

Society of Automotive Engineers
of China (SAE-China)
International Federation
of Automotive Engineering Societies (FISITA)
Editors

Proceedings of the FISITA 2012 World Automotive Congress

Volume 10: Chassis Systems
and Integration Technology



Lecture Notes in Electrical Engineering

Volume 198

For further volumes:
<http://www.springer.com/series/7818>

Society of Automotive Engineers of China
(SAE-China) · International Federation of
Automotive Engineering Societies (FISITA)
Editors

Proceedings of the FISITA 2012 World Automotive Congress

Volume 10: Chassis Systems
and Integration Technology



 Springer

The Springer logo, consisting of a stylized white chess knight piece on a black square, followed by the word "Springer" in a black serif font.

Editors
SAE-China
Beijing
People's Republic of China

FISITA
London
UK

ISSN 1876-1100
ISBN 978-3-642-33794-9
DOI 10.1007/978-3-642-33795-6
Springer Heidelberg New York Dordrecht London

ISSN 1876-1119 (electronic)
ISBN 978-3-642-33795-6 (eBook)

Library of Congress Control Number: 2012948289

© Springer-Verlag Berlin Heidelberg 2013

This work is subject to copyright. All rights are reserved by the Publisher, whether the whole or part of the material is concerned, specifically the rights of translation, reprinting, reuse of illustrations, recitation, broadcasting, reproduction on microfilms or in any other physical way, and transmission or information storage and retrieval, electronic adaptation, computer software, or by similar or dissimilar methodology now known or hereafter developed. Exempted from this legal reservation are brief excerpts in connection with reviews or scholarly analysis or material supplied specifically for the purpose of being entered and executed on a computer system, for exclusive use by the purchaser of the work. Duplication of this publication or parts thereof is permitted only under the provisions of the Copyright Law of the Publisher's location, in its current version, and permission for use must always be obtained from Springer. Permissions for use may be obtained through RightsLink at the Copyright Clearance Center. Violations are liable to prosecution under the respective Copyright Law.

The use of general descriptive names, registered names, trademarks, service marks, etc. in this publication does not imply, even in the absence of a specific statement, that such names are exempt from the relevant protective laws and regulations and therefore free for general use.

While the advice and information in this book are believed to be true and accurate at the date of publication, neither the authors nor the editors nor the publisher can accept any legal responsibility for any errors or omissions that may be made. The publisher makes no warranty, express or implied, with respect to the material contained herein.

Printed on acid-free paper

Springer is part of Springer Science+Business Media (www.springer.com)

Contents

Part I Chassis Structure and Design

Modular Unification as One of the Possible Directions of Innovations in the Automotive Industry	3
F2012-G01-003 Tagir Gadelshin	
Ford Motor Company’s New Rear Suspension Architecture for the Global CD Platform	9
F2012-G01-005 Paul Zandbergen and Alberto Girelli Consolaro	
On the Structural Simplification, Compact and Light Design of a Vehicle Suspension, Achieved by Using a Colloidal Cylinder with a Dual Function of Absorber and Compression-Spring	21
F2012-G01-006 Claudiu Valentin Suciu and Shuuichi Buma	
Fractured Reasons Analysis and Structure Optimization of a Light Truck Steering Bracket	33
F2012-G01-011 Xiang Wang, Xiongjie He, Weiwei Jia and Dongfang Xiao	
Optimization Design of Suspension Structure Based on Multi-Body Dynamic Analysis	43
F2012-G01-015 Fulu Sun, Junping Jiang, Wei Liu, Zhijie Pan and Fuquan Zhao	

Analysis and Optimization of Torque Variation in Steering Column Assembly	57
F2012-G01-016	
Guohui Yan	
Analysis of the Mechanism Kinematic Interference of a Heavy Articulated Dump Truck's Balanced Suspension System	69
F2012-G01-017	
Zhijun Guo, Bo Yang, Zhongli Li, Jingbo Wo and Keming Meng	
A Probabilistic Optimization Approach to Vehicle Suspension Design Under Uncertainty	81
F2012-G01-018	
Xiaokai Chen, Qinghai Zhao, Yi Lin and Kang Song	
Design and Simulation of a Novel Wedge Disc Brake	95
F2012-G01-019	
Junnian Wang, Nannan Yang, Zhe Wang, Yu Yang and Liang Chu	
Research and Application on Dynamic Stiffness of Leaf Spring	105
F2012-G01-020	
Zhanfu Zhou, Wanfu Guo, Tiejun Shen, Fengdong Wang, Jianhui Ju, Haiyan Wang and Enzhang Song	
Study and Simulation of Isolation Performance of Torsional Vibration of DMF-CS with Centrifugal Pendulu-Type Absorber	121
F2012-G01-021	
Wei Li, Tieshi Gao, Yongkui Cui, Wanfu Guo and Wenku Shi	
Part II Chassis Controls and Integration	
Model-Based Recursive Least Square Algorithm for Estimation of Brake Pressure and Road Friction	137
F2012-G02-002	
Nenggen Ding and Xiaofei Zhan	
Preview Ride Comfort Control for Electric Active Suspension	147
F2012-G02-005	
Haruhiko Sugai, Shuuichi Buma, Ryo Kanda, Kenshiro Yoshioka and Masaaki Hasegawa	

Slippage Equalization for Energy Loss Minimization in a Four-Wheel Drive Vehicle 163
 F2012-G02-021
 Osamu Nishihara and Yuki Yoneima

Multi-Objective Optimization and Multi-Attribute Decision of Mini-Van Chassis 173
 F2012-G02-023
 Xulong Jin, Min Qin, Yongfeng Jiang, Wenbin Wang and Chao Cheng

Part III Tire and Wheel Design/ Tire Properties and Modeling

Project Adtyre: Towards Dynamic Tyre Inflation Control 185
 F2012-G03-002
 Klaus Augsburg, Valentin Ivanov, Katja Kruchkova, Kristian Höpping, Sebastian Gramstat, Marijonas Bogdevicius and Peter Kiss

Structure Analysis and Ride Comfort of Vehicle on New Mechanical Elastic Tire 199
 F2012-G03-005
 Wei Wang, Youqun Zhao, Jian Wang and Liguozang

Part IV Vehicle Controls on Handling and Stability

Active Compensation of Friction in Electric Power Steering 213
 F2012-G04-002
 Tsutomu Tamura, Aris Maroonian and Robert Fuchs

Vehicle Lateral States Estimation Using Kalman-Bucy Filter 227
 F2012-G04-005
 Jin Zhao, Rongchen Zhao and Feng He

A Study on Steering Reactive Torque for Steer-by-Wire Vehicle Using Driving Simulator 237
 F2012-G04-006
 Motoaki Hibi, Tatsuro Kobune, Daisuke Miki, Yoshio Kano and Masato Abe

Active Camber Control 247
 F2012-G04-007
 Munehisa Horiguchi, Akira Mizuno, Michael Jones and Kayo Futamura

Research on the Torque Dynamic Distribution Algorithm of In-Wheel-Motor Electric Vehicle	257
F2012-G04-008	
Zhengyi He, Yang Ou and Jingming Yuan	
Electric Power Steering Systems: Market Requirements and Application Range with Special Focus on Column-EPS	267
F2012-G04-012	
Eberhard Kuebler, Mathias Eickhoff and Martin Budaker	
Part V Subjective and Objective Evaluation on Dynamic Performance	
Vehicle Ease of Control Evaluation via Stochastic Driver Model.	283
F2012-G05-003	
Yan Bai, Hsin Guan and Yuchen Chen	
Shift Quality Assessment and Optimization for Dual Clutch Transmission.	301
F2012-G05-004	
Yulong Lei, Huabing Zeng and Hongbo Liu	
Correlations Between Subjective and Objective Evaluations of On-Center Steering Feel	313
F2012-G05-008	
Xianglei Zhao, Hui Chen, Bolin Gao, Liming Lou and Nakano Shirou	
Using Chassis Tuning Technology in Chassis Design of Car	329
F2012-G05-010	
Xiang Meng, Wei Chen, Huihui Xue, Wei Liu, Zhijie Pan and Fuquan Zhao	
Research of the Correlation of Vehicle Handling Subjective Evaluation and K&C Characteristics	339
F2012-G05-011	
Yanding Yang, Yinghao Li, Zhi Yue, Chaobin Wang, Mengchun Chen, Jianxian Chen, Gan Chen and Jie Bai	

Part VI Dynamics Modeling, Simulation and Experimental Validation

Ride Comfort and Wheel Load Fluctuation Compatible Control Using Variable Stiffness and Damping 355
 F2012-G06-001
 Yanqing Liu, Jin Hozumi and Masaaki Tabata

Hybrid Steering of Wheeled Wheels 367
 F2012-G06-005
 Muhammad Adeel Awan, David Purdy and Amer Hameed

Integrated Development of Vehicle Dynamics Demonstrated on the New Bmw 3 Series 379
 F2012-G06-008
 Pavel Kvasnicka and Peter Dick

Torque Feedback Control for the Hand-Wheel Actuator of SBW Based on Active Disturbance Rejection Controller 391
 F2012-G06-009
 Guangzheng Gao, Hui Chen, Liming Lou and Shirou Nakano

Simulation and Modelling of Steering Ripple and Shudder 405
 F2012-G06-013
 Jinhuai Lin and Peter E. Pfeffer

Vehicle Longitudinal Velocity Estimation with Adaptive Kalman Filter 415
 F2012-G06-014
 Yunlong Gao, Yuan Feng and Lu Xiong

Advanced Cost Functions for Evaluation of Lateral Vehicle Dynamics 425
 F2012-G06-015
 Valentin Ivanov, Klaus Augsburg, Dzmitry Savitski, Jiri Plihal, Pavel Nedoma and Jaroslav Machan

Effect of Differential Modeling on Handling and Stability 441
 F2012-G06-019
 Rui Huang, Jun Zhan and Jungang Wu

Research on the Impact of Derived Vehicle's Weight Change on K&C and Vehicle Performance	449
F2012-G06-020	
Wuming Wu, Junping Jiang, Xiang Meng, Wei Liu, Zhijie Pan and Fuquan Zhao	
New Nonlinear Bushing Model for Ride Comfort and Handling Simulation: Focussing on Linearization and the Implementation into MBS Environment	461
F2012-G06-021	
Christian Scheiblegger, Jinhui Lin and Hannes Karrer	
Research on Variable Steer Ratio of Active Front Steering System with Fluctuating Velocity	475
F2012-G06-023	
Jun Wang, Zhenhai Gao and Fangming Lou	
Suspension Kinematic and Compliance Correlation: Test and Simulation	487
F2012-G06-030	
Da Xu, Bo Zhu, Shigen Hu, Zhonghui Zhang, Bingyong Wang, Wei Chen and Yanghui Xu	
Decrease in Dynamic Loading of Transmission Elements of the Vehicle	495
F2012-G06-031	
Alexandr Taratorkin, Viktor Derzhanskii and Igor Taratorkin	
A Study on Pitching Characteristics of the Passenger Car in Braking Process	505
F2012-G06-033	
Xuanfeng Wang, Guang Shi, Lingge Jin, Guozeng Ying and Hongwei Yang	
 Part VII Other	
Development of Cost Saing and Sloshing Noise Reductive Baffles of Fuel Tant Using Triz and Taguchi Engineering Method	525
F2012-G07-005	
YunSeok Kim, ChiWeon Jeong, MinSup Lee and JaeGon Yoo	

Part I
Chassis Structure and Design

Modular Unification as One of the Possible Directions of Innovations in the Automotive Industry

Tagir Gadelshin

Abstract The aim of this research is to find ways to reduce the cost of designing, manufacturing and maintenance of cars. The research was conducted at the level of automobile architecture. The architecture consists of modules. Unification is proposed to be made through choosing the equity and alignment of external parameters of the modules. The research of different automobile architectures showed the opportunity of applying of the module unification methods to reduce costs for designing, manufacturing and maintenance of vehicles. The way of such unification can be used for vehicles with internal combustion engines, hybrid engines and electric motors. Implementing the technology of modular unification can be performed on the basis of existing production systems and technologies. Therefore, introduction of this technology does not require large expenditures. Globalization and extensive collaboration in the world automotive industry requires a search for ways to improve the efficiency of these processes. Above all, the ratio of benefits from the vehicle usage to its cost would not decline. These problems can be solved through the use of modular unification. Meeting these challenges requires the collaboration in the community level of automotive manufacturers. First and foremost, this is a wide discussion of issues and making the decisions on organizational and legal arrangements.

Keywords Vehicle architecture • Modular unification • Globalization • Economic efficiency

F2012-G01-003

T. Gadelshin (✉)

Moscow State University of Mechanical Engineering (MAMI), Moscow, Russia
e-mail: t_gadelshin@mail.ru

The automobile is possibly the most mass manufactured sophisticated product among those made in mechanical engineering. More than 60 million of automobiles are produced every year. The automobiles consume the enormous material and human resources required for their production and during their life cycle. That is why we need to seek and find the methods of how to reduce the consumption of these resources. To solve this problem we propose the method of the modularization and unification while designing and manufacturing the automobiles.

The chapter considers one of the ways of production efficiency improvement and vehicle maintenance based on the sustainable use of general design principles of the car, regardless of the place and method of production.

Design and manufacturing of the vehicle are determined by its demand, the production ability and its usage. Each of these conditions specifies characteristics and parameters of the car.

One of the formalized methods of the vehicle representation is its architecture. It can have its own peculiarities for each type and class of the automobile. The method offered in this chapter applies some general features that can be allocated without reference to the particular vehicle architecture.

The architecture components of the automobile are its units. We will name them as modules. In vehicle design the modules are interconnected with nodes and the coupling. Selection of them in the architecture makes it possible to obtain the innovative direction in the automotive industry.

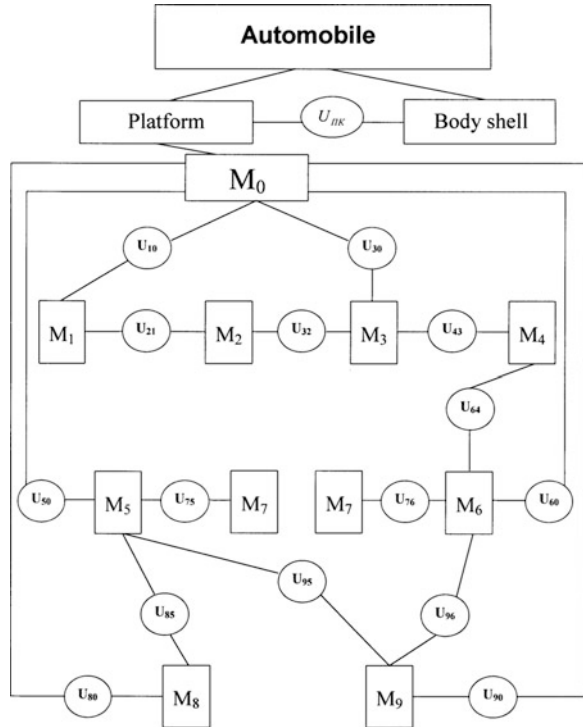
Research was performed at the level of the vehicle platform architecture. The method of unification by the set of platform modules external parameters, examined in the chapters [1, 2], was applied in this research.

Modularization is the decomposition of the whole product into its components—modules—without their destruction. The decomposition of the automobile into modules is naturally produced according to the standards accepted in automotive engineering. Platform and body shell are the two main components of any automobile. The platform module consists of functional modules. The basis of the platform is the frame module. The frame could be a separate module of the automobile. In this case the body module can be installed on the frame. The platform includes the engine module, the transmission module, the steering wheel module, and the brake system module. These modules are separate aggregates. The modules are connected together by joined and coupled units. This level of the platform modularization was chosen in our chapter to discuss the problem of the automobiles modular unification.

Every module could be described and identified by means of its parameters set. We divide the set of every module parameter into two subsets. The parameters determining the module joining with the rest of the platform modules are included in the first subset. We call these parameters as external ones. The other parameters are included into the second subset. These module parameters we call the internal ones. The external module parameters are essential to solve the problem of automobile structure modular unification.

Body shell is the main second module of the automobile. The versatility of the body shells gives us no possibility to decompose the body shells into unified

Fig. 1 The example of decomposition of the vehicle with FR layout (front-engine, rear-wheel drive layout) into separate modules and joining units of the modules



modules as we can do it with a platform. The platform requires more careful sophisticated technical service and maintenance than the body shell.

The modular architecture for division of the automobile is shown on Fig. 1. This is an example of the vehicle decomposition into body shell and platform.

This decomposition can be applied to the passenger vehicles, commercial vehicles, and buses having FR layout (front—engine, rear—wheel drive layout). The platform is divided into modules, which are unified according to the subset of the external parameters. Joined and coupled units are shown on Fig. 1 as circular figures. They are determined by the external parameters of the modules. These units are unified according to the subset of their external geometrical, technological, and functional parameters. The functional modules, shown on Fig. 1 as rectangles, are determined by internal parameters of modules. They may differ speaking about different models of automobiles and platforms of module manufacturers.

Modules: M_0 —frame module, M_1 —engine module, M_2 —clutch module, M_3 —gearbox module, M_4 —driving shaft module, M_5 —front axle module, M_6 —rear axle module, M_7 —wheel module, M_8 —steering wheel module, M_9 —braking system module.

The automotive platforms are much better adapted for modularization and unification in comparison with body shells of the automobiles. The platforms can

be almost completely decomposed into same unified, homogeneous modules. These decompositions are determined by external parameters of the platform modules. The unification of the platform could be implemented by means of choice of the platform modules equal external parameters of the same kind. We named it the unification method. This method is based on the unification according to the external parameters subset of the platform modules.

There is no doubt that the unification according to the subset of the platform external modules parameters can be done for the automobiles of the same type and class. The automobiles of various types and classes could be designed and manufactured on the same platform. The difference between such vehicles is determined by the characteristics of their body shells. Consequently such unification of the platform will broaden the types and classes of the vehicles which will have the platform unified according to that method.

The examples of unification can be found in automobiles as well. The passenger cars have four wheels. The road wheel disks parameters for tire mounting have got the unified standard range. The automotive tire industries produce various tires according to the accepted parameters. The other parameters, excluding standard parameters for road wheel rims, can vary depending on manufacturers. The octane numbers of the gasoline are unified too. The parameters of the engine compression ratio are unified according to those numbers. We can enlist more examples of such unification.

We will only mention some new possible directions of production and application development of the unified vehicles with standardized modules according to their external parameters.

Manufacturing of the automobiles with unified modules could give us possibility to gain certain advantages and benefits compared with nowadays situation.

The design and development of the automobiles can be simplified. The structures of the modules may fit to the structures of the automobiles being designed without their modules development. It will save time and reduce cost for their development.

The module production in automotive industry is a well known fact. Separate modules are produced on specialized plants manufacturing engines, transmission modules, steering system modules, braking system modules. The specialized production can be organized more economically and the products can have better quality than at automotive plants where all components are produced at one spot.

The usage of the unified functional modules could change the structure of the automotive plants. They could locate automotive production near their consumers. The unified modules for the platforms could be transported from the specialized manufacturing plants. These modules do not occupy much space and more easy to transport.

The replacement of the unified functional modules by the more advanced ones will broaden the possibility for the modernization of automobiles being used

nowadays. It could be one of the new directions of the activities referred to automobiles.

It is quite known that technical service and repair of the vehicles consume several times more resources compared with their production. The unification simplifies the assembly and disassembly of the structures if they consist of the unified functional modules. The unification enables production and usage of the unified tools and equipment for automobiles manufacture. It could also simplify the personnel training.

A lot of automobile manufacturers try to adapt their technical service facilities according to the automobiles of their own brands. But we should not forget that it will put limits to the automotive market of their automobiles in areas without the facilities for the repair and service of their vehicle brands.

At present we have got no unified standards for technical service and repair. The unification of the automotive structures could support the development and implementation of the new global standards for technical service and repair of the various companies automobiles and these standards will be obligatory for every automakers.

Modularization and unification could be useful for the production of the electric and hybrid vehicles. The manufacturing of these vehicles uses the modules of different industry branches. The modules must be unified.

The production of the automobiles and the business involved are becoming transnational. The automobiles influence politics in relations between countries. Modularization and unification in the automobile design and structures could be very helpful under modern level of the global motorization.

The problem of module technology realization involving the usage of the unified functional modules can be divided into technological, organizational, and legal problems. These problems should not be complicated from the technological point of view. The platform modules with different parameters of joined and coupled modules units are manufactured by makers of automotive platforms modules. The unification of the manufactured automotive designs is not a serious technological problem. Much more effort needs the solution of legal and organizational problems. Automakers of the world should find a compromise. The governments find agreements with difficulty. The numerous examples of profitable and beneficial cooperation between automakers are well known. The alliances of automakers are organized by automotive companies of various countries. The production of automobiles of various firms have been organized throughout the world. Versatile agreements and technological regulations are adopted and observed by automakers of various companies. The agreement on the modularization and unification while designing and manufacturing automobiles could be reached at the level of the automakers.

Conclusions

The external parameters of the platform modules are offered to be globalized. For example, the units connection of the wheel disks with tires are globalized.

Globalization is caused by the following objective reasons:

- Mass production of automobiles in different countries, irrespective of where the car company is situated;
- Collaboration in the design of vehicles between automotive firms;
- Production of modules on specialized enterprises and their usage in the automobile designing of different manufacturers;
- Selling and using of vehicles of the same producers throughout the world.

Through the use of module platform unification we could improve the economic efficiency of:

- Automobile designing;
- Automobile production;
- Servicing of automobiles and their utilization.

Using a modular unification of the platform does not limit the competition and business of car manufacturers.

References

1. Gadelshin TK, Gadelshin DT (2008) Parametrical unification of the vehicle design options during its construction and manufacturing. *Izvestia of Moscow State Technical University "MAMI"*, 1(5), Moscow, pp. 12–20
2. Gadelshin T, Gadelshin D (2010) Modularization and unification in the design and manufacture of automobiles. Book of abstracts, FISITA-2010, World Automotive Congress, 30 May–4 June, Budapest, Hungary, p. 405

Ford Motor Company's New Rear Suspension Architecture for the Global CD Platform

Paul Zandbergen and Alberto Girelli Consolaro

Abstract The objective was the development of a new suspension architecture for Ford's global CD platform. This suspension architecture was required to improve vehicle driving comfort and noise without compromising the high level of steering and handling performance of the Ford Mondeo to date. Moreover, the new suspension architecture had to fulfil a number of challenging package requirements. The newly developed rear suspension is an integral link suspension. This is an independent suspension system connecting a wheel carrier to an isolated subframe by means of a lower control arm, a camber link and a toe link. The wheel carrier is directly connected to the lower control arm via a pivot point and indirectly via an additional link, the integral link. This link decouples castor compliance from longitudinal compliance and prevents the need for a trailing link or control blade. The most important result is a substantial reduction of cruising interior noise. Impact harshness, noise and aftershake have significantly improved. The improvements in vehicle comfort have not affected the vehicle steering and handling performance. As a result, the new Ford Mondeo suits both relaxed and sporty driving styles.

Keywords Integral link suspension · Driving dynamics · Driving comfort · Suspension design principles

F2012-G01-005

P. Zandbergen (✉) · A. Girelli Consolaro
Ford Motor Company, Hamburg, Germany
e-mail: pzandber@ford.com

1 Introduction

Back in 1993 Ford introduced the so-called control blade SLA rear suspension on the Ford Mondeo wagon. Since then the concept migrated to many Ford applications like the Ford Focus, Kuga and Mondeo sedan. The steering and handling performance on these vehicles still proves the strength of the concept. However, to stay class leading for driving dynamics and comfort for all vehicles coming of the new global CD platform, Ford has felt the need to develop a concept that further improves the driving comfort, without degrading the steering and handling performance. The result is the so-called integral link suspension.

2 The New Integral Link Suspension

The new 2013 Mondeo builds on a new suspension architecture developed for the Ford global CD platform. The rear suspension system developed for this architecture is the so-called integral link suspension. The key components of this suspension system are indicated in Fig. 1 and the relevant suspension hardpoints are indicated in Fig. 2. The suspension comprises a lower control arm, which connects to a subframe in two pivot points. The rear pivot is a ball joint and the front pivot is a bushing. At the outer side, the lower control arm connects to a wheel carrier by means of a ball joint. This pivot point is positioned at a certain distance behind the wheel spin axis. The so-called integral link is positioned in front of the wheel spin axis. A lower pivot point connects the lower control arm to the integral link and a higher pivot point connects the integral link to the wheel carrier. Besides the lower control arm, two other links connect the wheel carrier to the subframe. The upper link is called the camber link and the lower link is called the toe link. The inner and outer pivot points of these links are all realized with bushings. The suspension further comprises a coil spring, a shock absorber and a stabilizer bar. The coil spring is supported by the lower control arm. The top of the spring connects to the vehicle body. The shock absorber is also supported by the lower control arm. It is located behind the wheel spin axis and outboard of the spring. On the top of the shock absorber an assist spring is mounted, which provides a progressive suspension rate. The subframe is isolated from the body by means of four rubber bushings.

3 Suspension System Requirements and System Targets

At the start of the design of the new suspension architecture, a number of requirements and targets were defined.

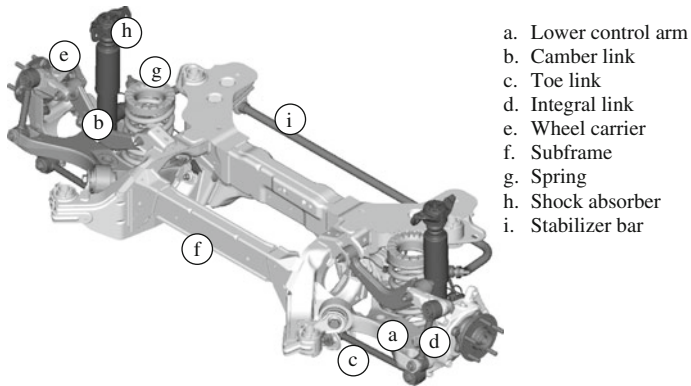


Fig. 1 The new Ford integral link suspension—components.

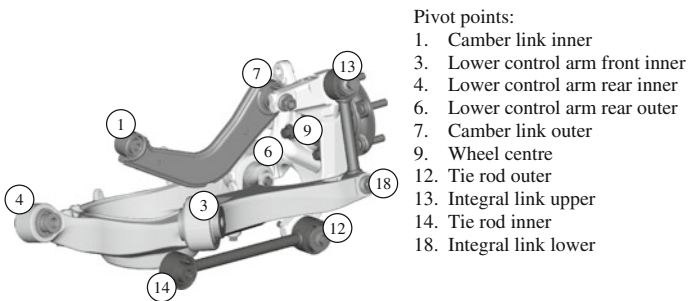


Fig. 2 The new Ford integral link suspension—definition of pivot points.

3.1 Requirements

The key requirements for the design of the new suspension are:

- Large wheel travel. This is important for ride comfort and road holding.
- A low underfloor and wide luggage compartment. This is especially important for the station wagon application and requires a package efficient suspension.
- All Wheel Drive (AWD) capability. This requires packaging space for a differential and drive shafts.
- Wheels and tyres ranging from 16" to 19" for sedan and wagon applications and from 17" to 21" for crossover vehicles.
- Exhaust routing under the suspension. This is important for optimal performance and efficient servicing capability.
- Improved driving comfort and reduced noise. The outstanding steering and handling performance of the Ford Mondeo to date is to be maintained.

3.2 System Targets

The key system targets related to driving comfort, steering and handling are discussed next.

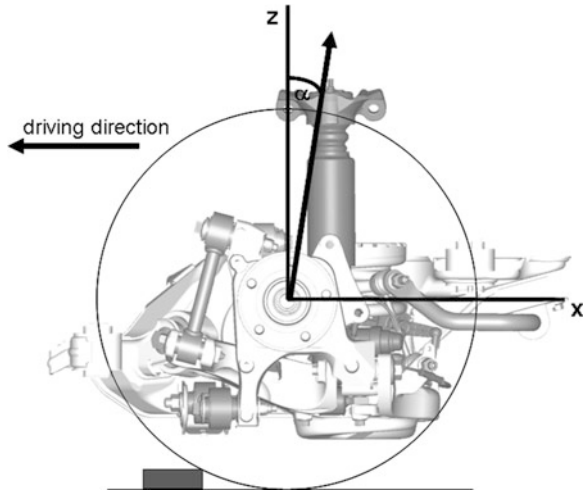
3.2.1 Driving Comfort

An important aspect of the vehicle driving comfort is the so-called impact harshness. Impacts due to road imperfection, e.g. expansion joints or tar strips, are to be absorbed in a smooth way. Related to impact harshness is the so-called aftershake, which is the remaining vehicle oscillation after the impact. This oscillation must be suppressed as quickly as possible via sufficient damping. During the course of this project multi-body CAE analysis was performed to simulate impacts. Accelerations in both X- and Z-direction were triggered at the driver seat rail. Via parameter studies the most important design parameters influencing the suspension impact harshness and aftershake were identified:

- Longitudinal mode frequency: this is determined by the dynamic stiffness of the suspension in longitudinal direction and the mass of components involved in the longitudinal motion. The dynamic stiffness is mainly determined by the dynamic rates of the suspension and subframe bushings. CAE studies have demonstrated that the impact harshness in X-direction is proportional to the longitudinal mode frequency: a lower longitudinal mode frequency results in better impact harshness. The lower limit for the mode frequency is driven by longitudinal mode frequencies of other relevant systems, e.g. the power train.
- Longitudinal damping: increasing the longitudinal damping in the suspension via the dynamic stiffness of the bushings would increase the longitudinal mode frequency, which as discussed above deteriorates the impact harshness. For a correct assessment of the effect of damping, the longitudinal frequency will have to stay constant via constant dynamic stiffness of the bushings. This can be achieved via a lower static stiffness of the bushings and increased damping. Increased longitudinal damping at constant longitudinal mode frequency demonstrates an improvement of the impact harshness and aftershake.
- Wheel trajectory angle: this is defined as the slope of the curve that plots the wheel centre vertical displacement versus the wheel centre longitudinal displacement. The angle is defined positive when the wheel moves rearwards during upward movement (Fig. 3). Several studies have demonstrated that the impact harshness deteriorates rapidly when the trajectory angle reduces below zero. A positive trajectory angle is beneficial for impact harshness up to a maximum of about 5 degrees. In this case, the wheel moves rearward and upward when it hits a bump.

The parameters listed above primarily influence the impact harshness and aftershake in X-direction. The characteristics of the shock absorbers, shock

Fig. 3 Wheel trajectory angle (α) beneficial for impact harshness



absorber mounts, springs and spring aids primarily determine the impact behaviour and aftershake in Z-direction. These parameters are considered as suspension tuning parameters rather than design parameters. One design parameter influencing the vertical dynamics is the unsprung mass. In general a lower unsprung mass is beneficial for ride comfort.

3.2.2 Steering and Handling

The steering and handling characteristics of a vehicle closely relate to the kinematics and compliance characteristics of the suspension. The suspension kinematics defines how the wheels translate or rotate during suspension vertical travel or suspension roll. For steering and handling the metric related to roll are of highest relevance. During cornering the vehicle body rolls and the resulting suspension travels should result in some level of understeer (roll steer). On a rear suspension, this is achieved via a certain amount of toe-in on at least the wheel on the outer side of the bend. On an independent suspension, the wheel on the outside of the bend usually loses camber angle with respect to the road. This so-called camber loss results in reduced grip. It is objected to minimize this camber loss via maximized suspension roll camber. Another important aspect of the vehicle roll behaviour is the roll axis, which is defined by the line connecting the suspension roll centres. The vehicle rolls with respect to the ground about this instantaneous axis [1].

The suspension compliance characteristics define how the suspension deflects when loads or moments are applied to the wheel. In general, lower suspension compliances are better for steering response and agility. A good steering that makes the driver feel connected to the road requires very low compliance in lateral direction. Crucial for low lateral compliance is low camber compliance. For

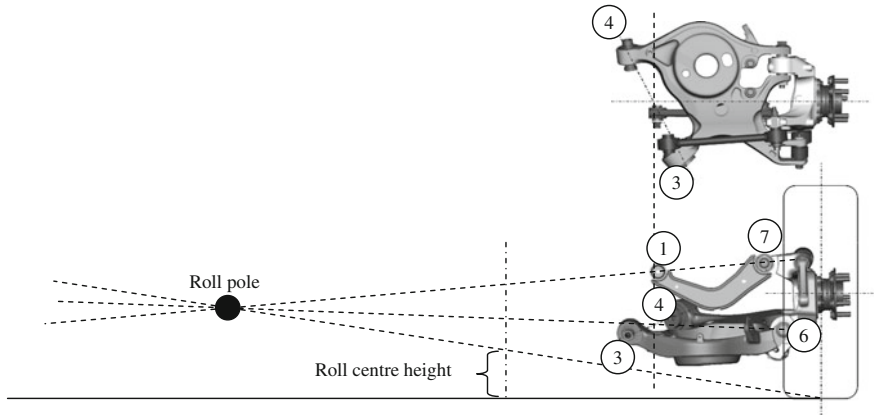


Fig. 4 Integral link roll pole and roll centre height

handling stability, the suspension ideally delivers a certain amount of compliance understeer during cornering and braking. This is defined by the lateral compliance steer and longitudinal compliance steer characteristics. During braking or other longitudinal wheel loading, e.g. impacts, the castor angle change should be minimal to prevent variations in bump steer, roll steer and mechanical trail. This is controlled via the castor compliance characteristic.

4 Suspension Design Principles

4.1 Roll Centre Height and Roll Camber

For a double wishbone suspension the roll centre can be constructed via a simplified, two dimensional approach known from the literature [2]. The same construction can be applied to the integral link suspension (Fig. 4). The roll pole is the intersection of lines drawn through the lower control arm and the camber link as projected on a vertical plane through the wheel centres. This is only a rough approximation, as in reality the toe link front view inclination will also effect the roll pole to some extent. A line connecting the centre of the tyre contact and the roll pole intersects the vehicle centre plane in the so-called roll centre. Besides the roll centre, the roll pole also determines the roll camber. Moving the roll pole inboard by more parallel front view inclination of the lower control arm and camber link, lowers both the roll centre and the roll camber.

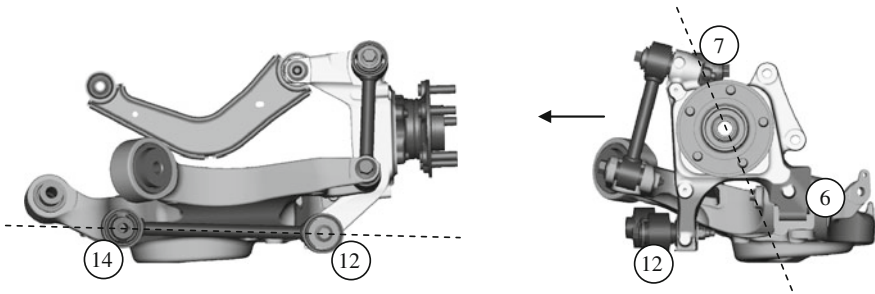


Fig. 5 Integral link front view (left) and side view (right)

4.2 Roll Steer

The roll steer of the integral link suspension is mainly dependent on the inclination of the toe link in the front view (Fig. 5 left). When the outer connection to the wheel carrier is raised, the roll steer gradient increases, which is a modification towards understeer. The wheel carrier steers about a virtual steer axis, which passes through point 7 and a point between point 6 and point 12 (Fig. 5 right). The location of this point depends on the stiffness of the pivot points 4 and 6 versus the stiffness of the pivot points 12 and 14. It is more biased towards point 6 as pivot point 4 and 6 are ball joints and the toe link pivot point 12 and 14 are bushings with some level of compliance.

4.3 Pitch Pole, Kinematic Recession and Anti-Properties

Figure 6 shows the bottom view of the integral link suspension. The line connecting point 3 and 4 and the line connecting point 6 and 18 are extended and the intersection point in this view is connected to the roll pole to form the suspension instantaneous axis. This is the axis about which the wheel rotates during suspension travel. The intersection point of the instantaneous axis and the plane through the wheel centre is named the pitch pole. As shown in the side view of the suspension (Fig. 7), the pitch pole is above the wheel centre. This provides kinematic recession during suspension jounce travel, anti-lift and anti-squat. The pitch centre is located far in front of the wheel centre, which results in relatively low bump castor. The pitch pole can be easily modified via the location of the lower control arm pivot points.

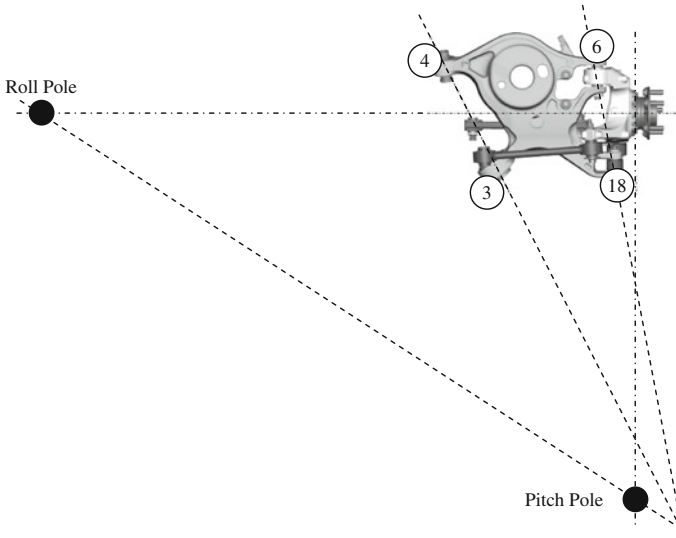


Fig. 6 Integral link instantaneous axis and pitch pole

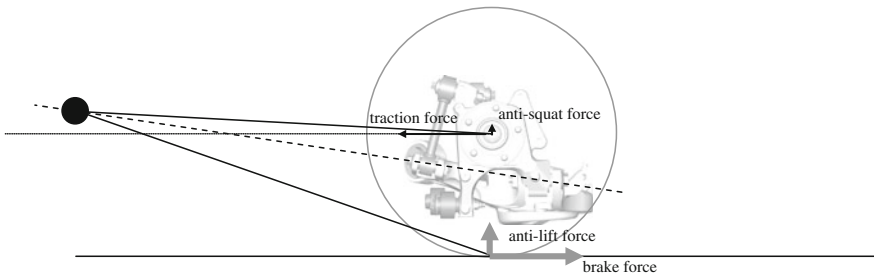


Fig. 7 Kinematic recession, anti-lift and anti-squat

4.4 Longitudinal Compliance Mechanism and Castor Compliance

As explained above, the integral link has a significant amount of longitudinal compliance in order to absorb road impacts smoothly. This compliance is mainly provided by the inner bushing of the lower control arm (3). When the wheel hits a bump, vertical and longitudinal forces are induced at the wheel centre. As a result of the longitudinal force, the lower control arm rotates around the rear pivot (4), which is a ball joint. The resulting translation in the bushing at the front of the lower arm is controlled by the stiffness of this bushing. The integral link connecting wheel carrier and lower control arm prevents rotation of the wheel carrier during impact or for example braking load. This reduces vibrations introduced to the suspension and prevents castor changes for wheel impacts or braking while driving in a corner. Such castor changes could cause instability due to varying roll

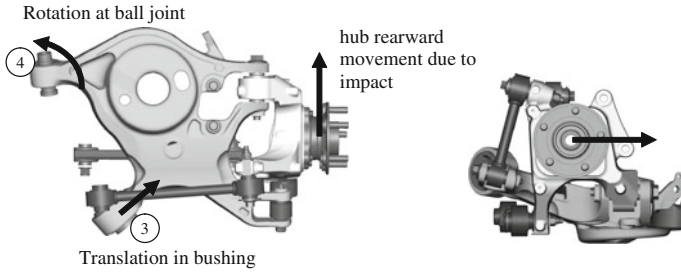


Fig. 8 Motion of lower control arm and hub during impact

steer and castor trail. When more longitudinal compliance is desired, the stiffness of the bushing in point 3 should be reduced. For a classical double wishbone suspension such a change would significantly reduce the castor stiffness. This is not the case for the integral link suspension because the castor load path is decoupled from the longitudinal load path via the integral link mechanism (Fig. 8)

5 Brake Pole

During braking, the lower control arm rotates as described for the longitudinal compliance mechanism. When the wheel would follow this arm rotation, the wheel would rotate to toe-out during braking, which is not desired. However, this rotation is restricted by the toe link. Depending on the bottom view angle of the toe link the wheel could even deflect to toe-in during braking. This is achieved via the mechanism displayed in Fig. 9. The line connecting point 4 and 6 and the line connecting point 12 and 14 are extended and the projected intersection in the bottom view is named the brake pole. This is the point about which the wheel rotates when a longitudinal load is applied. When the lines do not intersect, the pole is in infinity, resulting in zero longitudinal compliance steer (neutral brake steer). When the pole is outboard of the wheel centre line (as in Fig. 9), this gives toe-in under braking. Moving the pole towards the wheel centre line would increase toe-in. The lateral position of the pole can easily be adapted by the bottom view angle of the toe link. Brake forces are applied at the wheel contact patch and introduce a moment on the wheel carrier. This moment is transferred via the integral link to the lower control arm and the inner pivot points connecting the arm to the subframe. The rear pivot point is a ball joint and therefore very stiff. The front pivot point is a bushing responsible for the longitudinal compliance and therefore it is soft in the direction in plane with the lower control arm. To resist the moment induced by braking, the bushing must be stiff in the direction perpendicular to the lower control arm. To meet both requirements the bushing is voided in the soft direction.

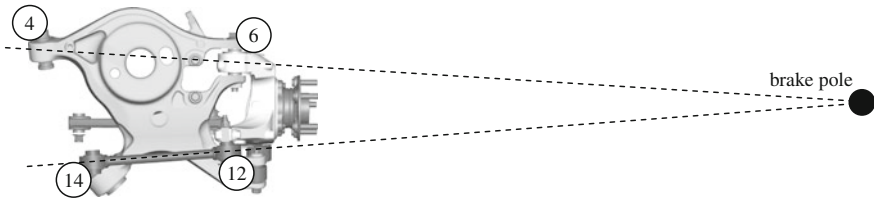


Fig. 9 Integral link brake pole

6 Results

The integral link suspension was assessed on the Ford proving grounds in a number of prototype vehicles. After initial subjective assessment of the built hardware, a tuning phase started in which springs, shock absorbers, link bushings, top mount bearings, etc. are varied following a systematic approach. The resulting improvements for impact harshness, aftershake and noise are demonstrated below. Despite clear improvements for comfort and noise, the steering and handling characteristics have not degraded over the control blade suspension in the Ford Mondeo to date. This was verified during several management drives and resulted to implementation of the integral link suspension for all applications built on the global CD platform.

6.1 Impact Harshness

Figure 10 shows the accelerations in X and Z, measured at the front seat rail versus time while driving over a strip of 30 mm height with a vehicle speed of 30 km/h. The highest peaks are obviously found at the point where the strip is passed by first the front wheels and then the rear wheels. The first cycle of body acceleration is the part of the signal reflecting the impact harshness (A). The remaining vehicle acceleration after the impact is the so-called aftershake (B). The vertical accelerations show very small differences between integral link and control blade. This is according expectations as the driven vehicle set-ups have very similar spring and shock absorber characteristics. In longitudinal direction the difference between the two suspensions becomes very clear. The integral link shows much lower accelerations during the rear suspension impact and also the aftershake accelerations are much lower. During the subjective evaluation it was clearly observed that for the integral link vehicle the rear impact was on a similar level as the front impact. For the control blade SLA vehicle the rear impact was much more pronouncing than the front impact. The observed difference between the two suspensions became even clearer for the rear passengers.

Fig. 10 Front seat longitudinal and vertical accelerations measured for control blade SLA and integral link suspension during impact

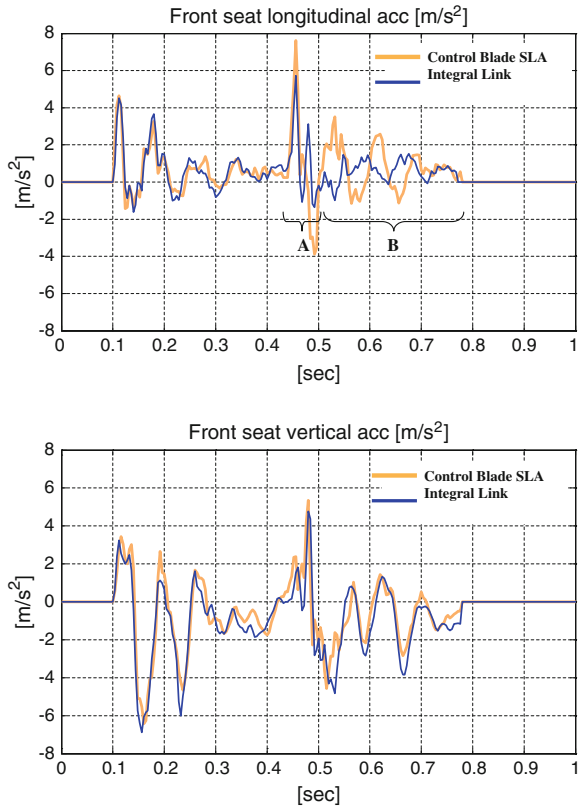
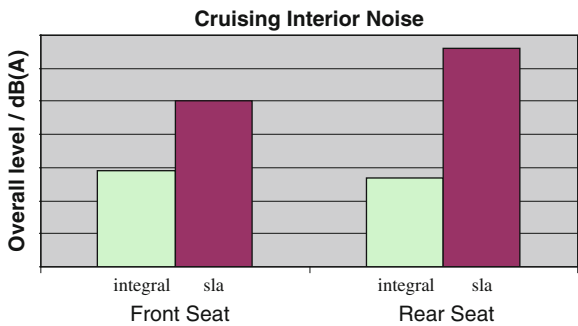


Fig. 11 Front and rear seat cruising interior noise measured on Lommel Proving Ground



6.2 Noise

The control blade SLA suspension on the Ford Mondeo to date has some known sources of vibrations that are transferred to the vehicle structure. The key contributor to noise is the flexible blade connecting the wheel carrier and the vehicle body. Taking away this blade via the new integral link concept does indeed take

away several vibration modes contributing to noise in the rumble range (80–200 Hz). The resulting cruising noise measured in the interior is shown in Fig. 11. On the front seat the integral link shows around 2 dB lower noise than the control blade SLA. On the rear seat the difference is even more pronouncing: 4 dB. During subjective evaluation this substantial reduction of noise was clearly experienced.

7 Conclusions

Ford has developed a new integral link suspension for the future global CD platform. The suspension was designed to meet a complex set of requirements related to vehicle package, driving comfort and driving dynamics. The new suspension layout significantly improves driving comfort and noise without compromising the strong steering and handling performance of the Ford Mondeo to date. As a result, the customer will benefit from a more relaxed driving experience.

References

1. Gillespie TD (1992) Fundamentals of vehicle dynamics. SAE, Warrendale
2. Reimpell J, Stoll H (1996) The automotive chassis: engineering principles. SAE, Warrendale

On the Structural Simplification, Compact and Light Design of a Vehicle Suspension, Achieved by Using a Colloidal Cylinder with a Dual Function of Absorber and Compression-Spring

Claudiu Valentin Suciu and Shuuichi Buma

Abstract Classical suspension (oil damper mounted in parallel with compression helical spring) is replaced by a colloidal suspension, in which case the spring can be omitted. Hence, structural simplification, accompanied by a compact and lighter design can be achieved. Oil is replaced by an ecological mixture of water and water-repellent nanoporous particles of silica (artificial sand). Travel tests using a V8 4.3L auto vehicle equipped with classical and colloidal suspensions were performed. Ride comfort (ISO 2631 method) was evaluated during travel (speed: 5–40 km/h) on a normal road with an asphalt step (height: 37 mm; width: 405 mm), for various values of the tire inflation pressure (150–250 kPa). On normal road without step the travel speed was increased up to 80 km/h. Acceleration at seat, seat-back, and feet surfaces was processed using the commercially available DEICY system for ride comfort evaluation. Spring omission, accompanied by 60 % reduction of the outer diameter, and 30 % reduction of the mass was achieved both for the frontal and rear colloidal suspensions. Results concerning the ride comfort were validated in the case of classical suspensions. Relationship between the travel speed of the vehicle and level of vibration perception was obtained for various values of the tire inflation pressure. Ride comfort decreased at augmentation of the travel speed and the tire inflation pressure. Since the colloidal spring constant was 6 times larger than the constant of the compression helical spring, colloidal suspension provided 1 rank lower ride comfort

F2012-G01-006

C. V. Suciu (✉)

Fukuoka Institute of Technology, Fukuoka, Japan

e-mail: suciu@fit.ac.jp

S. Buma

Toyota Motor Corporation, Toyota, Japan

e-mail: s@buma.tec.toyota.co.jp

than the classical suspension. Pitching and rolling movements were not considered during the estimation of the ride comfort. Relation between the lateral acceleration and the rolling attitude angle was experimentally determined. Ride comfort results were explained by taking into account the vehicle behaviour during frontal, rear and superimposed impact excitations, in correlation with the variation against travel speed of the frequency weighting proposed by the ISO 2631. Although the colloidal suspension was found to provide inferior ride comfort than the classical suspension, results obtained so far are encouraging since better performances are to be expected by softening the colloidal spring, and by redesigning the suspension including the stabilizers.

Keywords Ride comfort · Vehicle dynamics · Suspension · Colloidal cylinder · Absorber and spring

1 Introduction

Auto vehicle of the 21st century must be fabricated through ecological technologies and should be propelled by using “green” energies. Implicitly, future generations of hybrid and electrical auto vehicles are expected to employ improved suspension systems from various viewpoints, such as: development of environmental friendly working fluids to replace the oil; structural simplification of the conventional suspensions; compact and lighter design of suspension, etc. In this work, an oil-free absorber and spring is proposed to replace the conventional suspension. Since the annual reduction of oil consumption is estimated to be about 3,000 ton, only in Japan, such research subject occurs as appealing. Oil-free absorbers developed up-to-now, are using ecological fluids such as: air, water, solutions of water and glycerine, etc., but have various demerits such as: insufficient damping ability, structural complexity, etc. In this work, oil is replaced by a colloid, i.e., a mixture of water and water-repellent nanoporous particles of silica (artificial sand with controlled architecture), to obtain an ecological hydraulic absorber with high dissipative performances. In one particular design, colloid was encapsulated into elastic tanks, and such damping elements were introduced inside the cylinder of a conventional oil damper to obtain a hybrid absorber [1]. Aiming structural simplification and ecological benefits, in a different design, colloid was directly placed and sealed inside of the working cylinder [2–6]. In order to achieve an absorber suitable for vehicle suspensions, its life was extended by introducing the silica into a tank, separated from the main cylinder by a filter permeable [7, 8] or a diaphragm impermeable [9] to water. Although the conversion mechanism of mechanical energy was not fully understood, colloidal absorbers showed quite stable damping properties against temperature variation and surprisingly reduced

heating [10, 11]. In comparison with classical auto vehicle suspensions that employ for instance oil dampers mounted in parallel with compression springs, the latter providing for the necessary restoring force, in the case of a colloidal damper, since the liquid naturally exudes from the water-repellent silica matrix at decompression, the restoring force is intrinsically achieved, and the compression helical spring can be omitted [12]. In this way, structural simplification, accompanied by a compact and lighter design can be achieved. In this work, travel tests using a V8 4.3L auto vehicle equipped with classical and colloidal suspensions are performed. Ride comfort (ISO 2631 method [13]) is evaluated during travel (speed: 5–40 km/h) on a normal road with an asphalt step, for various values of the tire inflation pressure. On normal road without step the travel speed is increased up to 80 km/h. Results obtained are validated in the case of classical suspensions. Relationship between the travel speed of the vehicle and level of vibration perception is found for various values of the tire inflation pressure. Ride comfort results are explained by taking into account the vehicle behaviour during frontal, rear and superimposed impact excitations, in correlation with the variation against travel speed of the frequency weighting proposed by the ISO 2631. Methods to improve the ride comfort of vehicles equipped with colloidal suspensions are proposed.

2 Ride Comfort Evaluation

One traditional method to evaluate the ride comfort is to place the concerned vehicle over four expensive actuators and to excite it by using a complex controlling system able to simulate the real road conditions. Alternatively, in this work, tests of an auto vehicle travelling on normal road with an asphalt step are performed, and the equivalent (weighted composite) acceleration a_w is calculated as [13]:

$$a_w = \sqrt{\sum_i \left[W_c^2 \frac{16a_{xB}^2}{25} + W_d^2 \left(\frac{a_{yB}^2}{4} + \frac{4a_{zB}^2}{25} + a_{xS}^2 + a_{yS}^2 \right) + W_k^2 \left(a_{zS}^2 + \frac{a_{xF}^2 + a_{yF}^2}{16} + \frac{4a_{zF}^2}{25} \right) \right]_i}, \quad (1)$$

where $[W_c, W_d, W_k]$ are the frequency weightings or filters to be applied to acceleration data [13], and a is the acceleration in a Cartesian system of coordinates (subscripts x , y and z) measured at the feet surface (subscript F), at the seat surface (subscript S) and at the seat-back surface (subscript B), respectively. Concerning the human perception of vibration, for $a_w < 0.315$ the vibration is not uncomfortable, for $0.315 \leq a_w \leq 0.63$ the vibration is a little uncomfortable, for $0.5 \leq a_w \leq 1.0$ the vibration is fairly uncomfortable, for $0.8 \leq a_w \leq 1.6$ the vibration is uncomfortable, for $1.25 \leq a_w \leq 2.5$ the vibration is very

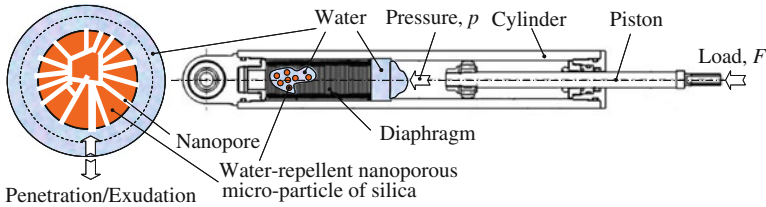


Fig. 1 Schematic view of the colloidal suspension (Specific design with colloid placed inside of a diaphragm)

uncomfortable, and for $a_w \geq 2$ the vibration is extremely uncomfortable. Thus, higher values of a_w mean worsened ride comfort.

3 Characteristics of the Evaluated Suspensions

Figure 1 illustrates a schematic view of the colloidal suspension, according to a specific design, in which the colloid is placed inside of a diaphragm. A nanoporous powder consisted of water-repellent silica micro-particles with diameters in the range of 10–70 μm and a mean particle diameter of 20 μm , was employed. After coating with alkyl chains (C_8H_{17}), properties of the nanoporous material were determined through nitrogen porosimetry, as follows: pore diameter range: 1–40 nm, mean pore diameter: 5 nm, specific pore surface: 440 m^2/g , specific pore volume: 0.55 cc/g and, bonding density of the grafted alkyl chains at the inner wall of the pore: 2 group/ nm^2 .

In this work, three types of suspensions are evaluated as follows: actual suspension consisted of oil damper mounted in parallel with compression helical spring, and proposed suspensions consisted of colloidal dampers with and without attached springs (Table 1). Outer diameter reduces from 135 to 55 mm (59 % reduction) and the mass reduces from 5.9 to 4.6 kg (22 % reduction) in the case of a frontal colloidal suspension without spring. Moreover, 120 g of oil are replaced by an ecological mixture of silica (8 g) and water (22 g). Similarly, the outer diameter reduces from 105 to 40 mm (62 % reduction) and the mass reduces from 2.8 to 1.9 kg (32 % reduction) in the case of a rear colloidal suspension without spring. Besides, 80 g of oil are replaced by 20 g of ecological colloid. Thus, structural simplification (spring omission) is accompanied by a compact and lighter design. Figure 2 presents the two degrees of freedom vibration model corresponding to a vehicle suspension consisted of an absorber mounted in parallel with a compression helical spring and Table 2 shows the associated mass elements, spring constants and damping coefficients. One takes $k_{CS} = 0$ for colloidal suspensions mounted without compression helical springs. Moreover, spring constant of the oil damper can be neglected ($k_{OD} \cong 0$). Table 3 illustrates variation of the tire spring constant versus the inflation pressure.

Table 1 Types of suspensions evaluated and their characteristics







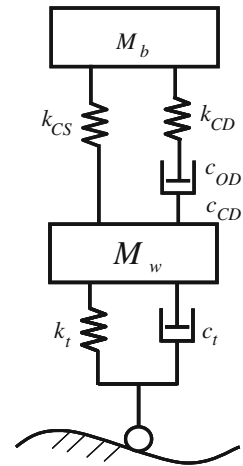
Type of suspension	Frontal suspension		Rear suspension	
	Photo, mass and outer diameter		Photo, mass and outer diameter	
Actual suspension	 Oil damper in parallel with spring	5.9 kg 135 mm	 Oil damper in parallel with spring	2.8 kg 105 mm
Proposed suspension	 Colloidal damper in parallel with spring	6.2 kg 135 mm	 Colloidal damper in parallel with spring	3.4 kg 105 mm
Proposed suspension	 Colloidal damper without spring	4.6 kg 55 mm	 Colloidal damper without spring	1.9 kg 40 mm

Table 2 Characteristics of the evaluated suspensions (Mass, spring constants and damping coefficients)

Parameter	Frontal suspension	Rear suspension
Body mass, M_b [kg]	240	240
Wheel mass, M_w [kg]	27	23
Constant of the compression helical spring, k_{CS} [N/mm]	21.6	18.6
Spring constant of the colloidal damper, k_{CD} [N/mm]	35	25
Damping coefficient of the oil damper, c_{OD} [Ns/m]	730	675
Damping coefficient of the colloidal damper, c_{CD} [Ns/m]	1,450	735
Damping coefficient of the tire, c_t [Ns/m]	81	81

Table 3 Variation of the tire spring constant versus the inflation pressure

Inflation pressure [kPa]	150	175	200	225	250
Tire spring constant, k_t [N/mm]	195	205	215	225	235

Fig. 2 Two degrees of freedom vibration model corresponding to the evaluated suspensions

4 Ride Comfort Evaluation from Impulse Tests of the Vehicle

Ride comfort was evaluated during travel tests on a normal road with a single semi-sinusoidal asphalt step of 37 mm height and 405 mm width. Travel speed was adjusted in the range of 5–40 km/h with an incremental step of 2.5 km/h by using a GPS speedometer. An impulse-like excitation was obtained when the vehicle passed the asphalt step at a certain speed, and the ride comfort was evaluated from the measured acceleration under the conditions specified by the ISO 2631 method [13]. Also the ride comfort was evaluated for halted vehicle, in which case the excitation was induced by the engine and air-conditioning system. Tire inflation pressure was adjusted in the range of 150–250 kPa with an

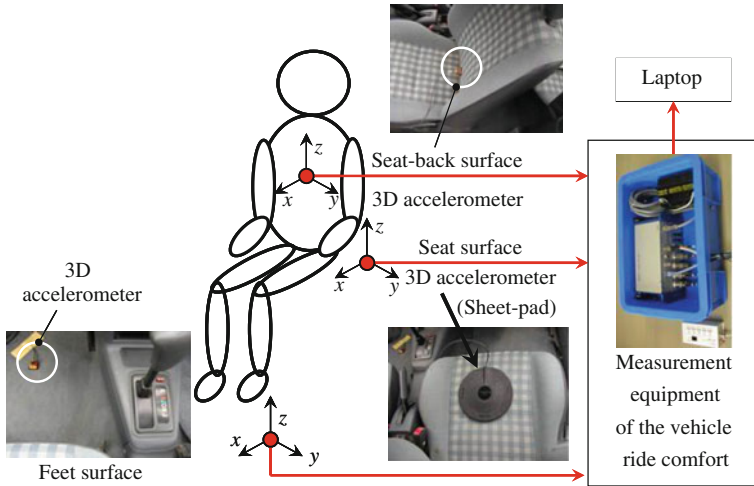


Fig. 3 Measurement equipment to evaluate the ride comfort

incremental step of 25 kPa (see Table 3). Figure 3 shows that during halt and travel tests, acceleration in the vertical, horizontal and lateral directions (z , x and y) was measured at 3 locations: seat, seat-back and feet surfaces. Recorded signal was automatically processed by using the commercially available DEICY system for ride comfort evaluation, which directly computed the equivalent acceleration a_w . As a limitation of this investigation, pitching and rolling movements were not considered during the estimation of the ride comfort.

5 Experimental Results and Discussions

Variation of the RMS equivalent acceleration versus the travel speed of a vehicle equipped at frontal and rear suspensions with oil dampers mounted in parallel with compression helical springs, for various values of the inflation pressure (150–250 kPa) is given in Fig. 4. One observes that the RMS equivalent acceleration increases, i.e., the ride comfort decreases at augmentation of the travel speed and the tire inflation pressure. This can be explained by the fact that, as the travel speed V increases, the excitation frequency $f = V/\lambda$ increases and becomes closer to suspension’s natural frequency f_n (here λ is the wavelength of the road roughness). Oppositely, the RMS equivalent acceleration decreases if travel speed exceeds the critical velocity ($V_n = \lambda f_n$). As expected, the vehicle’s ride comfort worsens at augmentation of the inflation pressure since the tire stiffness increases. In the right side of Fig. 4 one illustrates the corresponding domains for human perception of vibration. In this way, one finds the relationship between the travel speed and the level of vibration perception, for various values of the tire inflation pressure. Thus,

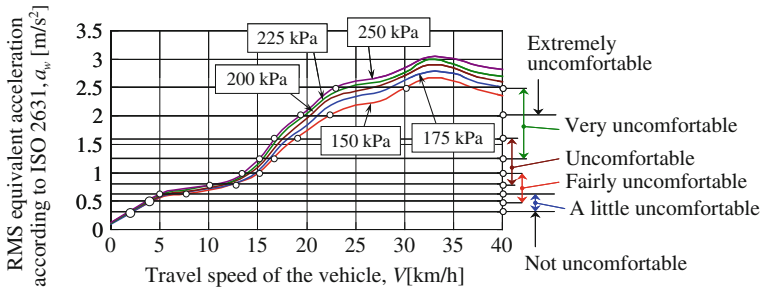
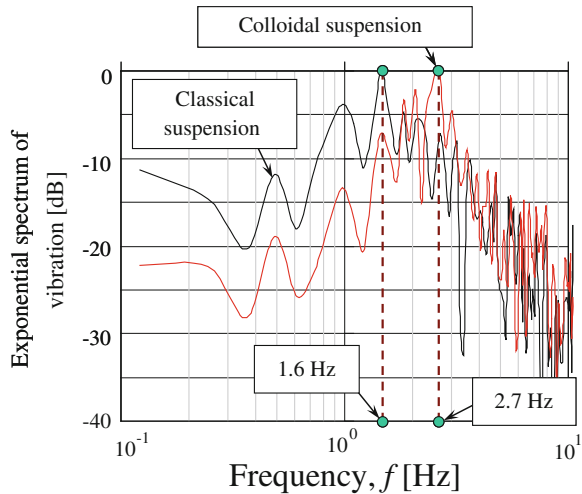


Fig. 4 Variation of the RMS equivalent acceleration versus the travel speed of a vehicle equipped at frontal and rear suspensions with classical suspensions, for various values of the tire inflation pressure

Fig. 5 Exponential spectrum of vibration obtained for a V8 4.3L auto vehicle travelling on a normal road without steps, at a velocity of 80 km/h



for $0 \leq V \leq 2$ km/h the vibration is not uncomfortable, for $2 \leq V \leq 4$ km/h the vibration is a little uncomfortable, for $V \leq 13-15$ km/h the vibration is fairly uncomfortable, and for $V \leq 23-30$ km/h the vibration is very uncomfortable, and at resonance, vibration is extremely uncomfortable. These reference results obtained for classical suspensions are necessary to validate the procedure proposed and to critically evaluate the performances of the novel colloidal suspensions.

Figure 5 shows the exponential spectrum of vibration, obtained through FFT transformation of the body acceleration under the DEICY system, for a V8 4.3L auto vehicle equipped with classical and colloidal suspensions, travelling on a normal road without steps at a velocity of 80 km/h. Actual suspension has a natural frequency of $f_n = 1.6\text{Hz}$ (Fig. 5), a helical spring constant of 36.1 N/mm and a damping coefficient of 1,120 Ns/m (oil damper). On the other hand, colloidal suspension without helical spring has a natural frequency of $f_n = 2.7\text{Hz}$ (Fig. 5), a colloidal spring constant of 213.2 N/mm and a damping coefficient of 1,742 Ns/m.

Table 4 Characteristics of the colloidal suspensions used for the of the V8 4.3L autovehicle

Cross-sectional area of the piston rod [mm ²]	201
Total volume of water [cc]	330
Total volume of silica powder inside the diaphragm [cc]	86.7
Spring constant of water [N/mm]	186.5
Spring constant of the colloid consisted of silica powder and water [N/mm]	35.1

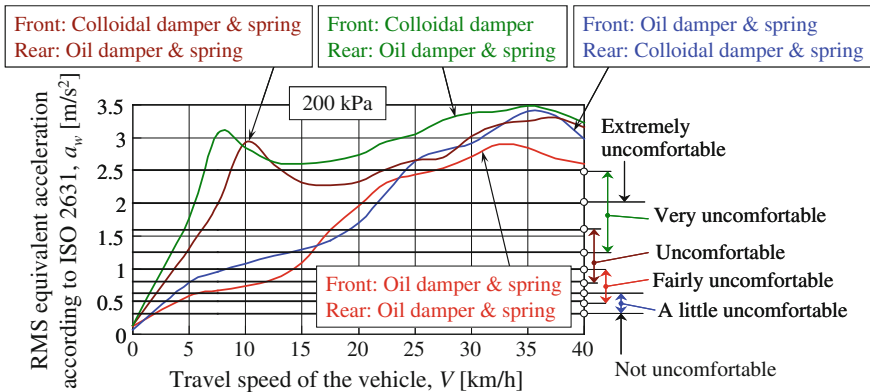


Fig. 6 Variation of the RMS equivalent acceleration versus the travel speed of a vehicle equipped with various types of frontal and rear suspensions, for a tire inflation pressure of 200 kPa

Details on the tested colloidal damper are given in Table 4. For ride comfort evaluation one calculates the equivalent accelerations as follows: $a_w = 0.38 \text{ m/s}^2$ for classical suspension, meaning a little uncomfortable, and $a_w = 0.77 \text{ m/s}^2$, for colloidal suspension, meaning fairly uncomfortable. Since the colloidal spring constant was 6 times larger than the helical spring constant, i.e., the colloidal suspension was too stiff, although the damping coefficient was higher, the damping ratio ($\zeta = \pi f_n c/k$) became 2.2 times lower. For this reason, the colloidal suspension was found to provide, according to the ISO 2631 method, 1 rank lower ride comfort.

In order to get a deeper understanding on the differences of behaviour between the classical and colloidal suspensions, for a tire inflation pressure of 200 kPa, one compares the variation of equivalent acceleration a_w versus travel speed, for the following four combinations (Fig. 6):

- (1) *Frontal suspension*: oil damper and spring; *Rear suspension*: oil damper and spring (red line in Fig. 6);
- (2) *Frontal suspension*: oil damper and spring; *Rear suspension*: colloidal damper and spring (blue line in Fig. 6);
- (3) *Frontal suspension*: colloidal damper and spring; *Rear suspension*: oil damper and spring (brown line in Fig. 6);
- and, (4) *Frontal suspension*: colloidal damper without spring; *Rear suspension*: oil damper and spring (green line in Fig. 6).

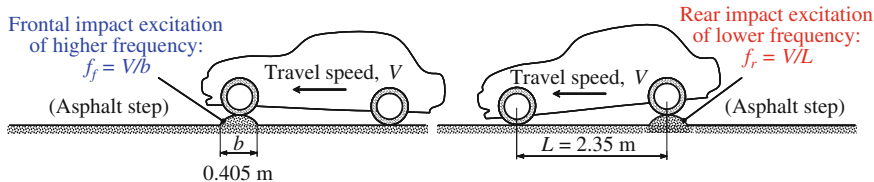
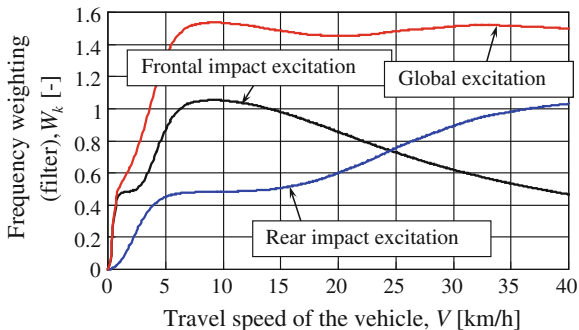


Fig. 7 Frontal impact excitation of higher frequency followed by the rear impact excitation of lower frequency of the tested auto vehicle

Fig. 8 Variation of the main filter W_k versus the travel speed of an auto vehicle subjected to frontal, rear and superposed (or global) impact excitations



As expected, the ride comfort worsens when colloidal suspensions are used, and this undesired effect is more prominent for frontal colloidal suspensions. When classical suspensions are used at the frontal wheels, on the graph of equivalent acceleration versus the travel speed, a single peak can be seen in the higher speeds region. Oppositely, for colloidal suspensions at the frontal wheels, two different peaks can be observed, one for lower speeds and the other in the region of higher speeds (Fig. 6). In order to explain these results, one considers the vehicle behaviour during frontal and rear impact excitations (Fig. 7), in correlation with variation versus the travel speed of the main filter W_k used by the ISO 2631 method for the ride comfort evaluation (Fig. 8).

Thus, during travel tests, firstly the frontal suspension receive an impact from the asphalt step, this producing an impulse-like excitation of higher frequency $f_f = V/b$, where b is the width of the step (Fig. 7). Then, the rear suspension receive an impact from the asphalt step, this producing an impulse-like excitation of lower frequency $f_r = V/L$, where L is the distance between the frontal and rear wheels (Fig. 7). Complementarily, Fig. 8 shows variation of the filter W_k versus the travel speed, obtained for the frontal impact excitation, rear impact excitation, and the superposed or global excitation, respectively. Comparison of Figs. 6 and 8 reveals that: for combinations (1) and (2) with frontal classical suspensions, mainly the rear impact excitation is responsible for the recorded response; for combinations (3) and (4) with frontal colloidal suspensions, a global superposed frontal-rear impact excitation is responsible for the recorded response.

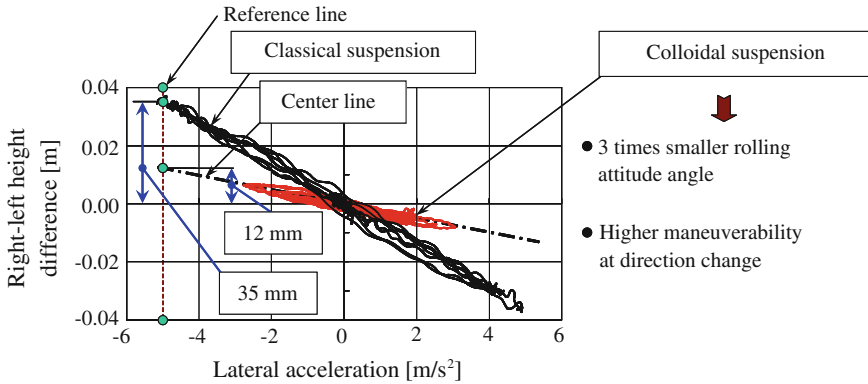


Fig. 9 Variation of the right–left height difference versus the lateral acceleration during the lane change test

In other words, while the vehicle body still vibrates due to the frontal impact, it receives a second rear impact, this producing a superposition of effects.

Figure 9 illustrates variation of the right-left difference versus the lateral acceleration during the lane change test of the V8 4.3L auto vehicle equipped with classical and colloidal suspensions. At the reference lateral acceleration of $\pm 5 \text{ m/s}^2$ the rolling attitude angle of the colloidal suspension (height difference: 12 mm) was about three times smaller than that corresponding to actual suspension (height difference: 35 mm). Thus, vehicle stability at lane change was improved due to the higher colloidal spring constant, this meaning increased degree of maneuverability at direction change.

6 Conclusions

In this work, a relatively inexpensive method was proposed to evaluate the ride comfort of a V8 4.3L auto vehicle equipped with classical and colloidal suspensions, during travel (speed: 5–40 km/h) on a normal road with an asphalt step, for various values of the tire inflation pressure. On normal road without steps the travel speed was increased up to 80 km/h. Due to the compression helical spring omission, 60 % reduction of the outer diameter, and 30 % reduction of the mass was achieved for the colloidal suspensions. Results concerning the ride comfort were validated in the case of classical suspensions. Ride comfort decreased at augmentation of the travel speed and the tire inflation pressure. Since the colloidal spring constant was considerably larger than the constant of the compression helical spring, colloidal suspension provided 1 rank lower ride comfort than the classical suspension, but the vehicle stability at lane change was improved (3 times smaller rolling attitude angle, i.e., higher degree of maneuverability at direction change). Ride comfort results were explained by the reduction of the damping ratio

under too stiff colloidal suspensions, and by taking into account the vehicle behaviour during frontal, rear and global (or superimposed) impact excitations, in correlation with the variation against travel speed of the filters proposed by ISO 2631. Although the colloidal suspension was found to provide inferior ride comfort than the classical suspension, results obtained so far are encouraging since better performances are to be expected by softening the colloidal spring, and by re-designing the suspension including the stabilizers. Results obtained are in agreement with the well known fact that the suspension design is always based on a trade-off between the vehicle's ride comfort and its maneuverability.

References

1. Eroshenko VA, Piatiletov I, Coiffard L, Stoudenets V (2007) A new paradigm of mechanical energy dissipation: experimental investigation and effectiveness of a novel car damper. *Automobile Eng* 221:301–312
2. Suciu CV, Iwatsubo T, Deki S (2003) Investigation of a colloidal damper. *Colloid Interface Sci* 259:62–80
3. Suciu CV, Iwatsubo T, Deki S (2004) Novel principle of mechanical energy dissipation. part 1: static performances of colloidal damper. *JSME Int C47*:180–188
4. Suciu CV, Iwatsubo T (2004) Novel principle of mechanical energy dissipation. part 2: dynamic performances of colloidal damper. *JSME Int C47*:189–198
5. Iwatsubo T, Suciu CV, Ikenaga M, Yaguchi K (2007) Dynamic characteristics of a new damping element based on surface extension principle in nanoporous. *Sound Vib* 308:579–590
6. Iwatsubo T, Washio K, Yano H, Miyazaki M (2008) Experimental study of a colloidal damper to practical application. *Sys Des Dyn* 2:1160–1169
7. Suciu CV, Yaguchi K (2009) Endurance tests on a colloidal damper destined to vehicle suspension. *Exp Mech* 49:383–393
8. Suciu CV, Tani S, Yaguchi K (2010) On the fatigue fracture at adsorption/desorption of water in/from liquid-repellent nanoporous silica. *Acta Mech* 214:195–203
9. Buma S. Investigation on the Possibility of Employing as Vehicle Suspension a Colloidal Cylinder, which Puts the Surface Tension to Practical Use [J]. *Trans JSAE*, 2012, 43, pp. 723–728 (in Japanese)
10. Suciu CV, Tani S, Miyoshi K (2010) experimental study on the thermal characteristics of a colloidal damper. *Trans JSME C76*: 1043–1049 (in Japanese). [J]. *System Design and Dynamics*, 2010, 4: 899–913
11. Suciu CV, Kimura Y (2012) Experimental study on the forced heating and natural cooling of a colloidal damper. *Trans JSME C78*: 1338–1351 (in Japanese)
12. Suciu CV, Tobiishi T (2010) Comfortableness evaluation of an auto vehicle equipped with colloidal suspensions. *Trans JSME C78*: 1378–1387 (in Japanese)
13. ISO 2631 (1997) Mechanical vibration and shock: evaluation of human exposure to whole-body vibration. Paris: International Organization for Standardization

Fractured Reasons Analysis and Structure Optimization of a Light Truck Steering Bracket

Xiang Wang, Xiongjie He, Weiwei Jia and Dongfang Xiao

Abstract In this paper, combination of a light truck's market issues, use HyperWorks software to do the finite element analysis of the fractured bracket, and improve the structure by topology optimization, optimized bracket compared with fractured bracket, obviously reduction of the maximum stress, and lighten the weight. Experimental verification of the final optimized stands by the reliability, indicating that the structure of CAE-based analysis and topology optimization, can provide the means for product failure analysis, find the optimal solution for product design, and is a also very important way for vehicle lightweight.

Keywords Steering bracket · Topology optimization · Experimental verification · CAE

1 Introduction

Steering bracket of a light truck bulk fracture appears on the market, this paper is to find fractured reasons of the steering bracket by finite element analysis, and the using of topology optimization software optimized the structure of the bracket, and finally through the bench test to verify the reliability of optimized bracket.

F2010-G01-011

X. Wang (✉) · X. He · W. Jia
Anhui Jianghuai Automobile Technology Center, Anhui, China
e-mail: kj_jszx@jac.com.cn

D. Xiao
Dongfeng Investment Casting Co., Ltd, Whuan, China

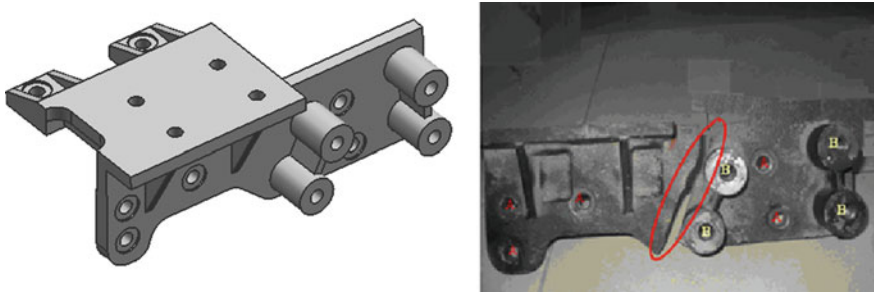


Fig. 1 3D & Fractured location of the steering bracket

Table 1 Bracket metallographic test data

Spheroidization grade	Matrix	Pearlite	Carbide
Grade 4	Ferrite	<10 %	<1 %
Eligibility	yes		

2 Steering Bracket Fractured Analysis

The bracket of the original assembly of the steering mechanical steering, the market did not appear fracture problems, the latter in order to improve the steering lightly, mechanical steering replaced the power steering, the steering bracket untouched steering maximum output torque of the original 960 N·m becomes 1,920 N·m. Replacement vehicle is sold an average of six months, travelling 10,000 km, finding bulk fracture, the fractured bracket are shown in Fig. 1.

The fractured bracket as a whole casting, its material is ductile iron QT450, and has done fractured market sample metallographic analysis, the results shown in Table 1.

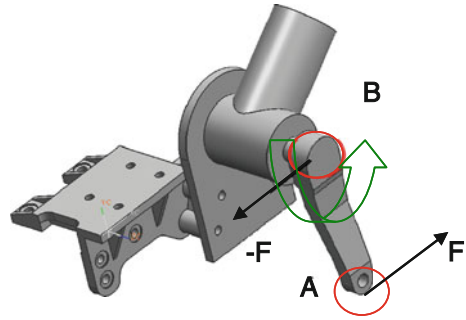
Bracket, according to test results, compliance with technical requirements, eliminate the problem of production quality, needs to do the structure stress analysis.

3 Finite Element Analysis of the Steering Bracket

3.1 Model Established

Steering bracket between the steering gear and the frame is connected to the outside through four threaded holes, fixed the steering inside with five through-hole and the frame bolted connections, installed above the cab tilting bracket, steering bracket is mainly affected by the steering gravity, the cab gravity and the

Fig. 2 Steering fixed structure sketch



reaction of the steering gear output torque, the steering gear gravity relative output torque can be neglected, the specific structure of the steering fixed structure in Fig. 2.

Point A as a springboard for the force size for steering the maximum output torque/rocker arm center point length = $1,920 \text{ (N/m)}/196 \text{ (mm)} \times 1,000 = 9,827 \text{ N}$, a condition known as the steering gear output shaft of torque through the rocker arm to pass along the F direction at point A force of 9,827 N, the rocker arm and redirector as a whole, the force of the reaction force acting on the steering gear output shaft is 9,827 N, direction, and F is the opposite. Take the steering gear output shaft and rocker arm intersects the center of the load to B, the force along the -F direction, the four fixed during the simulation will point B with the steering bracket holes rigid link (RBE2).

The cab of the force exerted on the steering on the installation according to the cab, steering gear on the plane four mounting holes with the cab connected to the center of mass, and apply 1/4 cab concentration.

Altair's HyperWorks finite element software to establish the finite element model (Fig. 3), the steering bracket model grid is divided into a higher order tetrahedral element 90,318,17 rigid elements, 393,361 nodes.

3.2 Result and Analysis

Of cracking scaffold model to calculate the apparent position of bracket cracking in the results of the analysis, we focus on the bracket cracking at stress contours and maximum. Stress cloud (Fig. 4) shows the crack at the maximum stress value 189.4 Mpa, the value of this stress and did not consider the impact loading conditions, and material fatigue notch limit is 210 MPa closer to the low safety factor in the long run withstand the steering force case, inevitably produce a fatigue fracture.

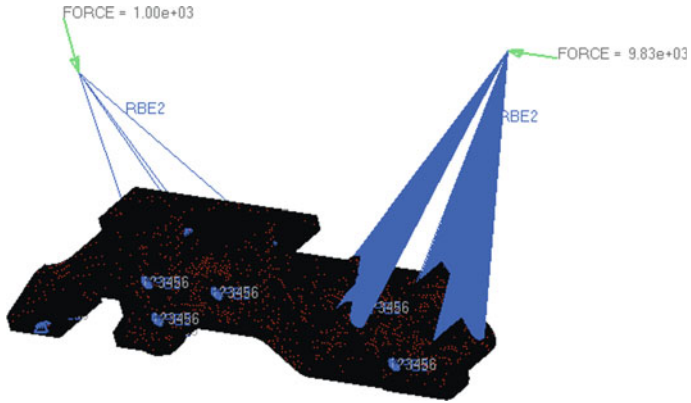


Fig. 3 Steering bracket finite element analysis model

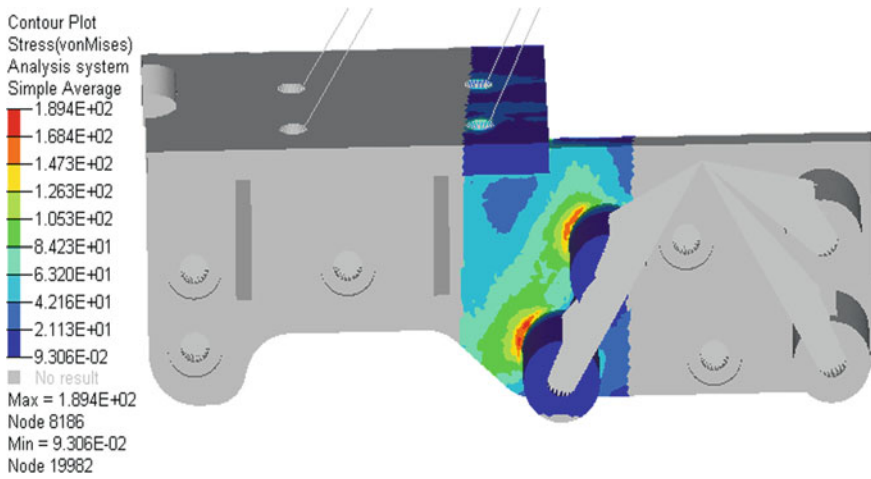


Fig. 4 Steering bracket cracking location of stress cloud

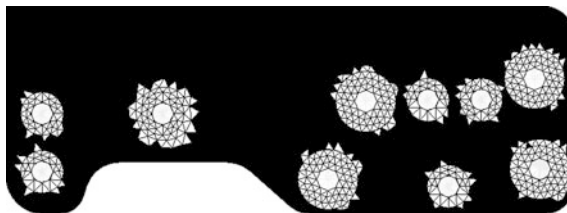


Fig. 5 Optimized regional settings (*black: optimized area*)

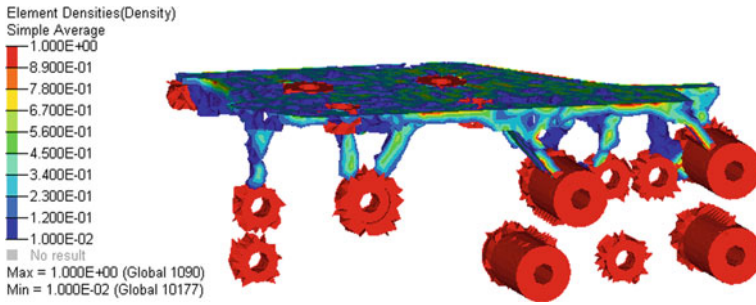


Fig. 6 Material optimization diagram (threshold of 0.12)

4 Topology Optimization of the Bracket Structure

Based on the above analysis, we can see now that the bracket cracking position's stress is too big, strength can not meet the actual power steering needs, must to optimize the structure.

4.1 Optimization Model Established

Use the topology optimization module of the HyperWorks to OptiStruct bracket, topology optimization goal is to find the best material of the support structure distribution program to get the structure of the optimal shape. Load or support based on the known constraints, solve the problem of the distribution of the material, so that the stiffness of the structure to achieve maximum output displacement, stress, etc. to achieve the requirements [1]. The topology optimization is divided into three steps: (1) as defined in the optimization of regional (2) define the optimal parameters (3) to optimize the calculation. Defined optimization parameter contains the definition of constraints, the objective function convergence tolerance, the Altair company's Optistruct module will set the density of the unit design variables, cell density in the 0 to a continuous change in 0 and 1 representing the Air or solid intermediate value represents the imaginary the material density [2].

Set the optimization of regional support structure (Fig. 5), non-optimized area for the bracket holes and steering fixed countersink hole area, less than the material fatigue notch stress value is set to optimize the constraints, the minimum quality as the optimization objective optimization The results shown in Fig. 6.

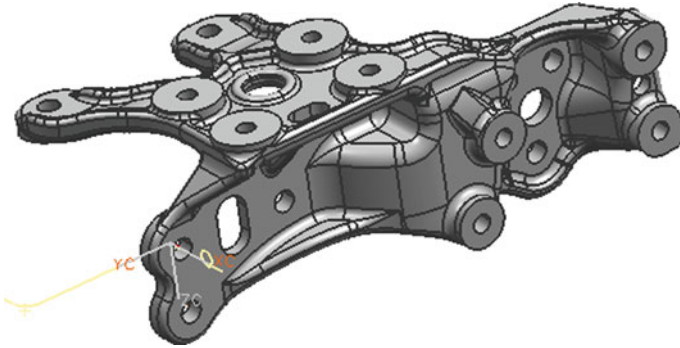


Fig. 7 The optimized final steering bracket model

4.2 Structure Refinement

The use of topology optimization to find the best distribution of the material, in conjunction with shape optimization, size optimization for details of the optimization, the use of HyperMorph tool to change the model grid shape. Morphing process to create and modify Domains (domain) and the Handles (handles), the model is divided into multiple domains. The shape of these domains is controlled by the handles, by moving the handle, you can change the shape of the domain, such as borders, chamfering, curvature, and the domain node location [2]. Optimization, we must also consider bracket manufacturing constraints for castings, to increase the draw direction and the maximum/minimum size constraints in the optimization process, the specific set of parameters with existing foundry mold and determine the level. Optimize the results using the HyperMesh OSSmooth tools converted to IGES surface format [3], the second design of the optimized geometry, import CAD software to finalize the steering bracket, the optimized structure of solid model shown in Fig. 7.

5 The Finite Element Optimized Analysis of Bracket

Optimized bracket to re-establish the finite element model to analyze its strength, and verify that optimize bracket performance advantages and disadvantages. Fracture bracket or brackets improve the analysis process, the optimization of the boundary conditions of the bracket, the force load, calculate the stress magnitude can be seen from Fig. 8, brackets in the crack at the maximum stress 142.4 Mpa bracket close to, and improvement than cracking bracket stress is reduced 47 Mpa, reduce the weight of 2.9 kg, the specific Table 2.

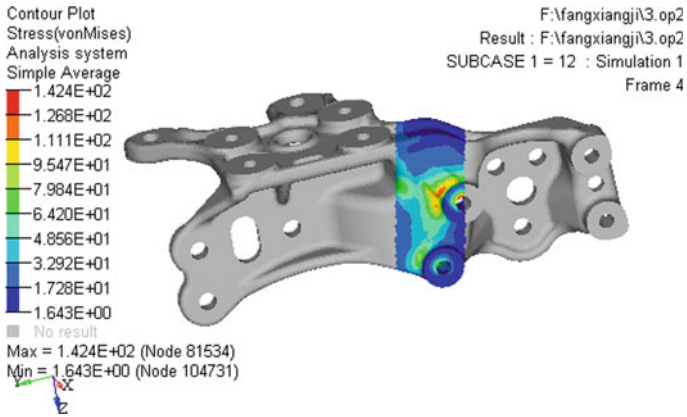


Fig. 8 Optimized bracket stress cloud

Table 2 Contrast between the optimized bracket and the original

	The maximum stress of cracking position/(MPa)	Weight/(kg)
Cracking bracket	189.4	7.6
Optimized bracket	142.4	4.7

Fig. 9 The fatigue life test bench



6 Bracket Fatigue Life Experiments

6.1 Experimental Test Program

Four-channel electro-hydraulic servo component fatigue testing system (Model PLS-L50B4, Fig. 9) to optimize bracket fatigue life experiments, steering the

Table 3 Bracket fatigue life test simulation conditions table

Case1: torque force point perpendicular to the direction install the geometric center line of the face, the torque size $-2,000$ to $2,000$ N·m (the output of the steering torque $1,920$ N·m), the frequency of 0.25 Hz,sine wave loading, until the product breaks or the number of cycles up to $50,000$ times.

Case 2: front suspension under the load point force perpendicular to the hanging bracket mounting face of the geometric center of the load size as $-3,000$ to $3,000$ N, frequency of 2.5 Hz sine wave load test until fracture or number of cycles to reach 20 million times, such as $200,000$ times without failure phenomenon, with the torque load to continue to do until the product fracture failure or the end of time (144 h).

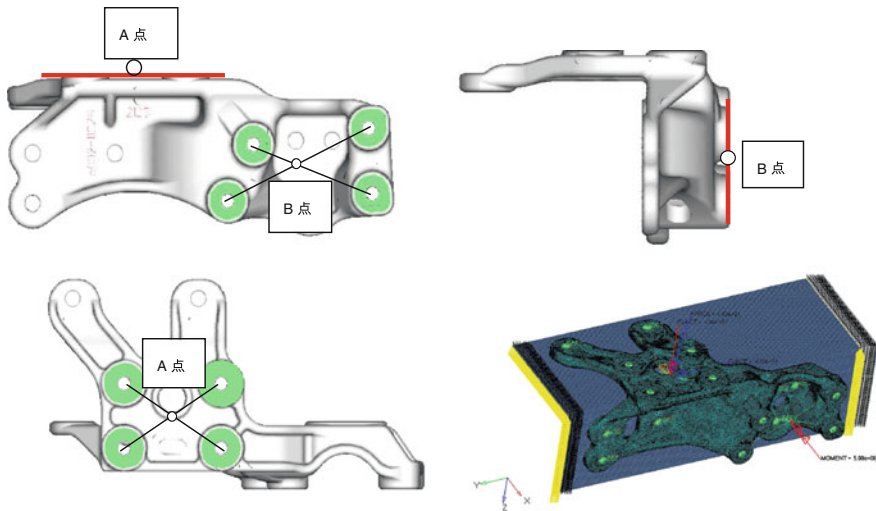


Fig. 10 Experimental loads and constraints

actual working environment to simulate the bracket at the same time impose two fatigue conditions (Table 3).

Specific of the applied loads and constraints, shown in Fig. 10.

6.2 Experimental Results

Under the test program, after the simulated condition $150,000$ times and conditions of up to $200,000$ times, the bracket has not permanent deformation, breakage or cracking (Fig. 11), optimize the bracket through the experimental technique requirements, see Table 4.



Fig. 11 Sample photos after experiment

Table 4 Experimental results

Experimental items	Technical requirements	Sample	Experimental results
Fatigue life	At the same time load simulation Case 1 and Case 2	Optimized bracket	Torque load reaches 50,000 (front suspension load up to 200,000 times then continue), the samples not result in fracture failure.

7 Conclusions

The above statement of the topology optimization based on the HyperWorks, testifies that the steering bracket optimization results significantly, optimized bracket cracking stress significantly reduced and weight mitigated, to meet the performance requirements. In addition we can see through this example, the topology optimization method, more accurate calculation in a given work situation and the given design space, a reasonable spatial distribution of the material, use this method to optimize the structure of the chassis, such as suspension parts, etc., can ensure strength of the part, at the same time greatly reducing the weight [4, 5]. CAE analysis with optimization methods and experimental validation, can enhance the designer's component design capabilities, verify that the feasibility of the optimized structure.

References

1. Ma Xun (2008) Finite element analysis and topology optimization of steering bracket structure design. *Trans ShenYang Industry University* 30(3): 313–317
2. Zhng S (2007) *Based on hyperworks structure optimization design technology*. China Machine Press, Beijing
3. Altair HyperWorks 10.0 Help[CP/OL],2009. <http://www.altair.com.cn>
4. Qu Y, Xu Y, Zhang L (2007) Application of topology optimization to automotive structure design. *Altair 2007 China disquisitions*
5. Ma Y, Kang L (2009) Design of engine fixed bracket based on topology optimization. *Proseminar of application and theory about structure and multi-subjects*. Dalian, China (9)

Optimization Design of Suspension Structure Based on Multi-Body Dynamic Analysis

Fulu Sun, Junping Jiang, Wei Liu, Zhijie Pan and Fuquan Zhao

Abstract Operation stability of vehicles is directly impacted by suspension K&C. Multi-body dynamic CAE analysis and suspension K&C design are two tools for suspension design, which are fundamental both in theory and test. Test and simulation analysis will be conducted to a benchmarking vehicle in the development of a sedan. Geely has established its chassis lab, which is equipped with K&C test equipment, operation stability performance test equipment, and owns subjective appraisers. Testing data can be accumulated by suspension K&C and vehicle operation stability and riding comfort test on competing vehicles and developing vehicles. Through analysis of the test data, a performance comparison of different suspension structures, i.e. McPherson strut, torsion beam, and multi-link, thus suspension structures appropriate for different vehicles of Geely's platforms are determined. In addition, optimization analysis is conducted to suspension structure and vehicle performance with ADAMS/CAR and CARSIM software to confirm the vehicle performance and system performance.

F2012-G01-015

F. Sun (✉) · J. Jiang · W. Liu · Z. Pan · F. Zhao
Zhejiang Geely Automobile Research Institute Co. Ltd, Hangzhou, China
e-mail: sfl_01@163.com

J. Jiang
e-mail: jiangjunping@rd.geely.com

W. Liu
e-mail: liuw@rd.geely.com

Z. Pan
e-mail: zhaofuquan10@163.com

F. Zhao
e-mail: panzhijie@rd.geely.com

Keywords Static design factors (SDF) · Setting targets · Suspension structure

1 Introduction

In the vehicle design process, subjective evaluation, objective testing, and simulation analysis of system of vehicle of operation stability are applied to development of vehicles. For estimates of vehicle performance, objectively measured data of automobile steering stability can be taken as the input of simulation analysis, through which the vehicle performance objective is confirmed and performance objective decomposition of each system can be implemented [1].

In this chapter, Model A, a vehicle in research and development on a platform of Geely is taken as the research object. Based on the foundation Model 3, operation stability of benchmarking Model 1, 2 and 4 is analysed through comparison of test data, optimization analysis of suspension structure and vehicle performance is conducted using ADAMAS/CAR and CARSIM. Finally, overall vehicle of Model A is designed and values of system targets are set.

2 Vehicle Target Setting and Decomposition Profile

2.1 Vehicle Targets Setting

Vehicle targets setting (VTS), indicates the confirmation of subjective and objective targets of vehicle operation stability and ride comfort ability. Through vehicle targets setting, decomposition of system targets can be further conducted [2].

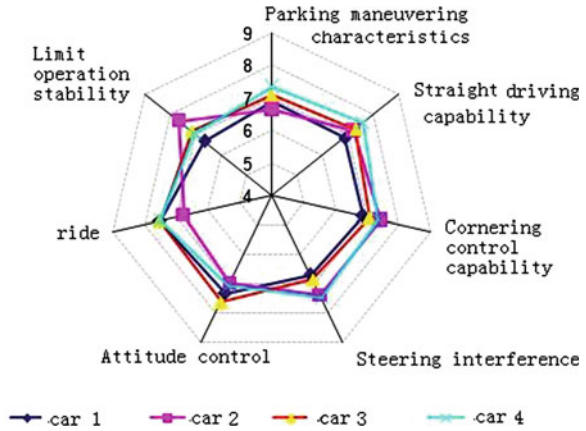
2.2 System Design Factors

The system design factors (SDF), indicates to conduct target setting to suspension systems, steering systems and braking systems according to the vehicle ride and operation targets [2, 3].

Suspension system performance consists of K&C characteristics. In the chassis design process, simulation analysis or test analysis of suspension K&C performance should be conducted for prediction and control of vehicle performance. K&C performance is directly related to vehicle operation stability and comfort ability, and K&C performance indicators include roll steer coefficient, variation coefficient of toe-in changes with longitudinal force, and etc.

In the steering system design, the key performance consists of steering tie rod plane angle, minimum turning diameter, the Ackermann rate, and Ackermann

Fig. 1 Of the vehicle ride and handling ride comfort subjective evaluation



deviation. And the Ackermann rate is an important indicator of automotive design, if the Ackermann rate is inadequate, steering force may be insufficient, which shall cause tire wear and a series of problems [4].

3 Vehicle Target Setting

The vehicle-level targets are set with vehicle database of competitive products the same level and with combination of product orientation of the designed model.

3.1 Subjective Evaluation of Operation Stability and Ride Comfort

Subjective evaluation result of operation stability of Model 1–4 is shown in Fig. 1, from which Model 3 is superior in ride comfort and attitude control; favourable in parking manipulation, straight running and limit operation; while poor in curve control and steering interference. For more details, see Table 1.

3.2 The Objective Test of Operation Stability and Ride Comfort

As shown in Table 2, performance of Model 3 is optimal in low speed aligning, serpentine and double lane, while poor in angle step and needs to be improved (Figs. 2, 3).

Based on subjective evaluation of vehicle performance and comprehensive steering performance, ride comfort, operability stability, vehicle performance of Model 3 and 4 are equivalent and superior to that of Model 1 and 2. According to

Table 1 Subjective evaluation of vehicle operation stability and ride comfort

Project	Elaborate	Car 1	Note	Car 2	Note
Parking handling characteristics—return ability	Residual angle of the steering wheel returning	7	Left turn and right back residual 15°, right turn and left back residual 5°, asymmetric	7	Residual 10° left turn and right back slightly larger, asymmetric
Straight-line driving capability—torque feedback	The return ability of the steering wheel speed, speed and uniformity	7	Appropriate speed and uniform	7.5	Appropriate speed and uniform
Bend control capability—torque feedback	Clear center of the steering wheel torque	6	Centers vague	6	Centers vague
Steering interference—torque steering	Increase or decrease of the steering wheel angle input lead to a corresponding increase or decrease of the steering wheel torque	6	Almost no torque to establish	7	The establishment of a small torque
Steering interference—steering wheel beater	Whether the steering wheel suddenly rotation by impact	7	Standing start and rapid acceleration, medium torque steering	7.5	Standing start and rapid acceleration, no steering torque
Steering interference—catch up	Whether the steering wheel torque will be increased significantly, resulting in not smooth steering	6.5	No significant impact	7	No significant impact
			Continuous wide-angle operating the steering wheel, the moment there is a moderate increase, but you can turn to	8	No torque is increased
Project	Elaborate	Car 3	Note	Car 4	Note
Parking handling characteristics—return ability	Residual angle of the steering wheel returning	6.5	Residue of about 20°	7	Residue of about 12°
	The return ability of the steering wheel speed, speed and uniformity	6.5	Slow return, uneven, catching	8	Appropriate speed and uniform

(continued)

Table 1 (continued)

Project	Elaborate	Car 3	Note	Car 4	Note
Straight-line driving capability—torque feedback	Clear center of the steering wheel torque	5.5	Center is not clear	6.5	The center is a little vague
Bend control capability—torque feedback	Increase or decrease of the steering wheel angle input lead to a corresponding increase or decrease of the steering wheel torque	6	The establishment of a small torque, left-right asymmetry, left turn is large, right turn is little	7.5	The establishment of small to medium torque
Steering interference—torque steering	Whether the vehicle exists steering	6	Standing start and rapid acceleration, medium to large torque steering, the steering wheel to the right	7.25	Standing start and rapid acceleration, little torque steering
Steering interference—steering wheel beater	Whether the steering wheel suddenly rotation by impact	6.5	Impact	7	No significant impact
Steering interference -catch up	Whether the steering wheel torque will be increased significantly, resulting in not smooth steering	6	Continuous large angle steering, steering torque is increased obviously, some difficulties	8	No torque increase

Table 2 Objective test data of handling stability

Project	Score content	Car 1	Car 2	Car 3	Car 4
Steady state	Understeer degree ($^{\circ}$)/ m/s^2	0.09	0.105	0.1	0.055
	Roll degree ($^{\circ}$)/ m/s^2	82.49	85.375	85	75.075
Step angle	Test value	0.51	0.465	0.505	0.425
	Score	100	100	100	100
Low speed return	Yaw rate response time s	0.18	0.15	0.215	0.19
	3 s yaw angular velocity residual ($^{\circ}$)/s	65.71	74.29	55.715	62.855
Serpentine	Test value	-0.975	0.115	-0.35	-0.28
	Score	80.5	87.1	90.6	82.2
Double lane change	Benchmark average speed steering angle ($^{\circ}$)	86.79	58.37	63.78	56.75
	The benchmark average speed yaw rate ($^{\circ}$)	91.07	97.59	98.74	100
	Test value	19.62	12.79	14.82	15.27
	Score	74.35	84.68	87.15	85.95
	Test value	95	100	105	100
	Score	85	90	95	90

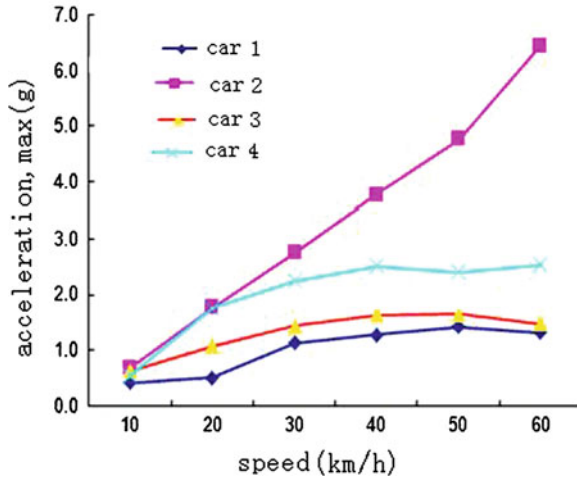


Fig. 2 Maximum value of acceleration at driver's foot position on floor

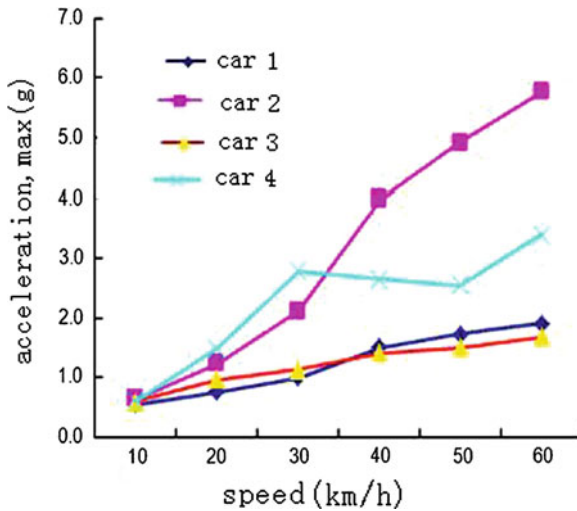


Fig. 3 Maximum value of acceleration at rear passengers' foot position on floor

local analysis, the steering system performance of Model 3 is weaker in steering system response, torque feedback and low speed aligning than that of Model 1, 2 and 4, so they should be improved;

According to the objective test result of operation stability and ride comfort, Model 3 is slightly inferior to Model 1, 2 and 4 in response, so it should be improved.

Table 3 Objective targets of operation stability and ride comfort of model A

Project	Performance index	Unit	Car 3	Car A		
Steady static circular	Understeer gradient	deg/g	2.56	2.2 ~ 2.6	Steady steering	
	Body roll angle @0.5 g	deg	2.23	≤ 2.3		
Response characteristics	Yaw rate steady state gain	dB	-12.85	-11 ~ -13	Response characteristics	
	Yaw rate of natural frequency	Hz	1.2	>1.2		
	Yaw rate the 1 Hz phase lag angle	deg	27.94	<35		
	Yaw rate response time	s	0.20	<0.19		
	Lateral acceleration response time	s	0.43	<0.35		
	Steering sensitivity		g/100 deg	1.25		>1.3

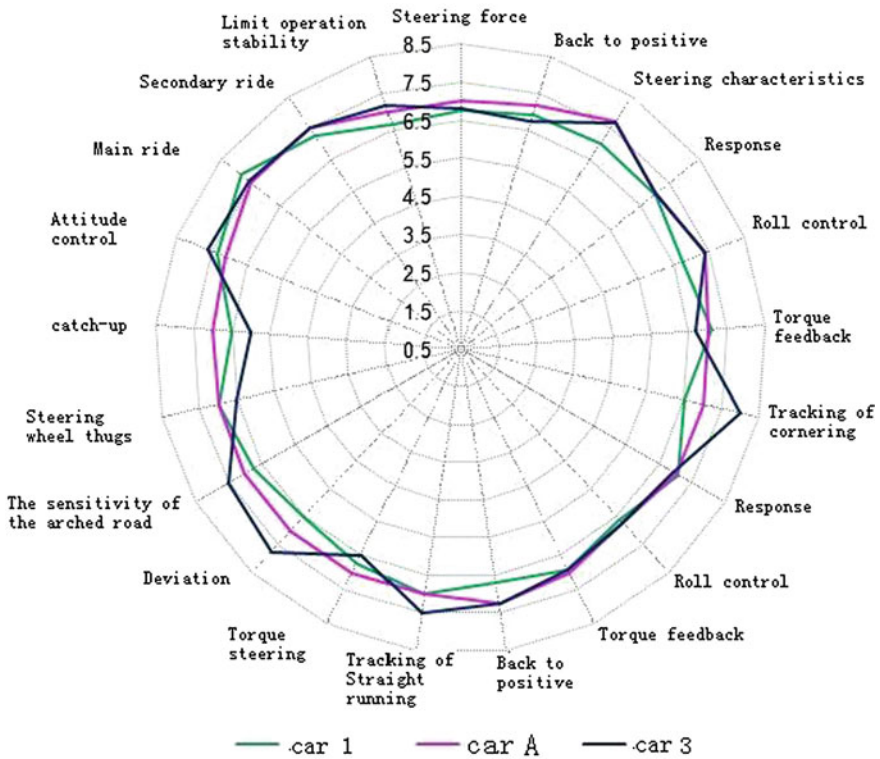


Fig. 4 Subjective targets setting of operation stability and ride comfort of model A

Fig. 5 Steady static circular—under steer

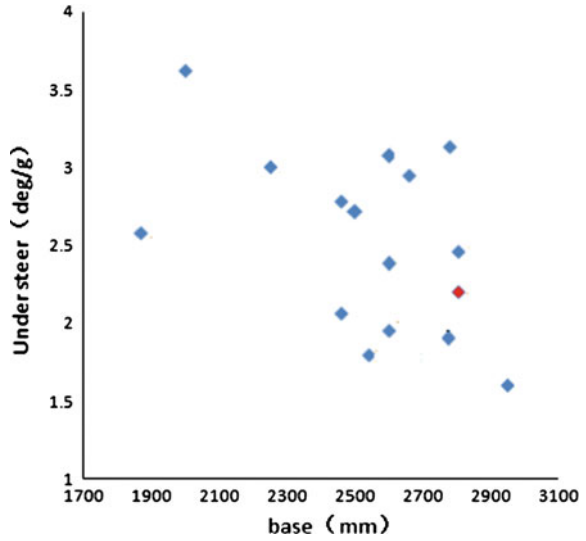
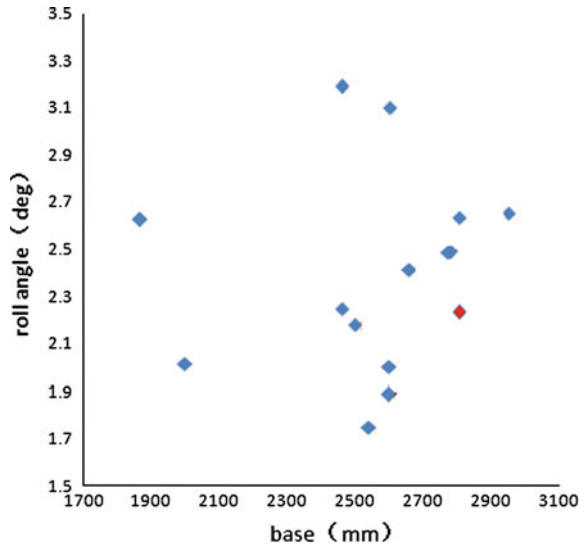


Fig. 6 Steady static circular—roll angle

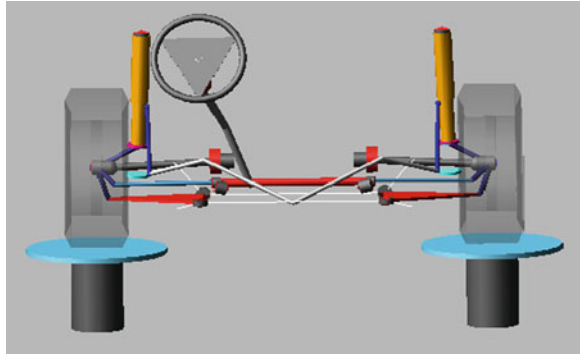
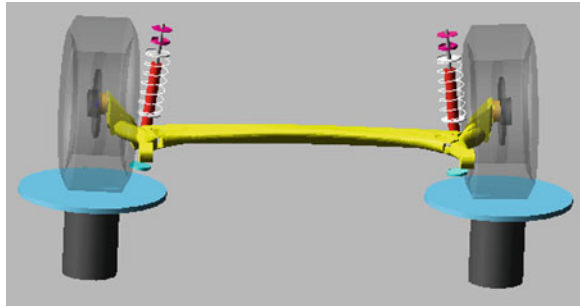


3.3 Vehicle-Level Targets Setting

According to the above analysis, Model 3 and Model 1 are close, and Model A is the improved Model 1, so Model 1 and 3 are selected as targets setting benchmark of vehicle operation stability and ride comfort. The subjective targets of Model A shall be improved on the basis of Model 1 and 3, and the specific target values are shown in Fig. 4.

Table 4 Objective targets of ride comfort of model A

Performance	Target	Unit	Car A	Remark
Pulse road	Driver's seat av_max	m/s^2	5.19	30 km/h
	The left rear passenger seat av_max	m/s^2	6.58	
	Driver's seat av_max	m/s^2	5.46	60 km/h
	The left rear passenger seat av_max	m/s^2	5.31	
Random road	Driver's seat the total aw_r.m.s	m/s^2	0.282	70 km/h
	The left rear passenger seat the total aw_r.m.s	m/s^2	0.293	
	Driver's seat the total aw_r.m.s	m/s^2	0.303	100 km/h
	The left rear passenger seat the total aw_r.m.s	m/s^2	0.309	

Fig. 7 Front suspension structure form**Fig. 8** Rear suspension structure form-one

Subjective targets of vehicle operation stability and ride comfort are set through simulation analysis with Carsim software [5]. For Model 3, response characteristics of operation stability and ride comfort need to be improved, so the target is promoted in setting, as shown in Table 3. Figures 5, 6 show the overall status of two design parameters, i.e. under steer degree and the car body roll angle in steady static circular mode in VTS parameters. The overall status is well and can be acceptable (Table 4).

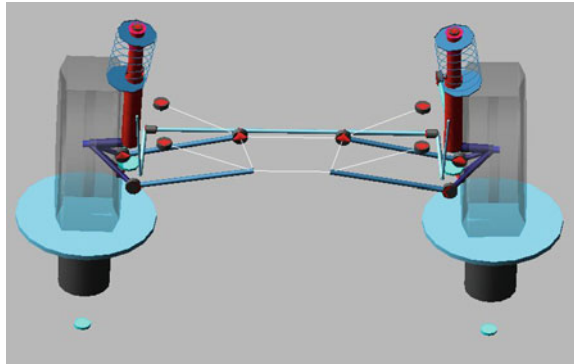


Fig. 9 Rear suspension structure form-two

Table 5 Model A suspension K&C performance targets setting

Parameter	Unit	Front sus	Rear sus
Roll center height	mm	88.6	140.4
Roll steer	%	- 1.19	-2.259
Roll camber	%	21.16	20.92
Toe/fy	deg/KN	-3.87E-06	7.34E-05
Camber/fy	deg/KN	1.41E-04	3.09E-04
Toe/fx	deg/KN	-1.42E-04	6.49E-05
Track/wheel travel	-	0.05065	-0.1072
Base/wheel travel	-	0.03856	0.1205

Fig. 10 Roll centre location—front suspension

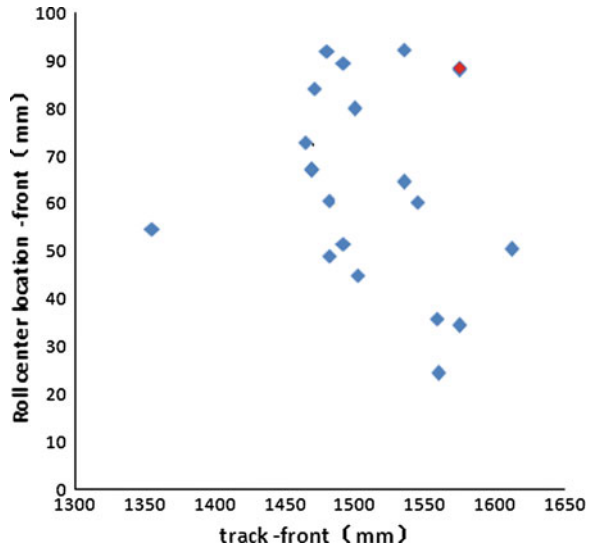


Fig. 11 Variation of Toe-In with roll steer—front suspension

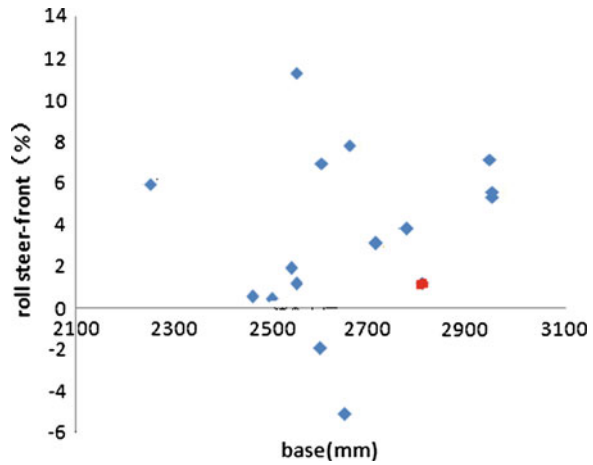
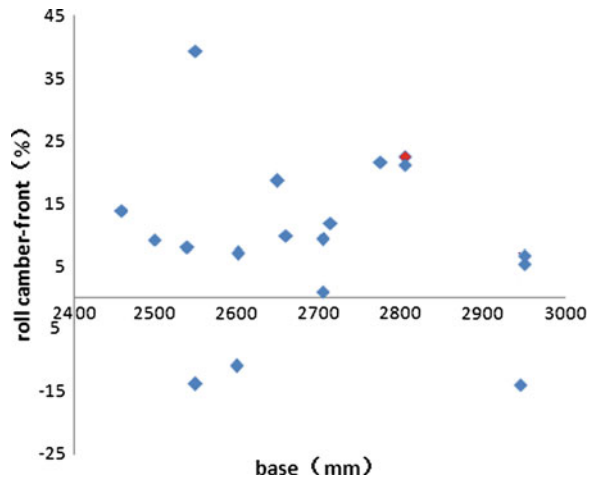


Fig. 12 Roll camber—front suspension



4 System Targets Setting

The system-level targets are confirmed through combination of test data and software [6].

4.1 Suspension System Targets Setting

The front suspension structure in Model 1–4 is McPherson (Fig. 7), the rear suspension form in Model 2 and 4 is torsion beam structure (Fig. 8), and rear suspension form in Model 1 and 3 is multi-link structure (Fig. 9). In the

Fig. 13 Lateral force camber stiffness—front suspension

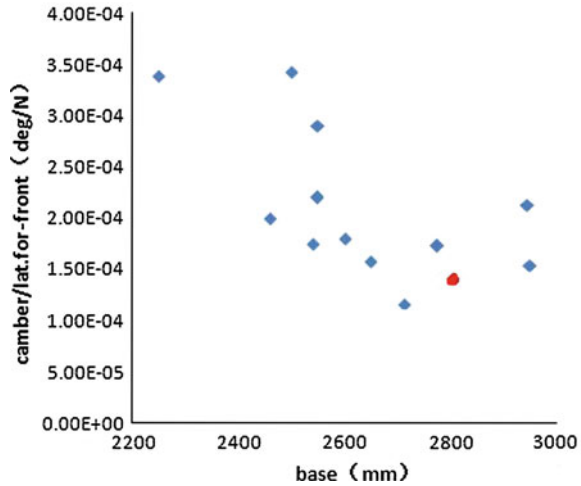


Table 6 Steering performance targets setting of model A

Steering performance	Car 3	Car A
The Ackermann rate left turn to the limit	63.87	>50 %
The Ackermann rate right turn to the limit	51.92	>50 %
Ackermann deviation revolver corner 25° (left)	2.82	<2.5°
Ackermann deviation revolver corner 25° (right)	3.39	<2.5°
Steering system transmission ratio	16.2	14 ~ 17
Steering rack such as the effectiveness of arm	135.63	>125 mm
Steering rod plane angle	7.24	<8
Minimum turning diameter	11.54	<11.5 m

comparison of performance of various models, Model 3 is favourable in overall performance; since the same suspension system of Model 3 is applied in Model A, performance targets setting of suspension K&C is similar to that of Model 3, as shown in Table 5. Figures 10, 11, 12 and 13 show the value range of Model A suspension system target setting in SDF parameter table, and the overall performance is favourable.

4.2 Steering System Targets Settings

The response performance of Model 3 is poor, and the steering performance needs to be improved. In addition, electric power steering is applied in Model A and facilitates to performance promotion, so steering performance targets setting of Model A is higher than that of Model 3, as shown in Table 6.

5 Conclusion

The vehicle performance targets include the subjective and objective performance targets of operation stability and ride comfort, and the system-level mainly consists of the performance targets of suspension, steering and braking system. In this chapter, through analysis of performance of Model 1–4, combined with the current VTS-SDF parameters database and based on the different performance design of the suspension forms, vehicle performance targets and system-level targets of Model A under research and development on some platform are finally determined, which shall provide reference for future development of models on the platform.

References

1. Kinstle MF, Hassler D, Johnson BS (2009) Vehicle dynamics benchmarking and simulation, SAE paper 2009-01-0465
2. Zhao SQ, Jin DF (2006) Vehicle dynamics foundation. Tsinghua University Press, Beijing
3. Yu ZS (2008) Auto theory. China Machine Press, China (In Chinese)
4. Guo KH (1991) Vehicle handling dynamics. Jilin Science and Technology Press (In Chinese)
5. Carsim Help (2008) Carsim Quick start Guide
6. MSC Software (2007) Adams/Car dynamic suspension analysis

Analysis and Optimization of Torque Variation in Steering Column Assembly

Guohui Yan

Abstract The steering torque variation which is an important evaluation index of the vehicle handling stability directly influences the feeling of driving. The objective of this chapter is to optimize the hard points and the phase angle of steering column assembly in order to reduce the torque variation to the minimum, and improve the vehicle handling stability. In this chapter, the formulas for accurate calculation of the angular velocity ratio and the torque variation in double cross universal joints system are deduced according to the transmission analysis of single cross universal joint. Based on the study of the formula for approximate calculation of the rotational angle deviation in double cross universal joints system and the calculation of the torque variation using MATLAB software, an effective optimization method of the phase angle which could be applied to reduce the angular velocity ratio and the torque variation is obtained. The torque variation could be calculated exactly and reduced to the minimum by using the optimization method and formulas in the early stage of steering column assembly layout. The formulas and optimization method could also be applied to other cross universal joints transmission system.

Keywords Torque variation · Universal joint · Angular velocity ratio · Phase angle · Steering column assembly

F2012-G01-016

G. Yan (✉)
China FAW co, ltd. R&d Center, Changchun, China
e-mail: yanguohui@rdc.faw.com.cn

1 Introduction

Steering column assembly is a very important transmission mechanism, which is composed by steering shaft, steering column tube, upper bracket, lower bracket and intermediate shaft, etc. Now steering column assembly mostly adopts double cross universal joints, which would cause the torque variation because of space, dimension tolerance of parts and assembly error. It would influence the feeling of steering, and then cause the driver to feel uncomfortable. So it is very important to reduce the torque variation to the minimum in steering column assembly. In this chapter, the torque variation of steering column assembly with double/three cross universal joints is optimized, the hard points and the phase angle are illustrated in detail, which could provide theoretical basis for the engineers in analysis and optimization of the torque variation in steering column assembly.

2 The Transmission Analysis of Single Cross Universal Joint

The transmission of single cross universal joint has advantages of simple structure, high transmission efficiency and lower noise. However, the transmission speed is not constant, the rotational angle of driven shaft fluctuates periodically when the rotational angle of driving shaft rotates with constant angular velocity.

As shown in Fig. 1 [1]:

$$\tan\varphi_1 = \tan\varphi_2\cos\alpha \quad (1)$$

Where

φ_1 is the rotation angle of driving shaft, the initial plane of the driving shaft yoke is the plane of driving shaft and driven shaft

φ_2 is the rotation angle of driven shaft

α is the axial angle between driving shaft and driven shaft ($0 \leq \alpha < \pi/2$).

By derivation from Eq. (1), the equation could be written as:

$$\frac{\omega_2}{\omega_1} = \frac{\cos\alpha}{1 - \sin^2\alpha\cos^2\varphi_1} \quad (2)$$

Where

ω_1 is the angular velocity of driving shaft

ω_2 is the angular velocity of driven shaft.

In Eq. (2), $\cos\varphi_1$ is a periodic function with 2π , so the angular velocity ratio is a periodic function with π . From Eq. (2), $(\omega_2/\omega_1)_{\max} = 1/\cos\alpha$, $(\omega_2/\omega_1)_{\min} = \cos\alpha$.

The rotational angle deviation of two shafts could be expressed as [1]:

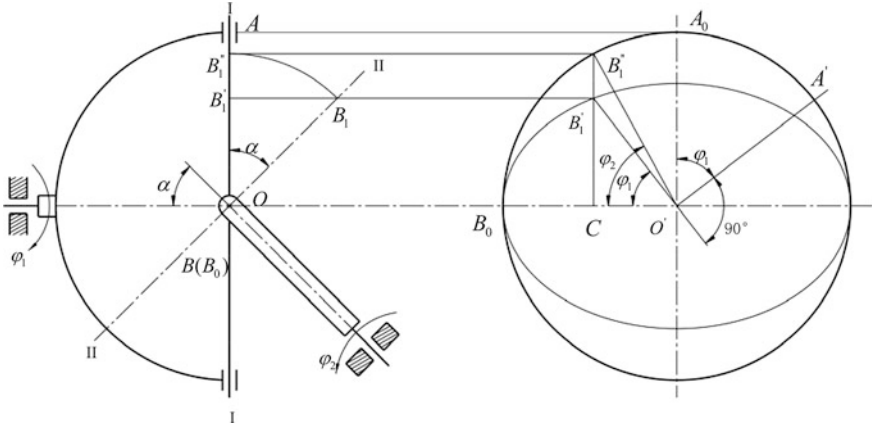


Fig. 1 The transmission of single cross universal joint

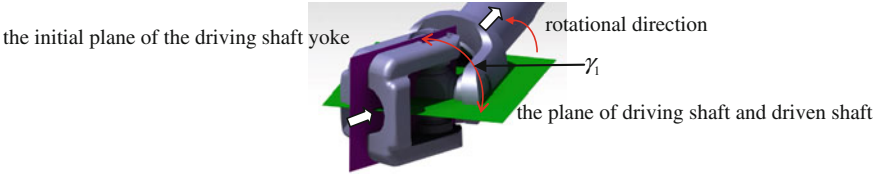


Fig. 2 The initial plane of the driving shaft yoke

$$\Delta\varphi_{2-1} = \varphi_2 - \varphi_1 = \arctan \frac{2 \tan \varphi_1 \sin^2(\alpha/2)}{\tan^2 \varphi_1 + \cos \alpha} \quad (3)$$

If the initial plane of the driving shaft yoke is perpendicular to the plane of driving shaft and driven shaft, Eq. (4) could be derived from Eq. (1).

$$\tan \varphi_2 = \tan \varphi_1 \cos \alpha \quad (4)$$

Eq. (1) and Eq. (4) are the transmission formulas of single cross universal joint, while the initial planes of the driving shaft yoke are different.

If the angle between the two planes is γ_1 as shown in Fig. 2 ($0 \leq \beta < \pi/2$), Eq. (1) can be written as:

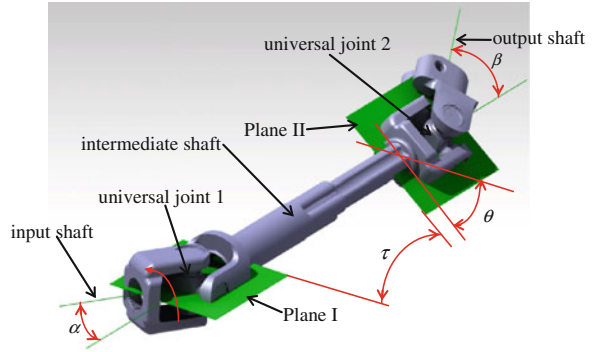
$$\tan(\varphi_1 + \gamma_1) = \tan(\varphi_2 + \varphi_{\gamma_1}) \cos \alpha \quad (5)$$

Where φ_{γ_1} is the rotation angle of driven shaft when the driving shaft rotates γ_1 from the plane of driving shaft and driven shaft.

By derivation from Eq. (5), the equation could be written as:

$$\frac{\omega_2}{\omega_1} = \frac{\cos \alpha}{1 - \sin^2 \alpha \cos^2(\varphi_1 + \gamma_1)} \quad (6)$$

Fig. 3 The transmission of double cross universal joints



Supposing that T_1, T_2 are torque of driving shaft and driven shaft respectively, and the transmission efficiency is ignored, we could draw the conclusion:

$$T_1 \times \omega_1 = T_2 \times \omega_2 \quad (7)$$

$$\frac{T_2}{T_1} = \frac{\omega_1}{\omega_2} = \frac{1 - \sin^2 \alpha \cos^2(\varphi_1 + \gamma_1)}{\cos \alpha} \quad (8)$$

The torque variation could be expressed as:

$$\Delta \lambda_{2-1} = \left| \frac{T_2 - T_1}{T_1} \right| = \left| \frac{1 - \sin^2 \alpha \cos^2(\varphi_1 + \gamma_1)}{\cos \alpha} - 1 \right| \quad (9)$$

The rotational angle deviation could be expressed as:

$$\begin{aligned} \Delta \varphi_{2-1} &= \varphi_2 - \varphi_1 = (\varphi_2 + \varphi_{\gamma_1}) - (\varphi_1 + \gamma_1) - (\varphi_{\gamma_1} - \gamma_1) \\ &= \arctan \frac{2 \tan(\varphi_1 + \gamma_1) \sin^2(\alpha/2)}{\tan^2(\varphi_1 + \gamma_1) + \cos \alpha} - \arctan \frac{2 \tan \gamma_1 \sin^2(\alpha/2)}{\tan^2 \gamma_1 + \cos \alpha} \end{aligned} \quad (10)$$

Eqs. (6, 9, and 10) are formulas of the angular velocity ratio, the torque variation and the rotational angle deviation of single cross universal joint respectively, which could be applied to any initial plane of the driving shaft yoke.

3 The Transmission Analysis of Double Cross Universal Joints

Plane I is the plane of input shaft and intermediate shaft.

Plane II is the plane of intermediate shaft and output shaft.

Universal joint 1 is the joint of input shaft and intermediate shaft.

Universal joint 2 is the joint of intermediate shaft and output shaft. (Fig. 3)

As for universal joint 1:

$$\frac{\omega_2}{\omega_1} = \frac{\cos\alpha}{1 - \sin^2\alpha\cos^2(\varphi_1 + \gamma_1)} \quad (11)$$

$$\Delta\varphi_{2-1} = \varphi_2 - \varphi_1 = \arctan \frac{2\tan(\varphi_1 + \gamma_1)\sin^2(\alpha/2)}{\tan^2(\varphi_1 + \gamma_1) + \cos\alpha} - \arctan \frac{2\tan\gamma_1\sin^2(\alpha/2)}{\tan^2\gamma_1 + \cos\alpha} \quad (12)$$

As for universal joint 2:

$$\frac{\omega_3}{\omega_2} = \frac{\cos\beta}{1 - \sin^2\beta\cos^2(\varphi_2 + \gamma_2)} \quad (13)$$

$$\Delta\varphi_{3-2} = \varphi_3 - \varphi_2 = \arctan \frac{2\tan(\varphi_2 + \gamma_2)\sin^2(\beta/2)}{\tan^2(\varphi_2 + \gamma_2) + \cos\beta} - \arctan \frac{2\tan\gamma_2\sin^2(\beta/2)}{\tan^2\gamma_2 + \cos\beta} \quad (14)$$

Where α is the axial angle between input shaft and intermediate shaft ($0 \leq \alpha < \pi/2$).

β is the axial angle between intermediate shaft and output shaft. ($0 \leq \beta < \pi/2$).

φ_1 , φ_2 and φ_3 are the rotational angles of input shaft, intermediate shaft and output shaft respectively ω_1 , ω_2 and ω_3 are the angular velocity of input shaft, intermediate shaft and output shaft respectively.

γ_1 ($0 \leq \gamma_1 < \pi$) is the angle between the initial plane of the input shaft yoke and Plane I in rotation direction.

γ_2 ($0 \leq \gamma_2 < \pi$) is the angle between the initial plane of the intermediate shaft yoke and Plane II in rotational direction.

$\Delta\varphi_{2-1}$ is the rotational angle deviation between intermediate shaft and input shaft.

$\Delta\varphi_{3-2}$ is the rotational angle deviation between output shaft and intermediate shaft.

The angular velocity ratio of double cross universal joints is derived from Eq. (11) and Eq. (13):

$$\frac{\omega_3}{\omega_1} = \frac{\omega_3}{\omega_2} \times \frac{\omega_2}{\omega_1} = \frac{\cos\alpha}{1 - \sin^2\alpha\cos^2(\varphi_1 + \gamma_1)} \times \frac{\cos\beta}{1 - \sin^2\beta\cos^2(\varphi_2 + \gamma_2)} \quad (15)$$

The torque variation of double cross universal joints could be expressed as:

$$\Delta\lambda_{3-1} = \left| \frac{1 - \sin^2\alpha\cos^2(\varphi_1 + \gamma_1)}{\cos\alpha} \times \frac{1 - \sin^2\beta\cos^2(\varphi_2 + \gamma_2)}{\cos\beta} - 1 \right| \quad (16)$$

The rotational angle deviation of double cross universal joints is derived from Eq. (12) and Eq. (14):

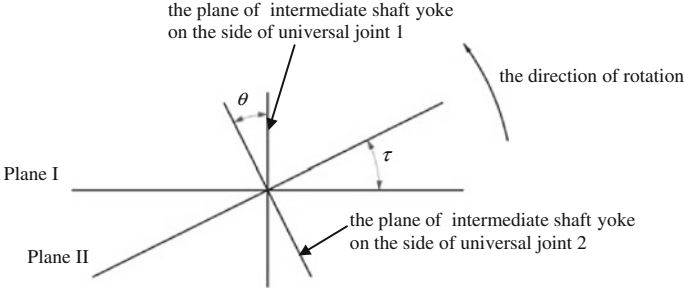


Fig. 4 The plane angle and the phase angle of intermediate shaft

$$\begin{aligned}
 \Delta\varphi_{3-1} &= \varphi_3 - \varphi_1 = (\varphi_3 - \varphi_2) + (\varphi_2 - \varphi_1) \\
 &= \arctan \frac{2\tan(\varphi_1 + \gamma_1)\sin^2(\alpha/2)}{\tan^2(\varphi_1 + \gamma_1) + \cos\alpha} - \arctan \frac{2\tan\gamma_1\sin^2(\alpha/2)}{\tan^2\gamma_1 + \cos\alpha} \\
 &\quad + \arctan \frac{2\tan(\varphi_2 + \gamma_2)\sin^2(\beta/2)}{\tan^2(\varphi_2 + \gamma_2) + \cos\beta} - \arctan \frac{2\tan\gamma_2\sin^2(\beta/2)}{\tan^2\gamma_2 + \cos\beta}
 \end{aligned} \tag{17}$$

α, β, γ_1 and γ_2 are known parameters. From Eq. (12), we could conclude that $\varphi_2 = \varphi_1 + \Delta\varphi_{2-1}$, so Eqs. (15, 16, and 17) are functions of φ_1 .

4 The Transmission Optimization of Double Cross Universal Joints

In Fig. 4, Plane I is the initial plane of the input shaft yoke, so that the intermediate shaft yoke of universal joint 1 is perpendicular to Plane I. Supposing that the angle τ ($0 \leq \tau < \pi/2$) is the angle of Plane II leading Plane I in rotational direction, and θ ($0 \leq \theta \leq \pi/2$) is the phase angle of intermediate shaft, we could conclude that the rotational angle deviation of double cross universal joints is [2]:

$$\Delta\varphi_{3-1} = \frac{\sqrt{\alpha^4 + \beta^4 - 2\alpha^2\beta^2\cos 2(\tau - \theta)}}{4} \sin 2(\varphi_1 + \sigma) \tag{18}$$

Where $\sigma = \frac{1}{2} \arctan \left(\frac{\beta^2 \sin 2(\tau - \theta)}{\alpha^2 - \beta^2 \cos 2(\tau - \theta)} \right)$.

The amplitude of $\Delta\varphi_{3-1}$ is:

$$|\Delta\varphi_{3-1}| = \frac{\sqrt{\alpha^4 + \beta^4 - 2\alpha^2\beta^2\cos 2(\tau - \theta)}}{4} \tag{19}$$

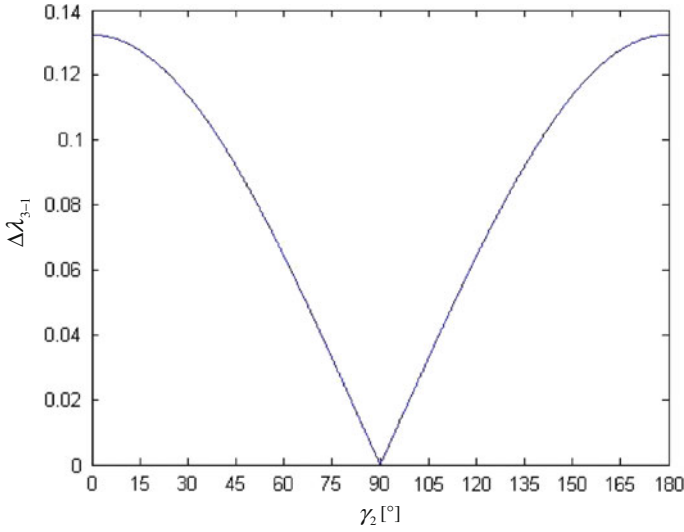


Fig. 5 $\alpha = \beta = 20, 0 \leq \varphi_1 < 2\pi$

In order to make $\Delta\varphi_{3-1}$ minimum, the amplitude $|\Delta\varphi_{3-1}|$ should be minimum. When $\theta = \tau$:

$$|\Delta\varphi_{3-1}|_{\min} = \frac{|\alpha^2 - \beta^2|}{4} \quad (20)$$

So the transmission of double cross universal joints is constant only when $\theta = \tau, \alpha = \beta$.

In Fig. 4, the torque variation of double cross universal joints could be expressed as:

$$\Delta\lambda_{3-1} = \left| \frac{1 - \sin^2\alpha\cos^2\varphi_1}{\cos\alpha} \times \frac{1 - \sin^2\beta\cos^2(\varphi_2 + \gamma_2)}{\cos\beta} - 1 \right| \quad (21)$$

$$\varphi_2 = \varphi_1 + \arctan \frac{2\tan\varphi_1\sin^2(\alpha/2)}{\tan^2\varphi_1 + \cos\alpha} \quad (22)$$

The curves of $\gamma_2 - \Delta\lambda_{3-1}$ derived by MATLAB are shown in Figs. 5 and 6. When $\gamma_2 = \pi/2, \theta = \tau$ and the torque variation is minimum.

To sum up, in order to realize constant-velocity driving, the condition $\theta = \tau, \alpha = \beta$ should be fulfilled in the system layout of double cross universal joints. If $\alpha \neq \beta$, the deviation between α and β should be minimum and keep $\theta = \tau$ (positive and negative of θ, τ also should be same) to obtain the minimum torque variation. The minimum

torque variation is $\left| \frac{\cos\beta}{\cos\alpha} - 1 \right|$ or $\left| \frac{\cos\alpha}{\cos\beta} - 1 \right|$.

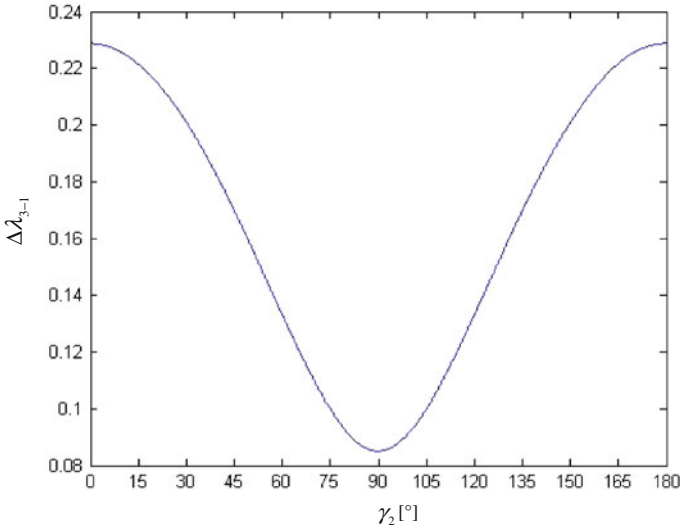


Fig. 6 $\alpha = 20$, $\beta = 30$, $0 \leq \varphi_1 < 2\pi$

5 Analysis and Optimization of Torque Variation in Steering Column Assembly

5.1 Steering Column Assembly with Double Cross Universal Joints

Now steering column assembly mostly adopts double cross universal joints, the axial angle of each cross universal joint should be 34° max, and the torque variation of steering column assembly is recommended 5 % max.

Steering column assembly is usually divided into non-adjustable type, tilt type (or rake type), telescope type, tilt and telescope type. To avoid the torque variation and realize constant transmission, the axial angle α between steering shaft and intermediate shaft should be equal to the axial angle β between intermediate shaft and steering gear input shaft, and the phase angle θ of intermediate shaft should be equal to the plane angle τ between Plane I and Plane II in the design position of steering column assembly. If $\alpha = \beta$ could not be met because of space limit, the deviation of α and β should be minimum and $\theta = \tau$ (positive and negative of θ , τ also should be same) must be kept to obtain the minimum torque variation. Then the torque variation should be checked in the upper and lower positions of tilt type (rake type, or tilt and telescope type). Take a vehicle steering column assembly for example as shown in the Table 1 and Fig. 7.

Table 1 The parameters of a vehicle steering column assembly (an example)

position	α [°]	β [°]	θ [°]	τ [°]	$\Delta\varphi_{3-1}$ [%]
upper	31.25	33.769	60.9	64.942	3.64
design	32.986	32.985		60.923	0
lower	34.866	32.203		57.313	3.76

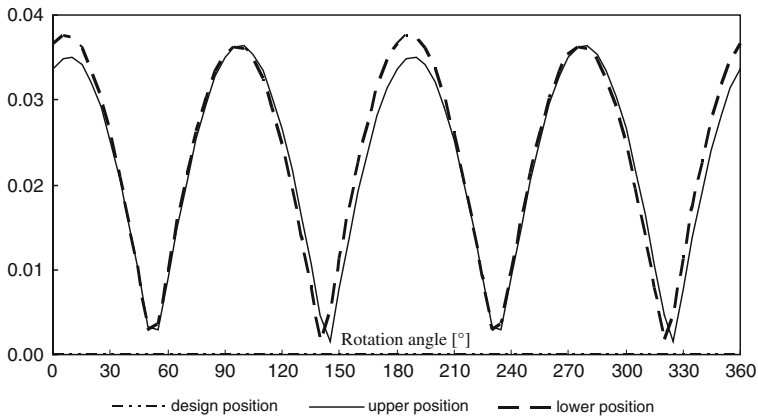


Fig. 7 The curves of the torque variation in different positions (an example)

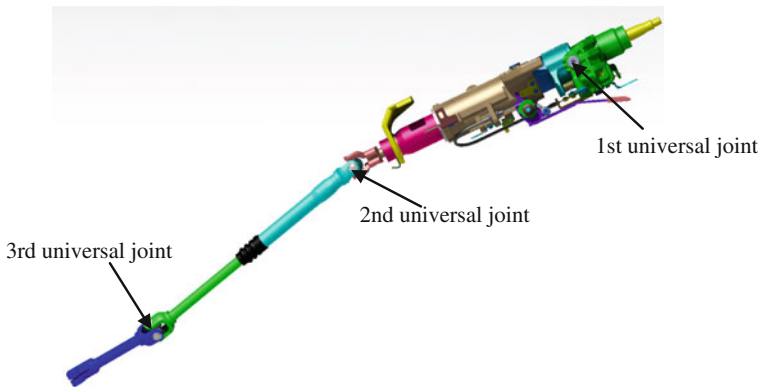


Fig. 8 Steering column assembly with three cross universal joints

5.2 Steering Column Assembly With Three Cross Universal Joints

Steering column assembly of up-tilt type usually contains three cross universal joints as shown in Fig. 8, the tilt angle is usually less than ± 10 , and the axial angle α_1 of 1st universal joint is usually 0 in the design position.

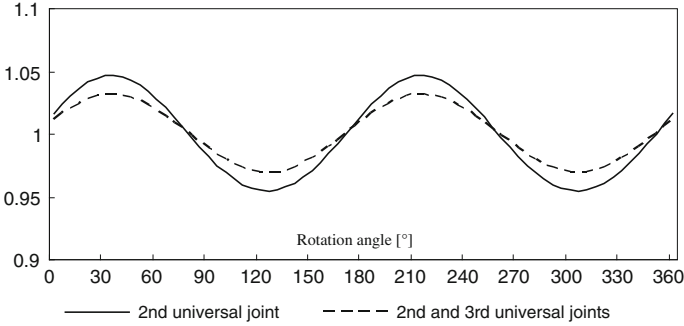


Fig. 9 The angular velocity ratio (an example)

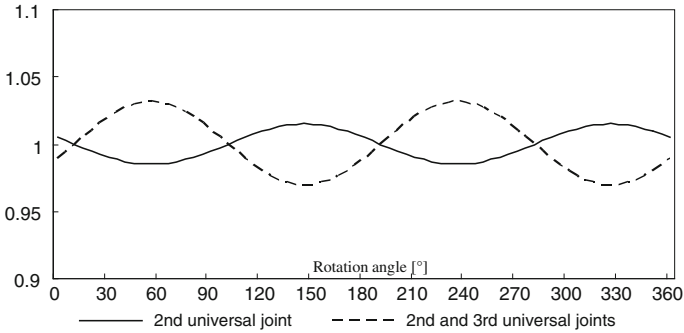


Fig. 10 The angular velocity ratio (an example)

In order to make the torque variation of the system to be minimum, the torque variation of the double cross universal joints connected by intermediate shaft should be minimum, the same as the optimization method of double cross universal joints, and the phase angle of the shaft connecting 1st universal joint and 2nd universal joint is very important. If $\alpha_2 \geq \alpha_3$ (α_2 is the axial angle of 2nd universal joint, α_3 is the axial angle of 3rd universal joint) and $\theta_2 = \tau_2$ (θ_2 is the phase angle of intermediate shaft, τ_2 is the plane angle of 2nd and 3rd universal joints system) could be met, the angular velocity ratio will be similar to Fig. 9, the phase angle θ_1 of the shaft connecting 1st universal joint and 2nd universal joint should be equal to the plane angle τ_1 of 1st and 2nd universal joints system in order to make the torque variation of steering column assembly to be minimum (positive and negative of θ_1, τ_1 also should be same), and the minimum torque variation is $\left| \frac{\cos \alpha_1 \cos \alpha_3}{\cos \alpha_2} - 1 \right|$ or $\left| \frac{\cos \alpha_2}{\cos \alpha_1 \cos \alpha_3} - 1 \right|$. If $\alpha_2 \leq \alpha_3$ and $\theta_2 = \tau_2$ could be met, the angular velocity ratio will be similar to Fig. 10, $\theta_1 = \pi/2 - \tau_1$ (positive and negative of θ_1, τ_1 should be opposite) must be kept to obtain the minimum torque variation, and the minimum torque variation is $\left| \frac{\cos \alpha_3}{\cos \alpha_1 \cos \alpha_2} - 1 \right|$ or $\left| \frac{\cos \alpha_1 \cos \alpha_2}{\cos \alpha_3} - 1 \right|$.

6 Conclusion

The formulas deduced in this paper could be applied to quantitative calculation of the torque variation in steering column assembly. The torque variation could be reduced to the minimum by using the optimization method in the early stage of steering column assembly layout. The formulas and optimization method could also be applied to other cross universal joints transmission system.

References

1. Mechanical Design Handbook Editorial Committee (2004) Mechanical design handbook new version volume 3. China Machine Press, Beijing
2. Zhendong F (1982) The calculation of angle deviation and equivalent angle in the transmission of multi cross universal joints system. Ji Lin: Academic Journal of Ji Lin University of Technology 01:104–110

Analysis of the Mechanism Kinematic Interference of a Heavy Articulated Dump Truck's Balanced Suspension System

Zhijun Guo, Bo Yang, Zhongli Li, Jingbo Wo and Keming Meng

Abstract The balanced suspension with rubber springs is widely used in heavy articulated dump truck's chassis to improve the power performance and the passing ability of vehicle. However, the congenital kinematics interference of the absorber and the guide linkage is in existence because of the natural structural feature of this kind of balanced suspension. On the basis of former dynamic analysis of the chassis' ride comfort by using vibration theory, the principle of mechanism kinematics is used to analyze the characteristics and the law of such a suspension system in this chapter. The kinematics sketch of the balanced suspension is obtained by way of hypothesis and simplification; the kinematics equations of the balanced suspension are further deduced; the relative movement law and the ways to reduce the interference are analyzed and surveyed by calculating the equations. It is concluded that it is beneficial to reduce the kinematics interference and prolong the life of the absorber and the guide linkage if the Guiding mechanism is parallel to X axis, and Panhard rod is parallel to Y axis of the vehicle coordinate while designing such balanced suspension. Compared with other chapters of the author, the kinematics interference of Panhard Rod was firstly analyzed in this chapter. However, the theoretical result needs more experimental support.

F2012-G01-017

Z. Guo (✉) · B. Yang · Z. Li · J. Wo · K. Meng
Vehicle and Motive Power Engineering College, Henan University of Science
and Technology, Luoyang, People's Republic of China
e-mail: gzhj1970@163.com

B. Yang
e-mail: yang34353@163.com

K. Meng
e-mail: 398235662@qq.com

Keywords Balanced suspension · Guiding mechanism · Kinematics · Interference

1 Introduction

Heavy articulated dump truck (HADT) can provide excellent performance in the Earth-rock transportation of water utilities, transport construction, mineral resources development and other large projects [1–5]. The balanced suspension, which is widely used in HADT, marking the wheels contact with the ground in complex conditions, to improve the dynamic performance and the passing ability of the vehicle [6, 7]. In the research of the balanced suspension, type A frame guiding mechanism was used to transmit longitudinal force between the frame and the axles, the rubber springs and Panhard Rod are used to transmit the vertical and lateral force between the frame and the axles [8–10]. In the small batch of real vehicle test process, the rubber springs shear failure happened. The form and the layout of the guiding mechanism and Panhard Rod had significant great influence on the balanced suspension components' force. The relative motion equations of the balanced suspension were deduced, and the relative movement law of the balanced suspension's main components was analyzed, to obtain the conditions which can avoid or reduce the interference.

2 Modeling

2.1 Physical Model

As the kinematics and dynamics interaction between HADT's front and rear body is relatively independent because of the articulated structure. Therefore, this study only establishes the rear body physical model for simplified analysis. The physical model of the rear body is shown in Fig. 1. In the 2D model, the articulated plate is simplified to be the combination motion pair with 4° ; type A frame is simplified to be the rigid rod, which hinged the frame with one end, and fixed on the corresponding axle with the other end; Panhard Rod was also simplified to be the rigid rod, which connected with the frame and the axle with revolution pair; the rubber spring was simplified to be the spring-damping component.

2.2 Mechanism Simplification

Figures 2 and 3 illustrate the kinematics sketches of the balanced suspension (the side and the back view). The assumptions are as follows: the frame is fixed; all

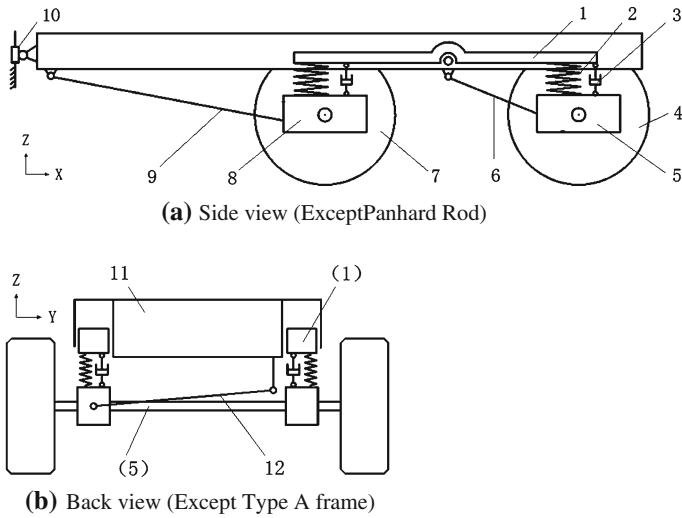


Fig. 1 Physical model of the rear body. 1 Balance beam, 2 spring, 3 damping, 4 rear wheel, 5 rear axle, 6 rear type a frame, 7 middle wheel, 8 middle axle, 9 middle type a frame, 10 articulated plate, 11 rear body, 12 rear panhard rod.

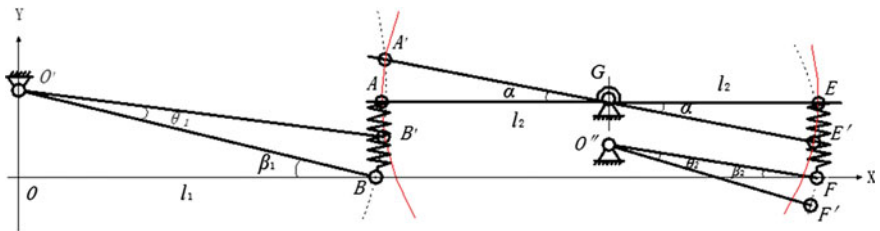
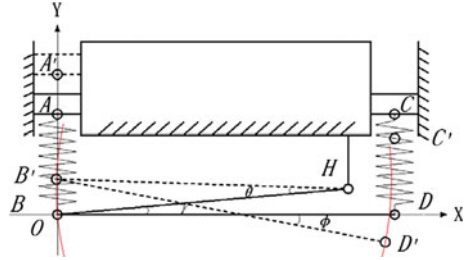


Fig. 2 Kinematic sketch of the balanced suspension (*Side view*)

components except the rubber spring are rigid rods. In Fig. 2, the middle and rear type A frame turn around O' and O'' , the balance beam turns around G . The rubber spring was simplified to be the special component AB and EF , which hinged balance beam with upper end points A and E and hinged the axle with lower points B and F . As the original vehicle used laminated rubber springs with allowable strain of 5 %, the deformation along the springs' centerline was very small. So it is assumed that AB and EF are incompressible along the Y axis. With the motion of the axle, the relative position between A and B (E and F) is changing along X . It is the important factor to affect of rubber spring's shear force and deformation, and also the main investigation index. Therefore, it was assumed that AB and EF could be stretched freely along the X axis. In the static equilibrium, take O point for the origin of the coordinates. According to the original vehicle size, G point coordinates is $(2932, 380)$, $OB = l_1 = 2,016$ mm, $AG = GE = l_2 = 916$ mm. The guiding mechanism trajectory is the dotted line, and the balance beam trajectory is

Fig. 3 Kinematic sketch of the balanced suspension (Back view)



the solid line. Provisions were as follows: when B is over the X axis, θ_1 and α are positive Angle, θ_2 is a negative Angle; conversely, when B is under the X axis, θ_1 and α are negative Angle, θ_2 is a positive Angle.

In Fig. 3, Panhard rod BH turns around H , the axle BD turns around B . The rubber spring was simplified to be the special component AB and CD , which hinged balance beam with upper end points A and C and hinged the axle with lower points B and D . It is also assumed that AB and CD are incompressible along the Y axis and could be stretched freely along the X axis. B point is the origin of the coordinates, and H point coordinates is $(l, l \tan \gamma)$. According to the original vehicle size, $l = 1,105$ mm, $BD = T = 1,380$ mm. The trajectory of Panhard rod is the solid line. Provisions were as follows: when B' is over the X axis, θ is a positive Angle, otherwise, θ is a negative Angle; if H is over the X axis, angle γ is positive, and otherwise, angle γ is negative.

3 Analysis of the Relative Movement Between the Guiding Mechanism and Balance Beam

3.1 Kinematics Equations

In Fig. 2, if the angle between the middle axis and X axis is β_1 , the coordinates of O' would be $(0, l_1 \tan \beta_1)$. When $O'B$ turns θ_1 to $O'B'$, assume that AG turns α to $A'G$.

$$A(l_1, b), A'(a - l_2 \cos \alpha, l_2 \sin \alpha + b)$$

$$B(l_1, 0), B' \left(\frac{l_1}{\cos \beta_1} \cos(\beta_1 - \theta_1), \frac{l_1}{\cos \beta_1} \sin \beta_1 - \frac{l_1}{\cos \beta_1} \sin(\beta_1 - \theta_1) \right)$$

Assuming that the vertical distance of AB is fixed, $(A'B')_y$ can be given by:

$$(A'B')_y = (AB)_y = l_2 \sin \alpha + b - l_1 \tan \beta_1 + \frac{l_1}{\cos \beta_1} \sin(\beta_1 - \theta_1) = b$$

$$\alpha = \arcsin \left[\frac{l_1}{l_2} \tan \beta_1 - \frac{l_1}{l_2 \cos \beta_1} \sin(\beta_1 - \theta_1) \right] \quad (1)$$

$$(A'B')_x = a - l_2 \cos \alpha - \frac{l_1}{\cos \beta_1} \cos(\beta_1 - \theta_1) \quad (2)$$

Taking Eq. (1) into Eq. (2) is rearranged by:

$$(A'B')_x = a - l_2 \cos \left\{ \arcsin \left[\frac{l_1}{l_2} \tan \beta_1 - \frac{l_1}{l_2 \cos \beta_1} \sin(\beta_1 - \theta_1) \right] \right\} - \frac{l_1}{\cos \beta_1} \cos(\beta_1 - \theta_1) \quad (3)$$

Assuming that the parallel distance of AB is $X = |(A'B')_x|$.

$$X = \left| a - l_2 \cos \left\{ \arcsin \left[\frac{l_1}{l_2} \tan \beta_1 - \frac{l_1}{l_2 \cos \beta_1} \sin(\beta_1 - \theta_1) \right] \right\} - \frac{l_1}{\cos \beta_1} \cos(\beta_1 - \theta_1) \right| \quad (4)$$

In Fig. 2, if the angle between $O''F$ and X axis is β_2 , the coordinates of O'' is $(l_1 + l_2, l_2 \tan \beta_2)$. When $O''F$ turns θ_2 to $O''F'$, EC turns α to $E'C$.

$$E(l_1 + 2l_2, b), E'(l_1 + l_2 + l_2 \cos \alpha, l_2 \sin \alpha + b)$$

$$F(l_1 + 2l_2, 0), F' \left(l_1 + l_2 + \frac{l_2}{\cos \beta_2} \cos(\beta_2 - \theta_2), l_2 \tan \beta_2 - \frac{l_2}{\cos \beta_2} \sin(\beta_2 - \theta_2) \right)$$

Assuming that the vertical distance of EF is fixed, $(E'F')_y$ can be described by:

$$(E'F')_y = (EF)_y = l_2 \sin \alpha + b - l_2 \tan \beta_2 + \frac{l_2}{\cos \beta_2} \sin(\beta_2 - \theta_2) = b$$

$$\alpha = \arcsin \left[\tan \beta_2 - \frac{\sin(\beta_2 - \theta_2)}{\cos \beta_2} \right] \quad (5)$$

$$(E'F')_x = l_2 \cos \alpha - \frac{l_2}{\cos \beta_2} \cos(\beta_2 - \theta_2) \quad (6)$$

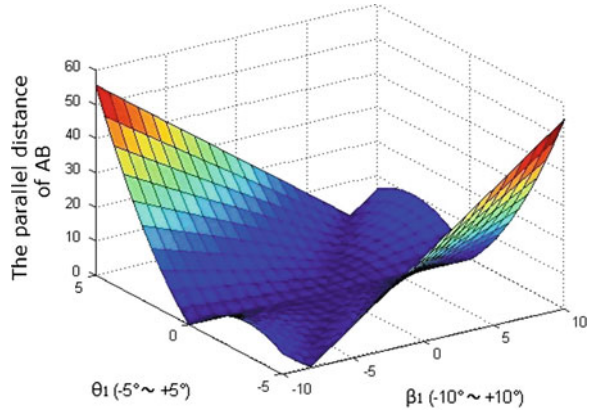
Taking Eq. (5) into Eq. (6) can be rearranged as:

$$(E'F')_x = l_2 \cos \left\{ \arcsin \left[\tan \beta_2 - \frac{\sin(\beta_2 - \theta_2)}{\cos \beta_2} \right] \right\} - \frac{l_2}{\cos \beta_2} \cos(\beta_2 - \theta_2) \quad (7)$$

Assuming that the parallel distance of EF is $X' = |(E'F')_x|$.

$$X' = \left| l_2 \cos \left\{ \arcsin \left[\tan \beta_2 - \frac{\sin(\beta_2 - \theta_2)}{\cos \beta_2} \right] \right\} - \frac{l_2}{\cos \beta_2} \cos(\beta_2 - \theta_2) \right| \quad (8)$$

Fig. 4 3D diagram of X changing along with θ_1 and β_1



3.2 Constraint Conditions

According to the real vehicle size, $\beta_1 = 9.2^\circ$ as O' reach the limit height. In the 2D diagram of mechanism, the angle range of β_1 was taken as $[-10^\circ, 10^\circ]$. As the limit frame fixed on the body plays a role in limiting the rotation of balance beam, the angle range of α was taken as $[-10^\circ, 10^\circ]$. According to Eq. (1), θ_1 is changing along with β_1 . The maximum $\theta_1 = 4.54^\circ$ and minimum $\theta_1 = -4.54^\circ$ through calculation. In the 2D diagram of mechanism, the angle range of θ_1 was taken as $[-5^\circ, 5^\circ]$.

Similarly, $\beta_2 = 26.8^\circ$ as O'' reach the limit height. In the 2D diagram of mechanism, the angle range of β_2 was taken as $[-27^\circ, 27^\circ]$. According to Eq. (5), θ_2 is changing along with β_2 . The maximum $\theta_2 = 9.58^\circ$ and minimum $\theta_2 = -9.52^\circ$ through calculation. In the 2D diagram of mechanism, the angle range of θ_2 was taken as $[-10^\circ, 10^\circ]$.

3.3 Result Analysis

Equation (4) reflects the relationship of X changing along with θ_1 and β_1 . The 3D diagram of the X changing along with θ_1 and β_1 is illustrated in Fig. 4. On the basis of Eq. (4), take 5 kind of β_1 as $-10^\circ, -5^\circ, 0^\circ, 5^\circ, 10^\circ$, the curve of AB horizontal spacing X in different β_1 as θ_1 being the independent variable was shown in Fig. 5.

From Figs. 4 and 5, it can be seen that in the two stages of θ_1 changing from -10° to 0° and from 0° to 10° , the variation of AB parallel spacing X in five kinds of β_1 Angle is generally opposite. AB parallel spacing average \bar{X} is taken for the comprehensive investigation. Different \bar{X} in five kinds of β_1 is shown in Table 1.

It can be seen from Table 1 that AB spacing average \bar{X} reduce gradually while β_1 increases from -10° to 0° ; AB spacing average \bar{X} increase gradually while β_1 increases from 0° to 10° ; and AB spacing average \bar{X} reach minimum value at

Fig. 5 2D diagram of X changing along with β_1

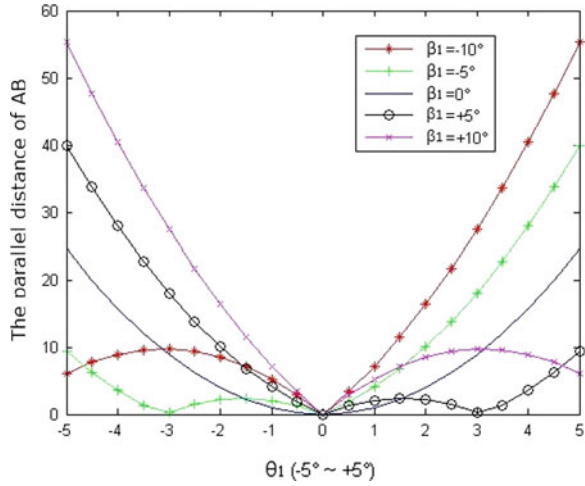
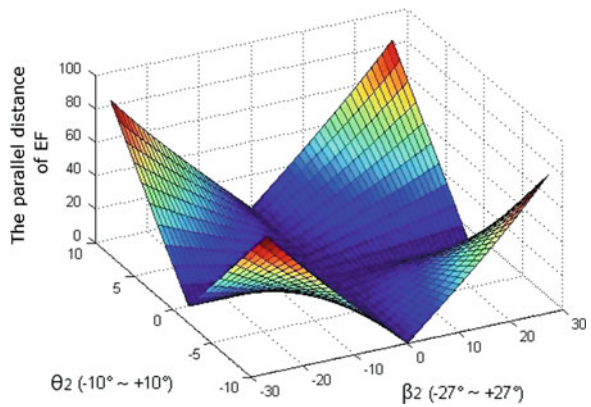


Table 1 \bar{X} values in five kinds of β_1 angle

$\beta_1(^{\circ})$	-10	-5	0	5	10
$\bar{X}(\text{mm})$	16.16	9.97	9.03	9.97	16.16

Fig. 6 3D diagram of X' changing along with θ_2 and β_2



$\beta_1 = 0^{\circ}$. Since the rubber force depends on its deformation, so it can be concluded that the X shear force average of rubber spring is the smallest as $\beta_1 = 10^{\circ}$.

Equation (8) reflects the relationship of X' changing along with θ_2 and β_2 . The 3D diagram of X' changing along with θ_2 and β_2 is reported in Fig. 6. On the basis of Eq. (8), take 5 kind of β_2 as -27° , -14° , 0° , 14° , 27° , the curve of EF horizontal spacing X' in different β_1 as θ_2 for the independent variable is shown in Fig. 7.

Fig. 7 2D diagram of X' changing along with θ_2

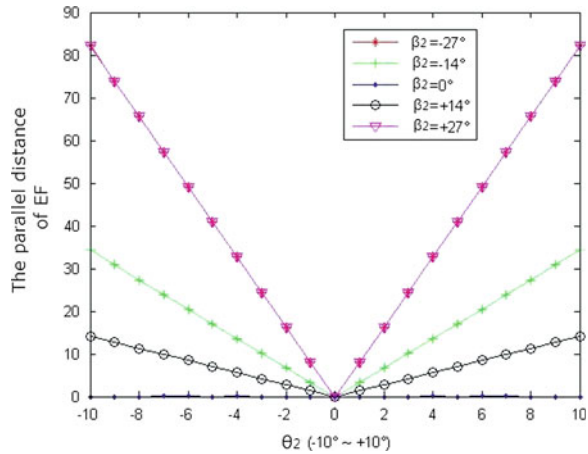


Table 2 \bar{X}' value in five kinds of β_2 angle

$\beta_2(^{\circ})$	-27	-14	0	14	27
$\bar{X}'(\text{mm})$	42.91	20.99	0.00	20.99	42.91

From Figs. 6 and 7, it can be found that in the two stages of θ_2 changing from -10° to 0° , and from 0° to 10° , the variation of EF spacing X' in five kinds of β_2 Angle is reducing firstly and then is increasing. EF spacing average \bar{X}' is taken for the comprehensive investigation. \bar{X}' in five kinds of β_2 Angle is shown in Table 2.

From Table 2, It can be seen that, when β_2 increases from -27° to 0° , EF spacing average \bar{X}' reduce gradually; When β_2 increases from 0° to 27° , EF spacing average \bar{X}' increase gradually; EF spacing average \bar{X}' reach minimum as $\beta_2 = 0^{\circ}$. Since the rubber force depends on its deformation, so it can be concluded that the X shear force average of rubber spring is the smallest as $\beta_2 = 0^{\circ}$.

4 Analysis of the Relative Movement Between Panhard Rod and Balance Beam

4.1 Kinematics Equations

In Fig. 3, the angle between Panhard rod HB and X axis is γ . When HB turns θ to HB' , assume A arrive A' .

$$A(0, a), A'(0, a + l \tan \gamma + l \cos \gamma \sin(\theta - \gamma))$$

$$B(0, 0), B'(l \cos \gamma [\cos \gamma - \cos(\theta - \gamma)], l \tan \gamma + l \cos \gamma \sin(\theta - \gamma))$$

As it was assumed that AB 's vertical distance of is fixed, the parallel distance of AB can be described as follows is as follows.

$$(A'B')_x = l \cos \gamma [\cos \gamma - \cos(\theta - \gamma)] \quad (9)$$

The parallel distance of AB was assumed to be $X = |(A'B')_x|$

$$X = |l \cos \gamma [\cos \gamma - \cos(\theta - \gamma)]| \quad (10)$$

In Fig. 3, When B turns θ to B' , horizontal ordinate of B' is $l \cos \gamma [\cos \gamma - \cos(\theta - \gamma)]$. When BD turns φ to $B'D'$, horizontal ordinate of D' is $l \cos \gamma [\cos \gamma - \cos(\theta - \gamma)] + T \cos \varphi$. As it was assumed that the vertical distance of CD is fixed, the parallel distance of CD is given by:

$$(C'D')_x = T - T \cos \varphi - l \cos \gamma [\cos \gamma - \cos(\theta - \gamma)] \quad (11)$$

The parallel distance of CD was assumed to be X' .

$$X' = |C'D'_x| = |T - T \cos \varphi - l \cos \gamma [\cos \gamma - \cos(\theta - \gamma)]| \quad (12)$$

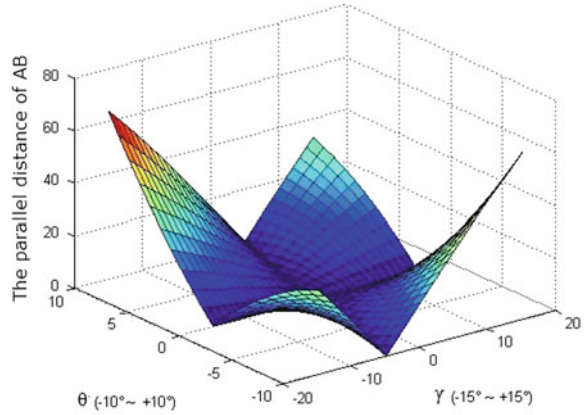
Equation (12) contains three variable values: γ , θ and φ . According to the trajectories of axle, if γ and θ were fixed, X' would get minimum value when $B'D'$ parallel to the X axis; When absolute value of angle φ between the X axis and $B'D'$ increase gradually, X' also increase; When D' reach the limit position, X' would get maximum value. For more convenient investigation of the relationship between X' and γ , BD 's limit position is calculated to eliminate the influence of the angle φ . CD 's maximum horizontal space X'_{\max} is analyzed, and equations of X'_{\max} changing along with γ and θ are deduced.

$$X'_{\max} = T - l \cos \gamma [\cos \gamma - \cos(\theta - \gamma)] - \sqrt{T^2 - [16l^2 + l^2 \tan^2 \gamma + l^2 \cos^2 \gamma \sin^2(\theta - \gamma)]} \quad (13)$$

4.2 Constraint Conditions

According to the real vehicle size, $\gamma = 15.4^\circ$ as H reach the limit height. In the 2D diagram of mechanism, the angle range of γ was taken as $[-15^\circ, 15^\circ]$. The angle range of α was taken as $[-10^\circ, 10^\circ]$. As θ is changing along with γ , the maximum $\theta_1 = 4.54^\circ$ and minimum $\theta_1 = -4.54^\circ$ through calculation. In the 2D diagram of mechanism, the angle range of θ was taken as $[-10^\circ, 10^\circ]$.

Fig. 8 *AB* horizontal spacing X change according to θ and γ



4.3 Result Analysis

Equation (10) reflects the relationship of X changing along with θ and γ . The 3D diagram of the *AB* horizontal spacing X change according to θ and γ is shown in Fig. 8. On the basis of Eq. (10), taking 7 kind of γ as -15° , -10° , -5° , 0° , 5° , 10° , 15° , the curve of *AB* horizontal spacing X in different γ is shown in Fig. 9.

Based on the results of Figs. 8 and 9, *AB* spacing average \bar{X} is taken for the comprehensive investigation in the stage of θ changing from -10° to 10° . \bar{X} values at different kinds of γ are shown in Table 3.

It can be seen from Table 3 that, *AB* spacing average \bar{X} reduce gradually when γ increases from -15° to 0° ; *AB* spacing average \bar{X} increase gradually when γ increases from 0° to 15° ; *AB* spacing average \bar{X} reach minimum value at $\gamma = 0^\circ$. Since the rubber force depends on its deformation, it can be concluded that the Y shear force average of rubber spring is the smallest at $\gamma = 0^\circ$.

Equation (13) reflects the relationship of X'_{\max} changing along with θ and γ . Figure 10 shows its 3D diagram. On the basis of Eq. (13), take 7 kind of γ as -15° , -10° , -5° , 0° , 5° , 10° , 15° , the curve of *CD*'s X'_{\max} in different θ is shown in Fig. 11.

It can be seen from Figs. 10 and 11 that, in 7 different γ , when θ increases from -10° to 10° , *CD* spacing maximum X'_{\max} occurs as θ was maximum or minimum. The variation is decreasing firstly and then increasing gradually. *CD* spacing maximum X'_{\max} reach minimum as $\gamma = 0^\circ$. X'_{\max} value in different kinds of γ is shown in Table 4.

From Figs. 10, 11, and Table 4, it is concluded that the Y shear force peak of rubber spring is the smallest at the point $\gamma = 0^\circ$.

Fig. 9 AB horizontal spacing X in different γ

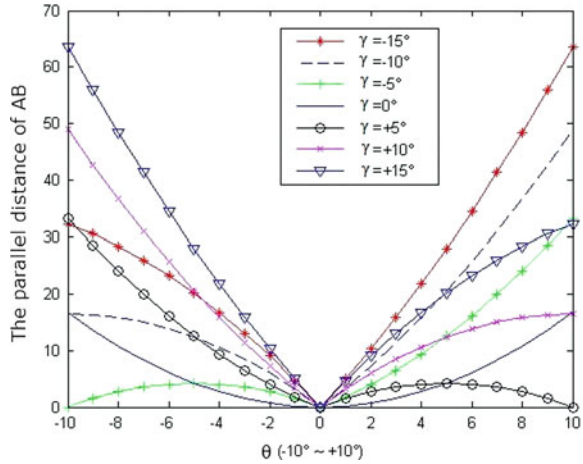
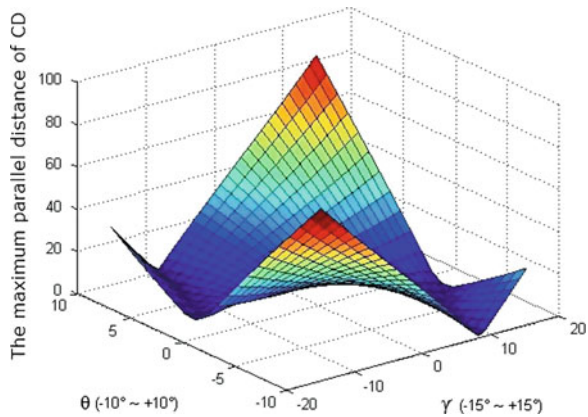


Table 3 \bar{X} values in different γ

$\gamma(^{\circ})$	-15	-10	-5	0	5	10	15
$\bar{X}(\text{mm})$	25.19	17.23	8.75	6.16	8.75	17.23	25.19

Fig. 10 X'_{max} change according to θ and γ



5 Conclusion

Both the angles between the HADT’s balanced suspension guiding mechanism and vehicle coordinate system X axis and between Panhard rod and the Y axis have significant effect on the rubber spring’s shear force. The rubber spring average or peak shear force could reduce to the minimum when both of the angles are 0° based on the calculation and analysis. In consideration of the vehicle’s overall layout and the minimum ground clearance, it is suggested to make the guiding mechanism parallel to the vehicle coordinate system X axis, and make Panhard rod parallel to

Fig. 11 X' max in different γ

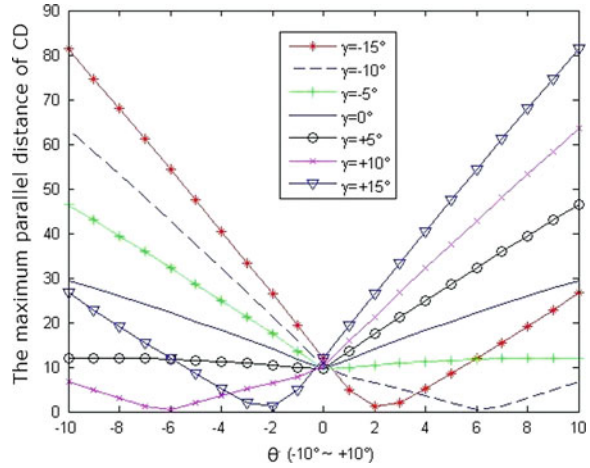


Table 4 X' max in different γ

$\gamma(^{\circ})$	-15	-10	-5	0	5	10	15
X' max(mm)	82.31	63.48	48.57	29.62	48.57	63.48	82.31

the Y axis in designing such heavy dump truck’s balanced suspension, which helps to receive the effect of reducing the balanced suspension’s interference.

References

- Liu J, Zhang W, Lan C (2003) Comparison of articulated dump truck and rigid dump truck. Min Process Equip 9:21–23 (in Chinese)
- Akbari A, Lohmann B (2008) Multi-objective preview control of active heavy vehicle suspensions. IFAC Proc Volumes 17(1):20–52
- Woodrooffe J (1996) Heavy truck suspension dynamics: methods for rubber suspension road friendliness and ride quality. Commercial Veh Highw Dyn 1201:17–23 SAE Special Publications
- Xu Z, Sun Q, Ma Z, et al. (2005) Articulated dump truck’s rubber spring suspension system dynamics simulation analysis and experimental study (in Chinese). Eng Sci 9:34–38
- Heinz H (2002) Advanced vehicle technology. Elsevier Limited Press, London
- Margolis D (2001) The stability of trailing arm suspension in heavy trucks. Int J Veh Des 25(3):211–229
- Zhang J, Chang L, Ma W (2009) Finite element analysis of the balance suspension failure mode and the effect. Automobile Technol 10:9–12 (in Chinese)
- Jiang Z, Streit DA (2001) El-Gindy moustafa. Heavy vehicle ride comfort: literature survey. Heavy Veh Syst 8(3):258–284
- Andersson D, Eriksson P (2004) Optimization of heavy dump truck suspension. Veh Sys Dyn 41(2):547–556
- Pang H, Li H, Fang Z et al (2011) Stiffness matching and ride comfort optimization of heavy vehicle’s suspension based on ADAMS. Appl Mech Mater, Frontiers Manufact Des Sci 44–47:1734–1738

A Probabilistic Optimization Approach to Vehicle Suspension Design Under Uncertainty

Xiaokai Chen, Qinghai Zhao, Yi Lin and Kang Song

Abstract The problem of vehicle development subject to uncertain parameters is of great significance in realistic engineering applications. A probabilistic optimization approach are proposed to deal with the uncertainty and demonstrated in vehicle suspension design application. The uncertainty propagation is realized by Sparse Grid Techniques. As a hierarchical multilevel Multidisciplinary Design Optimization (MDO) method with uncertainty, Probabilistic Analytical Target Cascading (PATC) is enhanced by considering the first two statistical moments of interrelated responses. The proposed methods were demonstrated by a suspension probabilistic optimization problem, and were solved by the proposed PATC and SGNI. Results show that the enhanced PATC has good effectiveness and efficiency.

Keywords Suspension · Probabilistic optimization · Uncertainty · Multidisciplinary design optimization (MDO)

F2012 -G01-018

X. Chen (✉) · Q. Zhao · Y. Lin · K. Song
School of Mechanical Engineering, Beijing Institute of Technology,
No. 5 Zhongguancun South Street, 100081, Beijing, China
e-mail: chenxiaokai@263.net

Y. Lin
Beijing Automotive Technology Center, No. 10 Huaweili, 100021 Beijing, China

1 Introduction

The design of suspension affects the vehicle performance in terms of ride, handling, rollover stability, braking and traction. Most research in suspension design and tuning was based on the assumption that all parameters are deterministic. Actually, the spring stiffness and damping rate may vary with respect to the nominal value due to production tolerances and/or wear, ageing. The tyre stiffness can have stochastic variations because of the variety of possible vehicle loading conditions and the uncertainty of the inflating pressure. In addition, the weight and CG position of vehicle often exhibit a significant variability. Hence, the problem of vehicle uncertain parameters is of great significance in realistic engineering applications.

Multidisciplinary Design Optimization (MDO) allows designers to incorporate all relevant disciplines simultaneously. There are two main challenges involved in MDO under uncertainty for hierarchical systems: the MDO framework and the uncertainty propagation. Probabilistic Analytical Target Cascading (PATC) is a hierarchical multilevel MDO method with uncertainty. Due to the need to describe the probabilistic character, at least the first two statistical moments should be matched. A wide variety of uncertainty propagation methods exist in literature, such as Monte Carlo simulation, Taylor series method, polynomial chaos expansion and the numerical integration-based methods. In this chapter, to realize the uncertainty propagation and to provide accurate and efficient solutions for high-dimension problem, Sparse Grid Numerical Integration was extended for estimating the first two moments of the system output performances and constraints. PATC was enhanced by considering the first two statistical moments of interrelated responses and linking variables.

In this chapter, [Sect. 2](#) discusses the deterministic Analytical Target Cascading and the Probabilistic Analytical Target Cascading formulation, respectively. Sparse Grid Technique as the new method of uncertainty propagation is presented with detail characterization to evaluate the first two moments in [Sect. 3](#). In [Sect. 4](#), the vehicle performance design is formulated based on Probabilistic Analytical Target Cascading, including system element and subsystem element. The response surface method is adopted to calculate the performance index and the reliability constraints are evaluated by Sparse Grid Technique. At last, the conclusion is presented in [Sect. 5](#).

2 Probabilistic Analytical Target Cascading Formulation

2.1 Review of the Deterministic Formulation

Product development includes a process of meeting targets T set by the enterprise level decision-making models [1], expressed as an optimization problem

$$\begin{aligned}
& \text{Given } T \\
& \text{find } \mathbf{X} \\
& \min \|T - R(\mathbf{X})\| \\
& \text{s.t. } g(\mathbf{X}) \leq 0
\end{aligned} \tag{1}$$

The vector X includes all design variables, while the vector R represents the system's responses. The vector T includes the target values for R , fixed during the optimization process. The design objective is to find a feasible design X that brings the responses R as close as possible to the assigned targets T . The quality of a design is measured by the deviation between R and T , using some (possibly weighted) norm). In this chapter, we use the l_2 -norm to measure deviations, but square the norms in the computational implementation of the process to avoid derivative discontinuities.

Using the concept of ATC, the problem in Eq. (1) is decomposed hierarchically into elements at multiple levels. Coupling among elements is captured by linking variables. Linking variables can be design variables shared among elements with the same parent or responses from "sibling" elements at the same level [2]. Each element is a subproblem of a smaller size. Inputs to an element include its local design variables, responses from its children elements, linking variables among its children elements, and linking variables from sibling elements. The design and analysis models at multiple levels are hierarchical by nature as the output of a lower-level model becomes the input of a higher-level model.

The deterministic ATC optimization of element j at level i (O_{ij}) with n_{ij} children is formulated in Eq. (2). The vector r_{ij} represents the element's responses. The optimization variables include local design variables x_{ij} , linking variables y_{ij} , targets for children responses $r_{(i+1)k}$, $k = 1, \dots, n_{ij}$, targets for children linking variables $y_{(i+1)j}$, and tolerance optimization variables ε^r and ε^y to coordinate children responses and linking variables for design consistency. The collective optimization variables will from now on be referred to as *decision variables*. Note that element O_{ij} collects all linking variables of its children in a single vector $y_{(i+1)j}$. The k th child of O_{ij} uses a selection matrix $S_{(i+1)k}$, to identify which components of $y_{(i+1)j}$ correspond to the linking variables $y_{(i+1)k}$ of that child [3]. Similarly, the O_{ij} itself uses its selection matrix S_{ij} to identify the target values for its linking variables from the vector y_{iq}^U , where q denotes its parent.

$$\begin{aligned}
& \text{Given } r_{ij}^U, y_{iq}^U, r_{ij}^U, y_{iq}^U, y_{(i+1)k}^L, S_{ij}, S_{(i+1)k}, \quad k = 1, \dots, n_{ij} \\
& \text{find } r_{(i+1)k}, x_{ij}, y_{ij}, y_{(i+1)j}, \varepsilon_{ij}^r, \varepsilon_{ij}^y, \quad k = 1, \dots, n_{ij} \\
& \min \left\| r_{ij} - r_{ij}^U \right\| + \left\| y_{ij} - S_{ij} y_{iq}^U \right\| + \varepsilon_{ij}^r + \varepsilon_{ij}^y
\end{aligned} \tag{2}$$

$$\begin{aligned}
s.t \quad & \sum_{k=1}^{n_{ij}} \left\| r_{(i+1)k} - r_{(i+1)k}^L \right\| \leq \varepsilon_{ij}^r \\
& \sum_{k=1}^{n_{ij}} \left\| S_{(i+1)k} y_{(i+1)j} - y_{(i+1)k}^L \right\| \leq \varepsilon_{ij}^y \\
& \sum_{k=1}^{n_{ij}} \left\| S_{(i+1)k} y_{(i+1)j} - y_{(i+1)k}^L \right\| \leq \varepsilon_{ij}^y
\end{aligned}$$

$$\text{where } r_{ij} = f_{ij} \left(r_{(i+1)1}, \dots, r_{(i+1)n_{ij}}, x_{ij}, y_{ij} \right)$$

In Eq. (2), superscripts U indicate targets assigned by the parent element, while superscripts L indicate values passed from children elements. The targets for responses and linking variables of element O_{ij} are r_{ij}^U and $S_{ij} y_{ij}^U$, respectively. The actual achievable values, $r_{(i+1)k}^L$ and $y_{(i+1)k}^L$, are passed up to O_{ij} from its children. Solving the problem in Eq. (2), element O_{ij} finds the achievable values of its responses and linking variables that are the closest to r_{ij}^U and $S_{ij} y_{ij}^U$, respectively. O_{ij} then passes them back to its parent element as r_{ij}^L and y_{ij}^L , respectively. It also determines the optimal values for its children responses and linking variables with the least inconsistency from $r_{(i+1)k}^L$ and $y_{(i+1)k}^L$. These optimal values are passed down as targets, $r_{(i+1)k}^U$ and $y_{(i+1)j}^U$.

2.2 Generalized Probabilistic ATC Formulation

In a probabilistic design optimization formulation, uncertain quantities are random variables that can be characterized by a probability density function (PDF), a cumulative distribution function (CDF), or descriptors such as moments [4]. We use the superscript v to denote probabilistic characteristics of a random variable. For example, for a normally distributed random variable X , $X^v = [\mu_X, \sigma_X]$. Still taking the objective as meeting design targets, the probabilistic AIO (PAIO) optimization formulation is

$$\begin{aligned}
& \text{Given } T^v \\
& \text{find } X^v \\
& \min \|T^v - R^v\| \tag{3} \\
s.t \quad & \Pr[g_m(X) \leq 0] \geq \alpha_m, \quad m = 1, \dots, M \\
& \text{with } R = f(X)
\end{aligned}$$

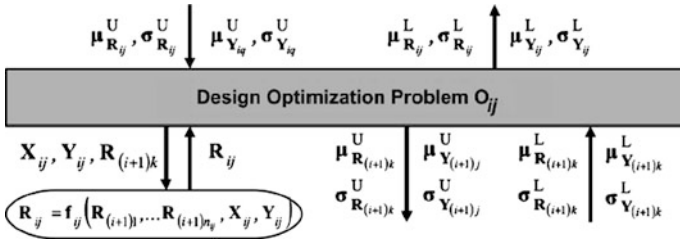


Fig. 1 Information flow for particular PATC formulation

where M is the number of constraints. In Eq. (3), capital letters R and X are used to represent the random variables [instead of r and x used in Eq. (2)]. We assume that an appropriate uncertainty propagation technique for computing R^v is available. Design constraints are posed using the probabilistic feasibility formulation [5], with α_m denoting the required reliability levels. Note that the system design targets vector T^v in Eq. (3) has a different meaning from T , the targets for deterministic responses in Eq. (2). In the presence of uncertainty, T^v consists of target values that correspond to the probabilistic characteristics R^v . Setting the targets for probabilistic characteristics is important because variations of system performance can lead to customer dissatisfaction and additional costs to the producer. On the other hand, reducing performance variations often causes increase in the cost of product development. For example, in considering vehicle engine noise under different operating temperatures, design targets should be set for both the nominal value of engine noise and its standard deviation.

2.3 PATC Formulation Based on Matching Mean and Variance

The particular implementation of the general PATC formulation presented in this article sets targets on mean and standard deviation for element performance based on robust design considerations and matches the first two moments of interrelated responses and linking variables. The information flow of the design optimization problem for element j at level i (element O_{ij}) is shown in Fig. 1.

R_{ij} and Y_{ij} are vectors of random responses and linking variables, respectively. R_{ij} are evaluated using analysis or simulation models $R_{ij} = f_{ij}(R_{(i+1)1}, \dots, R_{(i+1)n_{ij}}, X_{ij}, Y_{ij})$. Targets for mean and standard deviation of R_{ij} and Y_{ij} are assigned by the parent element as $(\mu_{R_{ij}}^U, \sigma_{R_{ij}}^U)$ and $(\mu_{Y_{ij}}^U, \sigma_{Y_{ij}}^U)$, respectively. Achievable values of mean and standard deviation for R_{ij} and Y_{ij} are the outputs of the optimization problem for element O_{ij} , feeding back to its parent element as $(\mu_{R_{ij}}^L, \sigma_{R_{ij}}^L)$ and $(\mu_{Y_{ij}}^L, \sigma_{Y_{ij}}^L)$. Similarly, achievable values of its children element responses and linking variables are passed to O_{ij} as $(\mu_{R_{(i+1)k}}^L, \sigma_{R_{(i+1)k}}^L)$ and $(\mu_{Y_{(i+1)k}}^L, \sigma_{Y_{(i+1)k}}^L)$, and must be taken into account for consistency. The optimization problem for element O_{ij} is solved to find the optimum values of the probabilistic characteristics (not limited

to the first two moments) of its local design variables X_{ij} and to determine the target values for the responses and linking variables ($\mu_{R(i+1)k}^U$, $\sigma_{R(i+1)k}^U$) and ($\mu_{Y(i+1)j}^U$, $\sigma_{Y(i+1)j}^U$), respectively, of its children elements.

Given $\mu_{R_{ij}}^U, \sigma_{R_{ij}}^U, \mu_{Y_{iq}}^U, \sigma_{Y_{iq}}^U, \mu_{R(i+1)k}^L, \sigma_{R(i+1)k}^L, \mu_{Y(i+1)j}^L, \sigma_{Y(i+1)j}^L, S_{ij}, S_{(i+1)k}, \quad k = 1, \dots, n_{ij}$

find $\mu_{R(i+1)k}, \sigma_{R(i+1)k}, X_{ij}^V, \mu_{Y_{ij}}, \sigma_{Y_{ij}}, \mu_{Y(i+1)j}, \sigma_{Y(i+1)j}, \varepsilon_{ij}^{\mu_R}, \varepsilon_{ij}^{\sigma_R}, \varepsilon_{ij}^{\mu_Y}, \varepsilon_{ij}^{\sigma_Y}, \quad k = 1, \dots, n_{ij}$

$$\begin{aligned} \min \quad & \left\| \mu_{R_{ij}} - \mu_{R_{ij}}^U \right\| + \left\| \sigma_{R_{ij}} - \sigma_{R_{ij}}^U \right\| + \left\| \mu_{Y_{ij}} - S_{ij} \mu_{Y_{iq}}^U \right\| + \left\| \sigma_{Y_{ij}} - S_{ij} \sigma_{Y_{iq}}^U \right\| + \varepsilon_{ij}^{\mu_R} + \varepsilon_{ij}^{\sigma_R} \\ & + \varepsilon_{ij}^{\mu_Y} + \varepsilon_{ij}^{\sigma_Y} \end{aligned} \quad (4)$$

$$s.t. \quad \sum_{k=1}^{n_{ij}} \left\| \mu_{R(i+1)k} - \mu_{R(i+1)k}^L \right\| \leq \varepsilon_{ij}^{\mu_R}$$

$$\sum_{k=1}^{n_{ij}} \left\| \sigma_{(i+1)k} - \sigma_{R(i+1)k}^L \right\| \leq \varepsilon_{ij}^{\sigma_R}$$

$$\sum_{k=1}^{n_{ij}} \left\| S_{(i+1)k} \mu_{Y(i+1)j} - \mu_{Y(i+1)k}^L \right\| \leq \varepsilon_{ij}^{\mu_Y}$$

$$\sum_{k=1}^{n_{ij}} \left\| S_{(i+1)k} \sigma_{Y(i+1)j} - \sigma_{Y(i+1)k}^L \right\| \leq \varepsilon_{ij}^{\sigma_Y}$$

$$\Pr [g_{ij,m}(R_{ij}, X_{ij}, Y_{ij}) \leq 0] \geq \alpha_{ij,m}, \quad m = 1, \dots, M$$

$$\text{where } R_{ij} = f_{ij}(R_{(i+1)1}, \dots, R_{(i+1)n_{ij}}, X_{ij}, Y_{ij})$$

We emphasize that Eq. (4) is a particular PATC formulation. Even though targets and interrelated random variables are matched using the first two moments, the probabilistic characteristics of local random variables X_{ij} are not restricted to the first two moments. It should also be noted that in the above formulation the number of optimization variables is approximately twice as large relative to that of the formulation since each random variable is represented by more than one descriptor [6].

A lot of efforts have been made to develop methods of uncertainty propagation in various fields such as structural reliability, stochastic mechanics, quality engineering and considerably many methods are now available. Among various methods, Full Factorial Numerical Integration (FFNI) [7] and Univariate Dimension Reduction (UDR) [8] are commonly used to evaluate the statistical moments through direct numerical integration. The two methods are flexible with the type of input distributions and their accuracy depends on the integration order of the quadrature rule adopted. While the computational cost increases exponentially in

FFNI, UDR has a linear increase of function evaluations with the number of input random variables. However, this outstanding efficiency is obtained by sacrificing accurate considerations of the interaction effects which may exist in the system. In this study, Sparse Grid Technique (SGT) [9, 10] is proposed to calculate the reliability constraints while reduce the CPU consumption and considering the interaction effects within input random variables.

When dealing with uncertainties that propagate throughout the multilevel hierarchy, one question is at which level the PATC process should begin. From an organization's viewpoint, the design process should start from the highest level, as usually overall targets are assigned and cascaded down from top to bottom. On the other hand, it may be beneficial to start at the level where uncertainty cannot be reduced, i.e., at the level where we cannot control the variation of random inputs. Typically, this occurs at the bottom level, where most random design variables have known distributions. The bottom-up coordination strategy imitates the uncertainty propagation process.

3 Sparse Grid Technique

Let U_1^i and w_1^i denote the collocation points and weights for one-dimensional. Thus, the collocation points space generated by SGT for d -dimensional space with k -level accuracy is [11]:

$$\vec{U}_d^k = \bigcup_{q-d+1 \leq |i| \leq q} U_1^{i_1} \otimes U_1^{i_2} \otimes \dots \otimes U_1^{i_d} \quad (5)$$

where $q = k + d$, $|i| = i_1 + \dots + i_d$.

It can be found that the direct tensor product scheme can result in the exponential increasing of the number of collocation points with respect to dimensionality, while Sparse Grid technique could reduce the number of required collocation points remarkably. Furthermore, the weight w_l corresponding to the collocation point $\vec{\xi}_l = [\xi_{j_{i_1}}^{i_1}, \dots, w_{j_{i_d}}^{i_d}] \in \vec{U}_d^k$ is:

$$w_l = (-1)^{q-|i|} \binom{d-1}{q-|i|} (w_{j_{i_1}}^{i_1} \dots w_{j_{i_d}}^{i_d}) \quad (6)$$

Then, the integration of nonlinear function $f(\vec{\xi})$ in terms of Gaussian random variables $\vec{\xi}$ can be computed as Eq. (7) up to $(2k + 1)$ -level accuracy.

$$\int_{\vec{\xi} \in \vec{U}_d^k} f(\vec{\xi}) p(\vec{\xi}) d\vec{\xi} \approx \sum_{l=1}^{P_s} w_l f(\vec{\xi}_l) \quad (7)$$

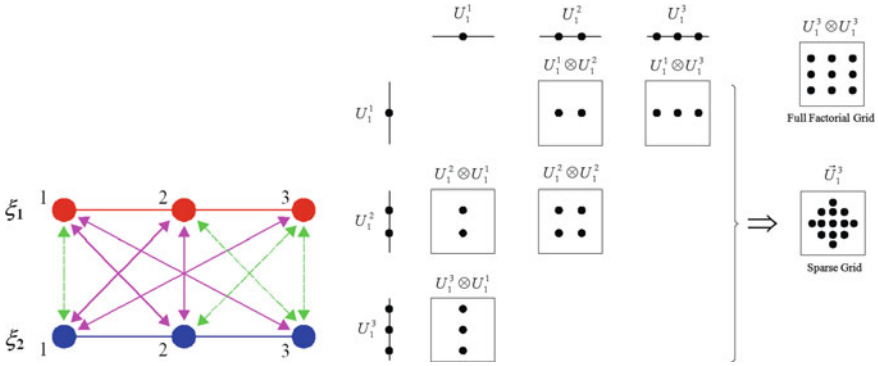


Fig. 2 Sparse grid and FFNI ($d = 2, k = 2$)

Sparse grids ($d = 2, k = 2$) are built based on the Gaussian integration points as shown in Fig. 2. Assumed that the two dimensions are equally important, FFNI method could obtain 9 ($3 * 3$) number of collocation point by direct tensor product scheme. However, for the sparse grids method, at first, multi-exponential combination $[i_1, i_2]$ need be calculated by satisfying the follow inequality condition:

$$3 \leq |i_1 + i_2| \leq 4 \tag{8}$$

$$[i_1, i_2] = \{12; 13; 21; 22; 31\}$$

Note that the number of nodes in the first dimension and the second dimension are set equal to the value of the index in the multi-exponential combination. Then the totally collocation points are obtained by sparse grid method, which treat the one dimension collocation points and weight by direct tensor product.

The process to estimate the moment based on the sparse grid technology is as follows:

Setup 1: At first, the level number $k (\geq 0)$ for spares grid should be determined. All possible index combinations $i = (i_1, \dots, i_d)$ that satisfy the follow inequality formulation:

$$q - d + 1 \leq |i| \leq q \tag{9}$$

Setup 2: For each combination $i = (i_1, \dots, i_d)$, according to the integration point number $i_j (j = 1, \dots, d)$ and the distribution of the random variable, the moment-matching method is used to obtain the corresponding one-dimensional Gaussian integration points and weights.

Setup 3: Based on the above points and weights, sparse grid collocation points and corresponding weights in d-dimensional random space are calculated using Eq. 6.

Setup 4: the formulation for the first second moments are obtained based on the sparse grid collocation points and weights as follows:

$$\mu_g = \int_{\vec{\xi} \in \bar{U}_d^k} g(\vec{\xi}) p(\vec{\xi}) d\vec{\xi} \approx \sum_{l=1}^{P_s} w_l g(\vec{\xi}^l) \quad (10)$$

$$\sigma_g = \int_{\vec{\xi} \in \bar{U}_d^k} (g(\vec{\xi}) - \mu_g)^2 p(\vec{\xi}) d\vec{\xi} \approx \sum_{l=1}^{P_s} w_l^s (g(\vec{\xi}^l) - \mu_g)^2 \quad (11)$$

4 Vehicle Performance Design Based on PATC

4.1 Building Approximate Model

Multibody model built in software ADAMS/Car could be used to accurately simulate handling and ride of vehicle. However, this model has complicated inner structure, including many modeling elements, connection and much information communication. So this model is not suitable for optimization, because it would largely increase computational complexity. In order to improve efficiency of computation, it is necessary to introduce approximate model.

In the optimization of handling and ride, front spring stiffness (x_1), rear spring stiffness (x_2), front damping (x_3), rear damping (x_4), diameter of front anti-roll bar (ARB) (x_5) and diameter of rear ARB (x_6) are selected as design variables. Optimization targets consist of understeer gradient (y_1), roll gradient of body (y_2), natural frequency (y_3), gain at the natural frequency (y_4), phase angle (y_5), average of maximum yaw angular velocity (y_6), average of maximum steering input (y_7), weight acceleration at driver seat (y_8) and weight acceleration at rear seat (y_9). In these optimization targets, y_1 and y_2 are used to characterize steady-state handling behavior (steady-state circular driving behavior); y_3 , y_4 and y_5 are used to characterize transient handling behavior (lateral transient response test methods); y_6 and y_7 are used to characterize handling behavior under close-loop driving; y_8 and y_9 are used to characterize ride behavior.

During building approximate model, cross-items in basis functions are ignored to reduce computational complexity, so the final basis functions is as follows.

$$x = [1, x_1, x_2, x_3, x_4, x_5, x_6, x_1^2, x_2^2, x_3^2, x_4^2, x_5^2, x_6^2, x_1^3, x_2^3, x_3^3, x_4^3, x_5^3, x_6^3] \quad (12)$$

Value ranges of design variables are $20.86 \leq x_1 \leq 38.74$, $20.86 \leq x_2 \leq 38.74$, $0.7 \leq x_3 \leq 1.3$, $0.7 \leq x_4 \leq 1.3$, $17.15 \leq x_5 \leq 31.85$, $13.65 \leq x_6 \leq 25.35$, respectively. Each design variable is assigned values in 5 levels according to its value range. With orthogonal test method, total 25 groups of combinations of design variables are applied in modeling. The obtained approximate model is

$$y_i = a_i x^T \quad i = 1, 2, \dots, 9 \quad (13)$$

in which, y_i represents the i th optimization target, a_i represents coefficient vector of the i th approximate function:

- a_1 [0.31939 -0.00561731 -0.0038368 -0.15906 -0.08891 -0.004797 0.0057403
0.00014616 0.00011137 0.14243 0.058794 0.00016756 -0.00039932 -1.2503e-
006 -1.101e-006 -0.041975 -0.01037 -1.907e-006 6.7919e-006];
- a_2 [3.2451 -0.049515 -0.035417 -1.8219 -1.3331 -0.043132 0.042491
0.0012286 0.00092793 1.6599 0.9779 0.00056947 -0.0028712 -1.0002e-005
-8.1547e-006 -0.49778 -0.21185 -1.9799e-007 4.8531e-005];
- a_3 [1.5957 -0.082149 0.012024 1.8153 -0.98984 0.023044 -0.0071399
0.0025286 -0.00055291 -1.9725 0.94603 -0.0010393 -3.6706e-005
-2.6125e-005 7.4642e-006 0.69136 -0.2963 1.3418e-005 -6.8172e-006];
- a_4 [17.686 -0.15199 -0.69133 -23.621 10.034 -0.84785 1.1163 0.0022785
0.022233 23.576 -11.625 0.030958 -0.066074 -1.9742e-006 -0.00023601
-7.652 4.3174 -0.0003876 0.0011815];
- a_5 [-39.608 3.2753 0.95191 2.5474 32.536 0.64574 0.45407 -0.09916
-0.026484 3.0195 -26.609 -0.02359 0.0041778 0.0009948 0.00024054
-2.4691 7.1654 0.00027519 -0.00016005];
- a_6 [22.235 -0.12584 -0.05293 -3.9039 0.094503 -0.2252 -0.34285
0.004373 0.0017691 3.9498 -0.097566 0.0085262 0.01733 -5.001e-005
-1.922e-005 -1.3037 0.024691 -0.00010936 -0.0002773];
- a_7 [126.48 -1.7118 -1.0421 -25.542 -7.8336 -2.1148 -0.80009 0.050153
0.03065 22.086 3.3403 0.086153 0.015408 -0.00048518 -0.00030379
-6.2617 0.13333 -0.0011148 -0.00015276];
- a_8 [-1.9798 0.027167 0.11113 0.97503 0.0019286 0.063003 0.10054
-0.00075639 -0.003471 -1.1689 -0.067492 -0.002522 -0.0047411
8.136e-006 3.7004e-005 0.46173 0.087407 3.8146e-005 7.6884e-005];
- a_9 [-2.3712 0.046753 0.11201 1.9216 -0.32951 0.083643 0.10493
-0.0015259 -0.0034472 -2.0751 0.20402 -0.003299 -0.0048236 1.7e-
005 3.7582e-005 0.74222 0.038025 4.6909e-005 7.4727e-005];

4.2 PATC Formulation

Geometric programming problems with polynomials (polynomials with positive constants) are known to have a unique global optimum. The PAIO problem is formulated in Eq. (14), and the purpose of solving it is to verify whether the PATC is capable of reaching the same optimal solution. In Eq. (14), capital letters are used to represent random variables, while lower cases are kept for deterministic quantities or realizations of random variables.

$$\text{Given } T_i^u, T_i^\sigma, \sigma_{x_1}, \sigma_D, \sigma_d, \sigma_n, \quad i = 1, \dots, 9$$

$$\text{find } \mu_{x_1}, x_2, x_3, x_4, x_5, x_6, u_D, u_d, u_n$$

$$\min \sum_{i=1}^9 (T_i^u - u_{y_i})^2 + \sum_{i=1}^9 (T_i^\sigma - \sigma_{y_i})^2$$

$$\text{s.t. } \Pr[g_i \leq 0] \geq \alpha_i, \quad i = 1, \dots, 6 \quad (14)$$

$$\text{where } x_1 = \frac{Gd^4}{8D^3n} \quad C = D/d \quad K = \frac{4C-1}{4C-4} + \frac{0.615}{C} \quad f_{\text{Max}} = \frac{8P_{\text{Max}}D^3n}{Gd^4}$$

$$20.86 \leq u_{x_1} \leq 38.74, \quad 20.86 \leq x_2 \leq 38.74, \quad 0.7 \leq x_3 \leq 1.3, \quad 0.7 \leq x_4 \leq 1.3,$$

$$17.15 \leq x_5 \leq 31.85,$$

$$13.65 \leq x_6 \leq 25.35, 3.325 \leq u_n \leq 6.175, 70 \leq u_D \leq 130, 7 \leq u_d \leq 13$$

$$g_1 = \frac{8PCK}{\pi d^2} - [\tau], \quad g_2 = 4 - C, \quad g_3 = C - 18, \quad g_4 = \frac{1.5}{C} + 0.5n - 5.3$$

$$g_5 = f_r - 0.356 \times 10^5 d/D^2 n, \quad g_6 = (n + 1.5)d - H_0 + f_{\text{Max}} \leq 0$$

where D is spring diameter; d is spring steel wire diameter; n is spring coil number; G is shear modulus ($=7.9 \times 10^4$ Mpa); $[\tau]$ is allowable shear stress ($=534$ Mpa); C is winding ratio; K is curvature coefficient; P is maximum axial load ($=7 \times 10^3$ N); H_0 is free height; f_r is load change frequency. The target values for the mean and the standard deviation of the system response $[x_1, \dots, x_6]$ were $[T_1^u, \dots, T_9^u] = [0.095, 0.65, 1.55, 2.43, 36.00, 13.7, 49.6, 1.20, 1.35]$ and $[T_1^\sigma, \dots, T_9^\sigma] = [0, 0, 0, 0, 0, 0, 0, 0, 0]$. We assume that design variables μ_{x_1} , u_D , u_d , and u_n are independent and normally distributed with constant standard deviations $\sigma_{x_1} = \sigma_D = \sigma_d = \sigma_n = 0.1$. The required reliability level α is 99.865 % for all probabilistic constraints.

We use Sparse Grid Technique (SGT) to evaluate the first two moments of responses to avoid the influence caused by approximation methods. All probabilistic constraints are evaluated by the moment-matching method:

$$u_{g_i} + k\sigma_{g_i} \leq 0 \quad i = 1, \dots, 6 \quad (15)$$

where k is a constant. Corresponding to the required reliability level set at 99.865 %, k is equal to 3. u_{g_i} and σ_{g_i} are also obtained by Eqs.(10–11). The probabilistic optimization models for the second elements O_0 , O_1 under the particular PATC formulation are formulated in Eqs. (16–17), respectively. Note that since the standard deviation of the random design variables x_1 , D , d and n are assumed constant (i.e., cannot be controlled). It is not included as a decision variable. In general, if we cannot control the standard deviation of a random response or a linking variable, we are forced to omit the corresponding standard deviation from the particular moment-matching formulation of Eq. (4).

$$O_0 : \text{ Given } T_i^u, \quad T_i^\sigma, \mu_{x_1}^L, \sigma_{x_1}^L \quad i = 1 \dots 9$$

$$\text{find } \mu_{x_1}, \sigma_{x_1}, x_2, x_3, x_4, x_5, x_6, \varepsilon^{u_x}, \varepsilon^{\sigma_x}$$

Table 1 The optimal values of design variables

Parameters	u_{x1} (N/ mm)	x_2 (N/ mm)	x_3	x_4	x_5 (mm)	x_6 (mm)	u_D (mm)	u_d (mm)	u_n (mm)
Initial point	29.8	29.8	1	1	24.5	19.5	120	12.7	5
Optimal value	21.25	28.02	1.3	0.73	21.38	14.04	108	10.6	4.75

Table 2 The optimal values of targets performance

Target	u_{y1}	u_{y2}	u_{y3}	u_{y4}	u_{y5}	u_{y6}	u_{y7}	u_{y8}	u_{y9}
Initial value	0.075	0.3469	0.92	0.834	37.35	15.17	54.90	1.1886	1.4137
Optimal value	0.090	0.517	1.04	1.70	33.77	15.15	57.39	1.100	1.328

$$\min \sum_{i=1}^9 (T_i^u - u_{y_i})^2 + \sum_{i=1}^9 (T_i^\sigma - \sigma_{y_i})^2 + w_1 \varepsilon^{\mu_x} + w_2 \varepsilon^{\sigma_x} \quad (16)$$

$$s.t. \left(\mu_{x_1} - \mu_{x_1}^L \right)^2 \leq \varepsilon^{\mu_x}$$

$$\left(\sigma_{x_1} - \sigma_{x_1}^L \right)^2 \leq \varepsilon^{\sigma_x}$$

$$O_1 : \text{Given } \mu_{x_1}^U, \sigma_{x_1}^U$$

find u_D, u_d, u_n

$$\min \left(\mu_{x_1} - \mu_{x_1}^U \right)^2 + \left(\sigma_{x_1} - \sigma_{x_1}^U \right)^2 \quad (17)$$

$$s.t. \quad u_{g_i} + 3\sigma_{g_i} \leq 0 \quad i = 1, \dots, 6$$

$$\text{where } x_1 = \frac{Gd^4}{8D^3n}$$

Starting from the top level requires an initial guess of $\left[\mu_{x_1}^U, \sigma_{x_1}^U \right]$ when solving O_1 for the first time. Starting from the obtained optimal solutions were identical under both coordination strategies. To be able to get the global optimal solution, and reduce the number of iterations, at the system level, combinatorial optimization algorithms, namely simulated annealing algorithm and sequential quadratic programming algorithm optimization algorithm are used; at the subsystem level, the sequence of quadratic programming algorithm is used. 246 cycles were used to reach the convergence for the design variables and the target optimal values. Tables 1 and 2 show the optimal mean value of the design variable and target, respectively.

5 Conclusions

The probabilistic Analytical Target Cascading formulation for suspension design problem is formulated, and sparse Grid technique is adopted to evaluate the first two moments for reliability constraints estimation. The design problem of a suspension system was formulated as a two-level (suspension level and component level) optimization problem. At the system level, the stiffness of spring, and damper rate were considered as stochastic parameters, at the subsystem level, the material character and geometry size of the spring were described as uncertain variables. The suspension robust design problem was solved by the proposed PATC and SGNI. Results show that the enhanced PATC has good effectiveness and efficiency.

References

1. Kim H, Kumar D, Chen W, Papalambros PY (2004) Target feasibility achievement in enterprise-driven hierarchical multidisciplinary design, 10th AIAA/ISSMO multidisciplinary analysis and optimization conference, paper no AIAA-2004-4546, Albany
2. Allison J (2004) Complex system optimization: a comparison of analytical target cascading, collaborative optimization and other formulations, MS thesis, University of Michigan, Ann Arbor, Michigan
3. Michalek JJ, Papalambros PY (2005) Technical brief: weights, norms, and notation in analytical target cascading ASME J. Mech Des pp 499–501
4. Ang AH-S, Tang WH (1975) Probability concepts in engineering planning and design, vol 1—Basic principles Wiley, New York
5. Du X, Chen W (2000) Towards a better understanding of modeling feasibility robustness in engineering, ASME J. Mech Des pp 385–394
6. Kokkolaras M, Mourelatos ZP, Papalambros PY (2006) Design optimization of hierarchically decomposed multilevel system under uncertainty. ASME J. Mech 128(3):503–508
7. Seo HS, Kwak BM (2002) Efficient statistical tolerance analysis for general distributions using three-point information. Int J Prod Res 40(4):931–944
8. Xu H, Rahman S (2005) Decomposition methods for structural reliability analysis. Probab Eng Mech V20(3):239–250
9. Klimke A, Wohlmuth B (2005) Computing expensive multivariate functions of fuzzy numbers using sparse grids. J Fuzzy Sets Syst 154(3):432–453
10. Klimke A (2007) Sparse grid interpolation toolbox—user’s guide IANS report. University of Stuttgart, Stuttgart
11. Tao J, Zeng X, Cai W et al. (2007) Stochastic sparse-grid collocation algorithm (SSCA) for periodic steady-state analysis of nonlinear system with process variations. Design Automation Conference, ASP-DAC ‘07, Asia and South Pacific, IEEE Xplore 474–479

Design and Simulation of a Novel Wedge Disc Brake

Junnian Wang, Nannan Yang, Zhe Wang, Yu Yang and Liang Chu

Abstract Though conventional hydraulic disc brake has better braking steadiness, it also has poor braking efficiency factor. As a fact, the conventional hydraulic disc brake has no large-scale application to heavy duty vehicle. A novel wedge disc brake is presented in this paper, which not only has the special characteristic of self-reinforcement, but also has better braking steadiness just like conventional disc brake. Firstly, the self-reinforcement principle of this kind of wedge disc brake is analyzed and concluded. The reasonable angle of wedge block is calculated and chosen according to the demand of self-reinforcement and unexpected self-lock phenomena. Based on that, the braking efficiency factor is derived from the wedge angle and the friction coefficient between the wedge block and brake disc. After that, the mechanical structure of designed wedge disc brake is presented, then some material strength of the components are revised. In order to validate this designed novel wedge disc brake, a AMESim vehicle model with Simulink wedge disc brake model are built. Several items such as the effect of self-reinforcement and reset of wedge block are simulated. Simulation results show that this novel wedge disc brake can generate the same brake force only at nearly one third multiple hydraulic pressure of conventional disc brake.

Keywords Disc brake · Wedge block · Design method · Self reinforcement · Simulation

F2012-G01-019

J. Wang (✉) · N. Yang · Z. Wang · Y. Yang · L. Chu
State Key Laboratory of Automotive Simulation and Control, Jilin University, Jilin, China
e-mail: junnianwang@126.com

1 Introduction

In the development of automotive technology, vehicle safety gets more and more attention. As a core component of the vehicle active safety system, the performance of brake system has great effect on the vehicle safety. Currently, the service brake of passenger car is mostly hydraulic disc brake. And the heavy duty truck also has a tendency to use disc brake. So it is obvious that disc brake is going to be the main service brake in the near future. While the brake efficiency factor of the conventional disc brake is relatively lower which restricts the widely use of the disc brake. Focusing on this problem, this paper presents a novel wedge disc brake which has much bigger brake efficiency factor.

2 Research Background

The Bosch GmbH has invented a new kind of brake device in which the brake pad is replaced by a wedge block [1]. Then in the same brake intensity, a smaller actuator force is needed. While the same actuator force is exerted, a much bigger brake force will be generated. This brake device adopts electric motor as the actuator which pushes the wedge block through a ball screw. But the dynamic response problem generated by the inertia moment of the motor rotor is not discussed. Because of the widely use of hydraulic system in passenger car nowadays, the adding of motor will result in high modification cost. And thinking about the high price of motor, this new kind of brake device is hard to apply to compact low-cost car. In addition, Bosch only shows us the working principle of the brake device and its lay out in car, but the physical structure was not discussed.

The eStop GmbH and Siemens AG used to developed a novel electronic wedge brake (EWB) eBrake[®] [2]. Several references introduced the basic design [2], simulation study [3], test process [4], prototype development [5] and application to ABS/ESP [6] of eBrake. eBrake is designed as one kind of electromechanical brake (EMB) for electronic parking brake system (EPB). The actuator of earlier EWB is a double motor system. Under the synergy of the double motor system, the wedge block is moved along tangential direction through ball screw, and the extrusion between wedge block and rollers makes positive axial pressure, in hence the brake works. Then later a new prototype generation with only one motor is designed [7]. The structure of EWB is complex and it is hard to fix such double motors in the wheel. Meanwhile, it is extremely necessary to take into account the high-cost and reliability of double motors.

Emam et al. [8] also designed a electronic wedge brake and the performance of its prototype is simulated and compared between different structures and control parameters. The results showed that the lower wedge mass, the bigger caliper stiffness and reasonable control are better for braking force and operation response. Mando Corporation designed a new electronic wedge brakes that have the feature

of cross-wedge with optimized volume and use no roller due to its weakness. The proposed cross wedge mechanism showed good performance and volume metric by generating sufficient braking force without distortion due to equally distributing the braking force to pad surfaces and optimistically designed lead screw and worm gear mechanism [9]. Jongsung Kim invented a single motor electro wedge brake. Besides the main braking function, the electro wedge brake implements various additional functions, such as a function for maintaining a set clearance of a pad, a Fail-Safe function, and an EPB function, by using a solenoid mechanism interlocked with a main braking motor [10]. Dong Hwan Shin et al. [11] provided a simple design review of the wedge profile related to the calliper stiffness, and design of calliper stiffness for reducing the weight of an electro wedge brake. Kwangjin Han et al. presented a sliding mode controller for electronic wedge brake to effectively control its self-energizing effect. The performance of the proposed controller is verified in simulations and experiments using a prototype brake [12].

From the above discussion, it is obvious to see the existing self-reinforcement brakes often utilize electric motors as their actuators which result in high cost, but the dynamic response problem is not solved. They have complex structure and it is hard to mount in the wheel due to greater axial length. The brake in present paper is actuated by hydraulic pressure, has a simple structure and with little size, reduces the cost of transformation and maintains the fast response. In this paper, the basic structure and design process is presented firstly, then theoretical relationship between the wedge angle and the performance of self-reinforcement, self-lock and thermal decay are introduced. At last, simulation is performed to verify the effect of self-reinforcement.

3 Basic Principle

The wedge brake in this paper (as seen in Fig. 1) is designed based on conventional hydraulic disc brake in which the activity brake pad is replaced by a wedge block. Wheel cylinder thrust is applied to the surface which is on the side of the smaller leg of the triangle, while the wedge block can slide along the caliper inside surface where rollers are mounted. So under the thrust of the wheel cylinder as well as the additional kinetic energy of a vehicle from brake disc, the wedge block will squeeze the brake disc and causes braking torque. Because of the adding of wedge block, the kinetic energy of a vehicle is transformed into braking power, that is to say, the equivalent brake efficiency factor becomes bigger than before, in hence it is self-reinforced.

Fig. 1 Schematic diagram of the structure of the wedge brake. 1—caliper; 2—wedge block; 3, 5—brake pad; 4—brake disc; 6—rollers; 7—sealing rubber ring; 8—cylinder

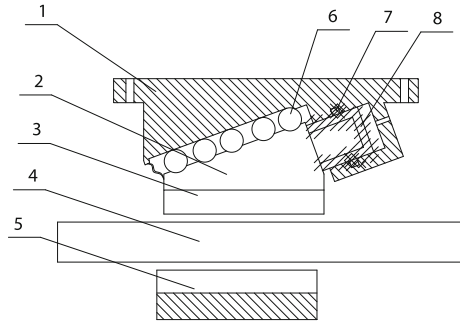
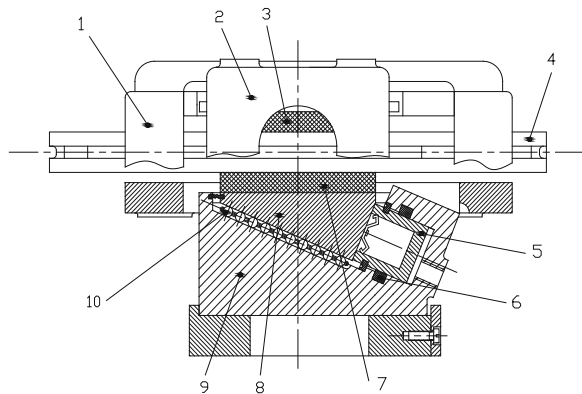


Fig. 2 Specific structure of wedge disc brake. 1—brake caliper mounting bracket; 2—brake caliper; 3, 7—friction plate; 4—brake disc; 5—brake cylinder; 6—friction limit ring; 8—wedge block; 9—wedge mechanism; 10—rollers



4 Structure

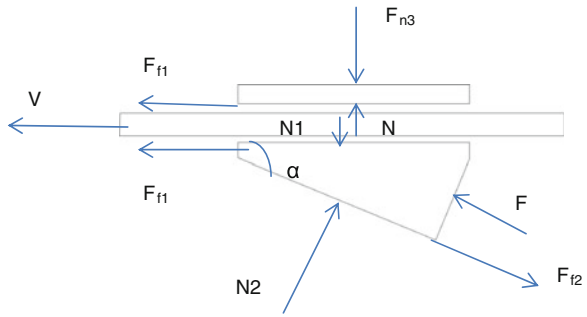
The specific structure of the wedge disc brake in this paper is shown in Fig. 2. It is designed based on traditional hydraulic disc brake, with only brake cylinder direction altered. The wedge angle is an important parameter which affects the self-reinforcement and self-lock. Several rollers are used to reduce the friction between the wedge block and calliper to prevent self-lock.

5 Performance Analysis

Based on the force analysis as shown in Fig. 3, it is easy to get the equation of force equilibrium:

$$\begin{aligned}
 x \quad & F \cos \alpha + F_{f1} = F_{f2} \cos \alpha + N_2 \sin \alpha; \\
 y \quad & F \sin \alpha + N_2 \cos \alpha = F_{f2} \sin \alpha + N_1. \text{ And: } F_{f1} = \mu_1 N_1, F_{f2} = \mu_2 N_2; \\
 F_{f1} \quad & \text{Friction between wedge block and brake disc;} \\
 F_{f2} \quad & \text{Friction between wedge block and calliper;} \\
 \mu_1 \quad & \text{Frictional factor between wedge block and brake disc;}
 \end{aligned}$$

Fig. 3 Force analysis on an simple wedge disc brake working status



- μ_2 Frictional factor between wedge block and wedge mechanism;
- F Thrust from wheel cylinder to wedge block;
- α wedge angle of wedge block;
- N_1 Pressure between wedge block and brake disc;
- N_2 Pressure between wedge block and calliper;

It can be solved from above equations that:

$$F_{f1} = \frac{F\mu_1}{\cos \alpha(\tan \alpha - \mu_1) + \mu_2 \cos \alpha + \mu_1\mu_2 \sin \alpha}$$

Because of the adding of rollers between wedge block and calliper, in this equation, the value area of μ_2 is 0.0008–0.0012. Since μ_2 is too small to effect the result of the equation, “ $\mu_2 \cos \alpha + \mu_1\mu_2 \sin \alpha$ ” is approximately equal to 0. As α is comparative smaller, $\cos \alpha$ is approximately equal to 1. So the equation above can be simplified as follows:

$$F_{f1} = \frac{F\mu_1}{\tan \alpha - \mu_1}$$

So it can be seen that, the equivalent brake efficiency factor of the wedge disc brake is:

$$K'_{ef} = \frac{2F_{f1}}{F} = \frac{2\mu_1}{\tan \alpha - \mu_1}$$

As we know, the brake efficiency factor of conventional disc brake is $K_{ef} = 2\mu_1$, so in the condition of the same actuator force, the brake torque generated by wedge disc brake is $1/(\tan \alpha - \mu_1)$ times bigger. In the present paper, this is named as reinforcement factor. The relationship curve between reinforcement factor and wedge angle is shown in Fig. 4. In Fig. 4 it can be seen that when wedge angle equals to $\arctan \mu_1$, the reinforcement factor changes suddenly, even changes to negative. At this point, wedge brake may work in bad condition such as getting lock. So it is required that $\alpha > \arctan \mu_1$. It also can be seen that if a bigger reinforcement factor is needed, the value of α should be close to $\arctan \mu_1$.

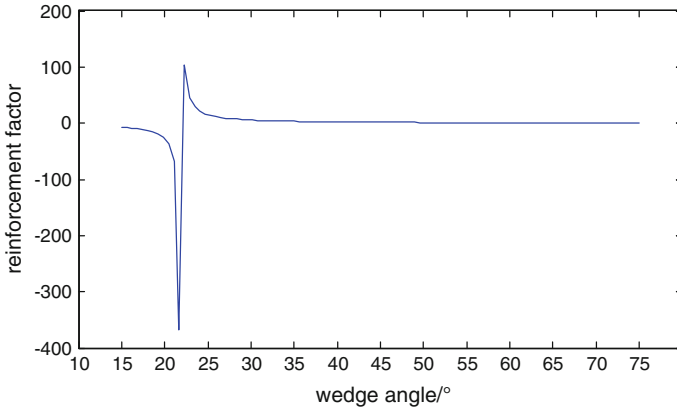
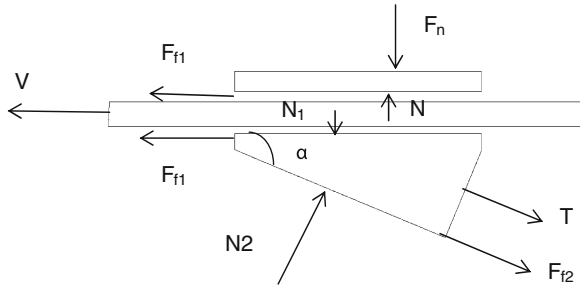


Fig. 4 Relationship curve between reinforcement factor and wedge angle

Fig. 5 Force analysis when wedge brake stops braking



Aiming at guarantee that the wedge brake can stop braking when the actuator force disappears, the condition when actuator force disappears should be taken into account. The force analysis in this condition is shown in Fig. 5. It is assumed that a return force T is required to pull back the wedge block, and at this moment the elastic deformation of wedge block keeps the same as that when wedge brake is braking, in other words, the pressure N_1 and N_2 do not change.

It can be got that:

$$T \cos \alpha + N_2 \sin \alpha = \mu_1 N_1 + \mu_2 N_2 \cos \alpha;$$

$$T \sin \alpha + N_1 = N_2 \cos \alpha + \mu_2 N_2 \sin \alpha.$$

It can be solved from equations above that:

$$T = N_1 \cos(\mu_1 + \mu_2 - \tan \alpha).$$

It is already known that μ_2 is extremely small and μ_1 is very close to $\tan \alpha$. So the return force T is extremely small too. Therefore T can be ignored in the theoretical calculation.

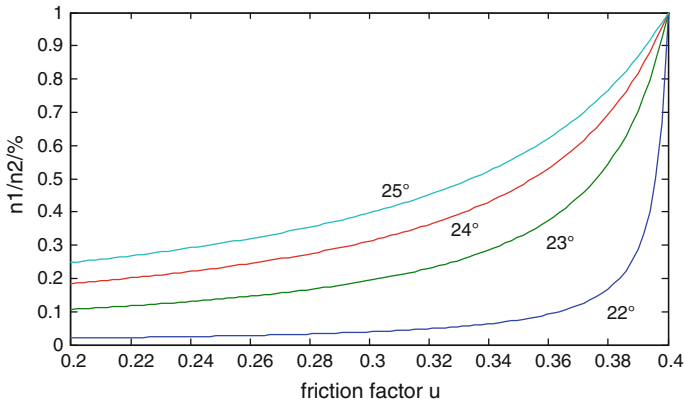


Fig. 6 Thermal decay tendency

In the working process of brake, big braking force may result in thermal decay and wearing happens all the times, and all these conditions lead to the change of friction factor. So it is necessary to study on the change of brake efficiency factor when friction factor changes. When all the components of the wedge brake are in good working condition, reinforcement factor is $n_1 = 1/(\tan \alpha - \mu_1)$. while after a long time of working or when the thermal decay happens, the friction factor changes to μ , reinforcement factor changes to $n = 1/(\tan \alpha - \mu)$. So n/n_1 can reflect the degree of thermal decay, the value is bigger, the thermal decay is slighter. Figure 6 shows relationship curve between n/n_1 and μ when α changes.

It can be seen from Fig. 6 that the value of α is smaller, the rate of change of n/n_1 is bigger, that is to say, a big reinforcement factor may cause a notable thermal decay. To prevent the wedge brake from losing brake capacity when thermal decay happens, the wedge angle α should be appropriately bigger.

6 Simulation

This present paper utilizes co-simulation of AMESim and Simulink to verify the performance of this novel hydraulic wedge disc brake. The AMESim vehicle dynamic model is built in AMESim (shown in Fig. 7) the conventional brake model is replaced by wedge brake model which is established in the Simulink (shown in Fig. 8).

In this model, the wedge angle is chosen as 23° . μ_1 is 0.1, μ_2 is 0.0001, so it can be calculated that the reinforcement factor is 3.3373. Given the same target velocity, two kinds of disc brake will generate the brake torque, then the input hydraulic pressure of the conventional disc brake should be 3.3373 times of that of wedge disc brake.

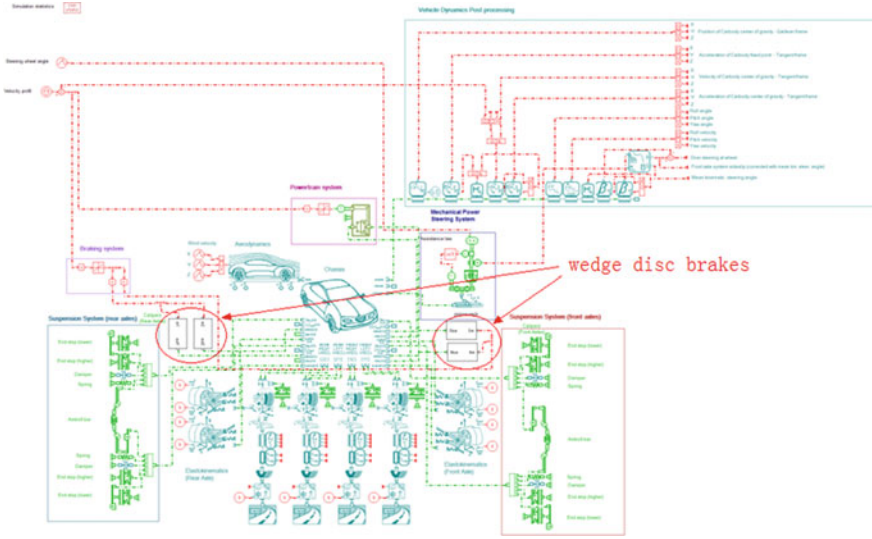


Fig. 7 Vehicle dynamic brake with wedge disc brake

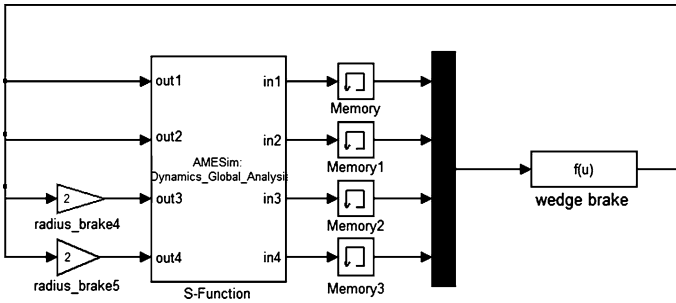


Fig. 8 Mathematical model of wedge disc brake

The result of simulation is shown in Figs. 9 and 10. Figure 9 shows the speeds of the same vehicle mounted different disc brake. Figure 10 shows the generated brake torque and applied brake press force. It is easy to see from the simulation results that two vehicles runs at the same velocity, two kinds of disc brake generate almost the same brake torque, but the input pressure of the wedge disc brake is much smaller, about 1/3 of that of conventional disc brake. These simulation results match the theoretical calculation.

Fig. 9 Speed of the vehicle. 1—real speed of the vehicle with wedge disc brake; 2—target speed; 3—real speed of the vehicle with conventional disc brake

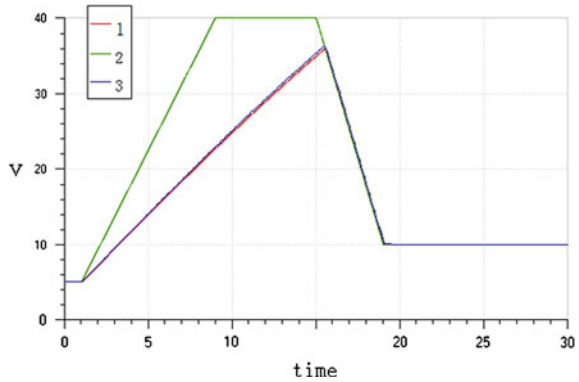
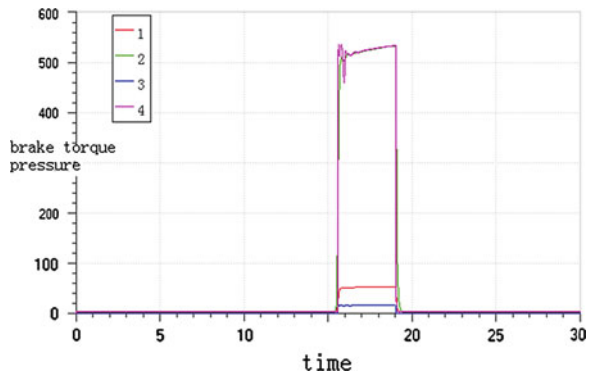


Fig. 10 Brake torque and pressure. 1—input hydraulic pressure of conventional disc brake; 2—brake torque of conventional disc brake; 3—input hydraulic pressure of wedge disc brake; 4—brake torque of wedge disc brake



7 Conclusion and Out Look

A novel low-cost hydraulic wedge disc brake is presented in this paper. Its mechanism and design process is introduced. As the most important structure parameter, wedge angle is calculated according to the its relationship with self-reinforcement, self-lock performance and thermal decay. Through theoretical analysis and computer simulation, it is proved that this novel wedge disc brake has a better self-reinforcement performance than the conventional disc brake. Given the same hydraulic pressure, the wedge disc brake can generate a bigger brake torque. While if the same brake torque is wanted, the wedge disc brake needs much smaller hydraulic pressure. Furthermore, prototype verification test is needed to conduct in near future.

References

1. Bowman D, Hoffman D, Wohlers H et al. (2006) Vehicle brake device. P. R. China Patent, ZL200480023981. 6, 2006-9-27 (in chinese)
2. Hartmann H, Schautt M, Pascucci A, Gombert B (2002) eBrake[®]—the mechatronic wedge brake. SAE Technical Paper 2002-01-2582
3. Roberts R, Schautt M, Hartmann H, Gombert B (2003) Modelling and validation of the mechatronic wedge brake. SAE Trans 112(6):2376–2386
4. Roberts R, Gombert B, Hartmann H, Lange D, Schautt M (2004) Testing the mechatronic wedge brake. SAE Paper no. 2004-01-2766
5. Man Ho L, Roberts R, Hartmann H, Gombert B (2006) The electronic wedge brake EWB. SAE Paper no. 2006-01-3196
6. Semsey Á, Roberts R (2006) Simulation in the development of the electronic wedge brake. SAE Paper no. 2006-01-0298
7. Fox J, Roberts R, Baier-Welt C, Ho LM, Lacraru L, Gombert B (2007) Modeling and control of a single motor electronic wedge brake. SAE Paper no. 2007-01-0866
8. Emam MAA, Emam AS, El-Demerdash SM, Shaban SM, Mahmoud MA (2012) Performance of automotive self reinforcement brake system. J Mech Eng 1(1):4–10
9. Joo Gon K, Myoung June K, Jong Ki K (2009) Developing of electronic wedge brake with cross wedge. SAE Paper no. 2009-01-0856
10. Jongsung K (2011) Single motor electro wedge brake system using solenoid mechanism for implementing additional functions. United States Patent, US 7987950B2
11. Dong Hwan S, Ji Nung A (2012) Study of stiffness design of caliper for reducing the weight of an electro wedge brake. Appl Mech Mater, 138–139:159–162
12. Kwangjin H, Myoungjune K, Kunsoo H (2012) Modeling and control of an electronic wedge brake. Proc Inst Mech Eng, Part C: J Mech Eng Sci 226(7):1693–1704

Research and Application on Dynamic Stiffness of Leaf Spring

Zhanfu Zhou, Wanfu Guo, Tiejun Shen, Fengdong Wang, Jianhui Ju, Haiyan Wang and Enzhang Song

Abstract Based on product development and design of light trucks, the paper has deduced the main factors influencing the dynamic stiffness of the leaf spring through theoretical programming and optimization of the structure of the leaf spring; The law of the influence of friction, frequency and amplitude on dynamic stiffness is explored by means of experiment and finite element analysis; On the basis of the above research, the matching design of the leaf spring and the shock absorber has greatly improved vehicle ride comfort.

Keywords Leaf spring · Shock absorber · Dynamic stiffness · Ride comfort · Finite element analysis

1 Preface

As the elastic component of the suspension system, the leaf spring transfers force and torque between the wheels and the frame, reducing the impact of the ground on vehicle body and having an important influence on car handling stability and comfort. Tests have proved that friction between the springs greatly affects the dynamic stiffness and vehicle vibration, and the friction produced by relative

F2012-G01-020

Z. Zhou (✉) · W. Guo · T. Shen · F. Wang · J. Ju · H. Wang · E. Song
FAW Group Corporation R&D Center, 130011 Changchun, China
e-mail: zhouzhanfu@rdc.faw.com.cn

movement between the springs is instable, leading to inconvenient control of the size of the resistance. Especially on better roads, the dynamic load produced by uneven pavement is too small to overcome the friction between the leaves, resulting in a “lock” phenomenon, which will pass impact to the body and damage ride comfort. In this paper, features of the dynamic stiffness of the leaf spring, which play important roles in improving the ride comfort of the vehicle, have been elucidated from the perspectives of structural design, vibration frequency and sports travel etc.

2 Calculation and Analysis of the Dynamic Stiffness of the Leaf Spring and Friction Relative Damping Ratio

Generally speaking, when surfaces of the two parts of the mechanical structure contact and are subjected to dynamic load, joints surface damping or coulomb friction damping will be generated. Joints damping usually refers to no relative sliding between the contact surfaces, while coulomb friction damping is generated by the dry friction energy dissipation of the relatively macroscopic motion between surfaces. The dissipated energy can be obtained through the analysis and computing of the area surrounded by friction-displacement hysteretic back line. Therefore, we can conclude that the damping generated by friction between leaf spring plates is Coulomb friction damping. From the mechanism of damping we can know that relative damping ratio ζ of leaf spring friction is closely related to the excitation frequency, amplitude, temperature and friction energy loss. If damping caused by friction between leaf springs is equivalent to speed damping with a damping coefficient k , then relative damping ratio ζ of leaf spring friction can be derived as follows

$$\zeta = \frac{k}{2\sqrt{MC}} \quad (1)$$

Among them, $k = \frac{E}{2\pi^2fA}$; A : Amplitude; C : Static stiffness values; M : Mass; E : friction power; f : Frequency.

The formula of Dynamic Stiffness:

$$K_S = \frac{\Delta F_r - 2F_c}{\Delta S} \quad (2)$$

Among them, Coulomb friction $F_c = \frac{E}{2\Delta S}$; K_S : Dynamic stiffness value; ΔF_r : Load amplitude; ΔS : Displacement amplitude.

The following formula can be derived from formula (1) and (2)

$$K_S = \frac{\Delta F_r - (4\pi^2 f A \zeta \sqrt{MC}) / \Delta S}{\Delta S} \quad (3)$$

Table 1 Calculation list of relative damping ratio between leaf spring plates

Serial number	C static stiffness	K _s dynamic stiffness	E friction power	M mass	F _c Coulomb friction	ΔF _r load amplitude	ζ damping ratio
1	14.2	33.5	507.1	356	12.68	41.74	0.057
2	15.2	45.5	853.2	379	21.33	48.28	0.090
3	17.8	55.6	942.3	445	23.56	64.06	0.085
4	21.1	57.0	518.0	527	12.95	88.11	0.039
5	21.4	53.3	301.1	534	7.53	91.62	0.023
6	29.9	104.7	604.1	747	15.10	179.29	0.032
7	32.9	119.0	394.0	823	9.85	218.29	0.019
8	36.6	152.7	712.0	915	17.80	269.89	0.031
9	40.9	190.2	860.1	1022	21.50	337.44	0.034
10	9.4	19.6	415.2	235	10.38	18.53	0.071
11	20.0	74.5	1316.6	500	32.92	83.14	0.106
12	21.5	95.0	1853.8	537	46.34	97.24	0.138
13	23.5	130.6	2830.1	588	70.75	119.62	0.193
14	26.4	131.3	2307.0	660	57.68	147.34	0.140
15	27.1	126.7	1993.2	678	49.83	153.76	0.118
16	29.2	173.7	3264.6	730	81.61	184.25	0.179
17	30.1	182.1	3376.8	754	84.42	195.38	0.180
18	14.2	33.5	507.1	356	12.68	41.74	0.057

Note: the former nine are small leaf springs, while the latter ones are multileaf springs

From formula (3), it is known that the dynamic stiffness of the leaf spring changes with the frequency, amplitude, friction energy loss. In order to facilitate our analysis, by assuming the excitation frequency $f = 2$ Hz and amplitude $A = 15$ mm, tests have been conducted on the dynamic stiffness of the leaf spring. Through experimental data and theoretical calculation, data in Table 1 can be deduced.

Through Table 1, we can carry out statistical analysis of the relative damping ratio of leaf springs of different forms, frequencies, and amplitudes in order to obtain the related motion characteristics. Its curve is shown below (Figs. 1, 2, 3).

Fig. 1 Relative damping ratio of small and multi-leaf springs

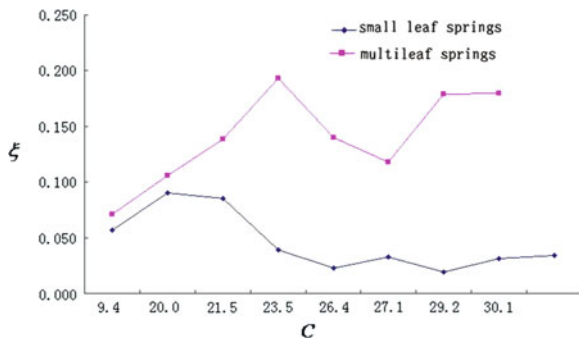


Fig. 2 Relative damping ratio of the same pair of leaf springs at different frequencies

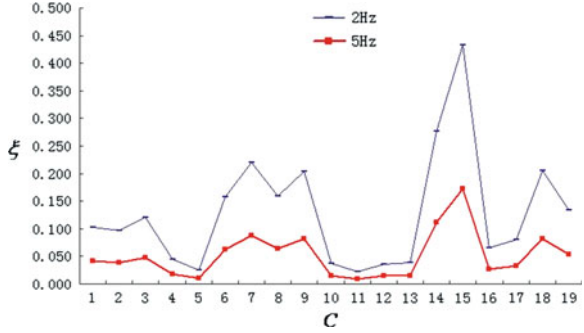
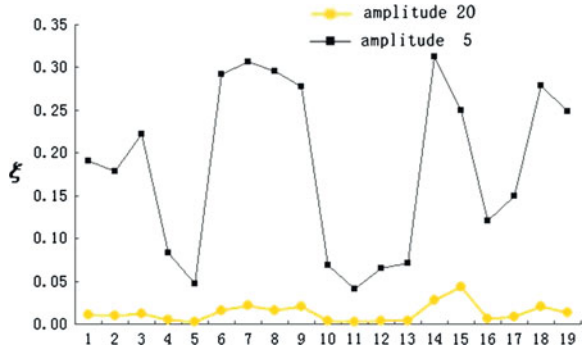


Fig. 3 Relative damping ratio of the same pair of leaf springs with different amplitudes



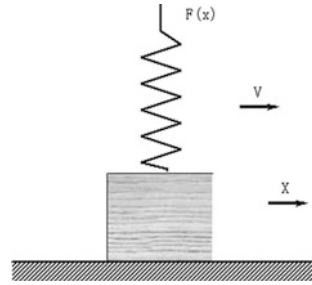
Thus it can be inferred that:

- (1) The dynamic stiffness of leaf spring is greater than the static stiffness. The greater the amplitude, the closer the dynamic stiffness is to the static stiffness.
- (2) In general, the relative damping ratio of the multi-leaf spring is greater than that of the small leaf spring.
- (3) As to the same leaf spring, the higher the frequency, the smaller the relative damping ratio and the dynamic stiffness; The bigger the amplitude, the smaller the relatively damping ratio and dynamic stiffness of the leaf spring. The size of the amplitude exerts great influence on the dynamic stiffness of the leaf spring.

3 Influence of the Structural Design of Leaf Spring on Dynamic Stiffness

Through the above analysis and study on the dynamic stiffness of leaf spring, we can know that when the leaf spring is in small-amplitude vibration at high frequency, the damping generated between the plates is very great. Especially

Fig. 4 Block slippage



between plates of multi-leaf springs, the relative damping ratio ranges from 0.1 to 0.2, close to the damping demand of the vehicle; While in large amplitude vibration at low frequency, damping between the plates is small, shock absorber is needed to provide certain damping to meet the need of the vehicle. Therefore, improvement in vehicle comfort can be achieved by reducing friction between leaf spring plates and decreasing friction damping generated in small amplitude at high frequency. Ordinary friction theoretical analysis shows that the dynamic stiffness of leaf spring is closely related to friction between the spring plates, and through structure design of the leaf spring friction can be reduced.

As shown in Fig. 4, the sample, subjected to variable pressure $F(X)$, moves on a flat plate with a friction coefficient of μ . Among them $F(X) = ax + b$, the equation for friction work is

$$\begin{aligned}
 W &= \int_{x_0}^{x_1} \mu F(x) dx \\
 &= \int_{x_0}^{x_1} \mu(ax + b) dx \\
 &= \mu \left[\left(\frac{1}{2}ax_1^2 + bx_1 \right) - \left(\frac{1}{2}ax_0^2 + bx_0 \right) \right] \tag{4} \\
 &= \mu(x_1 - x_0) \left[\frac{1}{2}a(x_1 + x_0) + b \right] \\
 &= \mu \left[\frac{\Delta F}{2} + F(x_0) \right] \Delta x \\
 &= \mu \frac{\Delta F \Delta x}{2} + \mu F(x_0) \Delta x
 \end{aligned}$$

From formula (4), it can be inferred that friction work is related to pre-load, relative displacement, increment of force and friction coefficient. Thus reducing friction between the plates is one of the effective ways to improve the dynamic stiffness of leaf spring.

In actual assembly, due to different curvature radius of each piece of leaf springs, prestressing will be caused. For easy calculation, assuming that the

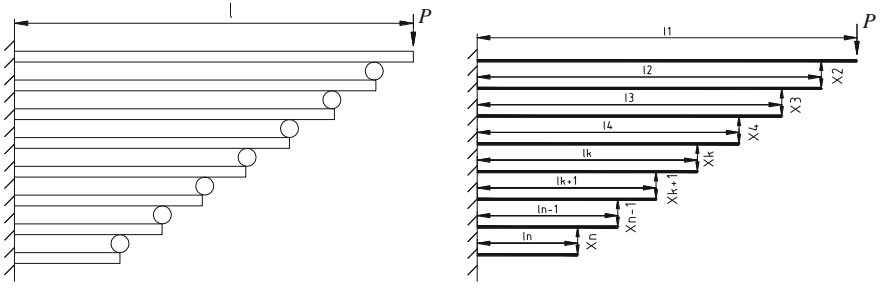


Fig. 5 Model of concentrated load calculation method

pressure $F(x_0) = 0$, then in the period of loading and unloading, the friction energy dissipation between plates of the whole spring leaf is:

$$W_{fr} = 2\mu F_1 x_i \tag{5}$$

Among them, F_1 : Contact pressure at the end of the i and $(i + 1)$ leaf spring x_i ; Relative displacement at the contact point at the end of the i and $(i + 1)$ leaf spring.

From the formula (5), we can conclude that the friction work between leaf spring plates is closely related to the contact stress at the end of the leaf spring. In order to simplify our analysis, when calculating the friction work of the leaf spring, we assume the relative displacement between spring plates is a constant. Then only the positive contact pressure F needs to be calculated. In solving the positive pressure, we adopt concentrated load calculation method, assuming load at the main spring eye is P and force generated at the end point of other plates is X_k . According to the principle of equivalent deformation at the contact point between adjacent spring plates, we can work out the load at the end of each spring plate. The model is shown in Fig. 5.

The specific calculation is as follows:

$$\begin{cases} A_2P + B_2X_2 + C_2X_3 = 0 \\ A_3X_2 + B_3X_3 + C_3X_4 = 0 \\ A_4X_3 + B_4X_4 + C_4X_5 = 0 \\ \text{hellip;} \\ A_nX_{n-1} + B_nX_n = 0 \end{cases} \tag{6}$$

Among them,

$$\begin{cases} A_K = 0.5 \frac{I_K}{I_{K-1}} (3 \frac{l_{K-1}}{l_K} - 1) \\ B_K = -(1 + \frac{I_K}{I_{K-1}}) - \frac{\eta(l_K - l_{K+1})^3}{l_K^3} \\ C_K = 0.5 (\frac{l_{K+1}}{l_K})^3 (3 \frac{l_K}{l_{K+1}} - 1) \end{cases}$$

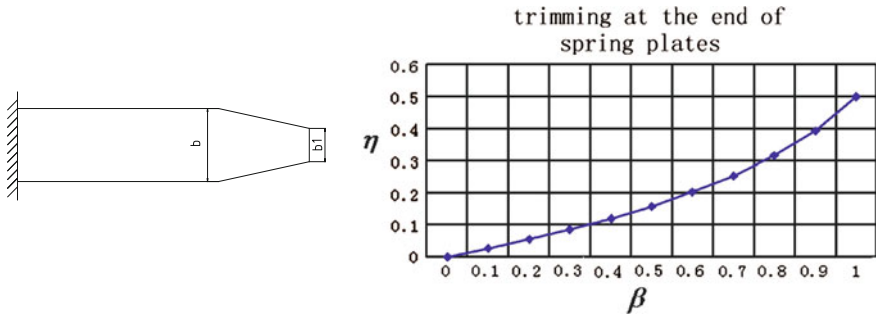


Fig. 6 Trimming at the end of spring plates

When there is no processing at the end of spring plates $\eta = 0$:

$$\begin{cases} A_K = 0.5 \frac{I_K}{I_{K-1}} (3 \frac{I_{K-1}}{I_K} - 1) \\ B_K = -(1 + \frac{I_K}{I_{K-1}}) \\ C_K = 0.5 (\frac{I_{K+1}}{I_K})^3 (3 \frac{I_K}{I_{K+1}} - 1) \end{cases}$$

When the end of the spring plates is trimmed, the calculation formula of η and the coefficient curve when the trimming shape of each spring plate is different are as follows (Fig. 6)

$$\eta = \frac{3}{\beta} \left[\frac{3}{2} - \frac{1}{\beta} - \left(\frac{1-\beta}{\beta} \right)^2 \ln(1-\beta) \right] - 1 \tag{7}$$

$$\beta = 1 - \frac{b_1}{b}$$

When the end of the spring plates is rolled, the calculation formula of η and the coefficient curve when the rolling shape of each spring plate is different are as follows (Fig. 7)

$$\eta = \frac{3}{\beta} \left[-\frac{1}{2} - \frac{1}{\beta} - \frac{1}{\beta^2} \ln(1-\beta) \right] - 1 \tag{8}$$

$$\beta = 1 - \frac{h_1}{h}$$

Among them, P : Load at the main spring eye, N ; l_1 : Half of the stretched length of the main spring plate, m ; l_{k+1} : Half of the length of the $k + 1$ th plate, m ; l_k : Half of the length of the k th plate, m ; I_i : Moment of inertia of the i th plate, m^4 ; X_k : Load at the end of k th plate, N .

Through $n - 1$ th power linear equations of Formula 6, we can work out the value of the load X_2, X_3, \dots, X_n at the end of each spring plates. Taking the multi-leaf spring of light vehicles as an example, the above method is used to calculate loading conditions at the end of each spring plate with three structures, namely, spring end rectangular, slimming and rolling, as is shown below.

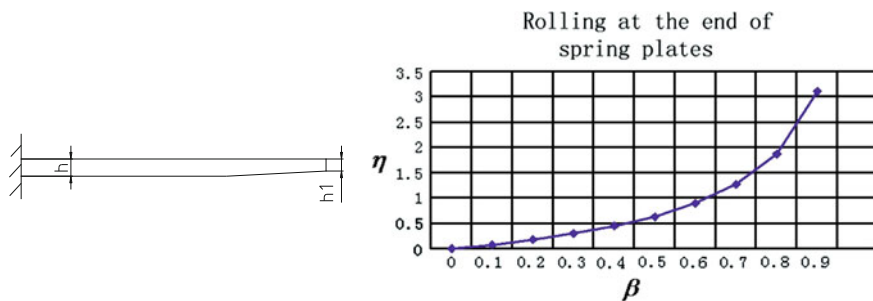


Fig. 7 Rolling at the end of spring plates

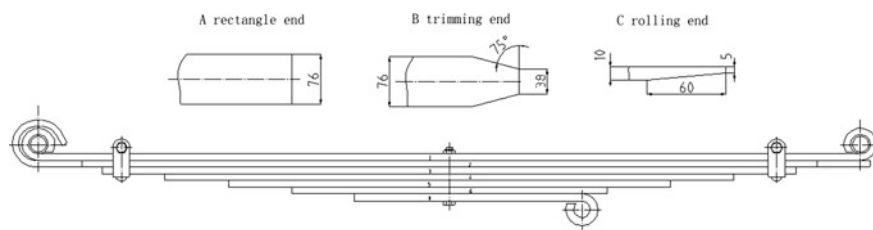


Fig. 8 Structure of multi-leaf spring

Table 2 Spring end load calculation table

	Rectangle end	Trimming end	Rolling end
Load/N at the end of 3th plate	10,300	10,200	10,000
Load/N at the end of 4th plate	9,940	9,760	9,390
Load/N at the end of 5th plate	9,200	8,840	8,100
Load/N at the end of 6th plate	7,360	6,550	4,920
Sum of pressure N	36,800	35,400	32,400
Static stiffness N/mm	187	186.4	185.7
Pressure reduction ratio	–	4 %	12 %
Stiffness reduction ratio	–	0.3 %	0.7 %

When the loading force P at the spring eye of the leaf spring in Fig. 8 is 12860 N , leaf spring end load are given in the following table.

From the analysis in Table 2, we can conclude that it is possible to decrease the spring end load and cut the friction work between spring plates through trimming and rolling the end of the leaf spring, yet without changing the static stiffness. A sharp decrease in pressure, as much as 12 %, has been seen in leaf springs with rolling ends.

To decrease friction between spring plates, small leaf spring is used instead of multi-leaf spring on the premise of maintaining the leaf spring stiffness invariable.

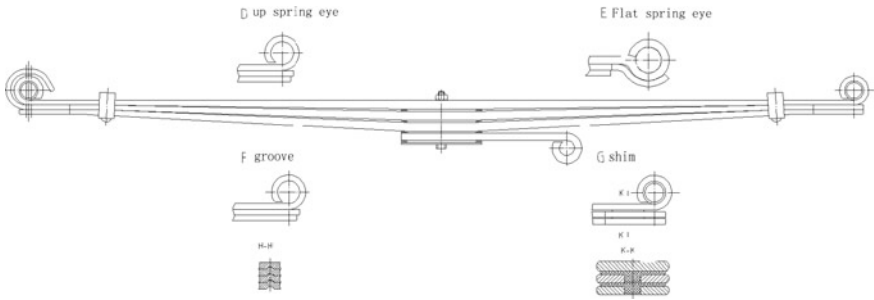


Fig. 9 Structure of small leaf spring

Fig. 10 Leaf-spring bench test



Meanwhile, an optimized design has been applied on the structure of leaf spring eyes and spring ends for the purpose of decreasing the dynamic stiffness of leaf spring. The concrete structural design is shown in Fig. 9.

4 Bench Test of Leaf Spring Dynamic Stiffness and Test Analysis of Vehicle Comfort

4.1 Bench Test of Leaf Spring Dynamic Stiffness

Based on the above-mentioned A–E schemes for the leaf-spring bench test, the change law in leaf-spring dynamic stiffness is verified through variable frequency and amplitude, shown as follows

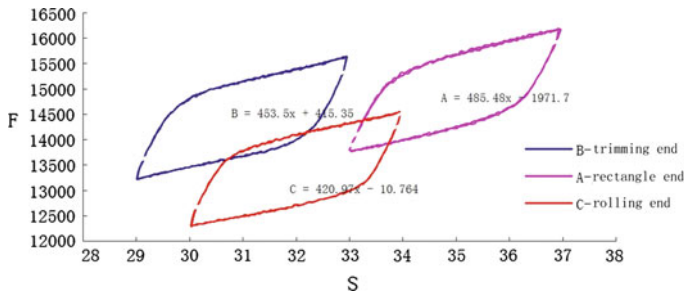
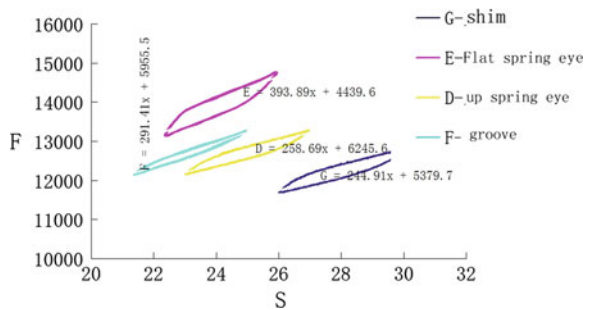


Fig. 11 Dynamic stiffness test curve of A, B, and C multi-leaf springs

Fig. 12 Dynamic stiffness test curve of D, E, F, G small leaf springs



- (1) Test loading is shown in Fig. 10.
- (2) Test conditions: The leaf spring clamping stiffness is 183.5 N/mm. It is loaded and run in at random before the test. Leaf spring displacement is 0 ~ 30 mm, frequency is 3 Hz and running-in period is 0.5 h.
- (3) Leaf spring force–displacement characteristics: $S = \pm A \cdot \sin(2\pi ft)$
- (4) Experiments of dynamic stiffness on multi-leaf spring A, B and C and small leaf spring D, E, F, G have been conducted. The test conditions are as follows: the same frequency and amplitude. The experimental results are as follows (Figs. 11, 12), (Table 3).
- (5) Distribution of dynamic stiffness bench test curves of the same leaf spring at different frequencies and amplitudes (Fig. 13).

Table 3 Test results of leaf spring dynamic stiffness

Multi-leaf spring dynamic stiffness, N/mm			Small leaf spring dynamic stiffness, N/mm			
A-rectangle end	B-trimming end	C-rolling end	D-up spring eye	E-Flat spring eye	F- groove	G-shim
485.48	453.5	420.97	258.69	393.89	291.4	244.91
Static stiffness $187 \pm 6 N/mm$						

Fig. 13 Dynamic stiffness bench test curves at different frequencies and amplitudes

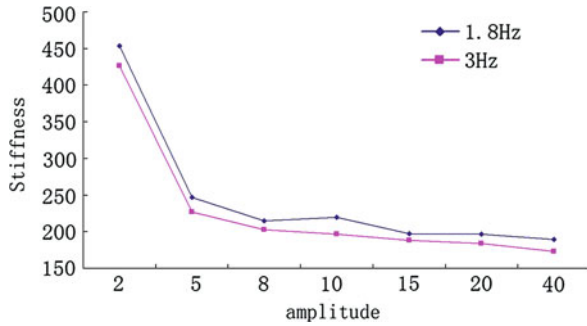
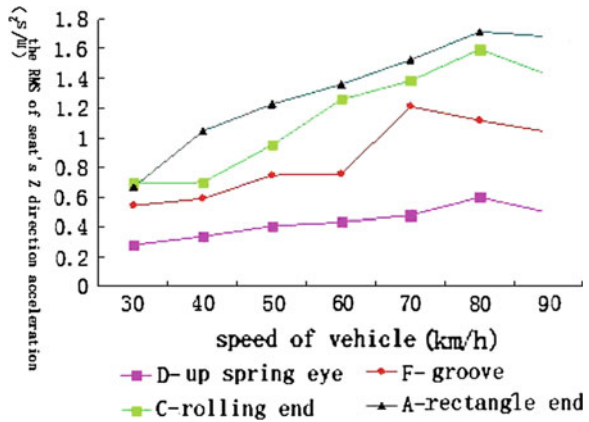


Fig. 14 Different schemes of vehicle comfort test



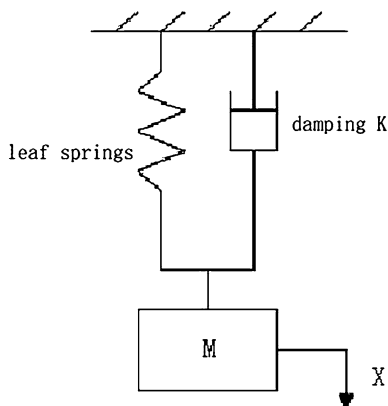
4.2 Comfort Test of Vehicles Mounted with Leaf Springs

Comfort tests have been conducted on vehicles mounted with the above-mentioned A–F types of leaf springs. The experimental method takes GB4970-1996 Vehicle comfort random input driving test method as reference. The test results are as follows (Fig. 14).

4.3 Test Analysis and Conclusions

- (1) The dynamic stiffness of leaf spring can be reduced by rolling at the end of multi-leaf spring; the form of the spring eye and rolling at the end of the leaf spring have very big effect on dynamic stiffness.
- (2) The dynamic stiffness of small leaf spring is 34 % lower than that of the multi-leaf spring, which plays an important role in improving vehicle ride comfort.

Fig. 15 Undammed free vibration model with single degree of freedom



- (3) The dynamic stiffness of leaf spring decreases as the amplitude and frequency increase.

Based on the above experimental and theoretical foundation, given the manufacturing cost, process and vehicle comfort, ride comfort can be improved by adopting D-rollup ear scheme of small leaf spring and C-end rolling plan of multi-leaf springs.

5 Match Between Leaf Spring and Shock Absorber Damping Characteristics

Suspension system vibration can be simplified as an undamped free vibration model with single degree of freedom, as shown in Fig. 15.

The vibration differential equation is:

$$\ddot{x} + \frac{k}{m}\dot{x} + \frac{c}{m}x = 0 \quad (9)$$

Relative damping ratio $\xi = \frac{k}{2\sqrt{mC}}$

When $\xi < 1$, namely in small damping situation, vibration system is no longer simple harmonic vibration of equal amplitude. With the passage of time, vibration decreases and eventually disappears, so small damping free vibration is also known as attenuate vibration. Suspension system belongs to the category of small damping vibration system. Therefore, as to the suspension system, only situations in which the relative damping coefficient is less than 1 need to be considered.

Take 1/4 vehicle model as an example, the mean square value of the vertical acceleration of a vehicle driving on a certain kind of road A and with a speed of V can be solved:

Table 4 The typical road A values

Cross-country bad way	1
Ordinary road	0.1
Good road	0.01
Quality road	0.001

$$\begin{aligned} \bar{Z}^2 &= 2 \cdot \pi \cdot A \cdot V \frac{4 \cdot \varepsilon^2 \cdot \omega_k^2 + (1 + \mu) \cdot \omega_0^4}{4 \cdot \varepsilon \cdot \mu} \\ &= 2 \cdot \pi \cdot A \cdot V \cdot \omega_0^3 \left(\frac{C_k}{C} \zeta + \frac{1 + \mu}{4 \cdot \mu \cdot \zeta} \right) \end{aligned} \tag{10}$$

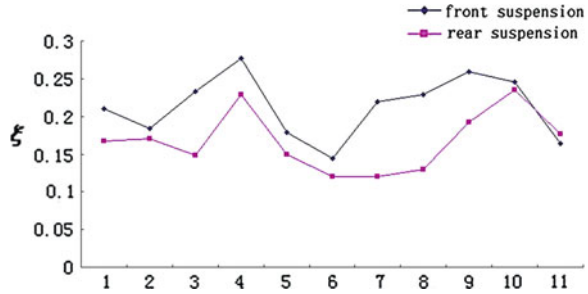
Among them, A : The extent of the road roughness, $cm^2 m/cycle$; V : Speed, m/s ; M : The sprung mass, kg ; m : Unsprung mass, kg ; C_k : Tire stiffness, kg/m ; $\omega_0^2 = C/M$; $\varepsilon = K/(2M)$; $\mu = M/m$; $\omega_k^2 = C_k/m$; C : The stiffness of the spring, kg/m ; K : Shock absorber damping coefficient, $kg \cdot s/m$.

The typical road A values are recommended in Table 4.

From formula (10), we could infer that only by selecting an appropriate relative damping ratio ζ can we get $\min \bar{Z}^2$. Therefore, full consideration has been given to the matching between leaf spring and damping of shock absorber in vehicle design. According to the above-mentioned motion characteristics of leaf spring dynamic stiffness, when driving on low frequency and large amplitude rolling roads or bad roads, the damping of shock absorber needs to be relatively large to improve the tires' road adhesion capacity for the friction damping of leaf spring is relatively small. While when running on better roads with high frequency and small amplitude, the dynamic load caused by rough road is small. Most of the vibration caused by ground excitation is filtered out by tires. Besides, the friction damping of the leaf spring is relatively large, thus demanding a relatively small damping of the shock absorber so as to improve vehicle ride comfort and ease the fatigue of the drivers.

The influence of damping in the suspension system on vehicle vibration mainly depends on relative damping ratio ζ . Considering simultaneous input of various frequencies on a random road, taking 0.2–0.45 as the value of ζ can make the mean square root value of body acceleration relatively small. By increasing the value of ζ , dynamic deflection and vibration of the wheels can be decreased, so can the relative dynamic load between the wheels and the ground. But improper increment would lead to the transfer of big impact on the road by the suspension system, even making it impossible for the wheels to quickly rebound to the ground, thus losing adhesion and buffering capacity against road excitation; when the value of ζ is small, the attenuation ability becomes relatively weak, and the vibration period becomes longer, which will not facilitate improvement in ride comfort. In addition, the design rules have been grasped through the analysis of the relative damping ratio ζ of suspensions of a dozen or more light vehicles home and abroad at frequency under no-load conditions, as is shown in Fig. 16:

Fig. 16 Relative damping ratio of suspensions of light vehicles at frequency under no-load conditions



The following conclusions can be drawn from the above:

- (1) The relative damping ratio of the front and rear suspensions of light vehicles at natural frequency is generally controlled at between 0.1 and 0.3.
- (2) The relative damping ratio of the front suspension is generally a little higher than that of the rear suspension.

Based on the damping characteristic test of the light car products, the damping ratio of the front suspension at frequency under no-load conditions is 0.15 ~ 0.24 and that of the rear suspension is 0.13 ~ 0.21, which has met the design requirements, reached the design level of similar foreign products and improved the vehicle ride comfort.

6 Conclusion Analysis

With the help of plenty of tests and CAE analysis method, the paper starts from theoretical calculations and explores the influencing factors and the law of motion of the dynamic stiffness of the leaf spring from several aspects. The experimental and simulation results are relatively close to those of actual application. Based on characteristic analysis of the dynamic stiffness of leaf spring, we've mastered the rules of matching design of the leaf spring and the shock absorber, and acquired certain means of design pre-evaluation on damping characteristics of the suspension system, which are of guiding significance on improving the vehicle ride comfort.

References

1. Jiang L, Dong X (1998) Automotive design manual vehicle chassis (4.4, 4.5). Changchun automobile research institute
2. Leaf spring design and performance test method. JIS B 2710-2000, 2000
3. Dai Depei (1991) Engineering application of damping technology. Tsinghai University press, Shenzhen

4. Yu Z (1996) Theory of automobile. Machinery Industry Press, Anyang
5. Yu A , et al (2007) Finite element analysis of the leaf spring stiffness characteristics. Automot Technol
6. Soviet H.B Kt Gaelic Saransk (1982) Friction and wear calculation principle. Machinery Industry Press, Anyang
7. Ding Nenggen, Ma Jianjun (2003) The finite element analysis of leaf spring hysteresis characteristics. Automot Eng, 25
8. Yersinia Lyme Pal (1992) The basis of automobile chassis. Popular science press, Germany
9. Xu Tianan (1996) BJ1045 Light truck ride comfort analysis. Beijing Auto, 4

Study and Simulation of Isolation Performance of Torsional Vibration of DMF-CS with Centrifugal Pendulum-Type Absorber

Wei Li, Tieshi Gao, Yongkui Cui, Wanfu Guo and Wenku Shi

Abstract The structure of DMF-CS with centrifugal pendulum-type absorber was analyzed, and the kinematics differential equation of DMF-CS was set up by using Lagrange principle. The natural frequency of pendulum was deduced and found proportional with the rotate speed of the second flywheel. With this characteristic, the torsional vibration from engine fire frequency can be absolutely eliminated theoretically by appropriately adjusting the structural parameters of the centrifugal pendulum. Further more, the isolation of the pendulum with the other lower frequencies vibration of engine was studied and the rule of vibration isolation was summarized. At last, virtual prototype technology was used to build the model of a domestic car drive-train torsional vibration and simulate the isolation performance of the absorber. It is found the simulation result is in accordance with the theoretical analysis.

Keywords Dual mass flywheel (DMF) · DMF-CS with centrifugal pendulum-type absorber · Natural frequency · Vibration isolation · Simulation analyses

F2012-G01-021

W. Li (✉) · T. Gao · Y. Cui · W. Guo
FAW Group Corporation R&D Center, Changchun, 130011, China
e-mail: nishihara@i.kyoto-u.ac.jp

W. Shi
State Key Laboratory of Automotive Dynamic Simulation, Jilin University, 130022, Changchun, China

1 Preface

The torsional vibration of DMF-CS with spiral spring-type absorber which was developed by German LUK company in 1989 and was constantly improved later on is the most typical DMF-CS in the world currently. The DMF-CS absorber with bigger rotation angle (generally more than 45°) can well solve the problem of achieving lower damper torsional stiffness in limited design space, and its excellent vibration isolation performance has been proved by plenty of test studies and practical application, and also reported by lots of literatures [1–4]. With the widespread use of high power engine and the increasingly higher requirements for ride comfort, the better performance of torsional vibration absorber is asked for [5, 6]. DMF-CS with centrifugal pendulum-type absorber was developed to meet this need.

The centrifugal pendulum-type absorber had been existed for decades and widely used in the aviation field. But so far, as the limitations of installation space for the pendulum and the complexity of the engine running conditions, the centrifugal pendulum-type absorber applied to automotive industry was limited [7]. In 2008, LUK found another feasible way to combine centrifugal pendulum-type absorber and transmission system—forming DMF-CS with centrifugal pendulum-type absorber by combining centrifugal pendulum-type absorber and DMF-CS into one. The DMF-CS absorber can attenuate the vibration of all-order excitations of the engine; and the centrifugal pendulum-type absorber not only can selectively absorb the vibration of all frequencies of engine through appropriate adjustments, but also can prevent the transmission of torsional vibration to achieve the best ride comfort, even in the case of high-torque engine. The birth of DMF-CS with centrifugal pendulum-type absorber was known as another milestone after the DMF-CS absorber in the history of the development of Dual Mass Flywheel. Now the first batch of the absorber has been produced for a world famous motor company [7].

2 Analysis of the Structure of DMF-CS with Centrifugal Pendulum-Type Absorber

There are two structural alternatives with DMF-CS with centrifugal pendulum-type absorber: one is the centrifugal pendulum installed in the first flywheel, the other is the centrifugal pendulum installed in the second flywheel, as shown in Fig. 1 [8]. When the centrifugal pendulum is mounted on the first flywheel, it can play an inhibitory effect on the excitation in the engine accessories at the same time, but more quality (3–5 kg) is required and more space is occupied, which is the main reason for hindering the centrifugal pendulum on the vehicle applications. When the centrifugal pendulum is mounted on the second flywheel, it cannot play an inhibitory effect on the excitations in the engine accessories. However, it can put the quality down to about 1 kg, which makes it possible for setting the centrifugal pendulum in the limited space.

Fig. 1 Two kinds of structure schematic drawing of DMF-CS with centrifugal pendulum-type absorber

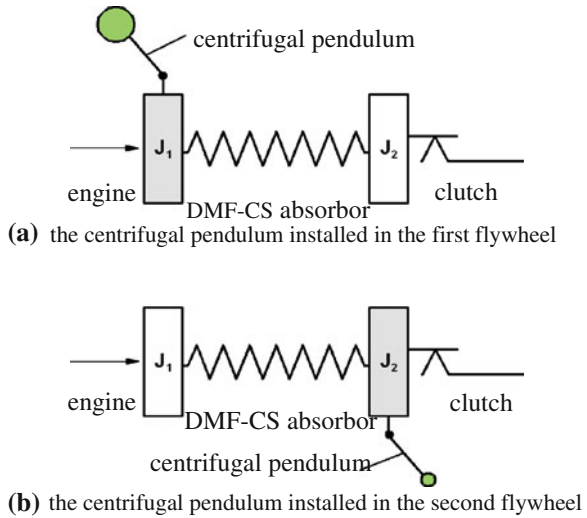
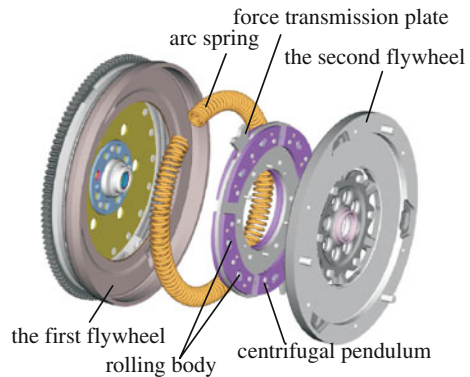


Fig. 2 DMF-CS with centrifugal pendulum-type absorber



The DMF-CS with centrifugal pendulum-type absorber produced by the LUK company is shown in Fig. 2, whose basic structure is identical with the structure of common DMF-CS absorber which consists of the first and second flywheel assembly and the spring-damper in between. The number of centrifugal pendulum is usually four, each is composed of two fan-shaped sheet metals of same shape by riveting. Centrifugal pendulum is arranged on the force transmission plate evenly, which is connected with the second flywheel. In this case, the centrifugal pendulum equals to be mounted on the second flywheel. The force transmission plate and the centrifugal pendulum are respectively provided with two arc slides. The centrifugal pendulum is connected with the force transmission plate actively through the roller body which diameter is slightly less than the diameter of the arc slide, as shown in Fig. 3. The main role of arc chute is guiding and limiting the centrifugal pendulum, which will prevent bigger impact on the flywheel in the case of sudden changes in speed such as starting or turning off the vehicle.

Fig. 3 Connection form figure of centrifugal pendulum

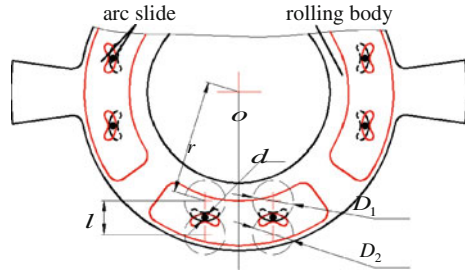
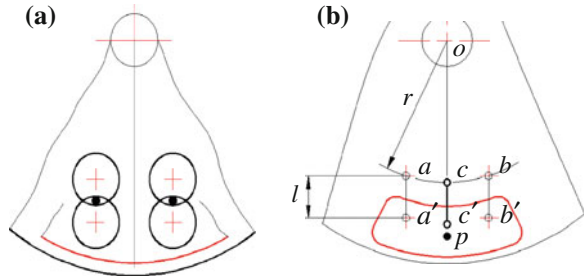


Fig. 4 a Hanging pendulum absorber. **b** Equivalent institution of hanging pendulum absorber

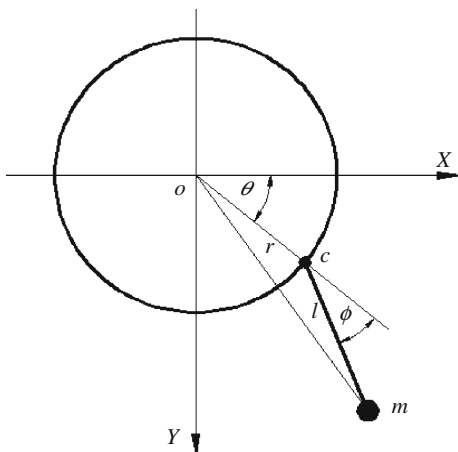


When the absorber runs smoothly, the relative relationship between the centrifugal pendulum and the force transmission plate shown in Fig. 3; When the speed fluctuates, angle between the centrifugal pendulum and the force transmission plate appears difference. Rolling body has a reciprocating motion along the arc slide under the action of “drag and drop” by centrifugal pendulum until the speed of the centrifugal pendulum is equal to the speed of force transmission plate, so as to realize the vibration damping. The system assembled by the centrifugal pendulum and the force transmission plate is essentially a hanging pendulum absorber shown in Fig. 4a. The institutions shown in Fig. 4b is in accordance with the hanging pendulum absorber, it is imaginary that a massless rod connects to the pendulum of mass m in the middle cc' , point c' swing relative to point c . r is the distance between suspension point of the centrifugal pendulum (a, b) to axis of rotation of the flywheel (o), as shown in Figs. 3 and 4. D_1 is the diameter within the arc of the force transmission plate, D_2 is the diameter within the arc of the slide of the centrifugal pendulum, d is the diameter of the roller body. Pendulum length can be expressed as $l = D_1/2 + D_2/2 - d$.

3 Study of the Isolation Performance of Centrifugal Pendulum Absorber

If centrifugal pendulum centroid position point p and point c' coincide, it can be further simplified as the model shown in Fig. 5. When the second flywheel makes constant turning motion at a speed of ω , centrifugal pendulum is adjust in oc of

Fig. 5 Principle diagram of centrifugal pendulum-type absorber



radial extension cord, and the system is in a stable operation condition. Engine output torque is always fluctuant, so the disturbing torque from the first flywheel is transferred to the second flywheel after DMF-CS absorber, and vibration amplitude is reduced but minor fluctuations of the second flywheel can still be caused, at this time the vibration angular of the centrifugal pendulum is ϕ , the corresponding velocity of the second flywheel is $\dot{\theta}$.

3.1 Establishment of Kinematics Differential Equation

In order to facilitate the deduction of formula, research the vibration problems in the operation process of centrifugal pendulum and the second flywheel without considering the influence of friction torque and gravity at the connection point c . Suppose that the rotational inertia of the second flywheel assembly is J , kinetic energy is $T_J = \frac{1}{2}J\dot{\theta}^2$. The mass of the centrifugal pendulum is m , the coordinates x, y are respectively

$$\left. \begin{aligned} x &= r \cos \theta + l \cos(\phi + \theta) \\ y &= r \sin \theta + l \sin(\phi + \theta) \end{aligned} \right\} \quad (1)$$

So

$$\left. \begin{aligned} \dot{x} &= -r \sin \theta \cdot \dot{\theta} - l \sin(\phi + \theta) \cdot (\dot{\phi} + \dot{\theta}) \\ \dot{y} &= r \cos \theta \cdot \dot{\theta} + l \cos(\phi + \theta) \cdot (\dot{\phi} + \dot{\theta}) \end{aligned} \right\}$$

Therefore, the synthesis velocity of particle m can be expressed by

$$\begin{aligned} v^2 &= \dot{x}^2 + \dot{y}^2 \\ &= r^2 \dot{\theta}^2 + 2rl\dot{\theta}(\dot{\phi} + \dot{\theta}) \cos \phi + l^2(\dot{\phi} + \dot{\theta})^2 \end{aligned}$$

The total kinetic energy of centrifugal pendulum and the second flywheel is obtained as

$$T = \frac{1}{2}J\dot{\theta}^2 + \frac{1}{2}mv^2 \quad (2)$$

Substituting Eq. (2) into Lagrange equation

$$\frac{d}{dt} \left(\frac{\partial T}{\partial \dot{q}} \right) - \frac{\partial T}{\partial q} = Mq$$

Where q is generalized coordinate ϕ, θ , the result as follows

$$\begin{aligned} mrl\ddot{\theta} \cos \phi - mrl\dot{\theta}\dot{\phi} \sin \phi + ml^2(\ddot{\phi} + \ddot{\theta}) \\ + mrl\dot{\theta}(\dot{\phi} + \dot{\theta}) \sin \phi = 0 \end{aligned} \quad (3)$$

$$J\ddot{\theta} + m(r+l)^2\ddot{\theta} + ml(r+l)\ddot{\phi} - mrl(\dot{\phi} + 2\dot{\theta})\dot{\phi} = 0 \quad (4)$$

Due to the small angular $\cos \phi \approx 1$, $\sin \phi \approx \phi$, the final part of Eq. (4) $mrl(\dot{\phi} + 2\dot{\theta})\dot{\phi}$ can be ignored for small vibration, kinematics differential equations of centrifugal pendulum can be respectively received by simplifying Eqs. (3, 4)

$$l(\ddot{\phi} + \ddot{\theta}) + r\ddot{\theta} + r\dot{\theta}^2\phi = 0 \quad (5)$$

The kinematics differential equation of the second flywheel assembly is obtained as

$$J\ddot{\theta} + m(r+l)^2\ddot{\theta} + ml(r+l)\ddot{\phi} = 0 \quad (6)$$

In most cases, centrifugal pendulum centroid position point p cannot coincide with point c' . Suppose that the distance between p and c' is e , centrifugal pendulum is simplified as the model shown in Fig. 6 and the centroid coordinate of centrifugal pendulum is as follows

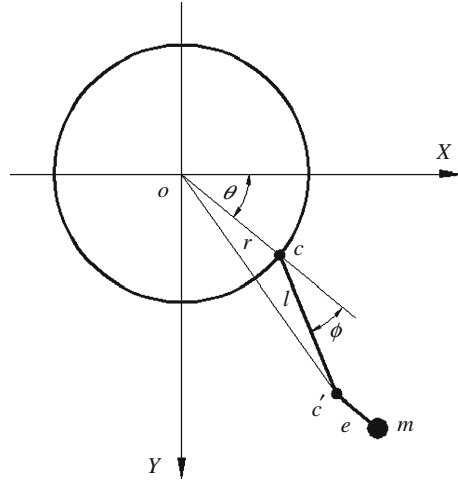
$$\left. \begin{aligned} x &= r \cos \theta + l \cos(\phi + \theta) + e \cos \theta \\ y &= r \sin \theta + l \sin(\phi + \theta) + e \sin \theta \end{aligned} \right\} \quad (7)$$

Repeat the above calculation process, kinematics differential equation of centrifugal pendulum and the second flywheel can be obtained as respectively

$$l(\ddot{\phi} + \ddot{\theta}) + (r+e)\ddot{\theta} + (r+e)\dot{\theta}^2\phi = 0 \quad (8)$$

$$J\ddot{\theta} + m(r+e+l)^2\ddot{\theta} + ml(r+e+l)\ddot{\phi} = 0 \quad (9)$$

Fig. 6 Principle diagram of centrifugal pendulum absorber



Suppose that $e = 0$, Eqs. (8, 9) equal to (5, 6). This proves the case that centroid and connection point coincide is special.

3.2 Calculation of Natural Frequency

Assuming $J_0 = J + m(r + e + l)^2$, we can receive the following equation by cancellation $\ddot{\theta}$ with Eqs. (8, 9)

$$\frac{J}{J_0} \ddot{\phi} + \frac{(r + e)\omega^2}{l} \phi = 0$$

From the above equation, it is shown that centrifugal pendulum (angular ϕ) does harmonic motion, and the circular frequencies is

$$p = \omega \sqrt{\frac{(r + e)J_0}{lJ}} \tag{10}$$

From Eq. (10), it can be found that natural frequency of centrifugal pendulum-type absorber is not constant, and its frequency p is proportional to the angular velocity ω of the second flywheel assembly in the stable operation, which lays a theoretical foundation for the design of DMF-CS with centrifugal pendulum-type absorber [9, 10].

3.3 Study of the Principle of Vibration Isolation of Centrifugal Pendulum

Assuming that the disturbing torque of the second flywheel assembly is $A \sin(\gamma\omega t)$, the kinematics differential equation of this system can be directly rewritten by Eqs. (8) and (9) as follows

$$\left. \begin{aligned} (r+e+l)\ddot{\theta} + l\ddot{\phi} + (r+e)\dot{\theta}^2\phi &= 0 \\ J_0\ddot{\theta} + ml(r+e+l)\ddot{\phi} &= A \sin(\gamma\omega t) \end{aligned} \right\} \quad (11)$$

We can get the special solutions of representative steady-state forced vibration by Eq. (11) as follows

$$\left. \begin{aligned} \theta &= C \sin(\gamma\omega t) \\ \phi &= B \sin(\gamma\omega t) \end{aligned} \right\} \quad (12)$$

Substituting Eq. (12) into Eq. (11), the amplitude B and C can be obtained, then return them back to Eq. (12), the steady-state solution of forced vibrations is gotten as follows

$$\left. \begin{aligned} \theta &= -\frac{A \sin(\gamma\omega t)}{\gamma^2\omega^2 J_0 \left\{ 1 - \frac{m(r+e+l)^2}{J_0 \left(1 - \frac{r+e}{\gamma^2 l} \right)} \right\}} \\ \phi &= \frac{A(r+e+l) \sin(\gamma\omega t)}{\gamma^2\omega^2 J_0 l \left(1 - \frac{r+e}{\gamma^2 l} \right) \left\{ 1 - \frac{m(r+e+l)^2}{J_0 \left(1 - \frac{r+e}{\gamma^2 l} \right)} \right\}} \end{aligned} \right\} \quad (13)$$

To illustrate the role of centrifugal pendulum, motion equation of the second flywheel assembly which has the same disturbing torque without installing centrifugal pendulum, can be expressed as follows

$$J\ddot{\theta} = A \sin(\gamma\omega t)$$

The steady-state solution of the above equation is

$$\theta = -\frac{A \sin(\gamma\omega t)}{J\gamma^2\omega^2} \quad (14)$$

By comparing the first formula of Eqs. (14) and (13), we can draw the conclusion that the role of the centrifugal pendulum is equivalent to increase the rotational inertia of the second flywheel assembly. The increased rotational inertia can be calculated as follows

$$\Delta J = J_0 \left\{ 1 - \frac{m(r+e+l)^2}{J_0(1 - \frac{r+e}{\gamma^2 l})} \right\} - J = \frac{m(r+e+l)^2}{1 - \frac{\gamma^2 l}{r+e}} \quad (15)$$

According to Eq. (15), when design, if selected

$$\gamma^2 = \frac{r+e}{l} \quad (16)$$

We can get $\Delta J \rightarrow \infty$, the role of centrifugal pendulum is similar to a great rotational inertia of the flywheel. In this case, the second flywheel stable operation will be not affected by disturbing torque theoretically. And centrifugal pendulum still does harmonic motion. Substituting $\ddot{\theta} = 0$ into Eq. (11) can be obtained as directly

$$\phi = -\frac{A \sin(\gamma \omega t)}{ml(r+e+l)\gamma^2 \omega^2} \quad (17)$$

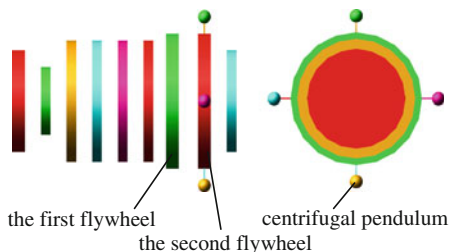
It can be seen that the direction of centrifugal pendulum's angular ϕ and disturbing torque is always opposite, and $ml\ddot{\phi}(r+e+l) = A \sin(\gamma \omega t)$, which makes that the vibration of centrifugal pendulum and the disturbing torque just cancel out.

For four-stroke four-cylinder engine is concerned, the most primary incentive is the second order. Six-cylinder engine, the third order is the most primary incentive. According to the above characteristics analysis of the centrifugal pendulum, if the ratio of sum of DMF-CS with centrifugal pendulum-type absorber's swinging radius and centroid slant distance $(r+e)$ and pendulum length l equals to the square of the main incentive order ($\frac{r+e}{l} = 2^2$ or $\frac{r+e}{l} = 3^2$), it can eliminate the most primary order excitation of engine theoretically, greatly improving the vibration isolation performance of DMF-CS absorber.

4 Analysis of Influencing Factors of the Performance of Vibration Isolation

From the above analysis, the role of the centrifugal pendulum is equivalent to increase the inertia of the second flywheel assembly, the increase of inertia (ΔJ) is closely related to the structure parameters (r, e, l) , the quality of pendulum(m) and the disturbance incentive-order (γ). Under the condition of speed ω , the centrifugal force $F_c = m(r+e+l)\omega^2$ is provided by the rolling body for the pendulum, when the centrifugal pendulum and the force transmission plate move relative to each other, the rolling body exists friction torque, and the greater the speed ω , the greater the friction torque. In the derivation of the performance of vibration isolation without considering the influence of friction torque, rolling body wear after use, manufacturing precision and many other factors, so satisfying Eq. (16) that

Fig. 7 The transmission idle model based on the virtual prototype technology



can thoroughly eliminate the influence of disturbance incentive is just an ideal state. In engineering practice, because of the complex operation conditions and more disturbance incentive -order whether the diesel engine or gasoline engine, the shock absorber can't completely isolate the torsional vibration of the transmission. However, DMF-CS with centrifugal pendulum-type absorber, shown in Fig. 2, can still make that the torsional vibration of the transmission was reduced by 60 % [7].

From the formula (15), in order to ensure enough increments of the rotational inertia, the quality of centrifugal m is required big enough. But the limitation of space and structure layout doesn't allow m too big. Because of the complex operating conditions, the rolling body not only provides centrifugal force for the pendulum, but also bears the impact of pendulum when vehicles start, shift and emergency brake, this requires that the rolling cylinder has strong abrasion resistance and enough strength, which is a more critical component to DMF-CS with centrifugal pendulum-type absorber.

5 Simulation of Performance of Vibration Isolation Based on the Virtual Prototype Technology

The vibration isolation model of the transmission system on different degrees of freedom was built utilizing the virtual prototype technology, the idling condition shown in Fig. 7. According to the Fourier, the frequencies of engine can be expressed as

$$T = T_0 + \sum T_n \sin(n\omega t + \varphi_n)$$

As the amplitude of the high-order harmonic disturbing torque is small, the influence of low-order (such as $n = 1/2, 1, 2, 4, 6, 8, 10$ and so on) can be just considered. For the disturbing torque of engine at different order, simulations of DMF-CS with centrifugal pendulum-type absorber were done, the result shown in Fig. 8. In Fig. 8a–g respectively represent the results of simulations, just as $n = 1/2, 1, 2, 4, 6, 8, 10$ and so on, and the result of the simulation of all the low-orders shown in Fig. 8h.

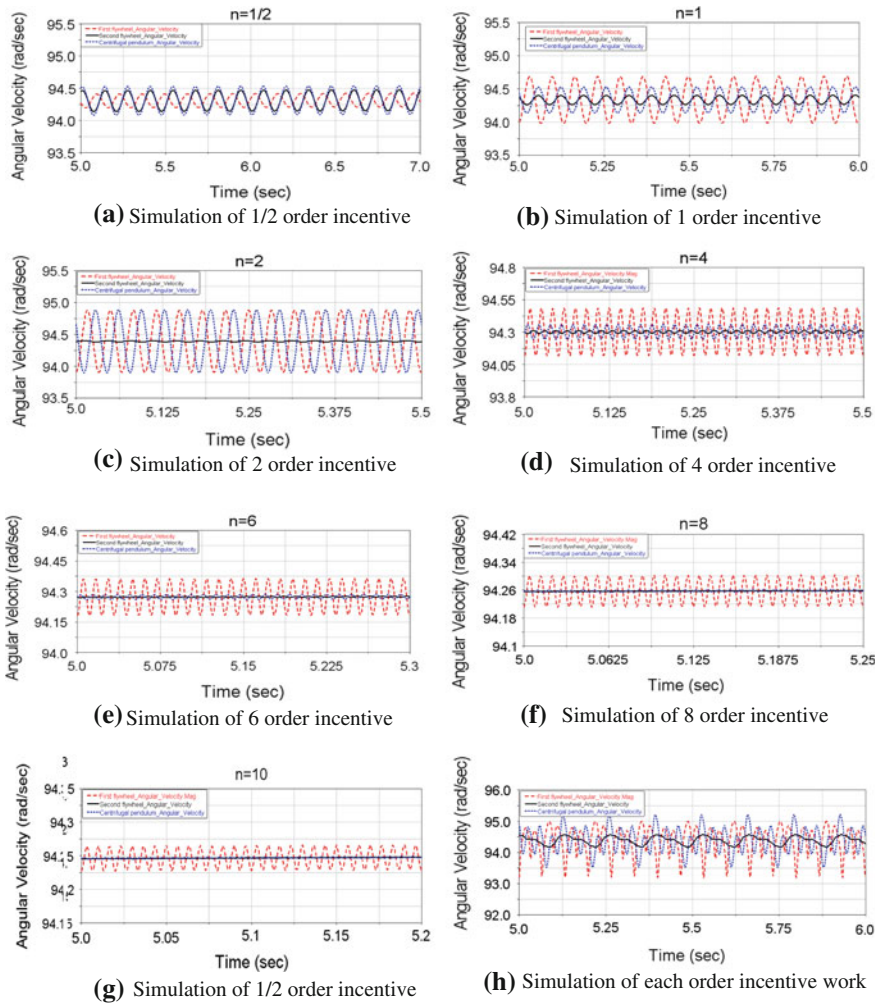


Fig. 8 Simulation of all the low-orders

From Fig. 8, we can come to the conclusion

- (1) When incentive order $n = 2$, based on the effect of the centrifugal pendulum-type absorber, the speed of the second flywheel is basically unchanged and the amplitude of the disturbing torque of the centrifugal pendulum-type absorber is large. The simulation results and theory analysis are consistent.
- (2) When incentive order $n > 2$, the amplitudes of the speed fluctuation of the second flywheel and the centrifugal pendulum are small, especially when $n \geq 8$, the amplitudes of angular velocity fluctuation is almost zero. This damper can effectively weaken the vibration at high-order, which is same with normal DMF-CS.

- (3) When incentive order $n < 2$, the effect of this damper on vibration isolation is not obvious, even when $n = 1/2$, the speed fluctuation of the second flywheel is larger than the first flywheel. Because when the idle speed is 900 rpm, the engine frequency is 15 Hz as $n = 1/2$, and the two order natural frequency of the transmission system is 11.6 Hz, which is the resonance time, so the effect of this damper on vibration isolation is poor.

Due to the result that the amplitude when $n = 1/2$ is far less than the amplitude of ignition frequency (when $n = 2$), even though the effect on vibration isolation is not ideal in this order, but it also can effectively weaken the disturbing torque by engine vibration (as Fig. 8h shown). The LUK Company did a lot of experiments for this damper, and the results show that it can reduce 60 % of the vibration of the transmission system [1].

Similarly, the model of the driving condition can be built and simulated, the result will be similar to the idling condition.

6 Results

- (1) In the paper, the mathematical model of the DMF-CS with centrifugal pendulum-type absorber was built and the differential equations were established. Utilizing the characteristics that the natural frequency of pendulum is proportional to the rotate speed of DMF-CS, the relation between parameters of DMF-CS with centrifugal pendulum-type absorber and the frequencies of engine was found.
- (2) The inertia moment in reverse of pendulum was counteracted to the disturbing torque of engine at ignition frequency by adjusting the parameters of pendulum.
- (3) Based on the virtual prototype technology, the model of power train which included the DMF-CS with centrifugal pendulum-type absorber was built, and simulation was done under different effect of engine. The simulation results and theory analysis are consistent, which validates the analysis and the method of modeling of the DMF-CS with centrifugal pendulum-type absorber.

References

1. Fidlin A, Seebacher R (2006) DMF simulation techniques-finding the needle in the haystack. In: 8th LuK symposium, pp 55–71
2. Reik W, Seebacher R, Kooy A (1998) The dual mass flywheel. In: 6th LuK symposium, pp 69–93
3. Reik W (1990) Torsional isolation in the drive train-an evaluation study. In: 4th LuK symposium, pp 125–146
4. Chen T, Lu Z, Su C (2006) Analysis method for elastic characteristics of arc spring. China Mech Eng 17(5):493–495

5. Luciano E, Vinicius D, Sidnei L, Galvani A, Emilio F (2004) Analyzing the torsional vibration of engines in dynamometer previewing the impacts in clutch disc calibration. In: SAE Paper 2004-01-3247
6. Steinel K (2001) Clutch tuning to optimize noise and vibration behavior in trucks and buses. In: SAE Paper 2001-01-3292
7. Bianchi J (2008) Centrifugal pendulum-type absorbers increase vibration damping. (2008-06-02)[2008-09-04].<http://www.reuters.com/article/pressRelease/idUS149916+02-Jun-2008+PRN20080602>
8. Kooy A, Gillmann A, Jäckel J, Bosse M 2002. DMFW-nothing new. In: 7th LuK Symposium, pp 5–14
9. Lin H (1990) Theory and application of mechanical vibration. Metallurgical Industry Press, Beijing
10. Wang H (1989) Mechanical kinetics. Chongqing University press, Chongqing

Part II
Chassis Controls and Integration

Model-Based Recursive Least Square Algorithm for Estimation of Brake Pressure and Road Friction

Nenggen Ding and Xiaofei Zhan

Abstract A recursive least square algorithm for estimation of brake cylinder pressure and road surface coefficients of adhesion using wheel speeds and control inputs for the hydraulic unit is proposed. It is intended for providing useful information for anti-lock brake systems (ABS) to improve the performance of control logic and diagnostic function. Based on the brake pressure model and wheel/vehicle dynamics, the errors between estimated wheel angular acceleration and its actual value according to the measured wheel speeds are minimized. Longitudinal load transfer is considered for calculation of tire normal forces based on the estimated deceleration according to the vehicle reference speeds from the ABS control logic. The proposed algorithm is evaluated using ABS simulation data under various braking conditions on a hardware-in-the-loop (HIL) test rig.

Keywords Brake pressure estimation · Road friction estimation · Recursive least square algorithm · ABS

F2012-G02-002

N. Ding (✉) · X. Zhan
e-mail: dingng@buaa.edu.cn

X. Zhan
e-mail: zxf_yh@yahoo.cn

1 Introduction

The performance of ABS relies on not only control logic itself, but also the information of road surface coefficient of adhesion and sometimes brake cylinder pressure. Both estimated road surface coefficient of adhesion and brake pressure are beneficial for determination of the control threshold and fault diagnosis of ABS.

As pointed out by Kevin Austin O’Dea [1], estimation of the difference in pressure across hydraulic valves can improve control of these valves and ultimately the performance of ABS. Mauer et al. [2], discussed means to adapt the braking pressure to variation of road conditions by analyzing the relation between brake torque and slip ratio in real time by the fuzzy logic controller. However, one drawback of the scheme is using of pressure sensors.

In recent years, Hassan Ali Shraim [3] identified and estimated tires longitudinal forces, vehicle side slip angle and velocity using sliding modes (SM) observers. Longitudinal forces are identified using high-order SM observers. Tire force estimation algorithms are also proposed for vehicle dynamic stability control (DSC) system to prevent the vehicle from deviation of the normal dynamics attitude and realize the improved dynamics stability in limited driving conditions [4].

A recursive least square algorithm for estimation of brake cylinder pressure and road surface coefficients of adhesion using wheel speeds and control inputs for the hydraulic unit is proposed. It is evaluated using ABS simulation data under a few braking conditions on a HIL test rig. Comparison between estimated results and their actual values shows that the proposed algorithm is valid for most ABS-activated situations and will be useful in enhancement of ABS control logic and its fault diagnosis.

2 Vehicle Model

A. Brake pressure model

For a vehicle with ABS, the brake pressure is modulated by the electromagnetic valves and a motor within the hydraulic unit. There are three basic pressure regulating states, i.e. pressure apply, pressure hold, and pressure release.

During a process of pressure apply, pressure of wheel cylinder, P_w , is governed by the following formula [5]

$$P_w(t) = P_m - \left[(P_m - P_{w0})^{\phi_{inc}} - K_{inc} \phi_{inc}(t - t_0) \right]^{\frac{1}{\phi_{inc}}} \quad (1)$$

Where P_{w0} is the pressure of wheel brake cylinder at time t_0 , P_m the pressure of master brake cylinder, and K_{inc} and ϕ_{inc} coefficients determined according to the pressure response characteristics of the hydraulic module and brake system used.

Similarly, during a process of pressure release, P_w is governed by

$$P_w(t) = \left[(P_{w0} - P_a)^{\phi_{\text{dec}}} - K_{\text{dec}} \phi_{\text{dec}}(t - t_0) \right]^{\frac{1}{\phi_{\text{dec}}}} + P_a \quad (2)$$

Where P_a is pressure of accumulator in the hydraulic module, and K_{dec} and ϕ_{dec} are similar coefficients.

B. Wheel dynamics

Wheel rotational motion is governed by the following equation

$$I_w \varepsilon = \mu_x \cdot F_z \cdot R - C_P \cdot P_w \quad (3)$$

Where ε is wheel angular acceleration, I_w wheel rotational inertia, C_P brake torque gain, R wheel static radius and F_z the tire normal force. F_z has a relationship with braking level Z , defined as vehicle deceleration divided by the gravity acceleration. Considering the longitudinal load transfer during braking operation, yield

$$F_z = F_{zs} \pm \frac{1}{2} m z g h_g / L \quad (4)$$

Where F_{zs} is static tire normal force, and signs “+” and “-” on the right side are suitable for front wheels and rear wheels, respectively.

C. Tire longitudinal forces and vehicle longitudinal model

As for longitudinal tire/road friction coefficient, a simple, velocity-independent three-parameter model proposed by Burckhardt [6] is used, i.e.

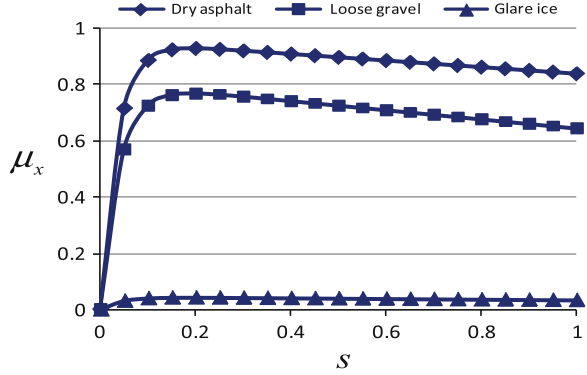
$$\begin{aligned} \mu_x &= c_1 (1 - e^{-c_2 s}) - c_3 s \\ s = \hat{s} &= 1 - \frac{\omega_w R}{\hat{V}} \end{aligned} \quad (5)$$

Where s is tire longitudinal slip ratio, $s \in [0, 1]$, μ_x longitudinal friction coefficient of tire, c_1 , c_2 , and c_3 road constants, and ω_w wheel angular speed.

Shown in Fig. 1 are various μ - s tire/road friction profiles, taken from [7] (Hamed et al.) and [6] (Canudas-de-wit et al.). For state estimation using Eq. (5), tire/road friction characteristics can be represented only by its peak value, which is restricted between those of dry asphalt and glare ice. With a given peak value for a specific road, the corresponding coefficients c_i 's can be determined using Eq. (6)

$$\begin{aligned} n &= (\mu_p - 0.044) / (0.93 - 0.044) \\ c_1 &= (1 - n) \times 0.0471 + n \times 0.958 \\ c_2 &= (1 - n) \times 23.9 + n \times 28.1 \\ c_3 &= (1 - n) \times 0.0125 + n \times 0.117 \end{aligned} \quad (6)$$

Where μ_p is peak value of longitudinal friction coefficient of tire. The longitudinal motion of the vehicle is governed by the following equations

Fig. 1 Burckhardt tire model

$$mD = F_{bfl} + F_{bfr} + F_{brl} + F_{brr} \quad (7)$$

$$F_{bij} = \mu_{xij} F_{zij}, \quad i = f, r \ \& \ j = 1, r \quad (8)$$

Where m is total vehicle mass, D vehicle deceleration, and F_b brake force. Note that a rear tire has the same peak value of longitudinal tire/road friction coefficient as the front tire on the same wheel track with a delay for travel of wheel base.

Road braking forces can be determined from Eq. (3) as

$$\mu_x \cdot F_z = \frac{I_w \varepsilon - C_P \cdot P_w}{R} \quad (9)$$

Substituting Eq. (9) first into (8) and finally into (7), yield

$$\frac{C_{Pf}(P_{wfl} + P_{wfr}) + C_{Pr}(P_{wrl} + P_{wrr})}{R} = mD - \frac{I_{wf}(\varepsilon_{fl} + \varepsilon_{fr}) + I_{wr}(\varepsilon_{rl} + \varepsilon_{rr})}{R} \quad (10)$$

Divide Eq. (10) by vehicle gross weight, mg , then

$$\eta = z - \frac{I_{wf}(\varepsilon_{fl} + \varepsilon_{fr}) + I_{wr}(\varepsilon_{rl} + \varepsilon_{rr})}{mgR} \quad (11)$$

Where η is called “BRAKE FORCE LEVEL”, which is defined as

$$\eta := \frac{C_{Pf}(P_{wfl} + P_{wfr}) + C_{Pr}(P_{wrl} + P_{wrr})}{mgR} \quad (12)$$

3 Estimation Algorithm

Define wheel brake force level as

$$\eta_{ij} := \frac{C_{Pi} P_{wij}}{mgR}, \quad i = f, r, \ \& \ j = 1, r \quad (13)$$

The coupling property of Eq. (10) or (11) indicates that brake pressure and angular acceleration of the four wheels are correlated by vehicle deceleration or vehicle brake level. For the purpose of formulating estimation algorithm for each individual wheel, the pseudo-measurement of brake force level η_m from Eq. (11) is apportioned to the four wheels proportionally to their vertical loads. Thus, the wheel brake force level has its pseudo-measurement value as follows

$$\eta_{fl} = \eta_{fr} = \frac{b + h_g \hat{z}}{2L} \eta_m, \quad \eta_{rl} = \eta_{rr} = \frac{a - h_g \hat{z}}{2L} \eta_m \quad (14)$$

where h_g is height of vehicle's center of gravity, and L wheel base.

To minimize computation work, only brake pressure is estimated for the rear wheels. As for front wheels, both tire/road friction and brake pressure are estimated. This strategy allows rear wheels utilize tire/road friction information of the front wheels.

For a rear wheel, the estimation architecture is

$$\begin{aligned} \theta_k &= (P_{0rj})_k \\ x_k &= \mu_{xj} F_{zsj} R - I_{wr} \varepsilon_{rj}, \quad j = 1, r \\ e_k &= x_k - \frac{C_{pr} P_{rj}}{(P_{0rj})_{k-1}} \hat{\theta}_k \end{aligned} \quad (15)$$

And for the front wheels, the estimation architecture after normalization of output vector is

$$\begin{aligned} \theta_k &= [\mu_{pj} \quad P_{0fj}]_k^T \\ x_k &= \begin{bmatrix} I_{wf} \varepsilon_{fj} \\ F_{zsf} R \quad w \cdot \eta_{fj} \end{bmatrix}_k^{-1} \\ e_k &= x_k - \begin{bmatrix} \frac{F_{zf} \mu_{xfj}}{F_{zsf} \hat{\mu}_{pj}} & -\frac{C_{pf} P_{fj}}{F_{zsf} R \hat{P}_{0pfj}} \\ 0 & \frac{w \cdot C_{pf} P_{fj}}{mgR \hat{P}_{0pfj}} \end{bmatrix}_{k-1} \hat{\theta}_k, \quad j = 1, ra \end{aligned} \quad (16)$$

where w is the relative weight for wheel brake force level.

As given with detailed derivation in [8], parameters can be estimated using RLS method to minimize the index as follows

$$\begin{aligned} \hat{\theta}_k &= \hat{\theta}_k + F_{k+1} B^T (x_{k+1} - B \hat{\theta}_k) \\ F_{k+1} &= \frac{1}{\lambda} \left[F_k - F_k B^T (\lambda I + B F_k B^T)^{-1} B F_k \right] \\ \hat{\theta}_k &= \theta_0, \quad F_1 = \sigma I \end{aligned} \quad (17)$$

It is reasonable to assume that w has a small value when the vehicle or wheel dynamics is in a transient state and vice versa. For example, when road friction changes suddenly or the wheel has a large slip rate, pseudo-measurement of wheel

Fig. 2 A brief flow chart of estimation architecture

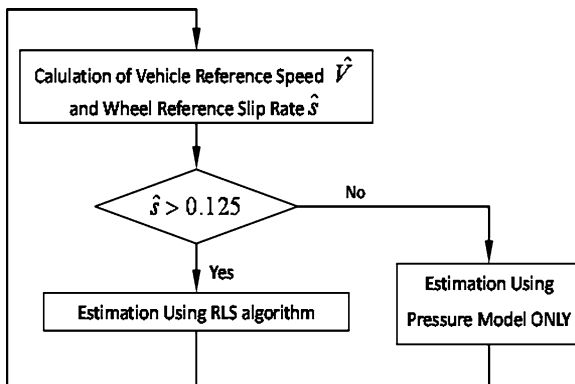


Fig. 3 A scenario of HIL simulation for braking on μ -split road surface



brake force level has a low credibility due to inaccurate estimate of braking level and longitudinal load transfer.

The accuracy of estimation highly depends on that of vehicle reference speed. From Fig. 1, it can be seen that at small slip ratios, both estimated slip rate and longitudinal force are more sensitive to these values. However, in the case of large slip, they will still have considerably high accuracy even if vehicle reference speed is misestimated, more or less. Thus the RLS algorithms Eq. (17) for individual wheel parameter estimation based on architecture in Eq. (15 and 16) are used only at large slip rates, combined with estimation using only brake pressure model at low slip rates. This modification is shown in Fig. 2.

4 Evaluation of the Algorithm

The algorithm for individual wheel parameters is evaluated using HIL simulation data. Braking conditions of the test are typically μ -jump, and μ -split road surfaces, and road friction coefficients are set to be 0.8 and 0.3 for high- μ and low- μ wheel tracks, respectively. A typical scenario of HIL simulation is shown in Fig. 3.

The initial brake pressure is assumed to be 3 MPa for four wheels, and the initial peak value of road friction coefficient is assumed 0.8.

For acquisition of required data from ABS tests, wheel speeds and brake cylinder pressure are measured and these data are sent to a personal computer from

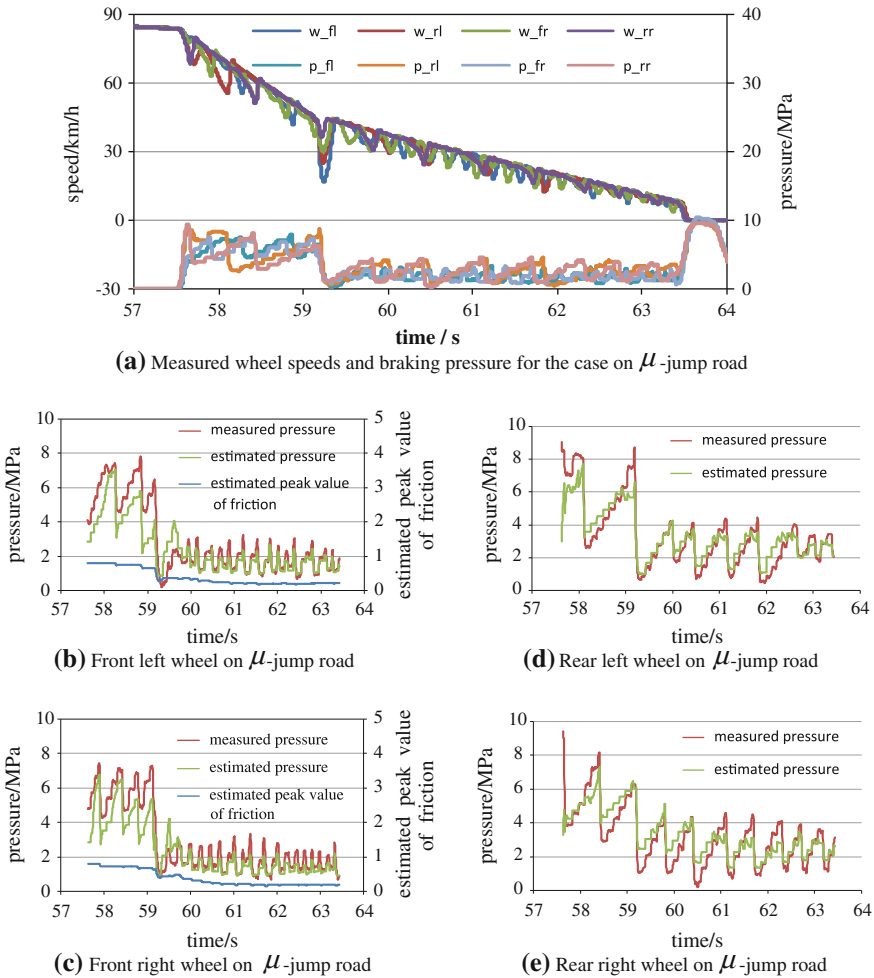


Fig. 4 Comparison of estimated results with road test data on μ -jump road

ABS ECU via serial port communication. The ECU also sends pressure regulating states to the computer. The measured pressure is used only for evaluation of estimation algorithms, and does not take part in the estimation process.

Test and estimated data are shown in Figs. 4 and 5. Comparison of measured and estimated data in figures shows that the estimated pressure in μ -jump, and μ -split cases coincides quite well with measured pressure except during the beginning phase after ABS is activated. This is due to the fact that brake pressure information is not available about at the beginning of the brake event. Often, the pressure is underestimated on the second half of the maneuvers, though the estimated results are generally satisfactory on the first half.

The estimated tire/road friction of coefficient is generally acceptable.

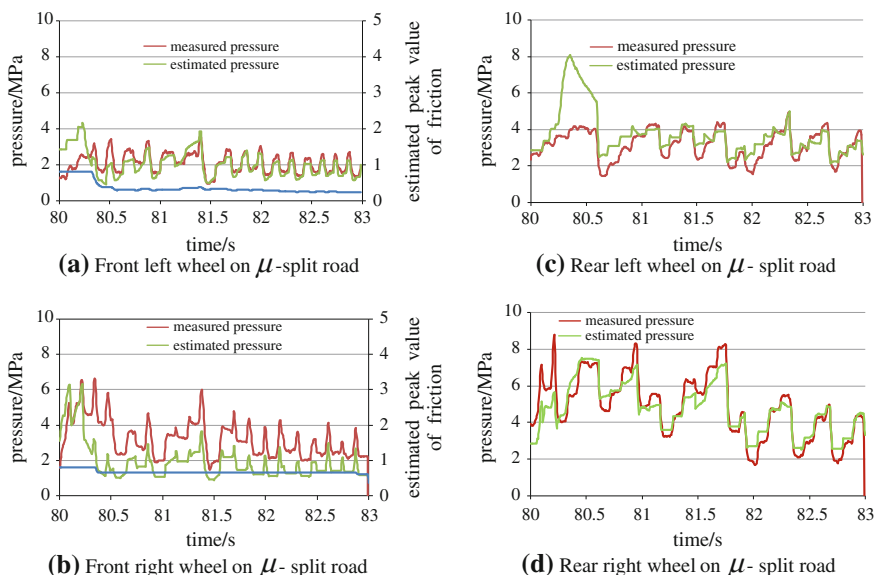


Fig. 5 Comparison of estimated results with road test data on μ -split road (low- μ on left side, and high- μ on right side)

5 Conclusion

A model-based recursive least square algorithm for estimation of brake cylinder pressure and road surface coefficient of adhesion using wheel speeds and control inputs for the hydraulic unit is proposed. Estimated results according to ABS HIL simulation data show that the strategy of estimation is valid and successful without using additional sensors.

References

1. O'Dea KA (2005) Anti-lock braking performance and hydraulic brake pressure estimation. SAE Paper Series 2005-01-1061, April 2005
2. Mauer GF, Gissinger GF, Chamaillard Y (1994) Fuzzy logic continuous and quantizing control of an abs braking system. SAE Paper Series 940830, Mar 1994
3. Shraim HA (2007) Robust virtual sensors and controller design to improve vehicle stability enhancement in the critical situations. SAE Paper Series 2007-01-0779, April 2007
4. Li L, Song J, Yang C et al (2007) Tire force fast estimation and compensation method for vehicle dynamics stability real time control. SAE Paper Series 2007-01-4244, Oct 2007
5. Guo K, Liu L (1999) A study on hydraulic characteristics of anti-lock brake systems. J Jilin Univ Technol (Nat Sci) 29:1-5
6. Canudas-de-wit C, Tsiotras P, Velenis E et al (2002) Dynamic friction models for road/tire longitudinal interaction vehicle system dynamics. Draft article, Oct 14

7. Harned J, Johnston L, Scharpf G (1969) Measurement of tire brake force characteristics as related to wheel slip (antilock) control system design. SAE Trans 78:909–925 (Paper 690214)
8. Yi K, Hedrick K, Lee S.(1999) Estimation of tire-road friction using observer based identifiers. Veh Syst Dyn, 31(4):233–261

Preview Ride Comfort Control for Electric Active Suspension

Haruhiko Sugai, Shuuichi Buma, Ryo Kanda, Kenshiro Yoshioka
and Masaaki Hasegawa

Abstract A preview control that acts in accordance with the road surface profile in front of the vehicle has been proposed as a way to enhance ride comfort. Although the effectiveness of this control has been verified, many issues remain to be resolved, including improving the road surface profile estimation accuracy while the vehicle is in motion. Consequently, as a way of enhancing the comfort of the vehicle and reducing energy consumption, this development aimed to construct preview ride comfort control logic capable of estimating road surface displacement more accurately. To improve estimation accuracy, this paper proposes a method of estimating the road surface displacement in front of the vehicle using preview sensors and the body displacement estimated using a full-order observer. It describes sky-hook control logic that performs feed-forward of control amounts proportionally to the lateral road surface displacement. The ride comfort performance in the roll direction and the energy-saving effect of this control was verified using a 4-wheel shaker and in actual driving tests. It was confirmed that the developed control estimates road surface displacement more accurately than the previous control, thereby improving ride comfort at low-frequencies and reducing energy consumption. The result is a more feasible preview control system that has made progress toward the aim of practical application.

Keywords Preview control · Ride comfort · Active suspension · Full-order observer · Laser displacement sensor

F2012-G02-005

H. Sugai (✉) · S. Buma
Toyota Motor Corporation, Toyota, Japan
e-mail: haruhiko@sugai.tec.toyota.co.jp

R. Kanda · K. Yoshioka · M. Hasegawa
Toyota Technical Development Corporation, Toyota, Japan

1 Introduction

Several examples of active suspension systems that aim to enhance both the ride comfort and stability of the vehicle have already been developed and practically adopted [1, 2]. At the same time, various reports have examined control laws for ride comfort using these systems [3] and control laws for correcting actuator response delays [4, 5].

Previous reports have verified the performance of sky-hook controls adopted in electric active suspension systems, such as one that performs feed-back of control amounts proportionally to the roll angular velocity of the body and one that performs feed-forward of control amounts proportionally to the lateral road surface displacement [6, 7].

Furthermore, a study has also verified the effectiveness of a preview control that calculates control amounts based on road surface information in front of the vehicle as a means of compensating for actuator delays and the like [8, 9].

This paper describes an overview of the development progress of this preview ride comfort control system.

2 System Outline

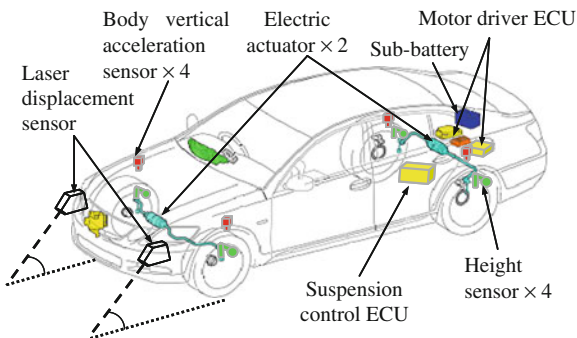
2.1 System Aims

ISO2631-1 [10] aims to improve ride comfort over a wide range, including close to the roll resonance frequency and the middle frequency band, centered on the 0.8 Hz frequency at which the human body is particularly sensitive to roll. It also aims to improve road holding performance and reduce energy consumption.

2.2 System Components

Figure 1 shows the components of the eActive2 system used by the test vehicle. The preview system uses laser displacement sensors to measure the road surface profile in front of the vehicle. These sensors have a measurement frequency of 0.1 ms and a measurement accuracy of 0.2 mm, which is sufficiently accurate for the test. The laser displacement sensors are located in the front bumper and are angled downward toward the front of the vehicle. The system uses the front and rear actuators in the existing electric active stabilizer system. Other components include body vertical acceleration sensors, height sensors, wheel speed sensors, and the like. The electric control unit (ECU) of the suspension uses the signals from these sensors to calculate the target control amounts and transmits control commands to each motor driver ECU. Based on these command values, the motor

Fig. 1 System components



drive ECUs drive the electric actuators, which then generate the active control force.

Figure 2 shows the frequency response characteristics of the actual actuator rotating angle with respect to the target angle. At 2 Hz, the gain decreases by 3 dB and at 1.4 Hz, the phase is delayed by 45°. These results were measured with the system installed on an actual vehicle under the following conditions. The input was a 0.1–15 Hz sine sweep and the amplitude was determined from the torque equivalent to 80 % of the accumulated operating frequency when driven at 80 km/h on the test road. The test road consisted of road surfaces equivalent to zones C and D in ISO 8608 at less than 5 Hz (good to rough road surfaces) and zones B and C at more than 5 Hz (good to normal road surfaces).

2.3 System Modeling

Figure 3 shows the vehicle model focusing on the roll motion of the system. This model considers road surface inputs to be virtually equal to inputs to the unsprung mass at frequencies where the actuator control force affects ride comfort. The model also ignores changes in tire deflection. The symbols in the model are defined as follows: θ_r is the body roll angle, I_r is the roll moment of inertia, x_{2ir} and x_{2il} are the body displacement at the right and left wheels, respectively, x_{1ir} and x_{1il} are the road surface displacement of the right and left wheels, respectively, c_{2i} is the damper coefficient, k_{2ci} is the coil spring stiffness, k_{2ti} is the stabilizer spring stiffness (at all wheel positions), T_i is the tread, and M_{acti} is the roll moment generated by the actuator. In addition, $i = f$ and r , which refer to the front and rear wheels, respectively.

Equation (1) shows the roll direction equation of motion derived from Fig. 3.

$$\begin{aligned}
 I_r \ddot{\theta}_r = & -(c_{2Rf} + c_{2Rr}) \dot{\theta}_r - (k_{2Rf} + k_{2Rr}) \theta_r + c_{2f} (\dot{x}_{1fl} + \dot{x}_{1fr}) \frac{T_f}{2} + c_{2r} (\dot{x}_{1rl} + \dot{x}_{1rr}) \frac{T_r}{2} \\
 & + (k_{2cf} + k_{2tf}) (x_{1fl} + x_{1fr}) \frac{T_f}{2} + (k_{2cr} + k_{2tr}) (x_{1rl} + x_{1rr}) \frac{T_r}{2} + M_{actf} + M_{actr}
 \end{aligned}
 \tag{1}$$

Fig. 2 Frequency response of electric actuators

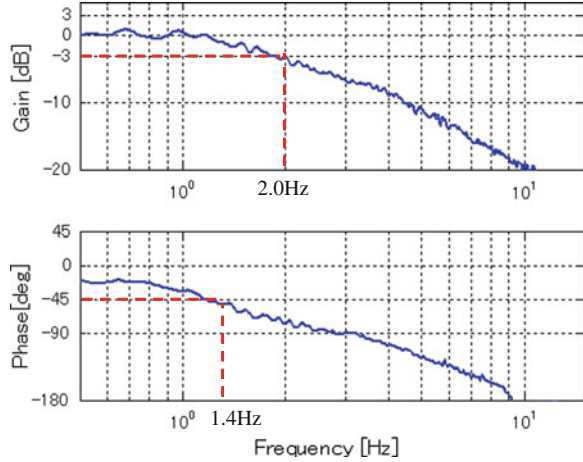
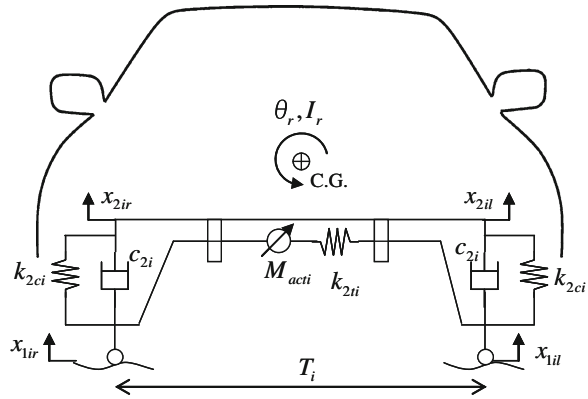


Fig. 3 Roll direction vehicle model

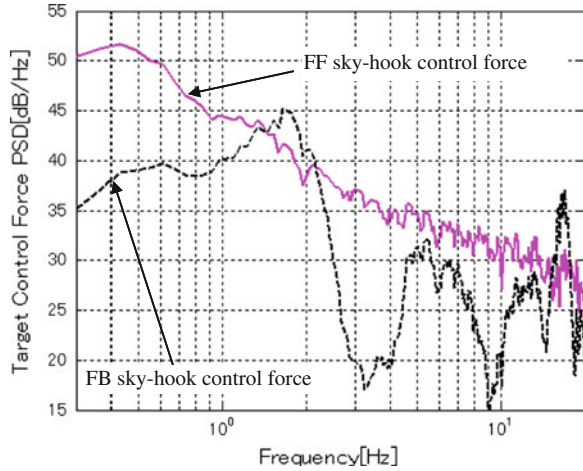


However, $c_{2Ri} = c_{2i} \frac{T_i^2}{2}$ and $k_{2Ri} = (k_{2ci} + k_{2ii}) \frac{T_i^2}{2}$. The first and second terms on the right of the equation express the vibration control force of the body, and the third to sixth terms express the vibration input force. The seventh and eighth terms on the right side of the equation express the active control force generated by the actuator. As described in the following sections, the roll vibration of the body is suppressed by calculating these terms using sky-hook control.

2.3.1 Ride Comfort Control Laws

Sky-hook control has excellent vibration insulation properties and is frequently used for the ride comfort control laws of active suspension systems. As described by Nagai [3], methods for achieving sky-hook control include the feed-back of control force proportionally to the angular velocity of the body (called FB sky-hook control below) and the feed-forward of control force proportionally to road

Fig. 4 Frequency characteristics of target control force



inputs such as the displacement or variation in the road surface (called FF sky-hook control below).

Figure 4 shows the frequency characteristics of the required control force assuming driving at 80 km/h on the test road using these control laws. Under these conditions, the greatest control force of the FB sky-hook control is close to the resonance point of the body. In contrast, the control force of the FF sky-hook control increases as the frequency decreases. Figure 5 shows the break down of the FF sky-hook control force. At 3 Hz or less, the control force proportional to the road surface displacement is dominant. However, above 3 Hz, the control force proportional to the road surface variation is dominant.

Therefore, this study adopted FF sky-hook control, which acts proportionally to the road surface displacement (i.e., the lateral differences in the road surface) and is capable of obtaining a major control effect at low frequencies. This control was selected considering the peak human sensitivity to roll (close to 0.8 Hz) and the actuator response (2 Hz). Equation (2) expresses the control value of the FF sky-hook control actuator.

$$M_{acti} = -k_{2Ri} \frac{(x_{1il} - x_{1ir})}{T_i} \tag{2}$$

The FB sky-hook control was studied for comparison. In this paper, the roll angular velocity is calculated using the vertical acceleration of the body at each wheel and the approximate integration [7]. The FB sky-hook control value is calculated following Eq. (3) by multiplying the roll angular velocity by the roll sky-hook damping coefficient. In this calculation, the phase of the roll angular velocity is advanced by a phase lead compensator [9].

$$M_{acti} = -c_{sRi} \dot{\theta}_r \tag{3}$$

Fig. 5 Break down of FF sky-hook control

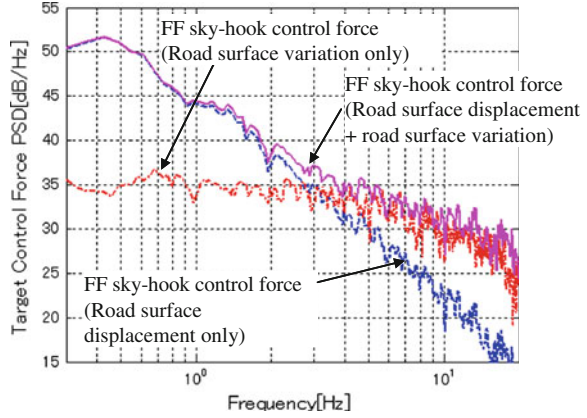
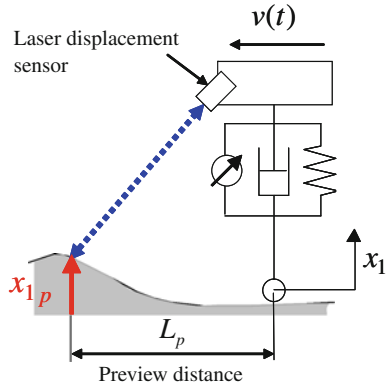


Fig. 6 Outline of preview control



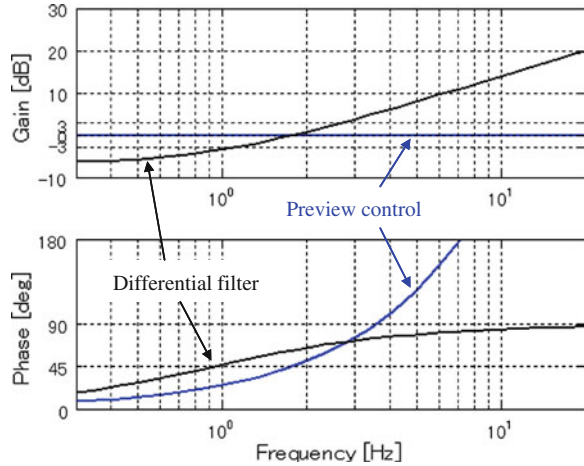
2.3.2 Phase Correction by Preview Control

This section describes how the preview control compensates for actuator response delays and the like. Figure 6 shows an outline of the preview control. The road surface profile in front of the vehicle is measured using the laser displacement sensors. This information is then used for the control. Equation (4) shows the control command value when this control law is adopted. It differs from Eq. (2) by including the control margin times $t_{pf} = L_p/v(t)$ and $t_{pr} = (L_p + L)/v(t)$ obtained by reading the road surface information at the front and rear in advance, and the preview compensation time τ_{pi} for correcting the actuator response delay and the like.

$$M_{acti} = -k_{2Ri} \frac{(x_{1pl}(t - t_{pi} + \tau_{pi}) - x_{1pr}(t - t_{pi} + \tau_{pi}))}{T_i} \tag{4}$$

In this equation, $x_{1pl}(t)$ and $x_{1pr}(t)$ represent the road surface displacement at the position of the laser displacement sensors above the left and right wheels, respectively, L_p is the preview distance to the road surface profile in front of the vehicle, L is the wheelbase, and $v(t)$ is the velocity of the vehicle body.

Fig. 7 Phase compensation characteristics



In this study, the preview distance L_p is set to a position 1.4 m forward of the center of the front axle based on the actuator response and the standard vehicle speed in the performance tests.

Figure 7 shows the frequency characteristics of the phase compensation performed under these conditions. For comparison, the figure also shows the characteristics of phase compensation using a conventional differential filter [9]. In the case of the differential filter, the gain fluctuates widely and the amount of phase lead is limited. In contrast, the preview control demonstrates no increases or decreases in gain in all the frequency bands, enabling the required control force commands to be generated. In addition, the amount of phase compensation increases in accordance with the frequency. This indicates that the control is more capable of achieving the optimum control timing even in middle and higher frequency bands at which the actuator phase delay increases. This should have the effect of reducing energy consumption.

Figure 8 shows a block diagram of the control after substituting Eqs. (4) into (1). The bold lines and boxes correspond to Eq. (4) and show the actuator control flow. This control is capable of reducing inputs from the road surface before transmission to the body by performing feed-forward of control force proportionally to the road surface displacement (i.e., the lateral differences in the road surface).

2.3.3 Road Surface Displacement Estimation

This section describes the method for estimating road surface displacement. The laser displacement sensors that detect the road surface profile in front of the vehicle are installed on the body and are therefore affected by the vehicle behavior. Consequently, the preview distance varies from the standard value (1.4 m) due to changes in the vehicle laden state or changes in vehicle posture (i.e., the sensor

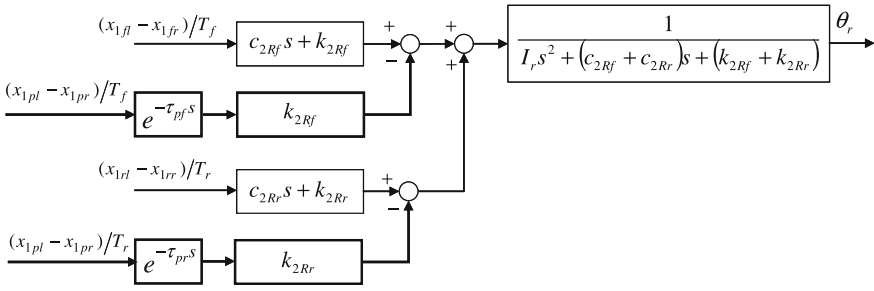


Fig. 8 Block diagram of FF sky-hook control + preview control

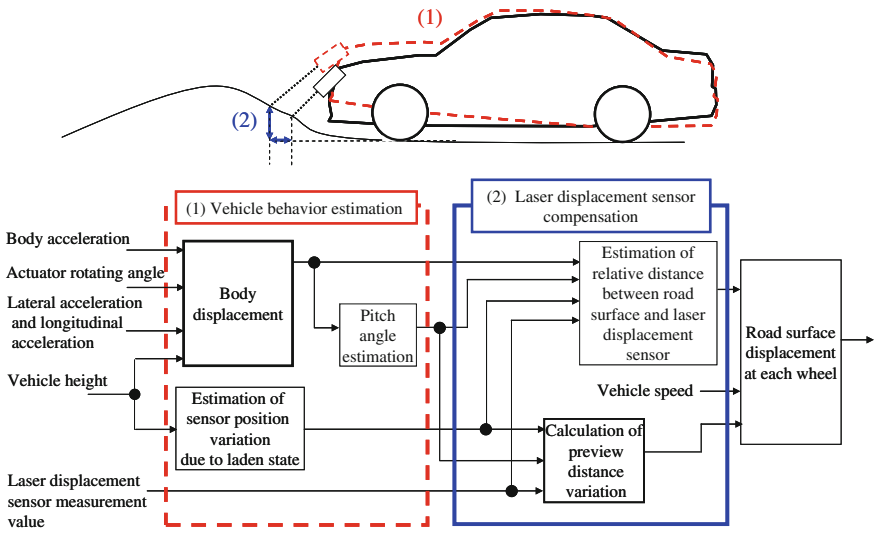


Fig. 9 Flow of road surface displacement estimation

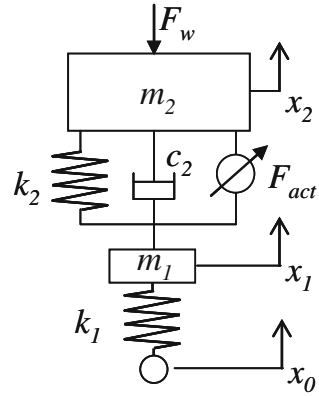
position) in response to road surface inputs. Therefore, compensation is required to prevent these changes affecting ride comfort.

The preview distance variation and the road surface displacement of the laser displacement sensor target position are estimated from the state quantities measured by each sensor. Figure 9 shows the flow from this estimation process to the calculation of the road surface displacement at each wheel.

First, the vehicle behavior is estimated in block [1]. As described in the following section, a full-order observer was used to estimate the body displacement and the pitch angle. The inputs to the full-order observer are the body vertical acceleration, actuator rotating angle, lateral acceleration, longitudinal acceleration, and vehicle height. The sensor position variation due to the laden state is also detected from the vehicle height.

Subsequently, laser displacement sensor compensation is performed in block [2]. In this block, the preview distance variation is calculated from the

Fig. 10 Single-wheel suspension model of full-order observer



sensor angle variation and the sensor measurement values to estimate the road surface displacement at this position. The road surface displacement at each wheel and the input timing can then be corrected by factoring this preview distance variation into the standard preview distance to calculate a preview time in accordance with the vehicle speed.

2.4 Estimation of Body Displacement

Estimation of the body displacement is a necessary part of this system to correct changes in the position of the laser displacement sensor due to vehicle behavior. This can be estimated from the second order integrals of the body vertical acceleration sensor values. However, since this method requires a high-pass filter, it is susceptible to phase lead and gain reduction at low frequencies. Therefore, this study estimated the body displacement using a full-order observer.

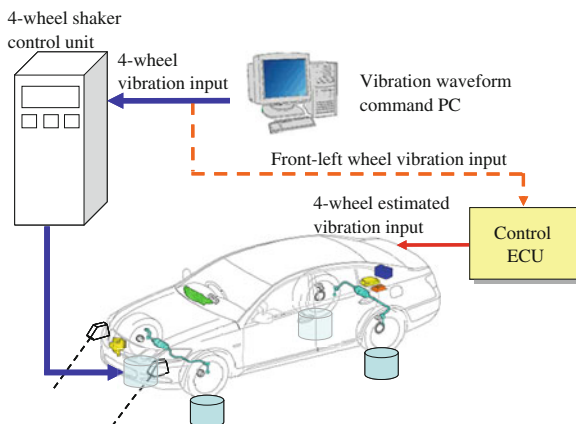
Figure 10 shows the single-wheel suspension model. Unlike a conventional single-wheel model for road inputs only, this model also factors in the pitch and roll moments with respect to longitudinal and lateral acceleration. The equation of motion is as follows.

$$\begin{aligned}
 m_2\ddot{x}_2 + c_2(\dot{x}_2 - \dot{x}_1) + k_2(x_2 - x_1) &= F_{act} + F_w \\
 m_1\ddot{x}_1 + c_2(\dot{x}_1 - \dot{x}_2) + k_2(x_1 - x_2) + k_1(x_1 - x_0) &= -F_{act}
 \end{aligned}
 \tag{5}$$

In this equation, $F_w = PitchSign(F_{gx}) + RollSign(F_{gy})$.

- F_{gx} : Pitch inertial force generated from longitudinal acceleration
- $PitchSign$: Symbol for each wheel [FL : 1, FR : 1, RL : - 1, RR : - 1]
- F_{gy} : Roll inertial force generated from lateral acceleration
- $RollSign$: Symbol for each wheel [FL : 1, FR : - 1, RL : 1, RR : - 1]
- F_{act} : Control force generated by actuator

Fig. 11 4-Wheel shaker system



The full-order observer was composed with respect to this model. The state quantity \hat{x}_2 estimated by the full-order observer for body displacement was used to estimate road surface displacement. This study set the target in the range from 0.8 to 1.8 Hz to an amplitude ratio of ± 3 dB and a phase difference of $\pm 45^\circ$, considering human sensitivity to roll angular acceleration and the actuator response. The full-order observer gain was determined by pole placement.

3 Actual Vehicle Tests

3.1 4-Wheel Shaker Test

To verify the effect of this ride comfort control law in actual vehicle tests, items such as the road surface displacement estimation accuracy, road holding performance, and the like must be evaluated accurately. Therefore, verification was performed using the 4-wheel shaker test system shown in Fig. 11. However, a 4-wheel shaker simulation does not have a road surface in front of the vehicle to measure. As a solution, the vibration start timing was read by the control ECU based on the vibration waveform acquired from the vibration waveform command PC. The vibration waveform in the ECU was then subtracted from the laser displacement sensor value based on this information to simulate laser displacement sensor values obtained in actual driving.

As an indication of the road surface displacement estimation accuracy, Fig. 12 shows a Bode plot of the correlation between the road surface displacement estimation value and the actual waveform data for the front left wheel. The preview compensation time τ_{pi} was 70 ms. As a result, the targeted amplitude ratio and phase difference of less than ± 3 dB and $\pm 45^\circ$, respectively, were achieved in the range from 0.5 to 6 Hz.

Fig. 12 Road surface displacement estimation accuracy

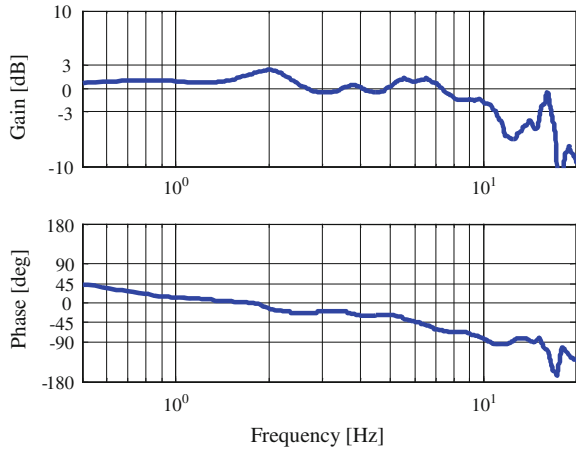
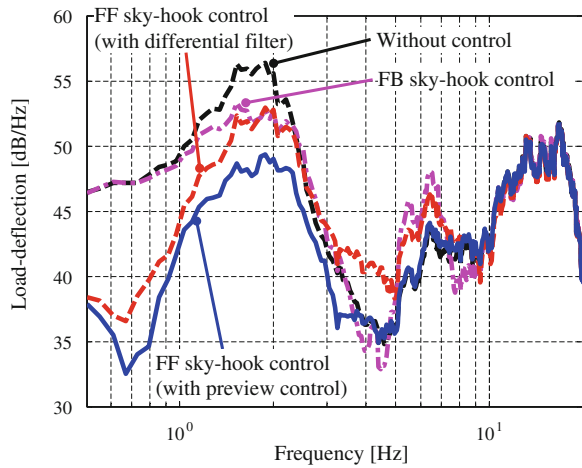


Fig. 13 Load deflection



Next, Fig. 13 shows the power spectral density (PSD) analysis results for load deflection in the roll direction. For comparison, the figure also shows the results without control, with FB sky-hook control, and with FF sky-hook control (phase compensation using differential filter). When the preview control was adopted in the FF sky-hook control, load deflection decreased at below 4 Hz compared to the results without the control. This effect was particularly noticeable at close to 0.8 Hz, at which the maximum reduction of 13 dB was achieved. These results verified that vibration inputs to the unsprung mass were offset by the actuator control force, thereby improving road holding.

Fig. 14 Ride comfort performance

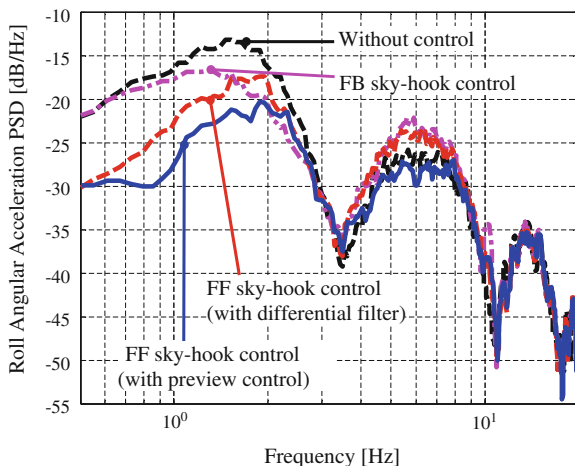
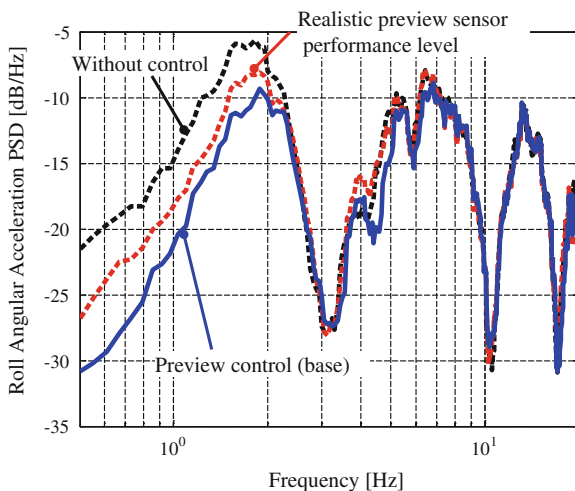


Fig. 15 Ride comfort performance (4-wheel shaker test)



3.2 Actual Road Tests

The ride comfort performance of the control was verified on actual roads. Figure 14 shows the PSD analysis results for roll angular acceleration after driving at 80 km/h on the test road. The effectiveness of the FB sky-hook control was greatest close to the roll resonance point (1–3 Hz). In contrast, the FF sky-hook control was effective at frequencies both close to the roll resonance point and even lower at between 0.5 and 1 Hz. Furthermore, adopting the phase compensation preview control instead of

Fig. 16 Energy consumption

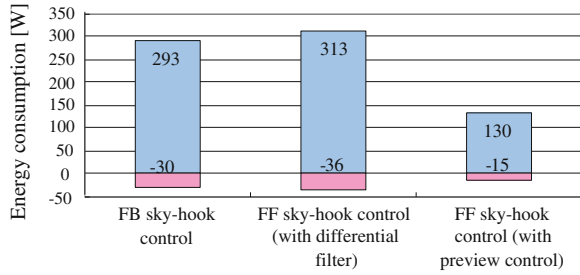
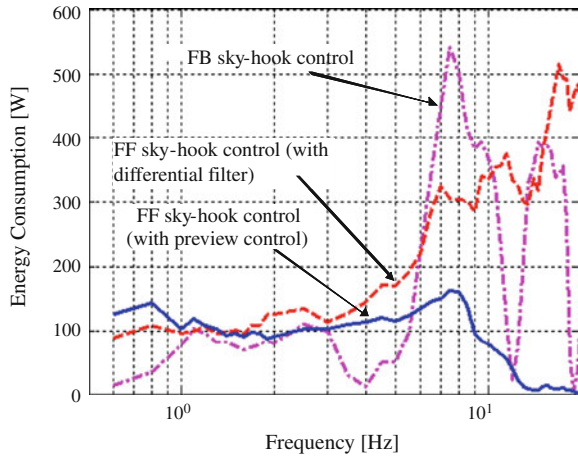


Fig. 17 Frequency characteristics of energy consumption



the differential filter improved ride comfort control performance by between 4 and 5 dB at low (2 Hz or less) and middle (4–8 Hz) frequencies.

In addition, line A in Fig. 15 indicates the ride comfort performance of the control when the preview sensor performance was reduced to a measurement frequency of 32 ms and a measurement accuracy of 10 mm, which represent realistic values reflecting the actual usage environment. This shows that substantial performance deterioration is unavoidable and underlines the necessity for developing a more accurate preview sensor.

3.3 Energy Consumption

Figure 16 shows the energy consumption for these results. Positive values indicate energy consumption and negative values indicate energy regeneration. In terms of the respective ride comfort control laws, the FB sky-hook and FF sky-hook

control consume approximately the same amount of energy. However, factoring in the different phase compensation methods, the preview control consumes roughly 40 % less energy than the differential filter control.

Figure 17 shows the energy consumption at each input frequency with sine sweep vibration. As demonstrated in Fig. 7, when the preview control is adopted in the FF sky-hook control, phase compensation does not cause variation in the control command values. Therefore, this control consumes much less energy than the differential filter control in middle frequencies. As a result, the overall energy consumption of the system was reduced.

4 Conclusion

Adopting the preview ride comfort control into an electric active stabilizer suspension system improved ride comfort and road holding over a wide frequency range and reduced the energy consumption of the system. Future development will aim to reduce the cost of the preview sensor while satisfying accuracy requirements as the next step toward practical application of this system. Development will also continue to examine the applicability of pitch and heave direction control to expand the effectiveness of the control.

References

1. Yonekawa T, Onuma T, Mori Y, Goto T, Buma S (1991) Effect of the active control suspension system on vehicle dynamics. *JSAE Rev* 12(2):40–45
2. Buma S, Okuma O, Taneda A, Suzuki K, Cho J, Kobayashi Y (2010) Design and development of electric active stabilizer suspension system. *J Syst Des Dyn, JSME* 4(1):61–76
3. Nagai M (1990) Fundamentals of vibration control of active suspension. *JARI Res J* 12(2):41–45
4. Shono A, Hiraiwa N, Nagiri S, Doi S (1991) Basic study of reducing vehicle vibration by preview control. *Proc Soc Automot Eng Jpn* 912-3:197–200
5. Kimura K, Akatsu Y, Tobata H, Fukuyama K (1994) Vehicle vibration control by active suspension using preview control. *Trans Soc Automot Eng Jpn* 25(3):93–97
6. Buma S, Kajino H, Takahashi T, Doi S (2008) Consideration of a human dynamic characteristic and performance evaluation of an electric active suspension. *AIM (IEEE/ASME)*
7. Kajino H, Buma S, Cho J, Kanda R (2008) Electric active suspension system development with driver's motion analysis. *FISITA, F2008-03-012*
8. Yoshioka K, Buma S, Kanda R, Yahagi T (2010) Study of preview control for electric active suspension. *Trans Jpn Soc Mech Eng C* 76(770):20–27

9. Kanda R, Buma S, Cho J, Yoshioka K, Yahagi T (2011) Study of ride comfort control logic for electric active stabilizer suspension system. *Trans Soc Automot Eng Jpn* 42(2):323–328
10. ISO2631-1, “Mechanical vibration and shock—evaluation of human exposure to whole-body vibration—Part 1: General requirements (1997)”

Slippage Equalization for Energy Loss Minimization in a Four-Wheel Drive Vehicle

Osamu Nishihara and Yuki Yoneima

Abstract Tire slippage will inevitably occur during vehicle acceleration and deceleration, with the amount of slippage depending on parameters such as tire force, vertical load, and road surface conditions. In a decelerating electric vehicle, tire slippage can result in considerable energy loss to a regenerative brake system. The purpose of this study is to derive the optimal drive/brake force distribution for minimizing slippage loss; doing this will help to determine an optimal torque distribution strategy for electric vehicles driven by individual motor/generators that are connected directly to the wheels. In this study the wheel slippage parameters of a four-wheel drive vehicle running straight on a uniform road lane are estimated. The tires are modeled using the brush model, and vertical load shifting is estimated as a function of longitudinal acceleration. By using conventional brush model assumptions, a cubic equation in terms of the slip ratio can be derived. The analytical solution to this equation can then be used to estimate energy loss during acceleration or deceleration; from this, a figure for energy efficiency in terms of what percentage of the energy consumed in driving is converted into kinetic energy of vehicular motion can be calculated. A similar index showing the percentage of the kinetic energy used to drive the motor/generators in the wheels during deceleration can then be defined. From these relationships, theoretical efficiencies can be precisely estimated, and it is found that energy loss can be closely approximated as a sum of quadratic functions of the slip ratios of the front and rear wheels. This result can be used to develop a torque distribution method that equalizes the slip ratios of all four wheels (which equates to synchronizing the revolution of all of the wheels) in order to minimize total

F2012-G02-021

O. Nishihara (✉) · Y. Yoneima
Kyoto University, Kyoto, Japan
e-mail: nishihara@i.kyoto-u.ac.jp

energy loss. The results of this study can therefore serve as a useful guide for implementing an efficient drive system controller. Although the quantitative estimation of relevant factors is driven by the brush model, slippage equalization is not essentially dependent on this estimation. This study provides a more firmly analytical description of an improved torque distribution method for minimizing slippage loss than has been previously developed; however, further study will still be needed to implement an actual drive system controller.

Keywords Electric vehicle · Motor drive system · Energy regeneration · Slip ratio · Range extension

1 Introduction

In recent times, electric vehicles (EVs) have attracted increasing attention as a means of reducing environmental impacts—particularly from carbon dioxide emissions—and of lowering energy costs. The development of EVs has been aided by research into and development of energy-efficient nickel-metal-hydride and lithium-ion battery modules and capacitor technologies that aim to provide higher power capacities at lower costs.

Some EVs are driven by in-wheel motors (IWMs) incorporated into their wheel hubs; these are beneficial in that they can considerably reduce energy loss in power transmission. Use of IWMs also facilitates the development and application of advanced technologies such as anti-slippage and integrated vehicle dynamics controls. However, the energy densities of secondary batteries are far lower than those of petroleum-based fuels, thus reducing the attainable mileage relative to a conventional internal combustion vehicle. Installing more battery cells will increase the mass—and thus the cost—of a vehicle. Control technologies, then, must be relied upon to maximize the effective use of battery modules of limited electrical capacity.

2 Model for Analysis

2.1 *Tire Slippage*

The primary focus of analysis in this study is the energy loss caused by slippage of the tires. As acceleration and deceleration are necessary components of vehicle travel, some amount of energy loss from slippage is unavoidable. Such energy losses, however, can be minimized if electrical energy can be effectively converted

into kinetic energy during acceleration, and if kinetic energy can be effectively converted into electrical energy by regeneration during deceleration. A quantitative analysis of the process by which slippage—as partly determined by the relative velocity between the tire and the road surface—leads to energy loss is not difficult to perform. In this study, the tire is approximated using the brush model in order to investigate the relation between slippage and energy loss [1].

2.2 Brush Model

In the brush model, the tire is simulated as numerous “bristles” (i.e., elastic bodies attached to the tread base) [2]. The forces and moments acting on the tire are estimated as elastic deformations of the bristles, with the coefficient of friction, μ , between the bristle tips and the road surface assumed to be a constant. As in standard examples, a parabolic distribution of vertical contact pressure is assumed in the longitudinal direction, while a constant pressure distribution is assumed in the lateral direction. The center point of the forward edge of the contact area is set as the origin, O ; the x -axis is defined to be along the centerline of the contact area; and the length and width of the contact area are denoted as a and b , respectively. The ground contact pressure can then be estimated as

$$p = \frac{6F_z}{ab} \frac{x}{a} \left(1 - \frac{x}{a}\right) \quad (1)$$

where F_z is the vertical load on the tire. Although, some of the parameters here might have varying definitions, Eq. (1) represents a common expression for contact pressure in the brush model.

The slip ratio in the longitudinal direction can be given as

$$\kappa_x = \frac{R\Omega - V}{V} \quad (2)$$

where V , Ω , and R are the velocity of the tire center, angular velocity of the tire, and effective radius of the tire, respectively. As the vehicle in this study drives straight along a uniform road lane, the slip angle of the tire can always be assumed to be null.

3 Front/Rear Drive Vehicle

As a first step toward modeling a four-wheel drive vehicle, a formulation for a front/rear drive system is first developed. The results of this will be used to provide a basis for comparison with a four-wheel drive system.

3.1 Equation of Motion

Using the brush model, the driving/braking force on the driven wheel can be estimated as

$$F_i = K_d \frac{\kappa_i}{1 + \kappa_i} - \frac{K_d^2}{3\mu F_{zi}} \frac{\kappa_i |\kappa_i|}{1 + \kappa_i} + \frac{K_d^3}{27\mu^2 F_{zi}^2} \left(\frac{\kappa_i}{1 + \kappa_i} \right)^3 \quad (3)$$

where K_d is the driving/braking stiffness, and F_{zi} is the vertical load to the drive wheel i . Although the dependence of the load on driving/braking stiffness is outside the scope of this study, essential properties of tire motion can still be discussed using this assumption. The stiffness can be assumed to be a constant determined by the road surface conditions:

$$K_d = \begin{cases} 50000 \text{ [N]} & (\mu = 0.89) \\ 25000 \text{ [N]} & (\mu = 0.4) \\ 10000 \text{ [N]} & (\mu = 0.2) \end{cases} \quad (4)$$

The suffix i in κ_i and F_i designates the various drive system layouts: $i = f$ indicates front-wheel drive and $i = r$, rear-wheel drive. The suffix j indicates a non-driving wheel. If $i = f$, then $j = r$; otherwise, $i = r$ and $j = f$.

The equation of motion can be simplified as

$$Ma_x = 2F_i - 2\mu_{rr}F_{zj} \quad (5)$$

where M is the equivalent mass of the vehicle:

$$M = m + \frac{2I_w}{R^2} \quad (6)$$

As the vehicle accelerates or decelerates, the vertical load on the tires will shift, and the dynamic load can accordingly be expressed as

$$F_{zf} = F_{zf,st} - \frac{mh}{2l} a_x \quad (7)$$

$$F_{zr} = F_{zr,st} + \frac{mh}{2l} a_x \quad (8)$$

where $F_{zf,st}$ and $F_{zr,st}$ are the static loads on the front and rear tires, respectively, h is the height of the center of gravity, and l is the width of the wheel base. Aerodynamic drag is not explicitly considered in this formulation. Additional resistances can be expressed by redefining the equivalent acceleration to include a virtual inertial force acting on the mass of the vehicle, but again, the numerical examples used in this paper do not take account of these terms.

Table 1 Vehicle parameters

m (kg)	1,100	I_w (kgm ²)	1.0
l (m)	2.55	R (m)	0.281
h (m)	0.56	μ_{rr}	0.011
$F_{f,st}$ (N)	2,695	$F_{r,st}$ (N)	2,695

3.2 Slip Ratio and Acceleration

If Eqs. (5)–(8) are substituted into Eq. (3) and this is rearranged, a cubic polynomial equation in κ_i can be obtained:

$$P_1(a_x)\kappa_i^3 + P_2(a_x)\kappa_i^2 + P_3(a_x)\kappa_i + P_4(a_x) = 0 \quad (9)$$

where $P_1(a_x)$, \dots , $P_4(a_x)$ are cubic polynomials in a_x . The unique real root of Eq. (9) will then give κ_i as a function of a_x .

In Table 1, the vehicle parameters assumed in this study are listed. These values have been carefully collected, and they can be treated as practically corresponding to a small electric vehicle. In Fig. 1, an example of the relation between the acceleration and the slip ratio is shown. Slip ratios of a few percent are observed with the accelerations or decelerations that can be seen in passenger cars under ordinary driving conditions. The front- and rear-drive systems yield relatively small differences, but the rear-drive system yields smaller slip ratios during acceleration than the front drive vehicle.

3.3 Energy Conversion Efficiency

For the purposes of this study, the energy conversion efficiency during acceleration, η , is defined as the ratio of the instantaneous power delivered by the drive system to the rate of kinetic energy increase. Similarly, the energy recovery efficiency during deceleration, ξ , is set as the ratio of the rate of vehicle kinetic energy decrease to the instantaneous power applied to the drive system. Figures 2 and 3 illustrate the relation between acceleration/deceleration and energy conversion efficiency, respectively.

4 Four-Wheel Drive Vehicle

It is assumed for the purposes of this study that the front and rear wheels are directly connected to the IWMs and that their rotations are precisely controlled to minimize the energy loss from slippage.

Fig. 1 Relation of vehicle acceleration and slip ratio ($\mu = 0.2$)

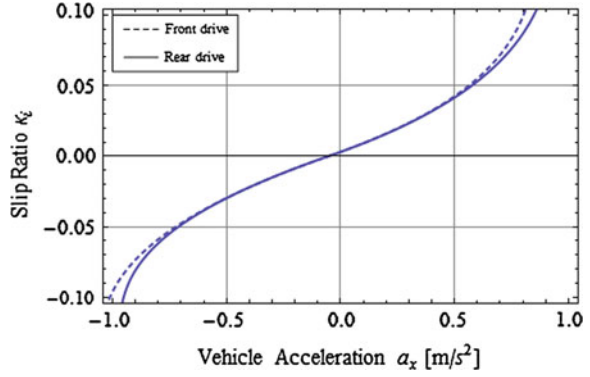


Fig. 2 Vehicle acceleration and energy conversion factor ($\mu = 0.2$)

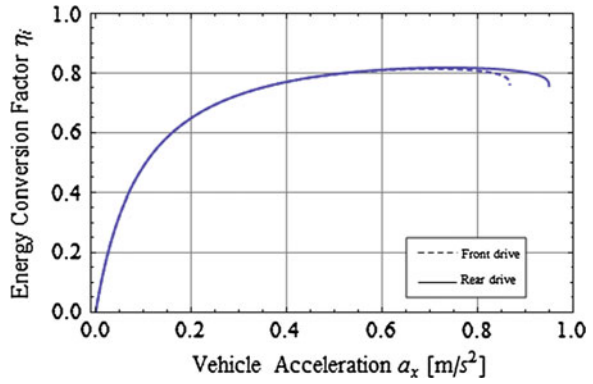
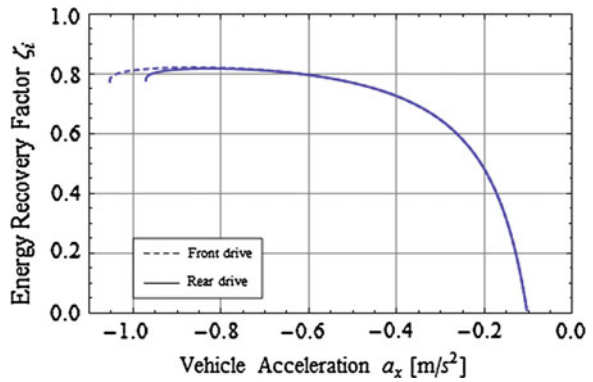


Fig. 3 Vehicle deceleration and energy recovery factor ($\mu = 0.2$)



4.1 Equations of Motion

The equations of motion of a four-wheel drive vehicle can be given using previously defined parameters:

$$ma_x = 2F_i + 2F_r \quad (10)$$

$$I_w \dot{\Omega}_f = T_f - RF_f - \mu_{rr} RF_{zf} \quad (11)$$

$$I_w \dot{\Omega}_r = T_r - RF_r - \mu_{rr} RF_{zr} \quad (12)$$

4.2 Slip Ratio Equalization

Analysis shows that, in the limits of small acceleration or deceleration, equalizing the slip ratios minimizes the energy loss caused by slippage; in other words, slippage energy loss is minimized by synchronizing the revolution of the front and rear wheels.

The energy loss caused by slippage can be approximated as

$$2F_f(R\Omega_f - V) + 2F_r(R\Omega_r - V) \cong 2K_{d,f}V\kappa_f^2 + 2K_{d,r}V\kappa_r^2 \quad (13)$$

where the equation of motion can be reduced to

$$ma_x = 2F_f + 2F_r \cong 2K_{d,f}\kappa_f + 2K_{d,r}\kappa_r \quad (14)$$

From these relations, it can be seen that equalizing the slip ratios of the front and rear wheels approximately minimizes the energy loss, even if the driving/braking stiffness of the front and rear tires are different.

Setting $\kappa_f = \kappa_r = \kappa_x$ and $K_{d,f} = K_{d,r} = K_d$ for simplicity, the equation of motion is reduced to

$$ma_x = 4K_d \frac{\kappa_x}{1 + \kappa_x} - \frac{2K_d^2}{3\mu} \left(\frac{1}{F_{zf}} + \frac{1}{F_{zr}} \right) \frac{\kappa_x |\kappa_x|}{(1 + \kappa_x)^2} + \frac{2K_d^3}{27\mu^2} \left(\frac{1}{F_{zf}^2} + \frac{1}{F_{zr}^2} \right) \left(\frac{\kappa_x}{1 + \kappa_x} \right)^3 \quad (15)$$

which can be rearranged as a polynomial with respect to the common slip ratio κ_x :

$$Q_1(a_x)\kappa_x^3 + Q_2(a_x)\kappa_x^2 + Q_3(a_x)\kappa_x + Q_4(a_x) = 0 \quad (16)$$

where $Q_1(a_x)$, ..., $Q_4(a_x)$ are cubic polynomials in a_x . As in the case of two-wheel drive, each real root κ_x is a function of a_x . As can be seen from Fig. 4, which shows the relation between the acceleration and the slip ratio, slip ratio equalization effectively reduces energy loss (Figs. 5, 6)

Fig. 4 Vehicle acceleration and slip ratio ($\mu = 0.2$)

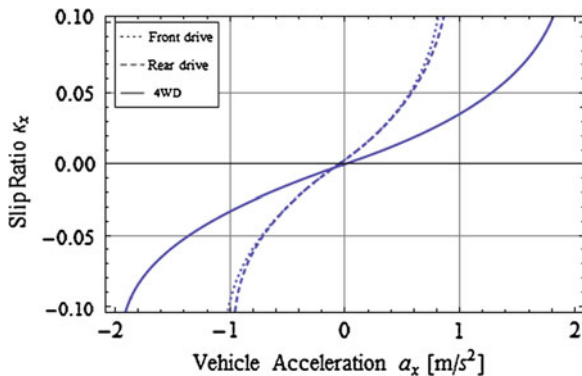


Fig. 5 Vehicle acceleration and power conversion factor ($\mu = 0.2$)

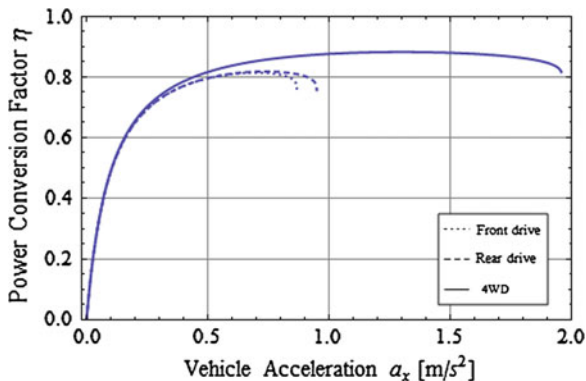
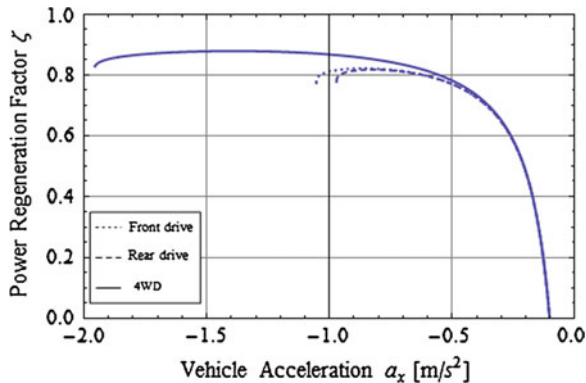


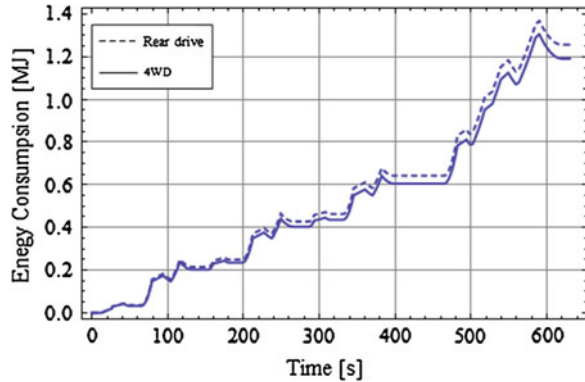
Fig. 6 Vehicle acceleration and power regeneration factor ($\mu = 0.2$)



5 Evaluation of Electric Mileage

In this section, evaluation of practical mileage using 10–15 mode (a Japanese emissions and fuel consumption test procedure) is discussed. Although this procedure has been abandoned for official use, it is simpler to conduct than the current JC08 procedure and is thus suitable for a discussion in this study.

Fig. 7 Cumulative energy
($\mu = 0.2$)



5.1 10–15 Mode

The 10–15 mode test procedure involves a three-cycle repeat of 10 patterns of model urban driving, followed by one cycle of 15 suburban driving patterns. This procedure typically involves measurements using the chassis dynamometer, where load shifting does not occur; however, for this study, the dynamic loads on the wheels from acceleration and the energy loss from slippage are evaluated.

5.2 Evaluation of Mileage

The energy conversion efficiency of both charging and discharging is assumed to be 80 %, while driving by motor and regeneration are assumed to have efficiencies of 90 and 80 %, respectively. The road surface condition varies as dry, wet, or icy, with corresponding road surface friction coefficients of 0.89, 0.4, and 0.2, respectively. Based on these assumptions, electric mileage is evaluated. Figure 7 shows comparative time series, for rear-drive and four-wheel drive vehicles, of cumulative energy consumption over one 10–15 mode cycle.

From this figure, the reduction in energy consumption owing to slippage equalization is apparent. Tables 2, 3 and 4 show the performance enhancements of using slip ratio equalization in a four-wheel drive. As can be seen in Tables 2 and 3, while the front- and rear-drive systems differ only slightly from each other in terms of consumed and regenerated energies, the four-wheel drive system requires less electric power for acceleration while regenerating more power in deceleration. Lower friction coefficients tend to enhance the advantages of the four-wheel drive. Table 4 shows the estimated vehicle mileages in both the rear- and four-wheel drive systems, further demonstrating the beneficial effects of slippage equalization with a four-wheel drive system.

Table 2 Consumed energy

μ	Front drive (MJ)	Rear drive (MJ)	4WD (MJ)
0.89	1.591	1.591	1.586
0.4	1.603	1.603	1.590
0.2	1.661	1.653	1.607

Table 3 Regenerated energy

μ	Front drive (MJ)	Rear drive (MJ)	4WD (MJ)
0.89	0.420	0.420	0.421
0.4	0.416	0.416	0.420
0.2	0.405	0.404	0.414

Table 4 Comparison of electric mileage

μ	Rear drive (km/MJ)	4WD (km/MJ)	Improvement (%)
0.89	3.557	3.575	0.51
0.4	3.509	3.560	1.43
0.2	3.335	3.491	4.48

6 Conclusions

In this paper, the energy conservation effects of slip ratio equalization in a four-wheel drive system were discussed. Slippage was shown to be reduced by slip ratio equalization, resulting in an improvement in energy efficiency. An improvement in electric mileage estimated using the 10–15 mode assessment also testifies to the benefit of slip ratio equalization. Overall, the use of slip ratio equalization with a four-wheel drive system improved performance parameters such as electric mileage by up to nearly 5 % as compared with a front- or rear-drive system, and lower friction coefficient tended to enhance these advantages.

References

1. Nishihara O, Masahiko K (2011) Estimation of road friction coefficient based on the brush model. Transactions of the ASME, Journal of Dynamic Systems, Measurement and Control 133(4):041006
2. Nishihara O, Yoneima Y (2012) Torque distribution for slip rate equalization of 4WD electric vehicle and energy saving effects (in Japanese). JSAE symposium text (trends of ecological and safety technology on tire), 19(11) 20124315:43–48

Multi-Objective Optimization and Multi-Attribute Decision of Mini-Van Chassis

Xulong Jin, Min Qin, Yongfeng Jiang, Wenbin Wang and Chao Cheng

Abstract Chassis developing is very important in vehicle performance. There are many chassis characteristic targets which may interfere with each other in most case. This efficiency function is difficult to confirm before optimization. We study the mini-van, build the multi-body suspension dynamic model, set up an optimization platform using Isight software by integrating ADAMS and MATLAB. Chassis design parameters of Multi-body Pareto optimization solutions were gotten by using multi-body genetic algorithm. The final chassis design parameters were confirmed by using multi-attribute decision.

Keywords Comprehensive performance · Dynamic simulation · Genetic algorithm · Multi-objective optimization · Multi-attribute decision

1 Introduction

Due to the inertia force and the braking force, mass transfer of the passenger car in the braking process leads to dynamic increase in the front axle load and decrease in the rear axle load, synchronously.

There is a huge market for mini-van in Chinese city and country and it is sure there will be a good future. At the same time the user has more requirements for performance of mini-van with the improvement of Chinese road conditions. Now

F2012-G02-023

X. Jin (✉) · M. Qin · Y. Jiang · W. Wang · C. Cheng
State Key Laboratory of Comprehensive Technology on Automobile Vibration and Noise & Safety Control, FAW R&D Center, Changchun, People's Republic of China
e-mail: qinmin@rdc.faw.com.cn

it is a huge challenge to develop a new mini-van which has good performance under the situation that most mini-van market was held by Wuling and Changan Company.

Chassis is a key subsystem of mini-van which its characteristics will influence the driving performance. Chassis characteristic designing is an important work during vehicle development. With the development of the Virtual Prototype, the vehicle performance can be analyzed by using the CAE technology before the physical prototype completed.

This paper studies the development of mini-van which has five-bar rear suspension. First the suspension model was built and validated by results of K&C test. Pareto optimization solutions of chassis design parameters were gotten by using Multi-objective genetic algorithm exploratory technique NSGA-II. Then we can confirm the parameters by multi-attribute decision. In this way the performances of suspension will be greatly improved.

2 Suspension Dynamic Modeling and Simulation

The dynamic model of mini-van was built in ADAMS software. Because the rear suspension is the base factor to the chassis, the process of developing of five-bar rear suspension is mainly described. The dynamic model five-bar of the rear suspension was calculated according to the K&C test. Because the simulation result is close to the test data, which is shown in Fig. 1, it is validated that the model is correct and can be used to optimize the characteristic of the chassis.

3 Multi-Objective Optimization

Because the changes of toe angle and the displacement of wheel center (imposed on lateral force) can directly influence the controllability and stability of mini-van. The straight performance of mini-van is mostly based on the toe angle change while imposing longitudinal force. So the stiffness of bushing in suspension control arm was considered as the factor. The response is toe angle, camber angle and the displacement at wheel center while the wheel center imposing on lateral force, toe angle while the wheel center imposing on longitudinal force. The multi-objective optimization of rear suspension was done to improve the compliance characteristic.

3.1 Theory of Multi-Objective Optimization

According to the different needs of vehicle performance, the suspension performance is usually contrary to one and another, suspension optimization is also a

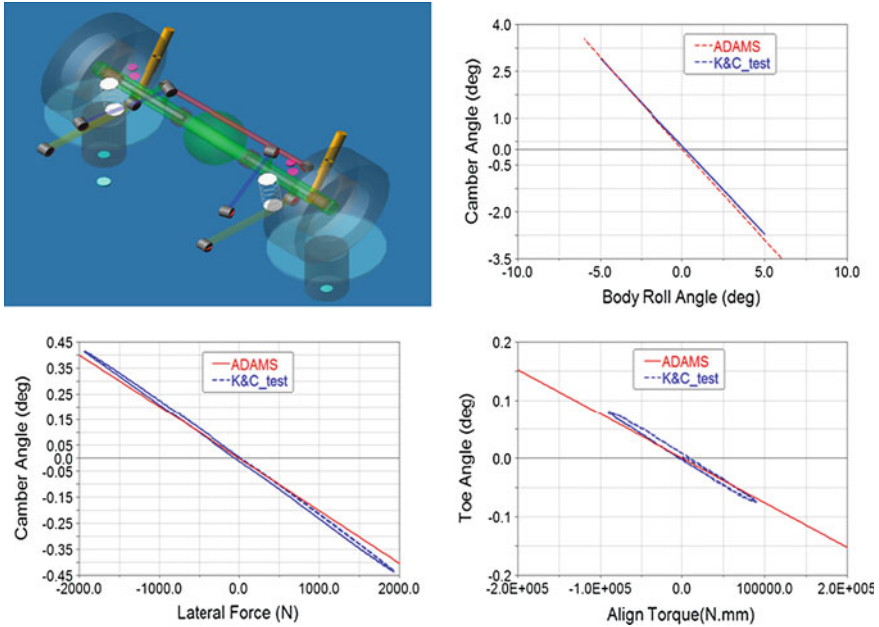


Fig. 1 ADAMS model of 5-bar suspension and simulation results

matching process. Under many norms or more design goal to match, if the goal is contrary to each other, we need to find the optimal design to satisfy these goals, namely the multi-objective optimization.

There are many conventional multi-objective optimization methods, including object planning and multi-objective weighting method, level planning, and so on, the characteristic of these algorithms is to translate the multi-objective to single objective. Unless we know the value of objective function beforehand, even if the single objective optimization is very successful, we also can't guarantee to achieve the optimal Pareto. In this chapter, we use the NSGA-II genetic algorithm (with the control strategy of the Non-Dominated Sorting Genetic Algorithm) to obtain the multi-objective optimization of Pareto optimal set.

The meaning of Pareto optimal set is as followed:

As for the question of minimum multi-objective optimization, n objectives f_k ($k = 1, 2, \dots, n$) constitute a vector $\vec{f}(\vec{x}) = (f_1(\vec{x}), f_2(\vec{x}), \dots, f_n(\vec{x}))$, $\vec{x}_v \in U, v = f(\vec{x}_v) = (v_1, \dots, v_n)$, dominate $u = f(\vec{x}_u) = (u_1, \dots, u_n)$, that is to say that there is none $\vec{x}_v \in U$ to make the follow expressions tenable:

$$\forall i \in \{1, \dots, n\}, \quad v \leq u \wedge \exists i \in \{1, \dots, n\} \quad v_i < u_i \quad (1)$$

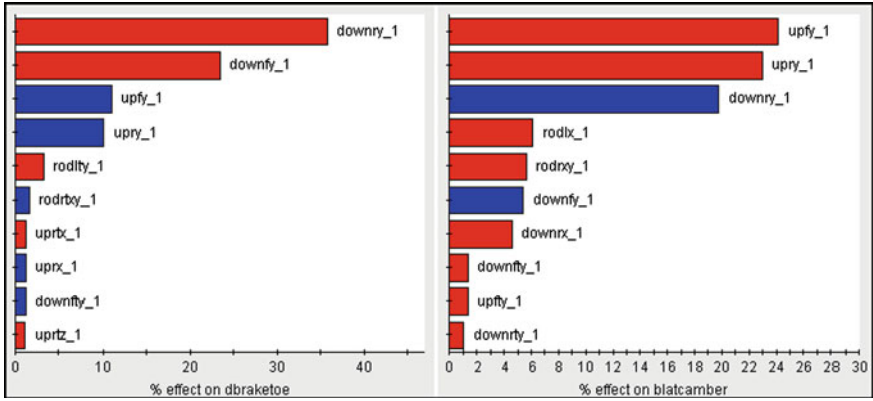


Fig. 2 Effects of all variables on factor

3.2 DOE Analysis

Set the optimization objectives as follows: alattoe is toe angle change on account of lateral forces; blatcamber is camber angle change on account of lateral forces; claty responsible for lateral wheel center displacement on account of lateral force; dbraketoe is toe angle change on account of longitudinal force. There are 34 directions bushing stiffness: front bushing of upper thrust bar has 6 directions stiffness (upfx, upfy, upfz, upftx, upfty, upftz); rear bushing of upper thrust bar has 6 directions stiffness (uprx, upry, uprz, uprtx, uprty, uprtz); front bushing of lower thrust bar has 6 directions stiffness (downfx, downfy, downfz, downftx, downfty, downftz); rear bushing of lower thrust bar has 6 directions stiffness (downrx, downry, downrz, downrtx, downrty, downrtz); left bushing of tie rod has 6 directions stiffness (rodly, rodly, rodly, rodltx, rodltx, rodltz); right bushing of tie rod has 6 directions stiffness (rodrtx, rodrtx, rodrtx, rodrtz, rodrtz, rodrtz).

There are many variables in this optimization analysis, but some variables have a little effect to the result, in order to improve the efficiency of optimization, we have to do the DOE analysis first, see Fig. 2, we select the furthest influence bushing stiffness as final optimization variables.

We use the Monte Carlo method to do the DOE analysis, and set the contribution of the target of 1.5 % for the constraints, and then we select nine main influence factors.

The factors were list as followed: upfy (Y direction of the upper front thrust bar), upry (Y direction of the upper rear thrust bar), downfy (Y direction of the lower front thrust bar), downrx (X direction of the lower rear thrust bar), downry (Y direction of the lower rear thrust bar), rodly (Y rotate direction of the left tie rod), rodrtx (XY direction of the right tie rod), rodrtx (XY rotate direction of the right tie rod).

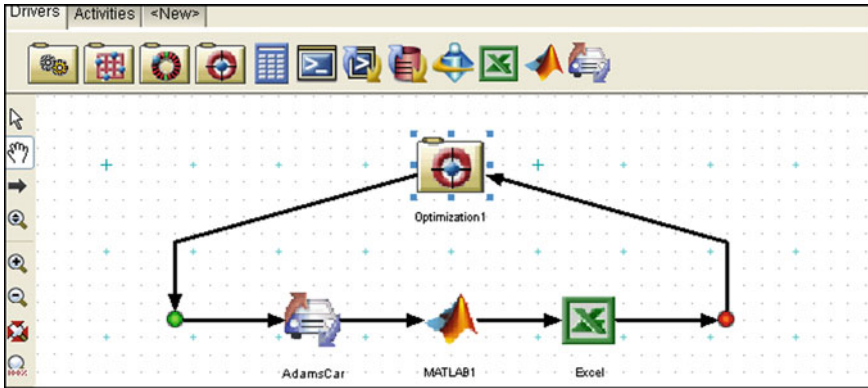


Fig. 3 Multi-objective integrated optimization

3.3 Suspension Optimization

We use Isight software integrating ADAMS and MATLAB to optimize the main suspension characteristic index (Fig. 3).

3.4 Objective of Optimization

It is very important in determining the appropriate design goal for five link type suspension performance in the designing optimization process. (Too few design goal may not satisfy the suspension performance requirements; but too many design goal will decrease the efficiency of design optimization process). Therefore we choose 4 important design goals of the five link independent suspension as the optimization objective.

- (1) toe angle while the wheel center imposed on brake force (\leq upper limit)
- (2) displacement gradient of wheel center while the wheel center imposed on lateral force (\leq upper limit)
- (3) toe angle gradient while the wheel center imposed on lateral force (maximum of the left wheel)
- (4) camber angle gradient while the wheel center imposed on lateral force (maximum of the left wheel)

3.5 Results of Suspension Optimization

After optimizing calculation, the integrated Pareto optimal and single detailed Pareto optimal is shown as Fig. 4.

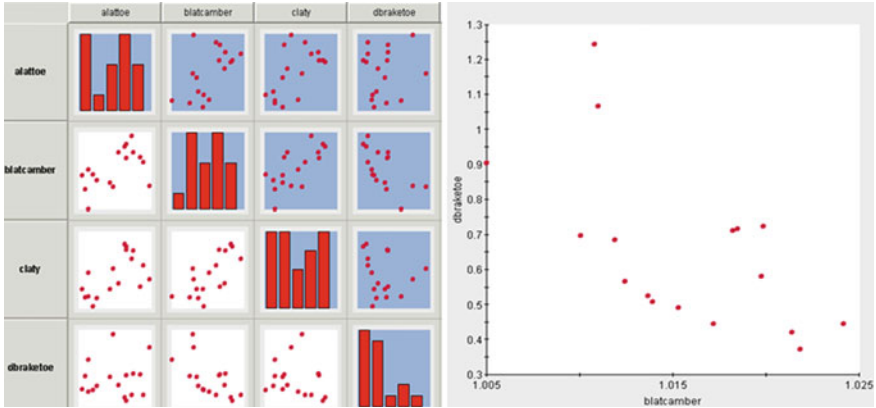


Fig. 4 Integrated Pareto optimal set

4 Multiple Attribute Decision Based on Maximum Difference

The integrated Pareto optimal set is aggregation of more optimization scheme after optimizing calculation for the five link type suspension, we needs to select the best scheme from the optimal set as a final design parameters of the chassis. We use multiple decision to select the optimal solution, set the change of toe angle, camber angle and lateral wheel center displacement under the action of lateral force and the change of toe angle under the action of longitudinal force as attribute set, we get the optimal scheme is Pareto set, form the decision matrix, $A = (a_{ij})_{n \times m}$, which n responsible for attribute number, m responsible for plan number, we use the multiple attribute decision to make method which based on the maximum deviation, sort and set the best one to the integrated Pareto optimal.

4.1 Consturct Matrix and Standardized Matrix

We use Pareto optimal set of five link type suspension optimization to form a decision matrix $A = (a_{ij})_{43 \times 4}$, as shown in Fig. 5, row of the matrix are four attribute value, it is the change of toe angle, camber angle and lateral wheel center displacement under the action of lateral force and the change of toe angle under the action of longitudinal force, The column of matrix is the optimal scheme of the 43 optimizations.

Attribute types usually have four types: benefit type, cost type, fixed type and offset type etc. In the suspension design goal, toe angle and camber angle under lateral forces are benefit type, and the other two types are cost type. Because each attribute unit is not unified, and the numerical magnitude is huge, so it needs to standardized the decision matrix. We use the left formula to standardize treatment

Attribute Set Scheme No.	Brake force toe angle	lateral force camber gradient	lateral force steer gradient	Lateral force Displacement gradient	Attribute Set Scheme No.	Brake force toe angle	lateral force camber gradient	lateral force steer gradient	Lateral force Displacement gradient
1	0.1670	0.1284	0.0163	0.1352	1	0.3125	0.6035	0.4503	0.8062
2	0.1863	0.0674	0.0143	0.1323	2	0.2802	0.3167	0.3938	0.8237
3	0.1433	0.0826	0.0205	0.1484	3	0.3592	0.3880	0.5643	0.7345
4	0.5267	0.0590	0.0208	0.1875	4	0.0991	0.2771	0.5719	0.5814
5	0.1843	0.0723	0.0207	0.1240	5	0.2833	0.3397	0.5697	0.8792
6	0.2049	0.1148	0.0363	0.2384	6	0.2547	0.5396	1.0005	0.4572
7	0.1390	0.2128	0.0193	0.2302	7	0.3756	1.0000	0.5314	0.4736
8	0.1369	0.1065	0.0172	0.1704	8	0.3812	0.5005	0.4730	0.6397
9	0.1892	0.0733	0.0142	0.2052	9	0.2760	0.3444	0.3444	0.5312
10	0.0807	0.0705	0.0184	0.1165	10	0.6472	0.3313	0.5080	0.9357
11	0.1984	0.0607	0.0181	0.1782	11	0.2632	0.2854	0.4986	0.6117
12	0.1865	0.0684	0.0221	0.1748	12	0.2799	0.3212	0.6089	0.6236
13	0.1123	0.0745	0.0137	0.1929	13	0.4647	0.3503	0.3782	0.5651
14	0.0692	0.0629	0.0144	0.1101	14	0.7541	0.2954	0.3971	0.9902
15	0.0576	0.0880	0.0158	0.2274	15	0.9055	0.4134	0.4346	0.4792
16	0.1108	0.0598	0.0161	0.1303	16	0.4719	0.2809	0.4424	0.8364
17	0.0822	0.0683	0.0158	0.1494	17	1.0000	0.3211	0.4351	0.7298
18	0.1466	0.0766	0.0163	0.2137	18	0.3560	0.3600	0.4495	0.5102
19	0.1013	0.0728	0.0130	0.1325	19	0.5155	0.3422	0.3573	0.8227
20	0.4456	0.0680	0.0182	0.1325	20	0.1171	0.3196	0.5010	0.8226
21	0.1036	0.0809	0.0221	0.2414	21	0.5037	0.3800	0.6100	0.4516
22	0.0803	0.0765	0.0164	0.1408	22	0.6500	0.3596	0.4510	0.7741
23	0.2957	0.1230	0.0205	0.1531	23	0.1765	0.3718	0.5639	0.7118
24	0.0922	0.0619	0.0146	0.1446	24	0.5659	0.2907	0.4018	0.7538
25	0.1346	0.0773	0.0140	0.1221	25	0.3879	0.3631	0.3866	0.8925
26	0.1568	0.0603	0.0168	0.1381	26	0.3328	0.2832	0.4641	0.7894
27	0.1596	0.1170	0.0177	0.1738	27	0.3271	0.5500	0.4869	0.6272
28	0.2179	0.0788	0.0254	0.1789	28	0.2396	0.3701	0.6991	0.6093
29	0.2843	0.0849	0.0127	0.1313	29	0.1836	0.3990	0.3512	0.8300
30	0.1774	0.1655	0.0163	0.1628	30	0.2943	0.1778	0.4499	0.6695
31	0.4607	0.1114	0.0241	0.1372	31	0.1133	0.5237	0.6644	0.7947
32	0.1347	0.0690	0.0149	0.1688	32	0.3876	0.3243	0.4098	0.6456
33	0.2502	0.0781	0.0217	0.2371	33	0.2086	0.3672	0.5988	0.4597
34	0.3546	0.0864	0.0202	0.2015	34	0.1472	0.4060	0.5557	0.5410
35	0.2268	0.0617	0.0287	0.2060	35	0.2301	0.2900	0.7903	0.5291
36	0.2165	0.0745	0.0289	0.1417	36	0.2411	0.3503	0.7950	0.7692
37	0.0833	0.1535	0.0158	0.1090	37	0.6267	0.7212	0.4361	1.0000
38	0.0686	0.0863	0.0145	0.1632	38	0.7604	0.4058	0.4008	0.6680
39	0.1305	0.0740	0.0126	0.1372	39	0.4001	0.3476	0.3464	0.7945
40	0.2251	0.0589	0.0168	0.2260	40	0.2319	0.2766	0.4632	0.4822
41	0.1151	0.0864	0.0186	0.1989	41	0.4533	0.4058	0.5124	0.5479
42	0.0851	0.0678	0.0182	0.1936	42	0.6137	0.3185	0.5024	0.5629
43	0.1084	0.1502	0.0132	0.1167	43	0.4815	0.7057	0.3642	0.9339

Fig. 5 Decision matrix A and R

for 2, 3 columns of attribute values, and then to standardize treatment for 1, 4 columns of attribute values, so we get the standardization decision matrix $R = (r_{ij})_{43 \times 4}$ as shown in Fig. 5.

$$r_{ij} = \frac{a_{ij}}{\text{Max}(a_{ij})}, \quad i \in [1, \dots, 43], \quad j \in [2, 3];$$

$$r_{ij} = \frac{\text{Min}(a_{ij})}{a_{ij}}, \quad i \in [1, \dots, 43], \quad j \in [1, 4]$$

4.2 Computation of Optimal Weight Vector ω

Suppose that the weight vector is $\omega = (\omega_1, \dots, \omega_m)$, $\omega_j \geq 0$, and it is satisfied unitary subject condition.

$$\sum_{j=1}^m \omega_j^2 = 1$$

Then we can defined the integrated attribute value of every scheme:

$$z_i(\omega) = \sum_{j=1}^m r_{ij}\omega_j \tag{4}$$

Generally, multiple attribute decision is to make sorted and compared comprehensive attribute value of these solutions. The smaller of the difference in the attribute of all scheme showed, the smaller this attribute decision made and sorted [1]. Therefore, considered the scheme sorting, [the greater the deviation of the scheme attribute value properties (no matter how important itself) should give the greater weight?]. In particular, if all the attributes of the scheme are equal under attribute value of u_j , the attributes of u_j will not work on the ranking. So the weight can set as zero. In this paper, $V_{ij}(\omega)$, equals to the difference between optimization scheme x_i and all other optimization schemes under attribute value of u_j , can be defined as:

$$V_{ij}(\omega) = \sum_{k=1}^{43} |r_{ij}\omega_j - r_{kj}\omega_j|, \quad i \in [1, \dots, 43], \quad j \in [1, 2, 3, 4] \tag{5}$$

As

$$V_j(\omega) = \sum_{i=1}^{43} V_{ij}(\omega) = \sum_{i=1}^{43} \sum_{k=1}^{43} |r_{ij} - r_{kj}| \cdot \omega_j, \quad j \in [1, 2, 3, 4] \tag{6}$$

So $V_j(\omega)$ is equal to total deviation between optimization scheme and all the other optimization schemes under the attribute value of u_j . According to the above analysis, the choice of the weighted vector ω should be able to make the total deviation largest to all scheme. Therefore, the objective function can be defined as:

$$\max V(\omega) = \sum_{j=1}^4 V_j(\omega) = \sum_{j=1}^4 \sum_{i=1}^{43} \sum_{k=1}^{43} |r_{ij} - r_{kj}| \cdot \omega_j \tag{7}$$

Solving weight vectors ω from the objective function and the optimal solution is normalized as:

$$\omega_j = \frac{\sum_{i=1}^{43} \sum_{k=1}^{43} r_{ij} - r_{kj}}{\sum_{j=1}^4 \sum_{i=1}^{43} \sum_{k=1}^{43} r_{ij} - r_{kj}}, \quad j \in [1, 2, 3, 4] \tag{8}$$

Base on the standardization of decision matrix $R = (r_{ij})_{43 \times 4}$, the optimal weight vector is as followed:

$$\omega = (0.9543, 0.015, 0.00977, 0.00901)$$

Base on the comprehensive attribute value definition, the comprehensive property values of scheme x_i is as followed:

$z_i(\omega), i \in [1, \dots 10]$	0.319	0.283	0.361	0.11	0.289	0.265	0.383	0.382	0.277	0.636
$z_i(\omega), i \in [11, \dots 20]$	0.267	0.284	0.458	0.737	0.879	0.466	0.97	0.354	0.508	0.129
$z_i(\omega), i \in [21, \dots 30]$	0.496	0.637	0.189	0.555	0.387	0.334	0.331	0.247	0.192	0.303
$z_i(\omega), i \in [31, \dots 40]$	0.13	0.385	0.215	0.157	0.236	0.25	0.622	0.742	0.398	0.234
$z_i(\omega), i \in [41, 42, 43]$	0.449	0.6	0.482							

4.3 Ranking of Scheme

According to the value of $z_i(\omega), i \in [1, \dots 43]$, we list all scheme Pareto optimal set of the five-bar suspension. The biggest was the value of $z_{17}(\omega)$ which equal to 0.97 so the optimum scheme in Pareto optimal set was the No. 17 scheme. The design variables of bushings stiffness in No. 17 scheme was set as the final chassis bushing design value.

5 Conclusion

The quality of the vehicle is decided by various performance. This chapter study the developing of five-bar suspension of new mini-van and the multi-objective optimization design and Multi-attribute Decision.

- (1) We calculate the chassis design parameters based on the Pareto solutions.
- (2) Base on information entropy, Multi-attribute Decisions of Pareto optimization solutions had made to match vehicle productive object.

Reference

Xu Z (2004) Method and application of uncertainty multiple attribute decision

Part III
Tire and Wheel Design/ Tire Properties
and Modeling

Project Adtyre: Towards Dynamic Tyre Inflation Control

**Klaus Augsburg, Valentin Ivanov, Katja Kruchkova,
Kristian Höpping, Sebastian Gramstat,
Marijonas Bogdevicius and Peter Kiss**

Abstract The paper presents the results of the research project ADTYRE that is concentrated on the development of dynamic tyre pressure control systems (TPCS) with the aim to reduce rolling resistance and to improve driving safety. The project is coordinated by the Ilmenau University of Technology (Germany) in cooperation with Gumpert Sportwagenmanufaktur GmbH (Germany), senTec Elektronik GmbH (Germany), Vilnius Gediminas Technical University (Lithuania), and Szent István University (Hungary). The paper covers the following content: (1) State-of-the-art of tyre pressure monitoring and control systems; (2) Simulation study to

F2012-G03-002

K. Augsburg · V. Ivanov · K. Kruchkova (✉) · K. Höpping · S. Gramstat
TU Ilmenau, Ilmenau, Germany
e-mail: katsiaryna.kruchkova@tu-ilmenau.de

K. Augsburg
e-mail: klaus.augsburg@tu-ilmenau.de

V. Ivanov
e-mail: valentin.ivanov@tu-ilmenau.de

K. Höpping
e-mail: kristian.hoepping@tu-ilmenau.de

S. Gramstat
e-mail: sebastian.gramstat@tu-ilmenau.de

M. Bogdevicius
Vilnius Gediminas Technical University, Vilnius, Lithuania
e-mail: marius@vgtu.lt

P. Kiss
Szent Istvan University, Gödöllo, Hungary
e-mail: Kiss.Peter@gek.szie.hu

estimate the potential of high-dynamic tyre pressure adaptation to the actual driving situation and operational state of the tyres; (3) TPCS design procedure using complex simulation tool (AMESim, IPG CarMaker); (4) Design of a data acquisition system with high sampling rate to monitor the tyre pressure and temperature; (5) Functional validation of the TPCS approach with experiments on the test rig and real car. Results of the laboratory and vehicle testing point out that the developed dynamic tyre pressure control system has an evident potential in increasing the vehicle safety and performance.

Keywords Tyre pressure control system · Vehicle dynamics · Rolling resistance · Vehicle safety

An efficient way to reduce the rolling resistance losses and to improve the vehicle performance lies in the proper maintenance of tyre pressure during the vehicle driving. For this purposes the market proposes a variety of tyre pressure monitoring systems (TPMS). In accordance with the sources [1, 2], the TPMS can secure the fuel or electrical energy saving of about 6 % for city driving and up to 5 % in highway driving per year; subsequently, the CO₂ emissions are reduced by these measures for about 9.6 million tonnes per year (calculated for EU-15 countries).

The European Commission proposes the obligatory introduction of tyre pressure monitoring systems to all new vehicles in 2012 [3] and to all existing vehicles in 2014. The NHTSA's FMVSS 138 document published in 2005 has obliged automobile manufacturers to install the TPMS on light passenger vehicles in period from 2006 to 2008 [4]. An additional impact of influence of the NHTSA's rules on medium and heavy vehicles was also discussed [5].

Existing TPMSs have functions of the maintenance of specified pressure, the short-time support of safe driving with one or more defective tire, and informing the driver about tire pressure level. Figure 1 proposes the classification of possible variants of tire pressure monitoring and control systems.

Depending on the type of pressure measuring, the TPMSs are divided into two groups: direct TPMS and indirect TPMS. A *direct TPMS* measures pressure using pressure sensors, which are installed in each wheel [6, 7]. The direct systems can also use the integrated pressure and temperature sensors. The main advantage of direct TPMSs is high accuracy. But otherwise such systems complicate the design and maintenance of wheel unit and have increased price due to the installation of not only additional sensors but corresponding power supply and transmitting devices. Several researches and industrial solutions have recently proposed the application of battery-less TPMSs that can eliminate some existing disadvantages [8, 9].

An *indirect TPMS* uses sensors from the anti-lock braking system to calculate the tyre pressure from angular wheel velocities. Implementation of such systems has no huge influence on the cost. The indirect TPMSs need no new hardware and require some changes in existing ECU software only [10]. It is one of the main

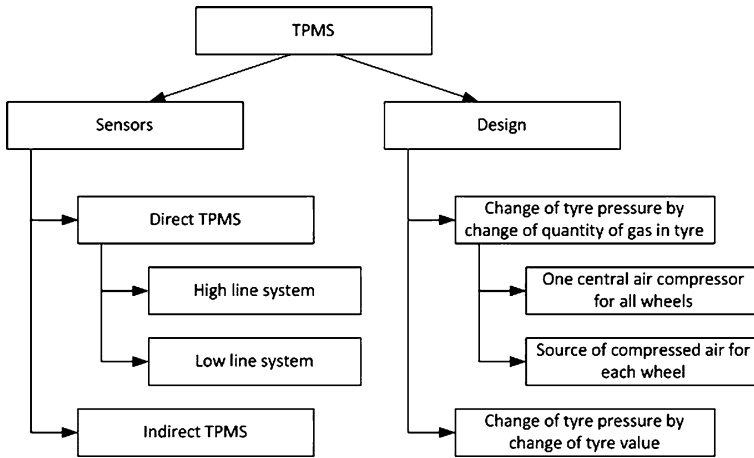


Fig. 1 Classification of tire pressure systems

arguments why majority of automotive manufacturers prioritize the application of indirect TPMSs [11].

Another variant of classification of tyre pressure systems relates to methods of dynamic change of tyre pressure. In such a case it should be spoken about the tyre pressure *control* systems (TPCS). The known TPCSs use two approaches: (1) changing a quantity of gas in the tyre and (2) changing the internal tyre volume. The general problem of the dynamic systems is that an optimal tyre pressure is not constant and changes according to the driving mode and environmental conditions. Hence the fast pressure adaptation can be required. However, the known TPCS solutions have relatively slow dynamics. For example, the relevant system described in [7] takes approximately from 12 to 3 min to inflate the 28”-tyre from 15 to 30 psi.

Review of the dynamic tyre pressure systems shows that one of the rare explored areas is the influence of tyre pressure on the lateral vehicle dynamics. However, the undoubted potential of the TPCSs can be confirmed by various experimental results introduced in the research works:

- Lower tyre inflation pressure produces understeer tendency at low and medium forward speeds (less than 18 m/s) and oversteer tendency at high speeds [12];
- Influence of tyre pressure on lateral tyre stiffness has nonlinear character; deflated tyres can ensure more stable motion at some operational conditions [13];
- Tyre pressure influences the transient handling response, roll stiffness and slip angle [12];
- Lateral friction coefficient has nonlinear dependence from the tyre pressure; the deflated tyres can better transfer lateral contact forces at low wheel loading [14].

Analysis of existing TPMS and TPCS variants as well as analysis of eventual effects from the dynamics tyre pressure control allows to formulate a number of design challenges:



Fig. 2 Apollo Gumpert test vehicle

- Tyre pressure systems require dynamic adaptation of the inflation/deflation in real-time mode to improve fuel economy and vehicle safety;
- Control strategy of tyre pressure systems has to apply a complex methodology to assess the influence of vehicle dynamics parameters on the required level of the tyre pressure;
- Development of the TPCS should consider optimization of pneumatic components to reduce total cost of the system.

These challenges have provided a basis for the new tyre pressure control system that is under development in the project ADTYRE performed by the consortium of Ilmenau University of Technology, Gumpert Sportwagenmanufaktur GmbH, senTec GmbH, Vilnius Gediminas Technical University, and Szent Istvan University. Next sections of the paper will describe the concept of the ADTYRE tyre pressure control system, discussion of relationship between the tyre pressure and lateral vehicle dynamics, the procedures relevant to the design of sensor and actuator parts of the TPCS, and methods of the system validation on the stage of the development design.

1 Definition of Functional Requirements to Tyre Pressure Control System

1.1 Target Vehicle

The TPCS variants, which are under development in the ADTYRE project, concern the sport car and light-weight truck. Within the framework of the presented paper, the architecture and functions of the system will be considered for the sport car Gumpert Apollo, Fig. 2, with technical data given in Table 1.

Taking into account specific character of the target vehicle, the functions of relevant TPCS should be concentrated first of all on the support of the car stability during the lateral dynamics manoeuvres. From this position, the first development stage has covered setting of reasonable pressure range where an effect from

Table 1 Specification of Gumpert apollo car

Curb weight	1200 kg
Maximum speed	360 km/h
Dimensions, mm	4460 × 1998 × 1114
Front tires	265/30 ZR19, air volume 47 l
Rear tires	345/30 ZR19, air volume 83 l
Max. steering angle, °	1044
Min. turning radius, m	12
Drag coefficient	0,57
Front area	1.99 m ²
Engine	V8-cylinder-Biturbomotor 4.2 l (478 kW nominal output)
Gearbox	Sequential six-speed gearbox

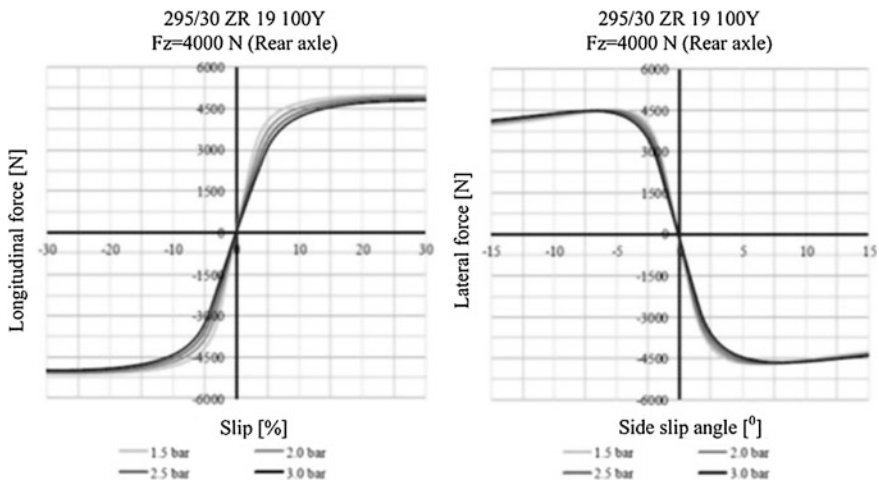


Fig. 3 Tyre characteristics as function of pressure

dynamic tyre inflation/deflation on vehicle stability can be expected. Additional important information to be defined relates to the time limits when the duration of tyre pressure control process is enough to support the vehicle performance during a certain manoeuvre. For this purpose, the preliminary modelling of vehicle dynamics has been performed using IPG CarMaker software.

1.2 Simulation of Vehicle Dynamics

The preliminary modelling covers the study of lateral dynamics of the Gumpert Apollo simulator during (1) ISO 4138 steady-state skidpad test and (2) ISO 3888-2 lane change manoeuvre. Because the test programme includes variation of tyre pressure, the simulator has special requirements to the proper choice of tyre

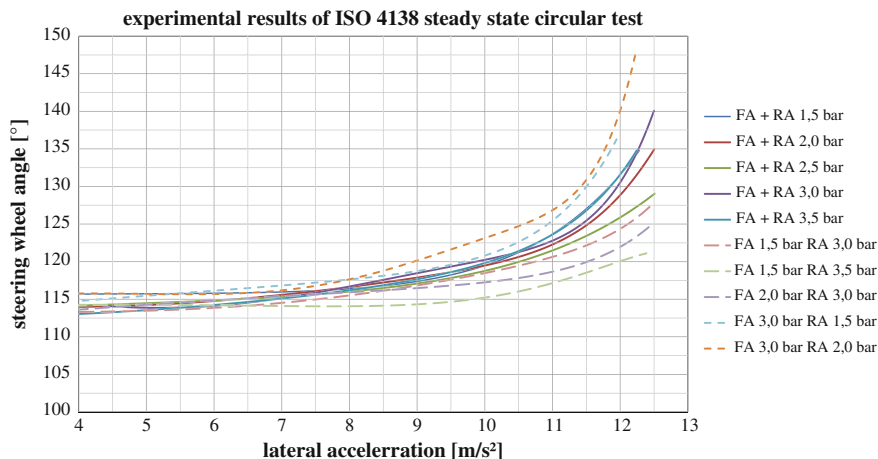


Fig. 4 Results of simulation of ISO 4138 steady-state skidpad test: steering angle vs. lateral acceleration

models. By modelling the tyres of the Gumpert Apollo car, the Magic Formula 6.1 tyre model with variable tyre pressure and temperature has been used. Examples of tyre characteristics are given on Fig. 3.

Using the proposed tyre models, a series of simulations of skidpad tests and lane change manoeuvres has been performed with both axis-selective and wheel-selective variation of tyre pressure. To illustrate the modelling, Figs. 4, 5, 6 display a number of typical dependencies characterizing the lateral vehicle dynamics. The analysis of simulation results has allowed to draw a number of conclusions, which are of special relevance for the further design stages:

- Total pressure range to be covered by the TPCS control processes is 1.5...3.5 bar (relative pressure); at that the reasonable boundaries of the tyre pressure alteration can be 1.8...2.3 bar (from viewpoint of achievable effect on stability);
- The change of tyre pressure can essentially influence the understeer characteristics of the vehicle; it was observed the transfer from understeer to oversteer behaviour of the vehicle in the cases of (1) high pressure level—3.0 bar—in all tyres and (2) low pressure level—1.5 bar—in front tyres and high pressure level—from 2.5 bar—in rear tyres;
- The change of tyre pressure influences the slip angle behaviour to a certain extent; within the total pressure range, the difference between maximal and minimal values of slip angle has reached 0.4° (in steady-state area) with variations of the “slip angle –lateral acceleration” gradient from 0.4 to 0.6 /m/s²;
- As opposed to steady-state tests, the tyre deflation can give more apparent positive effect on the vehicle stability during the transient manoeuvres; for instance, the tyre deflation from maximal to minimal value during the lane change manoeuvre has reduced maximal amplitude of slip angle on 1° and more;

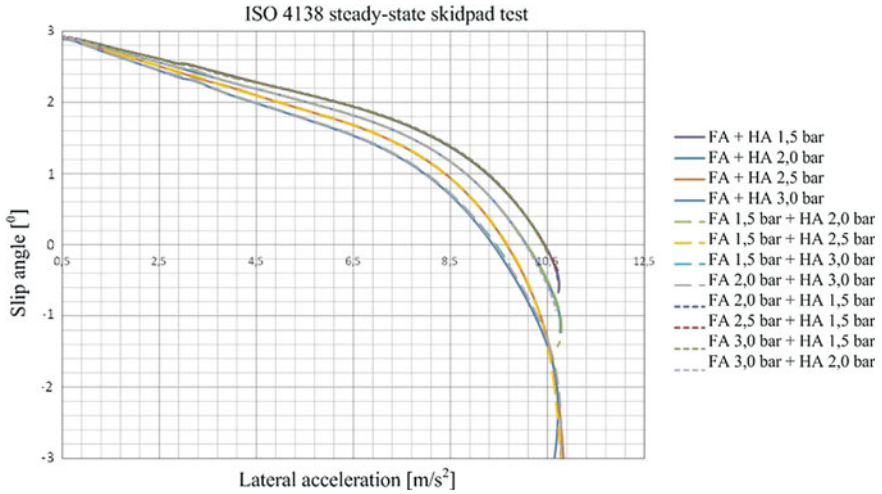
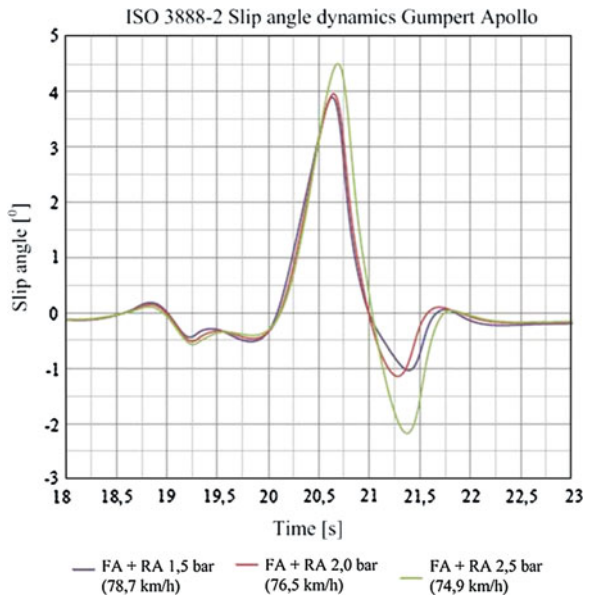


Fig. 5 Results of simulation of ISO 4138 steady-state skidpad test: slip angle vs. lateral acceleration

Fig. 6 Results of simulation of ISO 3888-2 lane change manoeuvre: slip angle vs. time



- Considering the appointed pressure range 1.8–2.3 bar appointed for the effective operation of the TPCS, corresponding time limits should be no more than 1 s for the inflation process and 1.5 s for deflation process.

The listed theses have allowed to form the requirements to the TPCS concept that will be introduced in next sub-section.

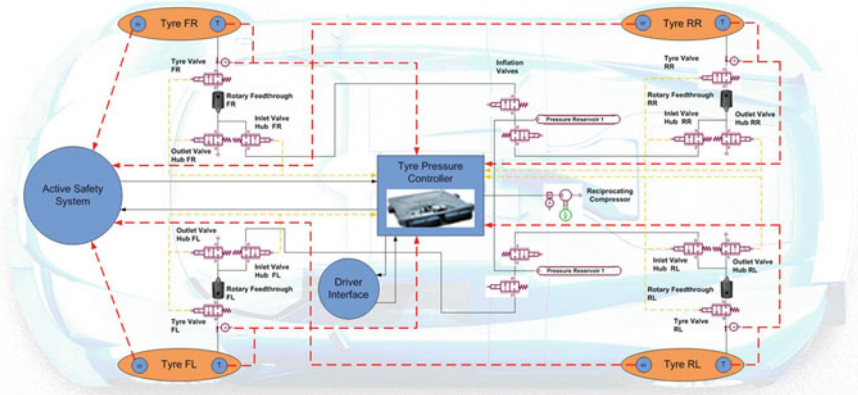


Fig. 7 Scheme of the ADTYRE dynamic tyre control system

1.3 Formulation of TPCS Concept

The main components of the proposed TPCS concept are introduced in Fig. 7. The general function of the discussed TPCS is the dynamic control of tyre pressure according to actual driving condition for improvement of active safety and vehicle performance. It means that system should monitor not only the pressures in each tyre but also the driving conditions such as longitudinal and lateral velocities, angular velocities of wheels, yaw rate and other. To smooth a human factor and to simplify the driver's work, it is necessary to combine the automatic maintenance of optimal level of tyre pressure automatically with providing the driver with the relevant feedback.

The following section is dedicated to the design of actuator and sensor components, which were developed for the proposed system concept. However, the detailed description of the logic of the TPCS controller will not be discussed in the work due to patent pending.

2 Technical Realization of TPCS Concept

2.1 Pneumatic System

The procedure of the design of the actuator part covers the stages of preliminary simulation of pneumatic components, validation of the actuator layout on test rig, and the final experiments on the real vehicle to assess the functionality of proposed engineering solutions. Modelling of the TPCS actuators has been performed in AMESim software, Fig. 8. The proposed configuration consists of two air storage devices, inlet and outlet valves, and rotary feedthrough at each wheel. The valve

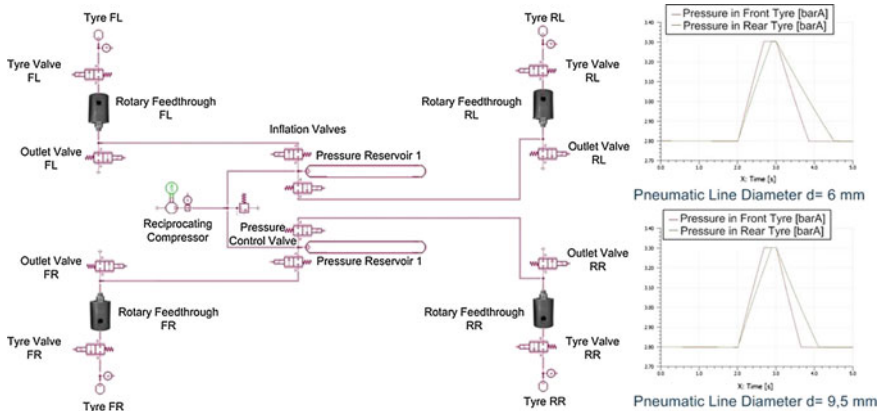


Fig. 8 Scheme of pneumatic system model with compressor in AMESim simulation

logic is based on the fact that during the vehicle driving it is necessary to inflate tyre (input signal “1”) for realization of one type of manoeuvres and to deflate tyre (input signal “0”) for realization of other type of manoeuvres. In that way, the control of opening and closing of pneumatic valves of the TPCS by processing of signals from two sources: the first one depends on type of manoeuvre (0 or 1) and the second one is received from the pressure sensor (value of tyre pressure).

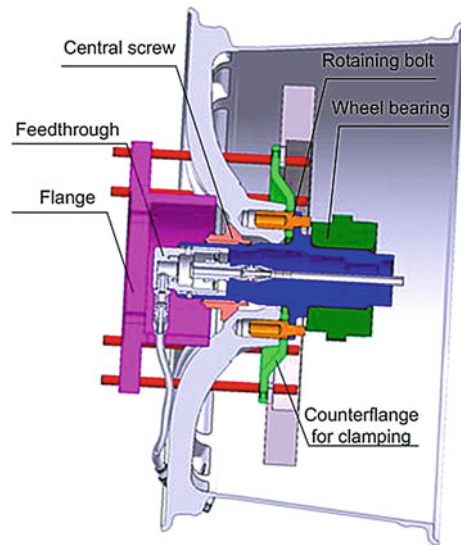
The simulation results have allowed to choose the TPCS components, which satisfy the requirements to the high-dynamic tyre inflation and deflation in term of operating time. For the tyres of Gumpert Apollo car (265/30ZR 19 and 345/30ZR 19), the expected inflation time from 1.8 bar to 2.3 bar is 0.6 s for front tyres and 0.7 for rear tyres, and deflation time is 1.08 s for front tyres and 1.15 s for rear tyres.

The complex technical problem, which has arisen by designing the TPCS actuator part, is the organization of rotary feedthrough to provide the tyres with air supply. Several related constructions are known from patents and industrial applications. However, most of them complicate the wheel unit packaging or have constructive limitations, especially for vehicles with high operational velocities. This problem was solved by providing a flexible design of feedthrough optimized both for driven and driving wheels, Fig. 9. The proposed solution allows the air supply with minimal losses and makes no complex changes in the wheel hub construction. The rotary feedthrough is also damage-proof due to the installing flange.

2.2 Sensor System

The estimation of tyre conditions requires monitoring of two operational parameters: tyre pressure and temperature. Both sensors in the developed TPCS are

Fig. 9 Construction of rotary feedthrough developed for tire test rig



mounted inside the tyre and fulfil several requirements: pressure range 1–5 bar; temperature range $-40\dots+120\text{ }^{\circ}\text{C}$; sampling rate $> 100\text{ Hz}$. Within the framework of the ADTYRE project, the original sensors “Intersema MS5535C” developed by the company senTec Elektronik GmbH are embedded in the TPCS. The initial testing of the sensors was performed using the chassis and brake test rig at the automotive engineering department at the Ilmenau University of Technology as shown on Fig. 10.

The sensor plate is mounted on tyre rim and includes a radio transmitter. This solution provides wireless transmitting of signal from the sensor. The sensor unit can be equipped with two variants of power supply. The unit can be either battery-less, with power supply from electrical valve (12 V on board voltage), or it can use a 3 V battery. The developed construction has reduced weight about 15 g.

Both actuator and sensor parts of the TPCS were investigated on the test rig and on the car in real conditions. The procedures of real car tests are being introduced in the next section.

3 Experimental Investigations

The first series of road tests performed in the project ADTYRE has aimed at:

- Proof of effect of improvement of lateral vehicle dynamics by changing of tyre pressure;
- Validation of developed IPG software simulator of Gumpert Apollo car;
- Proof of functionality of the developed actuator and sensor components.



Fig. 10 Intersema MS5535C: mounting and testing

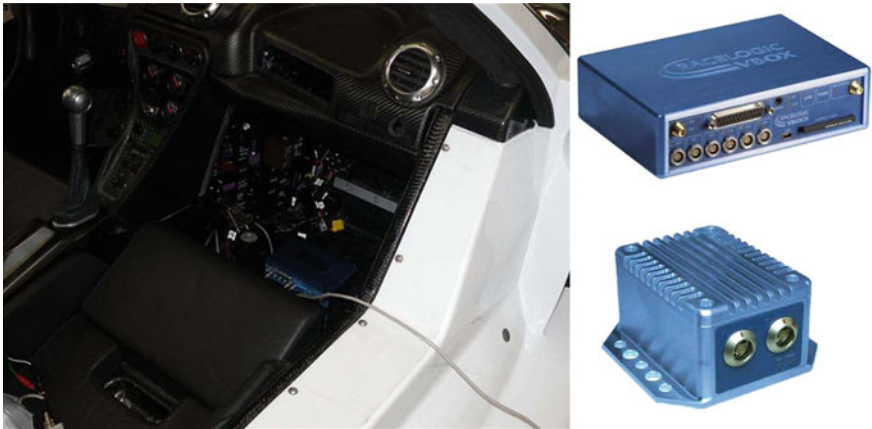


Fig. 11 GPS-Datenlogger VBOX in test vehicle [15]

The vehicle-demonstrator is equipped with GPS-Datenlogger device “VBOX”, which is connected to the CAN system and is used for monitoring of parameters of vehicle dynamics (longitudinal and lateral acceleration, wheel velocity, brake actuation etc.), Fig. 11. The previously described original sensors of pressure and temperature are installed on the tyre and wheel rim, Fig. 12.

The programme of experiments was developed from viewpoint of the most detail studying of influence of different tyre pressure on vehicle dynamics and also



Fig. 12 Pressure and temperature sensors installed on wheels

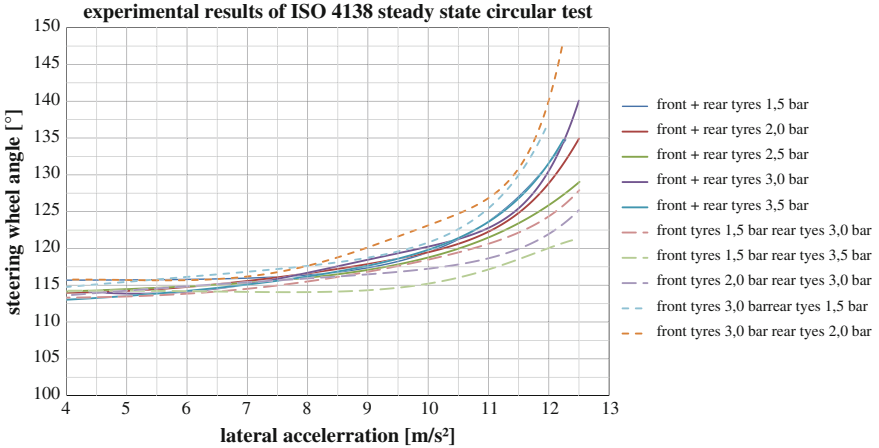


Fig. 13 Example of experimental results of ISO 4138 open-loop test

in accordance to the existing standards of vehicle dynamics. The driving tests were realized at the ADAC driving safety centre in Nohra (Germany). To give an illustration, some results of ISO 4138 open-loop test—Steady-state circle driving—are introduced on Fig. 13 (as applied to the radius of the circle test track of 27.5 m).

The tests were realized with the same tyre pressure in all tyres and different tyre pressure in axles from 1.5 till 3.5 bar. The following observations done from the analysis of experimental results should be especially mentioned for the test car:

- An equal change of the pressure level of front and rear tyres has less influence on the value of understeer gradient but gives a noticeable effect on transient

behaviour of the vehicle; at that the difference between maximal magnitudes of lateral acceleration achieved with the variation of tyre pressure from 1.5 to 3.5 bar can average more than 1.5 m/s^2 ;

- Axis-selective difference in pressure level on front and rear tyres influences essentially the boundaries of sensitivity of the vehicle steering; smaller pressure in rear tyres and higher pressure in front tyres calls for tendency to neutral steer behaviour, reverse proportion of tyre pressure increases understeer and reduces initial steady-state area of “steering angle—lateral acceleration” characteristic;
- A marginal influence of tyre pressure alteration on the slip angle and yaw rate dynamics was observed; for instance, the difference in maximal side slip values did not exceeded 1° , however, more significant effect could be expected in the case of transient manoeuvres.

It should be concluded in addition that the tests have fully validated and verified the simulator of Gumpert Apollo car created in the IPG CarMaker software as well as have proved all operational functions of the developed actuator and sensor parts of the tyre pressure control system. The detailed analysis of the experimental results will be given in coming publications of authors.

4 Summary/Conclusions

The presented work introduced several outcomes of the research project ADTYRE that aims at the development of the tyre pressure control system for improvement of vehicle dynamics. The relevant technical solutions have being developed as applied to sport car Gumpert Apollo.

The consistent modelling of lateral dynamics manoeuvres of the target vehicle has allowed to define requirements to the functional and operational characteristics of the TPCS. The successive design of pneumatic components of the system as well as integrated wireless tyre pressure and temperature sensors has been performed on the basis of defined requirements.

The experimental investigations of the developed components have confirmed high-dynamic operation of the proposed TPCS concept. The achieved operational time does not exceed 1 s for tyre inflation and 1.5 s for tyre deflation as applied to the appointed pressure range of 1.8–2.3 bar.

The actual works within the project ADTYRE are connected with refinement of the control strategy with adaptation to driving conditions and parameters of driving environment. Of particular interest are integrated functions of vehicle dynamics control through the tyre pressure alteration. The related approach proposes (1) stand-alone operation of the TPCS with partial carrying-out of the anti-lock braking and traction control functions (reduction of wheel slip through the change of tyre pressure) and (2) integration of the TPCS with the electronic stability control system to demonstrate the gain in yaw stabilization by cornering manoeuvres. The authors plan to introduce the results of these investigations in further works.

Acknowledgments This work is being funded by the European Regional Development Fund. The authors would also like to acknowledge the contribution of project partners Gumpert Sportwagenmanufaktur GmbH and senTec Elektronik GmbH. The authors express particular gratitude to Mr. Martin Heiderich for his valuable contribution to simulation and experimental activities.

References

1. Smokers R et al (2006) Review and analysis of the reduction potential and costs of technological and other measures to reduce CO₂-emissions from passenger cars. TNO report 06.OR.PT.040.2/RSM
2. <http://www.umweltdaten.de>
3. EUROPA—Press releases, improving the safety and environmental performance of vehicles. <http://europa.eu/rapid/pressReleasesAction.do?reference=IP/08/786&format=HTML>, 23 May 2008
4. U.S. Department of Transportation NHTSA, Tire pressure maintenance—a statistical investigation. April 2009
5. Greenly CL, Beverly JA (2005) Concerns related to FMVSS no. 138 “tire pressure monitoring systems” and potential implementation of a similar standard on commercial vehicles. SAE Technical Paper 2005-01-3517
6. Alexander M et al (2006) Dynamically-self-inflating tire system. Department of Mechanical Engineering, Document ADP-2006-07, University of Michigan, Michigan (Dec 12)
7. Drain J et al (2008) Tire pressure management system. Department of Electrical and Computer Engineering, University of Arizona, Arizona (April 29)
8. Benedict R et al (2003) Talking tires—a basis for tire diagnostics. SAE Technical Paper 2003-01-1279
9. Ho IH et al (2009) A battery-less tire pressure monitoring system. In: Proceedings of 69th vehicular technology conference
10. Forssell U (2009) A sensor fusion approach to tire pressure monitoring, presented at vehicle dynamics Expo. Stuttgart (June 18)
11. Harm GS, Singer R, Harris S (2002) Tire pressure monitoring systems and the automotive assembly process. SAE Technical Paper 2002-01-1308
12. Al-Solihat MK, Rakheja S, Ahmed AKW (2010) Influence of tyre pressure on an urban bus transient and steady state handling performance. Proceedings of the IMechE, Part D. J Automobile Eng 224:893–908
13. Fancher PS (ed) (1981) Descriptive parameters used in analyzing the braking and handling of heavy trucks—measurements of the longitudinal and lateral traction properties of truck tyres, report UM-HSRI81-19-3-4, vol 3. Highway Safety Research Institute, University of Michigan, pp 357–373
14. Kasprzak EM, Lewis KE, Milliken DL (2006) Inflation pressure effects in the nondimensional tire model. SAE Technical Paper 2006-01-3607
15. <http://www.racelogic.co.uk/>

Structure Analysis and Ride Comfort of Vehicle on New Mechanical Elastic Tire

Wei Wang, Youqun Zhao, Jian Wang and Liguo Zang

Abstract To improve the tire performance of puncture-proof, explosion prevention, safety and bullet-proof, a kind of new mechanical elastic tire(MET) used for vehicle is put forward. MET integrated tire and wheel combination is one of non-pneumatic tire (NPT) which has potential for improved handling, grip, low energy loss when impacting obstacles and reduced rolling resistance when compared to a pneumatic tire. The objective of this study is to analysis the structure and ride comfort of vehicle on the new MET. The MET is an innovative non-pneumatic tire. So, the structure and working principle of new MET with elastic rings and hinges are illustrated in detail. Mechanical relationship between the various components of the wheel will be obtained by analyzing the structure and basic principle of MET. The relationship of mechanical transmission of internal structure in the wheel is obtained under the wheels' driving and braking working conditions. The vehicle model concluding the MET is built in the software ADAMS and the results is compared with those of a pneumatic tire. By researching the MET, we can get two results. On the one hand, the new MET has effective mechanical transmission characteristics, ensuring the normal driving of the vehicle. On the other hand, the vehicle concluding the new MET meet the comfortable requirements and ride comfort regularity of pneumatic tire. In high speed, the ride comfort of vehicle concluding the pneumatic tire slightly better than the new mechanical elastic wheel. The results of the research will provide the theoretical support for the further experiment of the MET.

F2012-G03-005

W. Wang (✉) · Y. Zhao · J. Wang · L. Zang
College of Energy and Power Engineering, Nanjing University of Aeronautics
and Astronautics, Nanjing, People's Republic of China
e-mail: 1559449067@qq.com

Keywords New mechanical elastic tire · Non-pneumatic tire · Structure analysis · Ride comfort

1 Introduction

The pneumatic tire became the dominant wheel design for rolling transport shortly after its invention by John Boyd Dunlop in 1888. The pneumatic tire brought with it durability, reliability, and maintenance problems that are still present today. However, the pneumatic tire may have several disadvantages; catastrophic damage by flat while driving, requirement of maintenance of air pressure, and complicated manufacturing processes [1]. To reduce the pneumatic tire disadvantages, several tire engineers have attempted to develop non-pneumatic tires, such as Uniroyal Goodrich Tire, Bridgestone, Toyo Tire and Tweel [2–5]. In this study, mechanical elastic wheel, which has broken the boundaries of the traditional wheel and tire and integrated them in one body, is a special kind of the non-pneumatic tire. The mechanical elastic wheel aims at performance levels beyond those possible with conventional pneumatic technology because of its structural design, added suspension, and decreased rolling resistance. It delivers pneumatic-like load-carrying capacity, ride comfort, and as it has no pressurized air cavity, it cannot fail by loss of air pressure. Structural analysis of the non-pneumatic tire is rarely found in the literature [6]. Ju et al. developed the finite element models of non-pneumatic tires with cellular shear band and investigated one dimensional contact pressure [6] and computation method and nonlinear finite element analysis of Tweel [7, 8]. Thus, the objectives of this chapter are first, to describe a non-pneumatic structure that exhibits the same critical characteristics; second, to analysis the structural of the non-pneumatic tire to explain the relationship of mechanical transmission of internal structure; and finally, the ride comfort of vehicle on the MET is compared with those of a pneumatic tire.

2 The Structure and Working Principle of New Mechanical Elastic Tire

2.1 *The Structure of New Mechanical Elastic Tire*

MET is composed of the driving apron, elastic rings, the combo cards of elastic rings, hub, return spring, pins, hinges and other accessories. Its structure is shown in Figs. 1 and 2.

Fig. 1 Wheel geometry model

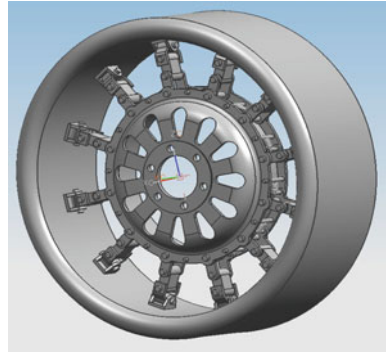


Fig. 2 The connection diagram of elastic ring



- (1) Twelve combo cards of elastic rings are distributed with the same angle and combined and locked a plurality of elastic rings together, as shown in Fig. 2.
- (2) By burying vulcanization in the rubber layer of driving apron and inner layer of cord fabric, the elastic outer-wheel is built.
- (3) The hub is put in the middle of the elastic outer wheel. One end of 12 groups of hinges is respectively installed with pins on the pin seat of the combo cards of elastic rings of the elastic outer wheel inner side. The other end of them is installed on the bolt hole of wheel hub.
- (4) A return spring at the bottom of the third hinge connected to the hub. In free state, the groups of hinges are slightly bending deflection. Because of ground shocking and the driving and braking torque, the hinges are curved in the vehicle driving process. The curved hinges can be returned through the return spring.

2.2 The Working Principle of New Mechanical Elastic Wheel

- (1) The load and torque by axle passed the hub make the groups of hinges from flexuosity to pretension state. Then, the hinges pull the elastic outer-wheel. The force is making the wheel roll.

- (2) The hub relying on the pull from the hinges hang into the outer-wheel and move down a distance due to vertical load. The hinges under the hub don't subjected to force and are slightly curved. The upper part of elastic outer-wheel due to the downward pull from the hub, outer-wheel transform into the appropriate class of elliptic elastic deformation with setting range.
- (3) Because of outer-wheel transforming into elliptic, the deformation of MET is different from local deformation of the pneumatic tire under the driving process. It shows the rolling resistance and energy consumption of MET is much smaller than that of the pneumatic tire and mechanical efficiency is much higher than that of the pneumatic tire.
- (4) The MET under the loading driving process, the force of each groups of hinges is from the tension gradually to the slightly bent not force, then to the tension, cycle replacement cycle. Because of the hub is put in the middle of the elastic outer wheel, the most of incentive of road roughness can only be suffered by the elastic outer-wheel. Because of deformation of the outer-wheel and the instantaneous curvature of each groups of hinges, incentive of road roughness cannot be sent to the wheel hub. The MET has a specific mitigation and buffering isolation performance different from the pneumatic tire.

3 Mechanical Transmission Characteristic Analysis of Met Structure

In order to more accurately describe the internal structure mechanics transmission characteristic of the MET, the mechanical characteristic under the driving and braking condition are respectively analyzed.

3.1 Mechanical Characteristic Analysis of Met Under Driving Condition

Mechanical analysis under driving condition is shown in Fig. 3.

Test pavement is hard. 12 groups of hinges in MET all receive tension, only excepting the following two groups showed a slightly bending deflection. The analysis is the same as the theory working principle. The internal structure mechanical characteristics analysis figure of the wheel under driving conditions is established, as shown in Fig. 4. The spring stiffness is small, and the role of it only let the hinges bending return. So relative to the wheel vertical load and driving force, the impact of the spring is very small, so the force of the spring will not be considered.

Mechanics theory is applied to respectively analysis the hub and outer-wheel. We can get that the outer-wheel pulling force is the opposing force of the hub pulling force, as shown in Fig. 4. Taking into account the 6 and 7th groups of hinges below the hub are slightly bending deflection, so the force is very small and can be ignored

Fig. 3 The analysis under driving condition

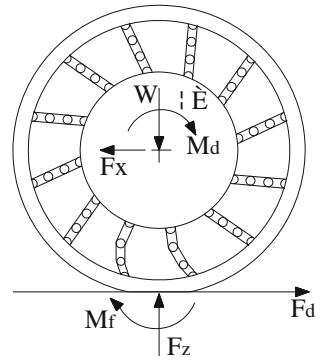
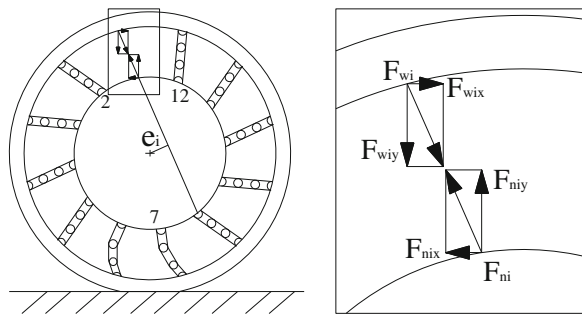


Fig. 4 The internal structure analysis



when analyzing wheel force, $F_{n6} = F_{n7} = F_{w6} = F_{w7}$. From the working principle of the MET, we can draw that the pull of the upper of elastic outer-wheel suffered from hub to surface is larger than the lower of elastic outer-wheel. In the driving conditions, the mechanical equations of hub and outer are as follows:

hub:

$$\sum_{i=1}^{12} F_{niy} + W = 0$$

$$\sum_{i=1}^{12} F_{ni}e_i + M_d = 0$$
(1)

outer:

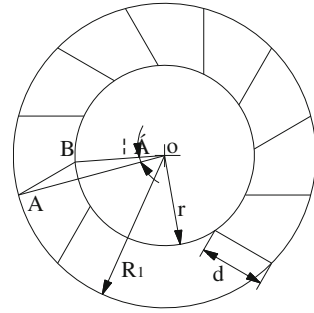
$$\sum_{i=1}^{12} F_{wiy} = W$$

$$F_z = W$$

$$M_a = F_b - F_x$$

$$J\ddot{\theta} = M_d - F_dR - M_f$$
(2)

Fig. 5 The lag angle



where, i represent the number of groups of hinges (number sequence as shown in Fig. 4), F_{ni} is the tension of a group of hinges to the hub, F_{nix} is the component of F_{ni} in the X direction, F_{niy} is the component of F_{ni} in the Y direction, W is the vertical loading, F_{wi} is the force from a group of hinges to the outer-wheel, F_{wix} is the component of F_{wi} in the X direction, F_{wiy} is the component of F_{wi} in the Y direction, e_i is the lever arm of F_{ni} , M_d is the drive torque acting on the hub, M is the quality of the MET, J is the inertia moment from the wheels to the center axis, a is the acceleration of the MET, $\ddot{\theta}$ is the angular acceleration of the MET, F_d is the driving force from the ground to the wheel, F_x is the horizontal force that the drive shaft acts on the MET, M_f is rolling resistance moment, R is the wheel radius.

Because the hub and the outer-wheel are connected by hinges in the MET, in stress situations, the hinges are inevitable after the transition from a free bend to the pretension state and the process will produce a lag angle.

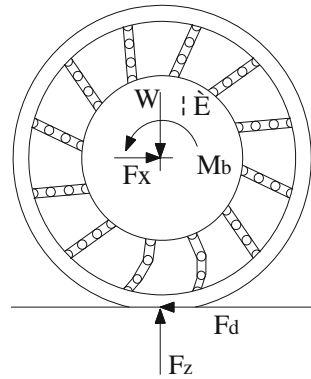
According to the geometric relationship in Fig. 5, the lag angle α is solved in $\triangle ABO$. In the figure, R_1 is the distance from the wheel center to the end of third hinge, r is the radius of hub, d is the length in the pretension state of hinges. $R_1 = R - D_1 - L_1$, D_1 is the thickness of the wheel outer ring, L_1 is a base length of the hinge and the elastic ring connected.

From the cosine theorem:

$$\alpha = \arccos[(R_1^2 + r^2 - d^2)/(2 \times R_1 \times r)] \times 180/\pi = 7.8^\circ \tag{3}$$

where, $R = 390\text{ mm}$, $D1 = 35\text{ mm}$, $L1 = 12\text{ mm}$, $r = 192\text{ mm}$, $d = 155\text{ mm}$. The angle makes the wheel from stationary to start. The inner-wheel and outer-wheel must go through a relative motion lag, and the process is clutch half joint state. In this state, the torsional vibration of transmission where the clutch will be greatly relieved due to the presence of lag angle. This is a thorough reform contrasting to the pneumatic tire, and it is important to design and research for off-road vehicle wheel.

Fig. 6 The analysis under braking condition



3.2 Mechanics Characteristic Analysis for Elastic Wheel Under Braking Conditions

Figure 6 is mechanical analysis diagram under braking condition. In the diagram, rolling resistance torque and inertia torque of deceleration time are negligible.

Mechanics analysis under braking condition is similar as driving condition. When the wheel suffers from braking torque, in fact, the hub suffers from the torque. The wheel still moves forward and the outer wheel to the hub has relative motion. Its internal structure mechanical characteristics are as shown in Fig. 7, the mechanical equations of hub and outer in the braking conditions are as follows:

Hub:

$$\sum_{i=1}^{12} F_{niy} + W = 0$$

$$\sum_{i=1}^{12} F_{ni}e_i + M_b = 0$$
(4)

Outer:

$$\sum_{i=1}^{12} F_{wiy} = W$$

$$F_z = W$$

$$Ma = F_b - F_p$$

$$J\ddot{\theta} = M_b - F_bR$$
(5)

where M_b is the brake torque, F_b is the braking force from the ground to the wheel, F_p is the thrust from the axle to the wheels. When the wheel converted from the driving state to the braking state, it will be accompanied by a 2α relative

Fig. 7 The internal structure analysis

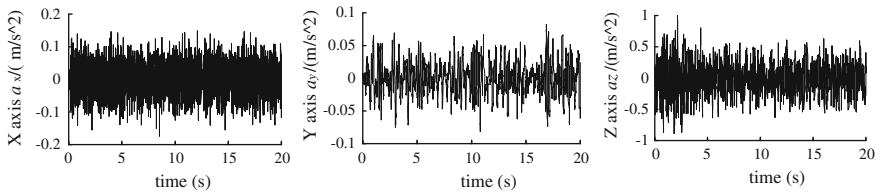
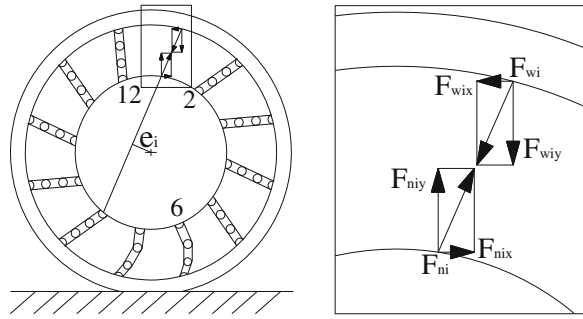


Fig. 8 The acceleration curves of the X axis, Y axis and Z axis on MET

movement of the inner-wheel and outer- wheel. The process is great significance for the relief of the braking load transfer impact.

4 Vehicle Ride Quality Simulation Comparison

In this paper, the mechanical elastic wheel model and the vehicle model are built in the using ADAMS. In this chapter vehicle model, ride comfort of vehicle between mechanical elastic wheel and pneumatic tire are comparative analyze. The vehicle is set in the B road at 60 km/h speed. Comparing the results of ride quality based on the mechanical elastic wheel vehicle centroid and the general tire vehicle centroid, we can get the acceleration curves of the X axis(vertical), Y axis direction(lateral) and Z axis direction(radial) shown in Figs. 8 and 9.

Using the Fast Fourier Transform (FFT) function of ADAMS post-processing to put the each direction acceleration curves into the acceleration power spectral density curves, and then the curves are obtained, shown in Figs. 10 and 11. It can be seen from the figure: the level X, Y direction acceleration power spectral density peak value of the vehicle based on the mechanical elastic wheel appear near the 4.2 and 10.7 Hz position, avoiding 0.5~2 Hz sensitive range; while, the X, Y direction acceleration power spectral density peak of the vehicle based on the pneumatic tire appears near the 5.6 and 11.5 Hz position, also avoiding 0.5~2 Hz sensitive range. From Figs. 10 and 11, we can see the vertical Z acceleration power spectral density peak of the vehicle based on the mechanical elastic wheel

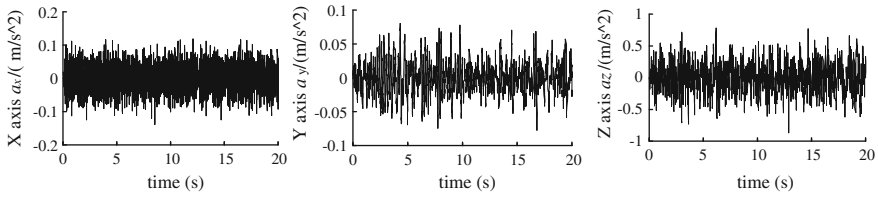


Fig. 9 The acceleration curves of the X axis, Y axis and Z axis on pneumatic tire

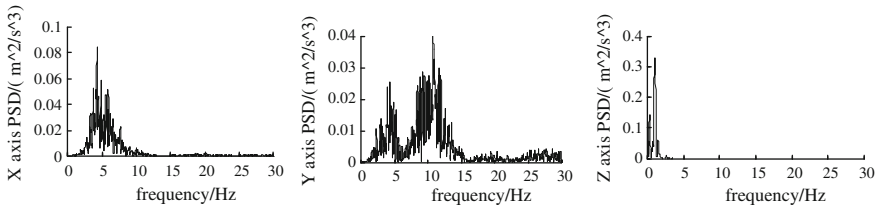


Fig. 10 The acceleration power spectral density curves of the X axis, Y axis and Z axis on MET

appears near the 1.1 Hz position, avoiding 4~12.5 Hz sensitive range. While, the vertical Z acceleration power spectral density peak of the vehicle based on the pneumatic tire near the 2.5 Hz position, also avoiding the sensitive range of 4~12.5 Hz.

From the analysis above, mechanical elastic wheel can replace the role of the pneumatic tire in Ride Comfort. According to the ISO 2631-1:1997 (E) standard, each axial frequency weighting function $W(f)$ is get from the formula 6. The each axial weighted acceleration mean square value a_{xw}, a_{yw}, a_{zw} are obtained according to the formula 7 and 8 in the ADAMS post-processing.

$$W_k(f) = \begin{cases} 0.5 & (0.5 \leq f < 2) \\ f/4 & (2 \leq f < 4) \\ 1 & (4 \leq f < 12.5) \\ 1.25/f & (12.5 \leq f < 80) \end{cases} \tag{6}$$

$$a_w = \left[\int_{0.5}^{80} W^2(f) G_a(f) df \right]^{\frac{1}{2}} \tag{7}$$

$$a_v = \left[(1.4a_{xw})^2 + (1.4a_{yw})^2 + a_{zw}^2 \right]^{\frac{1}{2}} \tag{8}$$

In the same method, the each axial weighted acceleration root-mean-square value and the total weighted root-mean-square acceleration are obtained at 40, 50, 70 km/h speed, the results are showed in Tables 1 and 2.

The results can be obtained from the two tables:

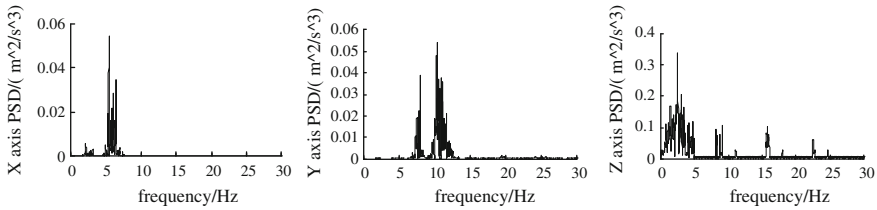


Fig. 11 The acceleration power spectral density curves of the X axis, Y axis and Z axis on pneumatic tire

Table 1 The each axial weighted acceleration root-mean-square value on MET

Speed (Km/h)	a_{xw} (m/s ²)	a_{yw} (m/s ²)	a_{zw} (m/s ²)	a_v (m/s ²)	Human subjective feeling
40	0.0799	0.0468	0.2237	0.2585	Comfortable
50	0.0869	0.0539	0.2454	0.2841	Comfortable
60	0.1015	0.0715	0.2484	0.3032	Comfortable
70	0.1163	0.0762	0.2671	0.3305	Some uncomfortable

Table 2 The each axial weighted acceleration root-mean-square value on pneumatic tire

Speed (Km/h)	a_{xw} (m/s ²)	a_{yw} (m/s ²)	a_{zw} (m/s ²)	a_v (m/s ²)	Human subjective feeling
40	0.0639	0.0388	0.1422	0.1766	Comfortable
50	0.0768	0.0443	0.1451	0.1909	Comfortable
60	0.0896	0.0507	0.1543	0.2111	Comfortable
70	0.0984	0.0649	0.2445	0.2950	Comfortable

- (1) As the speed increasing, the weighted acceleration root-mean-square value becomes large. It means that the ride comfort of the vehicle decreased with speed increasing. The ride comfort of the vehicle based on the pneumatic tire at the different speed is slightly better than that of the mechanical elastic wheel, but the ride Comfort of the vehicle based on the mechanical elastic wheel satisfy with the regularity of the ride comfort of the vehicle based on the pneumatic tire and conform with the characteristics of the pneumatic tire.
- (2) According to the weighted acceleration root-mean-square value and human subjective feeling: when weighted acceleration a_w is less than 0.315 m/s^2 , the body is not uncomfortable. No matter based on the mechanical elastic wheel or pneumatic tire, the body is not uncomfortable when the vehicle speed is less than 60 km/h in B road. The mechanical elastic wheel is committed to improve the controllability and stability of vehicle. So when the vehicle with mechanical elastic wheel drive at the speed of 70 km/h, driver’s seat vibration response exceeds slightly the limit and the body has some uncomfortable. When the vehicle with the pneumatic tire drive at the speed of 70 km/h, driver’s seat vibration response do not exceed the limit, the human feel comfortable. So, the ride comfort of mechanical elastic wheel under the condition of high speed needs to be improved.

5 Conclusions

In this study, we suggested mechanical elastic wheel with hinges. Major findings on the study are as follows:

- (1) Under the wheels' driving and braking working conditions, inner-wheel and outer-wheel are respectively mechanical analyzed. The relationship of mechanical transmission of internal structure in the wheel is obtained. The results show that the new wheel has effective mechanical transmission characteristics, ensuring the normal driving of the car.
- (2) The vehicle model concluding the new mechanical elastic wheel is built in the software ADAMS. The result shows that the vehicle concluding the new mechanical elastic wheel meet the comfortable requirements and ride comfort regularity of pneumatic tire. In high speed, the ride comfort of vehicle concluding the pneumatic tire is slightly better than the new mechanical elastic wheel. The results could be used as the thesis reference for design and improvement of new mechanical elastic wheel.

Acknowledgements This work was supported by Funding of Jiangsu Innovation Program for Graduate Education (CXLX12_0142) and the Fundamental Research Funds for the Central Universities.

References

1. Gent AN, Walter JD (1985) The pneumatic tire. National highway traffic safety administration, Washington
2. Alfredo RV (1967) Airless tire. US Patent US3,329192
3. Kubica W, Schmidt O (1979) Self-supporting motor vehicle tire. US Patent US4,169494
4. Manesh A, Terchea M, Anderson B, Meliska (2008) Tension-based non-pneumatic tire. World Intellectual Property Organization, WO 2008/118983 A1
5. Rhyne T, Cron SM (2006) Development of a non-pneumatic wheel. *Tire Sci Technol* 34(3):150–169
6. Ju J, Ananthasayanam B, Summers JD, Joseph P et al (2010) Design of cellular shear bands of a non-pneumatic tire-investigation of contact pressure. *SAE Int J Passeng Cars Mech Syst* 3(1):598–606
7. Manga KK (2008) Computation method for solving spoke dynamics on high speed rolling tweekTM. Master's Thesis, Clemson University, Clemson
8. Ramachandran M (2008) Nonlinear finite element analysis of tweekTM geometric parameter modifications on spoke dynamics during high speed rolling. Master's Thesis, Clemson University, Clemson

Part IV
Vehicle Controls on Handling and Stability

Active Compensation of Friction in Electric Power Steering

Tsutomu Tamura, Aris Maroonian and Robert Fuchs

Abstract The basic concept of the so-called *MS mimic control strategy* is developed and applied to a column assist electric power steering (C-EPS) in this paper. In this strategy, the friction of the assist column only is compensated assuming that the friction effects can be lumped into a single equivalent friction model and that its parameters are known and constant. The friction of the rack-pinion gear remains as in a manual steering system (MS). This strategy is of interest as the significant friction of the worm gear is compensated with the available sensors and actuators. This study addresses the potentials of an active compensation that could be generalized to the rack and pinion gear.

Keywords Vehicle dynamics · EPS · Steering feel · LuGre friction model · Friction compensation

F2012-G04-002

T. Tamura (✉) · A. Maroonian
JTEKT Corporation, R&D Center, Nara, Japan
e-mail: tsutomu_tamura@jtekt.co.jp

A. Maroonian
e-mail: aris_maroonian@jtekt.co.jp

R. Fuchs
JTEKT Europe, EU Representative Office of JTEKT R&D Center, Paris, France
e-mail: robert_fuchs@jtekt.co.jp

1 Introduction

Friction is known to deteriorate the dynamic characteristics of electric power steering (EPS) with effect on the “steering feel”. It is the design constrain of no backlash that requires the gear elements to be preloaded resulting in additional friction. More generally, friction in EPS is found at the gear meshes, the bearings, the rack bushes and the yoke support. Apart from altering the EPS sensitivity characteristic, friction influences the mechanical design resulting in tradeoffs well known in the industry. Furthermore, torque assisting control strategies often are based on the loose assumption of no friction limiting the tuning capability. Reducing the gap between the ideal frictionless EPS and an off-the-shelf EPS has not yet been addressed formally. Three complementary approaches are available to engineers to deal with friction in steering system (from the steering wheel to the wheel) of ground vehicle:

- Reduction of mechanical losses of independent components.
- Relative reduction of friction torque by increasing the wheel reaction (wheel castor and camber angles, etc.).
- Active compensation by mean of evolved control of the assist motor.

The first approach has been and is still one of the main design objectives for engineers of the steering supplier and the vehicle maker. The second is part of the core knowledge of the chassis engineers and is key to defining the vehicle dynamic behaviour. The third has not yet been explored. Commonly found methods for alleviating the effect of friction in EPS are based on assist motor angular speed dependent friction compensation [1] and the application of lead term in the current controller of the assist motor. These compensations are limited as empirically based and result in time consuming tuning procedure.

This paper introduces a first basic investigation on the active friction compensation of EPS. A previous work from the same authors presented an experimentally validated model of the dynamics of an EPS [2]. The LuGre model [3] was chosen for representing the friction because of its continuous formulation enabling the application of control theories and already widely exploited in robotics and machine tools [4, 5].

Friction compensation is investigated with the perspective of relaxing the tuning work, thus saving time. Furthermore, by achieving effective friction compensation, the mechanical design rules could be modified with, for examples, relaxed tolerances and the model-based control of steering will be closer to the ideal frictionless case. Nevertheless, steering, for the driver, is a subjective notion commonly referred to as “steering feel”. While friction compensation can be seen as a technical achievement, the value for the driver is likely to be found in the ability to design and control the EPS characteristic for a subjective optimal steering feel [6].

The remaining of this paper is organized as follows. The objectives of this work are presented in Sect. 2. Section 3 shows the structure of the EPS chosen. The model of the steering dynamics is summarized in Sect. 4. The friction compensation is developed in Sect. 5. The developed controller is experimentally validated on a power column test bench in Sect. 6. The controller is also validated on a vehicle dynamic simulation in Sect. 7. Finally, conclusions are given in Sect. 8.

2 Objective

By *active friction compensation*, it is mean the compensation of the mechanical friction found in an EPS with a feedback control using the assist motor as the actuator and the sensors available. Ideally, no additional sensor or modification of the existing hardware should be made for achieving this compensation. The modification of the hardware would be justified in the case of significant performance improvement only.

The objective is to increase the open-loop sensitivity of the EPS. An EPS can be seen as an actuator, which input is the driver torque applied to the steering wheel and the output the force developed by the rack to the wheels. Formally, sensitivity is the ratio between the output and the input signals. This will be the ratio of the rack force versus the steering wheel torque for a driver input of an EPS. The opposite definition can also be used for describing the sensitivity to a road input.

The sensitivity of an EPS is nonlinear for various reasons. First, the friction of the mechanical system causes the sensitivity to be null or close to zero for small inputs. Because of friction, the driver should apply a bias torque to the steering wheel for his command to be transmitted to the wheels. Also, small vibrations of the wheels are not transmitted to the driver affecting the “road feel”. Hence, friction filters small amplitude signals. Active friction compensation will enable small amplitude signals to be transmitted and therefore to render the EPS closer to the ideal frictionless actuator. Second, the assist control generates a torque, which is not proportional to the driver torque.

The basic concept of the so-called *MS mimic control strategy* is developed and applied to a column assist electric power steering (C-EPS) in this paper. In this strategy, the friction of the assist column only is compensated assuming that the friction effects can be lumped into a single equivalent friction model and that its parameters are known and constant. The friction of the rack-pinion gear remains as in a manual steering system (MS). This strategy is of interest as the significant friction of the worm gear is compensated with the available sensors and actuators. This study enables the development of an active compensation that could be generalized to the rack and pinion gear.

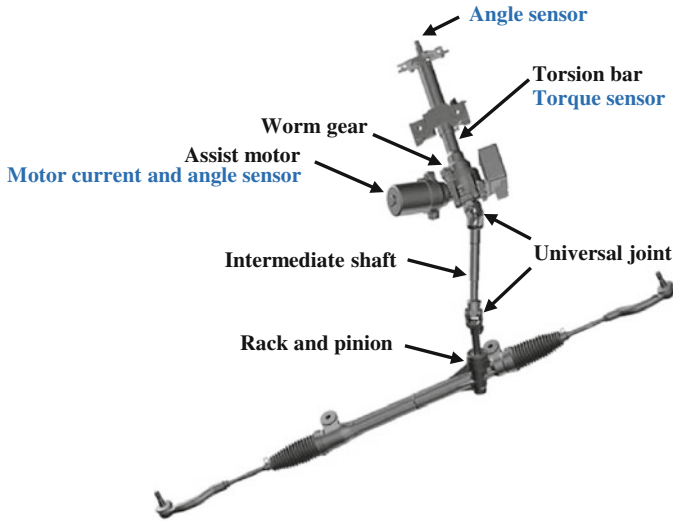


Fig. 1 Assembly view of JTEKT C-EPS and the available sensors

3 Structure of the C-EPS

Figure 1 shows the structure of the column assist electric power steering actuator. This system is composed of

- a torsion bar used as a torque sensor for detecting the driver input torque,
- a DC motor and an ECU (electric control unit) for generating the assist torque corresponding to the driver torque,
- a worm gear for amplifying the motor torque,
- an intermediate shaft with two universal joints for transmitting the combined torque of the driver and the assist motor to the pinion gear and
- a rack and pinion gear for converting the motion from rotation to translation.

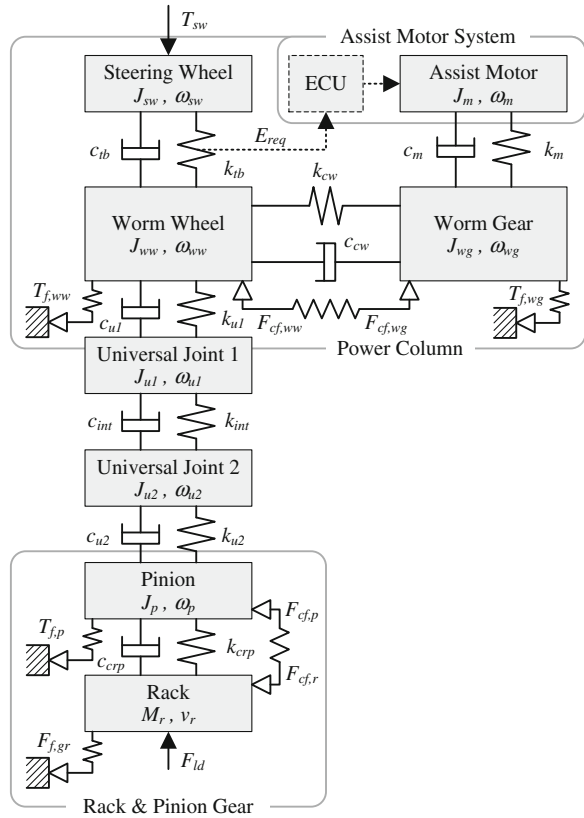
The parts located above the intermediate shaft form, what is called, the column. A C-EPS can be seen as a manual steering with an assist module located on the column. The available sensors are indicated in the same figure.

4 C-EPS Model

4.1 Simulation Model

Figure 2 shows the 8-dof (degree-of-freedom) structure of the C-EPS model introduced in [2]. Because of its high accuracy and relative complexity, it is

Fig. 2 Structure of the C-EPS model



considered as the *simulation model* or *plant model*. The inputs and the outputs of the system are the steering wheel torque T_{sw} , the rack axial force F_{ld} , and the assist torque command E_{req} . In this figure, J and M represent the rotational inertias and the masses, ω and v the angular and the translational velocities, k and c the stiffness and the damping coefficients. The frictions at the mesh points of the worm gear and of the rack and pinion gear $F_{cf,ww}, F_{cf,wg}, F_{cf,p}, F_{cf,r}$ as well as that at these gear support bearings $T_{f,ww}, T_{f,wg}, T_{f,p}$ and at the rack guide $F_{f,gr}$ are considered. The suffix *sw* indicates the steering wheel, *m* the assist motor, *ww* the worm wheel, *wg* the worm gear, *u1* and *u2* the universal joints, *p* the pinion gear, *r* the rack gear, *tb* the torsion bar and *int* the intermediate shaft.

This model has been experimentally validated in both static and dynamic conditions. Its characteristics are summarized as follows:

1. The representation of the friction transitions static to dynamic with the application of the LuGre model.
2. The replication of the efficiency in the two powerflow directions of the gear elements with a load dependent meshing friction model.

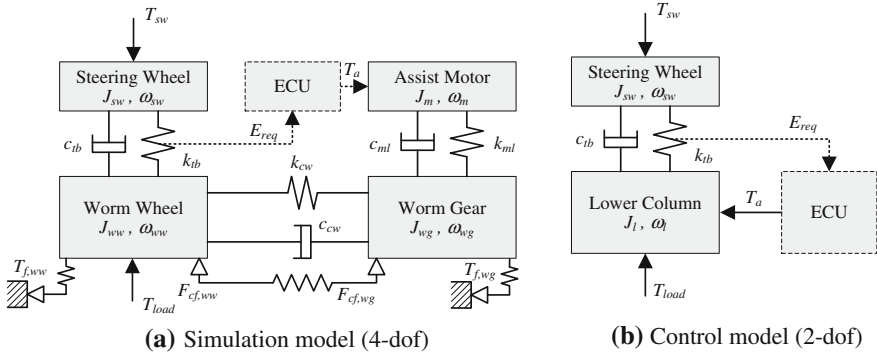


Fig. 3 Model of the power column of the C-EPS

3. The prediction of the friction induced hysteresis of the standard steering torque versus angle characteristic (Fig. 3).
4. A validated bandwidth of 5 Hz for a direct input and 15 Hz for an inverse input.

4.2 Control Model

A *control model* obtained from the reduction and simplification of the simulation model is required for the synthesis of the compensation controller. The power column originally represented as a 4-dof model is reduced to a 2-dof system as illustrated in Fig. 3. The three inertias, the worm wheel J_{ww} , the worm gear J_{wg} and the motor J_m , are lumped into the lower column inertia J_l . The two equations of motion write:

$$J_{sw}\dot{\omega}_{sw} = T_{sw} - T_{tb} \quad (1)$$

$$(J_{ww} + (J_{wg} + J_m)i^2\eta)\dot{\omega}_l = T_{tb} + T_{load} + T_a i \eta - \tau_0 \mu F_0 \frac{r_{ww}}{\sin(\gamma_w) \sin(\beta_w)} \quad (2)$$

where T_{sw} is the steering wheel torque, T_{tb} the torsion bar torque, T_{load} the load torque from the rack, T_a the worm gear torque by the assist motor, F_0 the preload force, μ the lumped friction coefficient of the power column which includes the friction coefficient of the worm gear mesh and the bearings, r_{ww} the worm wheel pitch radius, β_w the worm gear pressure angle, γ_w the worm gear lead angle. The gear ratio i , defined as ω_{wg}/ω_{ww} , and the efficiency of the worm gear η are represented as:

$$i = \frac{r_{ww}}{r_{wg}} \frac{1}{\tan(\gamma_w)} \quad (3)$$

Table 1 Condition of the contact state

Case	Condition	τ_0	τ_1	Contact state
(a)	$N_0 - dN_{1or2} > 0$	1	0	Double contact
(b)	$N_0 - dN_{1or2} \leq 0$ and $dN_1 \geq 0$	0	1	Single contact (Positive worm gear torque)
(c)	$N_0 - dN_{1or2} \leq 0$ and $dN_1 \leq 0$	0	-1	Single contact (Negative worm gear torque)

$$\eta = \tan(\gamma_w) \frac{\cos(\beta_w) - \tau_1 \mu \tan(\gamma_w)}{\cos(\beta_w) \tan(\gamma_w) + \tau_1 \mu} \quad (4)$$

with r_{wg} representing the worm gear pitch radius.

Because of the preload, single and double contact configurations are defined depending on the torque transmitted. This is modelled with the parameters τ_0 and τ_1 , which account for the difference between the initial contact force N_0 from to the preload and the variation of the contact force $dN_{1 or 2}$, defined as a function of T_{tb} , T_{load} , T_a and . Table 1 summarizes the condition of each contacting configuration.

Simulation results in quasi static condition of the worm wheel torque and the contact force versus the worm gear torque are shown in Fig. 4 in the two conditions of the gear with and without preload. The initial contact force defined by the preload and illustrated in Fig. 4b, generates a static friction at the gear mesh. As a consequence, a null sensitivity region appears for small values of worm gear torque (Fig. 4a). In other words, the worm gear torque is not transmitted until it overcomes the static friction caused by the preload. A second point of interest is the discontinuity observed in both figures originating from the change from a double to a single contact configuration. Also, the increasing width of the hysteresis with the worm gear torque illustrates the load dependent friction characteristics of this gear.

In terms of “steering feel”, the EPS responses for small driver torque input as well as the “on-center” condition are particularly important justifying the compensation of friction.

5 MS Mimic

The objective of the MS mimic control strategy is to replicate the same response as that of a manual steering. To this end, the assist motor should supply a torque for alleviating the effect of friction in the power column according to the gear contact configuration. Because an experimentally validated friction representation is available [3], a model-based friction compensation scheme is adopted.

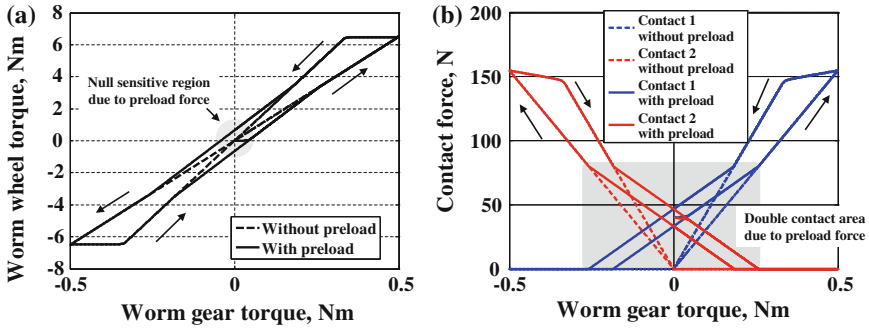


Fig. 4 Quasi static characteristic of the power column model. **a** Worm wheel torque versus worm gear torque. **b** Contact force versus worm gear torque

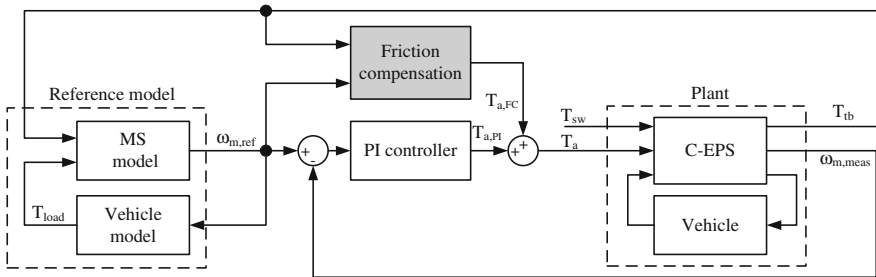


Fig. 5 MS mimic control strategy

5.1 MS Mimic Control Strategy

Figure 5 shows the block diagram of the MS mimic control strategy. The proposed model reference tracking control is composed of friction compensation and a PI controller. The friction compensation controller inputs are the torsion bar torque T_{tb} and the assist motor angular speed reference $\omega_{m,ref}$, which is defined by the reference model composed of a MS and a vehicle model. The friction compensation block outputs the assist torque command $T_{a,FC}$ according to the estimated friction loss in the power column. The PI controller is used for improving the robustness of the friction compensation with regard to unmodeled time varying parameters. The assist motor torque command T_a results from the combination of the friction compensation $T_{a,FC}$ and the PI controller effort $T_{a,PI}$.

5.2 Friction Compensation

The objective of this control is to modify the dynamics of the column (2) in such a way that the resulting dynamics seems frictionless. This can be formulated with the following relation.

$$(J_l + (J_{wg} + J_m)i^2)\dot{\omega}_l = T_{tb} + T_{load} \quad (5)$$

Two compensations schemes are developed because of the two contacting configurations. First, for the double contact configuration or small transmitted torque (case a in Table 1), the assist motor should generate a compensation torque corresponding to the third term of (2) as follows.

$$T_{a,FC} = \frac{1}{i} \frac{F_0 r_{ww}}{\sin(\gamma_w) \sin(\beta_w)} \hat{\mu} \quad (6)$$

where, $\hat{\mu}$ is the estimated friction coefficient from the LuGre friction model. The input of the LuGre model is the sliding velocity v_s along the friction angle of the worm gear.

$$v_s = \frac{r_{wg} \omega_m}{\cos(\gamma_w)} \quad (7)$$

The net contact force is constant in this configuration because when the force on one side increases, it decreases on the other side.

Second, for the single contact configuration or high transmitted torque (case b and c in Table 1), the assist motor should generate a compensation torque so as to satisfy (5). For that purpose, let's consider the compensation term Δx_1 and Δx_2 from (2).

$$\left(\frac{J_l}{\hat{\eta}} + \Delta x_1 + (J_{wg} + J_m)i^2 \right) \dot{\omega}_l = \frac{T_{tb} + T_{load}}{\hat{\eta}} + \Delta x_2 \quad (8)$$

where $\hat{\eta}$ is the estimated worm gear efficiency based on (4) and function of $\hat{\mu}$. From (5) and (8), Δx_1 and Δx_2 are defined respectively as follows

$$\Delta x_1 = J_l \left(1 - \frac{1}{\hat{\eta}} \right) \quad (9)$$

$$\Delta x_2 = (T_{tb} + T_{load}) \left(1 - \frac{1}{\hat{\eta}} \right) \quad (10)$$

The total torque that should be supplied by the assist motor can be written as

$$T_{a,FC} = \frac{1}{i} (-\Delta x_1 \dot{\omega}_l + \Delta x_2) \quad (11)$$

It shows that the compensation torque is a function of the external torque, the acceleration and the efficiency of the worm gear, which depends on the contact force. Therefore, in order to realize the proposed friction compensation, it is necessary to estimate the following ω unavailable states.

- Column friction coefficient μ
- Column load torque T_{load}
- Acceleration of the column $\dot{\omega}_l$

The column acceleration can be calculated from the differentiation of the assist motor angular speed and the gear ratio (3). Observers are required for the friction coefficient and the load torque.

5.3 LuGre Friction Coefficient Observer

The LuGre model is applied for estimating the column friction coefficient. It is formulated as a function of the gear sliding velocity v_s and the bristle deflection p :

$$\mu = \sigma_0 p + \sigma_1 \dot{p} + \sigma_2 v_s \quad (12)$$

$$\dot{p} = v_s - \sigma_0 \frac{|v_s|}{g(v_s)} p \quad (13)$$

$$g(v_s) = \mu_c + (\mu_{ba} - \mu_c) e^{-(|v_s|/v_{sb})^2} \quad (14)$$

where μ_c is the Coulomb friction coefficient, μ_{ba} the peak friction coefficient, v_{sb} the Stribeck velocity, σ_0 and σ_1 the contact stiffness and damping coefficients in the tangential direction and σ_2 the viscous friction coefficient. Typically, these six parameters, related to the bristle state, are experimentally identified. The input of the LuGre model is the slip v_s , which is calculated from (7) with the assist motor angular speed and the gear ratio (3).

5.4 Load Observer

The column load is defined from the wheel torque generating a force to the rack F_{ld} (Fig. 2) and transmitted through the rack and-pinion gear and the intermediate shaft. A vehicle and a rack and pinion gear model are required for defining that load.

Depending on the considered operation condition of the steering system, different models of the vehicle are available. As the on-center operation is essentially defined for small driver torque inputs where the friction effect is dominant, the nonlinear traction characteristics of the tire and the geometry of the steering linkage can be neglected. In that condition, a two-wheel vehicle [7] with a rack and pinion gear model [2] is sufficient. Such observer will need the assist motor angular speed ω_m as input for calculating the estimated column load torque T_{load} .

6 Controller Validation with Power Column Test Bench

The MS mimic control strategy is validated on a power column test bench. Figure 6 shows the experimental setup. The power column is loaded with a torsional spring in place of the actual rack load. A spring constant of 0.6 Nm/rad was

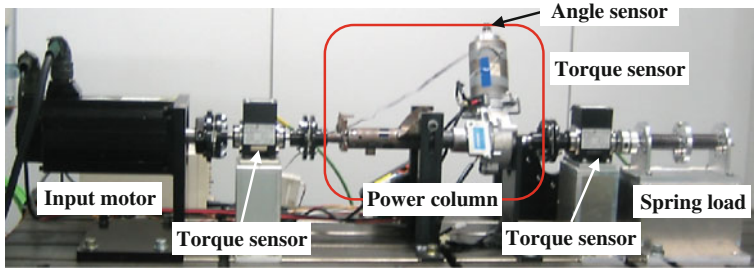


Fig. 6 Test rig set up for friction compensation

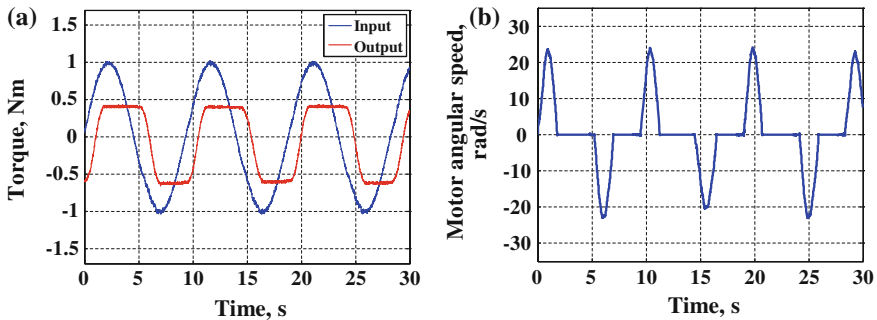


Fig. 7 Open loop performance of the power column. a Effect of friction on the transmitted torque. b Friction effect on speed

selected so that the effect of friction remained dominant against the generated load. The input torque is applied with a servo motor. The input and the output torques are measured with two torque sensors. The angle of the assist motor is measured with an encoder. Both the control functions and the sensors monitoring are made on a dSPACE platform. A sinusoidal torque input of small amplitude (1 Nm) and low frequency (0.1 Hz) is applied. Note that the conventional steering assist map is not adopted in this test.

Figure 7 shows the open loop performance of the power column (no friction compensation). The nonlinearity of the output torque response is observed at each transition when the input torque gradient sign varies (Fig. 7a). Consequently, discontinuity of the power column angular speed is observed (Fig. 7b). Figure 8 shows the result of the friction compensation. The nonlinearity of the output torque is eliminated (Fig. 8a) and the assist motor angular speed tracks the reference signal (Fig. 8b). Figure 8c shows that the friction compensation works effectively as the compensation term is greater than the PI controller effort. This is true in laboratory conditions where the friction characteristics have been identified. In actual situation, the effort of the PI controller is expected to be more significant.

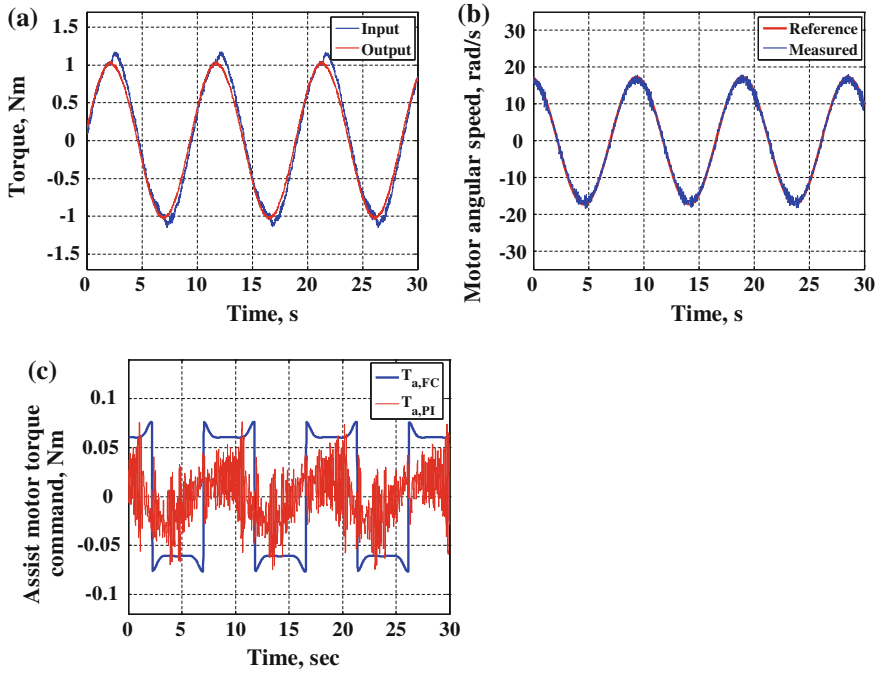


Fig. 8 Validation result of the friction compensation. **a** Improved torque transmission. **b** Speed tracking. **c** Friction compensation and PI controller efforts

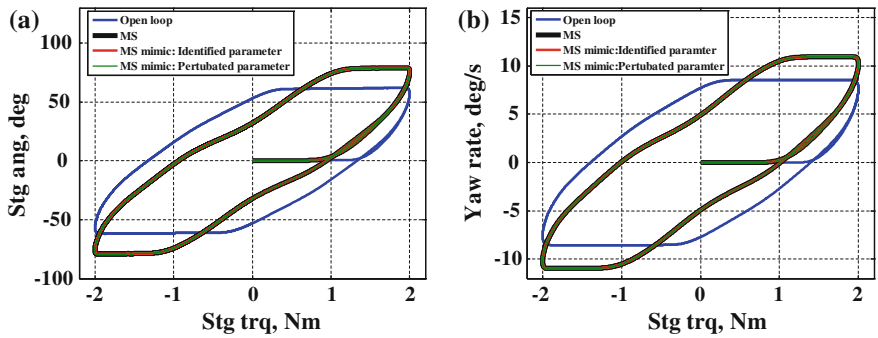


Fig. 9 MS mimic control simulation with vehicle model. **a** Steering angle versus steering torque. **b** Yaw rate versus steering torque

7 Controller Validation with Vehicle Simulation Model

The MS mimic control strategy is validated on simulation with an in-house developed vehicle model (Fig. 9). A sinusoidal driver torque input (frequency: 0.1 Hz, amplitude: 2 Nm) is applied with conventional motor assistance. The

vehicle longitudinal speed is kept constant at 30 km/h. The steering wheel angle and the vehicle yaw rate are simulated. The blue and the black lines show the response of the standard C-EPS (no friction compensation) and MS respectively. The red and the green lines illustrate the MS mimic control responses with the identified and with a 20 % higher friction parameters set. These results demonstrate the capability and robustness of compensating the power column friction embedded in a vehicle without any additional actuator.

8 Conclusion

The basic concepts of the so-called *MS mimic control strategy* has been developed and applied to a column assist electric power steering (C-EPS). In this model reference tracking control, the friction of the assist column is compensated based on an accurate representation of the friction with the LuGre model. The strategy is validated on a test bench. Test results show that the friction compensation is effective in alleviating the nonlinear characteristics caused by friction. The MS mimic strategy is also validated on a vehicle model demonstrating promising performance improvement without additional hardware cost.

In terms of the implementation of the proposed control on actual vehicle, stability, requirement of the sensor resolution and measurement limitations should be addressed. Moreover, adequate reference model definition should be clearly defined as having significant effect on the compensation of friction.

References

1. Kifuku T, Wada S (1997) An electric power-steering system. Mitsubishi Electric Advance, Vol. 78
2. Tamura T, Maroonian A, Higashi M, Fuchs R (2012) Modeling and simulation for the dynamic analysis of an electric power steering. Chassis-tech-plus
3. Candas-de-Wit C, Olsson H, Åström KJ, Lischinsky P (1995) A new model for control of systems with friction. IEEE Transactions on Automatic Control. Vol. 40, No 3
4. Zhu Y, Pagilla PR (2002) Static and dynamic friction compensation in trajectory tracking control of robots, IEEE
5. Altpeter F (1999) Friction modeling, identification and compensation. EPFL, PhD Thesis
6. Canudas-de-Wit C, Bechart H, Claeys X, Dolcini P, Martinez JJ (2005) Fun-to-drive by feedback. European J Control, 11:4–5
7. Jazar RN (2008) Vehicle dynamics: theory and application. Springer

Vehicle Lateral States Estimation Using Kalman-Bucy Filter

Jin Zhao, Rongchen Zhao and Feng He

Abstract This work concentrates on the estimation problems of vehicle lateral states. Based on the two-degree-freedom vehicle model, considering the impacts of the vehicle longitudinal velocity to the vehicle lateral states, we propose a vehicle lateral state observer using the Kalman-Bucy filter. The proposed observer was verified by the simulation experiments. The results show that the proposed method can effectively provide accurate estimation of the vehicle lateral velocity and yaw rate, and filter the process noise and measurement noise as well.

Keywords Vehicle lateral dynamics · Vehicle state estimation · Kalman-Bucy filter · Yaw rate · LTV system

1 Introduction

The vehicle state observation is an important issue in vehicle system dynamics, and it is also one of the key technologies for vehicle dynamics control. In the applications of vehicle lateral control, such as the Four Wheel Steering Control, Electronic Stability Program (ESP), Active Roll Control, need the vehicle yaw rate

F2012-G04-005

J. Zhao (✉) · R. Zhao · F. He
Department of Mechanical Engineering, Guizhou University, Guiyang 550025, China
e-mail: zhaojin1973@hotmail.com

or yaw angle as the very important control input. Although these states can be measured by the gyroscope sensor or other non-contact optical sensors, due to the limitations of sensor accuracy, cost, reliability and install requirement, these systems can be only equipped in the high-end models. Using state estimation, the yaw rate can then be estimated (indirectly measured) through other already equipped and low cost sensors, such as lateral acceleration sensor [1].

It should be noted that state estimation is also one of the key technologies for onboard fault diagnosis. Nowadays, the vehicles become more and more intelligent. A large number of vehicle motion control systems are used to improve the vehicle performance. This puts forward higher requirements of vehicle reliability. According to the configuration of vehicle sensor system, the physical sensors measure the vehicle states, at the same time, we using estimation technology to monitor these states. Thus, this will help us to find out the sensor faults immediately and effectively, and the reliability of the vehicle control system can then be improved [1, 2].

Different observation algorithms have been proposed in former literatures. For the linear system observation, the traditional Luenberger observer and Kalman filter are widely used. The Luenberger observer, which is based on the pole-placement of Linear Time Invariant (LTI) system, was proposed to estimate the states in vehicle lateral dynamics [3]. However, the problem of this method is that the poles are shifting, caused by changers of the system parameters (for example, the vehicle speed). In [4], the application of Kalman filter in vehicle dynamics observation was discussed. An example of using Kalman filter to estimate lateral velocity was introduced. Gao Z.H. proposed a “soft measurement” of vehicle yaw rate by using discrete Kalman filter [5]. The results showed that the proposed Kalman filter could provide accurate estimation of yaw rate, however, the experiment vehicle was assumed to be a constant (22 m/s). The results under the variations of vehicle speed have not been provided.

While, some nonlinear approaches have been also proposed, such as Extend Luenberger observer, Extend Kalman filter and sliding-mode observer [2, 6]. Besides, some more complex nonlinear observers have been also studied, such as H_∞ algorithm, neural network and fuzzy logic, and etc. [7–9]. However, these nonlinear approaches are too complicated for the real-time applications.

According to [10], the vehicle lateral dynamics can be described by the “Bicycle model” which is a 4th order linear time-variant (LTV) system. Although the bicycle model is simple, it has been proved to be a good approximation for vehicle dynamics when lateral acceleration is limited to 0.4 g on normal dry asphalt roads. Thus, the vehicle lateral dynamic state estimation is a problem of LTV system estimation. In this work, we try to observe the vehicle lateral dynamic by using the continues-time Kalman-Bucy filter.

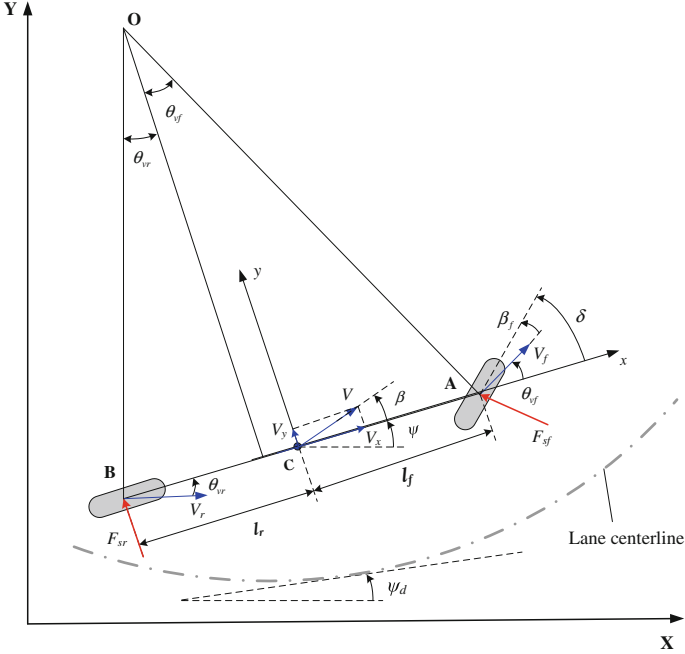


Fig. 1 Bicycle model for vehicle lateral dynamics

2 Vehicle Lateral Dynamics

The vehicle lateral dynamic model is shown in Fig 1. Under the assumption of small steering angle and yaw angle, negligible roll and pitch motion, and linear tire model, regards the longitudinal motion as a known motion, the ‘‘Bicycle model’’ can be represented here by standard state space form [10],

$$\dot{X} = AX + B\delta \tag{1}$$

where, X is the state vector, $X = [y, \dot{y}, \psi, \dot{\psi}]^T$, y and ψ denote the vehicle lateral displacement and yaw angle respectively, δ represents steering angle, and

$$A = \begin{bmatrix} 0 & 1 & 0 & 0 \\ 0 & -\frac{2C_{af}+2C_{ar}}{mV_x} & 0 & -V_x - \frac{2C_{af}l_f-2C_{ar}l_r}{mV_x} \\ 0 & 0 & 0 & 1 \\ 0 & -\frac{2C_{af}l_f-2C_{ar}l_r}{I_z V_x} & 0 & -\frac{2C_{af}l_f^2-2C_{ar}l_r^2}{I_z V_x} \end{bmatrix} \quad B = \begin{bmatrix} 0 & \frac{2C_{af}}{m} & 0 & \frac{2l_f C_{af}}{I_z} \end{bmatrix}^T$$

The meanings of the symbols in Eq. (1) are listed in Table 1. From Eq. (1), one can find that the system matrix A is a function of longitudinal velocity V_x . As the vehicle speed variation is considered in our research, therefore, the ‘‘Bicycle model’’ is a 4th order LTV system.

Table 1 Nomenclature of the bicycle model

δ	Steering angle (rad)
m	Mass (1,485 kg)
V_x, V_y	Longitudinal, lateral velocity (m/s)
I_z	Yaw moment of inertia (2,872 kgm ²)
l_f, l_r	Distance between the C.G. and the front/rear wheels (1.1/1.58 m)
C_{af}, C_{ar}	Cornering stiffness of the front/rear wheels ($C_{af} = C_{ar} = 42,000$ N/rad)

3 Kalman-Bucy Filter for LTV System

The Kalman filter is a set of mathematical equations that provides an efficient computational means to estimate the state of a process, in a way that minimizes the mean of the squared error.

Let us consider here LTV system defined by the following state space model:

$$\begin{aligned}\dot{x}(t) &= A(t)x(t) + B(t)u(t) + G(t)w(t), \\ y(t) &= C(t)x(t) + v(t)\end{aligned}\quad (2)$$

where $x(t)$ is the state vector, $y(t)$ denotes the measured signal, $u(t)$ is the control input, $w(t)$ and $v(t)$ represent the process and measurement noise respectively. The noises are assumed to be independent (of each other), white, Gaussian and with the following covariance matrices:

$$\begin{aligned}E\{w(t)w^T(t')\} &= Q(t)\delta(t-t'), \quad E\{v(t)v^T(t')\} = R(t)\delta(t-t'), \\ E\{v(t)w^T(t')\} &= 0, \quad E\{v(t)\tilde{x}^T(0)\} = 0, \quad E\{w(t)\tilde{x}^T(0)\} = 0, \quad E\{\tilde{x}(0)\tilde{x}^T(0)\} = p_0\end{aligned}\quad (3)$$

where, $\delta(t)$ is the Dirac delta, and $x(0)$ is a random variable with the expected value m_0 , $\tilde{x}(0) = x(0) - m_0$.

The filter consists of two differential equations, one for state estimate and one for the covariance:

$$\begin{aligned}\dot{\hat{x}} &= A(t)\hat{x}(t) + B(t)u(t) + K(t)[y(t) - C(t)\hat{x}(t)] \\ \dot{P}(t) &= A(t)P(t) + P(t)A^T(t) + G(t)Q(t)G^T(t) - K(t)R(t)K^T(t)\end{aligned}\quad (4)$$

where the second equation is a Riccati equation and the Kalman gain is given by:

$$K(t) = P(t)C^T(t)R(t)^{-1}\quad (5)$$

Equations (3–5) define the continues-time Kalman-Bucy estimator, which is also the Kalman-Bucy filter [11, 12].

4 Yaw Rate and Lateral Velocity Estimation Using Kalman-Bucy Filter

As the lateral acceleration sensor is a common sensor can be easily obtained, in our system, the lateral acceleration \ddot{y} is selected as the measure variable. Then from Eq. (1), we can get:

$$\ddot{y} = -\frac{2C_{af} + 2C_{ar}}{mV_x} \dot{y} + \left(-V_x - \frac{2C_{af}l_f - 2C_{ar}l_r}{mV_x} \right) \dot{\psi} + \frac{2C_{af}}{m} \delta \quad (6)$$

From Eq. (6), one can find that only the state variables \dot{y} and $\dot{\psi}$ are related with the measured variable \ddot{y} , while the state variable y and ψ do not have a one-to-one mapping to the measurement \ddot{y} . We eliminate the state y and ψ from Eq. (1). Then, the simplified state space model for observation and measurement equation can be given by:

$$\begin{aligned} \dot{X} &= A_1 X + B_1 \delta + G_1 \omega \\ \ddot{y} &= C_1 X + D_1 \delta + v \end{aligned} \quad (7)$$

where, X is the state vector, $X = [\dot{y} \quad \dot{\psi}]^T$ \ddot{y} is the measurement. δ , steering angle, is the system input. ω is the process noise, $\omega = [\omega_1 \quad \omega_2]^T$, v is the measurement noise, and

$$A_1 = \begin{pmatrix} -\frac{2C_{af} + 2C_{ar}}{mV_x} & -V_x - \frac{2C_{af}l_f - 2C_{ar}l_r}{mV_x} \\ -\frac{2C_{af}l_f - 2C_{ar}l_r}{I_z V_x} & -\frac{2C_{af}l_f^2 - 2C_{ar}l_r^2}{I_z V_x} \end{pmatrix}, \quad B_1 = \begin{pmatrix} \frac{2C_{af}}{m} \\ \frac{2l_f C_{af}}{I_z} \end{pmatrix}$$

$$C_1 = \left[\left(-\frac{2C_{af} + 2C_{ar}}{mV_x} \right) \left(-V_x - \frac{2C_{af}l_f - 2C_{ar}l_r}{mV_x} \right) \right],$$

$$D_1 = \left[\frac{2C_{af}}{m} \right], \quad G_1 = \begin{pmatrix} 1 & 0 \\ 0 & 1 \end{pmatrix}$$

As the vehicle speed variation is considered in our research, therefore, the vehicle state estimation problem described by Eq. (7) is a LTV system estimation problem. At first, we need to validate the observability of the system described in Eq. (7). The observability matrix of the system is

$$M = \begin{bmatrix} N_0 \\ N_1 \end{bmatrix} \quad (8)$$

where $N_0 = C_1$, and $N_1 = N_0 A_1 + \frac{dN_0}{d(V_x)} \frac{d(V_x)}{dt}$, Then we get,

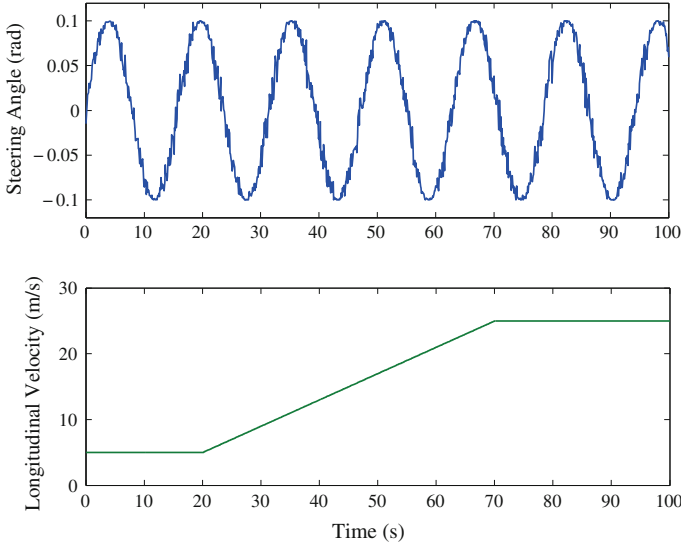


Fig. 2 Steering angle input and vehicle longitudinal velocity

$$M = \begin{pmatrix} \frac{a_1}{V_x} & -V_x - \frac{a_2}{V_x} \\ -a_3 + \frac{a_1^2 - a_2 a_3 - a_1 a_{cc}}{V_x^2} & \left(-a_{cc} - a_1 - a_4 + \frac{a_2 a_{cc} - a_1 a_2 - a_2 a_4}{V_x^2} \right) \end{pmatrix},$$

where a_{cc} is the vehicle acceleration, and

$$a_1 = -\frac{2C_{af} + 2C_{ar}}{m}, \quad a_2 = \frac{2C_{af}l_f - 2C_{ar}l_r}{m}, \quad a_3 = -\frac{2C_{af}l_f - 2C_{ar}l_r}{I_z},$$

$$a_4 = -\frac{2C_{af}l_f^2 - 2C_{ar}l_r^2}{I_z}$$

Rank of M is 2. Therefore, the system is observable.

Then, a Kalman-Bucy filter can be designed by following Eqs. (4) and (5), which can be used to estimate the state variables lateral velocity and yaw rate by using the lateral acceleration measurement.

5 Estimation Results

We will test the performance of the designed observer by using Matlab/Simulink. The vehicle parameters are given in Table 1. The vehicle performs a sinusoidal steering operation. The steering angle is given by:

$$\delta = 0.1 \sin\left(\frac{t}{2.5} + 0.1N(t)\right) \quad (9)$$

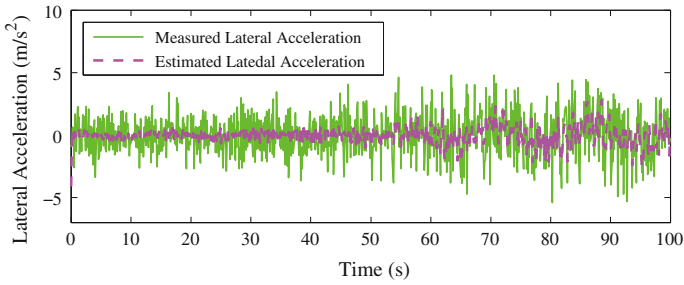


Fig. 3 Measured and estimated lateral acceleration

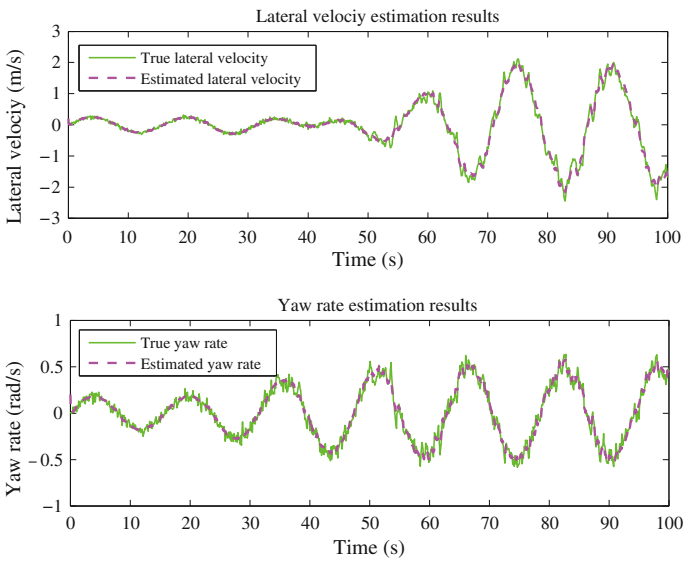


Fig. 4 Estimated lateral velocity and yaw rate

where, the unit of δ is rad , t denotes the time, and $0.1 N(t)$ represents the steering input noise caused by the steering mechanism and uncertainties of road condition, $N(t)$ is assumed to be normal distribution with mean 0 and standard deviation 1,

$$N(t) \sim \mathbb{N}(\mu, \sigma^2) \tag{10}$$

The vehicle speed variation is described as follows: from 0 to 20 s, the vehicle keeps a constant speed of 5 m/s (18 km/h), then the vehicle begins to accelerate from 5 to 25 m/s (90 km/h) with an acceleration of 0.4 m/s^2 , finally the vehicle keeps the final speed of 25 m/s.

The time histories of vehicle steering angle and speed variations are shown in Fig 2.

Figure 3 shows the plots of measured and estimated lateral acceleration. The “filtering” function of the Kalman filter is evident as the estimate appears considerably smoother than the noisy measurement.

The true and estimated values of lateral velocity and yaw rate are shown in Fig. 4. Although the vehicle velocity varies in a wide range, and lateral acceleration measurement is noisy, the estimated lateral velocity and yaw rate can closely follow the variations of the true values during the whole experiment period. The designed Kalman-Bucy filter is proved to be effective in the vehicle lateral dynamic estimation.

6 Conclusion

The proposed Kalman-Bucy filter was verified by a series of simulation experiments. The results show that the proposed method can provide accurate estimation of vehicle lateral states even the vehicle longitudinal velocity varies in a wide range, and filter the process noise and measurement noise as well. The estimated lateral velocity and yaw rate can closely follow the variations of the true values during the whole experiment period. The designed Kalman-Bucy filter is proved to be effective in the vehicle lateral dynamic estimation.

Acknowledgments This work was partially sponsored by the National Science Foundation of China (No. 61164007), and Science Foundation of Guizhou Province (No. [2011]2196)

References

1. Yu Z, Gao X (2009) Review of vehicle state estimation problem under driving situation. *Chin J Mech Eng* 45(5):20–33
2. ZHU S, GAO X, YU Z (2009) Vehicle sideslip angle estimation under extreme driving condition. *J Tongji Univ (Nat Sci)* 37:1070–1074
3. Kiencke U, Daifl A (1997) Observation of lateral vehicle dynamics. *Control Eng Pract* 5(8):1145–1150
4. Venhovens PJTH, Naab K (1999) Vehicle dynamics estimation using Kalman filters. *Veh Syst Dyn* 32(2):171–184
5. Zhenhai G (2003) Soft sensor application in vehicle yaw rate measurement based on Kalman filter and vehicle dynamics. In: *Proceedings of IEEE intelligent transportation systems*, 2 1352–1354 2003
6. Stephant J, Charara A, Meizel D (2004) Virtual sensor: application to vehicle sideslip angle and transversal forces. *IEEE Trans Ind Electron* 51(2):278–289
7. O’Brien RT Jr, Kiriakidis K (2006) A comparison of H_∞ with Kalman Filtering in vehicle state and parameter identification. In: *American control conference*, 3954–3959 2006
8. Sasaki H, Nishimaki T (2000) A side-slip angle estimation using neural network for a wheeled vehicle. *SAE Trans* 109(6):1026–1031
9. Shuming S, Lupker H, Bremmer P, Zuurbier J (2005) Estimation of vehicle side slip angle based on fuzzy logic. *Automot Eng* 4:426–430

10. Rajamani R (2006) Vehicle dynamics and control. Springer, New York
11. Kalman R, Bucy R (1961) New results in linear prediction and filtering theory. *AMSE J Basic Eng* 83:95–108
12. Borne P, Dauphin-Tanguy G, Richard J-P, Rotella F, Zamettakis I (1990) *Commande et optimisation des processus*. Éditions Technip, Paris

A Study on Steering Reactive Torque for Steer-by-Wire Vehicle Using Driving Simulator

Motoaki Hibi, Tatsuro Kobune, Daisuke Miki, Yoshio Kano and Masato Abe

Abstract Steering torque effects on vehicle handling quality is investigated by a driver model based evaluation method. A driving simulator with a precise steering torque generating device is used for this experimental study. It is found the steering reactive torque to steering angle composed of spring, damping and spring-friction is effective on good handling quality.

Keywords Handling quality evaluation · Driver model · Time lag · Damping · Friction

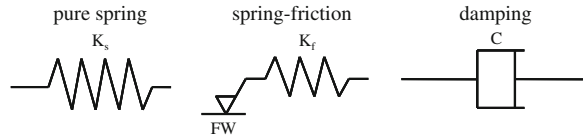
1 Introduction

A steer-by-wire vehicle is getting within our reach. Though the steering reactive torque has a big effect on the handling quality of the vehicle, it is not necessarily defined so far what sort of and how much steering torque should be provided for the SBW vehicle from the handling quality points of view. On the other hand, there has been no generic method other than subjective sensory or feeling test by the drivers to evaluate the handling quality itself. The purpose of this study is to evaluate the steering reactive torque from the handling quality view points using a novel method and contribute to the steering torque design for SBW vehicle.

F2012-G04-006

M. Hibi · T. Kobune · D. Miki · Y. Kano · M. Abe (✉)
Department of Vehicle System Engineering, Kanagawa Institute of Technology,
Atsugi, Japan
e-mail: abe@sd.kanagawa-it.ac.jp

Fig. 1 Steering torque components



A driving simulator with the steering torque generation device is used for the experimental study. The steering reaction torque provided is composed of pure spring, damping and spring-friction components depending on steering angle. Lane change tests of the vehicles with several types of steering reaction torque are carried out. Three driver parameters, gain constant, preview time and time lag in the steering angle control model of the driver are identified using the measured driver-vehicle-system behavior during the lane change. It has been found in the previous study that the identified time lag of the driver strongly related to the handling quality evaluation. The larger the time lag required for the driver, more relaxed behavior in his (or her) maneuvering during the lane change is expected, which corresponds with good handling quality.

It is found that the steering torque effects on handling quality is possible to be evaluated by the identified driver time lag in the driver model during lane change. The results show that spring, damping and spring-friction components are effective for good handling quality of the vehicle and the spring-friction component is essential for good handling quality at high vehicle speed over 100 km/h. Also it is found that there is an optimum value for the maximum friction torque as well as the spring constant in the spring-friction component of the steering reaction torque.

2 Steering Reaction Torque to Steering Angle

The steering torque components provided by the precise torque generating device installed in the driving simulator are spring, damping and spring-friction elements as shown in Fig. 1. The total steering torque is composed of the torques produced by the above three elements and their combinations and 6 types of steering reaction torque to steering angle shown in Fig. 2 are arranged for the evaluation of their effects on vehicle handling quality.

The Fig. 3 shows the driving simulator system for the experimental study with the steering reactive torque producing unit. A driver puts the steering angle to the DPS through the unit and the DSP calculates the reactive torque command and gives it to the unit. The driver can feel the reactive torque depending on the steering angle through the torque producing unit.

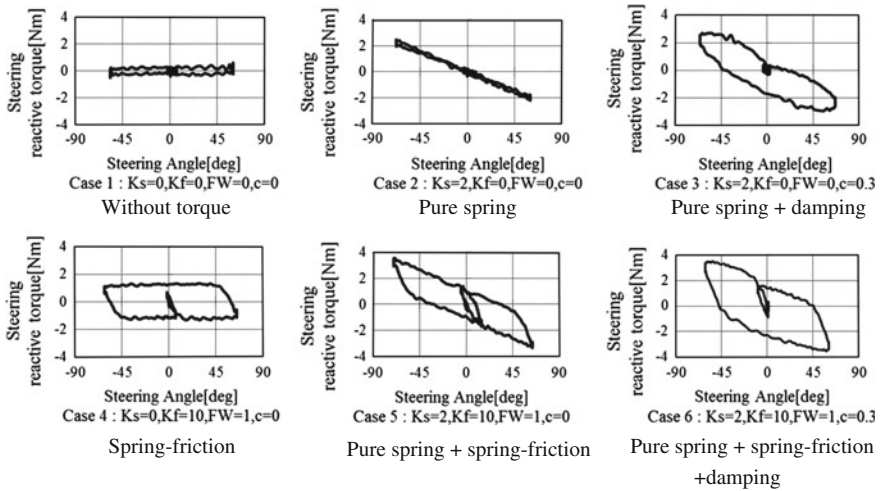
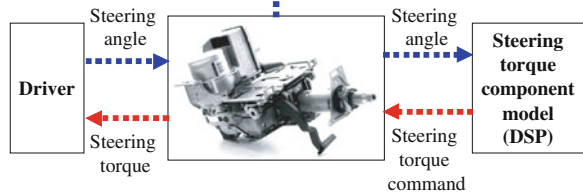
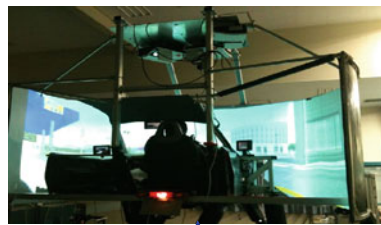


Fig. 2 Six types of steering reactive torque to steering angle

Fig. 3 Driving simulator with steering reactive torque producing device



3 Driver Model Based Evaluation

The existing first order preview driver handling model during lane change with the block diagram is shown in Fig. 4. Here, assuming $dy/dt \approx V\theta$ and $e^{-\tau_L s} \approx 1/(1 + \tau_L s)$, we can describe the steering angle of the driver as follows:

$$\delta(s) = -\frac{h}{1 + \tau_L s} \{ (1 + \tau_h s)y(s) - y_{OL}(s) \} \tag{1}$$

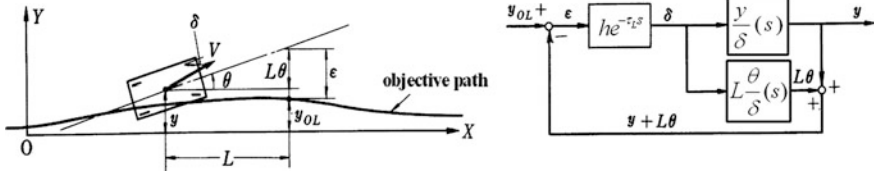
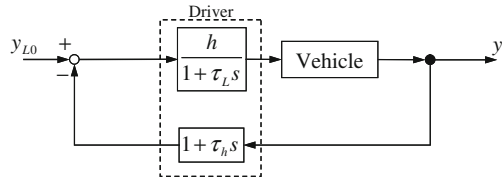


Fig. 4 Driver handling model

Fig. 5 Simplified driver model



We assume that τ_h represents the effects of the looking ahead behaviour (preview behaviour) including more or less the effect of the derivative control action of the driver and if any derivative control action in the driver behaviour is negligible, it is regarded to be just the preview time, L/V . Based on the above, the block diagram of the driver-vehicle model is redrawn as shown in Fig. 5 and the driver steering characteristics become possible to be represented by the three parameters, h , τ_h and τ_L .

The Eq. (1) is rewritten as follows:

$$(1 + \tau_L s)\delta(s) + h\{(1 + \tau_h s)y(s) - y_{OL}(s)\} = 0 \tag{2}$$

In order to find the parameters, h , τ_h and τ_L , which satisfy the Eq. (2) as much as possible to describe the experimentally measured driver behaviour by the above model, the following evaluation function is defined:

$$J = \int_0^T \left[\delta^* + \tau_L \frac{d\delta^*}{dt} + h \left\{ y^* + \tau_h \frac{dy^*}{dt} - y_{OL} \right\} \right]^2 dt \tag{3}$$

where, T is the time period long enough for the driver to finish the lane change. Since a typical behaviour of the driver-vehicle system can be seen in a lane change on a straight road, the experimentally measured time history of the driver steering angle, δ^* , and the lateral displacement of the vehicle, y^* , during the lane change are used for the identification of the parameters. Then, it is possible for us to find the parameters, h , τ_h and τ_L which minimize J by solving the following equations:

$$\frac{\partial J}{\partial h} = 0, \quad \frac{\partial J}{\partial \tau_L} = 0, \quad \frac{\partial J}{\partial (h\tau_h)} = 0 \tag{4}$$

The above equations are the first order linear algebraic equations of h , τ_L and $h\tau_h$ and easy to be solved by h , τ_L and $h\tau_h$, namely by h , τ_L and τ_h . The solved parameters are the identified driver parameters with which the driver steering

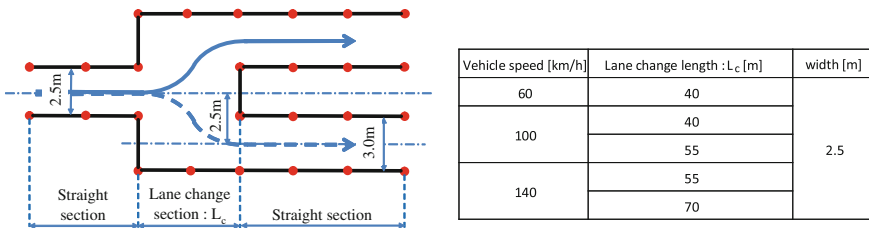


Fig. 6 Lane change test course in driving simulator

angle can be described by the model as close as possible to the real driver steering angle measured.

The driver parameters are expected to reflect the vehicle handling evaluation which depends on the vehicle handling characteristics. As h and τ_L represent responsiveness of the driver, if a vehicle stationary gain is small the driver is required to increase h to compensate for smaller stationary gain. If a vehicle is dynamically responsive, larger τ_L is allowable for the driver to control the vehicle. The larger the time constant, τ_L , is, the more relaxed the driver behaves during his (or her) maneuvering. The derivative time τ_h represents a level of the derivative action to stabilize the less stable vehicle motion or to compensate for the delay of the driver response due to larger τ_L . This is equivalent to preview behaviour of the driver by looking ahead of the vehicle. A larger value of required τ_h means a heavier tension on the driver and causes larger work load to the driver due to stabilizing less stable characteristics of the vehicle or to compensating for larger delay of the driver response characteristics. The previous studies [1–4] have shown that especially τ_L is strongly related to the vehicle handling quality evaluation of the drivers. A large value of τ corresponds to a good handling quality.

4 Effects of Steering Torque on Handling Quality

An experimental investigation is carried out to find how the six types of steering reactive torque mentioned earlier affect on the handling quality of the vehicle. The lane change test course on which the evaluation is conducted with the driving simulator is shown in Fig. 6.

The driver parameters are identified using the measured driver behaviour and the vehicle path during the lane changes. The attentions are focused on the driver’s time lag identified for the evaluation of the handling quality. The averaged relative value of the identified time constant of first order lag of 10 drivers is shown in Fig. 7 for each steering reactive torque. The Fig. 8 shows the average value of the driver’s subjective rating on handling quality together with the distribution of the identified time constant of 10 drivers for each steering reactive torque. The identified time constant τ_L and the subjective rating significantly correlate with

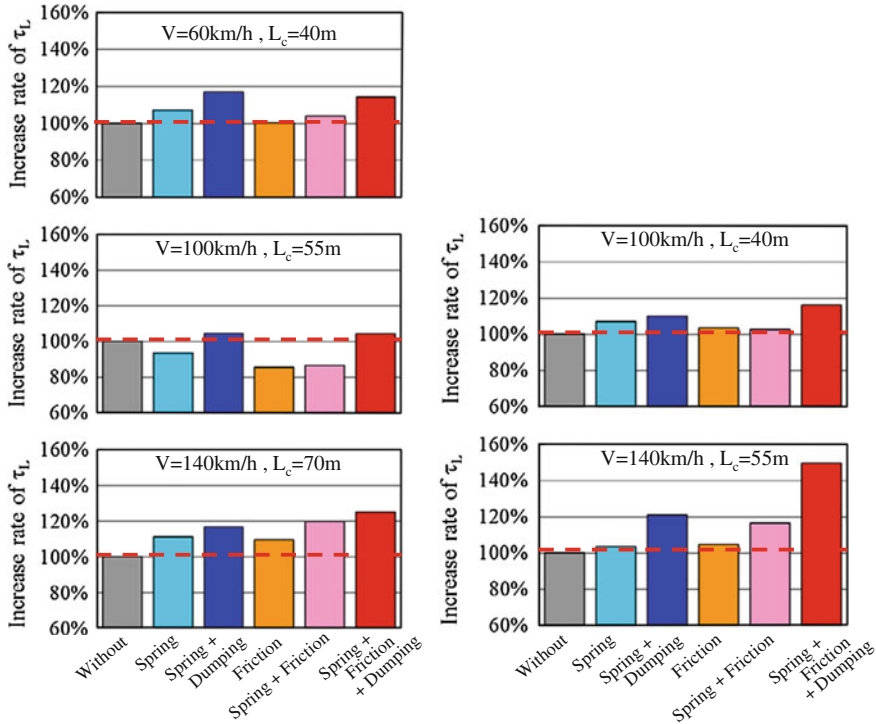


Fig. 7 The averaged relative value of the identified time constant τ_L of 10 drivers

each other and verify that the time constant τ_L reflects the subjective evaluation of the steering torque effects on handling quality. The results show that the steering torques with pure spring + damping and with pure spring + spring-friction + damping have favourable effects on handling quality. The spring-friction component is especially effective on good handling quality at high vehicle speed.

As the spring-friction component is effective, the effects of the spring constant K_f and the maximum friction force F_w in the spring-friction component as shown in Fig. 9 on the handling quality are investigated in a same way as the above at vehicle speed 60 km/h. The relations of steering reactive torque to steering angle for various spring constant and maximum friction torque are shown in Fig. 10.

The effects of the maximum friction force F_w on the averaged values of both time constant τ_L and subjective rating of 10 drivers are shown in Fig. 11. Also the effects of the spring constant of the spring-friction component K_f on the average values are shown in Fig. 12. Again a good correlation between the identified time constant τ_L and the subjective rating is recognized in the figures. From the results obtained, it is found that there are optimum values of both maximum friction torque and spring constant of spring-friction component from the handling quality view point.

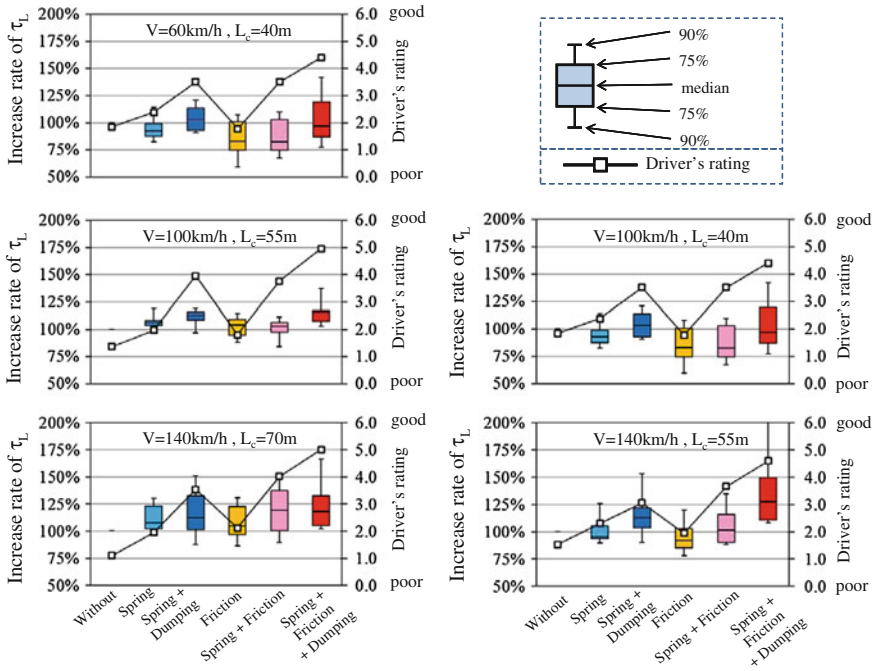
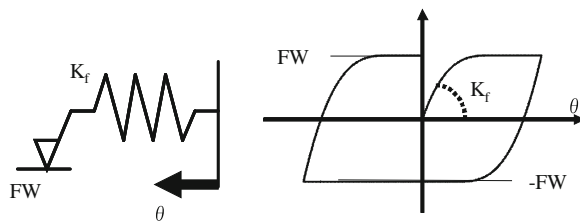


Fig. 8 Average value of subjective rating and the distribution of the time constant of 10 drivers

Fig. 9 Spring constant K_f and maximum friction torque FW



The interesting point in the results obtained in this study is that the steering torque has the effects on the driver steering angle control parameters as if the vehicle response characteristics to steering angle input changes, even though there is no change in the vehicle response to steering angle input itself. Actually it is clear that the steering torque has nothing to do with the open-loop transfer function in the control block diagram of steering angle control driver-vehicle system as shown in Fig. 13. Even so, the drivers change their parameters according to the steering reactive torque as though the vehicle response to steering angle input was changed.

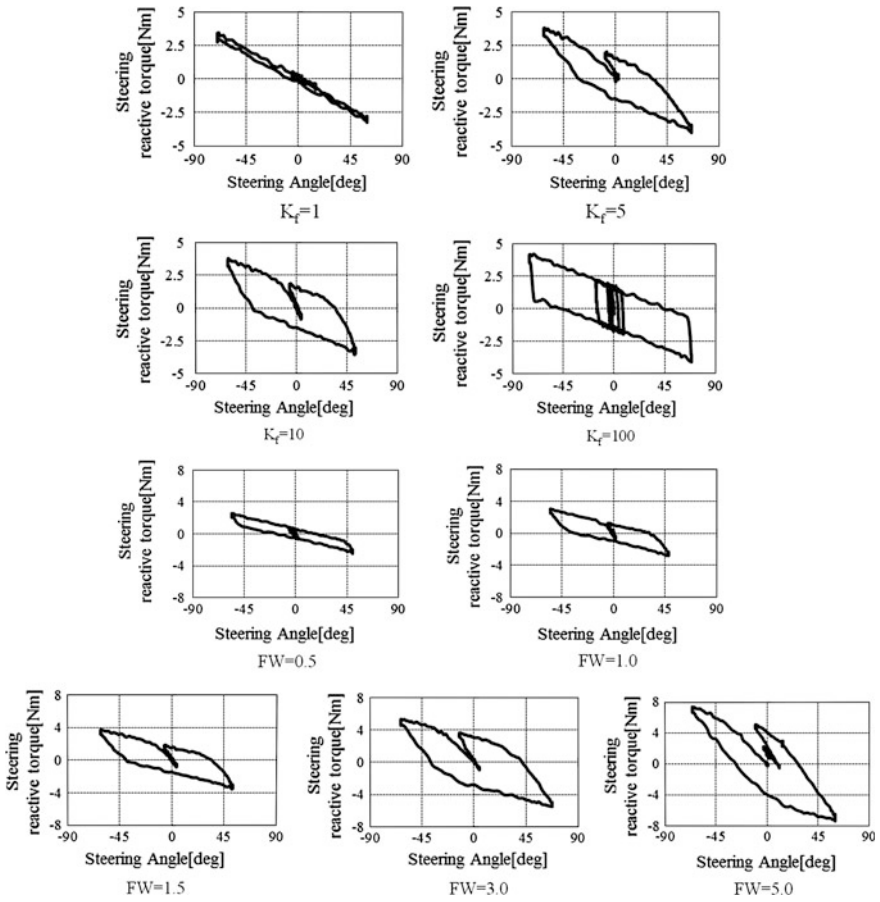


Fig. 10 Steering reactive torque to steering angle for various spring constant and maximum friction

Fig. 11 Effects of the maximum friction force FW on vehicle handling quality

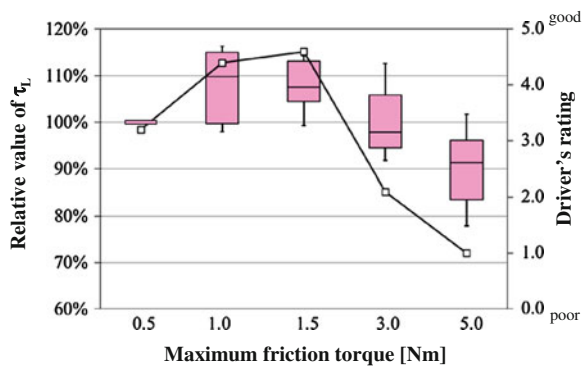


Fig. 12 Effects of spring constant of spring-friction component K_f on vehicle handling quality

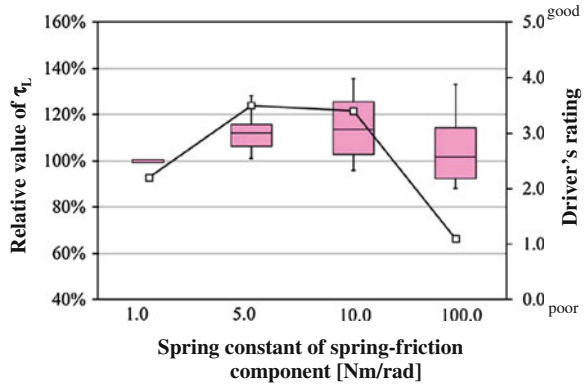
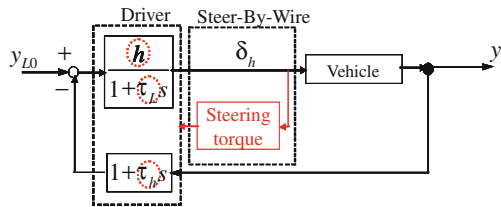


Fig. 13 Driver-vehicle system with driver model of steering angle control



5 Conclusions

The effects of the steering torque components in SBW steering system on handling quality is evaluated by the identified time lag in the steering angle control driver model. The results show that steering torques produced by combination of pure spring and damping and also produced by the combination of pure spring, spring-friction and damping bring us good handling quality evaluation and the spring-friction component is essential in the steering torque especially at high vehicle speed. This may give us a knowledge how the spring-friction component should be provided in the steering torque depending on vehicle speed. The optimum property of the spring-friction component from the handling quality point of view is also investigated.

The knowledge based on the results obtained in this study is valid only for the case of the lane change. The handling quality evaluations in other conditions such as on-centre handling characteristics etc. are needed. Also the validation of the results using the real SBW vehicle is required.

References

1. ISHIO J et al (2007) Vehicle handling quality evaluation through model based driver steering behavior. In: Proceeding of 20th IAVSD symposium, Berkeley, Aug 2007

2. Abe M et al (2009) Investigation of steering torque effects on handling quality evaluation based on steering angle control driver model. In: Proceedings of 21st IAVSD symposium, Aug 2009, in CD
3. Aoki Y et al (2011) Variable stability vehicle with response parameters controlled by active chassis control devices. In: Proceedings of 22nd IAVSD symposium, Aug 2011, in CD
4. Kushiro I (2010) Concept of steering torque hysteresis for better steering feel and steering behavior. In: Proceedings of JSAE annual meeting, 20105092, May 2010

Active Camber Control

Munehisa Horiguchi, Akira Mizuno, Michael Jones
and Kayo Futamura

Abstract Current major trends in the automotive industry include vehicle weight and size reduction, and the use of low rolling resistance tires. Along with these trends, techniques for increasing vehicle stability have become necessary. At Equos Research a rear camber control system has been developed which directly makes use of roll steer to increase vehicle stability. The potential of the system has been investigated for actual vehicles. In this report we present the details of this system and show its potential for improving vehicle stability.

Keywords Vehicle dynamics · Camber control · Stability · Rolls steer · Lever crank mechanism

1 Introduction

Recently, requirements for vehicle fuel economy improvement have become increasingly stringent. Hence it is anticipated that the current trend toward smaller, lighter vehicles and the use of low rolling resistance tires will continue. The tread

F2012-G04-007

M. Horiguchi (✉) · A. Mizuno · M. Jones · K. Futamura
Equos Research Co., Ltd, Tokyo, Japan
e-mail: i20674_horiguchi@aisin-aw.co.jp

A. Mizuno
e-mail: i73066_mizuno@aisin-aw.co.jp

M. Jones
e-mail: i73067_jones@aisin-aw.co.jp

and wheelbase of such small, light vehicles will probably be shorter, and hence their dynamics will be more subject to the effects of lateral wind and road irregularities, for example. In addition, the reduced sidewall stiffness of low rolling resistance tires may potentially lead to degradation in handling characteristics.

Various techniques for vehicle stability improvement, such as four-wheel steering [1, 2] and active suspensions [3, 4] have been presented. However these techniques are implemented not just for stability improvement, but also for improved handling, and tend to be relatively expensive. Hence they are generally intended for high-end vehicles.

Equos Research has developed a system which focuses on improving vehicle stability only, by actively varying the rear wheel camber angle. The system has been implemented using a simple mechanism on actual vehicles. In the present chapter we present a summary of the system mechanism and control concept, and its effect on vehicle stability.

2 System Description

2.1 Active Camber Control Concept

One way to represent the degree of stability of a vehicle is via the stability factor, defined in Eq. (1) [5].

$$A = -\frac{m}{2l^2} \frac{l_f \cdot C_f - l_r \cdot C_r}{C_f \cdot C_r} \quad (1)$$

The function of the Active Camber System is to increase the stability factor by increasing the rear wheel equivalent cornering coefficient C_r . This is accomplished by controlling the (negative) camber angle of the rear wheels, which indirectly results in an increase in the toe angle variation due to vehicle roll (i.e., an increase in roll steer).

In Eq. (2), C_r is represented as a combination of the tire cornering coefficient C_{pr} and the amplifier e_r , using the method described in Murata [6] (based on the analysis in Bundorf [7].)

$$C_r = e_r \times C_{pr} \quad (2)$$

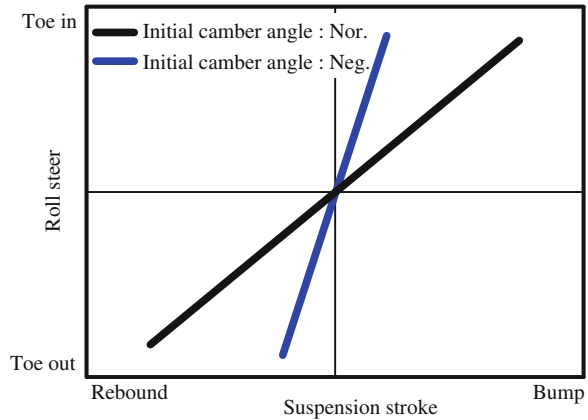
The dependence of e_r on the cornering compliance coefficient $eCCr$ ($eCCr$ encapsulates the effect of suspension) is shown in Eq. (3).

$$e_r = \frac{1}{1 + eCCr \cdot C_{pr}} \quad (3)$$

$eCCr$ is the sum of a number of contributions, as shown in Eq. (4)

$$eCCr = eYr + eGsr + eRr + eRcr + eYcr \quad (4)$$

Fig. 1 Roll steer (image)



The above three equations reveal the way in which increased roll steer (eRr) leads to an increase in the equivalent cornering coefficient. Figure 1 shows in conceptual form the effect of camber setting on roll steer. Increased negative camber results in an increase in the variance of toe angle with roll (suspension stroke), and correspondingly an increase in the roll steer coefficient R_s . (In this chapter, the vehicle normal camber setting is represented as ‘Nor.’, and the increased camber setting as ‘Neg.’).

2.2 Experimental Vehicles

The Active Camber System has been developed and implemented on a number of vehicles. An example of the overall system design is shown in Fig. 2 (in this case the vehicle is a Lexus HS250 h.) A mechanism which provides for two camber settings is added to the rear suspension. The signal received from the wheel speed sensors, steer angle sensor, and the accelerometer, is processed at the camber ECU, and based on the results of the control algorithm the appropriate camber angle is applied.

2.3 Mechanism

An active camber control mechanism was designed which allows for two distinct camber angles. For the Lexus HS250 h, the system was implemented on the body side joint of the trailing arm double wishbone suspension upper arm. A crank shaft, which can be rotated using a motor, was placed in the joint. As illustrated in Fig. 3, rotating the crank shaft (pink) moves the upper arm joint, changing the wheel camber angle. Hence it was possible to implement the system with only a slight modification to the existing suspension.

As shown in the figure, the crank shaft has two dead points. When the crank shaft is at one of the two dead points the system is resistant to rotation, even during

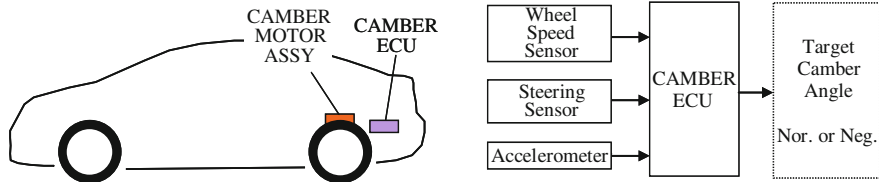
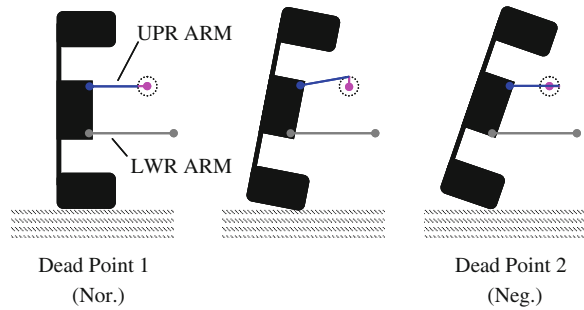


Fig. 2 Experimental vehicle system map

Fig. 3 Self-lock concept



large lateral force inputs from the wheel, so the camber angle setting can be maintained. By this method a self-locking, two-state variable camber system has been realised.

For the present vehicle, when stationary, there is a compression load on the upper arm due to vehicle weight, which leads to a natural tendency toward negative camber. Hence by taking advantage of the vehicle's weight, negative camber can be added when necessary using little power and within a short time. In addition, since camber can be changed by 3° using a crank radius of 5 mm, even during large loads only a small torque is needed to rotate the crank shaft.

The primary benefits of this design are:

1. a separate mechanism for maintaining camber angle is unnecessary;
2. a large gear ratio can be used (since the gear is not used for locking);
3. the motor/gear assembly is situated on the sprung mass, and so is not directly subject to suspension vibrations (improving durability), and does not add to unsprung weight.

Taking advantage of the above features, a small, simple mechanism could be implemented. The individual components of this mechanism are shown in Fig. 4.

From right to left, the DC motor output is increased by the planetary gear (reduction ratio: 49), and transferred to the crank shaft, which replaces the upper arm joint. Camber is actuated by a 180° rotation of the crank shaft. The crank shaft rotation is measured at the position sensor, and this measurement is fed back to allow accurate camber angle control. Using this system a camber actuation time of 0.3 s has been realised.

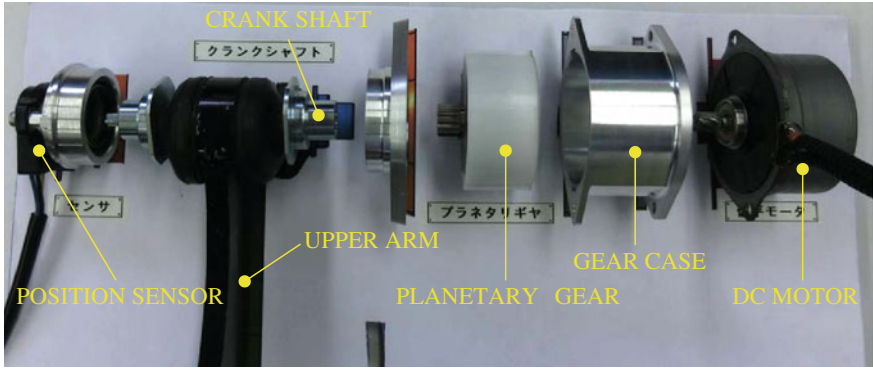
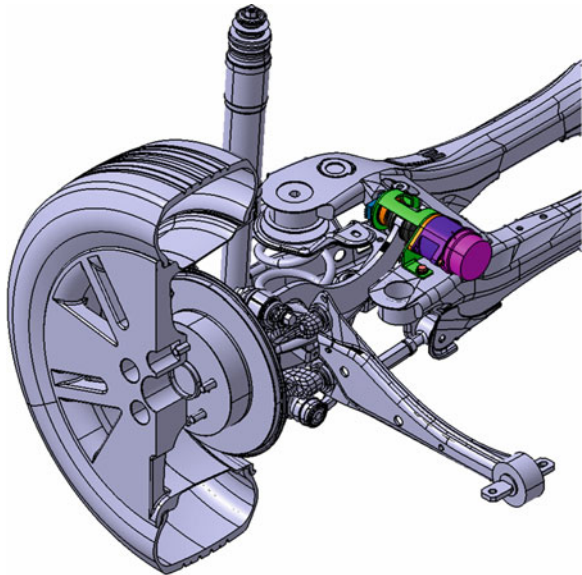


Fig. 4 System components

Fig. 5 Schematic of the installed system assembly



In the schematic in Fig. 5 the separate components of Fig. 4 are shown installed as the completed assembly. The assembly is fixed to the suspension member using bolts.

Photographs of the right rear wheel of the vehicle with the Active Camber System installed are shown in Fig. 6. The wheel is shown at both camber settings.

2.4 Control

The purpose of the active camber system is to increase stability. However, if the camber is maintained at a high setting, this can have negative consequences for

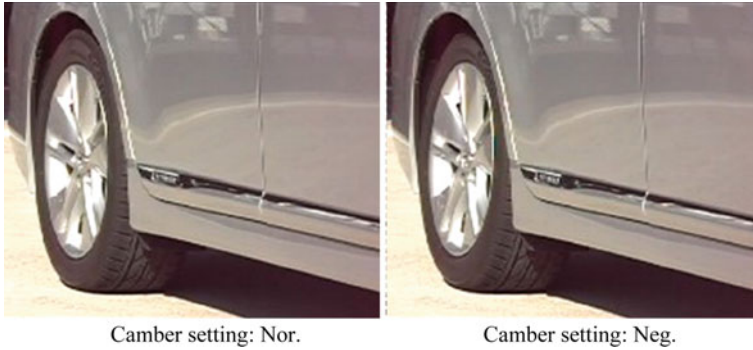
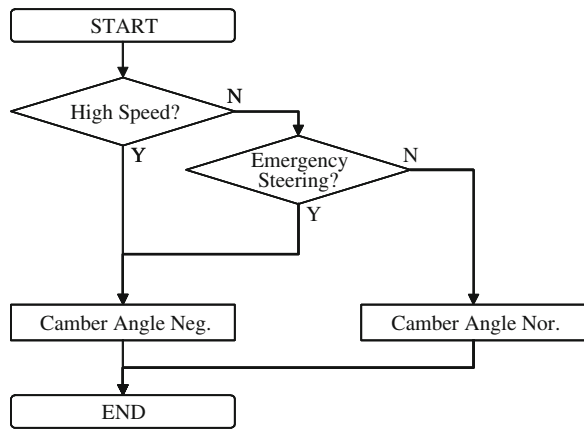


Fig. 6 The right rear wheel at both camber settings

Fig. 7 Camber angle control flow



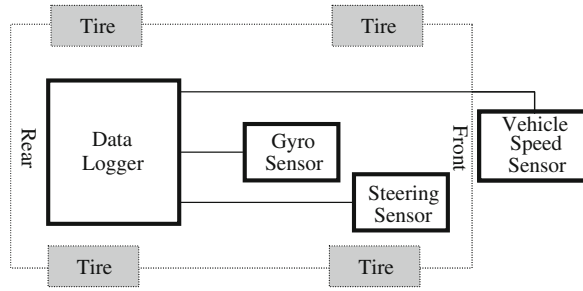
fuel economy and tire wear. Therefore control logic has been developed which adds rear negative camber only when it is required. The control flow is shown in Fig. 7.

Hence additional negative camber is implemented only at high speeds and during emergency steering manoeuvres.

3 Camber Effect on Vehicle Stability

3.1 Experiment Outline

Vehicle experiments were conducted to determine the effect of rear wheel camber on vehicle stability improvement. Two types of experiments were conducted: a pulse steer input response experiment to determine the fundamental vehicle response, and a single lane change experiment to determine the characteristics for

Fig. 8 Instrumentation system

a more realistic driving scenario. In order to compare the effects for different vehicles, in addition to the Lexus HS250 h, a Volkswagen Golf and Lexus RX350 were also included in the testing.

Instrumentation

The instrumentation system is shown in Fig. 8

Vehicle Conditions

Vehicles: Lexus HS250 h, Volkswagen Golf, Lexus RX350.

Crew: Driver and 1 (front seat) passenger.

Camber angles: -1.0 , -4.0° (approximate).

Method

Pulse steer input response experiment (JASO Z110 [8]).

Speed: 100 km/h.

Steer input: 30° of steer applied then returned to zero within 0.3–0.5 s, followed by 3 s of zero steer.

Single lane change experiment

Speed: 80 km/h.

Lane change lateral distance: 5 m (approximately).

Lane change period: 2 s.

3.2 Pulse Steer Input: Results

The results for each of the vehicles are shown as the yaw rate gain response to pulse steer input in the Bode plots in Fig. 9.

The vehicles' primary parameters were also determined, and are shown in Table 1

For all vehicles the trends were the same: stability factor and natural frequency increased, and the phase lag decreased, with negative camber. One undesirable effect is also apparent: the peak ratio increased (i.e., the damping coefficient decreased).

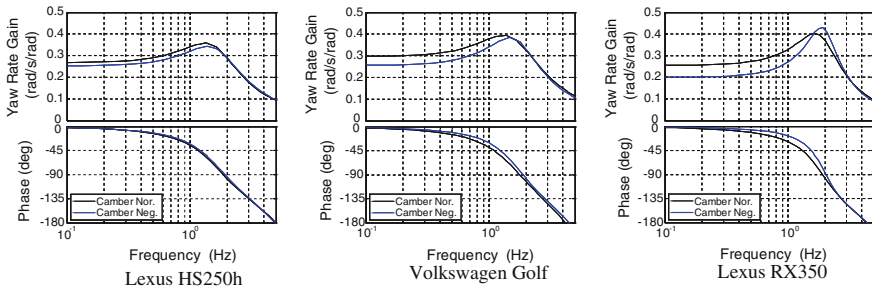


Fig. 9 Vehicle characteristics (yaw rate gain Bode plots)

3.3 Single Lane Change: Results

In the x-y plots of Fig. 10 the vehicle responses are compared. From the plots it can be seen that additional negative camber results in a reduction in the loop size, the yaw rate response lag is reduced, and the steer angle overshoot at the end of the manoeuvre is also reduced.

For reference the driver comments regarding the effects of camber are also summarized below; in particular, the evaluation of high speed stability was favorable.

- At high speed the steering firmness was improved (especially near the steer neutral point).
- At high speed the steering response speed improved.
- At high speed the required steering correction was reduced.
- Roll was reduced.
- Yaw rate gain became milder.

4 Analysis

The amount of roll steer is determined by the roll ratio and bump steer characteristics of the suspension. The roll ratio is independent of camber angle, hence the effect of camber angle on the roll steer characteristics can be seen from its effect on bump steer.

The variation in toe with stroke (bump steer) was determined by experiment, and the results are shown in Fig. 11. With the addition of negative camber the variation in toe with stroke increases, by a factor of approximately 2.3. The increase in roll steer resulting from this additional bump steer is thought to be the cause of the improvement in vehicle stability.

Table 1 Analysis results: primary parameters

	Lexus HS250 h		Volkswagen golf		Lexus RX350	
	Nor.	Neg.	Nor.	Neg.	Nor.	Neg.
Stability factor [s/m ²]	0.00232	0.00255	0.00176	0.00208	0.00180	0.00226
Yaw rate gain [rad/s/rad]	0.268	0.256	0.284	0.255	0.253	0.197
Natural frequency [Hz]	1.32	1.37	1.31	1.48	1.66	1.86
Phase angle [deg]	-35.0	-33.3	-37.9	-30.5	-28.1	-17.0
Peak ratio [-]	1.34	1.37	1.24	1.36	1.49	1.86

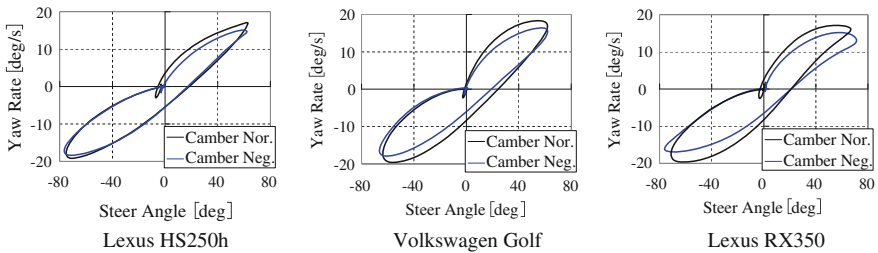
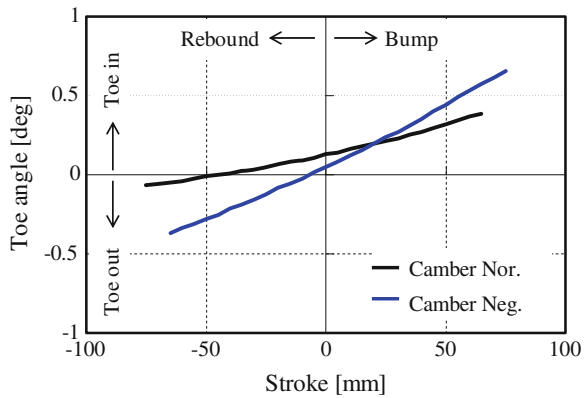


Fig. 10 Vehicle response analysis results (plots of yaw rate vs steer angle)

Fig. 11 Toe angle vs suspension stroke



5 Conclusions

- A system which modifies roll steer characteristics by controlling rear wheel camber has been proposed, and its effect on vehicle stability demonstrated.
- A primary system benefit is its implementation using a simple mechanism.
- The system provides a stability factor increase in excess of 11 %.
- The system has demonstrated stability improvement for various vehicles.

Appendix

Symbol	Definition	Symbol	Definition
A	Stability factor	er	Rear C_p amplifier
m	Vehicle mass	Cpr	Rear tire cornering coefficient
l	Wheelbase	eYr	Lateral steer compliance
lf	Distance from front axle to C.O.G	$eGsr$	Aligning torque compliance
lr	Distance from rear axle to C.O.G	eRr	Roll steer compliance
$C.O.G$	Centre Of Gravity	$eRcr$	Roll camber compliance
Cf	Front equivalent cornering coefficient	$eYcr$	Lateral force camber compliance
Cr	Rear equivalent cornering coefficient	$eCCr$	Rear cornering compliance coefficient

References

1. Yoshiki Yasuno, Takeshi Katayama, Tomoaki Oida (2007) Development of 4 wheel active steering system, JSAE Symposium, 1(7): 30–35 (in Japanese)
2. Yoshimi Furukawa (1986) Improvement of vehicle handling by four wheel steering system, 40(3): 290–296, Automotive Technology, (in Japanese)
3. Bose Suspension System, www.bose.com
4. Unkoo Lee, Sangho Lee, Alexandre Catara (2007) Active Geometry Control System (AGCS) for four wheel steering possibilities on the new hyundai sonata, symposium on international automotive technology, SAE Paper No. 2007-26-062
5. Masato Abe (1992) Vehicle dynamics and control, Sankaido, Tokyo, (in Japanese)
6. Satoshi Murata, Hirofumi Ohtake, Mitsuhiro Hoshino, Satoshi Uchida, Shinichi Fujiwara (2009) Development of vehicle dynamics and suspension for micro FF car, JSAE Autumn Conference, (in Japanese)
7. Bundorf RT, Leffert RL (1976) The cornering compliance concept for description of vehicle directional control properties, SAE Automobile engineering meeting, Dearborn, Michigan
8. JASO Z110 Road vehicles—Lateral transient response test methods: open-loop test (in Japanese)

Research on the Torque Dynamic Distribution Algorithm of In-Wheel-Motor Electric Vehicle

Zhengyi He, Yang Ou and Jingming Yuan

Abstract This paper focuses on developing the torque dynamic distribution algorithm of In-Wheel-Motor electric vehicle. The algorithm is developed to regulate the vehicle body yaw rate by changing the motor drive torque distribution between front wheel and rear wheel. The control aim is to control the vehicle yaw rate approach to the desired yaw rate. The proposed control strategies are evaluated with simulation, and the results show that the proposed method can improve the vehicle stability.

Keywords Four-wheel independent drive · In-wheel motor electric vehicle · Torque distribution algorithm

1 Introduction

Vehicle chassis control of All-Wheel-Drive vehicle has made great progress in the past decades. Bosch ESP [1] and Toyota VDC system help the Four-Wheel-Drive vehicle achieve better handling and stability performance in emergency conditions by using hydraulic braking system. Also some other advanced system such as

F2012-G04-008

Z. He (✉) · Y. Ou · J. Yuan
China Automotive Engineering Research Institute, Pingdu, People's Republic of China
e-mail: hezy05@gmail.com

Y. Ou
e-mail: ouyang@evchina.org

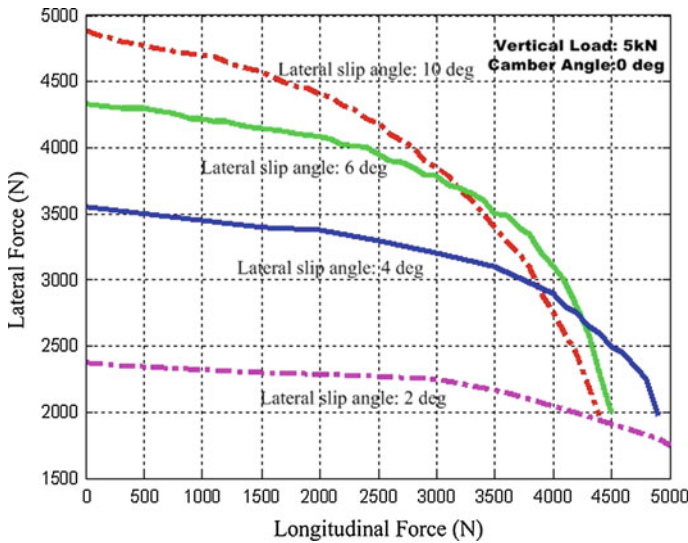


Fig. 1 195/65 R15 tire friction ellipse curve (Toyota)

BMW xdrive [2], Honda SH-AWD [3], Mitsubishi's AYC [4] are developed to improve handling and stability performance and driving fun.

As to the All-wheel independent drive electric vehicle, which uses In-Wheel-Motors, the power train can be used as the subsystem and actuator in chassis control system, which has the potential to realize the active safety function [5, 6].

It is well know that the vehicle have different handling performance with different drivelines, such as front-drive, rear-drive, four-wheel-drive. Consider the fact that the output torque of the four motors can be regulated to any value without requiring any additional hardware, it is naturally to consider to develop the control strategy to change the drive force distribution between the front axle and rear axle, in order to change the understeer/oversteer tendency according to different drive situations.

This paper aims to develop the driving force distribution control strategy for in-wheel-motor electric vehicle, and carry out the simulation to verify the proposed method.

2 Principle of Front/Rear Driving Force Distribution System

It has been known that the lateral force of tire is affected by its longitudinal force, and the relationship can be described by the friction ellipse curve. Figure 1 shows the measured data of 195/65 R15 tires, which is published by Toyota researchers [7].

Here, with the tire data of Toyota, we give the result to show the relationship between distribution coefficient and yaw moment, which can be seen in Fig. 2.

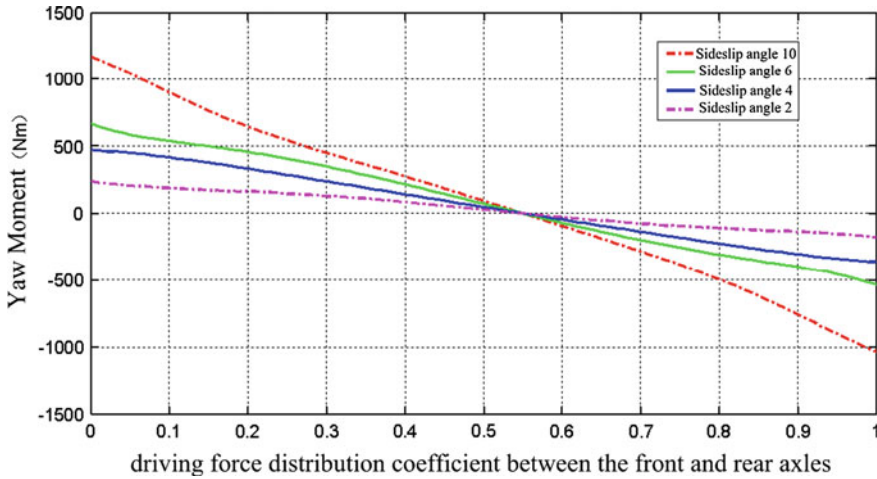


Fig. 2 Distribution coefficient VS. yaw moment

During the calculation process, we have applied the fact that, under normal situation, the vehicle has little under steering, then front and rear tire slip angle can be treated as approximately equal.

According to Fig. 2, we have the following conclusions:

- (1) The yaw moment that acts on the center of gravity of vehicle changes monotonously with the driving force distribution coefficient between the front and rear axles. This feature is the main basis of the distribution control system in this paper.
- (2) From the overall trend, the larger the tire slip angle is, the greater potential yaw moment produces.

3 Driving Torque Dynamic Distribution Algorithm

3.1 The Driving Torque Dynamic Distribution Control System

Similar to the ESP system such as from Bosch, the system calculates the deviation between the actual and desired yaw rate to determine whether the vehicle is in an over steering or an under steering state [8], in which the desired yaw rate uses 2DOF linear vehicle model steady-state response, as shown in Fig. 3.

The working process of the controller goes follows: if the yaw rate deviation is greater than the positive boundary of the dead zone, it indicates that the vehicle tends to be under steering, and then reduces PI output of controller, then reduces the front axle driving force while increasing the rear axle driving force in order to restrain under steering trend; On the other hand, if the yaw rate deviation is smaller

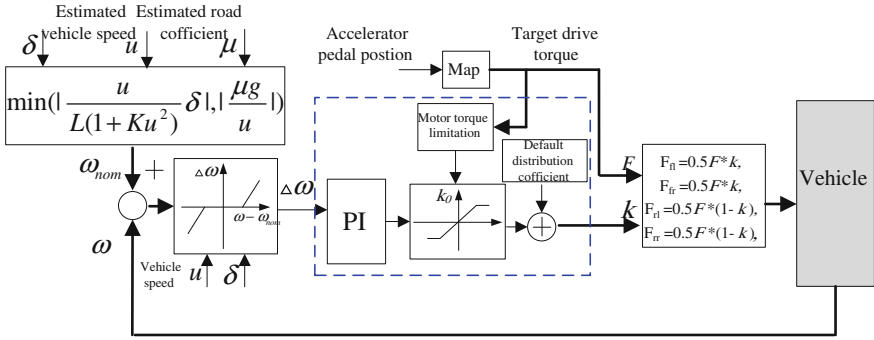


Fig. 3 Controller of front/rear axle driving force distribution

than the negative boundary, it means over steering, and then increases PI output of controller, reduces the rear driving force while increasing the front driving force in order to restrain over steering trend. It is to be noted that the total drive force is only determined by the accelerator pedal, and do not influenced by the PI regulator.

3.2 The Default Distribution Coefficient

In the system of Fig. 3, when the yaw rate deviation remain in the dead zone, the coefficient of front axle driving force and the rear axle driving force is only determined by the default distribution coefficient.

During accelerating and braking, the load transfer between the front and rear axle will determine the ideal I curve, which makes the front and rear tire have the same slip. Ideal I curve under braking situation has been discussed a lot before, and the method to get the ideal brake curve also can be applied in accelerating case.

Without considering the wind resistance, rolling resistance as well as the road grade, the ideal accelerating curve consider the front and rear axle load transfer can be described as:

$$\frac{F_2}{F_1} = \frac{a + zh}{b - zh} \tag{1}$$

Where, h is the height of CG (center of gravity), a is the distance from CG to front axle, b is the distance from CG to rear axle, z is the longitudinal acceleration, F_1 is front axle driving force, F_2 is the rear axle driving force. Then according to (1), F_1 and F_2 can be expressed as:

$$F_1 = \frac{-(2F_2 + \frac{G}{h}a) \pm \sqrt{4\frac{GL}{h}F_2 + (\frac{G}{h}a)^2}}{2} \tag{2}$$

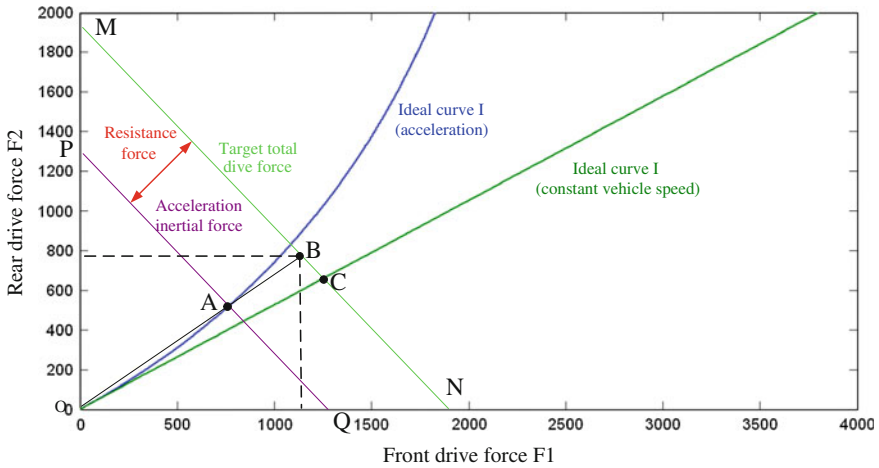


Fig. 4 Ideal drive torque distributions curve

In which L is wheel base, G is the vehicle weight. The ideal curve determined by (2) is shown in Fig. 4, which named as the ideal acceleration curve I.

In fact, the result calculated by (2) should be corrected while considering the wind resistance, rolling resistance. There are two methods to correct Eq. (2). The first method need to estimate longitudinal resistance force, which can be estimated according to the vehicle speed, rolling resistance coefficient, etc. The second method need to employ sensors to measure longitudinal acceleration signal z , and then calculate the ideal distribution according to acceleration load transfer Eq. (1).

As shown in Fig. 4, Line MN represents the target total driving force. The target driving force subtracts the estimated longitudinal resistance equals to the acceleration inertial force, which is PQ. Where PQ cuts acceleration I curve is point A, and the slope of point A is exactly the load transfer expression (1). Afterwards, extending OA intersects the line MN at B, the coordinate of point B is the ideal force distribution under the target driving force. Then the slope of point B is the default distribution coefficient.

When the acceleration is zero, which means the vehicle remains constant speed, then line PQ degrades to the origin O, which means the ideal drive force distribution is determined by the point C, then we have:

$$\frac{F_1}{F_2} = \frac{b}{a}, \tag{3}$$

In this case, the default distribution coefficient is determined by (1).

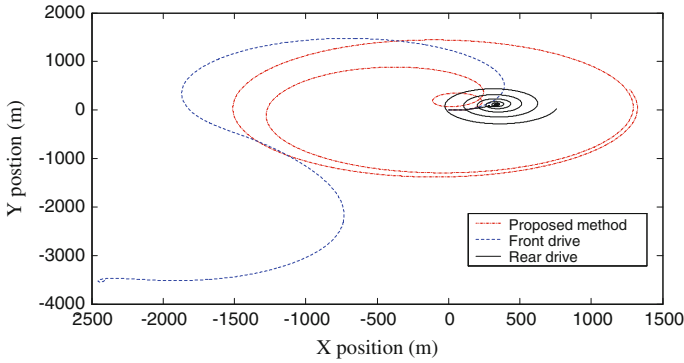


Fig. 6 The vehicle trajectories with steering wheel angle step input. (Torque dynamic distribution, front wheel drive and rear-wheel drive)

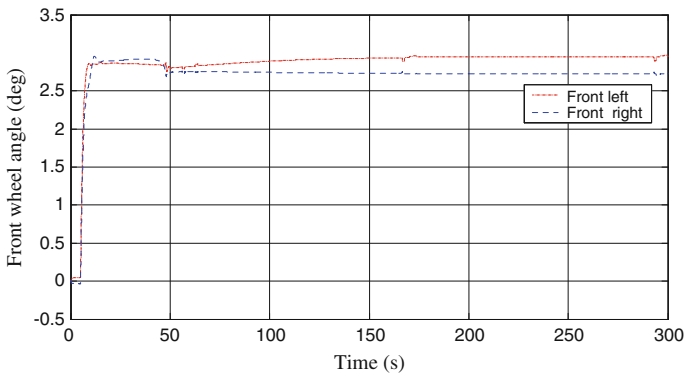


Fig. 5 Front wheel steering angle with step input

4 Control System Simulation

4.1 Control Model

The control algorithm is tested with MATLAB/Simulink. The vehicle sprung mass is set to 1,200 kg, with 185/65R15 tire, while the road coefficient is set to 0.4. The peak torque of single motor is 300 Nm.

4.2 Result Analysis

The following sections show the simulation results in the case of the step input steering angle. The front wheel steering angle is shown in Fig. 5.

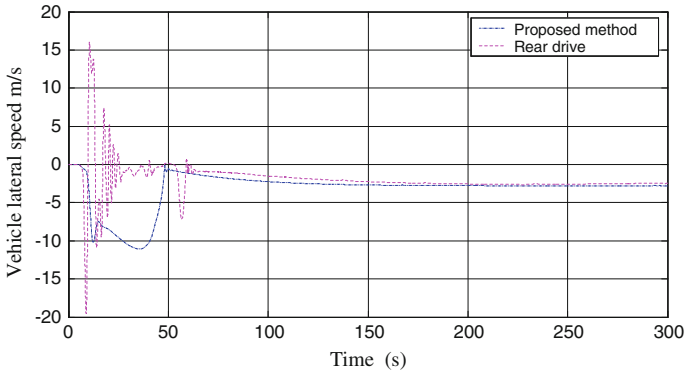


Fig. 7 Lateral speed at center of mass

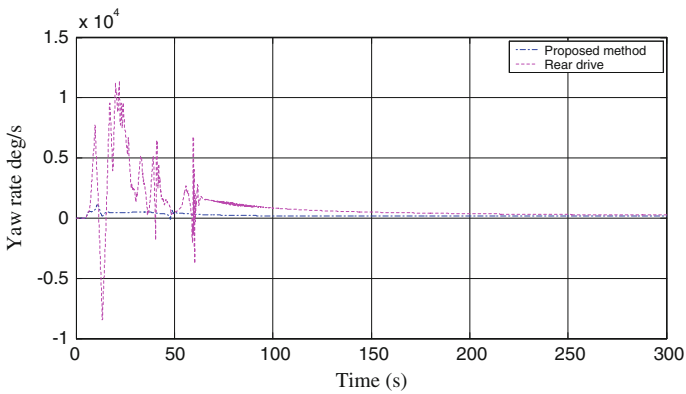


Fig. 8 Yaw rate

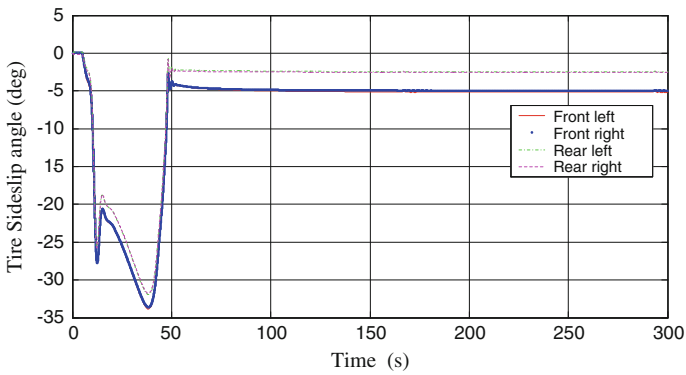


Fig. 9 Tire sideslip angle of four wheels

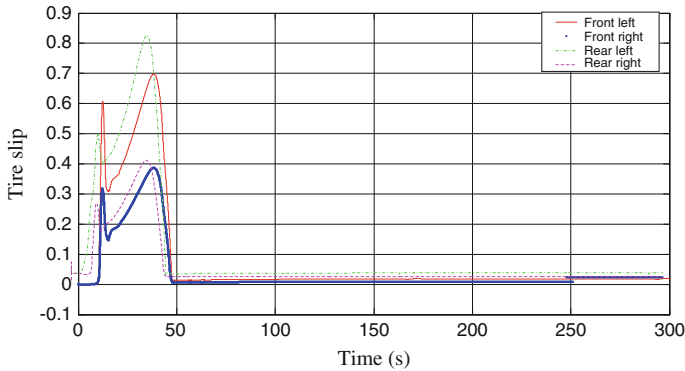


Fig. 10 Tire slip rate of four wheels

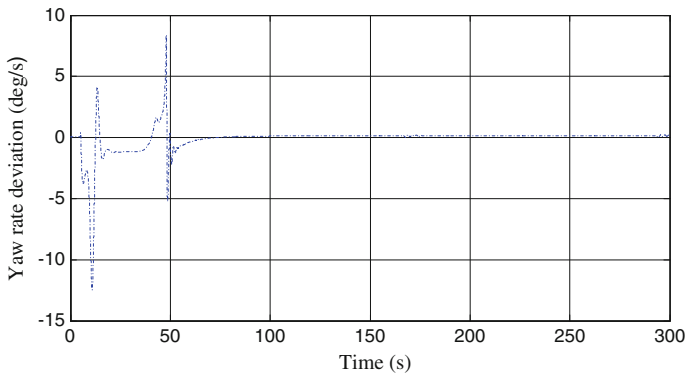


Fig. 11 Yaw rate deviation

With step input of steering angle, the vehicle trajectories of three cases, drive torque applying the dynamic distribution algorithm in this paper, front wheel drive and rear-wheel drive, are shown in Fig. 6. The centers of trajectories are not at the origin is due to the fact that the input steering angle remain zero until 5 s. As can be seen in Fig. 6, it is easier to find that rear-wheel drive vehicle over steers, whereas front wheel drive vehicle under steers and even lose stability.

In Figs. 7 and 8, during 5 to 45 s, the vehicle lateral speed and yaw rate oscillations because the tire sideslip angle is large enough to enter the lateral saturation area, as shown in Figs. 9 and 10.

The dead zone area of the yaw rate deviation (see Fig. 3) in the simulation system is set to be ± 1.2 degree. At the interval from 0 to 5 s, due to the steering wheel angle is zero, the yaw rate has no deviation; then the PI controller output equals to 1, which can be viewed as rear-drive case. After 5 s, front wheel angle starts to input, the yaw deviation becomes negative, the vehicle over steers, so the PI regulator output decreases, transferring driving force to front wheel, finally

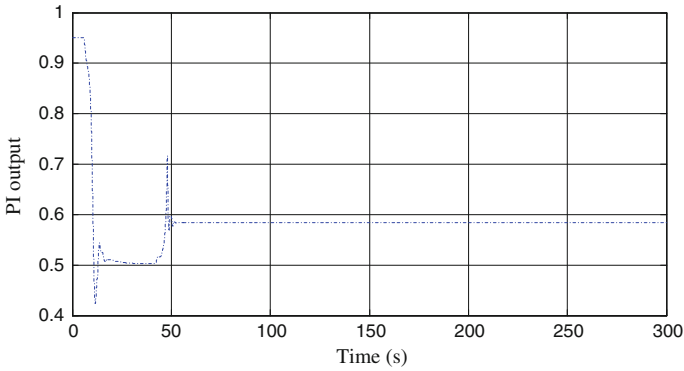


Fig. 12 PI controller output

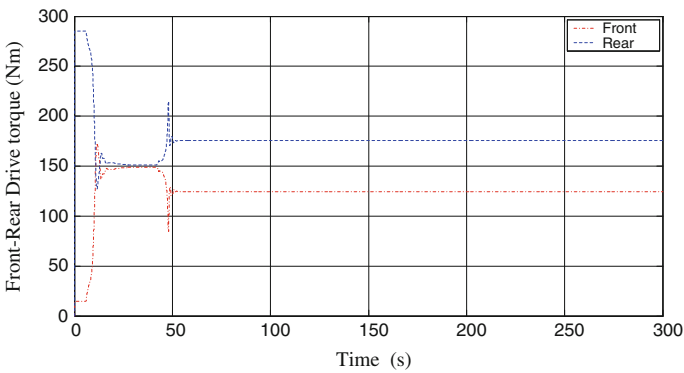


Fig. 13 Driving torque of front and rear axle

stops over steering. At about 40 s, the yaw deviation becomes positive, the vehicle under steers, and PI output increases, transferring driving force to rear axle, restrains under steering.

Figure 11 means, the yaw rate deviation goes into the dead zone after 50 s, then PI controller does not need to regulate the output. This result also indicates that the dead zone will help to prevent long-time oscillation derived from the slow integral drift (Fig. 12).

Figure 13 is the front and rear axle driving torque when applying the algorithm in this paper.

5 Conclusion

In this paper, we develop the torque distribution algorithm for All-wheel drive electric vehicle using in-wheel-motors. The simulation results show that the system can improve vehicle handling and stability. It is noted that the proposed method is an indirect yaw moment control strategy. We have to point that the system in this paper needs to combine TCS (Traction Control System) and DYC (Direct Yaw Moment Control) in order to ensure vehicle remain stable under any driving conditions.

Acknowledgments This work has been supported by National “863” Plan (2011AA11A253) and CSTC (2010AA6039).

References

1. Liebemann EK, Meder K, Schuh J, Nenninger G (2004) Safety and performance enhancement. The Bosch electronic stability control (ESP). SAE Institute, Warrendale 2004-21-0060
2. Fischer G, Pfau W, Braun HS, Billig C (2004) xDrive: the new four-wheel drive concept in the BMW X3 and BMW X5. ATZ Worldwide 106:92-103
3. Atsumi Y (2005) Development of SH-AWD (super handling-all wheel drive) system, presented at the Veh. Dyn. EXPO, Stuttgart
4. Ushiroda Y, Sawase K, Takahashi N, Suzuki K, Manabe K (2003) Development of super AYC. Tech Rev 15:73-76
5. Loos S, Eckstein L (2011) Vehicle dynamics control for electric vehicles with single wheel drive. 20th aachen colloquium automobile and engine technology
6. Schwarz R, Meissner T (2011) Quattro with electrical torque distribution Michael wein. 20th aachen colloquium automobile and engine technology
7. Takahashi T (2003) Modeling, analysis and control methods for improving vehicle dynamic behavior (overview). R&D Rev Toyota CRDL 38(4)
8. Piyabongkarn D, Lew JY, Rajamani R, et al (2007) On the use of torque-biasing systems for electronic stability control:limitations and possibilities. IEEE Trans control syst technol 15(3) may 2007

Electric Power Steering Systems: Market Requirements and Application Range with Special Focus on Column-EPS

Eberhard Kuebler, Mathias Eickhoff and Martin Budaker

Abstract The global trend of power steering systems for passenger cars, SUVs, pickup trucks and even light commercial vehicles clearly shows the replacement of hydraulic power steering systems (HPS) by electric power steering systems (EPS). In the mature vehicle markets Japan, Europe and NAFTA this development has already started about 15 years ago and is now more or less finalized for the whole range of passenger cars. The emerging markets in Asia/Pacific, South America and Russia are following with a delay of several years but increasing speed. In these markets the demand for cost efficient solutions is one of the main drivers for the technology decision of the OEMs. Column drive EPS (EPSc) is very often the technology of choice to cover this requirement.

Keywords Electric power steering · Column- EPS · Performance range · Durability · Cost efficiency

1 Introduction

The development of electric power steering systems has started already about 20 years ago. In the beginning it was mainly targeting to reduce the drivers steering effort in parking condition for micro and small vehicles which had been

F2012-G04-012

E. Kuebler (✉) · M. Eickhoff · M. Budaker
ZF Lenksysteme GmbH, chwäbisch Gmünd, Germany
e-mail: Eberhard.Kuebler@ZF-Lenksysteme.com

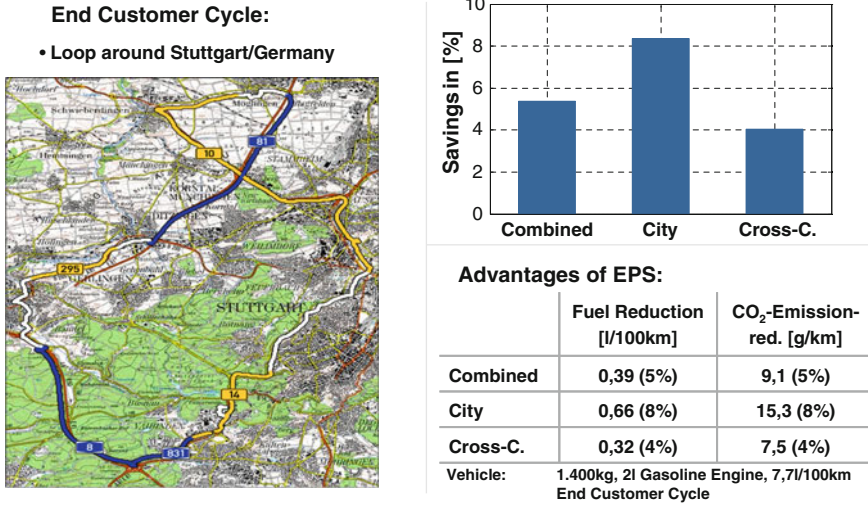


Fig. 1 Reduced fuel consumption by EPS application compared to HPS

equipped with manual steering before. The main technology at that time was already the integration of an electric support motor to the steering column. The requirements in regards of steering performance, steering feel, on-center precision, steering stiffness etc. have been quite low for this kind of vehicles. For the well performing premium vehicles of the medium upper and luxury class HPS was still the standard technology.

With the rising public discussion about fuel consumption caused by individual traffic, governmental rules on CO₂ emissions coming up and the increasing efforts of all international car manufacturers to improve the fuel efficiency of their fleet, EPS technology moved into the focus of the vehicle engineers. With the potential to reduce fuel consumption significantly by replacing the hydraulic steering pump, EPS started to replace HPS step by step (Fig. 1).

In the meantime nearly all newly launched passenger cars and SUVs in the western hemisphere and in Japan are equipped with EPS. For most applications in the medium, upper and luxury class different versions of rack drive EPS will be applied. Column EPS for long time has been used only in small cars for different reasons. In the meantime, also with the growing demand for cost efficient EPS solutions, the application of EPS_c is extended also to larger vehicles, even SUVs. Marketing studies show that EPS_c will cover about 50 % of the global EPS market for passenger cars and SUVs in the future (Fig. 2). Especially in the rapidly growing markets of China and Asia/Pacific a wide range of applications can be predicted.

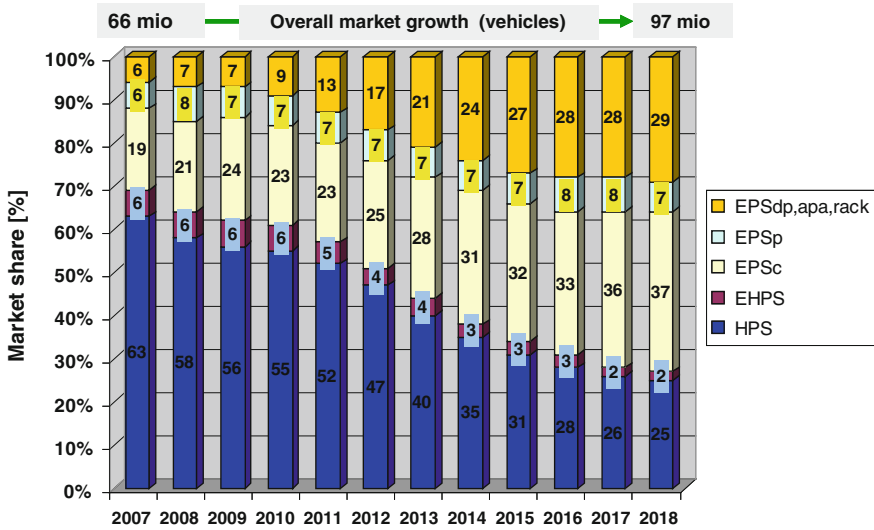


Fig. 2 Market development of steering technologies (ZFLS internal market study)

2 Engineering Objective

Within this paper the application range of the different EPS technologies as well as their advantages and limitations shall be discussed. Special focus will be on the growing range of EPSc and the components which need to be improved to meet the requirements of steering performance, steering feel and durability. The customer demand for comfort and safety features even in emerging markets and thus also for low cost vehicles has grown significantly in recent years. Development of adequate and cost efficient design, layout and performance of EPSc with high quality and life cycle durability will be the most important tasks of steering system suppliers.

3 Technical Approach

To cover the requirements of different vehicles in the range between small passenger cars and light commercial vehicles it is important to develop the specification of the steering system in a close cooperation with the customer. ZF Lenksysteme (ZFLS) offers different EPS technologies for the respective performance requirements (Fig. 3). In general three different systems are available (Fig. 4).

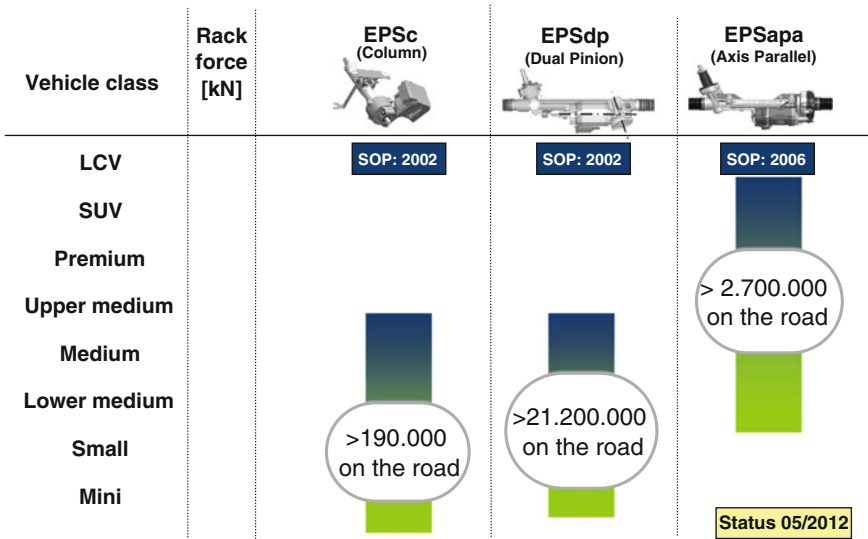


Fig. 3 Application range of EPS technologies

ZFLS covers all application requirements with :

- EPS Column (EPSc)
- EPS Dual Pinion (EPSdp)
- EPS Axis Parallel Assist (EPSapa)

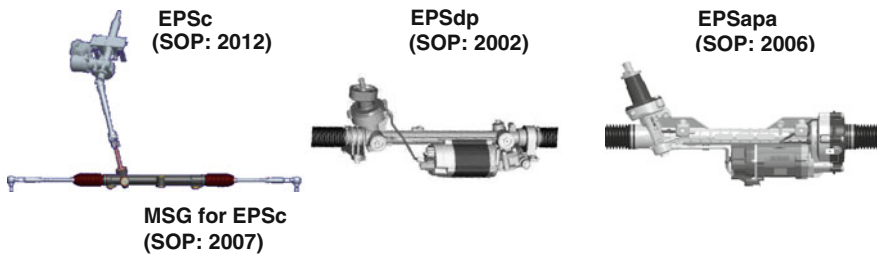


Fig. 4 EPS technology comparison

- In the column-EPS (EPSc) the power support is integrated into the steering column and the assist torque will be transferred via the steering column and intermediate shaft to the mechanical steering gear.
- In the dual pinion system (EPSdp) the input of the support torque is realised via a worm gear working on a second pinion which is attached to the steering gear.
- The highest output performance for luxury cars and even light commercial vehicles can be applied with the rack drive system (EPSapa) where the support torque is transferred to the rack via a belt drive and a ball and nut gear.

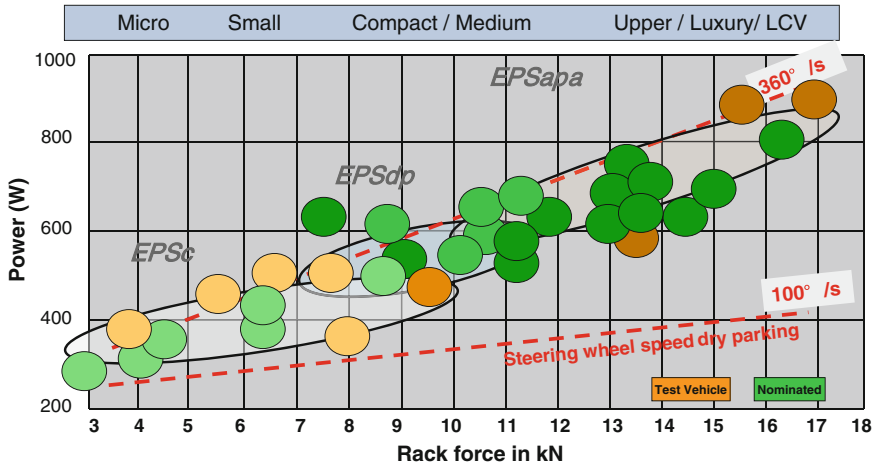


Fig. 5 Performance requirements to EPS systems in different customer specifications

In order to develop the best solution for the customer, the important parameters which influence the performance and thus also the cost, need to be optimized.

The support torque as the parameter of the steering system design, that has the highest impact on cost, is a result of the customer specification which requires the steering performance based on the vehicle data. Main influence on the performance requirements is given by:

- Rack force of the vehicle (F)
- Steering gear ratio (C)
- Steering speed requirement (ω)

Based on these data the steering system performance will be calculated as $P = F \times C \times \omega \times \eta$. The efficiency (η) can only be influenced within a relatively small range. EPSc will be applied in a performance range up to about 800 W. For higher requirements a technology switch to EPSdp or EPSapa would be recommended. Both systems can offer higher steering performance, but the system cost normally will exceed the EPSc cost.

4 Special Requirements for EPS Column Components

With the broadening of the application range of EPSc not only in terms of performance but also in terms of the target cost expectations most of the key components (mechanical and electric/electronic) need to be adapted to these requirements. Small and low cost vehicles at the lower end of applications and small SUVs or mid size sedans on the upper end require a modular design for the

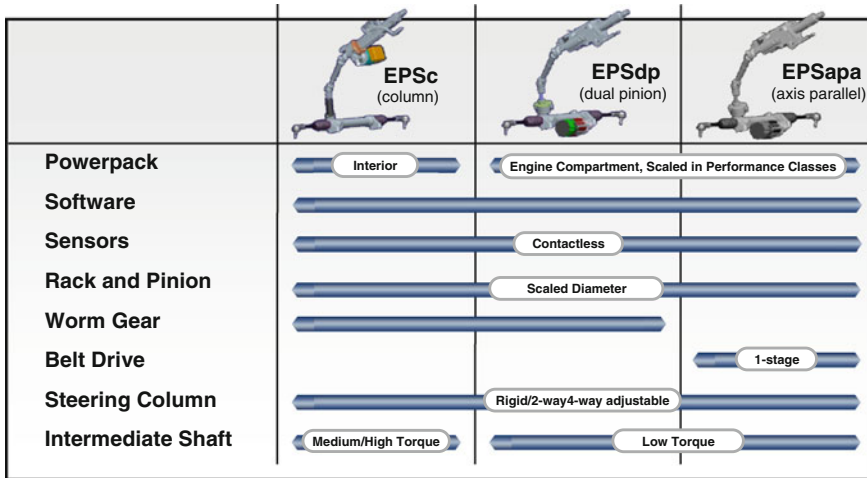


Fig. 6 Common parts in different EPS technologies

main components of EPSc which can be used in a flexible way for customer applications (Fig. 5).

4.1 Motor and ECU

For EPSc applications brushed motors have been used for many years as a standard technology. With the increasing requirements for performance and lifecycle durability brushless direct current motors (BLDC), also known as permanent synchronous motors (PSM) are more and more used also for EPSc. The lifecycle durability of BLDC motors is superior due to no brush wear. Also the application in vehicles with rack loads above 8–9 kN requires high performing BLDC motors. With this background, ZFLS has taken a basic decision to only use BLDC motors for all EPS applications.

Core element of the EPS technology of ZFLS is a modular approach for the key components like motor, ECU, software functions and also mechanical components like the worm gear. With this approach the component maturity for different applications can be increased significantly, application cost and time can be reduced, the overall product quality will be improved as well (Figs. 6 and 7).

The ECU has two main functions, the processing of signals and data and the power output stage. The microcontroller and the most important components like ASICs have been developed in close cooperation between ZFLS, the ECU-supplier and the suppliers for the components (Figs. 8 and 9). The microcontroller is scalable in its size and capacity; this means it can be adapted to the functional requirements of the customers.

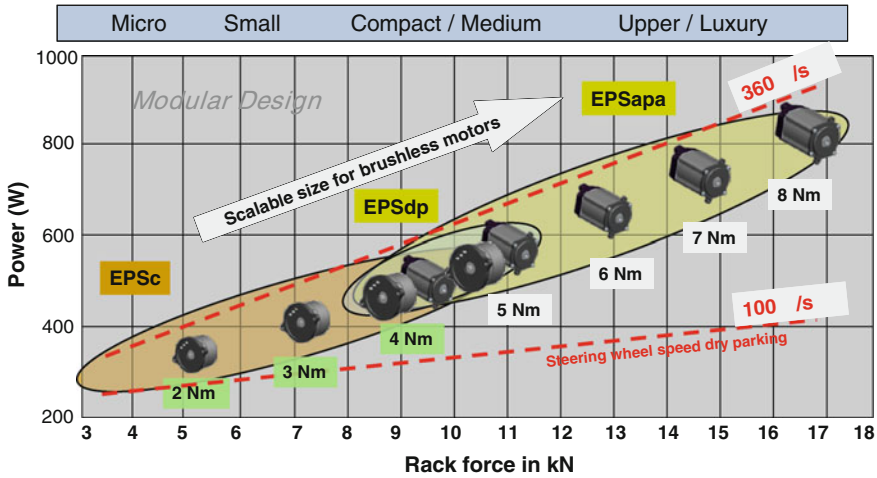


Fig. 7 Modular design of brushless EPS motors for different performance requirements

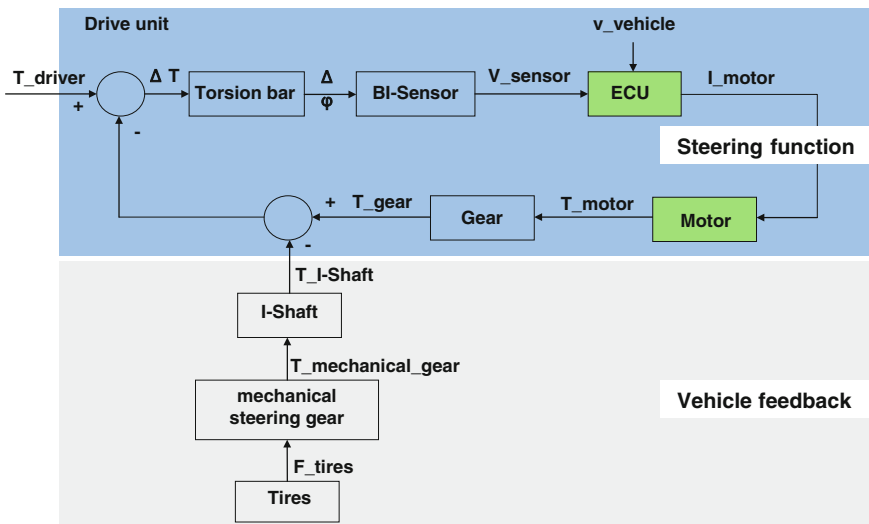


Fig. 8 Basic control loop of EPS

The main influence on the size of the microcontroller is given by the number of steering functions, their complexity and size. Also the hardware and software safety concept needs to be considered for the selection of the controller size.

The PCB layout is designed internally by ZFLS to meet all requirements of functions, EMC and also the safety requirements of IEC 61508, ISO 26262 and Automotive Spice (Fig. 10). In parallel to the logic part of the ECU also the power output stage can be adapted to the system performance requirements in order to generate a cost optimized system.

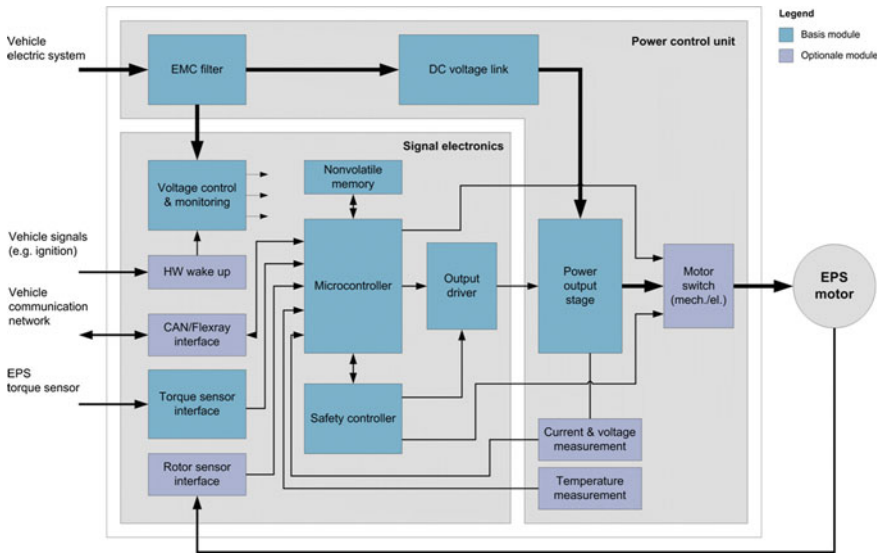
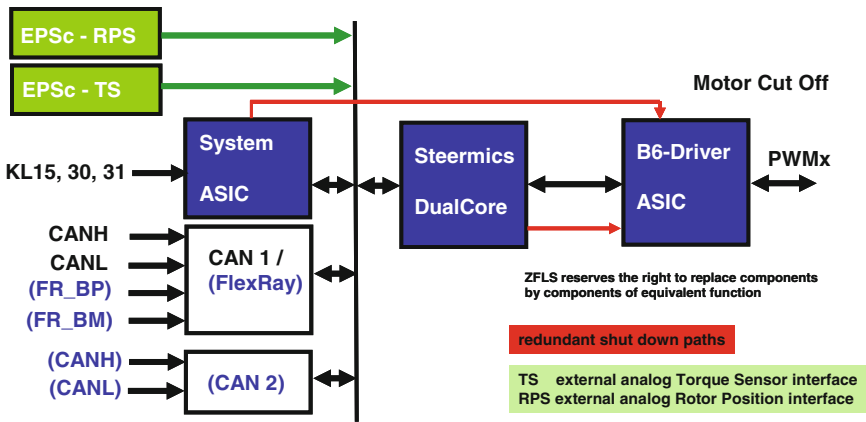


Fig. 9 Basic layout of ECU [1]



Options: FlexRay and CAN 2 for Steermics 2 and 3

Fig. 10 Structure of ECU and hardware communication and safety layout

4.2 Software Steering Functions

ZFLS has developed a set of standard steering functions which can be chosen by the customer (Fig. 11).

Based on the continuous and exact calculation of the actual steering angle a very precise speed sensitive steering support, which can be tuned exactly to the vehicle, can be realized. The steering angle signal can also be used as source for

Speed dependent steering assistance	Steering support in dependence of steering torque and vehicle speed
Active return function	Active return of the steering system to the vehicles center line position
Active damping function	Stabilization of uncontrolled vehicle movement
Friction compensation	Compensation of mechanical friction to improve steering comfort
Active end stop	Protection of mechanical components and increase of comfort by gradually slowing down the rack bar movement
Shudder detection	Reduction of uncomfortable road feedback on rough roads
Integrated steering angle sensor	Calculation of a steering angle signal from rotor position sensor signal and wheel speeds
Overheat protection	Reduction of motor support in dependence of measured ambient temperature
Over voltage protection	Reduction of motor support in dependency of battery voltage level
Network management	Control of CAN communication in a master slave network topology
Diagnostics	UDS (Unified Diagnostic Standard)

Fig. 11 Standard software functions in EPSc

vehicle dynamics management e.g. for functions like ESP. In addition to the standard functions advanced functions like the interface for semi-automatic parking or lane keeping systems can be provided.

On the other hand for low cost applications the functionality can also be reduced to a simple steering support comparable to standard HPS systems. The size of the microcontroller and also its cost can be minimised in that way.

4.3 Mechanical Components

In the wheel-to-wheel EPSc-System the main components are the steering column, the drive unit which includes motor, ECU, steering torque sensor and rotor position sensor and also the reduction gear (worm gear), the intermediate shaft (i-shaft) and the mechanical steering gear (Fig. 12).

The steering column of EPSc has to meet all requirements of a normal steering column. Most important are the adjustability as a comfort function and the crash energy management as a safety feature (Fig. 13). In addition to that the noise and vibration properties are more and more important and need to be tuned in combination with the drive unit.

The adjustability and also crash requirements to the steering column can be varied and have also significant cost influence. The column can be rigid (no adjustability) or be equipped with 2-way or 4-way adjustability. The crash travel and the respective loads (breakaway and travel load) can be adapted to the vehicle and tuned in a wide range.

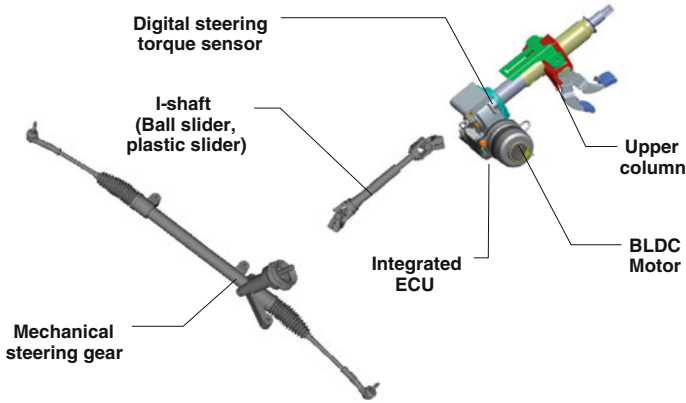


Fig. 12 EPSc main components wheel-to-wheel

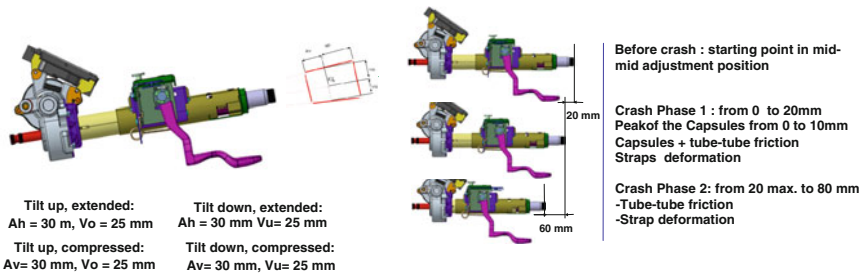


Fig. 13 Steering column requirements of EPSc (adjustability and crash energy management)

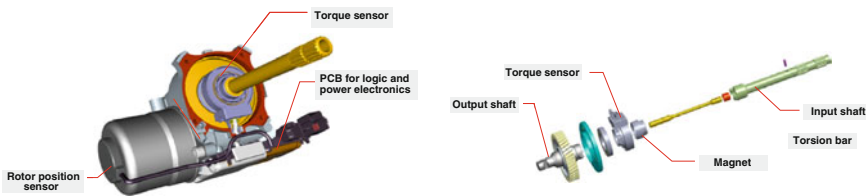


Fig. 14 Drive unit (left) and sensor unit (right) of EPSc

The drive unit contains the electronic components as explained above and also the sensor unit and the reduction gear which transfers the support torque of the motor to the steering column (Fig. 14).

The intermediate shaft has to be specially adapted to the torque which has to be transferred from the drive unit to the mechanical steering gear. Also stiffness requirements for excellent steering feel are more and more important. ZFLS has also for this component a modular kit which can meet customer requirements at different cost levels. More or less all single components have to be considered,

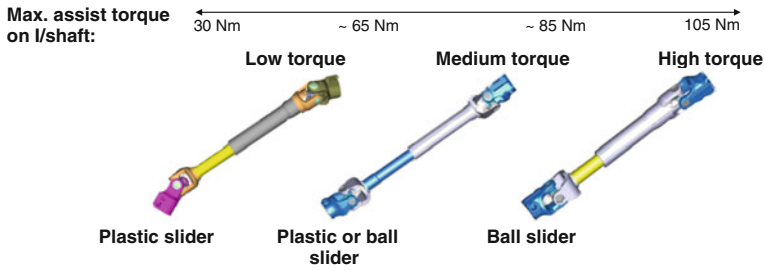


Fig. 15 Modular design of intermediate shafts for EPS

		← Low-end → High-end →			
Mechanical Steering Gear	Gear ratio	Constant			
	Rack bar diameter [mm]	22	24	26	28
Mechanical Steering Gear	Tie rod ends	Straight		Curved	
	Yoke design	With coil spring (Standard)		With additional damping	
	Gear mount	Rigid		Elastic (rubber mounts)	
	End stops	Mech. hard stops		Mech. soft stops	

Fig. 16 Modular components of the mechanical steering gear

especially bearings, yokes and the slider technology. For medium torque applications plastic slider and also ball slider can be used, for high torque applications only the ball slider technology is recommended, which can transfer torques up to 105 Nm (Fig. 15).

The mechanical steering gear must transfer the rotational movement of the steering column to a lateral movement of the rack bar (Fig. 16). Also for the main components of the mechanical steering gear the high input torque requirements need to be considered and the rack, pinion and also the bearings need to be designed to the summarized loads of the whole life cycle.

4.4 System Integration

The mechanical and electrical integration of the systems modular components needs to follow the customer requirements mainly. The main targets on the system level are cost efficiency and also compact design due to the packaging space which is normally very squeezed especially in the cockpit area. The ZFLS approach is

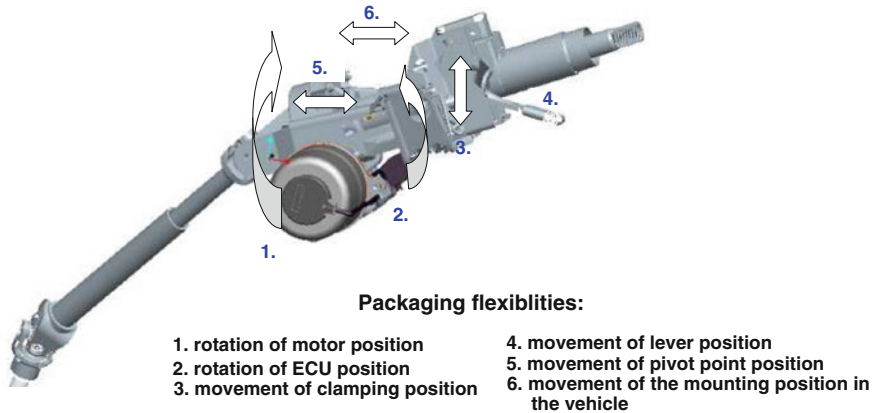


Fig. 17 Packaging flexibility of the ZFLS modular design

especially targeting these requirements by a high degree of component integration and packaging flexibility (Fig. 17). The direct integration of the ECU to the motor and the housing of the reduction gear reduces the number of components, packaging space and cost. The packaging flexibility allows a quite easy modification of the packaging without significant and costly modifications of the components themselves.

5 Conclusion

For many vehicle applications, column EPS (EPSc) would be the most cost efficient power steering system. Given by the technical concept (transfer of the support torque via the steering column and i-shaft) the economical application range of this technology will be limited at a certain performance.

The solutions for customer applications will be developed based on modular components for motor, ECU and the main mechanical components of the EPS system. Especially for cost efficient solutions in emerging markets, the performance optimisation of the steering system offers potentials to reduce the application cost.

The cost efficiency of EPSc steering technology application in a wide range of vehicles depends on a close interaction of the performance requirements on one hand and the application of a modular design of the main components of EPSc systems on the other hand. Electric power steering systems and especially EPSc offer a cost efficient solution to equip passenger cars and light commercial vehicles with comfortable steering systems. Their application can reduce the fuel consumption significantly compared to vehicles which are equipped with HPS. The

growing demands in emerging markets can be covered; however, the best results will be achieved by a close cooperation of the steering gear supplier and the vehicle manufacturer.

Reference

1. Lenkungshandbuch, Vieweg Teubner Verlag, 1. Auflage 2011, Herausgeber Harrer/Pfeffer, ISBN 978-3-8348-0751-9

Part V
Subjective and Objective Evaluation
on Dynamic Performance

Vehicle Ease of Control Evaluation via Stochastic Driver Model

Yan Bai, Hsin Guan and Yuchen Chen

Abstract Due to randomness of driver's control and various driving habits, the optimal performance of the driver-car closed-loop system is not always guaranteed in reality. Since the main aim of the car manufacture is to release new product that could be accepted by more customs, driving dynamics concerning handling always receives particular attention, if the influence of driver uncertainty input on the closed-loop performance was considered during vehicle design stage, it will be benefit to the modern automotive design and this is one of the cutting-edge trends. This paper focuses on the need for research on simulation method of ease of control to forecast the ability of vehicle to adapt to driving population at the early stages of vehicle design.

Keywords Ease of control · Driver model · Monte-carlo · Driver-car closed-loop system

F2012-G05-003

Y. Bai (✉)

Chang'an University, Xi'an, China
e-mail: baiyanjilin@gmail.com

H. Guan · Y. Chen

National Automobile Dynamics Simulation Lab, Jilin University, Changchun, China
e-mail: Guan.Hsin@ascl.jlu.edu.cn

1 Introduction

Due to randomness of driver's control and various driving habits, the optimal performance of the driver-car closed-loop system is not always guaranteed in reality. Since the main aim of the car manufacture is to release new product that could be accepted by more customs, driving dynamics concerning handling always receives particular attention, if the influence of driver uncertainty input on the closed-loop performance was considered during vehicle design stage, it will be benefit to the modern automotive design and this is one of the cutting-edge trends. This paper focuses on the need for research on simulation method of ease of control to forecast the ability of vehicle to adapt to driving population in design stage.

In 1968, Chiesa [1] carried on research to vehicle dynamics characteristics by changing steering input model, producing emergency driving condition and normal driving condition. Although driver model was not involved, it revealed that driver characters could influence closed loop performance. With intelligent assistance system and activity safety system being introduced extensively in modern automobile, research on performance evaluation via driver-vehicle closed loop to optimize design has received particularly attention, since during driving, drivers and systems interact with each other [2, 3].

According to the difference of emphasis and assumption, closed loop performance analysis methods could be divided into three categories [4]. The first category includes analysis methods of optimal closed loop performance. The second emphasizes on physiological perception features or modeling parameters [5]. The last one refers to evaluation criterion in terms of driving burden. The first one researches closed loop performance based on cybernetics, claiming that the optimal driver characteristics parameters can be approached through adjusting personal parameters artificially. By referring to cost function, usually is optimal weighted sum of square, driver model parameters of the optimal closed loop performance can be determined. Then the closed loop performance can be evaluated in terms of the optimal driver. According to whether or not the driver model is constructed based on optimal control theory and whether or not the driver model includes a cost function, such kind of evaluation problem can be divided into two types. One is using classic controller driver model with combination of cost function to look for optimal closed loop performance [6–14]. Another one is using driver characteristics parameters as evaluation indexes, based on optimal control theory [15]. The optimal closed loop performance analysis method assumes that the driver would adapt the vehicle by adjusting personal parameters. Apparently, the improvement of closed loop performance and of ease of control would possibly result from the improvement of driver performance, not always from the improvement of vehicle performance. The advantage of researching driver physical sense of vehicle is that it could forecast how driver perception dynamic behavior influences driver's subjective evaluation to vehicle handling performance. The application of closed loop performance research from feeling in airplane dates back to 40 years ago [16]. Modeling driver-vehicle real features is

conducive to researching human-vehicle dynamical behavior trait, which can provide the basis for improving closed loop performance. In order to make the model work like a real person, Cole has made lots of related researches in the domain of human nerve muscle dynamics [17–22]. A well designed control object should always be able to guarantee perfect closed-loop performance while cost as little output compensation as possible from driver. With this assumption, driving burden can be regarded as the measurement criteria of handling characteristics [23–26].

In this paper the definition of ease of control refers to the ability of vehicle to adapt to the driver population. The criterion of the ability is the range of the population who can easily control the vehicle under a certain closed loop condition. In another word, the paper analyzes robust performance of the whole closed-loop system with control inputs serving as random signals in a limited range. This analysis is obviously different from the analysis of determinate driver-vehicle closed loop system as mentioned before. Since there are differences of characteristics between common driving group and optimal individual driver, the optimal closed loop performance is hard to achieve. In terms of real drivers, as they have different psychological and physiological factors, their inputs to vehicle manipulation are also randomized. Therefore, the real driver closed loop performance is not a theoretically optimal performance. But instead, it is an acceptable one within the limitation of physiological condition and safety driving. Through reducing requirement from optimal performance indexes to acceptable ones, a larger crowd of qualified drivers can be obtained, thus making the designed vehicle more adaptable. In the next section, the driver-car closed-loop system with a stochastic driver model is described. The closed-loop safety index and closed-loop performance index are then outlined. In the last section, simulation and result with Monte-Carlo method is given.

2 Driver-Car Closed-Loop System with a Stochastic Driver Model

When the randomization of driver population is introduced into the closed-loop system, the performance will also be random. Then the closed loop could be written as following,

$$\begin{cases} \dot{X} = F(X, \Lambda, \tau, t) \\ Y = H(X, t) \end{cases} \quad (1)$$

where, $X = [X_1, X_2, \dots, X_n]$, $Y = [Y_1, Y_2, \dots, Y_h]$, $\Lambda = [\Lambda_1, \Lambda_2, \dots, \Lambda_m]$. X is state vector, Y is response vector, and Λ is random vectors of driver random parameters. F and H are functions described the closed-loop.

From Eq. (1), X and Y are random variable, and the closed-loop performance could be expressed as integral solution forms.

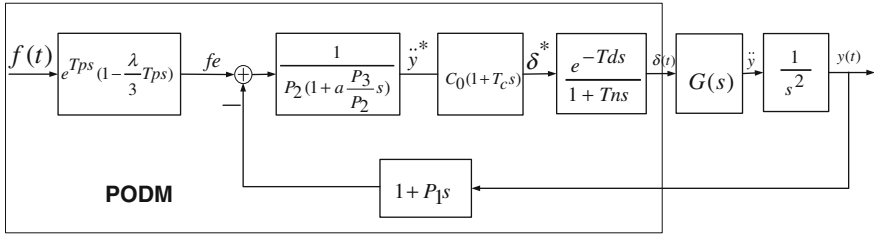


Fig. 1 Structure of POPADM

Table 1 Vehicles parameters

Name	Symbol	Car U (under-steering car)	Car N (neutral-steering car)	Car O (over-steering car)
Mass	m	1346.54 (Kg)	–	–
Moment of inertia (Z)	Iz	2454.2 (Kgm2)	–	–
Distance between cg. to front axle	Lf	1.022 (m)	–	–
Distance between cg. to rear axle	lr	1.628 (m)	–	–
Front cornering stiffness	kf	82,614 (N/rad)	114,590 (N/rad)	146,570 (N/rad)
Rear cornering stiffness	kr	71,936 (N/rad)	–	–
Steering ratio	i _{sw}	18.5	–	–
lf × Kf – lr × Kr		–32,680	0	32,680

$$I = \int_{a_1}^{b_1} \dots \int_{a_m}^{b_m} \Phi(\lambda_1, \dots, \lambda_m) f(\lambda_1, \dots, \lambda_m) d\lambda_1 \dots d\lambda_m \quad (2)$$

In the equation, $\lambda_1, \dots, \lambda_m$ are integral variables with their appropriate random variables $\Lambda_1, \dots, \Lambda_m$ and $[a_1, b_1], \dots, [a_m, b_m]$ are limited integrating ranges. $f(\lambda_1, \dots, \lambda_m)$ is joint probability density of random vector Λ . $\Phi(\lambda_1, \dots, \lambda_m)$ is a function directly or indirectly related to random vector Λ .

2.1 PO Driver Model and Random Variables

In this paper, the driver model, POPADM, derived based on Optimal Preview Acceleration Driver Model (OPADM) proposed by Prof. Guo’s [27], and considered both the position and orientation following trait during driving is introduced. The structure is shown as following [28] (Fig. 1).

The driver population could be represented by a driver model constructed with combination of deterministic structure driver model and some randomized parameters. According to Large Number theory, the parameter should be normal

Fig. 2 Distribution of T_p at 80 km/h for understeering car

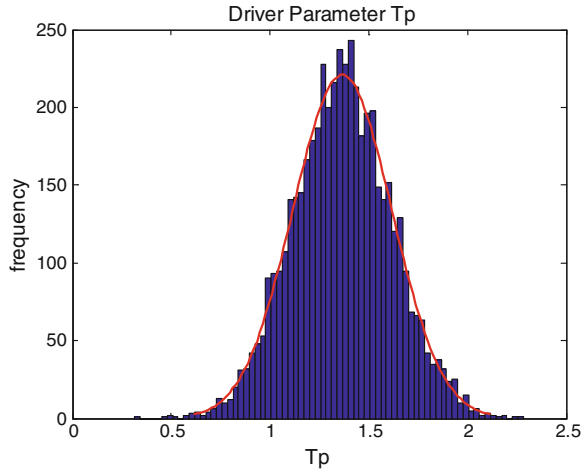
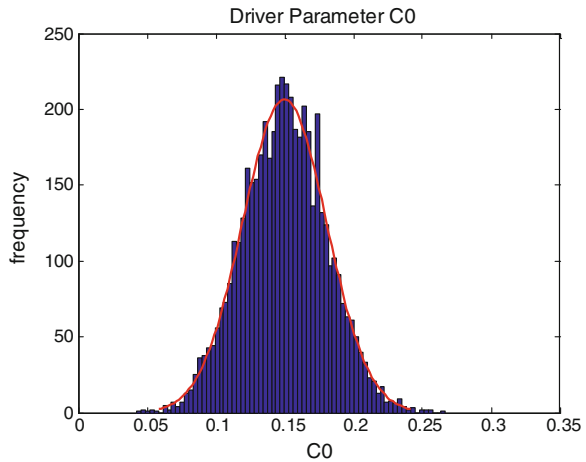


Fig. 3 Distribution of C_0 at 80 km/h for understeering car



distribution. Assuming the mean of the statistical variable is the optimal driver, the std. refers to the acceptance value that the general driver could not achieve the best driver level.

2.2 Closed-Loop Safety Index

The most direct evaluation index of driving safety is the actual track should be within permitted deviation of the desired track [29]. Assuming that the permitted positive and negative lateral deviation range is respectively D_u and D_l , within the limitation of lateral acceleration, assuming the maximum allowable lateral

Fig. 4 Distribution of T_p at 60 km/h for understeering car

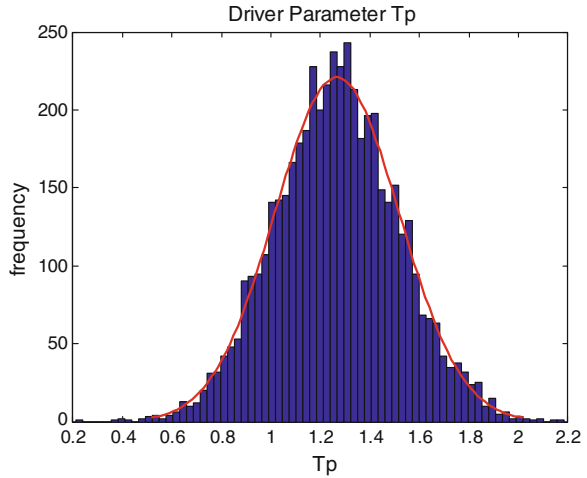
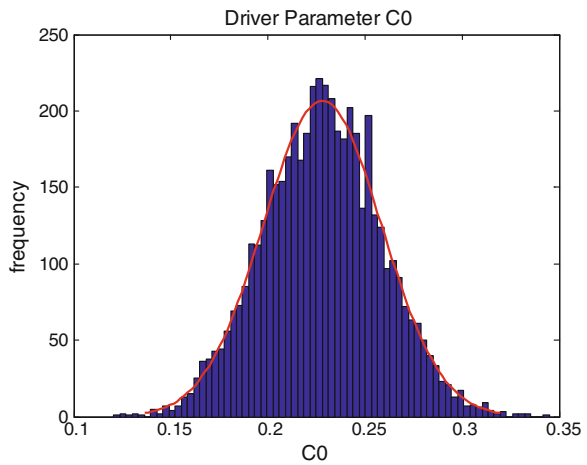


Fig. 5 Distribution of C_0 at 60 km/h for understeering car



acceleration is A_y , and vehicle lateral deviation and lateral acceleration in actual track is D and a_y , when there is one point in driving satisfies the equation:

$$\Phi(\lambda_1, \dots, \lambda_m) = \frac{1}{8} \left(1 - \frac{D - Du}{|D - Du|} \right) \left(1 + \frac{D - Dl}{|D - Dl|} \right) \left(1 + \frac{a_y + A_y}{|a_y + A_y|} \right) \left(1 - \frac{a_y - A_y}{|a_y - A_y|} \right) \tag{3}$$

When the deviation falls within the range of $[Dl, Du]$ and without the allowable lateral acceleration, $\Phi(\lambda_1, \dots, \lambda_m) = 1$, it is recorded that the vehicle can pass through this point safely.

In actual simulation, the general method is to make time into limited numbers of discrete moments. In terms of the whole expected path, assuming that there are N sampling time points, the safe driving random function of all points is:

Fig. 6 Distribution of T_p at 80 km/h for oversteering car

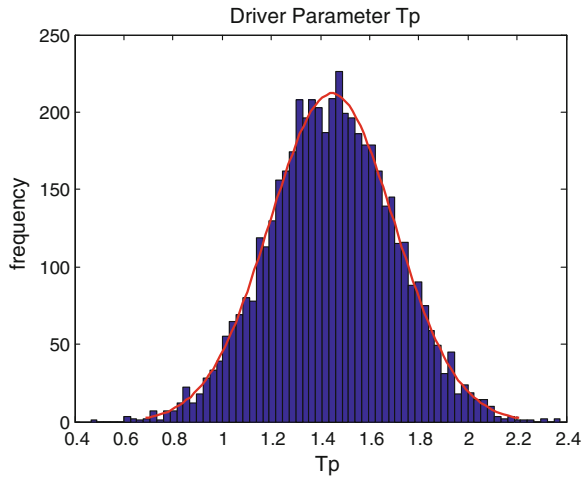
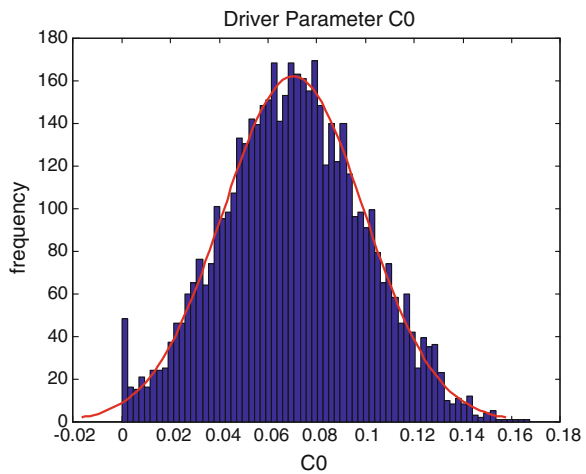


Fig. 7 Distribution of C_0 at 80 km/h for oversteering car



$$\Phi(\lambda_1, \dots, \lambda_m) = \prod_{k=1}^N \frac{1}{8} \left(1 - \frac{D(k) - Du}{|D(k) - Du|} \right) \left(1 + \frac{D(k) - Dl}{|D(k) - Dl|} \right) \left(1 + \frac{ay(k) + Ay}{|ay(k) + Ay|} \right) \left(1 - \frac{ay(k) - Ay}{|ay(k) - Ay|} \right) \tag{4}$$

If the driving condition satisfies Eq. (4) in simulation, it can be regarded that the vehicle can pass the expected path safely.

2.3 Closed-Loop Performance Index

According to the assumption that the driver usually keep coincidence the actual track with the desired track under the limitation of safety driving and himself

Fig. 8 Distribution of T_p at 60 km/h for oversteering car

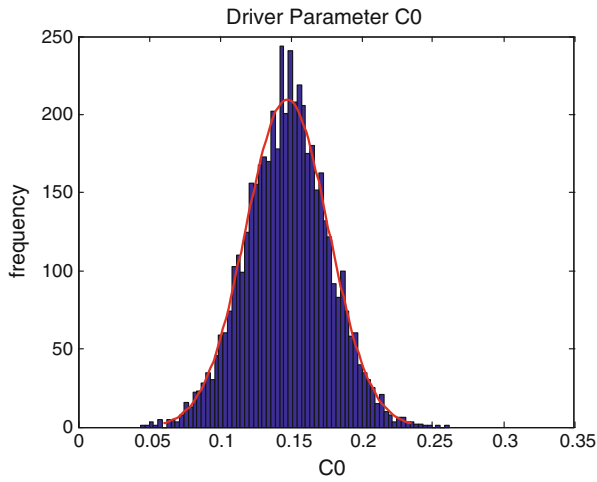
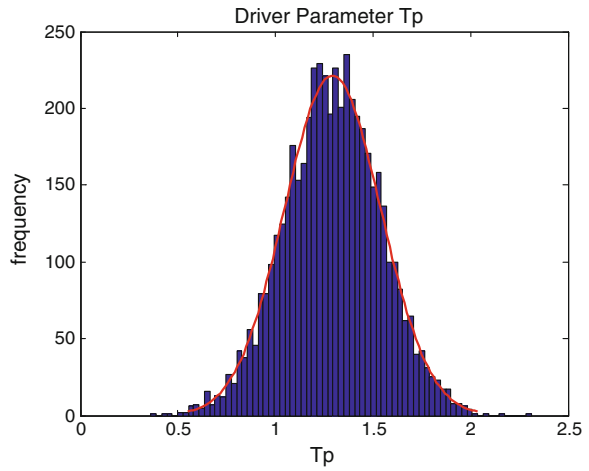


Fig. 9 Distribution of C_0 at 60 km/h for oversteering car

physiological limitation during driving [30]. And In terms of double lane change test, the calculation of indexes of driver-vehicle closed loop performance would be the cost function written as follows:

$$J = J_e + J_{SW} + J_{Latac} \tag{5}$$

where

$$J_e = \frac{1}{T} \int_0^T \left[\frac{f(t) - y(t)}{D_1} \right]^2 dt \tag{6}$$

Fig. 10 Distribution of T_p at 80 km/h for neutral-steering car

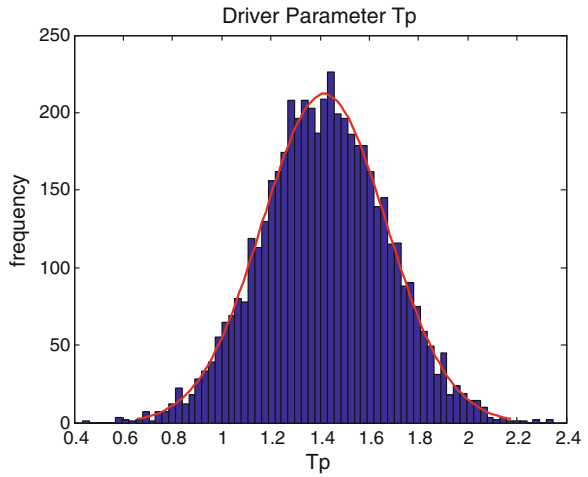
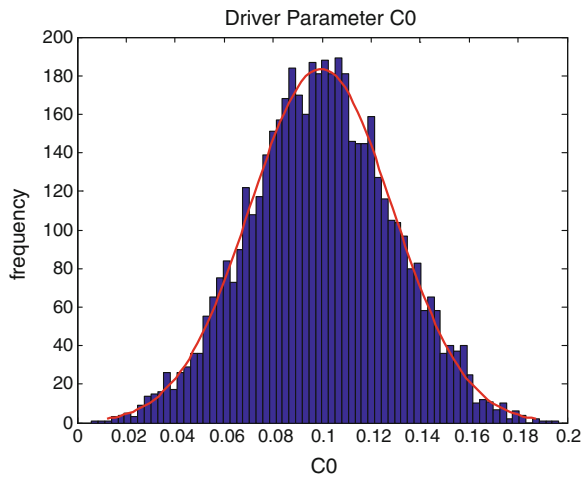


Fig. 11 Distribution of C_0 at 80 km/h for neutral-steering car



$$J_{SW} = \frac{1}{T} \int_0^T \left[\frac{\delta(t)}{D_2} \right]^2 dt \tag{7}$$

$$J_{Latac} = \frac{1}{T} \int_0^T \left[\frac{a_y}{D_3} \right]^2 dt \tag{8}$$

- J is the index of closed loop performance;
- J_e is the index of lateral displacement deviation performance;
- J_{SW} is total variance of steering angle;
- J_{Latac} is total variance of lateral acceleration;

Fig. 12 Distribution of T_p at 60 km/h for neutral-steering car

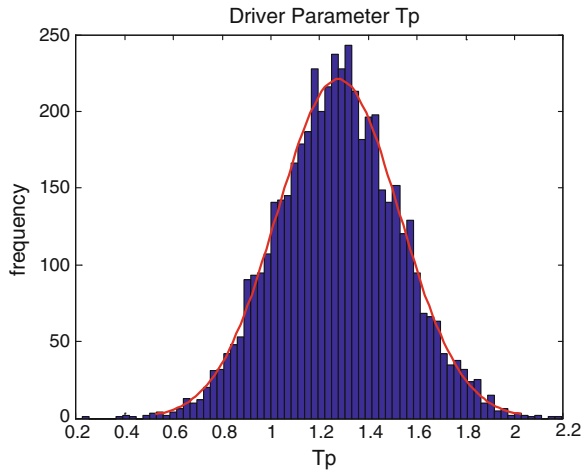
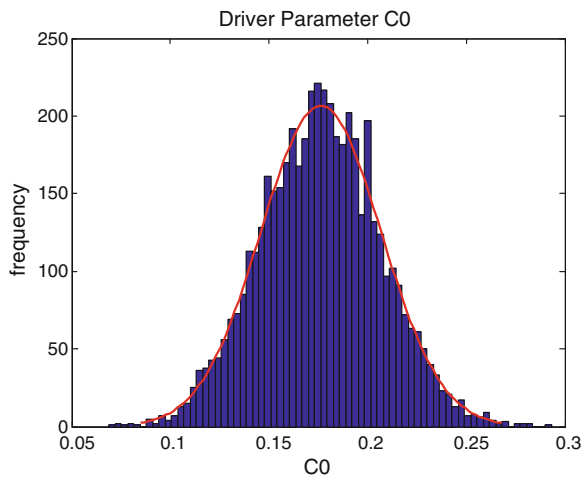


Fig. 13 Distribution of C_0 at 60 km/h for neutral-steering car



- $f(t)$ is desired driving path (m);
- $y(t)$ is actual driving path (m);
- $\delta(t)$ is steering angle (deg);
- T is simulation time (s);
- D_1, D_2 and D_3 are the threshold values of their correspondence index, which have penalty function to response values greater than, respectively, 0.5 (m), 360 (deg), 3 (m/s^2)

Fig. 14 Performance level of understeering car at 80 km/h

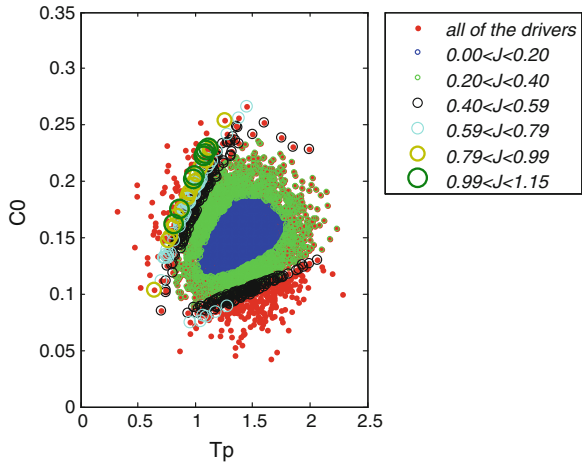
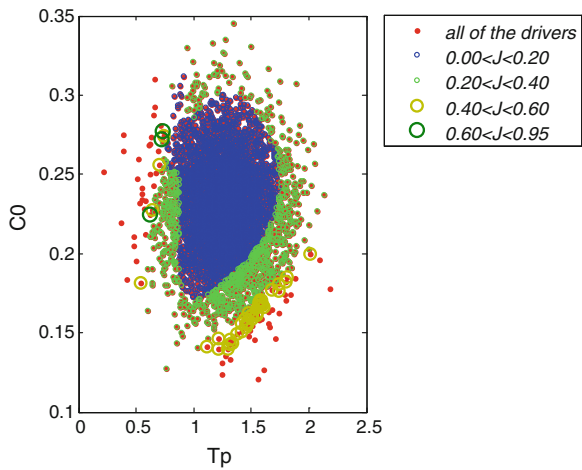


Fig. 15 Performance level of understeering car at 60 km/h



3 Simulation via Monte Carlo

3.1 Principle of Monte Carlo

Theoretically, it is hard to obtain analytic solution from Eq. (2), since the analytic expression of the integrated is hard to deduce. The general method for numerical integration, such as rectangle, trapezoidal rule and Simpson formula, can successfully avoid the demanding of awareness of analytic expression. These approximate calculation formulas could derive satisfactory conclusion, however, compute capacity would surge, with increasing integral dimension, to a point at which the computer cannot solve. One solution of random process in engineering is that setting up precise expression between stimuli and responses by using

Fig. 16 Performance level of oversteering car at 80 km/h

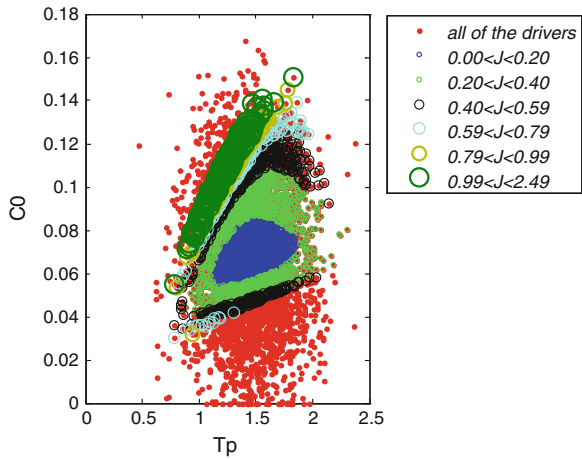
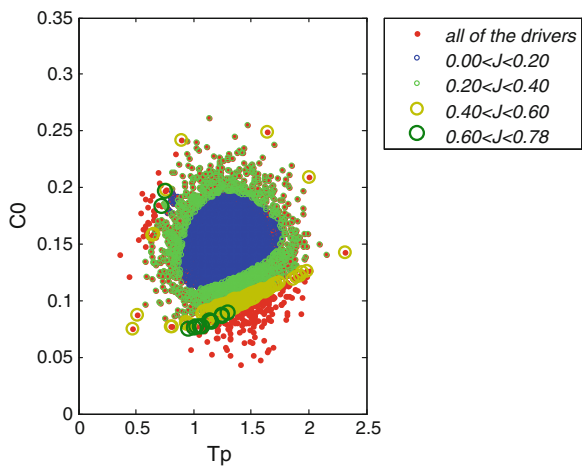


Fig. 17 Performance level of oversteering car at 60 km/h



control formula FPK which can describe probability density function. But there are some limitations, such as the stimulus must be white noise and the expression must use Markov process, not to mention the difficulty of precisely solving formula FPK. Therefore, some alternative methods, such as random perturbation method, Monte Carlo method, Gaussian closure technique, stochastic averaging method, stochastic finite element method, can be adopted to obtain approximate solution. Monte Carlo method, based on statistics, is very helpful in obtaining approximate solution and solving nonlinear complex probability problems. Since the computer is of high-speed and huge capacity, it can quickly accomplish simulations and process statistical treatment to derive the results.

Fig. 18 Performance level of neutral-steering car at 80 km/h

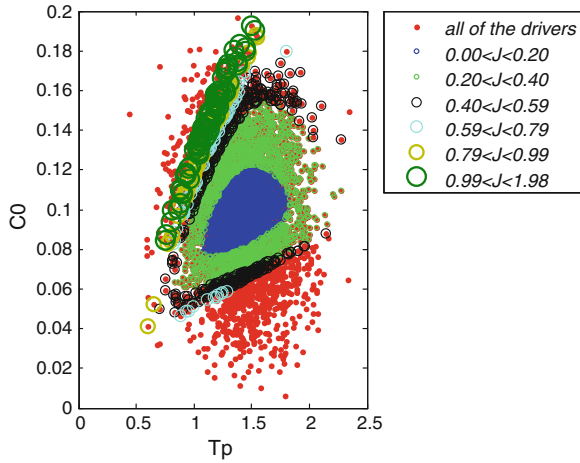
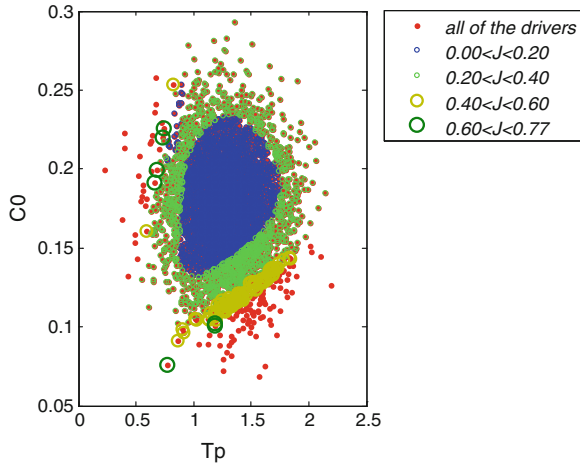


Fig. 19 Performance level of neutral-steering car at 60 km/h



3.2 Vehicle Parameters

Since 2DOFs vehicle model is simple and enough to present main kinetics characteristics in the linear regime, this model will be used in this paper. The paper analyzes ease of control by comparing under-steering vehicles, over-steering vehicles and neutral-steering vehicle, obtaining different steering characteristics by adjusting equivalent concerning stiffness of front axle (Table 1).

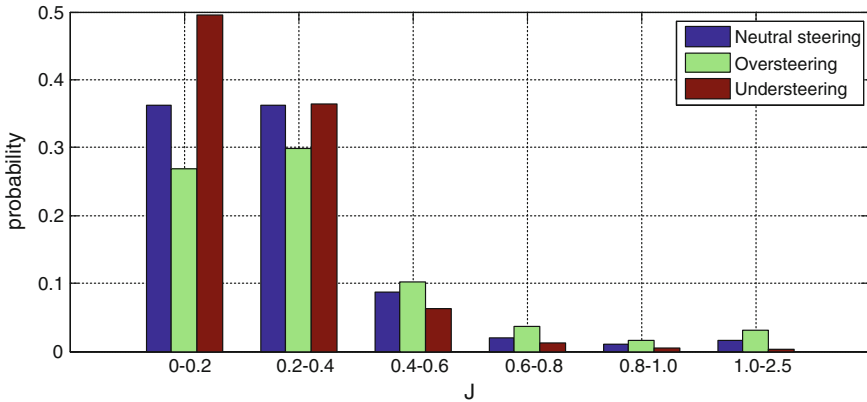


Fig. 20 Performance level comparison at 80 km/h for the 3 cars

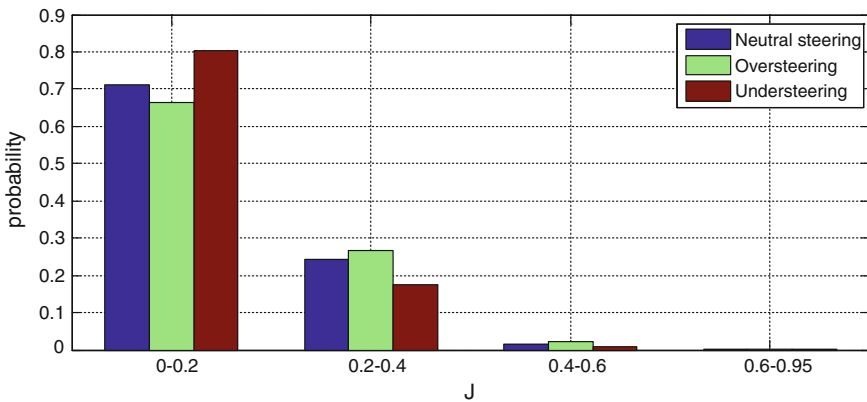


Fig. 21 Performance level comparison at 60 km/h for the 3 cars

3.3 Driver Model Parameters

In POPADM, C_0 and T_p were selected as the statistical variables, the frequency of the 5000 samples are shown as in the following figures (Figs. 2, 3, 4, 5, 6, 7, 8, 9, 10, 11, 12, 13).

4 Results

The simulation will be repeated using the driver parameter from every sample, and then both Closed-loop Performance Index and Closed-loop Safety Index are calculated for each sample. In the following figures, the red points represent the

whole driver population from the samples, all of other colors represent the drivers who could pass the desired path safely, but different color means different level of the closed-loop performance or the drivers' skill for the specific car (Figs. 14, 15, 16, 17, 18, 19).

From the figures, for all of the three cars, the performance levels are obviously better at 60 km/h than at 80 km/h, because the safety points (color points rather than red ones) are more than those at 80 km/h.

The comparisons between different cars at each performance level are shown in the following figures. The safety possibilities are 0.859, 0.752 and 0.940 for neutral steering, over steering and under-steering cars respectively at 80 km/h, and 0.974, 0.957, 0.99 at 60 km/h. The under-steering car could be controlled safely for more drivers than the other 2 cars and more drivers could also handle the under-steering car at better performance (the smaller J, the better performance) (Figs. 20, 21).

5 Conclusion

There are two methods to realize the analysis of ease of control. One is a subjective method which obtains required data by lots of trials carried out by different drivers on driving simulators or on real car. The other one is an objective method which can process virtual simulation analysis and forecasting through computer by using digital driver model. In this paper, the ease of control evaluation is based on analysis of the distribution of control parameters in safe driving situation and the distribution of inherent control parameters of real driver population. In order to consider the randomness feature of driver handling characteristics, the driver model is constructed with combination of deterministic structure driver model and randomized parameters. Three cars are set up to be evaluated by the proposed method, and the results shown this method could discern the ease of control by the driver population that could control it safely and closed-loop performance index.

Since the response indexes are a function of driver random parameters and it is difficult to derive the analytical solution of the closed-loop system. Monte-Carlo method was used to analyze the characteristics of calculation of random driver model-vehicle closed loop system response indexes. By adopting random sampling using this method, the randomness of drivers can be simulated, and random closed loop performance indexes can be obtained. Based on the analysis of parameter match ability of ease of control, the paper presents the proposed method to analyze and evaluate vehicle ease of control. It is worth to mention that the 3 cars presents in this paper does not necessary to represent all of the understeer, oversteer and neutral cars, since it is too simple to get the 3 steering characteristic cars.

References

1. Chiesa A, Rinonapoli L (1968) A new loose inverse procedure for matching tyres and car using a mathematical model. In: Proceedings of institution of mechanical engineers, Yo1183 Pt 3H
2. Auckland RA, Manning WJ, Carsten OMJ, Jamson AH (2008) Advanced driver assistance systems: objective and subjective performance evaluation. *Veh Syst Dyn* 46:S1, 883–897
3. Wang B, Abe M, Kano Y (2004) A driver-centred safety evaluation model of lane change operation for the aged driver. In: Proceedings of the institution of mechanical engineers. Part D: *J Automobile Eng* 218:7
4. Bai Y (2012) Ease of control evaluation via stochastic driver model. PhD thesis, Jilin University
5. Newberry AC, Griffin MJ, Dowson M (2007) Driver perception of steering feel. In: Proceedings of the IMechE vol 221. Part D: *J Automobile Eng* 405–415
6. Ishio J, Ichikawa H, Kano Y, Abe M (2008) Vehicle-handling quality evaluation through model-based driver steering behavior. *Veh Syst Dyn: Int J Veh Mech Mobility* 46(1):549
7. Wang B, Abe M, Kano Y (2002) Influence of driver's reaction time and gain on driver-vehicle system performance with rear wheel steering control systems: part of a study on vehicle control suitable for the aged driver. *JSAE Rev* 23:75–82
8. Harada H (1994) Stability criteria and evaluation of steering maneuver in driver-vehicle system. *JSME Int J* 37(1, C):115
9. Harada H (1997) Stability criteria of driver-vehicle system and objective evaluation of vehicle handling performance. *Int J Veh Des* 18(6):597–615
10. Harada H (1995) Control strategy of active rear wheel steering in consideration of system delay and dead times. *JSAE Rev* 16:171–177
11. Zong C, Guo K (2000) Objective evaluation index for handling and stability of vehicle. *Nat Sci J Jilin Univ Technol* 30(1):1–6
12. Zong C, Guo K, Li B (2001) Theoretical prediction and comprehensive evaluation for vehicle handling stability. *Automot Eng* (1):5–8, 12
13. Zong C, Liu Y, Fansen K (2001) Closed-loop evaluation and test method of vehicle handling and stability on driving simulator. *Automot Eng* 03:205–208
14. Horiuchi S, Yuhara N (2000) An analytical approach to the prediction of handling qualities of vehicles with advanced steering control system using multi-input driver model. *J Dyn Syst Measur Control* 122:490–497
15. Sharp RS (2005) Driver steering control and a new perspective on car handling qualities. In: Proceedings of IMechE vol 219. Part C: *J Mech Eng Sci* 1041–1051
16. Hess RA (2009) Analytical assessment of performance, handling qualities, and added dynamics in rotorcraft flight control. *IEEE Trans Syst, Man Cybern. Part A: Syst Hum* 39(1):162–271
17. Pick AJ, DJ Cole (2008) A mathematical model of driver steering control including neuromuscular dynamics. *J Dyn Syst, Measur, Control* 130:031004.1–031004.9
18. Pick AJ, Cole DJ (2007) Dynamic properties of a driver's arms holding a steering wheel. *Proc Inst Mech Eng, Part D: J Automobile Eng* 221(12):1475–1486
19. Pick AJ, Cole DJ (2008) A mathematical model of driver steering control including neuromuscular dynamics. *Trans ASME, J Dyn Syst Meas Control* 130(3):031004
20. Pick AJ, Cole DJ (2007) Driver steering and muscle activity during a lane-change manoeuvre. *Veh Syst Dyn* 45(9):781–805
21. Cole DJ (2011) Influence of steering torque feedback and neuromuscular dynamics on driver and vehicle response to lateral force disturbance. *IAVD*
22. Cole DJ (2011) A path-following driver-vehicle model with neuromuscular dynamics, including measured and simulated responses to a step in steering angle overlay. *Veh Syst Dyn*
23. Hess RA, Modjtahedzadeh A (1990) A control theoretic model of driver steering behavior. *IEEE Control Syst Mag* 10(5):3–8

24. Modjtahedzadeh A, Hess RA (1993) A model of driver steering control behavior for use in assessing vehicle handling qualities. *J Dyn Syst, Measur, Control* 115:456–464
25. Tokutake H, Miura Y, Okubo H (2004) Workload analysis method via optimal driver model. SAE paper 2004-01-3536
26. Miura Y, Tokutake H, Fukui K (2007) Handling qualities evaluation method based on actual driver characteristics. *Veh Syst Dyn: Int J Veh Mech Mobility* 45(9):807
27. Guo K, Fancher PS (1983) Preview-follower method for modeling closed-loop vehicle directional control. In: Proceedings of the 19th annual conference on manual control, 23–25 May 1983, Massachusetts institute of technology
28. Guan H, Bai Y, Jia X, Chen Y (2012) Identification of driver model parameters. VTI Changchun, China
29. Guan H (1992) Researches on the directional control model of drivers and its application to prediction of closed-loop driving safety. PhD thesis, Jilin University of Technology, China
30. Guo K (2011) Vehicle dynamics. Jiangsu phoenix science press

Shift Quality Assessment and Optimization for Dual Clutch Transmission

Yulong Lei, Huabing Zeng and Hongbo Liu

Abstract The shift quality is one of the most important factors that affect the performances of comfort, ride and drivability for vehicles equipped with dual-clutch transmission (DCT). Assessing the shift quality and then optimizing shift control strategy and algorithm by the guidance of assessment results to improve the vehicle performance is a useful idea for the development of DCT, and also for other types of automatic transmissions. This paper defines the shift quality assessment indexes in detail for DCT from the control point of view. The vehicle model for DCT is built using MATLAB/Simulink tools. And then a shift quality assessment system is developed. Through the co-simulation of DCT vehicle model and assessment system, the shift quality control objectives, namely expected control range of each assessment index, are determined, which provide reference and guidance for the optimization of shift control strategy and algorithm for DCT. The highest level of shift quality assessment is selected as the objective optimization function and the multi-objective genetic algorithm (MGA) is used to optimize the control strategy of clutch switch timing during the torque phase and inertia phase. The simulation results about shift quality before and after the optimization are observed, which verify the correctness and effectiveness of the shift control strategy after optimization, thus improving the shift quality of DCT.

F2012-G05-004

Y. Lei (✉) · H. Zeng · H. Liu
State Key Laboratory of Automotive Simulation and Control, Jilin University,
No. 5988, Renmin Street, 130022, Changchun, China
e-mail: leiyl@jlu.edu.cn

H. Zeng
e-mail: zenghb11@mails.jlu.edu.cn

Keywords Vehicle engineering · Shift quality assessment · Optimization · Dual clutch transmission · Genetic algorithm

1 Introduction

Dual clutch transmission (DCT), with its advantages of the no-torque-interrupt shift pattern, high transmission efficiency and good production inheritance has become a hot spot topic in the field of automotive transmission technology [1]. At present, the research of DCT technology mainly focuses on the launch control, gear-shift control and shift schedule making, etc. Assessing shift quality first and then guiding the optimization of shift quality by the assessment results is a new idea and one of the key technologies for the development of the DCT and other types of automatic transmissions. This paper studies on the assessment and optimization of the shift quality for DCT vehicles. On the one hand, through the assessment, the control objectives for DCT shift control, namely expected control range of each assessment index, are determined, and it provides the guidance and reference for the objective assessment and calibration of DCT; On the other hand, according to the control objectives of DCT, the control strategy and control algorithm are optimized so as to improve the shift quality.

2 Assessment Index

To assessment shift quality objectively, a primary issue is how to select a group of appropriate parameters, namely assessment index, to reflect the shift quality truly and effectively. To facilitate the assessment work, these indexes should have clear physical meaning and can be easily measured. The traditional shift quality assessment indexes are fewer that mainly include the jerk, slipping work and the shift time [2]. Since the difference in each shift condition, these indexes cannot characterize the shift quality fully and accurately. In order to solve the problems of unspecific shift control objectives and unclear assessment indexes for DCT, from the point of view of control, a group of subdivided indexes are defined according to the different phases at different shifting conditions. These indexes are easy to be acquired online and can scientifically and comprehensively characterize the shift quality. The indexes are defined in Table 1 and Fig. 1.

Table 1 Assessment indexes of shift quality

Assessment index	Symbol	Unit
Fluctuation of acceleration when engaging	Δa	m/s^2
Negative greatest jerk	j_{p-n}	m/s^3
Positive greatest jerk	j_{p-p}	m/s^3
Overshoot of engine speed when disengaging	$\Delta\omega_{e-o}$	rpm
Undershoot of engine speed when engaging	$\Delta\omega_{e-u}$	rpm
Decreasing of engine speed when upshift	$\dot{\omega}_{e-de}$	r/s^2
Increasing of engine speed when downshift	$\dot{\omega}_{e-in}$	r/s^2
Shift delay time	t_{delay}	s
Shift time	t_s	s
Delay time of engine speed	$t_{Spd-delay}$	s

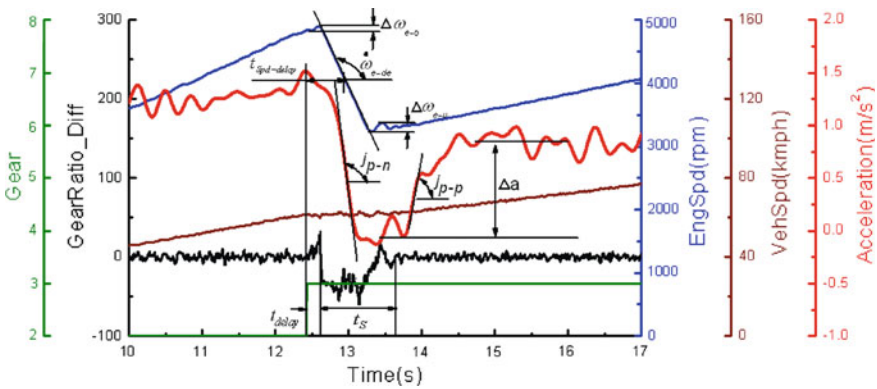


Fig. 1 Illustration of assessment indexes of shift quality

3 Vehicle Model and Assessment System

3.1 Design of Vehicle Model

The vehicle system model for DCT is built in Matlab/Simulink environment, which includes the sub-models of engine, dual clutch and its actuators, transmission and synchronizer, load, vehicle dynamics, controller (TCU) and driver[3, 4]. The overall design of simulation model is as shown in Fig. 2. Main function and data flow of sub-models are described as below:

- (1) Engine model calculates the engine output torque T_e according to the inputs of throttle opening adjustment volume $\Delta\alpha$ and engine speed ω_e ;
- (2) Model of dual clutch and its actuator calculates the dual clutch delivered torque T_{c1}, T_{c2} according to the inputs of engine torque T_e , resistance torque T_l , difference between dual clutch driven disc speed and engine speed $d\omega_{c1}, d\omega_{c2}$ and clutch engaging rate given by controller v_{c1}, v_{c2} ;

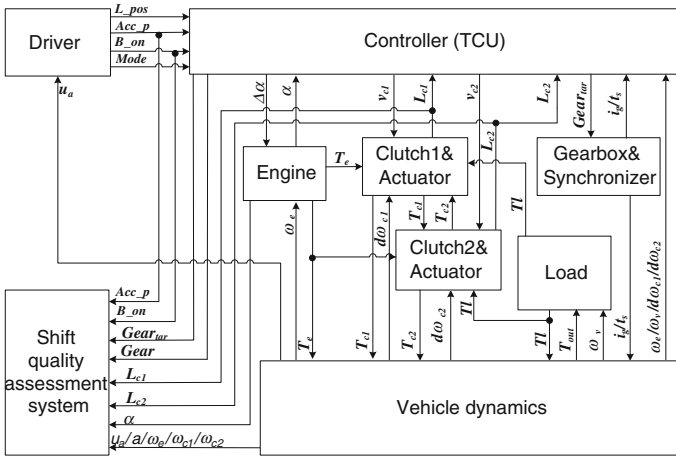


Fig. 2 Design of DCT vehicle model

- (3) Transmission and synchronizer model calculates synchronizer torque T_s , synchronization time t_s and current gearbox ratio i_g according to the target gear given by controller;
- (4) Load model calculate the resistance torque T_l according to the inputs of vehicle driven torque T_{out} and vehicle speed u_a ;
- (5) Vehicle dynamics model calculates longitudinal acceleration of vehicle a , dual clutch driven disc speed ω_{c1} , ω_{c2} , vehicle driven torque T_{out} and vehicle speed u_a according to the inputs of T_e , T_{c1} , T_{c2} , T_l ;
- (6) Controller model outputs the clutch engaging rate v_{c1} , v_{c2} and throttle opening adjustment value $\Delta\alpha$ to control the clutch and engine according the vehicle working state;
- (7) Driver model outputs the signals that represent the driver’s intention, including lever position L_pos , acceleration pedal position Acc_p , brake switch B_on and drive mode (sport/economy) mode.

3.2 Design of Assessment System

The shift quality assessment system was developed using Matlab/Simulation tool and integrated with the DCT vehicle system model. Its inputs include Acc_p , B_on , L_{c1} , $Gear$, u_a , a , ω_e , ω_{c1} , ω_{c2} etc. and these signals are used to extract assessment index of shift quality and calculate assessment level.

The shift quality assessment system can extract the assessment indexes at different driving condition by the input data and the signals, and then, it gives a corresponding objective assessment result by these indexes, and the result is divided into 1–10 levels [5, 6]. Figure 3 is the steps for calculating the objective

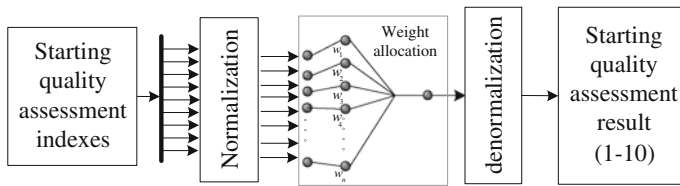


Fig. 3 Calculation steps for objective shift quality assessment

assessment result. As the dimension of each index is different, it is needed to normalize these indexes into 0–1 before calculation. Then the calculation is taken according to the different weight assigned to each index. The result is still in 0–1 range at this point. Finally, we obtain the corresponding shift control quality objective result by a process of denormalization (1–10).

3.3 Objectives of Shift Control

Based on the integrated simulation platform of DCT vehicle model with assessment system, the expected control interval of each index when shift quality is the optimal is gotten through assessment, as shown in Table 2. The results given in the table are the expected control objectives during the process of DCT shift quality optimization. When each index is considered synthetically and all falls within the corresponding control interval, a good DCT shift quality can be achieved. But it should be noted that because the table values are based on the simulation results, they need to be adjusted slightly when applied in actual vehicle.

4 Optimization of the Shift Quality

4.1 Genetic Algorithm Based Optimization

In this paper, the optimization of DCT shift control strategy is done by co-calculation of the software iSIGHT and MATLAB, which are connected seamlessly by the interface between them. In iSIGHT, the multi-objective genetic algorithm (GA) is selected as the optimization method. First, we need to initialize the input parameters and optimization range and set the indexes provided by shift assessment system as the design objectives (control objectives). Then, the iSIGHT invokes the MATLAB program to carry out the optimization work. In this step, a group of output parameters values are got, and the analysis operation to determine that whether the value is the optimal objective is taken. The iSIGHT repeats this operation until the optimal values which meet the design objectives are got.

Table 2 Desired control interval of shift quality assessment indexes

Index	Δa (m/s ²)	j_{p-p} (m/s ³)	j_{p-n} (m/s ³)	$\Delta\omega_{e-o}$ (rpm)	$\Delta\omega_{e-u}$ (rpm)
Interval	1 ~ 5	0 ~ 10	-10 ~ 0	0 ~ 300	0 ~ 300
Index	$\dot{\omega}_{e-de}$ (r/s ²)	$\dot{\omega}_{e-in}$ (r/s ²)	t_{delay} (s)	t_s (s)	$t_{Spd-delay}$ (s)
Interval	-1500 ~ -800	800 ~ 1500	0 ~ 0.2	0.5 ~ 1.5	0.2 ~ 1

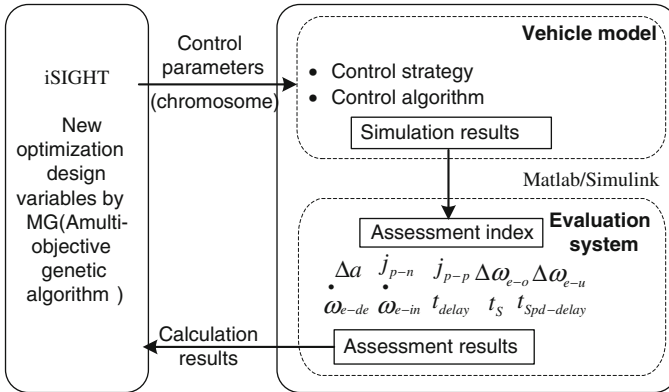


Fig. 4 Co-calculation steps for optimization

Finally, these final optimized values are adopted as the optimal solution of DCT shift control strategy to achieve the purpose of the optimizing the shift quality [7, 8].

The optimization process based on co-calculation of the DCT vehicle model and iSIGHT is as shown in Fig. 4. The steps are as follows:

- (1) Build the parameterized model in MATLAB and form the data tables that describe the DCT shift control strategy;
- (2) Invoke the simulation model from iSIGHT and initialize the control parameters;
- (3) Run the simulation model, evaluate the simulation data, and get the assessment indexes and results;
- (4) Re-assign the control parameters according to the multi-objective genetic algorithm (MGA), then run the model and output the result.

The shift quality optimization of the DCT is a complex multivariable and nonlinear optimization problem. The characteristics of the genetic algorithm determine that it is a kind of very effective way to solve this kind of problem. Through the calculation of MGA in iSIGHT software, the DCT gearshift control strategy is optimized globally at different conditions. It reduces the computation time, gets a group or groups of feasible solutions, and accurately determines the optimal solution for shift control strategy. To a great extent, the solution set

improved DCT shift quality, and made the assessment index reached the requirements of expected control objectives.

4.2 Optimization Scheme

In process of shifting, the core step of dealing with multi-objective optimization is to transfer multi-objective function into the single objective function. We use the linear weighted method to construct the objective function, namely assessment fitness function, which is defined as follows:

$$G_{SQ}(x) = w_1\Delta a + w_2j_{p-p} + w_3j_{p-n} + w_4\Delta w_{e-u} + \dots + w_6\dot{\omega}_{e-de} + w_7t_{delay} + w_8t_S + w_9t_{Spd-delay} \quad (1)$$

In this formula, $w_1 \sim w_9$ represent weights of control objectives respectively, i.e. weights of assessment indexes assigned by expert advice.

The maximum and the minimum of each control objective are got by the expected control interval of corresponding index. The optimization objective function can be expressed as follow:

$$\min(G'_{SQ}(x)) = \min(w_1\Delta a' + w_2j'_{p-p} + w_3j'_{p-n} + w_4\Delta w'_{e-u} + \dots + w_6\dot{\omega}'_{e-de} + w_7t'_{delay} + w_8t'_S + w_9t'_{Spd-delay}) \quad (2)$$

Because the higher the assessment level (1–10) means the better shift quality, so the assessment level function U'_{SQ} is constructed as follow:

$$U'_{SQ} = 1 - G'_{SQ} \quad (3)$$

Finally, by denormalization of U'_{SQ} , the result of corresponding objective assessment level is got.

When we apply the multi-objective genetic algorithm to solve the optimization problem, the too many chromosome genes may cause long calculation process, and the problem that the optimization results is not the optimal solution will happen. Therefore, the degree of influence of control variables on objective function should be analyzed to reduce the number of variables and simplify the optimization operation. Here, the individual gene is defined as disengaging clutch off-going rate $v_{offgoing}$ and engaging clutch on-coming rate $v_{oncoming}$. The two parameters together form a chromosome and represent a solution to the problem, which is

$$X = [x_1, x_2]^T = [v_{offgoing}, v_{oncoming}]^T \quad (4)$$

In this case, solving the optimal solution of the dual clutch switching rate can be boiled down to optimization problem that makes the shift quality assessment level U_{SQ} the highest. Through calculation of the dynamic models, the vehicle model simulation is carried out for each determined chromosome. The corresponding

Table 3 Interval and step length of control parameters optimization

Control parameters	Minimum value	Maximum value	Step length
$v_{offgoing}$	$0.1v_0$	v_0	$0.02v_0$
$v_{oncoming}$	$0.1v_0$	v_0	$0.02v_0$

fitness G_{SQ} , U_{SQ} , are obtained to determine the optimal solution of clutch switching rate when output meets $array*20cminx \in X(G_{SQ}(x))$, i.e.

$$\max_{x \in X} (U_{SQ}(x)).$$

Before seeking the most optimal solution using the genetic algorithm, the string should be encoded, considering the requirements of the change range and precision of each parameter, the paper used the genetic code of 16-bit fixed length binary number to represent a variable for solving the minimum value of the objective function G'_{SQ} and the optimal solution of corresponding design variable. The interval and step length of parameter optimization for control strategy are in Table 3. There, v_0 is the initial value for the clutch engaging and disengaging rate.

Figure 5 is the relationship between different optimization schemes and shift quality assessment in the process of DCT shifting gear from 1 to 2. It can be seen from the figure that: to improve the shift quality, what most needed to be optimized is the dual clutch switching speed or switch timing of control strategy. In the top left corner is a two-dimensional coordinate system that the horizontal axis is $v_{offgoing}$ and the vertical axis is $v_{oncoming}$. The two axes have their own boundary condition which is denoted by dotted line that the maximum is v_0 and the minimum is $0.1v_0$. Every dot in the figure represents an optimization scheme, namely a chromosome. For the chromosomes which are not within the boundary, its corresponding shift quality is poor, so it cannot be used as optimization scheme and can be ignored. The bottom left corner shows that the chromosomes in different areas can result in the different dual clutch overlap areas (a, b and c) when shifting. The a is the overlap area when $v_{offgoing}$ is a constant value and $v_{oncoming}$ is different; the b is the overlap area when $v_{offgoing}$ and $v_{oncoming}$ are equal; and the c is the overlap area when $v_{oncoming}$ is a constant value, and $v_{offgoing}$ is different. The right side of the figure shows the different shift quality assessment indexes and assessment results when applying the three optimization schemes. Through the optimization, when U_{SQ} is maximum, the corresponding chromosome is selected as the optimal solution of optimization.

4.3 Optimization Results

Through the optimization of the clutch switching speed during the shift process, the optimal solution set for the control law of engaging clutch and disengaging clutch when switching the clutch under the different throttle opening is obtained,

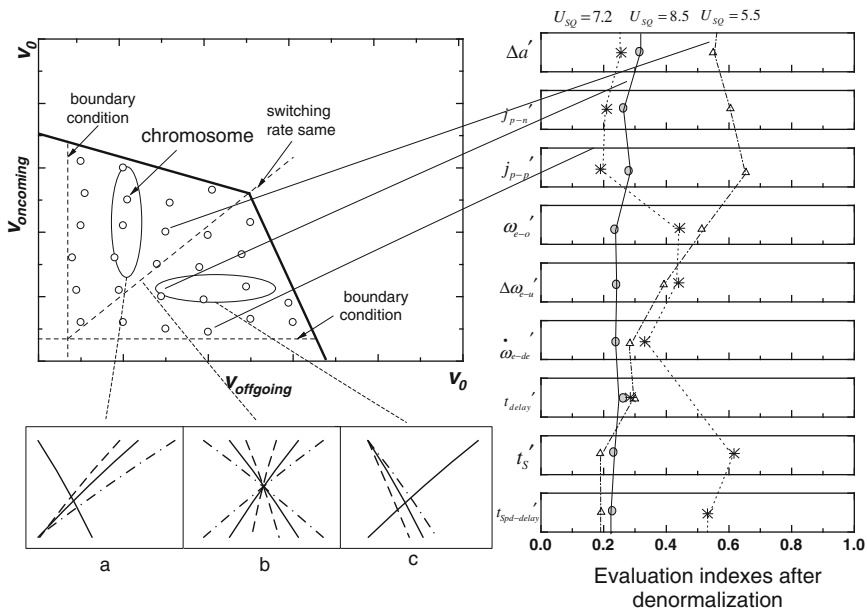


Fig. 5 Relationship between optimization and shift quality assessment

just as shown in Figs. 6 and 7. The $v_{oncoming}$ and $v_{offgoing}$ represent the switching speed of engaging clutch and disengaging clutch and they meet the relationship that $v_{oncoming}(v_{offgoing}) = x \cdot v_0$, where x is the solution for control law and v_0 is the initial value of the clutch running speed. The v_0 can be adjusted according to the system structure characteristics of dual clutch. From the two charts we can see that: $v_{oncoming}$ and $v_{offgoing}$ are greater when shifting to high-gear under large throttle opening; $v_{oncoming}$ and $v_{offgoing}$ are smaller when shifting to low-gear under light throttle opening. Thus, it ensures the shift quality when shifting to different gear effectively.

Above optimization for shift control parameters is gained based on the weights that an expert gave. Because different evaluators can pay different attention to each index and to influence factors of man and vehicle etc., we can adjust the weight as needed or we can take the average value of weights given by many experts. In this case, we change the optimization objective function and then get the optimal solution for control strategy that concerned about one or more assessment targets.

5 Comparative Analysis

Figure 8 is the simulation curves before and after optimization when DCT vehicle model shifts from gear 2 to 1 at the 50 % throttle opening. The black line in the figure is the downshifting process that the clutch switching time and overlap area

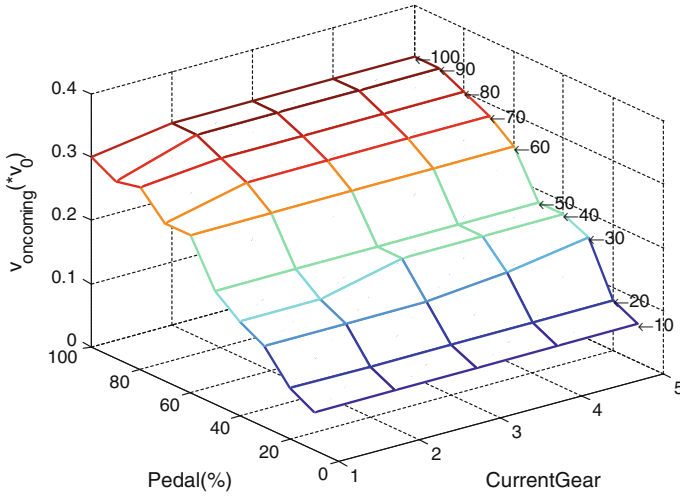


Fig. 6 Control law for $v_{oncoming}$ after optimization

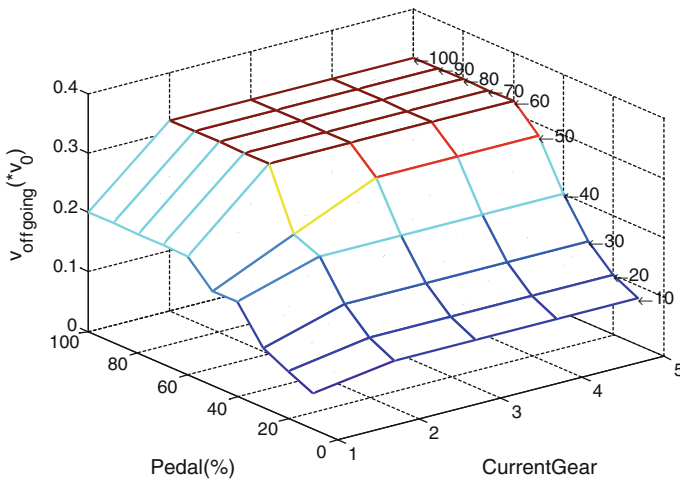


Fig. 7 Control law for $v_{offgoing}$ after optimization

both are appropriate, which is plotted after optimization; the red line is the downshifting process that the clutch overlap area is too great and the blue line is that when overlap area is too small, which is plotted before optimization. As shown in Table 4, the shift quality assessment system extracts the assessment indexes and gives the objective level by simulation results respectively before and after the optimization. The results show that each shift quality indexes get a very good compromise when the optimized control strategy and algorithm are adopted

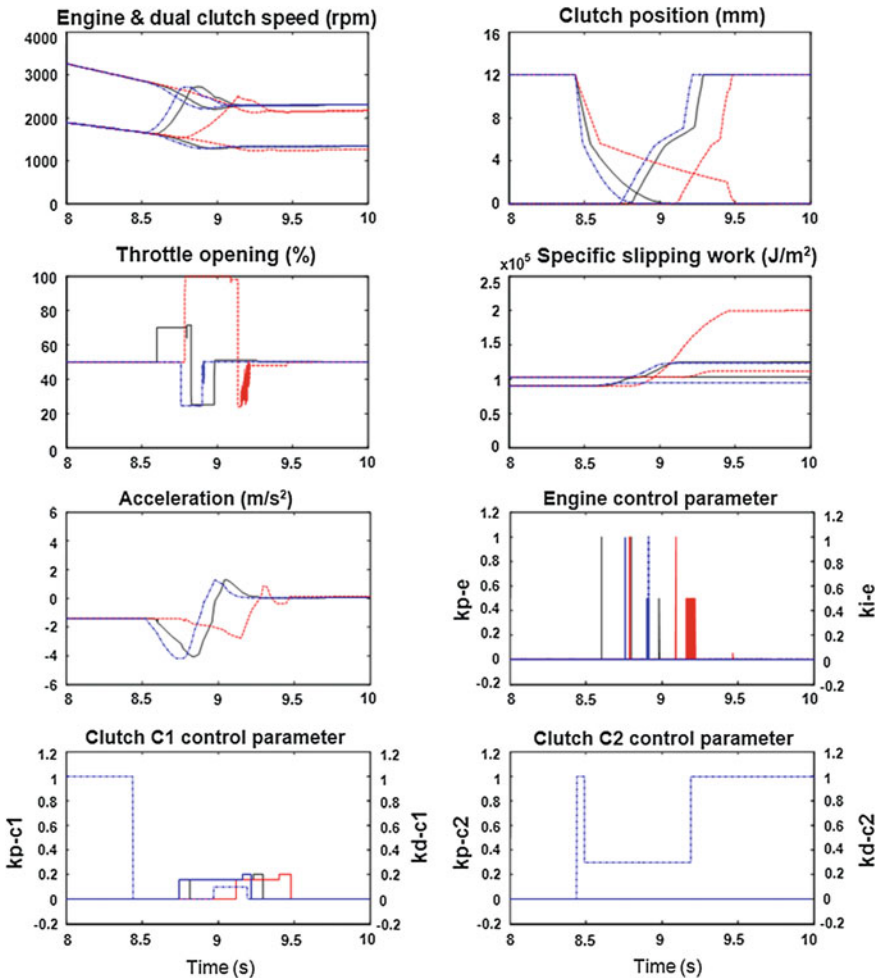


Fig. 8 Simulation curves of shift 2-1 at 50% throttle opening

in downshifting process; it meets the requirements of desired control area and makes the shift quality assessment reach the highest level.

6 Conclusions

This paper studies on the DCT shift quality assessment and optimization. On one hand, it determines the control target and control method through the assessment, providing guidance and reference for objective assessment and calibration; on the other hand, according to the specific control target, the control strategy and control

Table 4 Comparison of shift quality before and after optimization

Working condition	Control objective (assessment index)		Overlap too great	Overlap too small	Overlap good
Shift gear 2-1	Δa	(m/s ²)	2.8	2.5	2.9
	j_{p-n}	(m/s ³)	-2.5	-2	-1.5
	j_{p-p}	(m/s ³)	10	8	3
	$\Delta\omega_{e-o}$	(rpm)	0	0	0
	$\Delta\omega_{e-u}$	(rpm)	350	486	420
	$\dot{\omega}_{e-in}$	(r/s ²)	420	507	500
	t_{delay}	(s)	0.13	0.15	0.12
	t_S	(s)	1.05	0.77	0.85
	$t_{Spd-delay}$	(s)	0.52	0.22	0.30
	Overall target U_{SQ}		7.75	7.34	8.19

algorithm of DCT shift system is optimized to improve the shift quality. Assessing the DCT shift quality for its next improvement is a new idea for developments of DCT, and also for other type of automatic transmission.

Acknowledgments This study was supported by Technology development project of Jilin Province of China (No.20096008), Chinese National Natural Science Foundation (No. 51075182, No. 50505014), Program for Changjiang Scholars and Innovative Research Team in University (No. IRT1017) and “985 Project Automotive Engineering” of Jilin University.

References

- Matthes B (2005) Double clutch transmissions—lessons learned and future potential. SAE paper doi:10.4271/2005-01-1021
- Anlin GE (1993) Theory and design of vehicle automatic drive. China Machine Press, Beijing
- Andreas A, Schreiber U, Schindler J (2006) Engine and gearbox modeling and simulation for improving the shifting behavior of powertrains with manual or automated transmission. SAE 2006-01-1641
- Song X, Liu J, Smedley D (2005) Simulation study of double clutch transmission for medium duty truck applications. SAE paper 2005-01-3590
- Wang J, Guo K, Lei Y, Tian H (2007) Support vector machine theory based shift quality assessment for automated mechanical transmission (AMT). SAE 2007-1558
- Zhang J, Lei Y, Zong C, Liu H, Hu T (2010) Shift quality assessment system based on neural network for DCT vehicles. Sixth international conference on natural computation (ICNC 2010), 4267–4271
- Tong X (2009) Shift schedule and simulation of automatic transmission. College of automotive engineering, Jilin University, Changchun
- Morteza MG, Amir P (2006) Application of genetic algorithm for optimization of control strategy in parallel hybrid electric vehicles. J Franklin Inst 343:420–435

Correlations Between Subjective and Objective Evaluations of On-Center Steering Feel

Xianglei Zhao, Hui Chen, Bolin Gao, Liming Lou and Nakano Shirou

Abstract With the involvement of SBW system, a total of 12 extensively distributed force feedback characteristics for on-center steering are generated by specific arrangement of adjustable parameters. These characteristics are rated subjectively by 12 drivers in a driving simulator and meanwhile are simulated off-line objectively in accordance with international standards of on-center weave test and transition test. Then the correlations between subjective evaluation items and objective evaluation indices are analysed by multiple regression and logarithmic regression. The results show that for each subjective evaluation item, the mean absolute proportional error of the ratings predicted by each correlation equation is less than 4 %. The proposed methodology can acquire reliable correlations between subjective and objective evaluations and has potentials to be extended to cover other aspects of handling quality.

Keywords Steer-by-wire · On-center · Subjective evaluation · Objective evaluation · Multiple regression

F2012-G05-008

X. Zhao (✉) · H. Chen · B. Gao
School of Automotive Studies and Clean Energy Automotive Engineering Center,
Tongji University, Shanghai, People's Republic of China
e-mail: zhaoxianglei@126.com

H. Chen
e-mail: hui-chen@tongji.edu.cn

L. Lou · N. Shirou
Research and Development Center, JTEKT Co., Ltd, Kashihara, Japan

1 Introduction

Development efforts regarding handling quality of modern cars still primarily depend on purely subjective evaluation, which is subjected to deficiencies in reproducibility, and the period and cost of vehicle evaluation. In order to take full advantage of objective evaluation to make up these deficiencies, several investigations have been conducted to explore the correlations between subjective and objective evaluations by Crolla et al (1-3), Harrer et al (4), Zschicke and Albers (5), and Rothhamel et al (6). One major purpose is to predict the subjective evaluation ratings by the correlations in the development of a new car, including target setting and design optimization [7]. And it is mentioned that the prediction is credible on the condition that the distributions of handling quality in the predictions should be within the ranges of that in the establishment of correlations.

However, in the course of vehicle design and development, the distributions of handling quality may be not merely restricted to the given selections of vehicles in the contemporary automobile market [4, 5], and to the changes of several structural parameters in one vehicle (or vehicle model in the driving simulator) [1, 6]. More extensive distributions probably exist even beyond the capacity of conventional steering system with mechanical linkage. Mean-while, it is assumed that within certain limits the more extensive the distributions of handling quality are, the more significant the correlations between subjective and objective evaluations are. Based on the two aspects above, SBW (Steer-by-Wire) system is proposed as the instrument in correlation analysis to generate relatively extensive distributions of handling quality. It is expected that the correlations obtained with SBW are more reliable, and in this way, the predicted subjective ratings, depending on objective evaluation test, are more credible.

On-center handling quality has been identified as a combination of steering activity, steering feel, and vehicle response. Steering activity mainly refers to steering angle changes. Steering feel mainly refers to reaction torque with regard to steering angle. Vehicle response mainly refers to response characteristics of yaw rate and lateral acceleration [8]. This paper primarily focuses on the development of a methodology which is able to provide reliable correlations between subjective and objective evaluations of on-center steering feel. First, 12 force feed-back characteristics of on-center steering are generated by means of an adjustable force feed-back characteristics model. After subjective and objective evaluation tests, the two sets of test data are analysed with the help of regression analysis to acquire reliable correlations. Finally, another 8 force feedback characteristics are retested to verify the effectiveness of predictions of subjective ratings on basis of correlations.

Fig. 1 Force feedback characteristics model (reaction torque vs. steering angle)

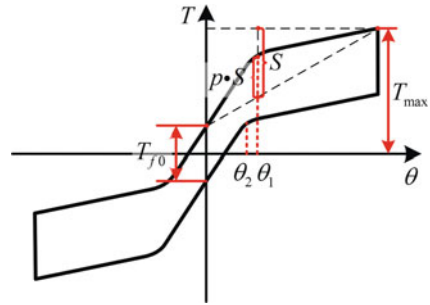


Table 1 Adjustable parameters of the model

Parameter	Description
T_{max}	Peak value of reaction torque
T_{f0}	Friction torque at zero steer
θ_1	Turning angle during steering
θ_2	Turning angle during returning
p	Proportion coefficient

2 Force Feedback Characteristics

2.1 Adjustable Force Feedback Characteristics Model

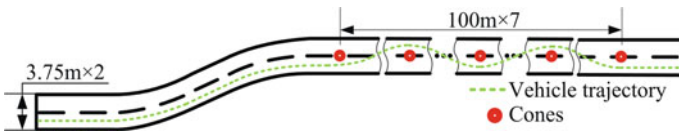
Force feedback of handwheel is obtained by torque map-based method. An adjustable force feedback characteristics model is established depending on steering angle and steering rate. Given that the speeds in the objective and subjective tests are both constants (100 km/h), vehicle speed is not involved in the model. There are 5 adjustable parameters to determine the force feedback characteristics (see Fig. 1 and Table 1) in total, with the hypothesis that the gradients of reaction torque with steering angle when steering and returning are identical.

2.2 Distribution of Force Feedback Characteristics

The combination of different values of 5 adjustable model parameters can generate myriads of force feedback characteristics. Uniform design [9], particularly suitable for multi-factor and multilevel experiments, is employed to acquire more experiment information with less experiment times. For more extensive distributions of steering stiffness at zero steer, turning angle during steering θ_1 is set to be a constant closer to zero. The specific arrangement of remaining four parameters is shown in Table 2.

Table 2 Arrangement of model parameters

Characteristic No.	T_{f0} (N·m)	T_{max} (N·m)	θ_2 (deg)	p
1	0.96	1	2.8	0.42
2	2.16	1.25	4	0
3	0.24	1.5	5.2	0.49
4	1.44	1.75	6.4	0.42
5	2.64	2	2.4	0.56
6	0.72	2.25	3.6	0.14
7	1.92	2.5	4.8	0.63
8	0	2.75	6	0.21
9	1.2	3	2	0.7
10	2.4	3.25	3.2	0.28
11	0.48	3.5	4.4	0.77
12	1.68	3.75	5.6	0.35

**Fig. 2** Road in the virtual scene

3 Subjective Evaluation Test

3.1 Test Drivers and Driving Simulator

A total of 12 normal drivers who have at least one year of highway driving experiences and are familiar with the subjective evaluation items are selected. Furthermore, they are all male and at the age of 20–30. The 12 test drivers are asked to rate the 12 force feedback characteristics in random order in a fixed-base driving simulator. The switch of different characteristics takes less time in the driving simulator than in a vehicle test, which benefits the drivers to compare a new steering feel with the previous one. Because human memory regarding to steering feel usually doesn't last long. The driving speed is set as 100 km/h with cruise control, which is consistent with the objective evaluation test. In the virtual scene, the road (see Fig. 2) is designed to assure that driving manoeuvres on the straight line with cones share similarities with the weave test described in ISO 13674-1 [10] and driving manoeuvres on the corners are generally in line with the transition test described in ISO 13674-2 [11]. The vehicle model is a highly precise passenger car model of vehicle dynamics (veDYNA) provided by TESIS DYNAware.

Table 3 Definition and description of subjective evaluation items

No.	Subjective evaluation Item	Definition	Description of feeling
1	Steering effort	Magnitude of reaction torque over the whole steering angle range	Light/heavy
2	Solid feel	Feel of rigidity of the reaction torque over the whole steering angle range	Flabby/tight
3	Center Feel	Feel of the center position of the handwheel according to reaction torque	Vague/clear
4	Reluctant feel at zero angle	Feel of friction in the area nearby zero angle	Lack of friction/ reluctant
5	Reluctant feel at other angle	Feel of friction in the area besides zero angle	Lack of friction/ reluctant
6	Overall evaluation	A overall rating about the steering feel of certain steering characteristic	Undesirable/ desirable

3.2 Subjective Questionnaire Design

The collection of subjective ratings is guided principally by a questionnaire, so that the test drivers are able to evaluate the steering feel in a quantitative way. The questionnaire includes six subjective evaluation items, i.e. five partial items and one overall item (see Table 3).

To acquire more information about the preferred steering feel, test drivers are asked to rate by means of absolute rather than comparative judgement. Five partial items are expressed using a semantic differential scale [6] ranging from -4 to 4 . Each item is rated on a bipolar scale between two antonymous description words of feeling (see Table 4), where zero equals to the just appropriate feel. In this case, each item has an optimal value, and the judgement has to point out which direction the deviation is perceived. However, in terms of the overall item, the higher the mark, the better the overall steering feel is. So it is expressed by using another semantic differential scale ranging from 1 to 9 (see Table 5). In addition, to reduce the burden of test drivers and assist them to give accurate ratings, all ratings have to be given by two judgements. The first is to judge the current feel is acceptable or not, or desirable or not. The second is to judge the concrete level based on the first judgement. So the judgement of nine levels is converted into two judgements of three levels separately. It is also allowed for drivers to award half mark for increasing the scale resolution. A remark of “don’t know” is available to avoid drivers’ guesses where uncertainty exists. Besides rating, additional comments are encouraged, which is helpful for understanding drivers’ perception of steering feel.

Table 4 Subjective rating scale for partial items

Distinction		Rating
Unacceptable	Extremely (Heavier/tighter...)	+4
	Quite (Heavier/tighter...)	+3
	relatively (Heavier/tighter...)	+2
Acceptable	Slightly (Heavier/tighter...)	+1
	Appropriate	0
	Slightly (Lighter/flabbier...)	-1
Unacceptable	Relatively (Lighter/flabbier...)	-2
	Quite (Lighter/flabbier...)	-3
	Extremely (Lighter/flabbier...)	-4

Note half mark and “don’t know” is available

Table 5 Subjective rating scale for overall item

Distinction		Rating
Desirable	Outstanding	9
	Excellent	8
	Good	7
Marginal	Barely satisfactory	6
	Fair	5
	Unsatisfactory	4
Undesirable	Poor	3
	Deficient	2
	Unsecure	1

Note half mark and “don’t know” is available

4 Objective Evaluation Test

4.1 Test Condition

In objective evaluation test, standardized handling manoeuvres corresponding to on-center weave test [10] by sinusoidal input and transition test [11] by ramp input are implemented successively. In order to avoid the influences caused by drivers’ unstandardized manoeuvres on the measured results, the test is simulated off-line with the same vehicle model as that in the subjective evaluation test.

Table 6 Description of objective evaluation indices

No.	Objective evaluation index	Unit	Description
1	Steering stiffness	N·m/ rad	Average gradient over range $\pm 10\%$ of peak steering angle
2	Torque hysteresis at zero steer	N·m	Ordinate deadband
3	Torque hysteresis at 70 % peak angle	N·m	Torque differences between steering and returning at 70 % of peak steering angle
4	Angle hysteresis	rad	Abscissa deadband
5	Torque at 50 % peak angle	N·m	Torque level at 50 % of peak steering angle
6	Peak value of torque	N·m	The maximum torque level over the whole steering angle range
7	Lateral acceleration at 0 N·m	m/s^2	Lateral acceleration level at 0 N·m
8	Torque hysteresis at 0 m/s^2	N·m	Ordinate deadband
9	Torque gradient at 0 m/s^2	N·m/ (m/s^2)	Gradient evaluated at 0 m/s^2
10	Torque at 1 m/s^2	N·m	Torque level at 1 m/s^2
11	Torque gradient at 1 m/s^2	$\text{N·m}/(\text{m/s}^2)$	Gradient evaluated at 1 m/s^2
12	Torque hysteresis at 1 m/s^2	N·m	Torque differences between steering and returning at 1 m/s^2
13	Steering stiffness at low level of steering angle	N·m/rad	Gradient of straight-line fit to data for right turn direction at low level of steering angle
14	Steering stiffness at high level of steering angle	N·m/rad	Gradient of straight-line fit to data for right turn direction at high level of steering angle
15	Torque deadband reference lateral acceleration	N·m	Abscissa deadband at ordinate threshold of $\pm 0.6 \text{ m/s}^2$

Note The 1st to 12th indices are derived from weave test, and the other indices are derived from transition test

4.2 Derivation of Objective Evaluation Indices

Steering angle, reaction torque, and lateral acceleration are recorded separately. Then the three measured variables are mapped in pairs against each other in a Cartesian coordinate system. Thus the corresponding hysteresis curves are generated, which enables the derivation of objective evaluation indices (see Table 6).

5 Correlations Between Subjective and Objective Evaluations

Owing to the complexity of steering feel, multiple linear regression analysis is more suitable than single. So multiple linear regression analysis based on ordinary least squares estimation is applied for each partial subjective evaluation item respectively. Moreover, the influences of 5 partial items on the overall item are also identified.

5.1 Data Preprocessing

To obtain the credible regression coefficients, fundamental data preprocessing is necessary to be conducted. For subjective evaluation ratings, since the entire test drivers are selected from normal drivers, instead of professional drivers, outliers in the ratings are obliged to be rejected to ensure the consistency and reliability of 12 ratings of each subjective evaluation item. Because of the relatively small sample size ($n = 12$), Chauvenet's criterion [12] is applied, according to which, the ratings outside $\pm 2.03\sigma$ (when $n = 12$) are supposed to be rejected. After that, the remaining qualified ratings are averaged as the values of dependent variable in the regression equation. For objective evaluation indices, the unconvincing independent variables are removed preliminarily from all the indices according to their physical meaningful sense by engineers. For example, when "Steering Effort" is chosen as the dependent variable, "Angle Hysteresis" and "Lateral Acceleration at 0 N·m" is not accountable enough to be selected as independent variables and have to be removed, even if they show a strong linear correlation with "Steering Effort".

5.2 Establishment of Regression Model

The multiple regression equation is specified as follows:

$$y = \beta_0 + \beta_1 x_1 + \beta_2 x_2 + \dots + \beta_p x_p \quad (1)$$

Where, there are a total of p independent variables. $\beta_0, \beta_1, \dots, \beta_p$ are partial regression coefficient. y denotes the dependent variable, i.e. subjective evaluation item. And x_i denotes the independent variable, i.e. objective evaluation index. To determine the involvement of qualified independent variables further, stepwise selection [13] is used. Besides, the independent variable that shows multicollinearity with other variables is excluded during the establishment of regression equations.

5.3 Statistical Test

Without statistical tests, the acquired regression equations cannot go to analysis and prediction in practice directly. In general, the statistical tests mainly includes test of goodness of fit, significance test of regression equations, significance test of regression coefficient, and residual analysis as well.

Test of goodness of fit serves to measure the quality of the fit of model to the data, which can be assessed by adjusted coefficient of determination \bar{R}^2 . Only the

regression equation that satisfies the condition $\bar{R}^2 \geq 0.85$ is considered as qualified. Significant test of regression equation is used to decide if the linear relationship between dependent variable and all the independent variables is significant, while significant test of regression coefficient is employed to check whether each independent variable in the regression equation could interpret the linear variation of dependent variable effectively. The observed p value in F-test and t test (except for constant term) should be both less than significance level α , set as 0.05. Residual analysis assumes two main tasks: (1) to detect whether the residuals conform to normal distribution with mean zero and equal variance; (2) to check whether residual sequence is independent. Both of the tasks are fulfilled using residual diagram that is plotted by independent variable on the horizontal axis, and unstandardized residual on the vertical axis.

5.4 Results

Multiple regression analysis results are shown in Table 7. For five partial items, partial regression coefficients which allow the prediction of subjective evaluation ratings are pointed out. Their uncertainties are quantified by the lower and the upper limits of 95 % confidence interval. Further, to discriminate the major and minor objective evaluation indices that correlate with the same subjective evaluation item, standardized regression coefficients are also figured out. The larger the absolute value of standardized regression coefficient is, the more important the corresponding objective evaluation index is. For the overall item, it is rated by unipolar scale while all the other partial items are rated by bipolar scale. To explore the linear influence that each partial item has on the overall one, the absolute value of five partial subjective evaluation items are regarded as the independent variable.

The linear correlations between six subjective evaluation items and their corresponding independent variables all enjoy suitably high values of the statistical indicators: $\bar{R}^2 > 0.85$, p -values in F test and p -values in t test are less than significance level 0.05 and the residuals are all scattered randomly around zero without evident regularity and tendency as the increase of the major independent variable, which meets statistical tests. Figure 3 is an example of residual diagram.

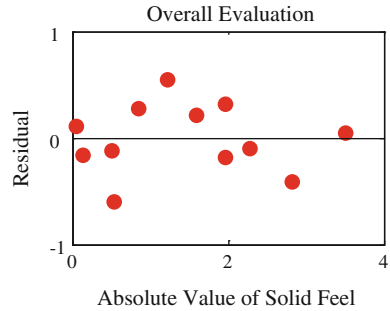
5.5 Discussion

“Steering Effort” is found to correlate most to “Peak Value of Torque”, which is reasonable to understand. In most cases, a higher “Peak Value of Torque” usually leads to a stronger feeling of heaviness over the whole steering angle range.

Table 7 Multiple regression analysis results

Subjective evaluation item	Objective evaluation index	Regression coefficient (standardized)	Confidence interval	p-value in t-test	p value in F-test	\bar{R}^2
Steering effort	Peak torque	1.739(0.978)	(1.476, 2.002)	0	0	0.952
	Constant	-3.918(-)	(-4.953, -3.243)	0		
Solid feel	Steering stiffness at low level of steering angle	0.138(0.778)	(0.111, 0.166)	0		0.953
	Torque gradient at 1 m/s ²	2.784(0.402)	(1.708, 3.859)	0	0	
	Constant	-3.357(-)	(-3.824, -2.890)	0		
Center feel	Angle hysteresis	-6.250(-0.644)	(-8.671, -3.829)	0		0.943
	Torque gradient at 0 m/s ²	0.595(0.394)	(0.219, 0.972)	0.006	0	
Reluctant feel at zero angle	Constant	-0.639(-)	(-1.570, 0.293)	0.155		0.915
	Torque hysteresis at zero steer	1.603(0.147)	(1.276, 1.931)	0	0	
	Constant	-2.402(-)	(-2.922, -1.882)	0		
Reluctant feel at other angle	Torque hysteresis at 70 % maximum angle	1.511(0.952)	(1.245, 1.776)	0		0.940
	Peak Torque	-0.294(-0.204)	(-0.534, -0.053)	0.022	0	
Overall evaluation	Constant	-2.144(-)	(-2.876, -1.413)	0		0.914
	Absolute value of solid feel	-0.950(-0.899)	(-1.162, -0.738)	0		
	Absolute value of reluctant feel at zero angle	-0.747(-0.425)	(-1.100, -0.394)	0.001	0	
	Constant	6.383(-)	(5.810, 6.956)	0		

Fig. 3 An example of residual diagram



“Solid Feel” correlates best to “Steering Stiffness at Low Level of Steering Angle” derived in the transition test and “Torque Gradient at 1 m/s²” derived in the weave test. The former is the major influencing index. This result means drivers assign more importance to the stiffness of reaction torque with steering angle at lower steering rate when steering activities are less, and begin to pay more attention to the stiffness of reaction torque with lateral acceleration as the steering activities increase. Since drivers are mostly driving with less steering activities at high speed, so “Steering Stiffness at Low Level of Steering Angle” is more essential.

“Center Feel” has a strong linear correlation with “Angle Hysteresis” and “Torque Gradient at 0 m/s²”, and the linear relationship with the former is stronger. As far as “Angle Hysteresis”, the lower its value is, the better the returnability is, which gives rise to easier detection of center position. However, just a low level of “Angle Hysteresis” is insufficient. A higher level of “Torque Gradient at 0 m/s²” is also indispensable to build a favourable “Center Feel”.

“Reluctant Feel at Zero Angle” is fully self-explanatory by “Torque Hysteresis at Zero Steer”. It is mentionable that drivers are more likely to experience the reluctant feel on the hysteresis curve of reaction torque vs. steering angle, rather than reaction torque vs. lateral acceleration.

“Reluctant Feel at Other Angle” is described in a linear manner by “Torque Hysteresis at 70 % Maximum Angle” and “Peak Torque”. There is no doubt the former is primary influencing factor. Whereas it may be confusing that “Peak Torque” is another independent variable. Practically, this is caused by inherent physical senses of humans. With the rise of reaction torque, the subjective reluctant feel will be weaker. This is also confirmed by drivers’ comments during the subjective evaluation test. However, “Reluctant Feel at Zero Angle”, similar with “Reluctant Feel at Other Angle”, has nothing with any objective evaluation index related to reaction torque. It is because the reaction torque around zero angle is generally not large.

“Overall Evaluation” is chiefly covered by “Solid Feel” and “Reluctant Feel at Zero Angle”. The former is more significant in judging the overall on-center steering feel. However, it cannot illustrate that the other three partial items are of little contributions on “Overall Evaluation”. It is shown that the correlation coefficient R between “Steering Effort” and “Solid Feel” is 0.914. And “Center Feel” is a combination of “Solid Feel” and “Reluctant Feel at Zero Angle”, in

which the multiple regression coefficient is 0.991. These two relationships are accountable by the descriptions of corresponding subjective evaluation items and can be elicited from the drivers' comments as well. Besides, the correlation between "Reluctant Feel at Zero Angle" and "Reluctant Feel at Other Angle" is also significant ($R = 0.954$). This is found to be caused by the strong correlation between "Torque Hysteresis at Zero Steer" and "Torque Hysteresis at 70 % Maximum Angle" ($R = 0.958$), which results from the present arrangement of parameters in the adjustable force feedback characteristics model.

As a whole, \bar{R}^2 in the 6 regression equations are all greater than 0.91. It verifies the hypo-thesis effectively that more extensive distributions of steering feel give rise to the detection of more significant correlations between subjective and objective evaluations. So the predictions of subjective ratings based on acquired regression equations are likely to be more credible.

6 Verification

To verify validity of the predictions, another 8 force feedback characteristics are distributed in accordance with uniform design again, in which the ranges of four adjustable parameters are within the ranges of that in the previous 12 characteristics. Then the subjective evaluation test and objective evaluation test are performed in the same way as the previous tests. Figure 4 shows the prediction results of each subjective evaluation item in the shape of radar map. The 8 numerical axes represent 8 force feedback characteristics. It can be seen that the predicted ratings are comparatively close to the average ratings given by test drivers, and almost all the predicted ratings are located within 95 % confidence interval, apart from the prediction of "Steering Effort" for the 8th characteristic. Also, it can be seen from Table 8 that the maximum and mean absolute error of predictions of "Steering Effort" are both larger than that of others. It is speculated that there is a more convincing relationship accountable for the correlation between "Peak Value of Torque" and "Steering Effort". Taking advantage of scatter diagram (see Fig. 5), it is found that all the data point are likely to be fitted better by logarithmic curve. The form is as follows:

$$y = \beta_0 + \beta_1 \ln(x) \quad (2)$$

Essentially, it is also a linear regression model, since $\ln(x)$ can be considered as transformation of variable x . The results (see Table 9) show that the logarithmic regression equation meets all the requirements of statistical tests. Most importantly, the adjusted coefficient of determination \bar{R}^2 is improved from 0.952 to 0.978, and the maximum and mean absolute error is reduced from 1.023 to 0.786 and from 0.392 to 0.318 respectively. The revised prediction results are also shown in Fig. 4.

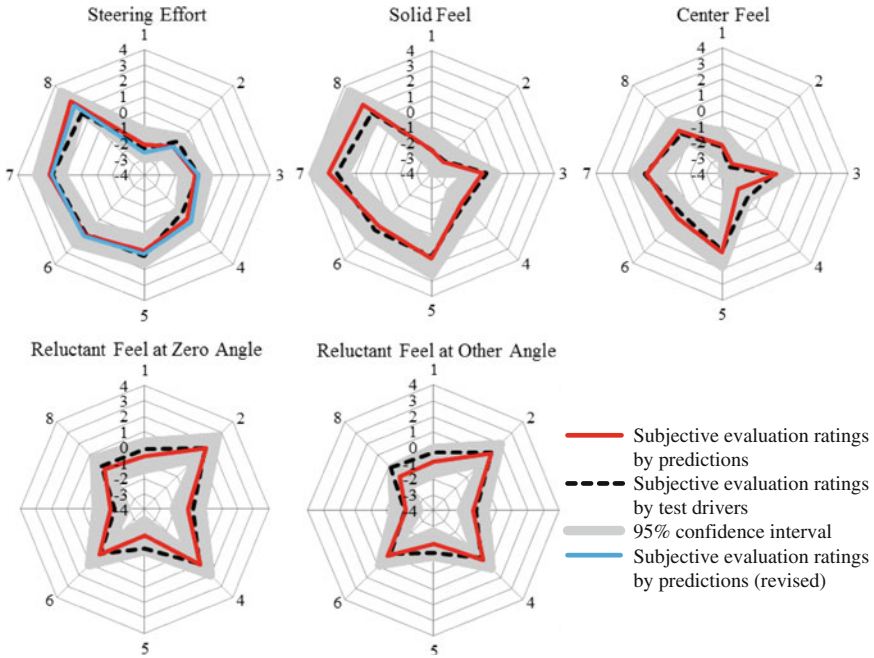


Fig. 4 Comparison of subjective evaluation ratings by prediction vs. by test drivers

Table 8 Error statistics of the predictions

Statistical Error	Steering Effort	Solid Feel	Center Feel	Reluctant Feel at Zero Angle	Reluctant Feel at Other Angle
Maximum Absolute Error	1.023	0.794	0.816	0.856	0.828
Mean Absolute Error	0.392	0.313	0.286	0.310	0.341

Fig. 5 Scatter diagram of "steering effort"

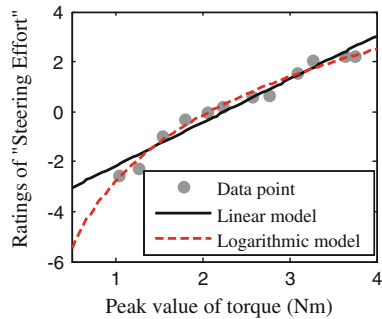


Table 9 Logarithmic regression results for “Steering Effort”

Subjective Evaluation Item	Objective Evaluation Index	Regression Coefficient	p-value in t-test	p-value in F-test	\bar{R}^2	Absolute Error	
						Maximum	Mean
Steering Effort	Logarithm of Peak Torque	3.382	0	0	0.978	0.786	0.318
	Constant	-2.811	0				

To sum up, for each subjective evaluation item, the maximum absolute error is around 0.8, while the mean absolute error is around 0.3. Comparing with the range of the rating scale, i.e. 9, the mean absolute proportional error is less than 4 %. So it can be concluded that the acquired five regression equations are available to predict the corresponding subjective ratings.

7 Conclusion

In this paper, a new methodology with the involvement of SBW is proposed to gain reliable correlations between subjective and objective evaluations. With multiple regression and logarithmic regression, the adjusted coefficients of determination \bar{R}^2 in 6 regression equations are all greater than 0.91, which serves as proof that extending the distributions of steering feel is constructive to the identification of significant correlations. The predictions based on regression equations work well with the mean absolute proportional error for each subjective evaluation item less than 4 %. In addition, “Steering Stiffness at Low Level of Steering Angle”, “Torque Gradient at 1 m/s²” and several other objective evaluation indices are regarded as key factors to achieve an exceptional on-center steering feel.

As future work, the ideal ranges of key objective evaluation indices are supposed to be identified for target setting in vehicle development on basis of acquired regression equations. Also, if the proposed methodology can be extended to cover vehicle response in a moving-base simulator, the complex handling quality will be interpreted more subtly.

References

1. Crolla DA, Chen DC (1998) Vehicle handling behavior: subjective V. Objective comparisons. FISITA World Automotive Congress, Paris
2. Crolla DA, King RP, Ash HAS (2000) subjective and objective assessment of vehicle handling performance. FISITA World Automotive Congress, Seoul

3. King RP, Crolla DA, Ash HAS (2002) Identification of subjective-objective vehicle handling links using neural networks for the foresight vehicle. SAE World Congress, Detroit
4. Harrer M, Pfeffer PE, Johnston DN (2006) Steering feel-objective assessment of passenger cars—analysis of steering feel and vehicle handling. FISITA World Automotive Congress, Yokohama
5. Zschocke AK, Albers A (2008) Links between subjective and objective evaluations regarding the steering character of automobiles. *Int J Automot Technol* 9(4):473–481
6. Rothhamel M, Ijkema J, Drugge L (2011) A method to find correlations between steering feel and vehicle handling properties using a moving base driving simulator. *Veh Syst Dyn* 49(12):1837–1854
7. Data SC, Frigerio F (2002) Objective evaluation of handling quality. *Proc Instn Mech Engrs, Part D: J Automobile Eng* 216:297–305
8. Farrer DG (1993) An objective measurement technique for the quantification of on-center handling quality. *Int Congr Exposition, Detroit*
9. Fang KT (1980) The uniform design: application of number-theoretic methods in experimental design. *Acta Mathematicae Applicatae Sinica* 3(4):363–372
10. International Standard ISO 13674-1(2003) Road vehicles—test method for the quantification of on-centre handling—Part 1 weave test 1st ed Switzerland
11. International Standard ISO 13674-2 (2006) Road vehicles—test method for the quantification of on-centre handling—Part 2 transition test 1st ed Switzerland
12. Taylor JR (1997) An introduction to error analysis: the study of uncertainties in physical measurements. University Science Books, Sausalito, pp 166–170
13. Wei X (2011) Data analysis on basis of SPSS. China Renmin University Press, Beijing, pp 234–235

Using Chassis Tuning Technology in Chassis Design of Car

Xiang Meng, Wei Chen, Huihui Xue, Wei Liu, Zhijie Pan
and Fuquan Zhao

Abstract Good or bad automotive quality mainly reflected in the advantages and disadvantages of vehicle performance, Tuning Technology use method of combining subjective and objective, adding simulation to give product correct position in the process of earlier scheming, to ensure product has good performance in the process of designing, to optimize product performance, and to ensure good chassis performance and vehicle performance. Summarize chassis tuning flow which provides basis for future car.

Keywords Chassis tuning · Design objectives · Hardpoints design · ADAMS/Car

F2012-G05-010

X. Meng (✉) · W. Chen · H. Xue · W. Liu · Z. Pan · F. Zhao
Zhejiang Geely Automobile Research Institute CO. LTD, Hangzhou, China
e-mail: mengfei197993@163.com

W. Chen
e-mail: chenwei@rd.geely.com

H. Xue
e-mail: xuehh@rd.geely.com

W. Liu
e-mail: liuw@rd.geely.com

Z. Pan
e-mail: panzhijie@rd.geely.com

F. Zhao
e-mail: zhaofuquan10@163.com

1 Introduction

With the rapid development of auto industry in modern society, people demand more and more requirements on the quality of auto, every OEM must raise the product performance on the basis of low-cost, like this platform design become a hot topic today. Platform design ensure product has better basic performance, but can't ensure every car has unique properties, so chassis tuning technology is paid more attention to automotive designing and developing. The purpose is to meet demand of projection by tuning damper, tire, spring, anti-rod, bushing, steering, body and parameters of suspension, to optimize and balance handling and riding by theoretic analysis and tuning [1]. the basic flow chart is shown in the Fig. 1.

The traditional design only designs vehicle itself, but now performance is ensured in automobile design from all aspects and each link, For example, safety, riding comfort, durability, reliability and operation stability etc. Due to the limited context, take A car as an example, this paper expounds using chassis tuning technology in chassis design of car from the view of handling and stability, comfort, product design. Expounding the process how chassis tuning technology ensure product performance in every stage of design, the paper summarizes the flow chart of chassis tuning to guide the further automotive design (Fig. 2).

2 Chassis Tuning Technology can Properly Recognize the Quality of Auto

OEM designs vehicle to sell, in order to have better profit, the car must meet the needs of customers and market. With the improvement of living standard, people have more in pursuit of the car, different customer have different request. So the quality of auto should be recognized in the early stages of product development. The handling and stability and the comfort are two aspects of conflict, chassis tuning technology synthetically evaluate the performance of competitive vehicle from subjective evaluation and objective testing, to ensure the target of performance based on market positioning of auto. A car is Sport multifunctional Vehicle, and its competitive vehicles are B car and C car, we evaluate competitive vehicles from subjective evaluation and objective testing to ensure the performance target of A car. The evaluation results are shown in Fig. 3.

The main sale market is China for A car, in China, consumers demand better comprehensive performance, meanwhile, the road is not good, so the final design target for A car : primary ride and secondary ride close to B car level, partial performance exceed it, handling close to B car level and the quality target car is B car.

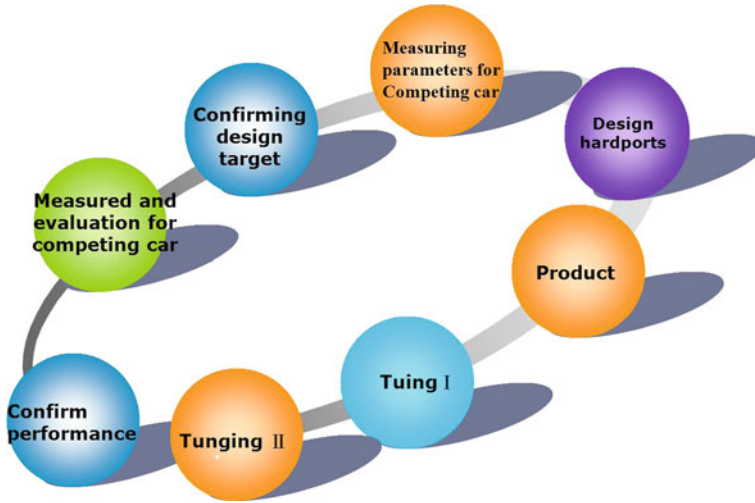
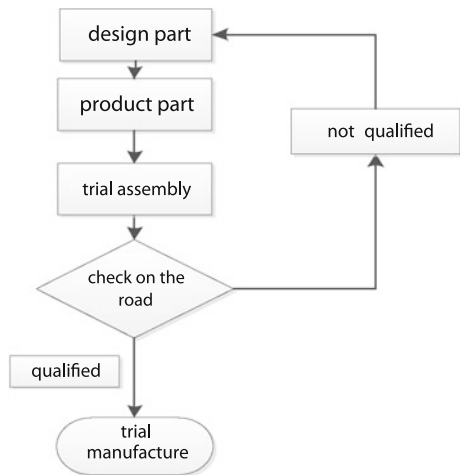


Fig. 1 Flow of chassis tuning

Fig. 2 Traditional design flow



3 Chassis Tuning Guides Design at Performance Point

How to ensure the designed product meets design target which is complicated and arduous task. Chassis tuning emphasizes on design hardpoints in the stage of designing because hardpoint is the basis of chassis design, whether the hardpoint is reasonable or not directly affect chassis and vehicle performance. Its main evaluating indicator is K&C features, chassis tuning emphasizes on the K&C of new car must meet target car. Only using simulation to analyze performance at the stage of designing, now, ADAMS/Car is essential or minor design soft for auto, it

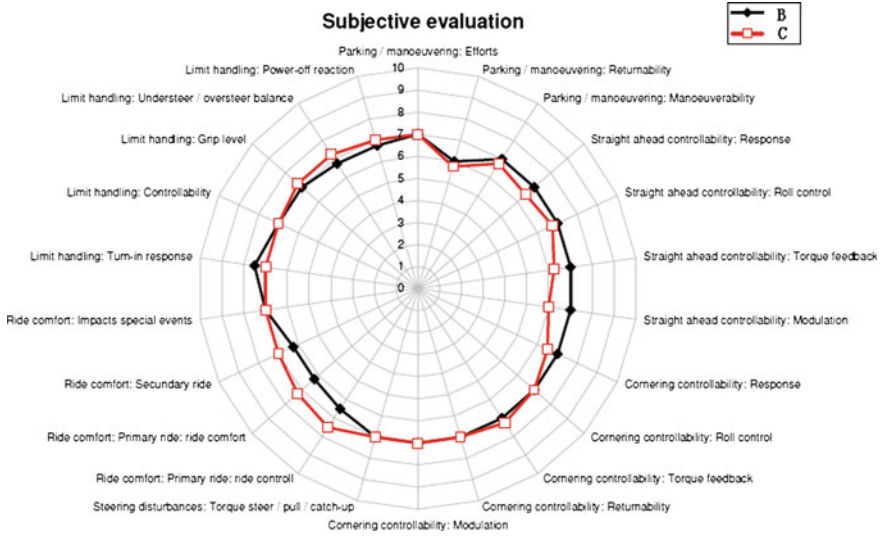
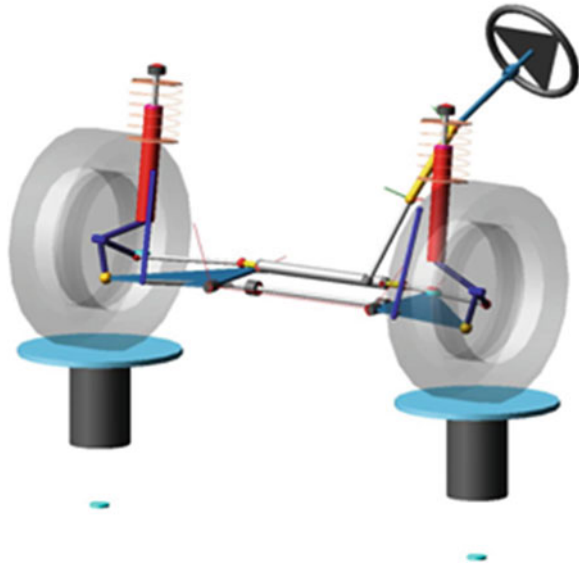


Fig. 3 Radar figure of B car and C car

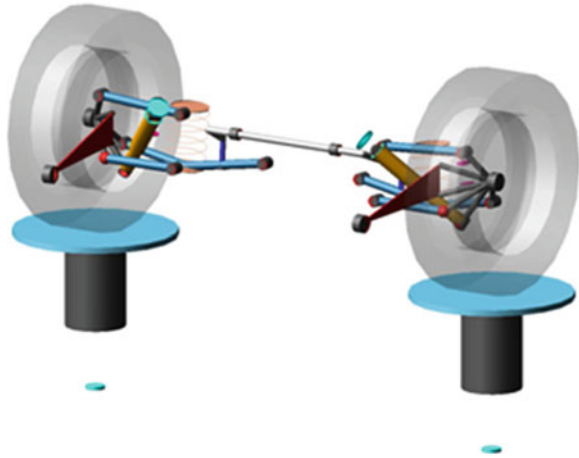
Fig. 4 A car ADAMS model of front suspension



has various kinds of functions of simulation and optimize, which is main tools of designing auto.

According to original hardpoints of A car to build ADAMS model, as shown in Figs. 4 and 5, the result of simulation shows the curve of toe VS travel cannot meets design target in the front suspension, shown in Figs. 6 and 7, Z coordinate of tierod Outer is main factor of affecting it [2], adjust the Z coordinate of tierod

Fig. 5 A car ADAMS model of rear suspension



Outer from -104 to -102 mm, as shown as blue curve in Fig. 6 which meets design target. Similarly, the curve of toe VS travel cannot meets design target in the rear suspension, shown as Figs. 8 and 9, adjust the Z coordinate of SCA outer from -124.2 to -120.7 mm, as shown as blue curve in Fig. 7 which meets design target. Like this, check every design target, and finish design work for hardpoints.

4 Chassis Tuning Make Product to has Exclusive Performance

Ride performance is dynamic performance of car [3], and has many factor affect it, for example, spring, bump stop, bushing in the suspension system, top mount, stiffness, weight, inertia of part etc., that cannot be optimized by calculating and simulation. For instance, spring, we have difficult to hold moving weight performance of it. Meanwhile, stiffness of bushing and pad is non-linear, we cannot correctly describe its performance, so real car tuning is absolutely necessary.

1. Simulation to confirm specifications of tuning part

Stiffness of spring, radial of anti-rod and damp of damper are main factor affecting handling and riding, so real car tuning has two steps, tuning spring and anti-rod, tuning damper. We adopt subjective to match different spring and anti-rod to confirm final project, but we cannot confirm optimization direction if we do not fully know performance of A car before tuning, we must prepare a lot of different specification spring and anti-rod to meet tuning demand. Like this, we adopt simulation and adjust stiffness of spring and radial of anti-rod, to tuning optimal performance parameter in the computer, to induce the number of spare part. The Table 1 shows the process of confirm spring and anti-rod.

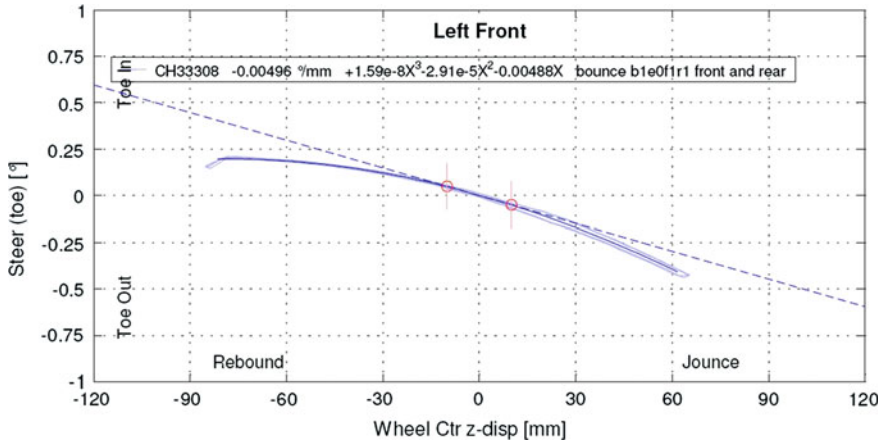


Fig. 6 B K&C test data of front suspension

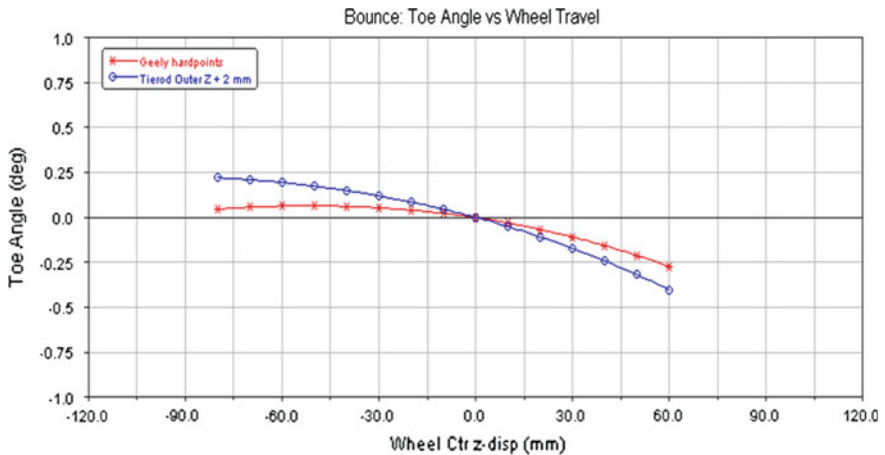


Fig. 7 A simulation curve of front suspension

2. Subjective evaluation

According to simulation result, we evaluate real car from Favor objective to Spare objective to confirm the specification of spring and anti-rod, and make sure the handling is acceptable; then adjusting damping of damper, mainly adjusting valve, spring, aperture inner the damper, relating to piston valve and base balve, the piston valve relate to rebound damper force and the latter relate to compression damper force. The Fig. 10 is the rebound force chart of damper, it shows the curve is divided into three sections, separately express damping curve which damper is working in the low speed, middle speed and high speed, adjusting them to confirm

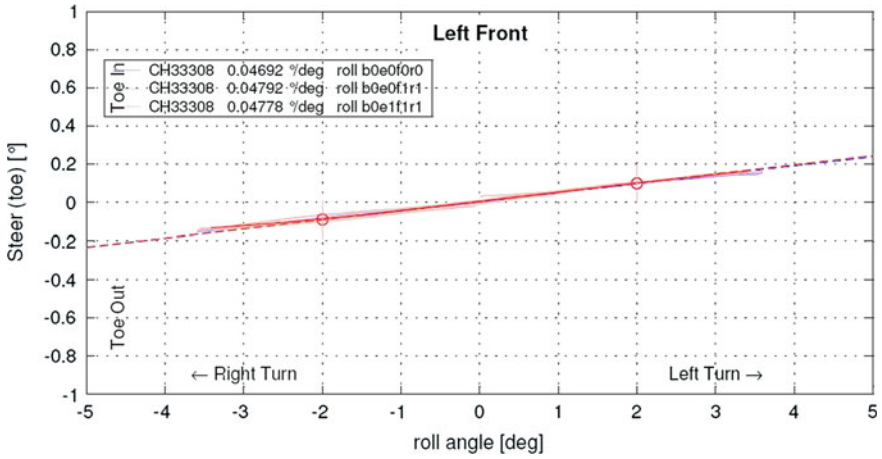


Fig. 8 B K&C test data of rear suspension

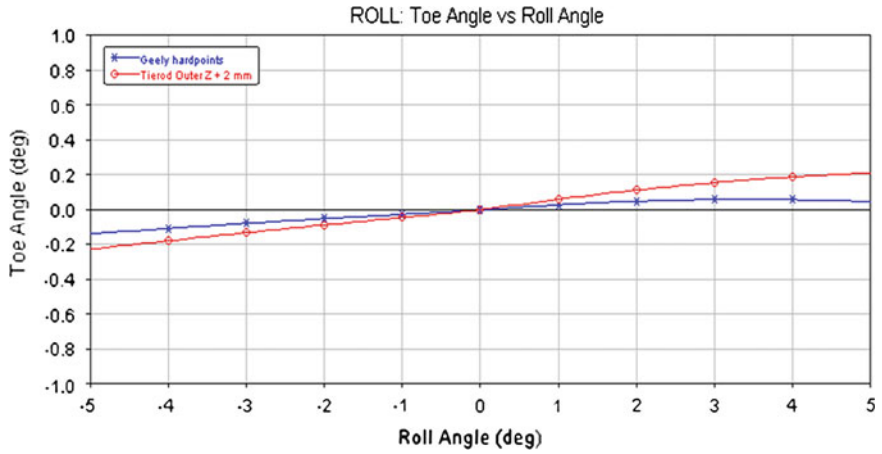


Fig. 9 A simulation curve of rear suspension

Fig. 10 The rebound force chart of damper

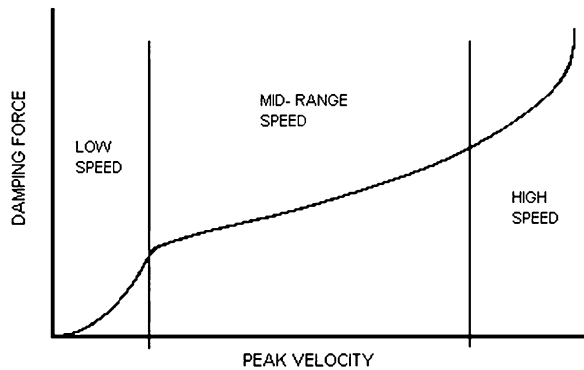


Table 1 The process of confirm spring and anti-rod for A car

Project	Front spring (K/mm)	Front anti-rod (mm)	Rear spring (K/mm)	Simulation result	Remarks
Initial	30	26	72.5	Every performance index are all acceptable	
Tuning 1	28.5	26	72.5	Degree of understeer get smaller, roll angle of body get bigger	
Tuning 2	31.5	26	72.5	Degree of understeer get bigger, resonant frequency get bigger, roll angle of body get smaller	Spare objective
Tuning 3	31.5	25	72.5	Roll angle of body get bigger, resonant frequency get smaller, responding of lateral acceleration get faster	
Tuning 4	31.5	27	72.5	Roll angle of body get smaller, resonant frequency get bigger, responding of lateral acceleration get slower	
Tuning 5	31.5	28	72.5	Roll angle of body get smaller, resonant frequency get bigger, responding of lateral acceleration get slower	
Tuning 6	31.5	26	70	Degree of understeer get bigger, roll angle of body get bigger, resonant frequency of body get smaller	
Tuning 7	31.5	26	75	Degree of understeer get smaller, roll angle of body get smaller, resonant frequency of body get bigger	Favor objective
Tuning 8	30	26	70	Degree of understeer get bigger, resonant frequency of body get smaller	Spare objective
Tuning 9	30	27	70	Degree of understeer get bigger, roll angle of body get smaller, resonant frequency of body get smaller	Spare objective

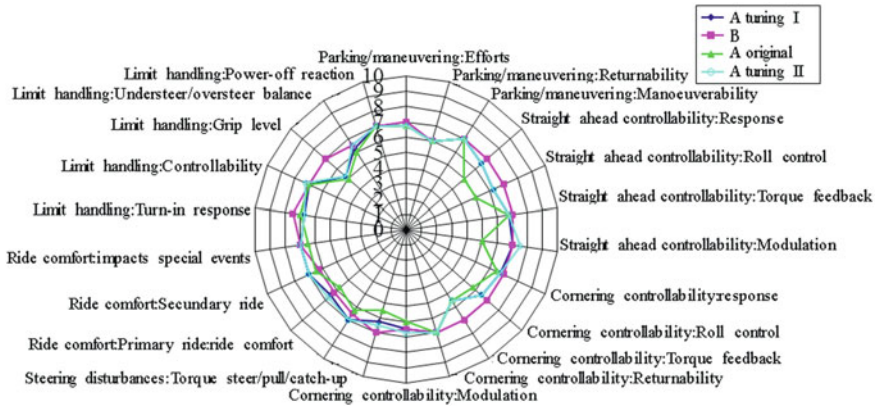


Fig. 11 Radar figure of B car and C car

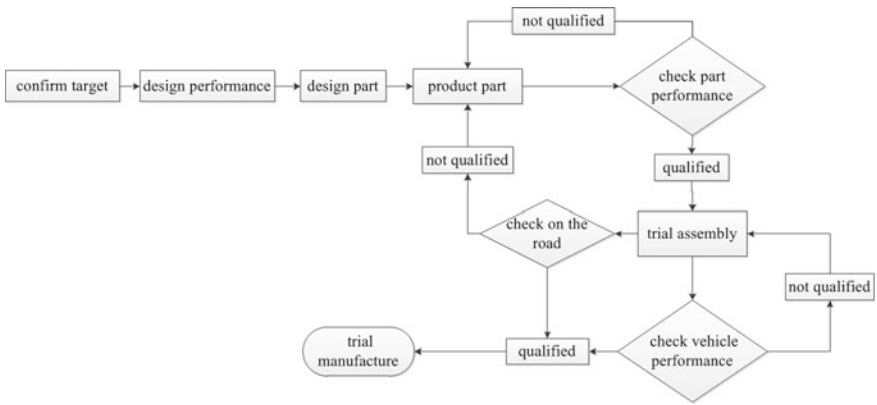


Fig. 12 Chassis tuning flow

riding, like this following to complete every tuning to achieve optimal combination handling with riding. the result of tuning for A car is shown in the Fig. 11.

5 Chassis Tuning Flow

Chassis tuning penetrates into each stage of chassis design to obtain better performance, including determine target, design performance, optimize and validate performance. Through setting reasonable target, accurate hard-point design and tuning, A car obtains better performance and achieves the design goal. The flow chart of chassis tuning we summarized is shown in the Fig. 12.

There are many factors affecting handling and stability, comfort, this paper mainly discuss spring, stabilizer bar and absorber. The tyre also impacts chassis

tuning, including velocity ranged, load capacity, tire noise, drainage performance, steering performance, rolling resistance, etc. If the tyre is soft, the car will has better comfort, but it will play down the performance of handing. On the other hand, hard tyre can increase the performance of handing, but it will increase tire noise. The paper only discuss handing and stability, comfort, not relate to NVH performance.

References

1. Zhang H (1999) Vehicle design. Mechanical industry Press, Beijing
2. Yu Z (2008) Automobile theory, 4th edn. Mechanical industry Press, Beijing
3. GB/T 12549-1990. Automotive controllability and stability-Terms and definitions

Research of the Correlation of Vehicle Handling Subjective Evaluation and K&C Characteristics

Yanding Yang, Yinghao Li, Zhi Yue, Chaobin Wang, Mengchun Chen, Jianxian Chen, Gan Chen and Jie Bai

Abstract *Research Objective* Vehicle ride and handling, which is important to the overall vehicle safety, is one of the performances that the customers are most concerned about. Therefore, the vehicle handling development, highly relied on subjective evaluation, is indispensable during the vehicle development process. Suspension K&C (Kinematics and Compliance) characteristics, which have direct influence on vehicle handling performance, are the key technique targets during vehicle design and validation processes. However, due to the lack of reliable link between subjective assessments and K&C objective measurements, lots of chassis tuning work still need to be done in order to accomplish the vehicle handling development targets, even though advanced design and CAE tools have already widely used in chassis design. In this paper, a methodology of analyzing the

F2012-G05-011

Y. Yang (✉) · Y. Li · Z. Yue · C. Wang · M. Chen · J. Chen · G. Chen · J. Bai
Dongfeng Motor Corporation Technical Center, Wuhan, China
e-mail: yangyd@dfmc.com.cn

Y. Li
e-mail: liyh@dfmc.com.cn

Z. Yue
e-mail: yuezhi@dfmc.com.cn

C. Wang
e-mail: wcb@nast.com.cn

J. Chen
e-mail: chenjx@dfmc.com.cn

G. Chen
e-mail: cheng@dfmc.com.cn

J. Bai
e-mail: baij@dfmc.com.cn

correlation between subjective evaluation and K&C measurements is further studied in order to reduce the developing time and cost. *Methodology* In this paper, six popular cars in Chinese market were chosen for subjective assessments by expert six drivers and K&C objective tests by test rig. In the subjective assessment, some parameters of the vehicle were evaluated. On the K&C test rig, the vehicles were measured in different load cases such as vertical test, roll test, side force test, brake force test, etc. And then a statistical methodology of multiple regressions was applied to analyze the correlation between K&C measurement results and subjective assessments. According to the multiple regression analysis, the correlations of K&C characteristics and subjective evaluation can be defined by coefficient, and the regression equation can be used to predict the subjective evaluation results of the vehicle. *Results* With this methodology, vehicle handling performance is more predictable and the relationships between subjective handling and K&C characteristics are more reliable. *Limitations of this study* The mainly limitation of this study is the accuracy of the regression equation. In order to increase the credit of regression equation, more vehicle samples need to be test in the future work. What does the paper offer that is new in the field: Although a lot of studies have already done in K&C and vehicle handling performance field, the link between K&C and vehicle handling subjective feelings is still lack of reliability. In this paper, using multiple regression to study the correlation between subjective evaluation of vehicle handling and K&C objective measurement is a new methodology in this field. *Conclusion* This research can reduce the chassis tuning work cycles during vehicle handling development and will also benefit the cost and time savings.

Keywords Subjective evaluation · K&C characteristics · Correlation · Regression analysis

1 Background

Customers of today have increasingly requirements for vehicle performance, especially for vehicle ride and handling. According to the purchasing intention analysis by J. D. Power 2011, the top three considerations for car purchasing are ride comfort, handling convenience and good-appearance [1]. Therefore, vehicle ride and handling is one of the major factors influencing vehicle sales, and thus need to pay special attention during the development process.

In the vehicle ride and handling development process, it is very difficult to achieve the target through early-stage design and simulation. Hence chassis tuning and optimization, mainly based on subjective evaluation and K&C object measurements, is still indispensable in order to achieve the best compromise between vehicle ride and handling. In this paper, we try to study the link between subjective evaluation and K&C objective measurements, and by the methodology we studied,

Table 1 Rating rules of subjective evaluation [5]

Rating	Vehicle condition	Customers' perception	Judgment from motor companies
1	Vehicle fails to meet safety requirements	All customers can feel	Not producible
2	Vehicle has a breakdown	All customers can feel	Not producible
3	Vehicle condition leads to customers' annoyance	All customers can feel	Not producible
4	Vehicle is deficient	Average customers' complain	Not producible
5	Vehicle is deficient	Average customers can reluctantly accept	Border Line
6	Vehicle is barely satisfactory	Critical customers can feel	Can be released to the market
7	Vehicle is good	Critical customers can feel	Can be released to the market
8	Vehicle is very good	Only experienced observers can feel	Can be released to the market
9	Vehicle is excellent	Only experienced observers can feel	Can be released to the market
10	Vehicle is outstanding	Not perceptible	Can be released to the market

it is imply that part of K&C characteristics are highly correlated with vehicle subjective handling feelings. The study results can reduce the chassis tuning work cycles during vehicle handling development and will also benefit the cost and time savings.

2 Method of Subjective Evaluation

2.1 Rating Rules of Subjective Evaluation

On the basis of customers' definition of their perception of vehicles, the subjective evaluation uses a 10-point scale. In the development process of vehicle ride and handling, each index of subjection evaluation must reach 5 points before the car is put on the market. See Table 1 for specific rating rules:

2.2 Items of Subjective Evaluation

In the development process of vehicle ride and handling, items of subjective evaluation include ride, acoustic comfort, steering comfort, starting performance, linear driving performance, steering pleasure, bend performance, and brake performance. See Table 2 for specifications of each item.

Table 2 Description of subjective evaluation [6]

Description	
Ride comfort	Spring response and road copying on rough road Replicating track surface lateral (left/right) Body damping, body vibration die-out
Acoustic comfort	Rolling noise Body damping, body vibration die-out Chassis noise (rumbling and rattle)
Steering comfort	Steering torque, parking effort Steering wheel vibration Steering wheel turn shocks
Drive-away characteristics	Drive-away squat Traction Direction stability
Straight-ahead driving	Direction stability on even road Direction stability on uneven road Sensitivity on longitudinal road joints Flick steer
Steering behavior	Steering response Center point feeling Reaction after steering input Steering torque characteristic Lane change Aiming accuracy
Cornering ability	Self steering response Rolling behaviour Rolling steering on uneven road Turn-in ability, lateral force response Load alteration effect
Brake performance	Brake stability straight ahead Braking behavior on uneven road Braking behavior in curves Brake diving/pitching

Table 3 Conditions and Items of K&C Measurement [2, 3, 7]

Conditions	Items of objective measurement
Steering kinematics	Caster (deg)
	Kingpin inclination (deg)
	Caster trail (mm)
	Scrub radius (mm)
Vertical travel	Steering ratio
	Wheel rate (N/mm)
	Tire vertical stiffness (mm/kN)
	Toe angle change (min/cm)
	Camber angle change (min/cm)
	Caster angle change (min/cm)
	Height of roll center change rate (mm/mm)
Rolling	Wheelbase change (mm/cm)
	Roll rate (N/mm)
	Axle steer (min/°)
Braking force	Toe angle change (min/kN)
	Camber angle change (min/kN)
Accelerating force	Longitudinal stiffness (mm/kN)
	Toe angle change (min/kN)
	Camber angle change (min/kN)
Lateral force	Longitudinal stiffness (mm/kN)
	Toe angle change (min/kN)
	Camber angle change (min/kN)
Aligning moment	Lateral stiffness (mm/kN)
	Toe angle change (min/kN)
	Camber angle change (min/kN)

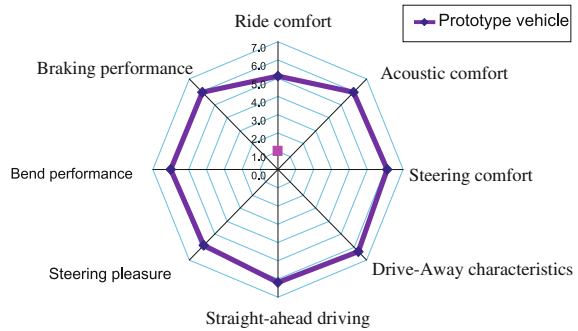
3 K&C Measurement

As one of most significant factors that determine the stability of vehicle handling [2, 3], the K&C characteristics of suspension impact vehicle steady-state and transient steering, lane stability, braking stability, linear stability and road sense. In the development process of vehicle ride and handling, K&C measurement is one of the essential steps. See Table 3 for general measuring conditions and items.

4 Case Study of Vehicle Ride and Handling Development

In the development process of a prototype engineering vehicle, deficiency in vehicle ride and handling is found through subjective evaluation of the vehicle. Major factors that influence vehicle ride and handling are found through K&C measurement of the prototype vehicle, and vehicle ride and handling are optimized by improving its K&C characteristic.

Fig. 1 Radar figure of subjective evaluation of prototype vehicle



4.1 Results of Subjective Evaluation of Prototype Vehicle

Subjective evaluation of the prototype vehicle is conducted in vehicle test ground on the basis of the items specified in Table 2. See Fig. 1 for results of the evaluation:

According to the subjective evaluation performance in Fig. 1, major problems of the prototype vehicle are concluded as follows:

- Vertical vibration comfort was not good;
- Pitching motion was apparent;
- Yaw stability was not good and dynamic under-steer is too small during lane;
- The force feel was not good when steering wheel is on center;
- Linearity of steering response was not good;
- Road feel was not good on steering wheel during driving.

4.2 K&C Measurement of Prototype Vehicle

K&C characteristics of the prototype vehicle are measured in accordance with the items in Table 3. See Table 4 for the result and analysis:

4.3 Optimization of K&C Characteristics

According to the above analysis of K&C and subjective evaluation, the optimization proposals for the K&C characteristics are specified by the changing of suspension hardpoints, bushing characteristics and steering gear characteristics. The K&C measurement results of the optimized prototype vehicle are listed in Table 5.

Table 4 Result and analysis of K&C measurement of prototype vehicle

Items of K&C measurement	Result of K&C measurement	Analysis
Vertical test— force versus suspension travel of front suspension		When jouncing, the front and rear suspensions reached the bump stop very early, and the rebound travels were too small. It may cause comfort problem
Vertical test— force versus suspension travel of rear suspension		
Vertical test— camber change of rear suspension		When Jouncing, the camber angle change of rear suspension was too small, it may affect the yaw stability of vehicle (oversteer tendency)
Lateral force— toe angle change of front suspension		The toe angle change was too much in lateral force and it was not linear, it may affect yaw stability of vehicle
Lateral force— toe change of rear suspension		The steering system was not stiff enough which may cause road feel and center point feel problem Too much toe out change when applied lateral force. It may affect yaw stability (oversteer tendency)
.....		

Table 5 Part of the K&C Measurement Result of the Tuned Prototype Vehicle

Items of K&C measurement	Result of K&C measurement	Description
Vertical jump—stiffness of front suspension		Rebound travel and stiffness of the front suspension were increased
Vertical jump—Stiffness of rear suspension		Rebound travel of rear suspension was increased and the stiffness was reduced
Vertical jump—camber angle change of front suspension		More negative toe change of front suspension
Roll—roll stiffness of front suspension		Roll stiffness of front suspension was increased

(continued)

Table 5 (continued)

Items of K&C measurement	Result of K&C measurement	Description
Lateral force— toe angle change of front suspension		Less toe angle change of front suspension under lateral force
Lateral force— toe angle change of rear suspension		More toe-in change tendency

4.4 Subjective Evaluation of Ride and Handling of the Tuned Prototype Vehicle

Subjective evaluation of the tuned prototype vehicle is conducted in vehicle test ground and the results of subjective evaluation are showed in Fig. 2:

As demonstrated by Fig. 2, by the optimization of K&C characteristics, the prototype vehicle is improved in the following aspects:

- Vertical vibration comfort had a great improvement;
- Pitch motion was smaller;
- Linearity of steering response had a great improvement;
- Yaw stability had a great improvement;
- Steering feel had a great improvement.

To sum up, the subjective feel of vehicle ride and handling is improved by optimizing the K&C characteristics of prototype vehicle. That is to say, the K&C characteristics of vehicles are correlated to the subjective feel of vehicle ride and handling. Research into this correlation holds great significance for the development of vehicle ride and handling, which can be more accurately predicted and controlled in the development stage.

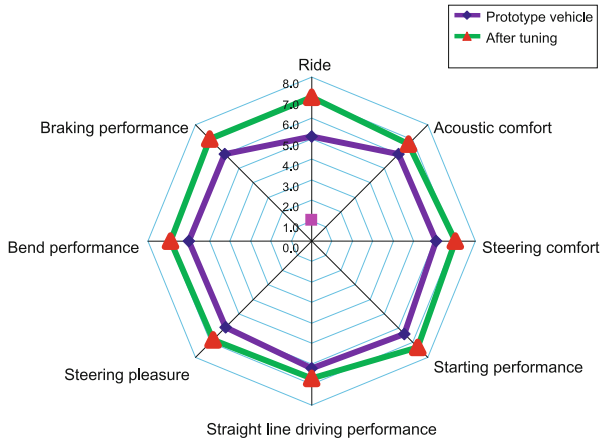


Fig. 2 Result of subjective evaluation of the refitted prototype vehicle

5 Research Into the Analysis Method of Correlation Between Vehicle Ride and Handling and K&C

5.1 Method of Correlation Analysis

The definition of correlation is that when one or several interrelated variables take a certain value, it still changes within a certain range on the basis of a certain law in spite of the uncertainty of the corresponding value of another variable, and this relationship among variables is called uncertain correlation.

Correlation analysis and regression analysis are two basic methods to study the correlation among phenomena. Correlation analysis uses an index to indicate the degree of the interdependence among phenomena. Regression analysis is that a specific form of correlation selects an appropriate mathematical model to approximately express the average change in the relationship among variables [4].

5.2 Method of Correlation Analysis Between Subjective Evaluation and K&C Measurement

In the development process of vehicle ride and handling, a considerable part of the work is subjective evaluation and objective measurement. On the basis of main driving conditions, subjective evaluation subdivides dynamics performance of chassis into several subjective evaluation indexes, and then sets specific evaluation standard and designing targets according to these indexes. Through the K&C test bench and relevant tests, objective measurement is the measuring of specific objective parameters that has significant impact on vehicle performance.

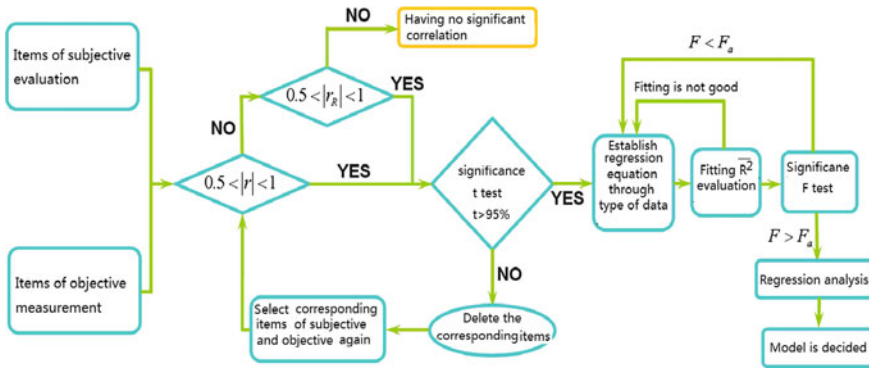


Fig. 3 Analysis procedure of the correlation between subjective evaluation and objective measurement

Actually, certain correlation exists between subjective evaluation results and specific parameters of objective measurement, and the correlation can be found by correlation analysis, of which the contents mainly include:

1. Between which subjective evaluation values and objective measurement values does the correlation exist?
2. In what form does the correlation appear between the correlated subjective evaluation values and objective measurement values, linear correlation or nonlinear correlation, for example and what is the degree of the correlation, judged by specific correlation coefficient?
3. Through correlation analysis, unitary or multiple regression model is accurately established.

As a certain vehicle performance is effected by many factors, usually a certain subjective evaluation value is related to many objective measurement parameters. For example, steering handiness is effected by kingpin inclination, caster, camber, tire pressure..., and also yaw characteristic is effected by steering stiffness, wheel alignment parameters, driving ratio, axle load distribution, tire cornering stiffness and so on. Hence, analysis should be based on multiple regression analysis, and one element regression analysis is supplemented.

See the following Fig. 3 for the correlation analysis between subjective evaluation and objective measurement as well as the procedure of building the final predicting model.

Table 6 Subjective Evaluation Result and Objective Measurement Result of Steer stiffness factors

	Subjective evaluation	Normalization (Y)	X1	X2	X3	X4	X5
Vehicle 1	5.7	-1.28	0.98	2.01	2.89	3.89	5.01
Vehicle 2	6.5	0.41	1.86	3.8	5.98	8.14	11.32
Vehicle 3	5.8	-0.64	1.13	2.07	3.78	5.35	7.94
Vehicle 4	6.5	0.41	1.03	1.92	3.47	5.64	7.27
Vehicle 5	7.5	1.28	2.16	3.72	7.74	16	34.67
Vehicle 6	6.3	-0.20	0.68	1.6	3.08	5.3	6.68

Note Because of sample volume are too less, results of subjective evaluation were normalized

Table 7 Multiple regression results

Assessment rating of center point feeling	Steering stiffness factors	Multiple R	R square
Y	X3, X4, X5	0.97	0.94

Regression equation: $Y = -2.91 - 0.60X3 + 1.41X4 - 0.39X5$

5.3 Case for Correlation Analysis of Subjective Evaluation and Objective Measurement that is Based on Multiple Regression

The case in this paper selects the center point feeling subjective evaluation result of some prototype vehicles and the objective measurement results of Steer stiffness factors for correlation analysis. See Table 6 for the result of subjective evaluation and objective measurement:

According to the above six samples, by regression analysis the correlation coefficient of Y with X1, X2, X3, X4, X5 are 0.72, 0.67, 0.81, 0.84, 0.78. The factor X3, X4 and X5 show relative high correlation to subjective center point feeling. Hence multiple regression method is further applied to analyze the correlation of X3, X4 and X5 (steering stiffness factors) to Y (center point subjective feeling), and the result is showed in Table 7.

This case is an analysis of the correlation and multiple regression of Y with X3, X4, and X5. According to the analysis result, 0.97 as the correlation coefficient of Y with X3, X4, and X5 indicates significant correlation. Its significant coefficient for correcting freedom is 0.86, which indicates that the regression equation has a good fitting.

6 Conclusion

By correlation analysis (multiple regression analysis) in the development process of vehicle handling and ride, and with large amounts of data from subjective evaluation and objective measurement, the following targets are achieved:

1. Establish a basically-accurate multivariate regression model by correlation analysis of objective measurement value which has a significant impact on subjective evaluation.
2. Through the regression model, predict subjective evaluation value which corresponds to objective measurement value.
3. In the early stage of vehicle design, predict the subjective evaluation value that can be acquired through vehicle correlation and thus offer help for vehicle design and improvement.

According to the above analysis and cases, correlation analysis can guide and help the development of vehicle handling and ride. However, due to lack of samples, some of the analysis results are yet deficient and the following research will focus on improving the accuracy of the correlation analysis results.

References

1. http://businesscenter.jdpower.com/DesktopModules/CustomizedUserControls/Compass/CustomizedPages/SpecialReportsDownloadRedirect.aspx?f=2011China_NVIS_CN.pdf. J.D. Power and Associates
2. Wang S (2008) Study on the suspension K&C characteristics of a mini-car and its influence on the vehicle handling stability. Jilin University, Jilin
3. Guo K (2011) Theory of vehicle handling dynamics, 1st edn. Phoenix Science Press, Nanjing
4. Zeng, W (2002) Introduction to statistics. Capital University of Economics & Business Press
5. Harrer M (2006) Steering system development in premium car segment. SAE paper, 2006-01-0935. doi: 10.4271/2006-01-0935
6. HaiSenying B, Jurgen H, Brand L (2010) Subjective evaluation vehicle dynamics, 1st edn, (trans: Shi X, Chen Z). China Communication Press, Beijing
7. Philip M (2004) Using K&C measurements for practical suspension tuning and development. SAE Paper, No. 2004-01-3547

Part VI
Dynamics Modeling, Simulation
and Experimental Validation

Ride Comfort and Wheel Load Fluctuation Compatible Control Using Variable Stiffness and Damping

Yanqing Liu, Jin Hozumi and Masaaki Tabata

Abstract A purpose of a vehicle suspension is to isolate the body from road disturbances. Simultaneously, it is to reduce wheel load fluctuations and improve road holding. However, in conventional variable damping control suspensions, it is a difficult issue to improve both the ride comfort and the wheel load fluctuations simultaneously in the whole frequency region. In this paper, a new compatible control algorithm using variable stiffness and variable damping was proposed. The variable stiffness and the variable damping were designed simultaneously using the nonlinear H infinite theory with frequency weighting functions. Twelve different control schemes involving passive, only variable damping, only variable stiffness, and variable stiffness and damping control algorithms were explored. The frequency and time responses of a quarter-car model to sinusoidal sweep and random excitations showed that the system with the proposed control algorithm provided excellent performances in the whole frequency region. Based on the comparisons between the controller designed separately and the controller designed simultaneously, the responses of the system with the proposed control algorithm were similar to those of the system using variable stiffness to reduce the low frequency responses of sprung mass accelerations, and using variable damping to reduce the high frequency responses of wheel load fluctuations.

F2012-G06-001

Y. Liu (✉) · J. Hozumi · M. Tabata
Toyota Motor Corporation, Toyota, Japan
e-mail: yqliu@con.tec.toyota.co.jp

J. Hozumi
e-mail: hozumi@giga.tec.toyota.co.jp

M. Tabata
e-mail: tabata@masa.tec.toyota.co.jp

Keywords Variable stiffness · Variable damping · Ride comfort · Wheel load fluctuation

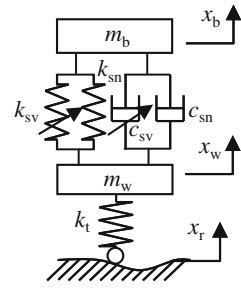
1 Introduction

Vehicle suspensions are utilized to support the weight, to isolate the body from road disturbances, and to maintain the traction force between the tire and the road surface. Therefore, the prime purposes of controlling suspensions are to improve the ride comfort, and to reduce wheel load fluctuations for improving road holding. Based on designs and energy requirements, suspension systems are categorized as: passive, active, and semi-active. For the passive suspensions, the ride comfort and the road holding were achieved trade-offs in the whole frequency [1]. For active suspensions, the ride comfort and the road holding was improved simultaneously [2, 3]. However, active actuators and lots of power are required. On the other hand, semi-active control systems expend small energy because only the system parameters, such as damping and stiffness, are altered. The idea of providing variable damping and stiffness in semi-active control suspensions had been studied by many researchers [4–8].

The semi-active control suspension with variable stiffness had an excellent performance at low frequencies. Nevertheless, it had less influence on the wheel vibration at high frequencies [1, 6–8]. In the semi-active control suspensions with variable damping, the body acceleration and the wheel load fluctuation at low frequencies was reduced. However, the wheel load fluctuation at high frequencies was reduced insufficient [3]. Therefore, in order to reduce the body acceleration and the wheel load fluctuation in the whole frequency, a new semi-active control system should utilize the variable damping and the variable stiffness simultaneously. Moreover, because of the limitations of effects at different frequencies, the variable damping and stiffness should be designed to reduce the body acceleration and the wheel load fluctuation at certain frequencies without influences on other frequencies. The nonlinear H infinite theory with frequency weighting functions was utilized in control suspension systems by automobile researchers [3–5]. The suspension performances could be controlled at certain frequencies using suitable frequency weighting functions.

In this paper, a new compatible control algorithm using variable stiffness and variable damping is proposed. The variable stiffness and the variable damping are designed using the nonlinear H infinite theory with frequency weighting functions. The responses of a quarter car model with the proposed control algorithm to sinusoidal sweep and random excitations are studied in numerically calculations.

Fig. 1 Quarter-car model



2 Quarter-Car Model

A quarter-car model with variable stiffness and damping is shown in Fig. 1. Table 1 shows the parameter names and values in Fig. 1. The variable damping coefficient c_{sv} and the variable stiffness k_{sv} express the variable damper and the variable spring, respectively. The equations of motion for the system shown in Fig. 1 are as follows.

$$m_b \ddot{x}_b = (k_{sn} + k_{sv})(x_w - x_b) + (c_{sn} + c_{sv})(\dot{x}_w - \dot{x}_b) \tag{1}$$

$$m_w \ddot{x}_w = -(k_{sn} + k_{sv})(x_w - x_b) - (c_{sn} + c_{sv})(\dot{x}_w - \dot{x}_b) + k_t(x_r - x_w) \tag{2}$$

Based on Eqs. (1) and (2), the state space expressions are shown in Eqs. (3) and (4).

$$\dot{x}_p = A_p x_p + B_{p1} w + B_{p2} u \tag{3}$$

$$z_p = C_p x_p + D_{p1} w + D_{p2} u \tag{4}$$

The matrices in Eqs. (3) and (4) are shown as follows. $x_p = \begin{pmatrix} x_r - x_w \\ x_w - x_b \\ \dot{x}_w \\ \dot{x}_b \end{pmatrix}$

$$u = \begin{pmatrix} c_{sv} & 0 \\ 0 & k_{sv} \end{pmatrix} \begin{pmatrix} \dot{x}_s \\ x_s \end{pmatrix} \quad \begin{pmatrix} \dot{x}_s \\ x_s \end{pmatrix} = \begin{pmatrix} \dot{x}_w - \dot{x}_b \\ x_w - x_b \end{pmatrix} \quad w = \dot{x}_r \quad z_p = \begin{pmatrix} \ddot{x}_b \\ k_t(x_r - x_w) \end{pmatrix}$$

$$A_p = \begin{bmatrix} 0 & 0 & -1 & 0 \\ 0 & 0 & 1 & -1 \\ \frac{k_t}{m_w} & -\frac{k_{sn}}{m_w} & -\frac{c_{sn}}{m_w} & \frac{c_{sv}}{m_w} \\ 0 & \frac{k_{sv}}{m_b} & \frac{c_{sn}}{m_b} & -\frac{c_{sv}}{m_b} \end{bmatrix} \quad B_{p1} = \begin{bmatrix} 1 \\ 0 \\ 0 \\ 0 \end{bmatrix} \quad B_{p2} = \begin{bmatrix} 0 & 0 \\ 0 & 0 \\ -\frac{1}{m_w} & -\frac{1}{m_w} \\ \frac{1}{m_b} & \frac{1}{m_b} \end{bmatrix}$$

$$C_p = \begin{bmatrix} 0 & \frac{k_{sn}}{m_b} & \frac{c_{sn}}{m_b} & -\frac{c_{sv}}{m_b} \\ 0 & 0 & -k_t & 0 \end{bmatrix} \quad D_{p1} = \begin{bmatrix} 0 \\ k_r \end{bmatrix} \quad D_{p2} = \begin{bmatrix} \frac{1}{m_b} & \frac{1}{m_b} \\ 0 & 0 \end{bmatrix}$$

Table 1 Parameter values in the model

Parameters	Names	Values
m_b	Sprung mass (kg)	375
m_w	Unsprung mass (kg)	38
k_{sn}	Suspension middle stiffness (kN/m)	21.5
k_{sv}	Suspension variable stiffness (kN/m)	
c_{sn}	Suspension middle damping coefficient (Ns/m)	2,500
c_{sv}	Suspension variable damping coefficient (Ns/m)	
k_t	Tire stiffness (kN/m)	240
x_b	Sprung mass displacement (m)	
x_w	Unsprung mass displacement (m)	
x_r	Road displacement (m)	

The controlled output z_p including the sprung mass acceleration and the wheel load fluctuation ($F_t = k_t(x_r - x_w)$) is evaluated. In a real car, the sprung mass acceleration is measured by an acceleration sensor. The wheel load fluctuation can be measured directly by a special implement or adopted an estimated value that is derived from measured variables, such as unprung mass accelerations. The control input u includes the variable damping coefficient c_{sv} , the variable stiffness k_{sv} , and the suspension deflection and velocity. The suspension deflection is measured by a displacement sensor and the velocity is derived from the displacement. The values of c_{sv} and k_{sv} are designed using the nonlinear H infinite theory with frequency weighting functions.

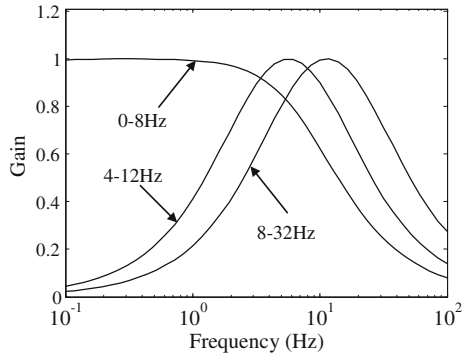
3 Controller Design

The controller using H infinite theory is designed using the generalized plant [2]. The generalized plant is composed of the system state expressions shown in Eqs. (3) and (4), and the weighting functions of the controlled outputs.

3.1 Weighting Functions

The ride comfort is evaluated by the sprung mass acceleration in the frequency region from 0 to 8 Hz, and the road holding is evaluated by the wheel load fluctuation in the vicinity of the unsprung mass resonant frequency region from 8 to 32 Hz. Moreover, to improve the ride quality, it is important to isolate the sprung mass from the road disturbances and to suppress the vertical vibrations from 4 to 12 Hz, which is known to be a sensitive frequency range to human body according to ISO 2631 [9]. Therefore, in this paper, band pass filters with the frequencies of 0–8 Hz, 4–12 Hz, and 8–32 Hz are adopted as follows.

Fig. 2 Weighting functions for different frequency regions



$$\dot{x}_w = A_w x_w + B_w z_p \tag{5}$$

$$z_w = C_w x_w + D_w z_p \tag{6}$$

where A_w, B_w, C_w, D_w are designed using a Butterworth filter. \dot{x}_w and z_w are the variables of weighting functions. To reduce the order in the controller, the Butterworth filter with one order is utilized and the gains of weighting functions are shown in Fig. 2.

3.2 Generalized Plant

Based on Eqs. (3)–(6), the state space expressions of the generalized plant are shown as follows.

$$\dot{x} = Ax + B_1 w + B_2 u \tag{7}$$

$$z = Cx + D_1 w + D_2 u \tag{8}$$

The matrices in Eqs. (7) and (8) are shown as follows.

$$x = \begin{pmatrix} x_p \\ x_w \end{pmatrix} \quad z = z_p \quad A = \begin{bmatrix} A_p & 0 \\ B_w C_p & A_w \end{bmatrix} \quad B_1 = \begin{bmatrix} B_{p1} \\ B_w D_{p1} \end{bmatrix} \quad B_2 = \begin{bmatrix} B_{p2} \\ B_w D_{p2} \end{bmatrix}$$

$$C = [C_w C_1 \quad C_w] \quad D_1 = [D_w D_{p1}] \quad D_2 = [D_w D_{p2}]$$

Based on the generalized plant, the controller is designed using the nonlinear H infinite theory [2]. The control input u is expressed as follows.

$$u = -B_2 P x \begin{pmatrix} \dot{x}_w - \dot{x}_b \\ x_w - x_b \end{pmatrix} \tag{9}$$

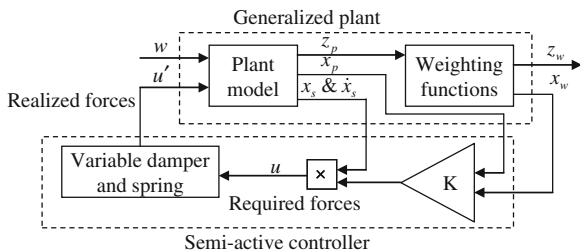


Fig. 3 Control scheme including weighting functions

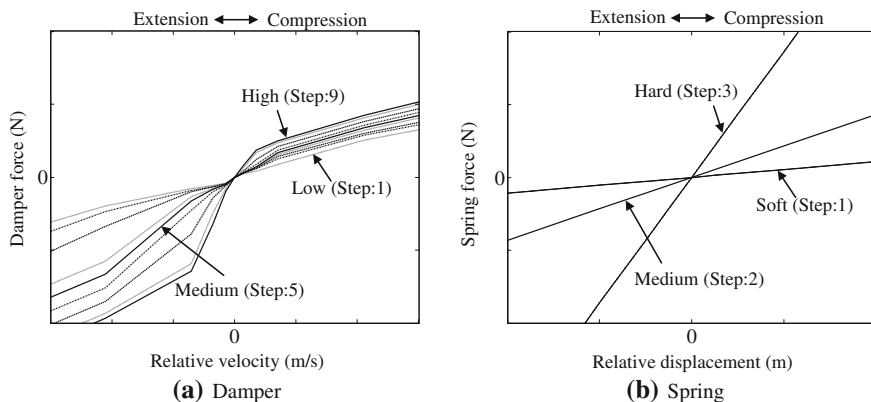


Fig. 4 Performances of variable

where P is calculated using Riccati Equation. Based on Eq. (9), the controlling gain K of the variable damping and stiffness are expressed as follows.

$$K(x) = -B_2Px \tag{10}$$

Therefore, the variable damping coefficient and the variable stiffness are the functions of x . The control scheme including weighting functions is shown in Fig. 3. In a vehicle suspension system with variable damper and variable spring, the forces designed in the controller are called required forces, and the forces realized by the damper and the spring are called realized forces.

3.3 Variable Damper and Spring

A damper with variable damping and a spring with variable stiffness are utilized. Figure 4 shows the performances of variable damper and spring.

Table 2 Types of control algorithms

Types	Control algorithms		Frequency region of the sprung mass weighting factor (Hz)	Frequency region of the wheel load fluctuation weighting factor (Hz)	Abbreviation
	Damping	Stiffness			
Type 1	Step: 5	Step: 2	–	–	Medium
Type 2	Variable	Step: 2	0–8	0	DCL
Type 3	Variable	Step: 2	0	8–32	DCH
Type 4	Variable	Step: 2	4–12	0	DCM
Type 5	Variable	Step: 2	0–8	8–32	DCLH
Type 6	Variable	Step: 2	4–12	8–32	DCMH
Type 7	Step: 5	Variable	0–8	0	SCL
Type 8	Step: 5	Variable	0	8–32	SCH
Type 9	Variable	Variable	0–8	4–32	DC + SC
Type 10	Variable	Variable	0–8 (Damping)	8–32 (Stiffness)	DCL + SCH
Type 11	Variable	Variable	0–8 (Stiffness)	8–32 (Damping)	DCH + SCL
Type 12	Variable	Variable	0–8 (Stiffness)	4–32 (Damping)	DCMH + SCL

The damper and spring forces can be set to a required step of nine steps and a required step of three steps, respectively. The required steps are designed based on the required forces and the suspension velocity and displacement, respectively.

3.4 Control Algorithms

Twelve types of control schemes shown in Table 2 are explored. For Type 1, Step 5 of the damper and Step 2 of the spring are adopted and called Medium.

For Type 2–Type 6, the damping coefficients are designed using the H infinite controller and the springs are always in the Step 2 state (called Variable damping control). For Type 7 and Type 8, the spring stiffnesses are designed using the H infinite controller and the damper are always in the Step 5 state (called Variable stiffness control). For Type 9, the spring stiffness and the damping coefficient are designed simultaneously in the H infinite controller (called Variable damping and stiffness control, and abbreviated to DC + SC). However, it is difficult to divide the effects of the damper and the spring on the sprung mass acceleration and the wheel load fluctuation, respectively. Therefore, the variable damping coefficient and the variable stiffness designed separately using two H infinite controllers were shown as Type 10 to Type 12.

4 Simulation Results

4.1 Frequency Responses to Sinusoidal Excitations

In the suspension as shown in Fig. 1, a logarithmic sinusoidal sweep input is adopted in calculations. Figure 5 shows the transmissibility $|\ddot{X}_b/\dot{X}_r|$ and $|F_t/\dot{X}_r|$ of

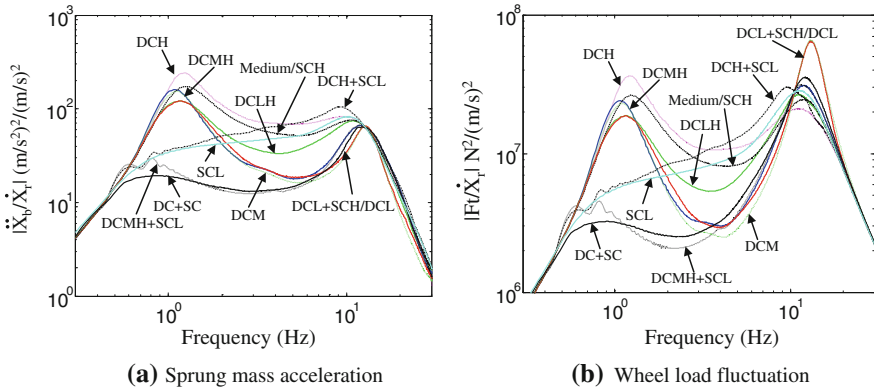


Fig. 5 Frequency responses of the system with control schemes

the twelve control schemes. Herein, \ddot{X}_b , \dot{X}_r , and F_t are the magnitudes of \ddot{x}_b , \dot{x}_r , and F_t . Because the required force of SCH is always around the Step 2 and the realized force is the same as that of Step 2, the responses of SCH and DCL + SCH are the same as those of Medium and DCL, respectively.

Based on Fig. 5, the DC + SC system has good performance in the whole frequency region, and are similar to those of DCMH + SCL. In other words, the distributions of the damper and the spring in DC + SC algorithm are similar to those in the DCMH + SCH algorithm. Therefore, in the proposed DC + SC algorithm, the responses of sprung mass accelerations in the low frequency region could be reduced using the variable stiffness control. Simultaneously, the responses of wheel load fluctuations in the middle and high frequency regions could be reduced using the variable damping control.

4.2 Time Responses to Random Inputs

The time responses to a random input and root means square (RMS) values of the control algorithms are shown in Figs. 6 and 7, respectively.

Based on Figs. 6 and 7, the responses of DC + SC and DCMH + SCL are similar and smaller than that of DCL. Regarding the RMS values shown in Fig. 7, the total sprung mass acceleration and the total wheel load fluctuation of DC + SC are smaller than those of DCL by 26 and 20 %, respectively. Moreover, the sprung mass acceleration in the low frequency region and the wheel load fluctuation in the high frequency region of DC + SC are smaller than those of DCL by 54 and 13 %, respectively. In the middle frequency region, the sprung mass acceleration and wheel load fluctuation of DC + SC are also smaller than those of DCL. Therefore, the system with the proposed control algorithm has excellent performances in the whole frequency region.

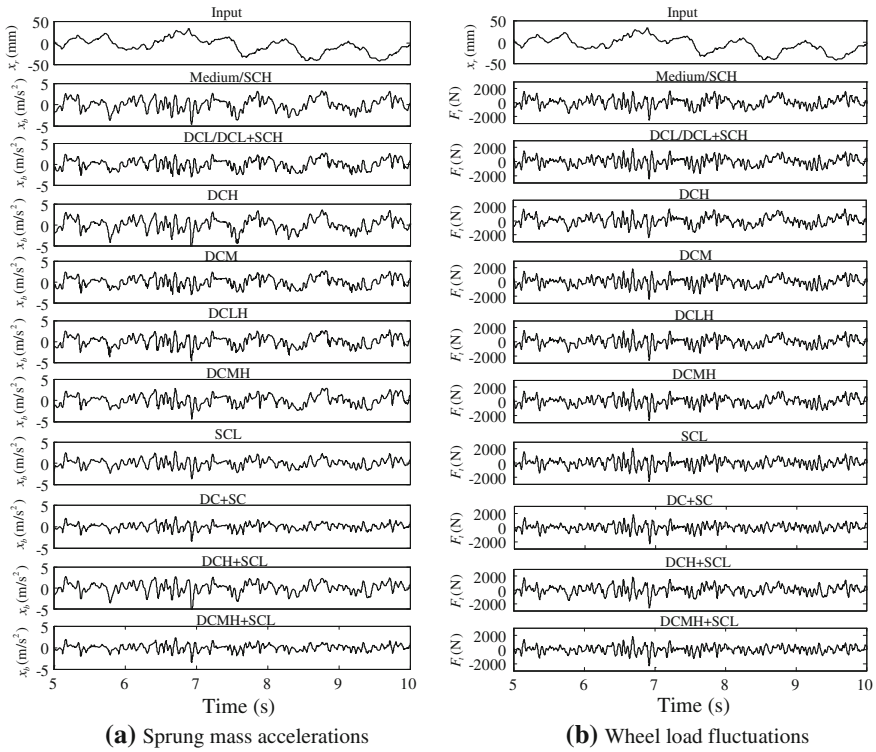


Fig. 6 Time responses of control systems with a random input

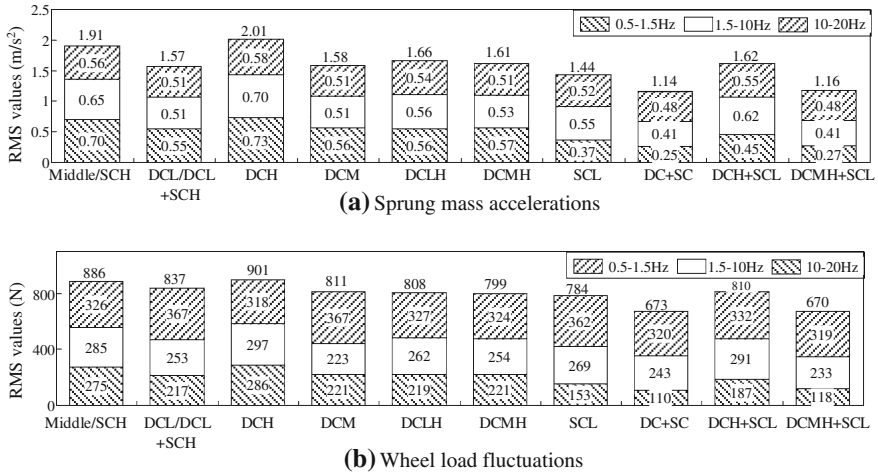


Fig. 7 RMS values of control systems with a random input

Table 3 Response differences as compared with the conventional damping control

Types	Abbreviation	Sprung mass acceleration(%)			Wheel load fluctuation(%)		
		0.5– 1.5 Hz	1.5– 10 Hz	10– 20 Hz	0.5– 1.5 Hz	1.5– 10 Hz	10– 20 Hz
Type 1 & 8	Medium/SCH	+27	+28	+10	+26	+12	–11
Type 2 & 10	DCL/ DCL + SCH	0	0	0	0	0	0
Type 3	DCH	+32	+36	+15	+32	+17	–13
Type 4	DCM	+2	0	0	+2	–12	0
Type 5	DCLH	0	+9	+7	+1	+3	–11
Type 6	DCMH	+3	+4	0	+2	0	–12
Type 7	SCL	–33	+7	+3	–29	+6	–1
Type 9	DC + SC	–54	–19	–4	–49	–4	–13
Type 11	DCH + SCL	–18	+20	+9	–14	+15	–9
Type 12	DCMH + SCL	–50	–19	–4	–46	–8	–13

–: Smaller (good)
 +: Larger (bad)
 0: Same (Similar))

The responses of conventional damping control DCL are regarded as comparing base, and differences of the control schemes in the low, middle and high frequency regions are shown in Table 3. The differences of DC + SC are similar to those of DCMH + SCL. Therefore, the proposed control algorithm could also be applied to a semi-active system using 2 electronic control units to design the variable damping and the variable stiffness, respectively.

5 Conclusions

A new compatible control algorithm using variable stiffness and variable damping was proposed. The variable stiffness and the variable damping were designed using the nonlinear H infinite theory with frequency weighting functions. The responses of a quarter car model with the proposed control algorithm to sinusoidal sweep and random excitations were numerically calculated.

Based on the calculation results, the system with the proposed control algorithm had better performances in the whole frequency region. Moreover, according to the comparisons between the controller designed simultaneously and the controller designed separately, the responses of the system with the proposed control algorithm were similar to those of the system using variable stiffness to reduce the low frequency responses of sprung mass, and simultaneously using variable damping to reduce the high frequency responses of wheel load fluctuations.

The case of the suspension excited by a force input on the sprung mass will be studied using the proposed control algorithm. Moreover, the testing will be executed in a real car in future.

References

1. Redfield RC, Karnopp DC (1989) Performance sensitivity of an actively damped vehicle suspension to feedback variation. *ASME J Dyn Sys, Meas Control* 111(1):51–60
2. Valasek M, Novak M, Sika Z, Vaculin O (1997) Extended ground-hook new concept of semi-active control of truck's suspension. *Veh Sys Dyn* 27(2):289–303
3. Sammier D, Sename O, Dugard L (2003) Skyhook and hinf control of semi-active suspensions: some practical aspects. *Veh Sys Dyn* 39(4):279–308
4. Ohsaku S, Nakayama T, Kamimura I, Motozono Y (1999) Nonlinear hinf control for semi-active suspension. *JSAE Rev* 20:447–452
5. Honma M, Hozumi J, Mizuta Y, Liu Y, Okimura K, et al. (2010) Ride comfort and body attitude compatible control using nonlinear hinf theory in semi-active suspensions. In: FISITA world automotive congress, F2010-B-017
6. Liu Y, Matsuhisa H, Utsuno H (2008) Semi-active vibration isolation system with variable stiffness and damping control. *Sound Vib* 313(1–2):16–28
7. Liu Y, Matsuhisa H, Utsuno H (2006) Variable damping and stiffness vibration control with magnetorheological fluid dampers for two degree-of-freedom system [J]. *JSME* 49(1):156–162
8. Spelta C, Previdi F, Savaresi SM, Bolzern P, Cutini M, et al. (2011) Performance analysis of semi-active suspensions with control of variable damping and stiffness. *Veh Sys Dyn* 49(1–3): 237–256
9. ISO2631-1 Mechanical vibration and shock-evaluation of human exposure to whole-body vibration, ISO, 1997

Hybrid Steering of Wheeled Wheels

Muhammad Adeel Awan, David Purdy and Amer Hameed

Abstract This paper is focussed to assess the performance of a low cost steer-by-wire system developed in the Vehicle Dynamics Laboratory at Cranfield University. The steering system plays an important role in vehicle's safety by influencing its handling performance and therefore considered as a critical vehicle system. The performance of a steer-by-wire system is predominantly linked to its actuators' behaviour. This paper contains the findings of experiments carried out to measure the actuators' response. As the steering commands can be represented by step, sinusoidal and combination of such inputs therefore the actuators are subjected to similar sort of inputs with varying frequencies and amplitudes. In the later part a controller is developed to improve the performance of the steering system using the torque vectoring technique.

Keywords Hybrid steer · Steer-by-wire · Yaw-control · LQR · Vehicle model

Nomenclature

α_f, α_r Front and rear tyre slip angles respectively
 δ_f Front steering angle of the vehicle
 $\dot{\omega}_{fl}\dot{\omega}_{fr}\dot{\omega}_{rl}\dot{\omega}_{rl}$ Angular velocities of the front left, front right, rear right and rear left wheels respectively

F2012-G06-005

M. A. Awan (✉) · D. Purdy · A. Hameed
Cranfield University, Cranfield, UK
e-mail: m.awan@cranfield.ac.uk

D. Purdy
e-mail: d.j.purdy@cranfield.ac.uk

A. Hameed
e-mail: a.hameed@cranfield.ac.uk

$\sum F_x$	Sum of forces acting on the vehicle in x-direction,
$\sum F_y$	Sum of forces acting on the vehicle in y-direction,
$\sum M_z$	Sum of moments acting on the vehicle in z-direction,
$\tau_{fl} \tau_{fr} \tau_{rr} \tau_{rl}$	Torque acting on the front left, front right, rear right and rear left wheels respectively
a	Distance between the front axle and the vehicle's centre of mass
b	Distance between the rear axle and the vehicle's centre of mass
F_d	Air drag force,
$F_{x_{fw}} F_{x_{rw}}$	Longitudinal tyre forces at front and rear respectively
$F_{y_{fw}} F_{y_{rw}}$	Lateral tyre forces at front and rear respectively
I_z	Moment of inertia about z-axis
m	Mass of the vehicle,
r	Yaw rate of the vehicle
$T_F T_R$	Track width at front and rear respectively
$R_{fl} R_{fr} R_{rr} R_{rl}$	Effective radius of the front left, front right, rear right and rear left wheels respectively
u	Longitudinal velocity of the vehicle
v	Lateral velocity of the vehicle
$C_{\alpha f} C_{\alpha r}$	Cornering stiffness of the front and rear tyre respectively

1 Introduction

Since the inception of high speed automobiles, the automotive engineers are in a constant pursuit to enhance their manoeuvrability and stability. The earlier versions of automobiles were steered by a tiller, which was replaced by a steering wheel. The steering wheel is connected to the wheels by means of mechanical linkages and transfers the driver's commands to the wheels through these linkages. This effort to enhance the steering system of a vehicle by introducing the steering wheel dates back to 1893 when a Frenchman, name Alfred Vacheron, introduced the steering wheel to his race car [1]. These efforts to improve the vehicle stability and steerability continued on and resulted in the form of anti-lock brake system (ABS), differential braking, yaw control, traction control, and active steering system, which made their way to the production models. Among these performance enhancement systems active steering phenomenon, being the least matured, still lures the researchers.

An active steering system is one which uses an auxiliary arrangement to assist the driver in controlling the vehicle. The active steering system can have various forms; it can be a conventional steering arrangement assisted by an electric motor/hydraulic pump or an arrangement in which the steering wheel is not directly connected to the wheels and the wheels are steered by actuators that receive

Fig. 1 The test vehicle fitted with the steer-by-wire vehicle



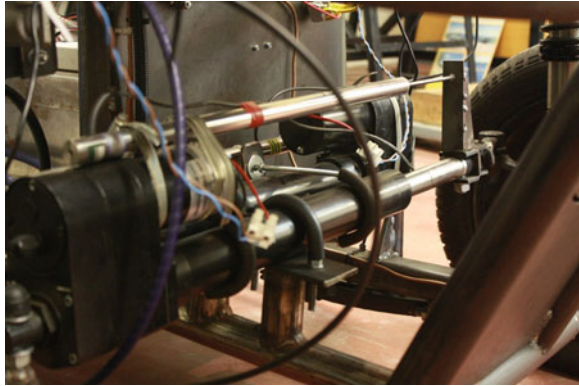
commands through a microprocessor. The latter steering arrangement is termed as steer-by-wire system and is one of the advanced forms of the active steering systems. The active steering goes back to at least the sixties [2] when Kasselman and Keranen [3] studied an active steering system in which a proportional feedback controller augmented the front steering angle by monitoring the vehicle yaw-rate with a gyro.

The motivation for this paper is to envisage a future vehicle with a low cost steer-by-wire system. This idea raises the need to explore the possibilities that allow the replacement of a conventional steering system with a steer-by-wire system. Due to its critical nature generally a steer-by-wire system contains high performance actuators. These high performance actuators/motors are costly and therefore do not provide a feasible solution for production vehicles. This paper investigates the possibility of using the low cost actuators as a part of the steer-by-wire system. In order to overcome the limited performance of these low cost actuators this paper explores the compensation by torque vectoring techniques. This provides control over the torque distribution to all wheels of a vehicle. Generally this technique is implemented by a mechanical differential; however, this work uses in-wheel electric motors to implement the torque vectoring mechanism as these are being considered for both civilian and military vehicles.

2 Experimental Setup

The test vehicle, on which the low performance steering system was fitted, is shown in Fig. 1. It is a dune buggy converted to include a steer-by-wire system comprising two low cost linear actuators, a potentiometer to convert steering commands into the respective voltages, a data acquisition (DAQ) module and a laptop for data manipulation and gathering. The front and rear McPherson strut suspension has been altered to accommodate four of such actuators to make the vehicle four wheels steerable. However, for this work the rear wheels have been

Fig. 2 Front steering actuator and LVDT replacing the conventional steering



kept fixed and only front two wheels were allowed to steer during the investigation. The actuator's performance data sheet, provided by the supplier, suggests that the actuator can travel at maximum speed of 45 mm/sec when a load of 2.3 kN is acting on it.

Figure 2 shows the steer-by-wire system replacing the conventional steering system. Due to physical limitations it was not possible to fit the actuators in-line to each other on the vehicle chassis. The kinematic arrangement on the right side of the vehicle was slightly modified to accommodate the actuator's offset and therefore both of the actuators travel in different lengths to steer the two wheels in parallel. The actuators were fitted with two calibrated LVDTs to measure the actuators' displacement during the experiments.

3 Actuator's Response

This section describes the experiments carried out to measure the response of the low cost actuators. As mentioned earlier the steering commands can be generally represented in the form of square and sinusoidal inputs. Therefore, the actuator was subjected to inputs of similar forms of various frequencies and amplitudes.

3.1 Square Wave Response

The layout diagram of the experimental set-up is shown in the Fig. 3. In order to investigate the actuators' response they were fed with an input in the form of a square wave.

Figure 4 shows the displacement versus time graph for the actuator. The data shown in the figure was collected when the actuator was commanded to move from one end to other at the frequency of 0.1 Hz. This frequency was chosen to allow the actuator to reach the end position fully and then move back.

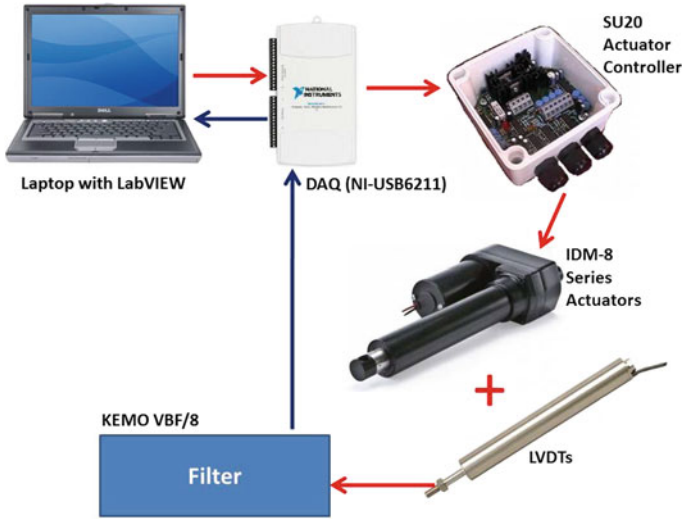


Fig. 3 Experimental set-up layout

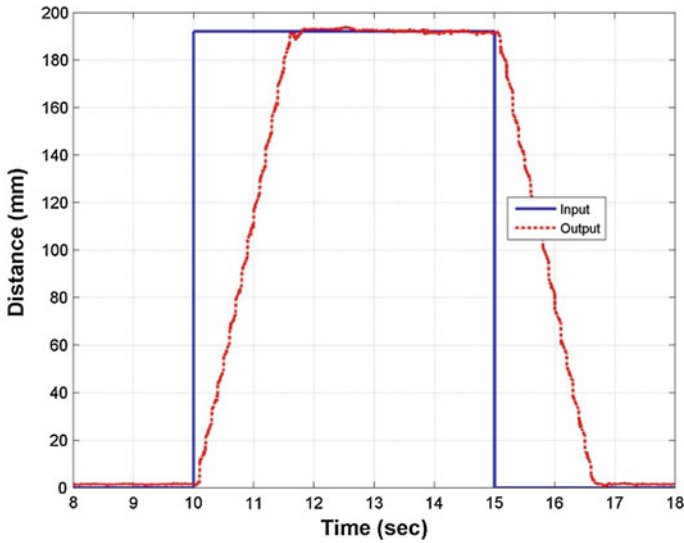


Fig. 4 Response of the actuator when subjected to the square wave input of 0.1 Hz

This experiment was repeated several times by varying input frequencies and amplitudes. The measured responses show a relatively simple behaviour consisting of a scaling factor to compensate for the steering kinematics and velocity saturation from the actuator. Using this analogy a Simulink model is developed that imitate the delayed actuator response. This model was validated by comparing its

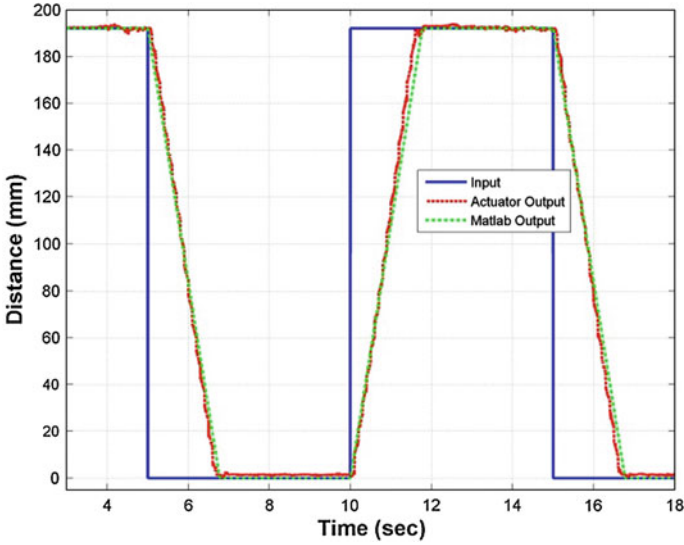


Fig. 5 Comparison of the Simulink model's response with the experimental output

output with that of the actuator, when subjected to an input of the same frequency and amplitude. This has been shown in Fig. 5, which compares the outputs of the Simulink model and the actuator when both are excited with a square wave of 0.1 Hz and maximum amplitude.

3.2 Sine Wave Response

In this set of experiments the actuator was driven by sine wave inputs of varying frequencies and amplitudes to identify its behaviour in manoeuvres representing lane-change or obstacle avoidance. Figure 6 shows the output comparison for the Simulink model and the actuator when subjected to a sine wave input having frequency of 0.2 Hz and maximum amplitude. These results show that the Simulink model of the steer-by-wire system represents the real system in an acceptable manner. The root mean square error value between the actual and simulated responses was within the range of 15–20 mm.

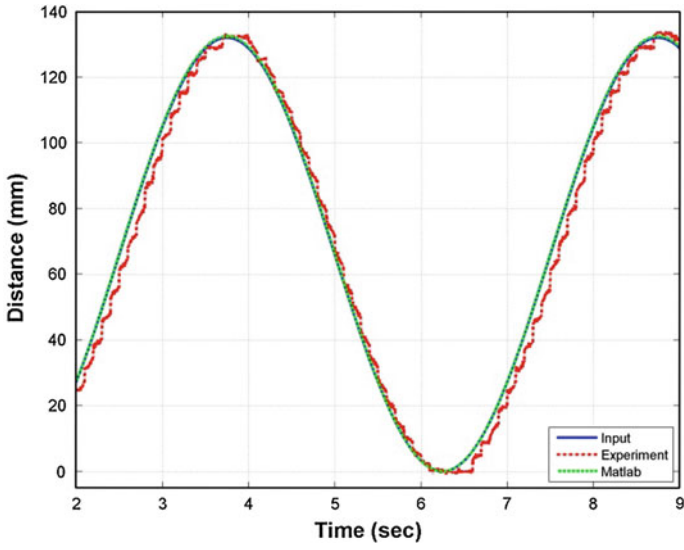
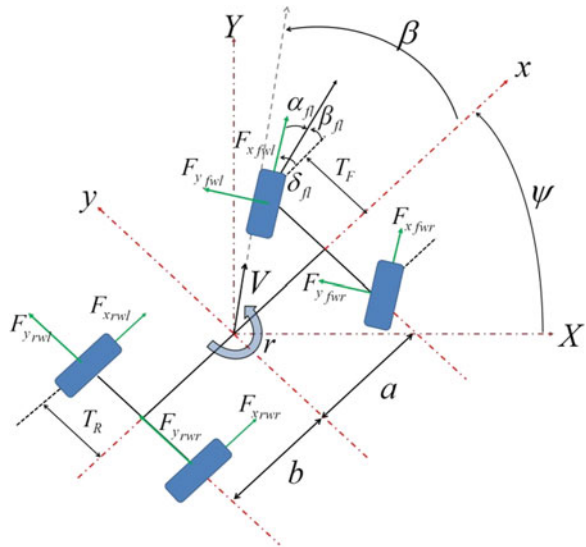


Fig. 6 Comparison of sine wave response of the Simulink model and actuator

Fig. 7 Vehicle model with seven degrees of freedom



4 Simulation and Analysis

4.1 Vehicle Model

In order to analyse the effect of the above discussed steer-by-wire system on the vehicle's handling performance, its Simulink model is integrated with a vehicle model, shown in Fig. 7, having seven degrees of freedom. This vehicle model is also developed using Matlab/Simulink and the degrees of freedom are vehicle's lateral, longitudinal and yaw motions along with the rotational degree of freedom for each tyre.

Applying the Newton's second law of motion, the equations of motion can be written as:

$$\sum F_x = F_{x_{fvl}} \cos \delta_{fl} - F_{y_{fvl}} \sin \delta_{fl} + F_{x_{fvr}} \cos \delta_{fr} - F_{y_{fvr}} \sin \delta_{fr} + F_{x_{rwl}} + F_{x_{rwr}} - F_d \quad (1)$$

$$\sum F_y = F_{x_{fvl}} \sin \delta_{fl} + F_{y_{fvl}} \cos \delta_{fl} + F_{x_{fvr}} \sin \delta_{fr} + F_{y_{fvr}} \cos \delta_{fr} + F_{y_{rwl}} + F_{y_{rwr}} \quad (2)$$

$$\begin{aligned} \sum M_z = & (F_{x_{fvl}} \sin \delta_{fl} + * \Phi_{\theta_{\phi\lambda}} \psi \omega \sigma \delta_{\phi\lambda} + \Phi_{\xi_{\phi\lambda\rho}} \sigma \nu \delta_{\phi\rho} + \Phi_{\theta_{\phi\lambda\rho}} \psi \omega \sigma \delta_{\phi\rho}) \times \alpha \\ & - (F_{x_{fvl}} \cos \delta_{fl} - * \Phi_{\theta_{\phi\lambda}} \sigma \nu \delta_{\phi\lambda} - \Phi_{\xi_{\phi\lambda\rho}} \psi \omega \sigma \delta_{\phi\rho} + \Phi_{\theta_{\phi\lambda\rho}} \sigma \nu \delta_{\phi\rho}) \times T_F \\ & - (F_{y_{rwl}} + F_{y_{rwr}}) \times b - (F_{x_{rwl}} - F_{x_{rwr}}) \times T_R \end{aligned} \quad (3)$$

For wheels the equations of motion are:

$$\dot{\omega}_{fl} = \frac{1}{I_{fvl}} (\tau_{fl} - R_{fl} F_{x_{fvl}}) \quad (4)$$

$$\dot{\omega}_{fr} = \frac{1}{I_{fvr}} (\tau_{fr} - R_{fr} F_{x_{fvr}}) \quad (5)$$

$$\dot{\omega}_{rr} = \frac{1}{I_{rwr}} (\tau_{rr} - R_{rr} F_{x_{rwr}}) \quad (6)$$

$$\dot{\omega}_{rl} = \frac{1}{I_{rwl}} (\tau_{rl} - R_{rl} F_{x_{rwl}}) \quad (7)$$

The torque values in the Eqs. (4)–(7) are the output of the in-wheel electric motors, which are transferring the torque through a reducer as discussed by Es-mailzadeh et al. [4].

4.2 Tyre Model

A simplified version of Dugoff's tyre model is used for this work. These equations are given in [5], which provides tyre forces in pure slip as well as combined slip scenario. The longitudinal and lateral tyre forces are written as:

$$F_x = -\frac{C_{S_x}S_x}{(1-S_x)}f(\lambda)$$

$$F_y = -\frac{C_\alpha \tan\alpha}{(1-S_x)}f(\lambda)$$

where λ is a non-dimensional parameter related to tyre/road friction coefficient μ and normal load F_z . The Dugoff's model assumes the normal load to be uniform and this has been represented by the definition of λ . It is given by:

$$\lambda = \frac{\mu F_z (1 - S_x)}{2 \left\{ (C_{S_x} S_x)^2 + (C_\alpha \tan\alpha)^2 \right\}^{1/2}}$$

where

$$\mu = \mu_O (1 - A_S u_w [S_x^2 + (\tan\alpha)^2]^{1/2})$$

The function $f(\lambda)$ is defined as:

$$f(\lambda) = \begin{cases} (2 - \lambda)\lambda, & \lambda < 1 \\ 1, & \lambda \geq 1 \end{cases}$$

In the above equations μ_O is the tyre road friction coefficient $u_w [S_x^2 + (\tan\alpha)^2]^{1/2}$ is zero, A_S is the friction reduction factor and u_w is the velocity component in the wheel plane.

4.3 Controller Design

The controller proposed in this paper is based on Linear Quadratic Regulator (LQR) theory, discussed in detail by Dutton et al. [6]. A two degrees of freedom bicycle model is used as the reference model for the controller design. The controller monitors the vehicle (7 DOF) yaw-rate and compares it with the reference yaw-rate generated by the bicycle model. The 2 DOF bicycle is derived in detail by Abe [7] and it can be written in state-space form as follows:

$$\dot{x} = Ax + Bu$$

where

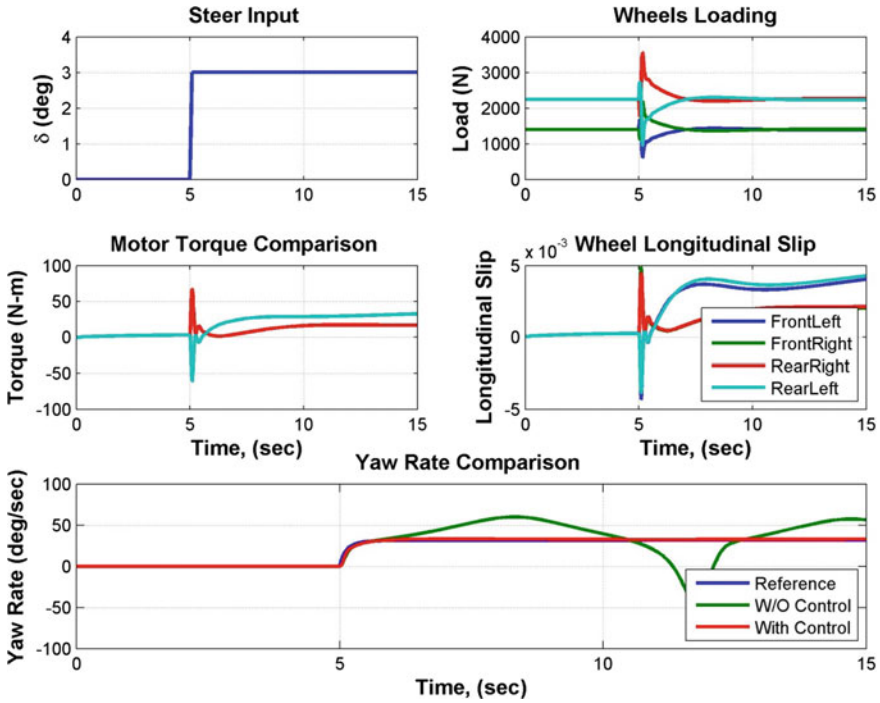


Fig. 8 Output recorded for a J-Turn manoeuvre at the speed of 65 km/h

$$A = \begin{bmatrix} \frac{-2(C_{zf} + C_{zr})}{2(C_{zr}b + C_{zf}a)} & \frac{2(C_{zr}b + C_{zf}a) - u}{l_z u} \\ \frac{mu}{l_z u} & -\frac{2(C_{zf}a^2 + C_{zr}b^2)}{l_z u} \end{bmatrix}, \quad B = \begin{bmatrix} \frac{2C_{zf}}{m} \\ \frac{C_{zf}a}{l_z} \end{bmatrix}$$

4.4 J-Turn Manoeuvre with a Constant Speed

The J-turn manoeuvre is a simple testing procedure which allows the evaluation of the vehicle’s transient response as well as its steady-state behaviour. In this manoeuvre the vehicle first runs in a straight line and then enters into a turn when the steering wheel is quickly rotated from the straight ahead position to a new one and held constant. This step change in the steer angle results into a steady-state cornering after the settling time is over. Figure 8 shows the outputs recorded during the simulation in which the 7 DOF vehicle model is subjected to step steer input of 3° when it was moving with the speed of 65 km/h. Due to this sudden input the vertical loading on tyres is disturbed and the vehicle’s load shifts from the left side towards the right. This can be observed in the second sub-figure of Fig. 8. The yaw-rate curves show that the steer-by-wire vehicle model without

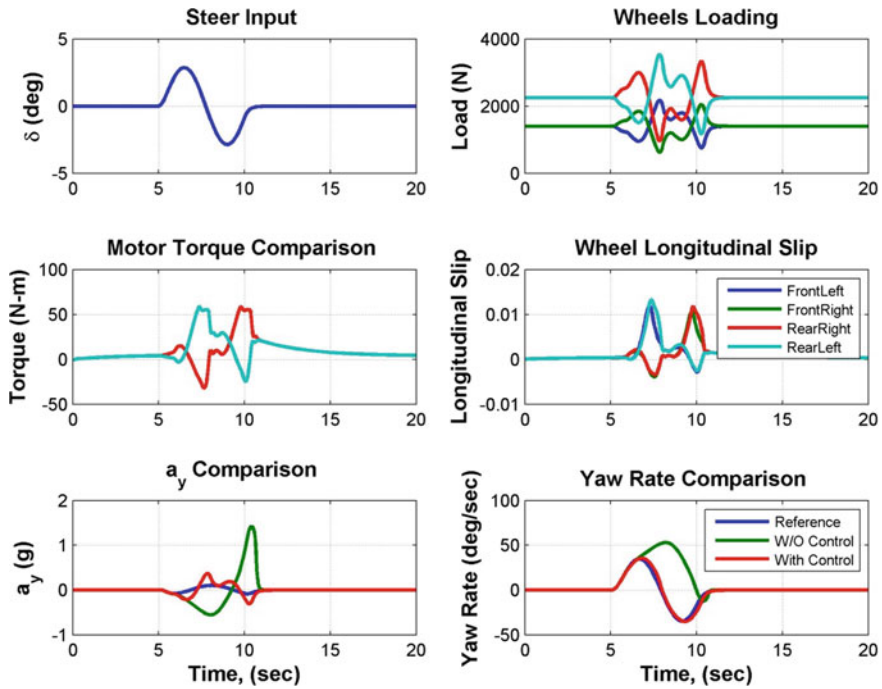


Fig. 9 Output recorded for a sine steer manoeuvre at the speed of 70 km/h

controller becomes unstable once subjected to this manoeuvre. This happens due to the lag induced by the actuators in vehicle’s response. On the contrary the vehicle model with the controller is able to complete the manoeuvre like the reference vehicle model. The control action is applied by varying the torque values for each wheel. This is shown in the third sub-figure, which shows the correcting torque induced by the controller for each wheel. The fourth sub-figure is showing the longitudinal slip for the all four wheels during this manoeuvre.

4.5 Sine Steer Manoeuvre

The sine steer manoeuvre is used to evaluate the vehicle’s transient lateral handling response. In this test a single sine wave has been used as a steer input for the vehicle. The amplitude and frequency of the sine steer command has been varied to test the control system’s effectiveness to keep the vehicle stable at different values of lateral acceleration. Figure 9 shows information about various parameters and states recorded during a sine steer manoeuvre when a vehicle moving with a velocity of 70 km/h was subjected to a sine steer input of amplitude 3° and frequency 0.2 Hz. During this manoeuvre the lateral acceleration value of the

uncontrolled vehicle shows that it enters into highly non-linear region where it is difficult for an ordinary driver to control. On the contrary the vehicle equipped with the designed control system follows the reference signal and remains stable. The root mean square error values for lateral acceleration and yaw-rate are 0.06 g and 1.8 deg/s respectively.

5 Conclusion

This paper introduces the Simulink model of a steer-by-wire system, validated by experimental results. This steering model, in-conjunction with a seven degrees of freedom vehicle model, is used to show that this low performance steering system influences the handling response of the vehicle. Further a yaw controller based on LQR theory is developed, which improves the vehicle response by introducing the torque vectoring. Thus based on these simulation results it can be suggested that there is a possibility for the future vehicles having in-wheel electric motors to use low cost actuators for steering purpose.

References

1. Dick R (2005) Mercedes and auto racing in the belle epoque 1895–1915. McFarland and Company, Inc. Publishers, Jefferson
2. Ackermann J, Bünte T, Odenthal D (1999) Advantages of active steering for vehicle dynamics control. In: In Proceedings of 32nd international symposium on automotive technology and automation, pp 263–270
3. Kasselmann JT, Keranen TW (1969) Adaptive steering. Bendix Tech J 2:26–35
4. Esmailzadeh E, Vossoughi GR, Goodarzi A (2001) Dynamic modeling and analysis of a four motorized wheels electric vehicle. Veh Sys Dyn 35(3):163–194
5. Guntur R, Sankar S (1980) A friction circle concept for Dugoff's tyre friction model. Int J Veh Des 1(4):373–377
6. Dutton K, Thompson S, Barraclough B (1998) The art of control engineering. Addison-Wesley Longman Publishing Co., Inc. Boston, MA
7. Abe M (2009) Vehicle handling dynamics: theory and application. Elsevier, Oxford

Integrated Development of Vehicle Dynamics Demonstrated on the New Bmw 3 Series

Pavel Kvasnicka and Peter Dick

Abstract This paper describes BMW's new integrated approach for chassis development. The chassis optimization process includes the evaluation of requirements ranging from customer expectations to component parameters, as well as testing and validation. BMW developed a novel systematic methodology for combining the various design tools and methods. The process starts with an assessment of customer requirements based on subjective criteria and objective measurements. BMW uses a standardized set of objective criteria. This makes it possible to compare vehicle performance through history and across the competitors. Based on these criteria and subjective impressions the goals are defined. These goals are then detailed into component requirements. For this purpose, iterative development and validation steps are planned together in order to refine the requirements, basing the new design on the results of the previous step. These are determined through simulation, with a test-rig, or through vehicle testing. This paper presents examples of chassis elastokinematics, the steering properties, and the vertical suspension properties. The objective goals from the first step are mapped to passive subsystems of the vehicle, such as suspension and steering, but also to control systems as well. After the layout process, tests of the vehicle hardware are performed and measured against the goals obtained from the customer requirements. The virtual development process is supported by scalable models and systems, starting with an expert system that demonstrates the dependencies between subsystems, components and customer needs. A fast concept

F2012-G06-008

P. Kvasnicka (✉) · P. Dick
Bmw Ag, Mexico, Germany
e-mail: pavel.kvasnicka@bmw.de

P. Dick
e-mail: peter.dick@bmw.de

model provides a convenient way to detail the requirements to subsystems and a subsequent transfer to further car derivatives. Finally, more complex MBS and FEM simulations are performed to optimize the component parameters. These steps result in an effective development process, combining the strengths of the hardware and virtual worlds. BMW uses these methods to develop derivatives primarily virtually while nonetheless ensuring outstanding driving dynamics.

Keywords Integrated vehicle design • Requirement assessment • Simulation, objective measurements

1 Introduction

BMW strives to create exciting cars with outstanding driving performance in a short and effective development process. This ensures an advantage in the current challenging market environment. For the new 3 Series and its derivatives BMW instituted an approach using integrated virtual and hardware optimization steps for the development of the chassis. In this approach simulation and hardware tests do not just co-exist but intelligently build upon one another.

This paper describes the new integrated approach for the development of the driving dynamics. The chassis optimization process includes the evaluation of requirements such as customer expectations and component parameters, as well as testing and validation. The novel methodology for combining the existing design tools and methods is presented.

2 Integrated Development

The vehicle development process involves defining and testing requirements. Starting with customer needs and developing them to component descriptions (Fig. 1).

These development requirements cannot be implemented directly, as there are many trade-offs which are partly solved in different teams. Moreover, a modern development engineer has the option to choose from different methods, such as simulation, hardware, prototypes and test rigs. A robust and time effective process has to be established to support the progress of the development.

The development process is divided in several stages. For every stage the main goals are predefined. The engineers are looking for the best combination of developing and testing methods over the stages. For example, a suspension system is selected by virtual methods. After this step, a prototype confirms this system and defines new goals for the set-up. This new set-up is then further developed and

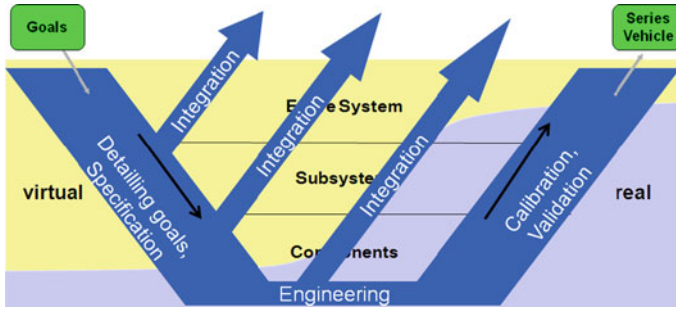


Fig. 1 Development process

Fig. 2 Validation landscape of the 3 series

	early stage	calibration	pre-series
Elastokinematics	S	S/HW	HW
Structure Interface	S	S/HW	HW
Steering	S	HW	HW
Vertical Components	S	S/HW	HW
ECU		S/HW	HW
Driver Assistance		HW	HW

tested on a virtual test-rig. The final set up is found in a prototype. These steps are done for every main sub-system of the vehicle as shown in the “validation landscape” (Fig. 2).

Because of these steps, an integrated plan was created. For example for the development prototype phase (Fig. 3).

An integrated approach with virtual and hardware prototypes was established. The hardware was mainly used to calibrate the knowledge and to establish a basis of vehicle data and subjective impression. The virtual vehicles were used to extrapolate the knowledge to derivatives.

3 Chassis

The chassis of the 3 Series was developed with the goal of significantly improving comfort compared to the previous model while remaining best in segment in driving dynamics. Despite the already outstanding handling qualities, it was necessary to improve some specific driving characteristics such as robustness in straight-line-driving and steering accuracy/steering feedback to ensure the next generation best in segment claim. Furthermore, improvements in objective criteria (press tests) were challenging due to the reduced rolling resistance to achieve CO2-reduction targets.

For the driving dynamics, objective values were selected: average ISO lane change speed, maximum lateral acceleration and stability criteria like braking

Motorisation	Elastokinematics /Structure	Vertical Components	Steering	HW-Prototype
Top Model				Calibration
				Virt. Prototype
				Risk. Mngmnt.
Standard Model				
Low-End Model				

Fig. 3 Combination of HW and Virt. Prototypes in the calibration stage

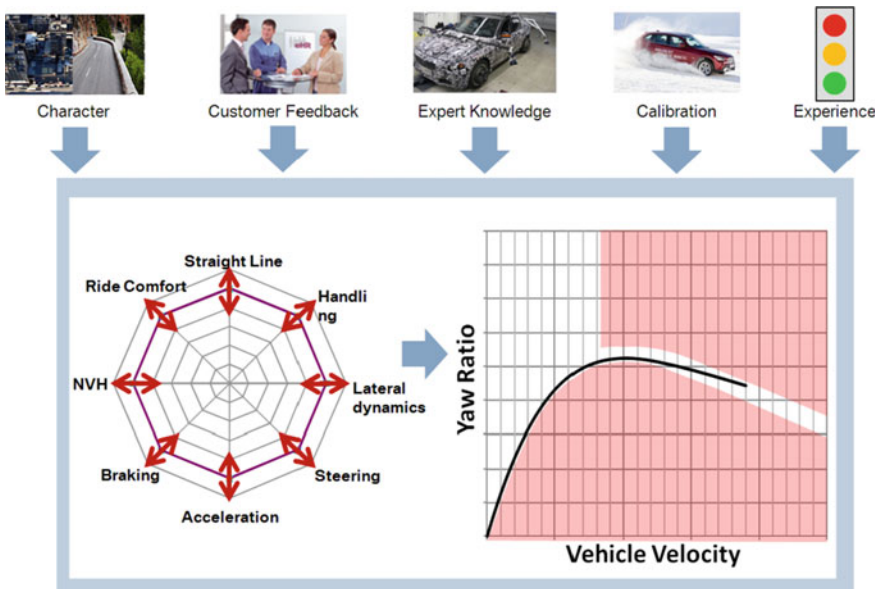


Fig. 4 Assessment of objective criteria for virtual layout

while cornering. These values are accompanied by subjective descriptions of how the vehicle has to perform in different customer use cases and driving conditions.

The values of the previous model and comparable vehicles on the market were acquired by measurements. For the subjective descriptions, BMW has a set of objective criteria to translate the textual requirements into criteria usable for the simulation.

For example, Fig. 4 shows a plot of the yaw gain with respect to the vehicle velocity, defined as a measure of the vehicle’s agility. Similar plots were established for stability criteria, steering properties etc. Based on these values and the

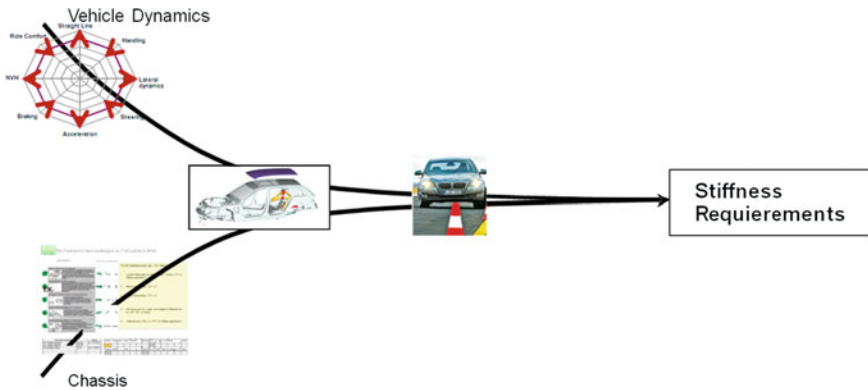


Fig. 5 Integrated Process for requirements of body stiffness

expert knowledge the suspension system in combination with the active systems was optimized.

Considering all criteria regarding function, packaging, mass and costs, the first set-up for the suspension is found using CATIA system [1]. This data is transferred by an automated process to ADAMS [2], where the system calibration is calculated.

After these initial virtual and hardware developments, the double-joint front axle with spring struts and the five-link axle rear suspension is selected.

One of the most important parts affecting the vehicle dynamics is the car body. BMW has developed a map of global and local stiffness values of the car body to handle the requirements of the driving dynamics. In a first step, these requirements are prepared in a virtual environment generating variations for the hardware set up (Fig. 5).

4 Steering

Similar to the overall driving dynamics, BMW has defined a set of goals to be achieved relative to the previous model regarding the specific steering behaviour. For example, the steering torque during a drive and a parking manoeuvre. The disturbance reaction is defined. In an iteration process, the main attributes (steering ratio, steering power) are pre-defined.

The sport steering of the 3 Series can be used as an example. The goal was to provide a more direct and agile behaviour of the vehicle lateral response for the city speeds and at the same time achieve a comfortable and robust behaviour for the highway speeds. The property requirements are depicted in Fig. 6.

To accomplish these requirements, virtual tests were done. With different types of variable steering ratios, the properties of the steering were tested (Fig. 7).

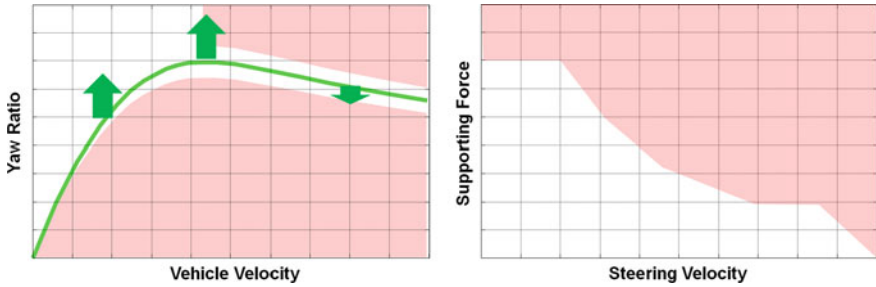
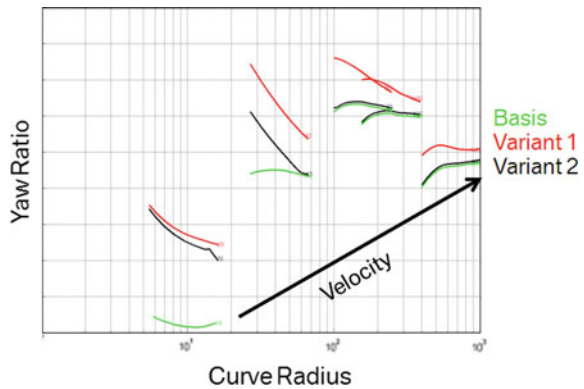


Fig. 6 Requirements for the sport steering

Fig. 7 Yaw ratio with different steering ratio set-ups



Variant 2 fulfils the driving requirements for more agile behaviour at low speeds, while being stable at highway speed. This set up was then tested and confirmed in the hardware test.

5 Vertical Dynamics

The optimisations of the vertical design parameters for ride comfort and handling can be decoupled under some circumstances [3]. The development process for the 3 Series is outlined in (Fig. 8).

Test drivers are able to sense even small differences in the stiffness of the main springs. Based on the previous model, the development engineers provide the spring stiffness for the front and the rear suspension according to the vehicle’s character.

The target function for the roll moment ratio is mainly derived from the requirements of agility and stability (Fig. 9). Using this target function, an optimisation of the vertical design parts is carried out. This optimisation delivers the initial set-up for the development engineers’ tests. The results are then discussed in

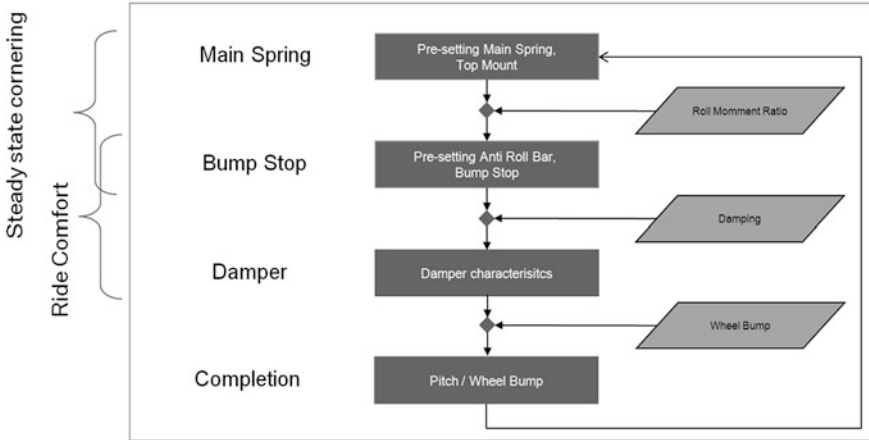
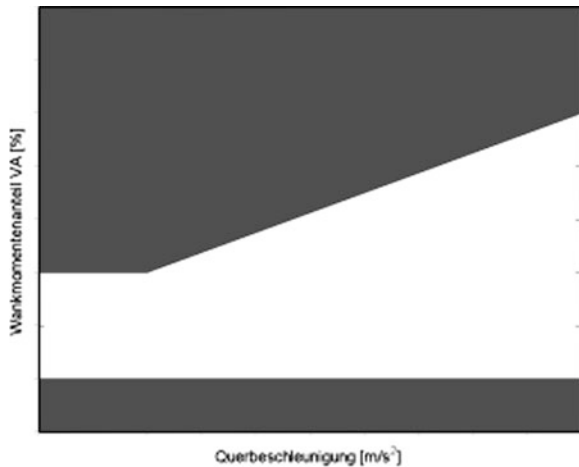


Fig. 8 Development process, using quasi-steady-state cornering for lateral vehicle

Fig. 9 Definition of the target function for the roll moment ratio



detail regarding the under-steering and stability behaviour depending on lateral acceleration. If needed, the target function is then adjusted and can be used for the initial optimisation of the derivative models (such as the convertible or coupé)

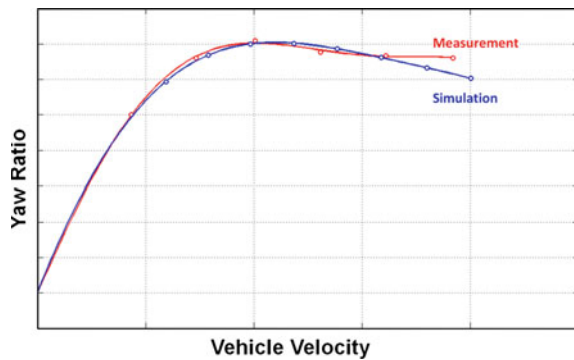
6 Anti-Roll Bar Setting

First generic combinations of stiffness of the front and rear anti-roll bars are simulated for the target functions initial roll moment ratio and overall stiffness. The results are plotted in an overview matrix (Fig. 10), which includes the target function overall stiffness in the lower part of each cell and the initial load transfer

Zielerfüllung: Oben: Wanksteifigkeit Unten: Wankmomentenverteilung		Stabivariante Hinterachse				
		1	2	3	4	5
Stabivariante Vorderachse	1	91	93	94	96	97
		100	98	97	95	94
	2	93	94	96	97	99
		102	98	97	95	95
	3	94	96	97	99	100
		102	100	98	97	95
	4	95	97	99	100	101
		103	100	98	98	97
	5	97	98	100	101	103
		103	102	100	98	97
	6	98	100	101	103	104
		105	102	100	100	98
	7	100	101	103	104	106
		105	103	102	100	98
	8	101	103	104	106	107
		105	103	102	100	100
	9	102	104	106	107	108
		106	105	103	102	100

Fig. 10 Example for an optimal anti roll bar set-up

Fig. 11 Measurement/
Simulation comparison for
yaw rate of the 3 series



in the upper part. The printed values are normalised to a theoretical optimum. The optimum is then found in the interception of the two target functions (in this example in the middle of the table).

7 Tool Landscape

The integrated development is enabled by an integrated tool landscape. For the suspension development, BMW uses numerous virtual and real tools. The effectiveness is realised by an automated process for exchanging the requirements and the data between the hardware and software tools. A comparison of the virtual and

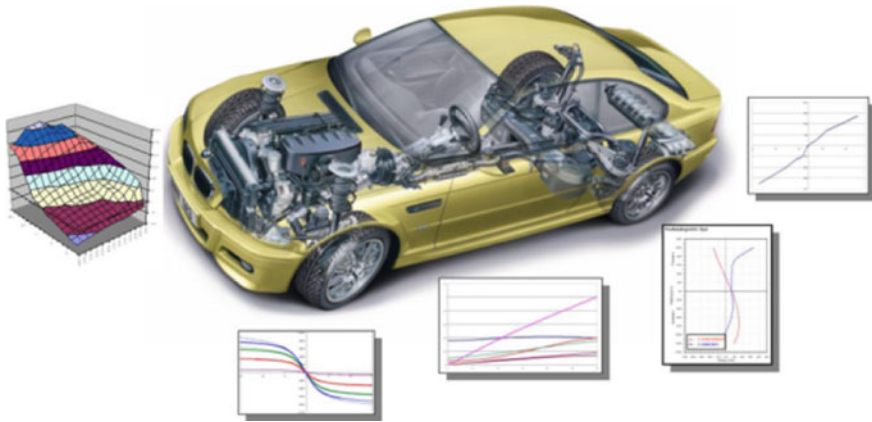


Fig. 12 Diagrammatical representation of the vehicle dynamics model

hardware results is performed periodically as depicted in Fig. 11 for the yaw rate behaviour.

8 Hardware Tools

In an integrated environment, data exchange between the virtual and hardware world is essential. BMW has established a PDM-CAE system which systematically couples the acquired data from the component and full vehicle measurements with the simulation data models. Additionally, communication between the hardware and virtual testing is implemented by integration teams, where hardware and virtual tools are used interchangeably.

9 Virtual Tools

For the optimisation of the lateral dynamics, BMW’s Two-Track Model is used [4]. The model (Fig. 12) includes mathematical representations for the properties of vertical dynamics, such as the main springs and dampers, bump stops, anti-roll bars and roll centres. The Elasto-kinematics is described by mathematical functions which are identified either from measurements or from simulation models, such as ADAMS. The tyres are described with the Pacejka Formula [5].

For the optimisation of the vertical components such as the damper and top mount, the vehicle is reduced to a one track model (Fig. 13). The model has four DOF, two for the body (vertical travel and pitch) and one vertical DOF for each suspension.

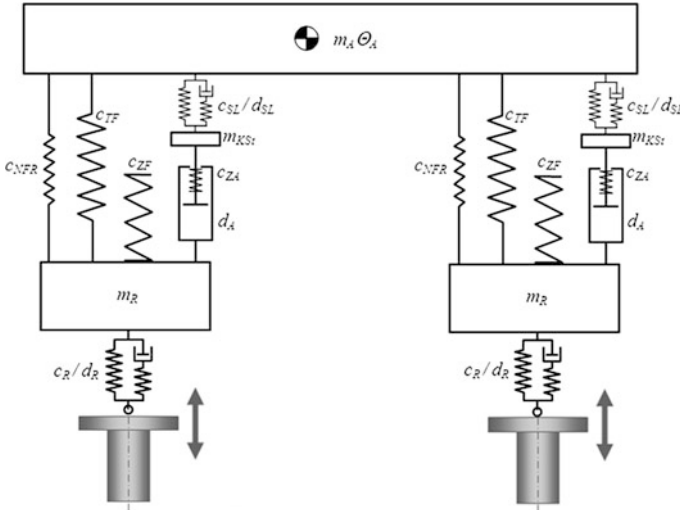
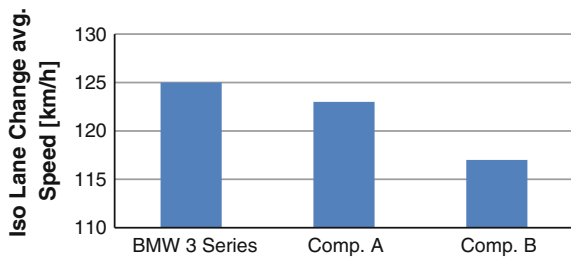


Fig. 13 Primary model for ride comfort

Fig. 14 Comparison Iso Lane change 3 Series vs. competitors



The model is stimulated by either measured or synthetic signals. The analyses can be done on a vehicle or a component level, which is important for the calculation of the operating points of the mounts and dampers.

When the load case is a highly non linear excitation, or component requirements are needed, the design criterion requires a detailed model and multi-body simulation with ADAMS/Car is used at BMW. The model includes single rods connected by elastic elements with non-linear properties. The tyre model includes a flexible belt [6], which enables the embedding of obstacles.

10 Conclusion

With this new integrated process it was possible to prepare a good basis for a final calibration to achieve the challenging goals over an increasing number of model variants whilst using fewer resources. Moreover, in the press manoeuvres such as

iso-lane change the 3 Series is a new benchmark in its class Fig. 14. Many test results of the international automotive press underline the achieved targets of the new 3 Series with respect to driving dynamics and road comfort.

References

1. Guldner J, Böttrich M, Berkan D, Kvasnicka P, Kriebel S, Sedlmayr M (2011) Vehicle dynamics—architecture and advanced development. Chassis Tech, Brompton
2. Wielenga TJ (1986) Analysis methods and model representation in ADAMS, Internal Document of Mechanical Dynamics, Inc.
3. Kvasnicka P, Schmidt H (2010) Conceptual layout for spring/damper set up of a prototype regarding vehicle dynamics and ride comfort. Chassis Tech, Brompton
4. Kvasnicka P, Prokop G, Dörle M, Rettinger M, Stahl A (2006) Comprehensive approach for the chassis control development SAE International Congress
5. Zegelaar P (1998) The dynamic response of tyre to brake variations and road variations, Delft
6. Gipser M (1999) FTire a new fast tire model for ride comfort simulations. International ADAMS User's Conference Berlin

Torque Feedback Control for the Hand-Wheel Actuator of SBW Based on Active Disturbance Rejection Controller

Guangzheng Gao, Hui Chen, Liming Lou and Shirou Nakano

Abstract The nonlinear friction, parameter perturbation and other inner or external disturbances existing in the hand-wheel actuator (HWA) of steer-by-wire system (SBW), have a bad effect on the torque feedback control of SBW. In this paper, a new torque feedback controller based on the active disturbance rejection control theory (ADRC) is proposed for the torque feedback control of the HWA of SBW. The ADRC controller includes three components: Tracking Differentiator (TD), Extended State Observer (ESO) and Nonlinear State Feedback (NLSF). It can estimate the inner and external disturbances including the nonlinear friction disturbance and compensate them in real time. The simulation results show that ADRC controller has better performance than PID controller in the robustness to the nonlinear friction disturbance.

Keywords Steer-by-wire · Torque feedback control · Friction compensation · Active disturbance rejection control · Extended state observer

F2012-G06-009

G. Gao (✉) · H. Chen

School of Automotive Studies and Clean Energy Automotive Engineering Center, Tongji University, Shanghai, People's Republic of China
e-mail: gaoguangzheng@163.com

L. Lou · S. Nakano

Research and Development Center, JTEKT Co., Ltd, Japan

1 Introduction

The SBW (steer-by-wire system) has many advantages over the traditional steering system in vehicle handling performance, safety, especially greater freedom in the force feedback characteristic design. It has great application prospects in the future automobile technology. Therefore, more and more scholars have paid close attention to the research of SBW [1, 2]. Normally, most mechanical components of the hand-wheel actuator (HWA) of SBW are the same as that of C-EPS (Column type Electric Power Steering), hence the HWA of C-EPS can be used to do research on SBW.

In order to simulate the real road feel, the torque feedback control of HWA needs to obtain both desirable torque command tracking performance and good robust performance. However, the inner or external disturbances, especially the nonlinear friction existing in the HWA of SBW, have a bad effect on the torque feedback control and make the torque feedback control particularly challenging. The friction torque existing in the HWA of SBW is normally large and it is characterized with strong nonlinearity, uncertainty and hysteresis. The mechanical friction torque can lead to tracking wave distortion at the zero-speed crossing point, system steady-state error and stick-slip phenomenon [3–5]. The friction disturbance is the main factor that affects the performance of the torque feedback control of SBW.

Some scholars proposed the friction compensation methods based on the friction model. The friction models, such as the Static Stribeck Model, the LuGre Model, etc. have been established [6]. The accurate friction compensation depends greatly on the degree of the precision of the friction model. However, in the practical application, some parameters are challenging to measure. In addition, the friction model is the function of the relative velocity, but accurate signal of relative velocity is hard to obtain at low velocity. All factors mentioned above reduce the precision of the friction model and thus it will affect the performance of friction compensation.

Other scholars proposed the friction compensation methods through improving the disturbance rejection ability of the system [3, 6]. These methods do not depend on the accurate friction model. Among these methods, PID (proportional-integral-derivative) controller is widely used because it's simple and effective. However, PID controller is sensitive to the disturbance and the parameter perturbation of the system. Steady-state error of the system and the tracking wave distortion at the zero-speed crossing point exist when PID controller is adopted in the friction compensation control. When the static friction is larger than the Coulomb friction, the limit cycle oscillation exists in the friction compensation method based on PID controller [7].

In this paper, a new torque feedback controller based on the active disturbance rejection control technique (ADRC) is proposed to realize the friction compensation and improve the torque feedback control performance of the HWA of SBW. The basic idea of ADRC controller is to estimate the real-time disturbances, including the friction disturbance, and compensate them in real time. The ADRC

controller doesn't depend on the friction model and it can achieve both desirable torque command tracking performance and good robustness to the system disturbances.

The paper is organized as follows. The model of HWA of SBW is established in Sect. 2. The torque feedback controller based on ADRC is designed in Sect. 3. The simulation test results are shown in Sect. 4. Finally, the conclusion is given in Sect. 5.

2 Model of the Hand-Wheel Actuator of SBW

2.1 Model of the Mechanical Structure of the HWA

The HWA of SBW introduced in this paper is modified from C-EPS, and the mechanical structure of the HWA of SBW is shown in Fig. 1.

According to the idea of reduced order modeling, the HWA of SBW can be simplified to two masses as shown Fig. 1, namely the steering wheel and the steering column, the DC motor. The dynamic model of the HWA can be described as follows:

$$\begin{cases} J_C \ddot{\theta}_C + C_C \dot{\theta}_C + K_S (\theta_C - \frac{\theta_M}{n}) = T_h \\ J_M \ddot{\theta}_M + C_M \dot{\theta}_M + \frac{K_S (\frac{\theta_M}{n} - \theta_C)}{n} + F_M = T_M \end{cases} \quad (1)$$

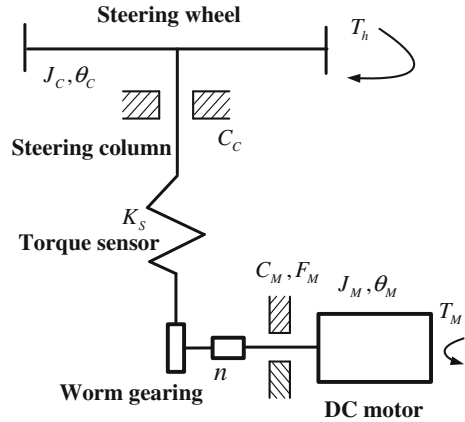
Where J_C is the moment of inertia of the steering wheel and the steering column, J_M is the moment of inertia of the DC motor; θ_C , θ_M are the angular displacement; C_C , C_M are the damping coefficient; K_S is the stiffness coefficient of the torque sensor; n is the transmission ratio of the worm gearing; F_M is the equivalent friction torque existing in SBW; T_h is the steering torque of the driver; T_M is the DC motor torque.

2.2 Electrical Model of the DC Motor

The PWM servo drive is used to drive the brush type DC motor applied in the HWA at a high switching frequency. The PI controller inside the PWM servo drive is applied to realize the current closed-loop control of the DC motor. The electrical model of DC motor can be described as follows:

$$\begin{cases} u_d = K_{pwm} u \\ Ri + L \frac{di}{dt} + K_e \dot{\theta}_M = u_d \\ T_M = K_M i \end{cases} \quad (2)$$

Fig. 1 Mechanical structure of the HWA of SBW



Where K_{pwm} represents the amplification factor of PWM servo drive, u is the control voltage of PWM servo drive, u_d is the terminal voltage of DC motor, R is the armature resistance, L is the armature inductance, i is the armature current, K_e is the back EMF constant, K_M is the DC motor torque constant, T_M is the electromagnetic torque of DC motor.

2.3 The Friction Model

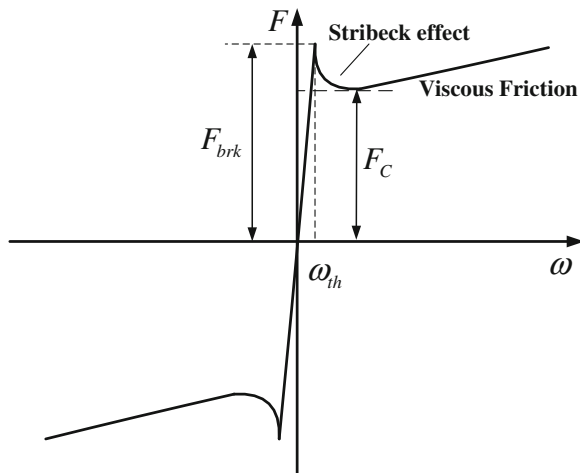
The mechanical friction torque is the main factor that affects the performance of the torque feedback control of SBW. In this paper, the friction model is established based on the Static Stribeck Model [3, 6, 8]. This friction model is the function of relative velocity and it is shown in Fig. 2. It takes the static friction, the Coulomb friction, the viscous friction, especially the Stribeck effect into account. Therefore, it is able to describe the friction characteristic roundly.

The static friction is simplified by a linear function and its peak value F_{brk} is the static breakaway friction torque. It is higher than the Coulomb friction F_C . The dip in the curve is called the Stribeck effect, which is the main factor causing the friction stick–slip phenomenon. The viscous friction works at the higher magnitudes of velocity, where the friction is the linear function of the velocity. The Static Stribeck Model can be described as follows:

$$F = \begin{cases} (F_C + (F_{brk} - F_C) \exp(-c_v|\omega|)) \text{sign}(\omega) + f\omega, & |\omega| > \omega_{th} \\ \omega \frac{f\omega_{th} + (F_C + (F_{brk} - F_C) \exp(-c_v\omega_{th}))}{\omega_{th}}, & |\omega| < \omega_{th} \end{cases} \quad (3)$$

Where ω is the relative velocity; f is the viscous friction coefficient; c_v is the transition approximation coefficient; and ω_{th} is the linear region velocity threshold.

Fig. 2 The static stribeck friction model



2.4 The Torque Feedback Control Structure of SBW

The structure diagram of the torque feedback control of SBW is shown in Fig. 3. The objective of the control system is to provide reaction torque to the driver as designed by the force feedback characteristic. θ_C represents the steering wheel angle, and it is the input of the control system. T_Cmd is the command of reaction torque to the driver, and it is the input of the torque feedback controller. T_Cmd is designed by the force feedback characteristic according to the steering wheel angle θ_C . w represents the disturbances to the HWA of SBW and in this paper, it mainly represents the nonlinear friction disturbance. T_S is the torque sensor signal. The compensation module includes inertia compensation and damping compensation. Through the compensation module, we can get the estimated value of the steering torque of the driver T_{h_est} . T_{h_est} is the feedback of the torque feedback controller. The torque feedback controller generates the current command of DC motor i_Cmd . i is the actual current of DC motor. T_M is the electromagnetic torque of DC motor and it is the input of the mechanical structure of the HWA, thus the driver can get reaction torque from SBW.

3 Torque Feedback Control of SBW Based on ADRC Controller

3.1 Active Disturbance Rejection Controller Design

Consider a second-order system as follows:

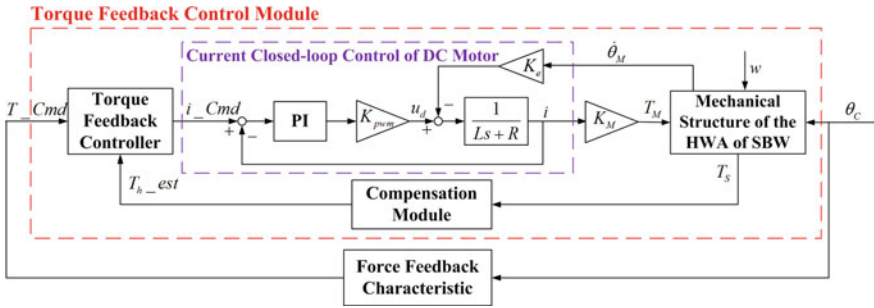


Fig. 3 The structure diagram of the torque feedback control of SBW

$$\begin{cases} \dot{x}_1 = x_2 \\ \dot{x}_2 = f(x_1, x_2) + w + b_0u \\ y = x_1 \end{cases} \quad (4)$$

Where x_1, x_2 are the state variables of the system. $f(x_1, x_2)$ is the dynamic characteristic of the system and it is regarded as the inner disturbance of the system. w is the unknown external disturbance. u is the input of the system and y is the output of the system. b_0 is the coefficient of the system input. The basic idea of ADRC controller is to regard all the disturbances of the system as the new state variable x_3 , as shown in Eq. (5) and Extended State Observer can estimate x_3 and make feed-forward compensation in real time, namely realizing the active disturbance rejection control.

$$\begin{cases} \dot{x}_1 = x_2 \\ \dot{x}_2 = x_3 + b_0u \\ \dot{x}_3 = f(x_1, x_2) + w \\ y = x_1 \end{cases} \quad (5)$$

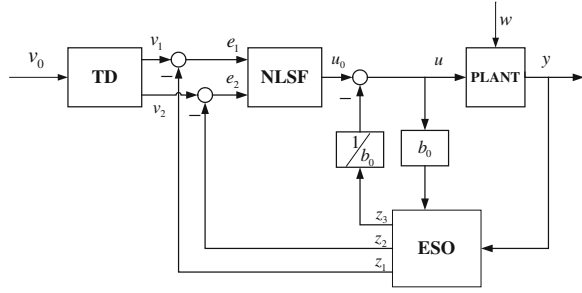
The ADRC controller includes three components: Tracking Differentiator (TD), Extended State Observer (ESO) and Nonlinear State Feedback (NLSF) [9]. The control block of ADRC controller is shown in Fig. 4.

The second-order discrete algorithms of ADRC controller are described as follows:

$$\text{TD} : \begin{cases} v_1(k+1) = v_1(k) + hv_2(k) \\ v_2(k+1) = v_2(k) + h(fst(v_1(k) - v_0(k), v_2(k), r, h_0)) \end{cases} \quad (6)$$

$$\text{ESO} : \begin{cases} z_1(k+1) = z_1(k) + h(z_2(k) - \beta_1e(k)) \\ z_2(k+1) = z_2(k) + h(z_3(k) - \beta_2fe + b_0u) \\ z_3(k+1) = z_3(k) + h(-\beta_3fe_1) \\ e(k) = z_1(k) - y(k), fe = fal(e(k), 0.5, \delta), fe_1 = fal(e(k), 0.25, \delta) \end{cases} \quad (7)$$

Fig. 4 Control block of ADRC controller



$$\text{NLSF} : \begin{cases} u_0(k) = k_p(\text{fal}(e_1(k), \alpha_1, \delta_1)) + k_d(\text{fal}(e_2(k), \alpha_2, \delta_2)) \\ u(k) = u_0(k) - z_3(k)/b_0 \\ e_1(k) = v_1(k) - z_1(k) \\ e_2(k) = v_2(k) - z_2(k) \end{cases} \quad (8)$$

Where w is the external disturbance of the system and y is the output of the system; h is the sampling step of the system; fst, fal are the nonlinear functions designed by Han Jingqing to improve the performance of the controller [10]. Nonlinear TD can arrange the transition process for the input signal v_0 of the system. TD provides the tracking signal v_1 and the differential signal v_2 for the input signal v_0 . It solves the problem of contradiction between the rapidity and overshoot existing in the PID controller. The NLSF adopts the nonlinear combination of the state variable error signals e_1, e_2 between TD and ESO to generate the control signal u of the system through dynamic feedback linearization. ESO is the most important part of ADRC controller. It estimates the state variables x_1, x_2 with z_1 and z_2 based on the input u and the output y of the system. Particularly, ESO regards the system disturbances (inner and external disturbances) as the new system state variable x_3 , namely the extended state variable. ESO can estimate x_3 with z_3 and compensates it in real time. In this way, ADRC controller can realize the active disturbance rejection.

3.2 Torque Feedback Control Based on ADRC Controller

The structure diagram of the torque feedback control of SBW based on ADRC controller is shown in Fig. 5. θ_C is the input of the control system. In this paper, the torque feedback control is focused, so the force feedback characteristic is simplified to be a simple linear model. The bandwidth of the current closed-loop control of DC motor (about 200 Hz) is much higher than that of the torque closed-loop control, thus the current command i_Cmd is nearly equal to the motor current i and the motor current i can be regarded as the input of SBW system. T_{h_est} estimates the steering torque of the driver, and it is the feedback to the ADRC controller. Hence the model of the HWA of SBW can be described as follows:

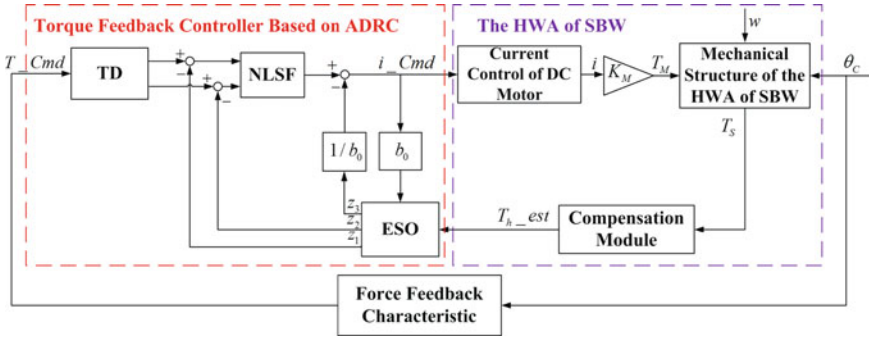


Fig. 5 The torque feedback control diagram of SBW based on ADRC controller

$$\begin{cases} J_M \ddot{\theta}_M + C_M \dot{\theta}_M + K_S(\theta_M/n - \theta_C)/n + F_M = T_M \end{cases} \quad (9)$$

$$T_{h_est} = K_S(\theta_C - \theta_M/n) + J_C \ddot{\theta}_C + C_C \dot{\theta}_C. \quad (10)$$

$$T_M = K_M i. \quad (11)$$

According to the Eq. (10),

$$\theta_M = n\theta_C - n(T_{h_est} - J_C \ddot{\theta}_C - C_C \dot{\theta}_C)/K_S \quad (12)$$

Substitute the Eqs. (11) and (12) into the Eq. (9), and define $x_1 = T_{h_est}$, $x_2 = \dot{T}_{h_est}$, the Eq. (9) is transformed into the Eq. (13).

$$\begin{cases} \dot{x}_1 = x_2 \\ \dot{x}_2 = x_3 + b_0 i \\ x_3 = f(x_1, x_2, \theta_C) + w \\ y = x_1 \end{cases} \quad (13)$$

Where x_3 is the extended state variable, $f(x_1, x_2, \theta_C)$ is regarded as the inner disturbance and $w = (K_S/(J_M n)) \cdot F_M$, represents the friction disturbance; $b_0 = -(K_S K_M)/(J_M n)$.

4 Simulation Results

The simulation model of the HWA of SBW and ADRC controller are designed. The simulation test condition is in accordance with on-center steering test [11]. The system input is the steering wheel angle, $\theta_C = (12\pi/180) \sin(0.4\pi t)$ rad. The force feedback characteristic is a linear model, $T_Cmd = (45/\pi) \cdot \theta_C$ Nm. The simulation parameters are shown in Tables 1, 2, 3, and 4 follows.

In order to show the good performance of ADRC controller, the control performance comparison is made between PID and the ADRC controller.

Table 1 Electric parameters of DC motor

Parameters	Value
L	300 μH
R	100 $\text{m}\Omega$
K_{pwm}	0.24
K_e	0.05 $\text{V}\cdot\text{s}/\text{rad}$
K_M	0.05 Nm/A

Table 2 Parameters of friction torque

Parameters	Value
F_C	0.055 Nm
F_{brk}	0.06 Nm
C_v	3
F	0.001 $\text{Nm}\cdot\text{s}/\text{rad}$
W_{th}	0.001 rad/s

Table 3 Parameters of the HWA

Parameters	Value
J_C	0.032 $\text{kg}\cdot\text{m}^2$
C_C	0.02 $\text{Nm}\cdot\text{s}/\text{rad}$
K_S	140 Nm/rad
J_M	0.00013 $\text{kg}\cdot\text{m}^2$
n	16.5
C_M	0.0044 $\text{Nm}\cdot\text{s}/\text{rad}$
–	–

Table 4 Parameters of ADRC controller

Parameters	Value	Parameters	Value
h	0.001	k_d	0.16
r	10,000	α_1	0.5
β_1	1200	α_2	1
β_2	700,000	δ_1	0.1
β_3	65,000,000	δ_2	0.1
δ	0.3	b_0	-3365
k_p	0.9	–	–

4.1 Simulation Without Disturbances

Considering the HWA of SBW without friction torque (namely $w = 0$), the parameters of PID and ADRC controller are properly tuned, and they almost have the same torque command tracking performance. Figure 6 shows the simulation results and Fig. 7 shows that ESO can estimate the disturbance of the system x_3 with z_3 .

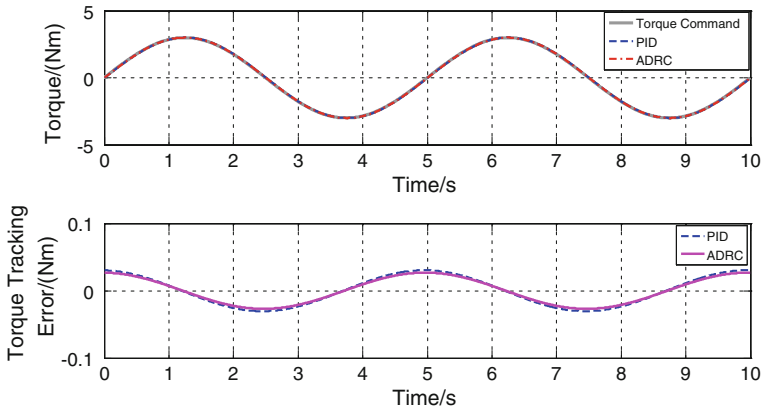
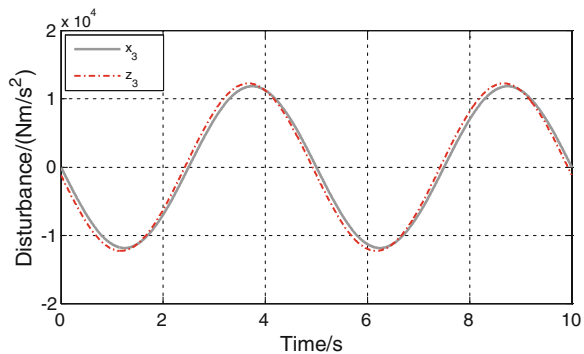


Fig. 6 Simulation result without friction

Fig. 7 Disturbance in SBW



4.2 Simulation with Friction Disturbance

Taking the influence of nonlinear friction disturbance existing in the HWA into account, the simulation results are shown as follows. Figure 8 shows that ADRC controller has better robustness to nonlinear friction disturbance than PID. Normally, the minimum torque that a driver can feel is about 0.2 Nm. The maximal torque error of ADRC controller is about 0.1 Nm, while the maximal torque error of PID controller is 0.23 Nm, which is larger than the torque threshold 0.2 Nm. Figure 9 shows the friction disturbance with strong nonlinearity existing in the HWA of SBW. Figure 10 shows that ESO can estimate the system disturbances x_3 with z_3 in real time accurately and realize the active disturbance rejection.

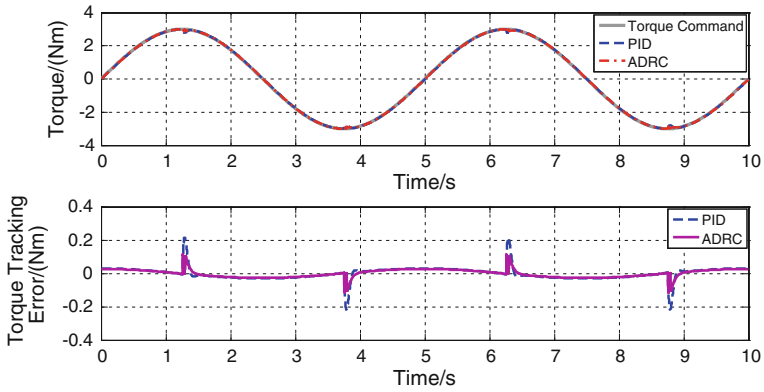


Fig. 8 Simulation result with friction disturbance

Fig. 9 Friction disturbance in SBW

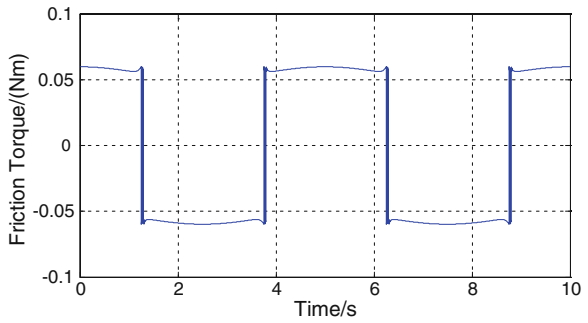
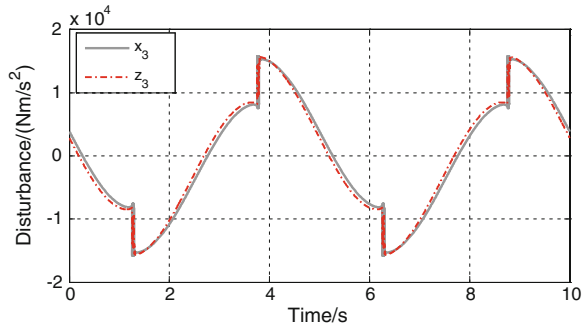


Fig. 10 Disturbances in SBW



4.3 Simulation with Parameter Perturbation

The friction torque existing in SBW may become larger for poor lubrication or other reasons. Taking the influence of parameter perturbation into account, the peak value of the static friction in DC motor is changed to be 0.08 Nm from

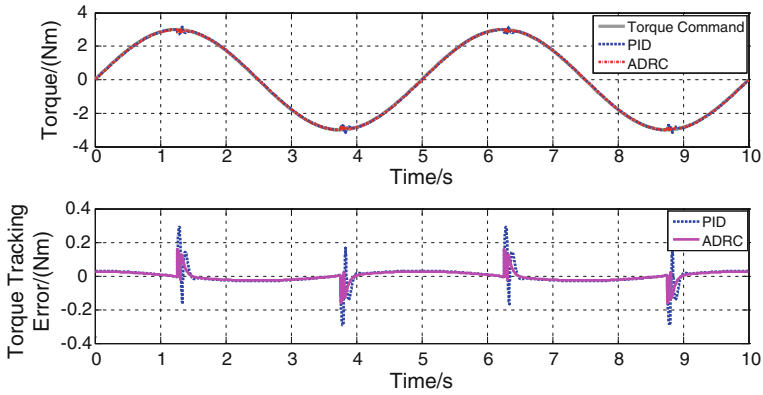


Fig. 11 Simulation result with parameter perturbation

Fig. 12 Friction torque in SBW

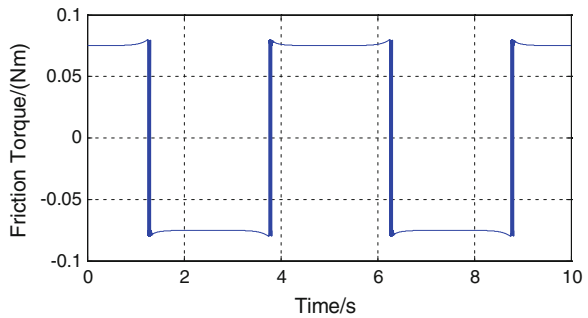
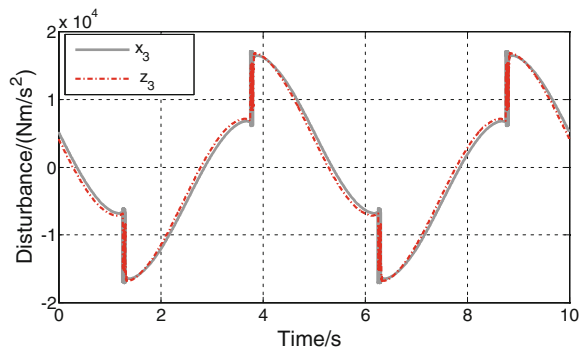


Fig. 13 Disturbances in SBW



0.06 Nm. The simulation results are shown as follows. Figure 11 shows that ADRC controller has stronger robustness to system uncertainty than PID. The maximal torque error of ADRC controller is 0.15 Nm, while the maximal torque error of PID controller is 0.3 Nm, which is larger than the torque threshold 0.2 Nm that a driver is able to feel. Figure 12 shows the friction torque in SBW and Fig. 13 shows that ESO can estimate the disturbances of the system x_3 with z_3 .

5 Conclusion

In this paper, a new control method based on ADRC controller is proposed for the torque feedback control of the HWA of SBW. The simulation results based on MATLAB/Simulink software show that a good performance on the nonlinear friction rejection is obtained and both good torque tracking performance and strong robustness to system uncertainty and external disturbances are realized. The simulation results show that the maximal torque error caused by friction disturbance is smaller than 0.2 Nm, the torque threshold a driver can feel, when the torque feedback control of SBW is realized by ADRC controller. Such kind of torque feedback control method could also be used in the hand-wheel actuator of driving simulator.

References

1. Werner H, Wolfgang P, Peter D, Gerhard R, Peter B (2000) Future electrical steering systems: realizations with safety requirements. SAE Paper 2000-01-0822
2. Se-Wook O, Seok-Chan Y, Ho-Chol C, Seok-Hwan J, Jae-Ho J, Chang-Soo H (2003) The development of an advanced control method for the steer-by-wire system to improve the vehicle maneuverability and stability. SAE Paper 2003-01-0578
3. Armstrong B, Dupont P, Canudas de WC (1994) A survey of models, analysis tools and compensation methods for the control of machines with friction. *Automatica* 30(7): 1083–1138
4. Zbigniew L, Dariusz Z (2007) Friction and stick-slip phenomena in steering system—modeling and simulation. SAE Paper 2007-01-1153
5. Zbigniew L, Dariusz Z (2002) Vehicle dynamics simulation with inclusion of freeplay and dry friction in steering system. SAE Paper 2002-01-0619
6. Qiang Liu, Lianjie Er, Jinkun Liu (2002) Overview of Characteristics, Modeling and Compensation of Nonlinear Friction in Servo Systems [J]. *Syst Eng Electron* 24(11):45–52
7. Armstrong B, Amin B (1996) PID control in the presence of static friction: a comparison of algebraic and describing function analysis. *Automatica* 32(5):679–692
8. Misovec KM (1997) Friction compensation using adaptive nonlinear control with persistent excitation. Massachusetts Institute of Technology, Massachusetts
9. Jingqing Han (2007) Auto disturbances rejection control technique. *Front Sci* 1:24–31
10. Jingqing H (2009) Active disturbance rejection control technique—the technique for estimating and compensating the uncertainties. National Defence Industry Press, Beijing
11. International Standard ISO 13674-1 (2003) Road vehicles—test method for the quantification of on-centre handling—part 1: weave test, 1st edn. Switzerland

Simulation and Modelling of Steering Ripple and Shudder

Jinhuai Lin and Peter E. Pfeffer

Abstract Vehicle dynamics simulation is very common nowadays at any stage of chassis development which saves development time and cost. An Advanced Steering System Model has been developed and implemented in virtual environment to simulate steering characteristics and handling performance. In the vehicle measurement, it was found that the steering friction decreases when driven on an uneven road. As steering friction is an important steering characteristics related to steering centre feel, the Advanced Steering System Model should be able to produce accurate results for such phenomenon. The objective of this study is to validate the Advanced Steering System Model at different levels of road excitation. A steering system test bench was built up to realize the hardware-in-the-loop tests. In order to investigate the influence of the road excitation to the steering system friction, left and right rack forces were recorded on the test bench when the vehicle was driven on an uneven road. These two signals were imposed to the steering rack force to simulate the random road excitation in vehicle measurements. The measurements were used to validate the Advanced Steering Model. The Advanced Steering Model comprises mechanical module and power assist module. The advanced friction element in the mechanical module consists of an Exponential-Spring-Friction-Element and a parallel Maxwell-Element. It represents the frequency and amplitude dependency of the steering system accurately with appropriately identified parameters. The current parameters for the friction model were identified implicitly in this paper. The imposed noise was generated on a predefined

F2012-G06-013

J. Lin (✉) · P. E. Pfeffer
Munich University of Applied Sciences, Munich, Germany
e-mail: jlin@hm.edu

P. E. Pfeffer
e-mail: peter.pfeffer@hm.edu

uneven road. Further effort should be made to characterize this effect with constant frequency and amplitude force inputs on the test bench. The Advanced Steering Model is capable of representing the system response to the random road excitation, typically the friction reduction of the system due to the random noise input.

Keywords Steering system modelling and simulation · Centre feel · Steering ripple · Steering shudder · Road excitation

1 Introduction

Vehicle dynamics simulation is very common nowadays at any stage of chassis development which saves development time and cost. An Advanced Steering System Model has been developed and implemented in virtual environment to simulate steering characteristics and handling performance [1].

In the handling performance evaluation, the steering friction is an important criterion to the steering centre feel [2]. In the vehicle measurement, it was found that the steering friction decreases when driven on an uneven road. Therefore, the Advanced Steering System Model must be able to represent such phenomenon. The objective of this study is to validate the Advanced Steering System Model at different levels of road excitation.

2 Steering Response to Noise

2.1 Measurements Setup

A steering system test bench was built up to realize the hardware-in-the-loop (HIL) tests such as weave test or steady state circular test. Figure 1 shows the fixing of the steering system on the test bench platform. Two linear motors, which are connected to the steering rack on the left and on the right, are used to apply the lateral forces. The steering wheel is connected to a steering motor, which applies the torque of the drive.

The steering system is set up on the test bench according to the positions measured on the vehicle. The steering system used in the study is a column assist electric power steering system (EPS). The two rack force actuators on the test bench apply the rack forces calculated by a vehicle model. For coupling of the steering rack with the test bench, tie rods are used that are parallel to the steering rack. The steering wheel motor simulates the driver input in steer-by-angle or steer-by-torque mode. The test bench is controlled via a dSPACE real time environment.

Figure 2 shows the interaction between test bench controller and the software environment CarMaker 3.5.1/HIL for dSpace. The two linear motors are force controlled and the steering motor is torque controlled or angle controlled. The

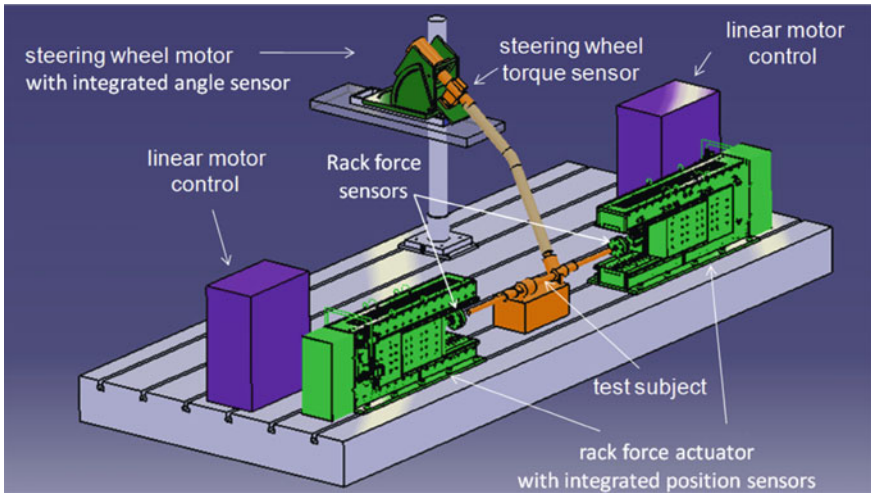


Fig. 1 Components of the steering test bench at Munich University of applied sciences

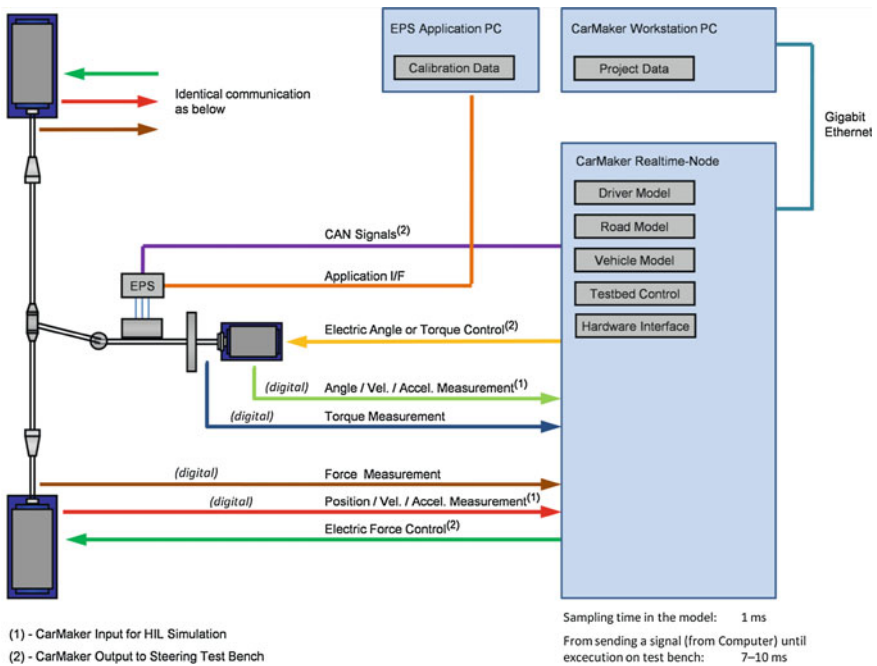


Fig. 2 Communication of the steering test bench with CarMaker

input signals for CarMaker are the measured position, velocity and acceleration for left and right linear motors and the steering motor. The CarMaker outputs to the

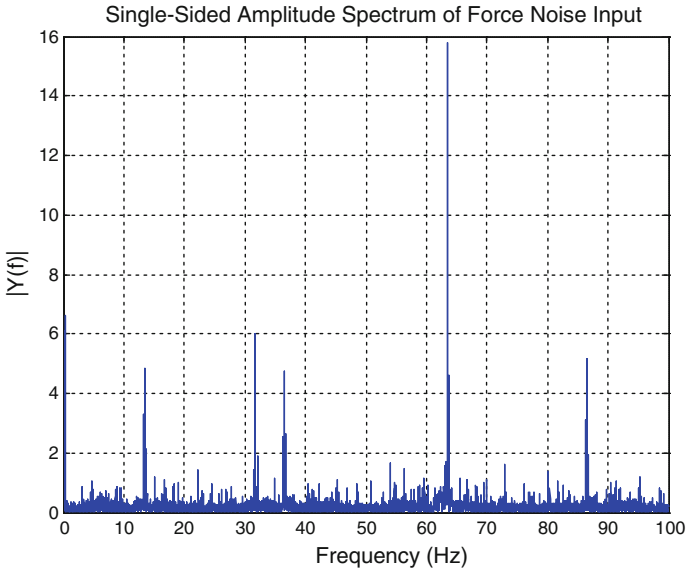


Fig. 3 Force noise single-sided amplitude spectrum

steering test bench are the desired steering wheel angle or torque and the left and right rack forces.

2.2 Steering Response to Noise

In order to investigate the influence of the road excitation to the steering system friction, rack forces for left and right were recorded on the test bench first while the vehicle was driven on an uneven road. These two signals were then added to the rack forces during HIL tests. The noise variations of 0, 10, 25, and 50 % were applied in addition to the rack force calculated by the vehicle model (Fig. 3).

Figure 4 shows that the friction levels of the steering system at different levels of the imposed noise during weave test. In order to derive the tendency of the steering friction deviation, the objective parameters (Table 1) from weave test were calculated. As shown in Fig. 5, the friction of the system decreases while the steering stiffness increases slightly.

3 Description of the Advanced Steering Model

The Advanced Steering System Models (ASM) was developed in order to represent and simulate the accurate characteristics of steering systems [1]. The model comprises of mechanical module and power assistance module. The required input

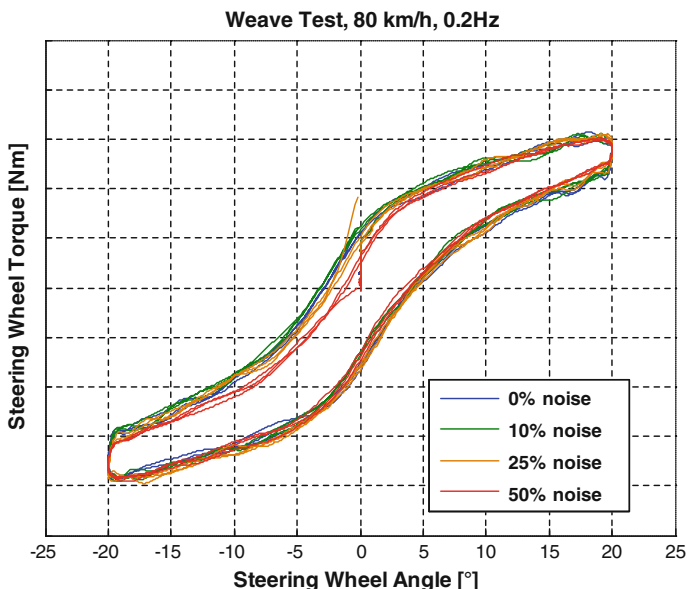


Fig. 4 Steering wheel torque vs. steering wheel angle during weave test at different noise levels

Table 1 Objective parameters in weave test

Steering stiffness (right) (Nm/°)	Gradient between +−20 % Ampl. steering wheel angle (clockwise)
Steering stiffness (left) (Nm/°)	Gradient between +−20 % Ampl. steering wheel angle (anticlockwise)
Steering friction (Nm)	Ordinate deadband
Angle hysteresis (°)	Abscissa deadband

signal of the model is either steering wheel angle or steering wheel torque. A single track vehicle model or a more advanced vehicle model such as the dynamic vehicle model in CarMaker provides the steering model the tie rod force input. The steering model supplies the vehicle model the steering rack position.

Figure 6 shows the steering model layout. The power assistance module refers to the assistance of the hydraulic powered steering system (HPS) or electric powered steering system (EPS) for respective steering systems. The mechanical module provides steering velocity and rack velocity to the power assistance module while the power assistance module feeds back the assisting force and the friction caused by the power assistance module such as the sealing friction caused by the pressure in HPS system.

The mechanical model was developed and shown in Fig. 7 schematically. It contains all mechanical components which transfer torque from the steering wheel to the tie rods, i.e. the steering wheel, steering column, hardy disc, torsion bar, pinion, steering rack and the occurring damping and friction effects.

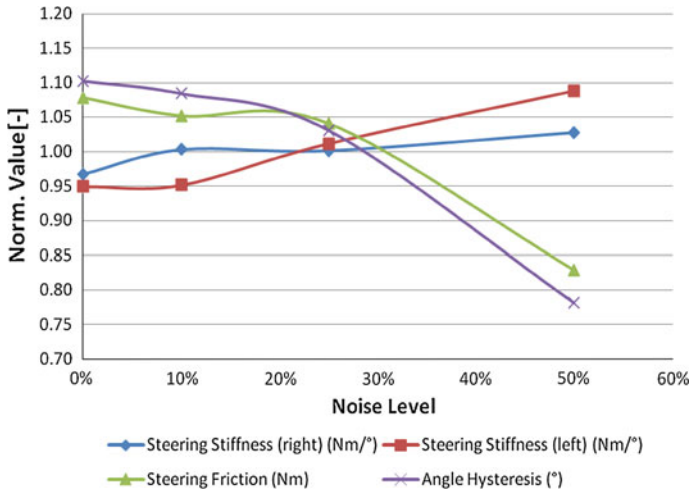


Fig. 5 Steering responses at different noise levels

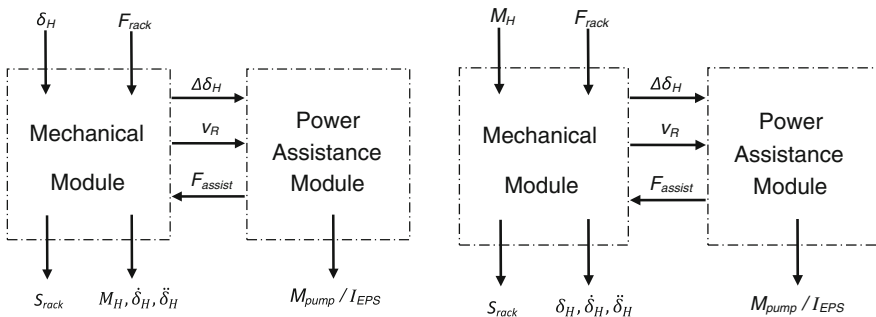


Fig. 6 Steering model layout (δ_H —steering wheel angle; v_R —steering rack velocity; $\Delta\delta_H$ —torsion bar twist angle; F_{assist} —assistant force of the power assistant module; M_H —steering wheel torque; M_{pump} —pump output torque of the hydraulic power assistance; I_{EPS} —EPS current)

The assist torque $M_{assist,C}$ is determined according to the torsion bar torque which is applied to the column close to the steering wheel. $M_{F,lc}$ is the lumped torque friction of the steering column. The upper steering column is implemented by the spring damper model (k_T, d_T) and it also includes the friction due to the torsion bar twist angle ($M_{F,torsion}$). A second degree of freedom is added to the steering column (J_{-1C}). Again, a spring damper model is used to model the intermediate shaft, hardy disc and the mesh stiffness. Along the steering rack, F_R is the steering rack force calculated by the CarMaker vehicle model. $F_{F,R}$ is the friction force along the rack. The friction elements are modelled by an Exponential-Spring-Friction-Element with parallel Maxwell-Element (Fig. 8) [3].

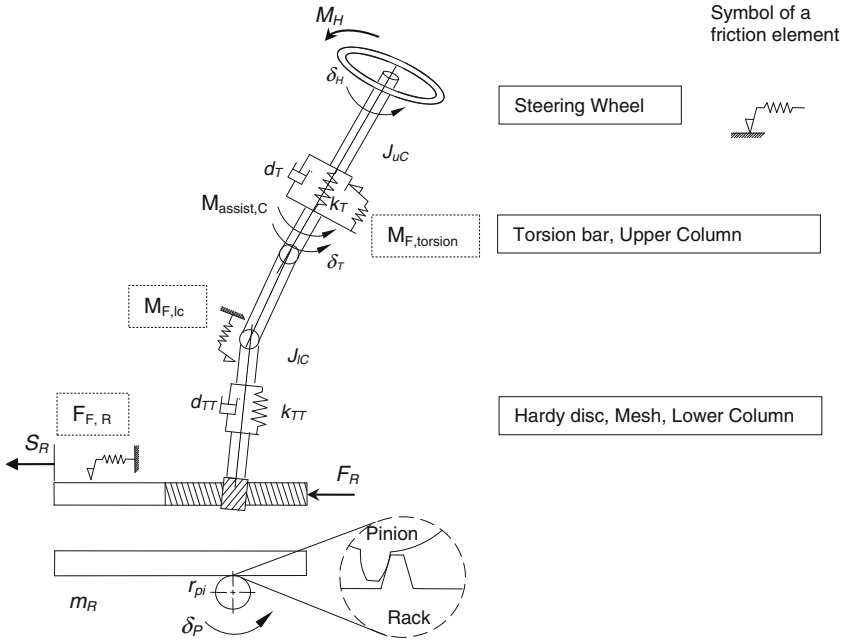


Fig. 7 The mechanical steering model (EPSc)

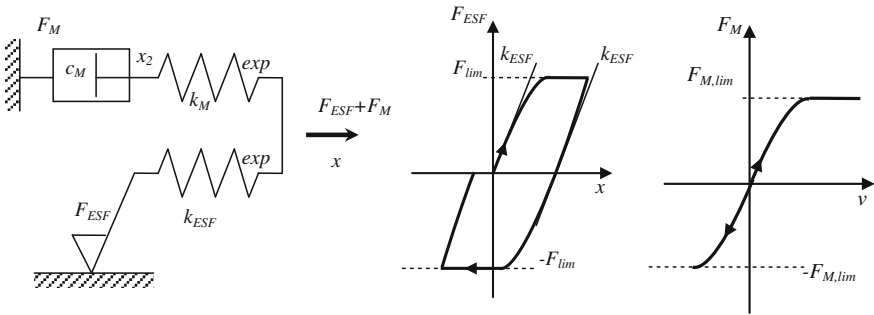


Fig. 8 Exponential-spring-friction-element with parallel Maxwell-element (ESFM)- F_{lim} : force limit; k_{ESF} : stiffness at zero force; friction force F_{ESF} increases exponentially; F_M : nonlinear Maxwell-Element force; k_M : the spring stiffness at zero force; $F_{M,lim}$: maximum spring force; c_M : the linear damping coefficient; x :displacement; v :velocity;

The ASM models were validated with measured data from test bench and on-vehicle testing data. Good agreements between the measurement and simulation for these tests further confirm the accuracy of the ASM models (Fig. 9).

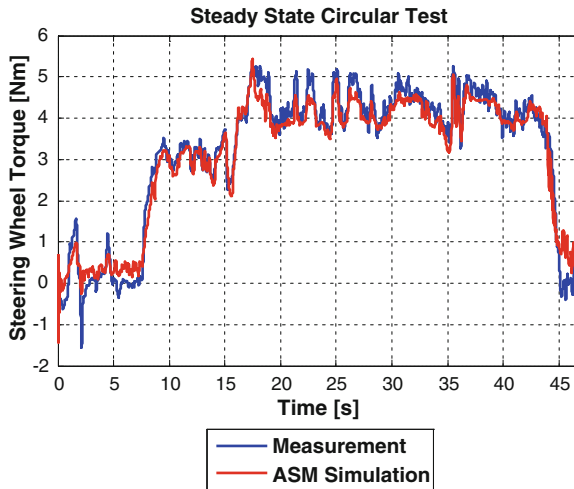


Fig. 9 Comparison of the advanced steering system model (ASM) with on vehicle testing data (steady state circular test) (1)

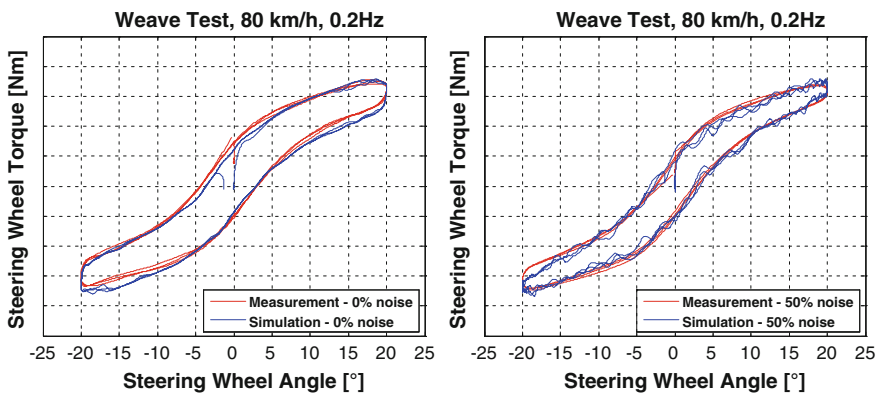


Fig. 10 Simulated response of ASM to noise compared to measurements

4 Response of the Advanced Steering Model to Noise

The ASM simulates the response of the steering system to noise as shown in Fig. 10. With the ESFM friction element, the ASM is capable to simulate similar response to the noise as in the experiment. A test rig with constant frequency and amplitude sinusoidal displacement input are used to generate the frequency response of the ESFM friction element. Figure 11 shows the dynamic stiffness and the loss angle of the ESFM friction element which exhibits similar trend to Fig. 5.

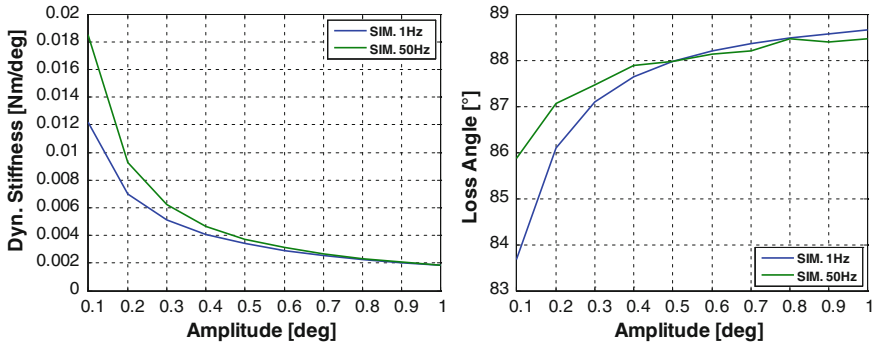


Fig. 11 ESFM friction element transfer function varied with amplitude and frequency

5 Conclusion

The ASM steering model is capable of representing the system response to the random road excitation, typically the friction reduction of the system due to the random noise input. Further effort should be made to characterize this effect with constant frequency and amplitude excitation on the test bench.

References

1. Lin J, Pfeffer PE, Schick W (2011) The application of advanced steering system models in vehicle dynamics simulation. In Proceedings of Chassis. Tech plus 2011 Vol 2, 7–8 June 2011, 441–451, Springer Automotive Media, Munich, Germany
2. Pfeffer PE, Harrer M (2011) Lenkungs-handbuch—Lenksysteme, Lenkgefühl, Fahrdynamik von Kraftfahrzeugen. ATZ/MTZ-Fachbuch, 1st edn. Vieweg+Teubner Verlag
3. Pfeffer PE (2006) Interaction of vehicle and steering system regarding on-centre handling. PhD Thesis, University of Bath, England

Vehicle Longitudinal Velocity Estimation with Adaptive Kalman Filter

Yunlong Gao, Yuan Feng and Lu Xiong

Abstract A new approach of vehicle longitudinal velocity estimation with adaptive Kalman Filter is proposed in this paper. An EV with four in-wheel drive motors is chosen as the study object. Adaptive Kalman Filter is used to estimate the longitudinal velocity and road ramp angle under unknown road conditions by measuring the wheel speeds and vehicle acceleration. Simulation of the algorithm is carried out to find out desired covariance matrices of Kalman Filter.

Keywords Longitudinal velocity estimation · Kalman filter · Gain matrix · Ramp angle

1 Introduction

The incorporation of dynamic control systems in vehicles, e.g. TCS/ASR/ABS, has greatly improved vehicle safety and manoeuvrability. The performance of these systems is based on longitudinal velocity observation accuracy. The direct measurement of longitudinal velocity requires relatively expensive sensors, thus inexpensive sensors is used to estimate the speed in this paper.

F2012-G06-014

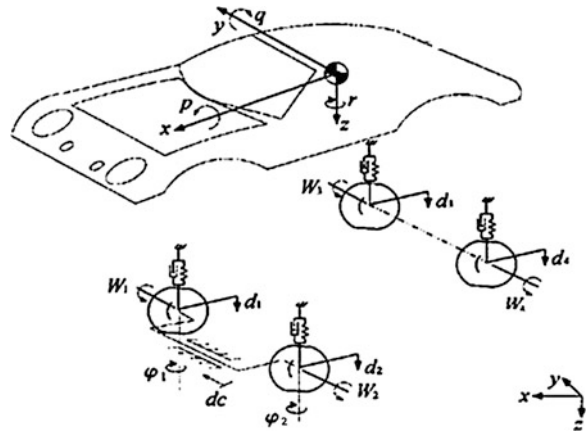
Y. Gao (✉) · Y. Feng · L. Xiong

Tongji Clear Energy Automotive Engineering Centre, Shanghai, People's Republic of China
e-mail: tj.ylgao@gmail.com

L. Xiong

e-mail: xionglu.gm@gmail.com

Fig. 1 Vehicle model
(16-Dof)



According to the published papers and patents, there are mainly two ways to estimate the longitudinal velocity. One is directly calculating the vehicle velocity by using the wheel speed and vehicle acceleration signals. Another is the indirect model-based method. Typical direct approaches such as maximum wheel speed method [1, 2], which uses the maximum wheel speed as the reference velocity when braking, is handy but get a large error. Another direct approach uses adaptive nonlinear filter [1] to estimate the longitudinal velocity on the basis of wheel speed or vehicle acceleration information. The larger value is chosen as the estimated velocity. It has a good adaptability to different road conditions, but the accuracy cannot be guaranteed. Liu proposed another method [2], which uses wheel speed and acceleration to calculate vehicle acceleration, and estimates velocity with integration of the acceleration. A method using both wheel speed sensor and vehicle acceleration sensor is put forward in [3–6], it corrects one signal by the other and improves the accuracy. However, when calculate the velocity, it have to find out the multi-dimensional matrix inversion, which is too complex in real-time estimation. Indirect approaches including force based and multi-variable based methods [7, 8]. These algorithms usually base on a model and can estimate the velocity when steering. In this paper, a novel method is proposed for longitudinal vehicle velocity estimation when slip occurs based on four wheel speeds and vehicle acceleration signals.

The paper is organized as follows. The brief introduction of adaptive Kalman Filter is explained in Sect. 2. Considered the road ramp angle compensation, Sect. 3 present a gradient estimation method and the simulation is carried out to validate it. The conclusion is drawn in the last section.

2 Physical Model of the Vehicle

The simulation model is based on the simplification of the vehicle into 16 Degree of Freedom (DOF) multi-body system and use MATLAB/Simulink s-functions describing and solving the elementary physical equations from the system dynamics. The 16 -DOF vehicle physical model shown in Fig. 1 is used to study the vehicle behaviour in longitudinal, lateral and vertical directions. A sprung mass of vehicle body and four unsprung masses of the wheels are included. The sprung mass has 6 DOF includes the longitudinal, lateral, vertical, roll, pitch, and yaw motion. x, y, z are longitudinal, lateral and vertical motion of the vehicle respectively. p, q, r are roll, pitch and yaw angle of the vehicle respectively. Every wheel has the 2 DOF, i.e. vertical motion d_i ($i = 1 - 4$) and rotation about the wheel centre W_i ($i = 1 - 4$). While front wheels also has steering angle ϕ_1 and ϕ_2 .

3 Longitudinal Velocity Estimation

3.1 Introduction of Algorithm

The typical Kalman Filter function is:

$$\begin{cases} K_k = P_k^- H_k^T (H_k P_k^- H_k^T + R_k)^{-1} \\ \hat{X}_k = \hat{X}_k^- + K_k (Z_k - H_k \hat{X}_k^-) \\ P_k = (I - K_k H_k) P_k^- \\ \hat{X}_k^- = \Phi_{k-1} \hat{X}_{k-1} + \Psi_{k-1} U_{k-1} \\ P_k^- = \Phi_{k-1} P_{k-1} \Phi_{k-1}^T + Q_k \end{cases} \quad (1)$$

where K_k is the gain matrix; P_k and P_k^- are respectively covariance matrixes of current and forecast estimation errors; H_k is the observation matrix, R_k is the covariance matrix of observation error; Q_k is the covariance matrix of system error; Φ_{k-1} is the transition matrix; $\Psi_{k-1} U_{k-1}$ is input variables; \hat{X}_k and \hat{X}_k^- are respectively current and forecast estimation variables; Z_k is the measured variable.

In velocity estimation model, four wheel speed signals are defined as state variables, and acceleration signal is the input variable.

Substitution of variables as follows,

$$H = \begin{bmatrix} 1 \\ 1 \\ 1 \\ 1 \end{bmatrix}; \quad R = \begin{bmatrix} 10 & 0 & 0 & 0 \\ 0 & 10 & 0 & 0 \\ 0 & 0 & 10 & 0 \\ 0 & 0 & 0 & 10 \end{bmatrix}; \quad Q = [0.01].$$

In the model, the observation function can be written as

$$y(k) = H(k)x(k) + e(k) \quad (2)$$

Substitute the variable,

$$\begin{bmatrix} v_{lf}(k) \\ v_{lr}(k) \\ v_{rf}(k) \\ v_{rr}(k) \end{bmatrix} = \begin{bmatrix} 1 \\ 1 \\ 1 \\ 1 \end{bmatrix} v(k) + \begin{bmatrix} e_{lf}(k) \\ e_{lr}(k) \\ e_{rf}(k) \\ e_{rr}(k) \end{bmatrix} \quad (3)$$

where $v_{lf}(k)$, $v_{lr}(k)$, $v_{rf}(k)$, $v_{rr}(k)$ are respectively the wheel speeds of left front, left rear, right front and right rear wheel, $e(k)$ is the measurement error.

In the model, the state function can be written as

$$\hat{x}(k+1) = A(k)x(k) + B(k)u(k) \quad (4)$$

where, $A = [1]$, $B = [\tau]$, τ is the sample time.

The following equation can be obtained from (Eq. 4)

$$\hat{x}(k+1) = v(k) + \tau \cdot a(k) \quad (5)$$

Substitute the variable in (Eq. 1), and get the follow functions.

$$\begin{cases} P^-(k) = P(k-1) + Q \\ K(k) = P^-(k)H^T(HP^-(k)H^T + R)^{-1} \\ \hat{v}(k+1) = v(k) + \tau a(k) \\ \hat{v}_m(k+1) = H\hat{v}(k+1) \\ v(k+1) = \hat{v}(k+1) + K(k+1)(v_m(k+1) - \hat{v}_m(k+1)) \\ P(k) = (I - K(k)H)P^-(k) \end{cases} \quad (6)$$

where $a(k)$ is the acceleration, $v(k+1)$ and $\hat{v}(k+1)$ are respectively the current and forecast estimation of velocity, $v_m(k+1)$ and $\hat{v}_m(k+1)$ are respectively the current and forecast measured value of wheel speed

In desired tire-road friction condition, the normal Kalman Filter works well. However, when wheel slip occurs, the approach cannot provide precise estimation. Therefore, bring in gain matrix control algorithm. In the model, the gain matrix K is $K = [k_{lf} \quad k_{lr} \quad k_{rf} \quad k_{rr}]$, where K_{lf} , K_{lr} , K_{rf} , K_{rr} are the respective gain values of left front, left rear, right front and right rear wheel.

When one wheel slips, control the relevant value in gain matrix and set it to zero.

The criteria of slip are shown as follows,

- (a) The difference between $v_m(k)$ and $\hat{v}(k)$ is greater than a pre-set value;
- (b) The difference between $\hat{v}(k)$ and a_m is greater than a pre-set value.

The pre-set values are decided by the simulation. When the condition meets any one in (a) or (b), set the relevant value in K to zero, and the estimation of velocity is the integral of the measured acceleration when all four wheels slip at the same time.

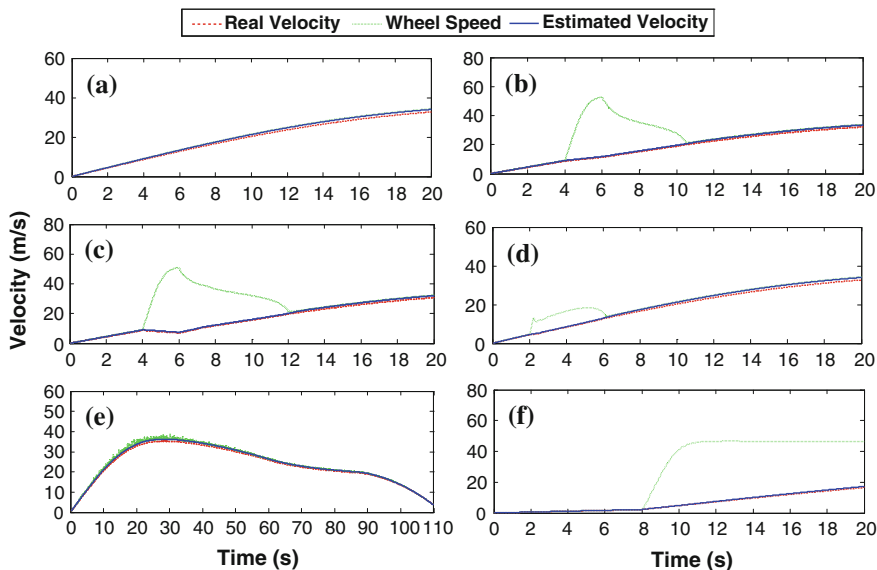


Fig. 2 Simulation results of adjusting gain matrix-based kalman filter method

3.2 Simulation Result

As shown in Fig. 2, the estimation of longitudinal velocity is just the same as typical Kalman Filter (Fig. 2a and b). But when all wheel slip, the adaptive method can also give out accurate estimation while typical one cannot (Fig. 2c). To validate the stability of the algorithm, simulations were carried out under some common driving conditions such as passing bump (Fig. 2d), long time acceleration and deceleration driving on rough road (Fig. 2e), sudden accelerating on low friction coefficient road (Fig. 2f). The velocity estimation is desired in all conditions mentioned above.

4 Longitudinal Velocity Estimation on Gradient Road

4.1 Introduction of the Algorithm

The acceleration signal will be influenced by the gradient of the road, as seen in Fig. 3. Where m is the mass of the vehicle, a is the real acceleration, α is the gradient of slope, $m \cdot a$ is the acceleration resistance.

The measured acceleration signal on gradient road composed of

$$a_m = a + g \cdot \sin \alpha \tag{7}$$

Fig. 3 Force analysis of the vehicle on gradient road

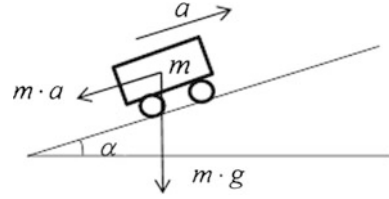
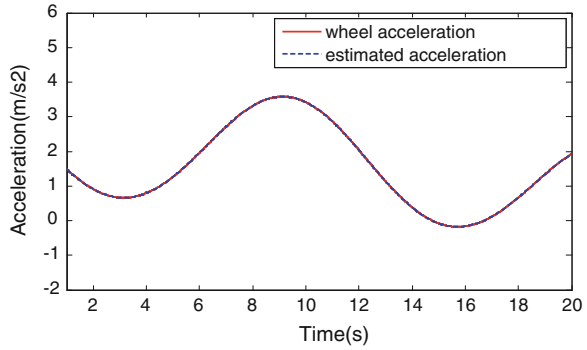


Fig. 4 Vehicle body acceleration and wheel acceleration



The vehicle acceleration should be estimated before obtaining the acceleration caused by gradient. Figure 3 shows the vehicle acceleration is approximately equal to the wheel acceleration, which calculated from derivative of the wheel speed multiplied by the tire radius.

As shown in Fig. 4, the vehicle acceleration curve is mostly covered by the one of wheel acceleration. Therefore the estimated acceleration can be written as

$$a_e = \dot{\omega} \cdot r_e \tag{8}$$

where a_e is estimated acceleration, $\dot{\omega}$ is derivative of the wheel speed, r_e is the radius of the tire.

From (Eq. 7), (Eq. 8), the slope of the road is

$$\alpha = \arcsin \frac{a_m - \dot{\omega} \cdot r_e}{g} \tag{9}$$

4.2 Longitudinal Velocity Estimation on Gradient Road

Using adjusting gain matrix-based Kalman Filter and considering the ramp angle compensation to estimate the longitudinal velocity. Algorithm flow chart is shown in Fig. 5.

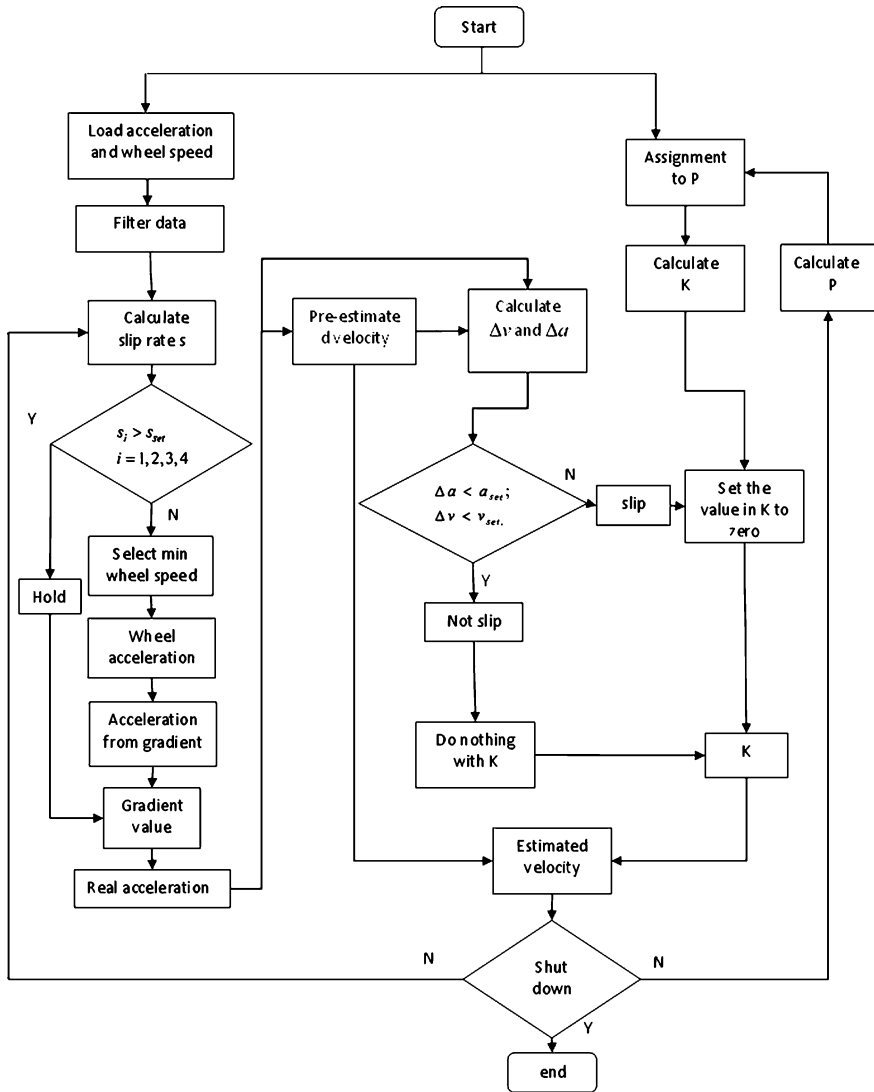


Fig. 5 Flow chart of the velocity and gradient estimation algorithm

4.3 Simulation Results of the Longitudinal Velocity Estimation on Gradient Road

When driven on the constant slope road, the simulation results of longitudinal velocity estimation are shown in Fig. 6. (Fig. 6a, c and e presents the results of the gradient estimation. Figure 6b, d and f are the results of the longitudinal velocity estimation).

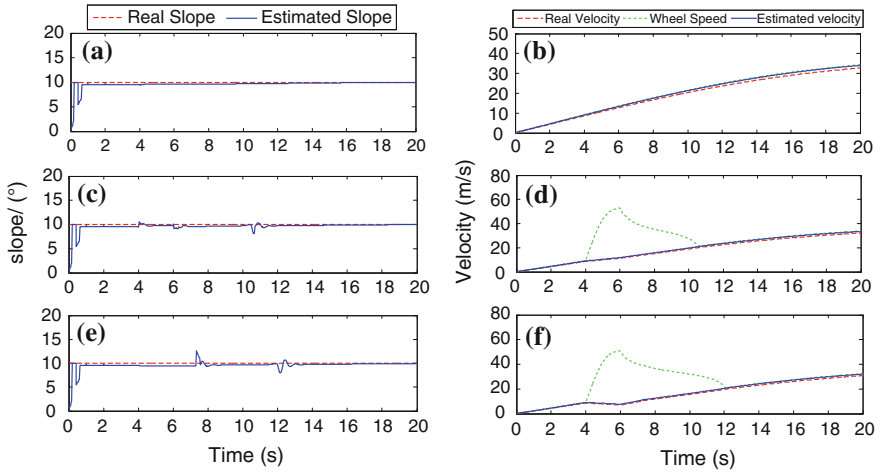


Fig. 6 Simulation results of velocity estimation on constant slope road

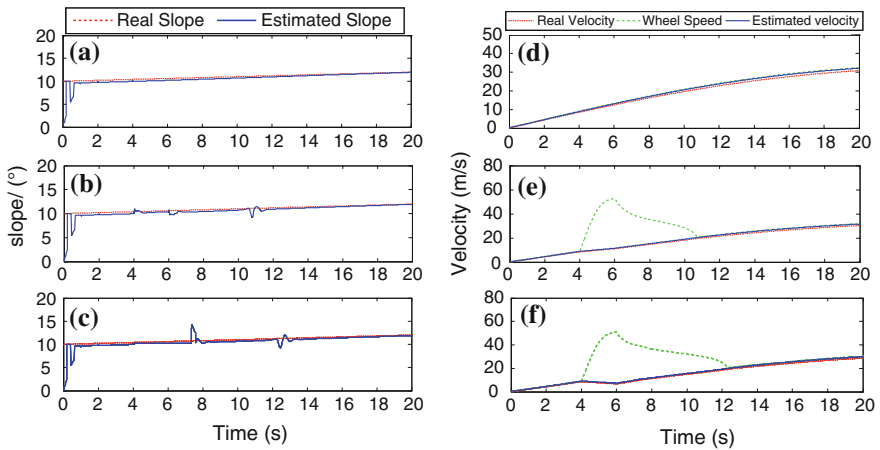


Fig. 7 simulation results of velocity estimation when single wheel slips

When driven on variable slope road, the simulation results of longitudinal velocity estimation are shown in Fig. 7.

The estimation of velocity and gradient is accurate on both constant and small variable slope road. The estimate velocity curve follows the real one and the results are satisfactory.

5 Conclusion

In this paper, gain matrix adjustment-based Kalman Filter is used to estimate longitudinal velocity based on the information of four wheel speeds and vehicle acceleration. Then design a gradient estimation algorithm with considering the compensation of ramp angle of the road when estimate velocity on gradient road. When wheel slip occurs, the adjusting gain matrix-based Kalman Filter can give out desired result. To validate the stability of the algorithm, simulate some common used driving conditions and the results are satisfactory. After simulation, modify algorithm to estimate the longitudinal velocity more accurately.

Acknowledgments This work was supported by National Basic Research Program of China (No.2011CB711200).

References

1. Jiang F, Gao Z (2000) An adaptive nonlinear filter approach to the vehicle velocity estimation for ABS. In: Proceeding of the 2000 IEEE international conference
2. Guofu L (2004) ABS system is based on data fusion technology, the speed estimation methods. J Sci Instrum
3. Daiss A, Kiencke U (1995) Estimation of vehicle speed fuzzy-estimation in comparison with kalman-filtering. IEEE
4. Song CK (2002) Vehicle speed estimation using accelerometer and wheel speed measurements. SAE paper, 2002-01-2229
5. Ming-yuan B (2002) Monitoring longitudinal vehicular velocity by using driving wheels information. J Beijing Inst Technol
6. Ungoren AY (1999) Experimental verification of lateral speed estimation methods. IEEE
7. M'sirdi NK (2006) Second order sliding mode observer for estimation of velocities, wheel slip, radius and stiffness. In: Proceeding of the 2006 American control conference
8. Krantz W (2002) Estimation of side slip angle using measured tire forces. SAE paper, 2002-01-0969

Advanced Cost Functions for Evaluation of Lateral Vehicle Dynamics

Valentin Ivanov, Klaus Augsburg, Dzmitry Savitski, Jiri Plihal,
Pavel Nedoma and Jaroslav Machan

Abstract The paper introduces the method of assessment of vehicle manoeuvres through a set of global cost functions. The corresponding cost functions can be derived for different domains like longitudinal and lateral dynamics, driving comfort and other. The procedures of the computation of the cost functions include in general: (1) Selection of vehicle dynamics parameters relevant to the domain; (2) Transformation the appointed parameter to the dimensionless form; (3) Definition of weighting factors for each of the appointed parameters with taking into account that the weighting factors can be variable depending on the type of the vehicle manoeuvre as well as on the driving conditions; (4) Calculation of the cost function for the selected domain; (5) Calculation of a global cost function in the case of the integrated assessment of the manoeuvre through several domains of the vehicle dynamics. The described procedures are discussed in the paper as applied to

F2012-G06-015

V. Ivanov (✉) · K. Augsburg · D. Savitski
Ilmenau University of Technology, Ilmenau, Germany
e-mail: valentin.ivanov@tu-ilmenau.de

K. Augsburg
e-mail: klaus.augsburg@tu-ilmenau.de

J. Plihal · P. Nedoma · J. Machan
Skoda Auto, Mladá Boleslav, Czech Republic
e-mail: j.plihal@volny.cz

P. Nedoma
e-mail: Pavel.Nedoma@skoda-auto.cz

J. Machan
e-mail: jaroslav.machan@skoda-auto.cz

J. Plihal
Institute of Information Theory and Automation of the ASCR, Prague, Czech Republic

the domain of lateral vehicle dynamics. The parameters chosen for the calculation of the corresponding cost function are the lateral acceleration a_y , the yaw rate $d\psi/dt$, and the sideslip angle β . To transform these parameters to a dimensionless form, the procedure is proposed that uses the function of root mean square of deviations between reference and actual values for each variable. This procedure implements also an original method of definition of reference values for lateral acceleration a_y and yaw rate $d\psi/dt$. The method is based on the variation of understeer characteristic of the baseline vehicle with the aim to extend the linear region and to reduce the understeer gradient as well as to increase the maximum level of lateral acceleration. The validation of the developed methods and procedures is illustrated by way of model-in-the-loop simulation. The test programme covers several standard manoeuvres—steady-state circle, slalom and avoidance manoeuvre—performed for a simulator, medium-sized passenger car. The numerical values of the cost functions for each manoeuvre are introduced and analyzed. The further applications of the developed technique can be: (1) Assessment of vehicle dynamics based on criterions of performance and stability; (2) Optimization of vehicle dynamics control systems; (3) Choice of proper control strategies/tuning of control gains and resolution of critical control situations by simultaneous operation of several systems like ABS, TCS, TV/vehicle dynamics control.

Keywords Vehicle dynamics • Cost functions • Stability • Weighting factors • Simulation

Modern methods of vehicle dynamics control meet various complex challenges due to the fact that different systems with individual set of functions can be simultaneously involved in the control process: anti-lock braking, traction control, torque vectoring, direct yaw control, active suspension and so on. Resulting system fusion raises the issue about the development of an analytical tooling estimating the combined efficiency of the vehicle manoeuvres from viewpoint of longitudinal and lateral dynamics, ride comfort, driver control comfort, agility and other factors. Such a tooling can include a set of objective functions and variables interconnected through weighting factors, which depend on conditions of the driving manoeuvre, operational state of the vehicle and so on. For practical applications, a reasonable formulation of cost functions can be done in a dimensionless form.

An analysis of research literature points to lack of complex approaches to the evaluation of vehicle dynamics based on cost functions. However, several relevant studies should be mentioned in such a context. Milliken and Milliken [1] as well as Radt and Glemming [2] have proposed normalised, dimensionless description of tyre forces and moments, camber and slip angles, and slip ratios. The mentioned works show that this approach is useful by assessment of combined lateral and longitudinal manoeuvres of the vehicle. Other studies have discussed more specified methods for the shaping the objective/cost functions in relation to the development of vehicle control systems. For example, the combined assessment of lateral and ride dynamics on the basis of frequency-dependent weighting index of

the lateral acceleration has been given in [3]. The work [4] introduces objective functions of tractive performance as optimum slip and optimum input power for drive wheels that can be used in traction control systems.

The authors of the present article propose an extended flexible methodology that allows both individual and integrated evaluation of vehicle dynamics through diverse sets of cost functions. Next sections of the paper will introduce a relevant general approach, example of calculation of cost functions for lateral dynamics, and the case study illustrating the application of proposed method.

1 General Approach to the Calculation of Cost Functions

The efficiency of a vehicle manoeuvre can be evaluated for different domains of vehicle dynamics: longitudinal and lateral dynamics, ride comfort, driver comfort etc. Each domain has a set of inherent parameters. A parameter within a certain domain can be both independent and interrelated with other parameters. These statements are illustrated with Table 1.

The resulting diversity of parameters of vehicle dynamics implies many variations of possible cost functions as well as related computational methods. The authors of the present paper have proposed an approach that aims at the dimensionless interpretation of cost functions and their in-domain and inter-domain composition through a set of weighting factors. This approach is presented in Fig. 1 and can be explained as follows:

1. A set of parameters $N_1 \dots N_k$ is being chosen to shape the cost function of a certain domain N . The interpretation of parameters is preferred in a dimensionless form in the range 0–1, for example, as ratio of actual value and base value, or ratio of actual value and an appointed threshold.
2. An individual weighting factor has to be designated to each of parameters: $w_{N_1} \dots w_{N_k}$. At that the condition takes place:

$$\sum_{i=1}^k w_{N_i} = 1 \quad (1)$$

The magnitudes of weighting factors are not static and can be changed in accordance with the type of performed manoeuvre or actual driving conditions.

3. The corresponding cost function E_N for the domain N is calculated as

$$E_N = \sum_{i=1}^k N_i \cdot w_i \quad (2)$$

4. In accordance with postulates (1) and (2), the E_N -value from Eq. (2) yields a variable within the range 0–1.
5. In the case of a simultaneous evaluation of the vehicle manoeuvre in different domains, additional weighting factors can be designated to each domain-based

Table 1 Domains and parameters of vehicle dynamics – Example

Domain	Longitudinal dynamics	Lateral dynamics	Driver comfort
Parameters	Vehicle velocity	Lateral acceleration	Throttle pedal velocity
	Longitudinal acceleration	Yaw rate	Brake pedal velocity
	Wheel slip	Sideslip angle	Steering wheel velocity

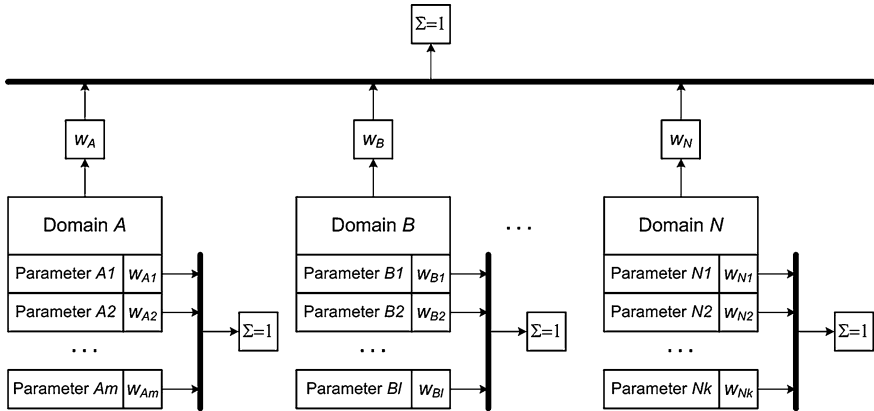


Fig. 1 Procedure of computing of cost functions

cost function (see factors w_A , w_B and w_N on Fig. 1). Their sum should be equal to 1, similar to postulate 2).

- Implementation of positions (1)–(5) allows to compute an integrated, global cost function:

$$E_{global} = E_A \cdot w_A + E_B \cdot w_B + \dots E_N \cdot w_N \tag{3}$$

The resulting cost function E_{global} lies also within the numerical interval 0–1.

Next parts of the paper will explain the proposed approach by the example of lateral vehicle dynamics.

2 Cost Functions of Lateral Vehicle Dynamics

2.1 Definition of Parameters of Lateral Vehicle Dynamics

The cost function, discussed in this section, is based on the vehicle parameters that (1) describe lateral vehicle dynamics and (2) can be measured by conventional on-board sensors, or sensors commonly adopted for vehicle testing: lateral

acceleration a_y , side slip angle β , and yaw rate $d\psi/dt$. In such a case the basic formulation of the cost function can be proposed as

$$E_{lat} = w_{ay} \cdot f(\Delta a_y) + w_{\beta} \cdot f(\Delta \beta) + w_{\psi} \cdot f(\Delta \dot{\psi}), \quad (4)$$

where w_i are the weighting factors and

$$\Delta a_y = |a_y^{ref} - a_y^a|, \quad (5)$$

$$\Delta \beta = |\beta^{ref} - \beta^a|, \quad (6)$$

$$\Delta \dot{\psi} = |\dot{\psi}^{ref} - \dot{\psi}^a|. \quad (7)$$

Indexes *ref* and *a* in Eqs. (5)–(7) are relevant to the reference and actual values of the corresponding parameter.

The kind of function f in Eq. (4) depends on the purpose of the specific optimization tasks of vehicle dynamics. The analysis of reference literature shows that one of the most conventional variants can be based on the root mean square functions (RMS-functions). In particular, the methods using RMS error, relative RMS error, the mean relative error, and the maximum relative error are known. Within the framework of the discussed approach, the function of *root mean square* of deviations between reference and actual variables in Eqs. (5)–(7) has been chosen to assess vehicle dynamics during a certain manoeuvre :

$$E_{lat} = w_{ay} \cdot RMS(a_y^{ref}, a_y^a) + w_{\beta} \cdot RMS(\beta^{ref}, \beta^a) + w_{\psi} \cdot RMS(\dot{\psi}^{ref}, \dot{\psi}^a) \quad (8)$$

Equation (8) is written in a general form. Aiming at the deduction of dimensionless quantitative magnitudes of E_{lat} , the variants of relative RMS-deviations of actual and reference values can be proposed:

$$E_{lat} = w_{ay} \cdot \frac{f_{RMS}(\Delta a_y)}{\max(a_y^a) - \min(a_y^a)} + w_{\beta} \cdot \frac{f_{RMS}(\Delta \beta)}{\max(\beta^a) - \min(\beta^a)} + w_{\psi} \cdot \frac{f_{RMS}(\Delta \dot{\psi})}{\max(\dot{\psi}^a) - \min(\dot{\psi}^a)}, \quad (9)$$

where

$$f_{RMS}(\Delta x) = \sqrt{\frac{\sum_{i=1}^n (x_i^{ref} - x_i^a)^2}{n}}. \quad (10)$$

Table 2 Technical data of the vehicle

Parameter	Value/description
Total weight	2,080 kg
Maximum speed	201 kph
Acceleration 0–100 kph	8, 4 s
Front axle	McPherson suspension with lower triangular links and transverse torsion stabiliser
Rear axle	Multi-element suspension with a longitudinal and transverse links and transverse torsion stabiliser
Steering	Direct rack-and-pinion steering with electromechanical power steering
Tyres	215/60 R16
Dimensions	4,223 mm × 1,793 mm × 1,691 mm
Wheelbase	2,578 mm
Outer turning circle diameter	10, 32 m

In Eq. (10) the parameter n is the number of observed time points during the manoeuvre, x^{ref} and x^a in relation to Eq. (9) are the vectors of reference and baseline and lateral accelerations, yaw rates, or side slip angles given for the vehicle manoeuvre, for which the cost functions are being estimated. The *max*- and *min*-functions in Eq. (9) are maximum and minimum values of corresponding actual variable during the test. Following the discussed methodology, the ratio $f_{RMS}(x)/(max(x)-min(x))$ —relative root mean square deviation—lies in the range [0, 1]. The value “0” should be considered as “the best case”: the actual values of a variable coincide with the reference values. The value “1” should be considered as “the worst case”.

The procedures of computing the reference characteristics for lateral acceleration, yaw rate and side slip angle are introduced in next sub-section.

2.2 Reference and Actual Values of Lateral Acceleration

The reference lateral acceleration is calculated as

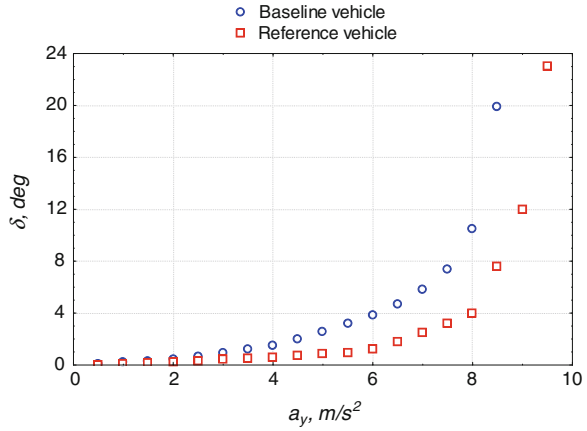
$$a_y^{ref} = \begin{cases} a_y^*, & a_y^* \leq a_{y\max} \\ a_{y\max}, & \text{otherwise} \end{cases} \quad (11)$$

The maximal lateral acceleration a_y^* can be defined from the tyre friction ellipse as

$$a_{y\max} = 9,81 \cdot \mu_{y\max}, \quad (12)$$

where $\mu_{y\max}$ is the maximal lateral friction coefficient at given level of longitudinal acceleration/deceleration. The parameter a_y^* in Eq. (11) identifies the reference lateral acceleration that does not exceed the friction limits and can be derived from

Fig. 2 Comparison of baseline and reference understeer characteristic at constant velocity



the look-up-table (LUT) given for the vehicle as a family of “Steering wheel angle—Lateral acceleration”—functions composed for different longitudinal accelerations. The procedure of shaping the reference characteristics is described below. The corresponding numerical examples are given for the vehicle with the technical data from Table 2.

Step 1. Calculation of understeer characteristic of the baseline vehicle.

The understeer characteristics can be derived from results of various standard steady-state tests on vehicle dynamics. The regulations such as ISO 4138 or SAE J266 recommend different procedures: constant radius test, constant steer angle test, constant speed variable radius test, constant speed and variable steer angle test, or response gain test. An example of the understeer characteristic for a baseline vehicle is shown in Fig. 2. In the case under discussion the initial gradient of the curve is 0,375 °/m/s². The linear part of the “Steering wheel angle—Lateral acceleration”-dependence is valid until $a_y = 4.0$ m/s². The maximum level of lateral acceleration is $a_y = 8,25$ m/s².

Step 2. Shaping the understeer characteristic of a reference vehicle for constant velocity conditions. The reference understeer characteristic can be shaped after analysis of the baseline vehicle behaviour. It defines the target behaviour of reference vehicle dynamics that is characterized by:

- Less understeer gradient in term of $\delta(a_y)$;
- Extended linear part of the $\delta(a_y)$;
- Higher maximum level of lateral acceleration.

An example of reference understeer characteristics is introduced in Fig. 2. It was computed taking into account the mass-geometry parameters of the baseline vehicle as well as relevant tyre characteristics. The main reference characteristic parameters are: the initial gradient of the curve is 0.2 °/m/s²; the extension of the linear part of the “Steering wheel angle—Lateral acceleration” characteristic-

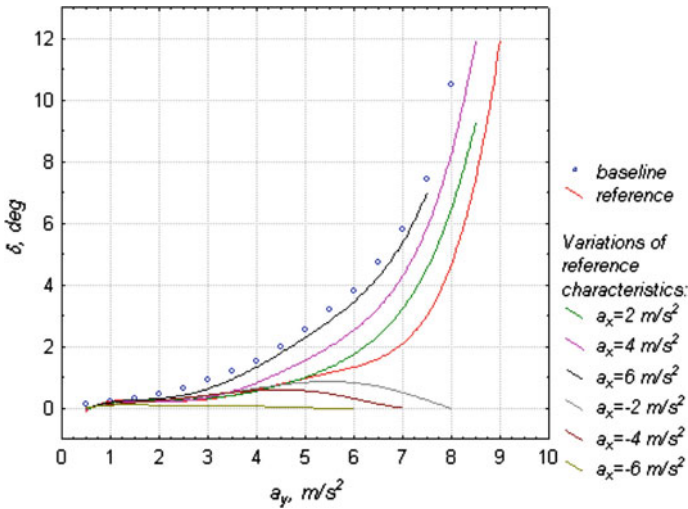


Fig. 3 A set of reference (a_y)-dependencies by variation of longitudinal acceleration

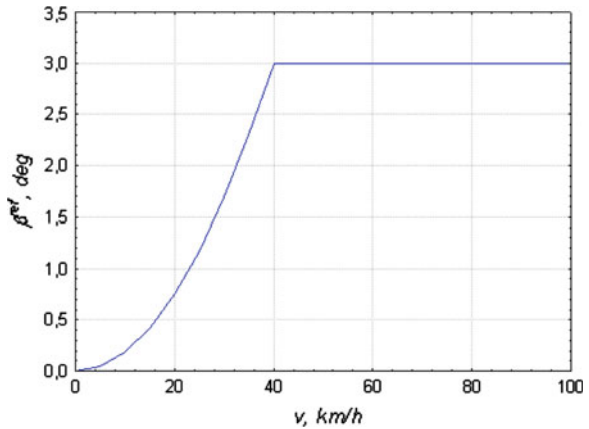
dependence (for the specific case the reference is linear until $a_y = 5.7 \text{ m/s}^2$); the maximum reference level of lateral acceleration is $a_y = 9.5 \text{ m/s}^2$.

Step 3. Variation of reference understeer characteristic. During this step, the behaviour of the reference understeer characteristic has to be defined for different levels of longitudinal acceleration a_x . Figure 3 proposes a tree of the reference $\delta(a_y)$ characteristics shaped for different a_x -levels. A set of displayed reference curves has common initial linear gradient. The end of the linear part depends on the given level of longitudinal acceleration. Such an approach is required to determine the variation of the understeer characteristic as a function of longitudinal acceleration. As it was evidenced by simulation and experimental results [5], the understeer characteristic can be influenced by the actual a_x -level with trends (1) to more understeering with the growth of a_x and (2) to oversteering by negative a_x -values. Hence, the reference $\delta(a_y)$ -dependencies are subject of variation. Referring to the tree of understeer characteristics from Fig. 3, the maximal a_y -value for each branch is limited by the corresponding a_x -level. Generally the shaped reference characteristics should have:

- Reduced understeer gradient during all a_x -range (while considering the traction of front wheel drive vehicle); in the case of rear wheel drive vehicle the reference characteristic can possess increased understeer;
- Reduced variation of the understeer characteristic subjected to a_x .

The value of actual lateral acceleration a_y^d is obtained either (1) with conventional lateral accelerometer being a component of vehicle dynamics control system or (2) from the vehicle simulator, or (3) from the vehicle model in the case of simulation [6]:

Fig. 4 The reference characteristic for side slip angle



$$a_y^a = \frac{1}{m_a} \left(\sum_{i=1}^4 F_{xi} \sin(\delta_{vi}) - \sum_{i=1}^4 F_{fi} \sin(\delta_{vi}) + \sum_{i=1}^4 F_{yi} \cos(\delta_{vi}) - m_s h_s \ddot{\theta} \right) \quad (13)$$

where F_{xi} are the longitudinal tire forces, F_{yi} are the lateral tire forces, δ_{vi} are the steer angles, F_{fi} are the tyre rolling resistance forces, m_a is the vehicle mass, m_s is the vehicle sprung mass, h_s is the roll height, and θ is the vehicle roll angle.

2.3 Reference and Actual Values of Vehicle Side Slip Angle

The reference side slip angle is calculated as

$$\beta^{ref} = \begin{cases} \beta^*, & v \leq v_{ss} \\ \beta_{Max_ss}, & \text{otherwise} \end{cases} \quad (14)$$

The β^* -value of side slip angle for steady-state conditions can be chosen as:

$$\beta^* = \beta_{max_ss} \frac{v^2}{v_{ss}^2} \quad (15)$$

where v is the actual absolute vehicle velocity, β_{max_ss} and v_{ss} are correspondingly the maximal side slip angle and absolute vehicle velocity given for the point where the influence of velocity on yaw rate becomes negligible. Equation (15) refers to the source [6], where $\beta_{max_ss} = 3^\circ$ and $v_{ss} = 40 \text{ m/s}$ have been recommended on the statistical basis from the experimental results for different types of vehicles. Therefore the reference characteristic for side slip angle is being proposed as shown on Fig. 4. It can be seen that a smooth increase of β^{ref} takes place in the range of velocities from 0 to 40 km/h. It is necessary while estimating the dynamic

situations on surfaces with the low friction, where the vehicle stability can be critical already at small driving velocities with low side slip angles.

The value of actual vehicle side slip angle β^a can be computed as follows [7]:

$$\beta^a = \tan^{-1} \left(\frac{v_y}{v_x} \right) \quad (16)$$

where the actual longitudinal velocity is estimated as

$$v_x = \int \left(a_x + v_y \cdot \frac{d\psi}{dt} \right) dt \quad (17)$$

and the actual lateral velocity can be found as

$$v_y = \int \left(a_y - v_x \cdot \frac{d\psi}{dt} \right) dt \quad (18)$$

The values of vehicle accelerations a_x and a_y as well as yaw rate $d\psi/dt$ are obtained from corresponding vehicle sensors. Instead of the vehicle model, other ways for the estimation of β^a are (1) the use of vehicle simulator or (2) measurement technique. Similar tooling can be used also for the estimation of the individual contributions v_x and v_y .

Unlike the reference lateral acceleration, the reference side slip angle should be considered as a maximum allowed value during the manoeuvre performed. In this regard the comparison of β^a and β^{ref} takes place only in the case $\beta^a > \beta^{ref}$.

2.4 Reference and Actual Values of Yaw Rate

The calculation of reference yaw rate $(d\psi/dt)^{ref}$ is similar with the procedure for lateral acceleration that is described above. Generally

$$\dot{\psi}^{ref} = \begin{cases} \dot{\psi}^*, & \dot{\psi}^* \leq \dot{\psi}_{max} \\ \dot{\psi}_{max}, & \text{otherwise} \end{cases} \quad (19)$$

By analogy with the lateral acceleration, the parameter $(d\psi/dt)^*$ in Eq. (19) can be derived from the look-up-table given for the vehicle as a family of “Steering wheel angle—Yaw rate”-dependencies composed for variable longitudinal accelerations. Figure 5 introduces a tree of corresponding curves that were computed from the steady state circle test 42,5 m similar to the reference a_y -curves from Fig. 3. The maximum value of yaw rate [6] can be in addition controlled as

$$\dot{\psi}_{max} = \frac{a_{ymax} - \dot{v}_x \cdot \sin \beta_{ref}}{v_x \cdot \cos \beta_{ref}} \quad (20)$$

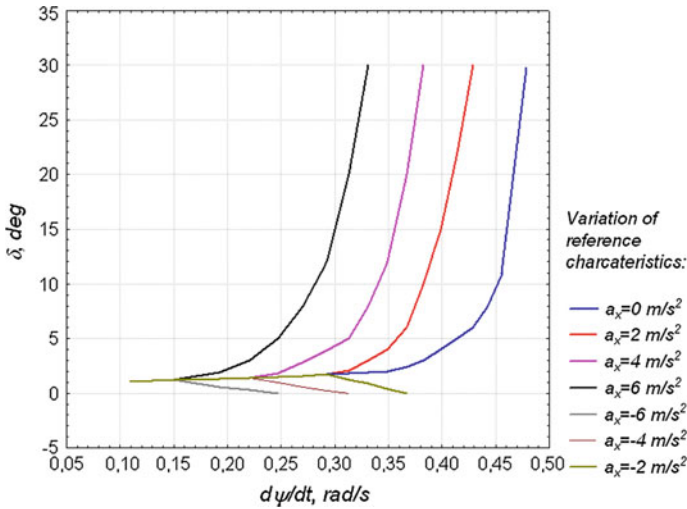


Fig. 5 A set of reference $\delta(d\psi/dt)$ -dependencies by variation of longitudinal acceleration

Table 3 Examples of composition of weighting factors

Manoeuvre	w_{a_y}	w_{β}	w_{ψ}	Comment
Avoidance, dry road	0,3	0,1	0,6	Priority for yaw dynamics
Avoidance, ice	0,2	0,3	0,5	Higher priority for side slip due to low road friction
Track keeping on circle	0,6	0,05	0,35	Priority for lateral acceleration
Braking on mixed road	0,1	0,4	0,5	Higher priority for side slip angle dynamics
Slalom	0,4	0,2	0,4	Equal priority for yaw and lateral acceleration

The value of actual yaw rate $(d\psi/dt)^a$ can be obtained with conventional yaw rate sensor being a component of vehicle dynamics control system.

2.5 Choice of Weighting Factors

The next step is the choice of weighting factors for Eq. (8). It can be done for different driving situations, for instance:

- On-road straight-line manoeuvres;
- On-road manoeuvres with lateral dynamics;
- Off-road straight-line manoeuvres;
- Off-road manoeuvres with lateral dynamics.

It is appointed that the sum of three weighting factors w_{a_y} , w_{β} and w_{ψ} is taken as 1. The magnitudes of weighting factors are selected depending on the kind of manoeuvre. The Table 3 gives examples of composition of weighting factors.

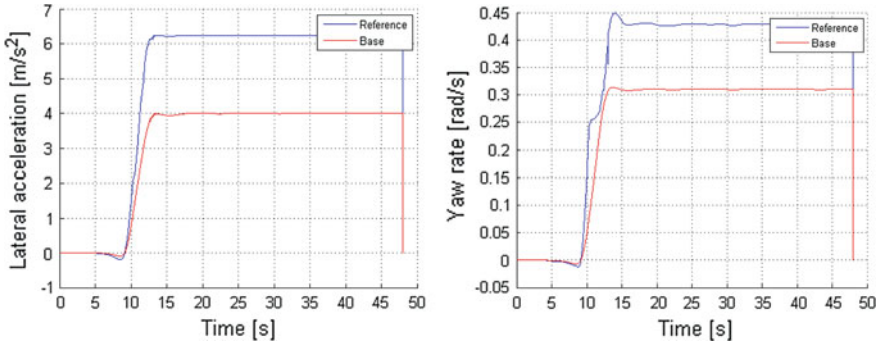


Fig. 6 Results of test of vehicle simulator, constant circle

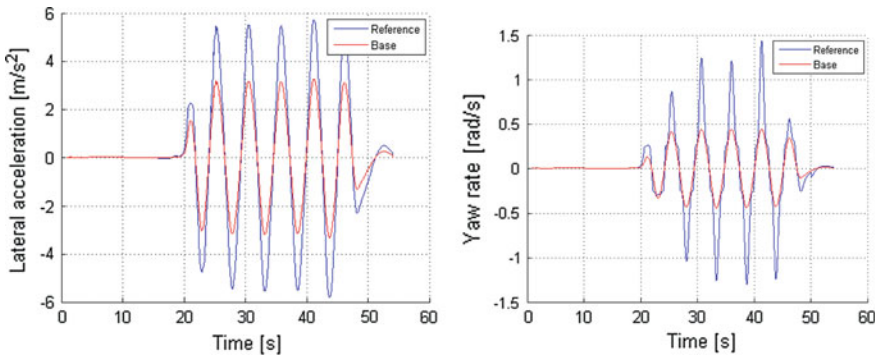


Fig. 7 Results of test of vehicle simulator, slalom

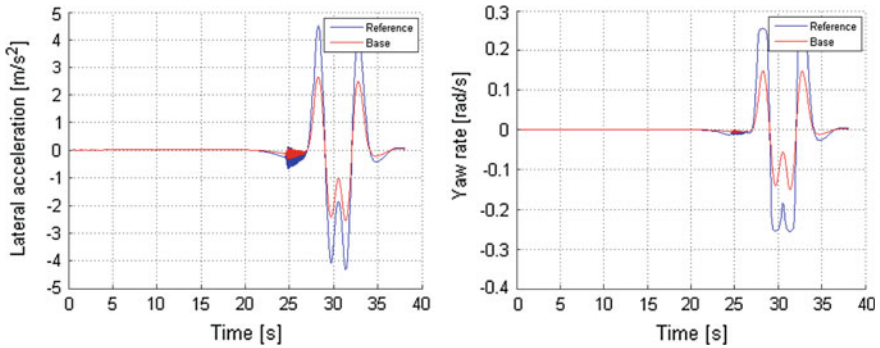


Fig. 8 Results of test of vehicle simulator, avoidance

It can be concluded from previous considerations that the magnitude of cost function E_{lat} from Eq. (9) for the certain manoeuvre will be always between 0 and

Table 4 Cost functions for results of tests of vehicle simulator (values given for the end of manoeuvre)

Test	Constant circle	Slalom	Avoidance
$f_{RMS}(\Delta a_y), m/s^2$	1,8552	1,1069	0,5111
$f_{RMS}(\Delta\beta), deg$	below threshold	1,1195	below threshold
$f_{RMS}(\Delta d\psi/dt), rad/s$	0,0979	0,2353	0,0503
$max(\Delta a_y)-min(\Delta a_y), m/s^2$	4,0064	6,5892	5,1872
$max(\Delta\beta)-min(\Delta\beta), deg$	below threshold	4,3916	below threshold
$max(\Delta d\psi/dt)- min(\Delta d\psi/dt), rad/s$	0,3103	0,8817	0,2990
w_{a_y}	0,6	0,4	0,3
w_{β}	0,05	0,2	0,1
w_{ψ}	0,35	0,4	0,6
E_{lat}	0,3883	0,3418	0,2590

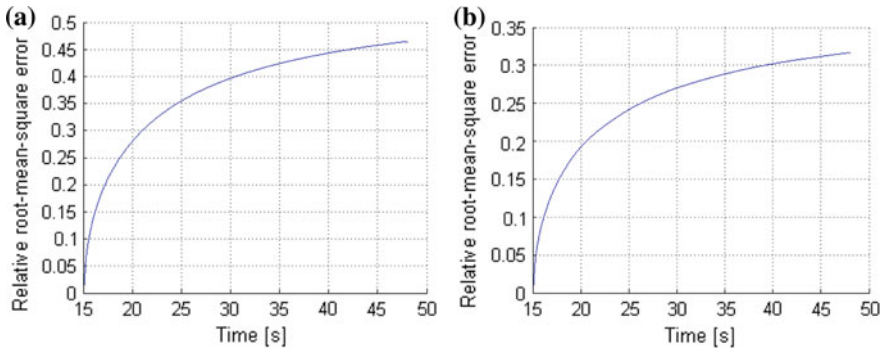


Fig. 9 The relative root mean square error functions from Eq. (9) Constant circle: **a** lateral acceleration; **b** yaw rate Critical part of the manoeuvre for calculation of cost functions - from 15 s

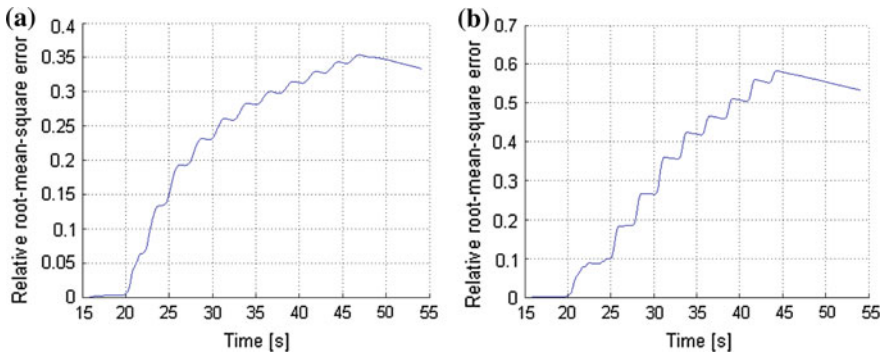


Fig. 10 The relative root mean square error functions from Eq. (9) Slalom: **a** lateral acceleration; **b** yaw rate Critical part of the manoeuvre for calculation of cost functions—15–55 s

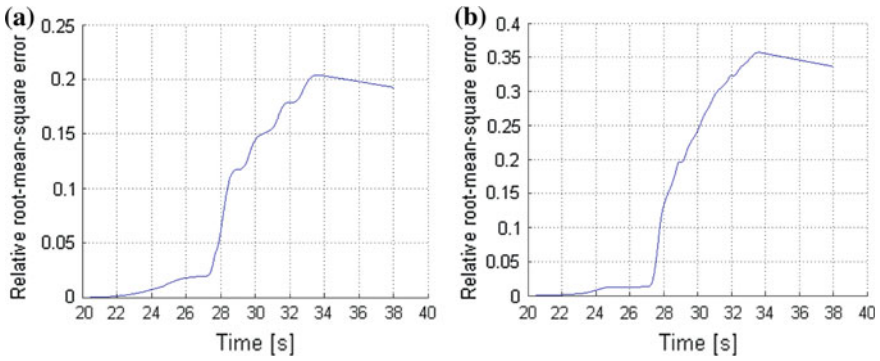


Fig. 11 The relative root mean square error functions from Eq. (9) Avoidance: **a** lateral acceleration; **b** yaw rate critical part of the manoeuvre for calculation of cost functions—20–38s

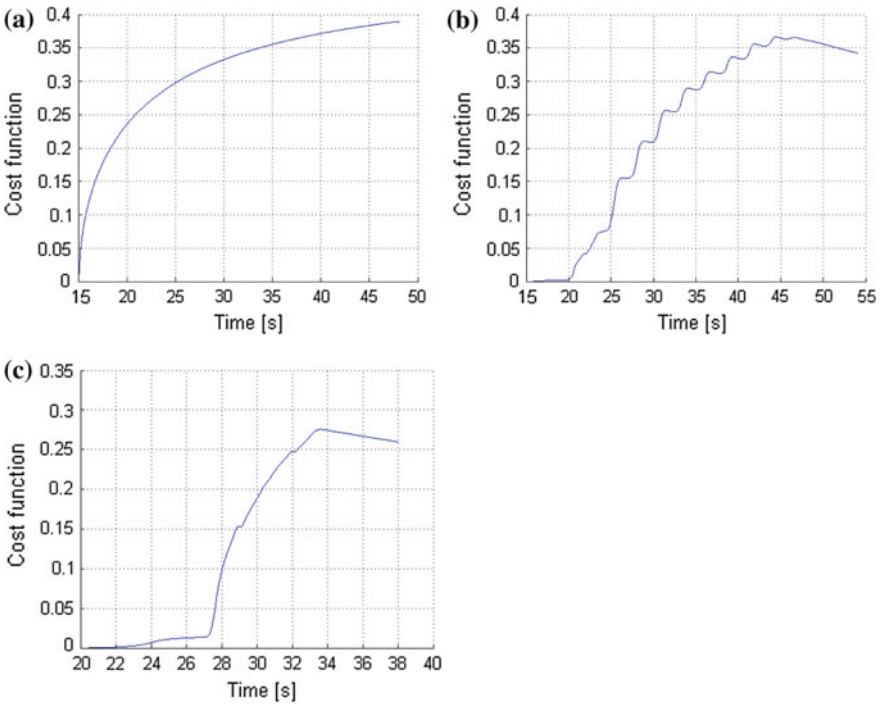


Fig. 12 Cost functions of lateral dynamics calculated in accordance with Eq. (9) **a** constant circle; **b** slalom; **c** avoidance

1. The more E_{lat} tends to 0, the more efficiently the manoeuvre is performed from viewpoint of the lateral dynamics.

3 Case Study for Application of Cost Functions

The case study was performed for the vehicle simulator created in the IPG CarMaker software for the car with the data from Table 2. Three following manoeuvres were simulated:

- Constant circle, radius 42,5 m;
- Slalom, 18 m;
- ISO avoidance manoeuvre.

The reference dependencies are similar with characteristics shown on Figs. 3, 4, 5. The comparison of actual and reference variables is shown on Figs. 6, 7, 8. The results of calculations of cost function are given in Table 4. The cost functions were computed for the critical parts of the manoeuvres. In addition Figs. 9, 10, 11 illustrates dynamics of the relative RMS-function for lateral acceleration and yaw rate, and Fig. 12 introduces dynamics of the cost function calculated in accordance with Eq. (9). It should be mentioned that the obtained results have indicated a proper evaluation of complexity of the performed manoeuvres.

The analysis of the case study allows to propose the following application areas of the cost functions:

- Assessment of vehicle dynamics based on criterions of performance and stability;
- Optimization of vehicle dynamics control systems;
- Choice of proper control strategies/tuning of control gains by simultaneous operation of several systems like ABS, TCS, and ESC.

4 Conclusions

The presented paper has introduced an approach to calculation of cost functions for the evaluation of lateral vehicle dynamics. The cost functions are based on the comparison of baseline and reference values of lateral acceleration, yaw rate and side slip angle. The following features can be especially mentioned in this context:

- The composition of reference variables can be obtained from the variation of understeer characteristics of the baseline vehicle. At that the reference vehicle should possess less understeering.
- The reference characteristics for lateral acceleration and yaw rate require the variation depending on the longitudinal acceleration.

- Composition of cost functions and weighting factors for singular components can be proposed in a dimensionless form in the range from 0 to 1.

The calculation of cost functions was illustrated with the case study for modelling of three different manoeuvres with the vehicle simulator.

The developed cost functions can be used for optimization of control strategy of automotive control systems and evaluation of vehicle dynamics.

Acknowledgments The research leading to these results has received funding from the European Union Seventh Framework Programme FP7/2007-2013 under grant agreement n°284708.

References

1. Milliken WF, Milliken DL (2002) Chassis design: principles and analysis. SAE International, p 676
2. Radt HS, Glemming DA (1993) Normalization of tire force and moment data. *Tire Sci Technol* 21(2):91–119
3. Peng H, Tomizuka M (1990) Vehicle lateral control for highway automation. In: Proceedings of american control conference, pp 788–794
4. Vantsevich VV (2007) Multi-wheel drive vehicle energy/fuel efficiency and traction performance: objective function analysis. *J Terramech* 44:239–253
5. Radt HS (1997) Variable dynamic testbed vehicle—analysis of handling performance with and without of rear steer, Milliken Research Associates Report
6. Kiencke U, Nielsen L (2005) Automotive control systems. Springer, Berlin-Heidelberg
7. Wong JY (2001) Theory of ground vehicles. Wiley, New York

Effect of Differential Modeling on Handling and Stability

Rui Huang, Jun Zhan and Jungang Wu

Abstract Research target: There are exists many principle types of limited slip differential. If simplify limited slip differential model to open differential, vehicle handling and stability simulation results will be uncorrected. So the paper's target is to build several principle differentials, prove that: different differential have different effects to handling and stability, different transfer case and drive style have the same effects additionally. Research method: Build several limited slip differential models and vehicle dynamic models, respectively; then, simulate different drive style vehicle with different differential or transfer case on the Steady State Cornering and steering wheel angle step input maneuver; compared the simulation results to prove the conclusion of the paper. Research production: Through research and analyses, build up several principle limited slip differential and transfer case models rightly, and connected with vehicle model perfectly. Innovation: Through vehicle dynamic simulation, it is easy for us to find effects of limited slip differential to handling and stability. Other papers in the field have not cover limited slip differential, transfer case model and vehicle drive style, comprehensively, this paper has researched all of those models, getting some general conclusion at last. Insufficiency: This paper shows different differential models how to affect handling and stability, but lacking of correlation of the corresponding differential and vehicle test. Conclusion: The compared simulation analysis of vehicle with different forms of differential and drive type shows that: limited slip differential in the low friction coefficient road affects more obviously,

F2012-G06-019

R. Huang (✉) · J. Wu

China Automotive Engineering Research Institute Co.,Ltd, Shanghai, P.R. China
e-mail: 15923567321@139.com

R. Huang · J. Zhan

State Key Lab. Of Automobile Simulation and Control, Jilin University, Jilin, P.R. China

and have more effects to front-drive vehicle, different differential models will have a significant impact to handling and stability. Remark: The work was completed with the assistance of National 863 plan (serial number is 2012AA111801).

Keywords Limited slip differential · Handling and stability · Differential model · Vehicle model · Simulation

1 Preface

The limited slip differential model is usually simplified to open differential at vehicle handling and stability simulation, this may lead to the simulation results are not accurate enough to reflect vehicle performance.

Predecessors have done much work to research differential's influence on handling and stability. the earliest, literature [1] compared differential of different principle influence vehicle; literature [2] analysis viscous differential's specific structure, principle and torque output characteristic; literature [3] analysis several scheme of arrangement of transfer case and differential how to effect power performance and handling used AMESim model; literature [4] use ADAMS software to build several differential models to explore vehicle performance; literature [5] use simulink toolbox to build open differential, self-locking differential, clutch active differential model to research their effects on handling; literature [6] research differential with different self-locking friction coefficients plate how to effect handling of rear-wheel drive.

This article mainly built several differential models, and researched different differential model how to affect handling.

2 Typical Differential Modeling

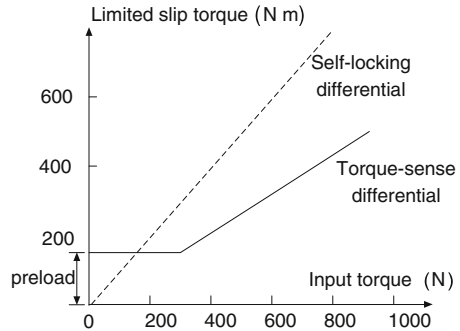
2.1 Open Differential Model

Open differential usually ignored inner-friction torque between gears, the average distribution input torque to differential shell, is calculated by the follow equation:

$$M_{xlf} = M_{xrf} = \frac{1}{2}M_d \quad (1)$$

In which, for front-drive vehicle, M_d is input torque to differential shell, M_{xlf} , M_{xrf} is left wheel and right wheel drive torque.

Fig. 1 Friction plate type differential performance curve



2.2 Friction Plate Type Differential Model

Friction effect radius, friction area number, pressing spring can affect anti-slip torque outputted by clutch, we can use performances curve received from bench to explain anti-slip differential.

Solid line in Fig. 1 means anti-slip torque vs. differential input torque, which is formed by two lines have different slopes. The first flat section is preload range of action, which is differential output torque before friction plate has not been flattened; the second section is differential output torque after friction plate has been flattened. The dotted line shows the performance of self-locking differential [7].

Ignoring anti-slip differential transmission efficiency, anti-slip torque is function of minus and plus between two output torque. Output torque by friction plate type anti-slip differential can express by the following function:

$$M_{LSD} = f(M_d) \tag{2}$$

$$M_{LSD} = M_{xlf} - M_{xrf} \tag{3}$$

$$M_d = M_{xlf} + M_{xrf} \tag{4}$$

Left drive, right drive torque:

$$M_{xlf} = \frac{1}{2} [f(M_d) + M_d] \tag{5}$$

$$M_{xrf} = \frac{1}{2} [-f(M_d) + M_d] \tag{6}$$

In which: M_{LSD} , $f(M_d)$ is anti-slip torque of torque sense differential.

Fig. 2 Vicious differential performance curve

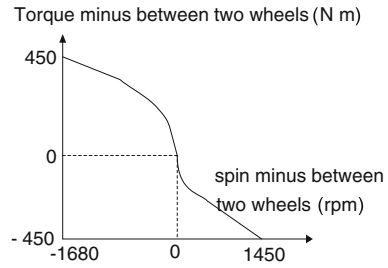
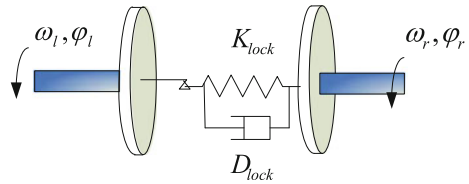


Fig. 3 Self-locking differential model



2.3 Vicious Limited Slip Differential Model

Besides structure factors, speed difference and temperature is the main factor effect output of vicious anti-slip differential. Ignored temperature, anti-slip torque is a function of spin difference between differential output ends, as in Fig. 2.

$$M_{LSD} = f(\omega_{lf}, \omega_{rf}) \tag{7}$$

Left drive, right drive torque:

$$M_{xlf} = \frac{1}{2} [f(\omega_{lf}, \omega_{rf}) + M_d] \tag{8}$$

$$M_{xrf} = \frac{1}{2} [-f(\omega_{lf}, \omega_{rf}) + M_d] \tag{9}$$

In which, $f(\omega_{lf}, \omega_{rf})$ is vicious anti-slip torque.

2.4 Self-Locking Differential Model

SUV and heave truck usually use self-locking differential, when it mounts between front axle and rear axle, lead to axles rigidly connected. When it mounts either front axle or rear axle, lead to half shaft rigidly connected.

Using torsion spring and damp model to simulate self-locking differential between two wheels, as in Fig. 3, self-locking torque is expressed by the follow equation:

$$T_{lock} = K_{lock} \times (\phi_l - \phi_r) + D_{lock} \times (\omega_l - \omega_r) \tag{10}$$

Fig. 4 Front-drive vehicle steady circle simulation displacements

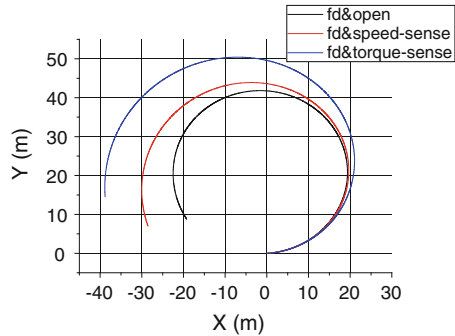
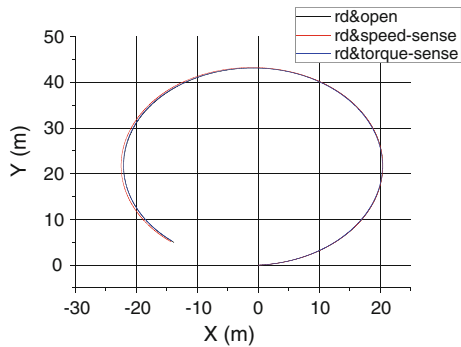


Fig. 5 Rear-drive vehicle steady circle simulation displacements



In which, K_{lock} is wheel axle torsion stiffness, D_{lock} is wheel axle torsion stiffness, ω_l, ω_r is left and right wheel spin velocity, φ_l, φ_r is left wheel and right wheel spin angle.

Front left, front right wheel drive torque:

$$M_{xlf} = \frac{1}{2}M_d - T_{lock} \tag{11}$$

$$M_{xrf} = M_d - M_{xlf} \tag{12}$$

3 Typical Simulation Maneuver Analysing

In order to compare different differential modeling may affect handling, chose several typical simulation maneuver.

In which, fd means front-drive vehicle, rd means rear-drive vehicle, 4wd means all-wheel drive vehicle, open means vehicle with open differential, speed-sense means vehicle with viscous differential, torque-sense means vehicle with friction plate type differential, fd&open means front-drive vehicle with open differential, etc.

Fig. 6 Front-drive vehicle on road with high coefficient of friction: yaw rate vs. lateral at steady circle simulation

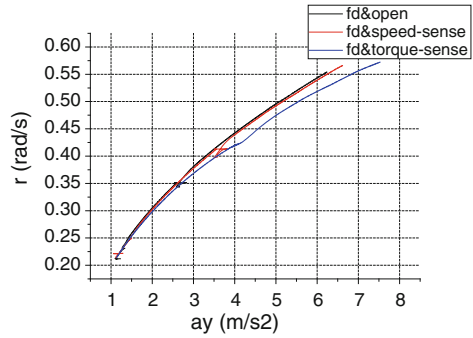


Fig. 7 Rear-drive vehicle on road with high coefficient of friction: yaw rate vs. lateral at steady circle simulation

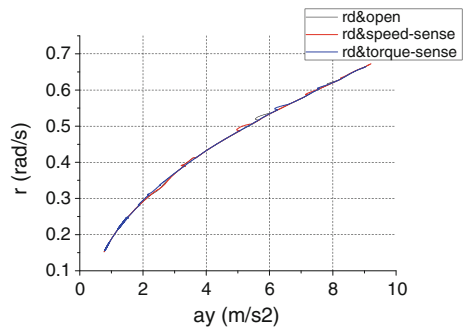
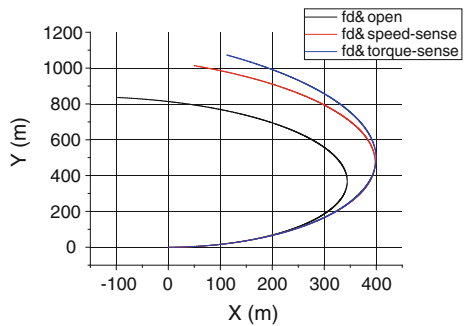


Fig. 8 Front-drive vehicle on road with low coefficient of friction: yaw rate vs. lateral at steady circle simulation

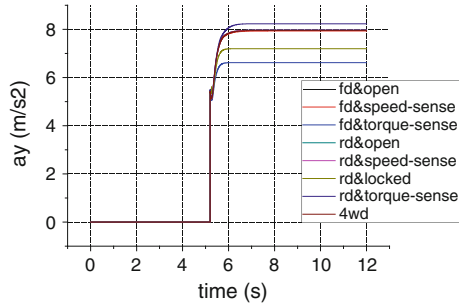


3.1 Steady Circle Maneuver on Road with High Coefficient of Friction

In simulation, guaranteed that the initial radius is 20 m, then keep steering wheel fixed, and accelerate slowly.

From Fig. 4, 5, 6 and 7, we can know that different differential models can cause these results difference: understeer, lateral acceleration, yaw rate, especially to front-drive vehicle.

Fig. 9 Lateral acceleration vs. time at step maneuver simulation



3.2 Steady circle maneuver on road with low coefficient of friction

From Fig. 8, friction plate type differential has strong understeer, viscous differential has less, and open differential is the worst. There is a conclusion that anti-slip differential have a more strong effect at low-road coefficient of friction.

3.3 Step Maneuver

In simulation, guaranteed that the velocity is 60 km/h, make steering wheel a step angle input when time is between 5 and 5.2, then keep the steering wheel stabilization. From Fig. 9, different combination of drive style and differential style can cause different results to lateral acceleration response.

4 Conclusion

The compared simulation analysis of vehicle with different forms of differential and drive type shows that: limited slip differential in the low friction coefficient road affects more obviously, and have more effects to front-drive vehicle, limited slip differential will make a more contribution to decrease adverse oversteer trend; different differential models have more significant effects to handling and stability.

References

1. Heinrich H, Heinz K (1996) The effect of various limited-slip differentials in front-wheel drive vehicles on handling and traction. In: SAE PAPER 960717
2. Gassmann T, Barlage J (1996) Visco-lok: a speed-sensing limited-slip device with high-torque progressive engagement. SAE PAPER 960718

3. Galvagno E, Morgando A, Sorniotti A, Vigliani A (2006) Differentials Modeling for Four Wheels Drive. SAE PAPER 2006-01-0581
4. Yue J, Wang T, Wang W, Li J (2005) Simulation study of light off road vehicle LSD in virtual environment. *J Jilin University (Engineering and Technology Edition)* 35(1):12–17
5. Danesin D, Girardin C. (2004) Driveline layout influence on four wheel drive dynamics. In: SAE PAPER 2004-01-0860
6. Wang J, Wang Y, Fu T, Zhang B (2006) A study on the effect of torque sensing LSD on the handling and stability of a RWD vehicle. *Automotive Engineering* 28(5):460–464
7. Wang J, Wang Y, Fu T, Zhang B (2009) Analysis and evaluation of structure and performance of the torque sensing limited slip differential. *Automotive Technology* 9:16-20.

Research on the Impact of Derived Vehicle's Weight Change on K&C and Vehicle Performance

Wuming Wu, Junping Jiang, Xiang Meng, Wei Liu, Zhijie Pan
and Fuquan Zhao

Abstract Due to the weight deviation between derived vehicle model and the original one, it is necessary to determine whether to maintain the original performance or re-design it when designing its performance parts. The vehicle model is established in ADAMS by taking a Geely's vehicle as the object. Adjusted according to the pre-set weight range of 3, 5 and 10 %, the model's K&C, riding comfort, steering stability are simulated and equivalent cornering stiffness can be calculated to compare the results with that of the original one. When the change of axle load or vehicle weight are higher than 5 %, its suspension K&C and vehicle performance obviously differ from the original one, thus the relative performance parts needs to be redeveloped since performance parts cannot meet the requirements.

Keywords Derived vehicle · Axle load · Steering · Riding comfort

F2012-G06-020

W. Wu (✉) · J. Jiang (✉) · X. Meng · W. Liu · Z. Pan · F. Zhao
Zhejiang Geely Automobile Research Institute Co. Ltd, Hangzhou, China
e-mail: wwm19851128@126.com

J. Jiang
e-mail: junping2007@163.com

F. Zhao
e-mail: zhaofuquan10@163.com

1 Introductions

To meet different market needs, OEMs will develop a series of derivative vehicles according to different customer groups, based on a mature vehicle by changing the interior and exterior adorn, replacement power, and change of surface. The front and rear axle load of derivative vehicle are different from that of original vehicle, but the wheelbase, wheel track, chassis hard points and structure will remain the same.

The Derivative vehicle's front and rear axle load are different from that of the original vehicle, so that compared with the vehicle performance the original model will have certain differences, for derivative vehicle's performance is consistent with original vehicle or has a little difference, therefore it needs to re-design performance parts to make the derivative vehicle's performance in line with that of the original vehicle.

Engineers are often unable to determine whether to maintain the original performance or re-design. For clear axle load changes on vehicle performance, taking a Geely's vehicle as the research object, the vehicle's each subsystem model in ADAMS is built and planned to adjust the axle-load analysis of the K&C and vehicle performance change, and it determines the axle load permitted range, so subsequently when engineers design performance parts, only by comparing the changes of axle load, they can immediately determine whether to maintain the original performance or re-design it.

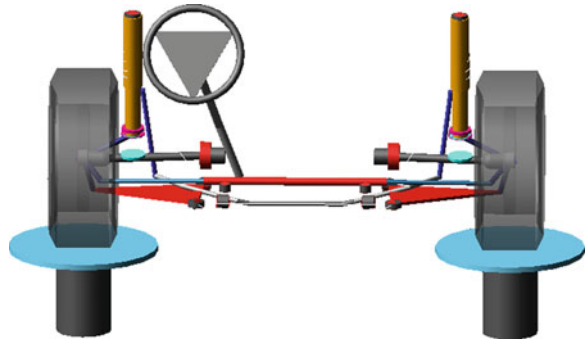
2 Suspension Kinematics and Compliances Analysis

The axle load changes will impact on suspension spring compression, suspension geometrical status, four-wheel location and deformation of the bush, resulting in the change of kinematics and compliances (K&C) performance and vehicle performance.

2.1 Front Suspension K&C Performance Analysis

Figure 1 is a Geely's vehicle front suspension assembly built in ADAMS, by increasing its front axle load 2.5, 5, and 10 %, analysis of its K&C performance change, Table 1 is the front suspension indexes change when the front axle load increases, by contrast can know, when front axle load increases to 5 %, suspension stiffness, roll center height, roll steer and suspension lateral stiffness variation exceeded the allowable variation range, K&C performance cannot be regarded as that of the original one. Suspension stiffness change causes front frequency and rear frequency matching unbalance, which may make the vehicle comfort turn bad.

Fig. 1 Front suspension assembly model



Roll center height and the roll steer have a greatly impact on vehicle under steer, therefore, when taking analysis of the vehicle performance, detailed analysis of those performance shall be needed [1].

2.2 Rear Suspension K&C Performance Analysis

Figure 2 is a Geely's certain vehicle rear suspension assembly built in ADAMS, by increasing its front axle load by 2.5, 5, and 10 %, analysis of its K&C performance change is conducted. Table 2 shows the rear suspension indicators changes with the axle load, by contrast, when rear axle load increases to 5 %, the roll center height, steer longitudinal stiffness and camber longitudinal stiffness variation has exceeded the allowed variation range, K&C performance cannot be regarded as that of the original one.

3 Calculation of Suspension Equivalent Cornering Stiffness

3.1 The Front Suspension Equivalent Cornering Stiffness Calculation

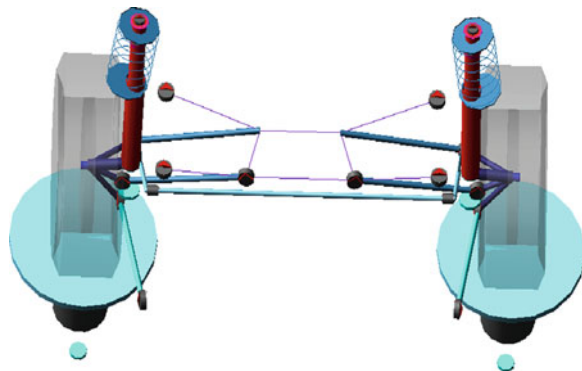
The relationship between K&C index is complementary or offset, so it is difficult to judge the impact on the whole suspension performance by change of an index. For more clearly overall performance change of front and rear suspension, through calculation of front and rear suspension and equivalent cornering stiffness, suspension performance change can be judged according the result [2].

Table 3 is the front suspension's equivalent cornering stiffness calculation result. From the table, with the increase in axle load, front suspension under steer is turning worse; when axle load variation reaches 10 %, under steer variation has exceeded the allowed range, and the front suspension performance cannot be regarded as that of the original one.

Table 1 Comparison the change of front suspension parameters

Condition	Target	Units	Original	Front axis load +2.5 %	Front axis load +5 %	Front axis load +10 %
Parallel wheel travel	Suspension stiffness	N/mm	29.83	29.77	29.3	28.94
	Roll stiffness	Nm/deg	1331	1333	1332	1335
	Roll center	mm	73	65	52	33
	Roll steer	%	9.91	10.02	10.17	10.61
	Roll camber	%	17	16	15	14
Lateral force	Toe/FY	deg/KN	-0.015	-0.015	-0.016	-0.016
	Lat.stiffness	N/mm	4967	4919	4827	4678
	Camber/fy	deg/KN	0.221	0.223	0.227	0.232
Longitudinal force	Toe/fx	deg/KN	0.024	0.024	0.024	0.024
	Long.stiffness	N/mm	790	792	797	799
	Camber/fy	deg/KN	-0.034	-0.034	-0.035	-0.035

Fig. 2 Rear suspension assembly model



3.2 The Rear Suspension Equivalent Cornering Stiffness Calculation

Table 4 is the rear suspension’s equivalent cornering stiffness calculation result. From the table, with the increase in axle load, rear suspension under steer is turning better, when axle load variation reaches 5 %, under steer variation has exceeded the allowable range, and the rear suspension performance cannot be regarded as that of the original one.

4 Handling Performance Simulation

From the preceding analysis, when the axle load variation is 5 %, K&C and equivalent cornering stiffness change has exceeded the allowable range, and the suspension performance cannot be regarded as that of the original status, so in the

Table 2 Comparison the change of rear suspension parameters

Condition	Target	Units	Original	Rear axis load +2.5 %	Rear axis load +5 %	Rear axis load +10 %
Parallel wheel travel	Suspension stiffness	N/mm	25.71	25.71	25.7	25.64
	Roll stiffness	Nm/deg	687	686	685	682
	Roll center	mm	173	167	161	149
	Roll steer	%	-0.7	-0.65	-0.6	-0.52
	Roll camber	%	20	20	19	18
Lateral force	Toe/FY	deg/KN	0.084	0.084	0.084	0.086
	Lat.stiffness	N/mm	5118	5104	5062	4964
	Camber/fy	deg/KN	0.1	0.11	0.11	0.12
Longitudinal force	Toe/fx	1000*deg/KN	1.8	-2.9	-3.8	-5.7
	Long.stiffness	N/mm	-397	-397	378	374
	Camber/fy	1000*deg/KN	-7.9	-8.3	-8.5	-9.1

Table 3 Front suspension equivalent cornering stiffness calculation

	Original	Front axis load +2.5 %	Front axis load +5 %	Front axis load +10 %
Roll steer coefficient	-0.3776	-0.3818	-0.3875	-0.4042
Toe/lat.force coefficient	-0.0672	-0.0676	-0.0719	-0.0773
Roll camber coefficient	-0.1121	-0.111	-0.1049	-0.0992
Lateral camber stiffness	-0.0244	-0.0246	-0.0251	-0.0256
Toe/Mz coefficient	-0.83	-0.8284	-0.8631	-0.8972
Equivalent cornering stiffness (%)	72.40	72.38	71.83	71.13

Table 4 Rear suspension equivalent cornering stiffness calculation

	Original	Rear axis load +2.5 %	Rear axis load +5 %	Rear axis load +10 %
Roll steer coefficient	0.0269	0.025	0.023	0.02
Toe/lat.force coefficient	0.2456	0.2517	0.2579	0.2767
Roll camber coefficient	-0.0786	-0.0767	-0.0788	-0.0794
Lateral camber stiffness	-0.011	-0.011	-0.0127	-0.0146
Toe/Mz coefficient	-0.0529	-0.0536	-0.0545	-0.0567
Equivalent cornering stiffness (%)	102.67	102.79	103.63	103.7

subsequent analysis of vehicle performance, only impact on vehicle performance within 5 % variation range of axle load is analyzed.

By adjusting the center of gravity position, moment of inertia and vehicle mass, the vehicle steering performance variation is analyzed with front axle load increase of 2.5, 5 %, rear axle load increase of 2.5, 5 %, and the vehicle weight increase of 5 % (front axle load increase of 2.5 % and front axle load increase of 2.5 %) respectively.

Fig. 3 Slip angle difference changes with the lateral acceleration

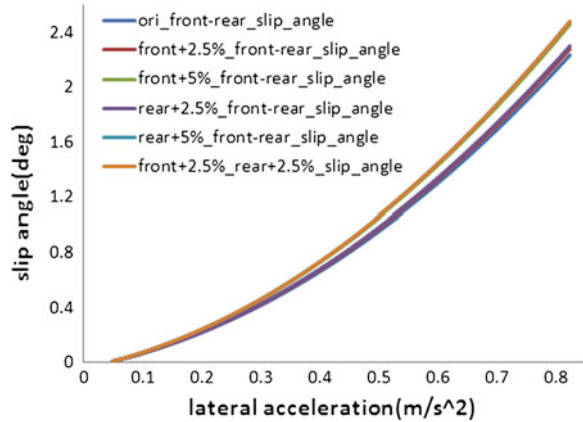
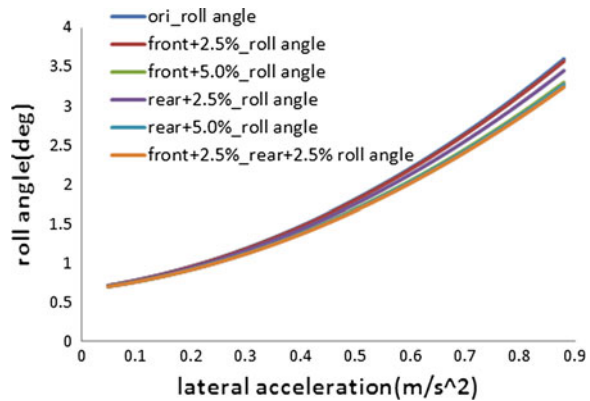


Fig. 4 Roll angle change with the lateral acceleration



4.1 Steady-State Rotation Simulation Analysis

According to the literature [3], the driver control files are built in ADAMS, and steady state circular test simulation analysis is conducted, the simulation speed is 100 km/h, and the simulation working mode is fixed steering angle. Figure 3 shows the variation curve of difference of the front and rear axle slip angle changes with the lateral acceleration, Fig. 4 is the variation curve of vehicle roll angle changes with the lateral acceleration, and Table 5 shows the degree of under steer when lateral acceleration is 0.2 g and roll angle value when lateral acceleration is 0.5 g.

From Table 5, when the front axle load increases by 5 %, the variation of degree of under steer is 10.1 %, the vehicle roll angle variation reaches 6.6 %; when rear axle load increases by 5 %, the variation of degree of under steer is

Table 5 Under steer and roll angle change

	Under steer (deg/g)	Roll angle 0.5 g (deg)
Original	1.79	1.81
Front axis load +2.5 %	1.83	1.8
Front axis load +5.0 %	1.97	1.69
Rear axis load +2.5 %	1.84	1.75
Rear axis load +5.0 %	1.99	1.68
Whole vehicle weight +5.0 %	1.99	1.67

Fig. 5 Yaw velocity gain

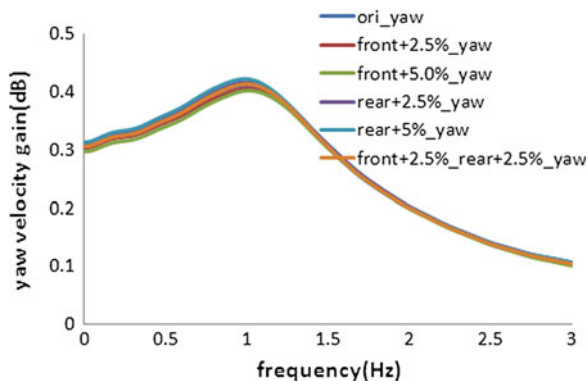
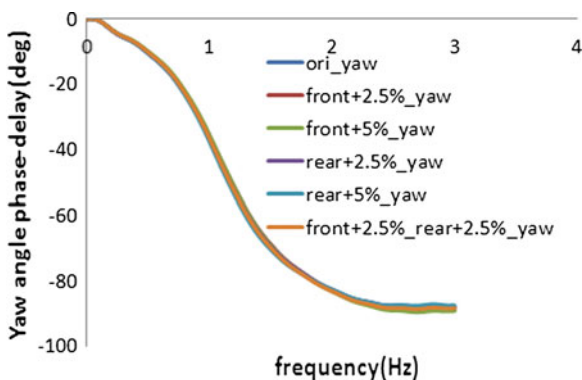


Fig. 6 Yaw velocity phase-delay

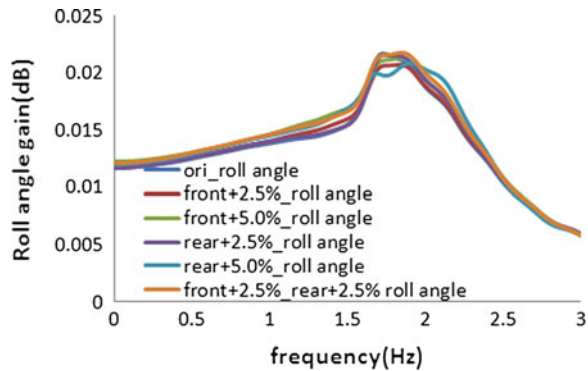


11.2 %, and the vehicle roll angle change reaches 7.7 %; and when the front and rear axle load both increase by 2.5 %, i.e., the vehicle weight increases by over 5 %, the under steer variation is 11.2 %, and the vehicle roll angle change reaches 7.7 %. From the above analysis, when the front and rear axle loads or overall vehicle weight variation reaches over 5 %, the variation of degree of under steer will exceed the allowable variation range and cannot be regarded as that of the original one (Fig. 5).

Table 6 Steering wheel angle pulse input simulation index

	Yaw velocity gain (dB)	Ay gain(dB)	Yaw velocity delay(deg)	Yaw _{max} /Yaw	Ay _{max} /Ay
Original	-10.206	0.147	-36.306	2.474	0.323
Front axis load +2.5 %	-10.39	0.144	-35.799	2.534	0.314
Front axis load +5.0 %	-10.568	0.141	-35.429	2.635	0.305
Rear axis load +2.5 %	-10.151	0.148	-36.859	2.522	0.32
Rear axis load +5.0 %	-10.103	0.149	-37.515	2.595	0.317
Whole vehicle weight +5.0 %	-10.305	0.145	-36.566	2.614	0.312

Fig. 7 Vehicle roll angle gain



4.2 The Steering Wheel Angle Pulse Input Simulation Analysis

According to the literature [4], pulse angle simulation is conducted in ADAMS, the simulation speed is 100 km/h. Figure 6 is the curve of yaw velocity changes with time, Fig. 7 is the variation curve of steer wheel roll angle, and Table 7 shows variation of each indicator. According to Table 7, when the front axle load increases by 5 %, variation degree of steering wheel angle is relatively large, namely 5 %. While when the rear axle load increases by 5 % and the vehicle mass increases by 5 %, variation degree of each indicator is little and can be regarded as same to the original one. From the above analysis, when the front and rear axle loads or overall vehicle weight variation reaches over 5 %, the variation of degree of under steer will exceed the allowable variation range and cannot be regarded as that of the original one.

Table 6 is the index curve changes with axle load, according to which the front axle load increases by 5 % for the yaw velocity gain and yaw velocity phase delay have a great impact; when the effect of rear axle load increases by 5 %, the yaw velocity phase delay is relatively large; the overall vehicle weight increase of 5 % (front axle load increase of 2.5 % and front axle load increase of 2.5 %) has little effect on the targets. Generally, the axle load increase of 5 % has little impact on the steering wheel angle pulse input and each other index (Fig. 8).

Fig. 8 Vehicle roll angle phase-delay

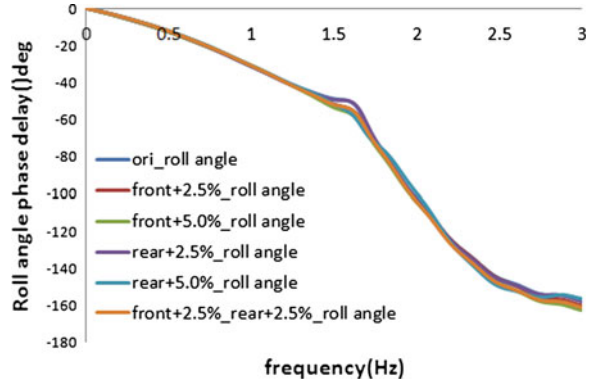


Fig. 9 Yaw velocity change with time

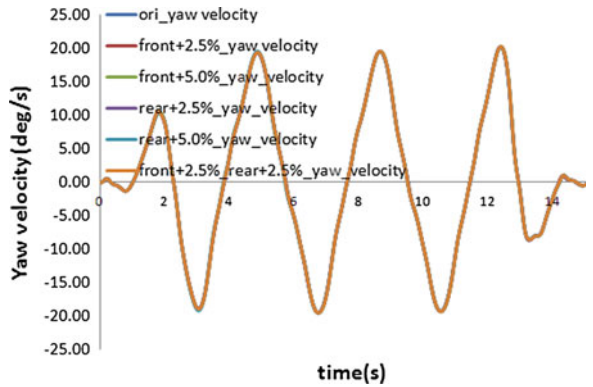


Fig. 10 Steering wheel angle change with time

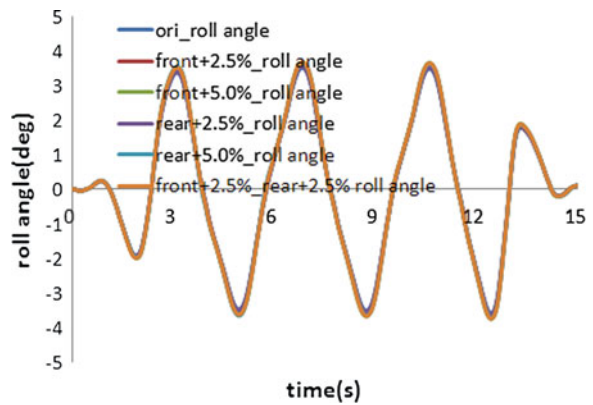


Table 7 Steering wheel angle pulse input simulation index

	Steering wheel angle (deg)	Roll angle (deg)	Yaw (deg/s)
Original	93.52	3.4975	19.3475
Front axis load +2.5 %	95.225	3.5525	19.375
Front axis load +5.0 %	98.155	3.6575	19.4
Rear axis load +2.5 %	93.275	3.525	19.35
Rear axis load +5.0 %	93.9425	3.655	19.42
Whole vehicle weight +5.0 %	95.8175	3.6575	19.4025

Fig. 11 Ride comfort simulation model

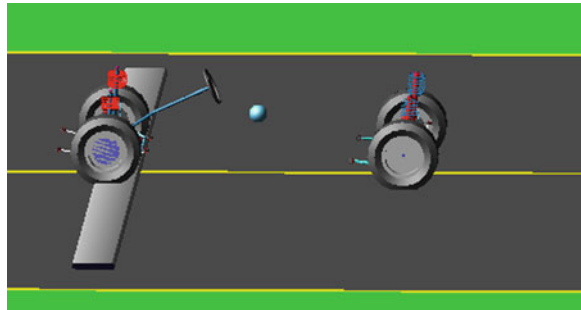
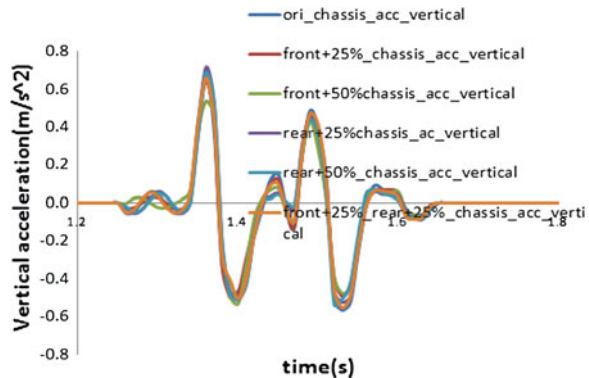


Fig. 12 Body center of mass vertical acceleration change with time



4.3 Pylon Course Slalom Simulation Analysis

According to the literature [5], pulse angle simulation is conducted; the simulation speed is 100 km/h. Figure 7 is the variation curve of steer wheel roll angle, and Table 7 shows variation of each indicator. According to Table 7, when the front axle load increases by 5 %, variation degree of steering wheel angle is relatively large, namely 5 %. While when the rear axle load increases by 5 % and the vehicle mass increases by 5 %, variation degree of each indicator is little and can be regarded as same to the original one. From the above analysis, when the front and

Table 8 Maximum vertical acceleration of the body center of mass

	Original	Front axis load +2.5 %	Front axis load +5.0 %	Rear axis load +2.5 %	Rear axis load +5.0 %	Whole vehicle weight +5.0 %
ver_acc _{max} (m/s ²)	6.82	6.49	5.38	7.17	6.89	6.6

rear axle loads or overall vehicle weight variation reaches over 5 %, the variation of degree of under steer will exceed the allowable variation range and cannot be regarded as that of the original one (Figs. 9, 10).

5 Ride Performance Simulation Analysis

According to the literature [6], pulse road surface simulation analysis is conducted as shown in Fig. 11. Figure 12 shows the variation curve of vertical acceleration of vehicle centroid when running through the rectangular pulse road. Table 8 is the maximum value of vertical acceleration of vehicle centroid. By contrast, when the front axis load increases by 5 %, variation of vertical acceleration of vehicle centroid reaches 21.11 %, which has exceeded the acceptable range, and cannot be regarded as with the original vehicle.

6 Conclusion

- (1) When axle load variation is 5 %, the relevant indexes of suspension K&C volume has exceeded the allowable variation range, and cannot be regarded as with the original suspension parameters.
- (2) When axle load variation is 5 %, front suspension equivalent cornering stiffness variation exceeds the allowable range; suspension performance cannot be regarded as with the original performance. When rear axle load variation is 5 %, rear suspension equivalent cornering stiffness variation exceeds the allowable range, and suspension performance cannot be regarded as with the original performance as.
- (3) When axle load variation is 5 %, the vehicle relevant index of handling and ride performance variation exceed the permitted range, cannot be regarded as with the original vehicle performance.
- (4) For the derived vehicle, when design the performance parts, First, determine the axle load variation, if the axle load variation is less than 5 %, the derived vehicle performance parts can be directly borrowed from the original vehicle. Otherwise, it needs to re-design performance parts, through changing the parameters of performance parts to reduce the impact of axle load change to the vehicle performance.

References

1. Gillespie write TD, Zhao L, Jin translation D (2006) Fundamentals of vehicle dynamics [M]. Tsinghua University Press, Beijing
2. Zhisheng Yu (2008) The theory of automotive (the fourth edition) [M]. China Machine Press, Beijing
3. GB/T 6323.6-1994. Controllability and stability test procedure for automobiles-Steady static circular test procedure [S]
4. GB/T 6323.3-1994. Controllability and stability test procedure for automobiles-Steering wheel angle pulse input [S]
5. GB/T 6323.1-1994 Controllability and stability test procedure for automobiles-Pylon course slalom test [S]
6. GB/T 4970-2009. Method of running test-Automotive ride comfort [S]

New Nonlinear Bushing Model for Ride Comfort and Handling Simulation: Focussing on Linearization and the Implementation into MBS Environment

Christian Scheiblegger, Jinhuai Lin and Hannes Karrer

Abstract A new nonlinear model for elastomer mounts and bushings has been developed that solves the conflicting criteria of model performance and flexibility on the one side and user-friendliness, computing time and stability on the other side. Research on this field is extensive but available models in MBS environment are often only linear model approaches that do not take into account the amplitude dependence due to the Payne effect [1]. On the other hand, some nonlinear models may map amplitude dependence well and show good performance under sinusoidal excitation; but research uncovered unexpected behaviour for time domain simulation of transient or superimposed sinusoidal excitation after implementation within MBS software environment. The investigation showed that this is due to numerical issues and principle model simplifications which are necessary for the implementation into MBS software. Therefore, the model code has been manually reprogrammed and changed to ideally fit the needs of the MBS software environment like MSC. Adams. For frequency domain analysis the new model can be switched to a simplified version (linearization) which calculates frequency dependence very well but cannot match the amplitude dependent characteristics. Similar linear models are available in some MBS applications but investigations showed that automatic linearization is often not carried out correctly and results in the time domain are different from frequency domain analyses. Therefore, such models can only be used for time domain simulation whereas for frequency

F2012-G06-021

C. Scheiblegger (✉) · J. Lin
Munich University of Applied Sciences, München, Germany
e-mail: christian.scheiblegger@hm.edu

H. Karrer
Audi AG, Ingolstadt, Germany
e-mail: hannes.karrer@audi.de

domain analysis a simple spring damper model is used. A linearized form of the new bushing model and its parameter identification are described in this paper; it leads to identical results in the time domain as well as in frequency domain analyses around the used operating point. In order to improve flexibility and user-friendliness the user can choose between a complex nonlinear model including coupling of directions as well as amplitude dependence or any possible simplification e.g. for linearization. The purpose of such a model is not to exactly describe given physical dependencies but rather to estimate the transient behaviour from a given (or expected or required) frequency response. In this paper the full nonlinear bushing model is described briefly. The model performance is validated and a concept for practical linearization is discussed with an example of the simplified linear model version. Using the given equations, this linear form of the model can be implemented into any MBS environment which is more accurate than a simple spring-damper model and can also be used for frequency domain analyses.

Keywords Elastomer model · Amplitude dependence · Linearization · Mounting · Pfeffer model

1 Introduction

For vehicle dynamics and ride comfort, engine mounts and suspension bushings have a high impact. The vehicle represents a complex vibration system where behaviour is affected not only by the tyre property, suspension system and the elasticity of the car body, but also by the tuning of the variety of different mounts and bushings. All mentioned components must be carefully tuned to achieve satisfying comfort and vehicle dynamic characteristics. This tuning process is very time consuming and expensive in an early phase of development where parts and vehicle availability are limited. Therefore simulation based development is necessary to offer a good choice of few part alternatives before actually manufacturing mounts and bushings for on-road test manoeuvres (Fig. 1).

In order to predict the ride comfort and handling behaviour of vehicles during the development process multi body simulation (MBS) tools are widely used. Starting from basic MBS philosophy using only masses and linear frequency dependent springs and dashpot elements the software tools developed to more detailed modelling of sub-modules like suspension dampers, tyres or flexible chassis structures. Bushings are usually modelled by a dashpot in parallel to a spring element, the so called Kelvin-Voigt model. Such models offer good agreement for dynamic stiffness over frequency but the damping characteristics are only estimation; it is important to know the layout frequency correctly as shown in Fig. 2. As another drawback, such linear models neglect amplitude dependent characteristics or calculate the behaviour wrongly, even if the nonlinear static stiffness characteristic is taken into account. In this paper a new nonlinear model

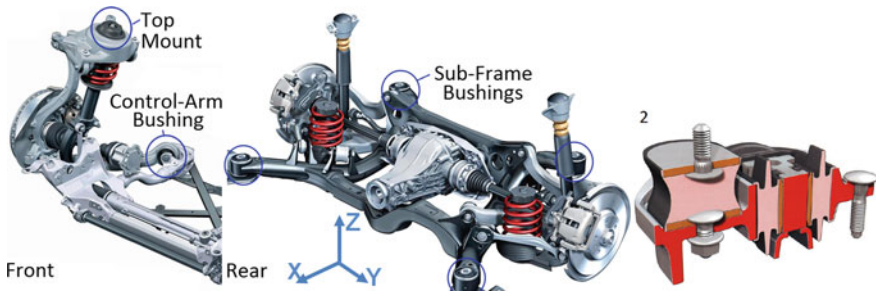


Fig. 1 Position of several elastomer bushings within vehicle and cross-sectional view of gearbox mount (right)

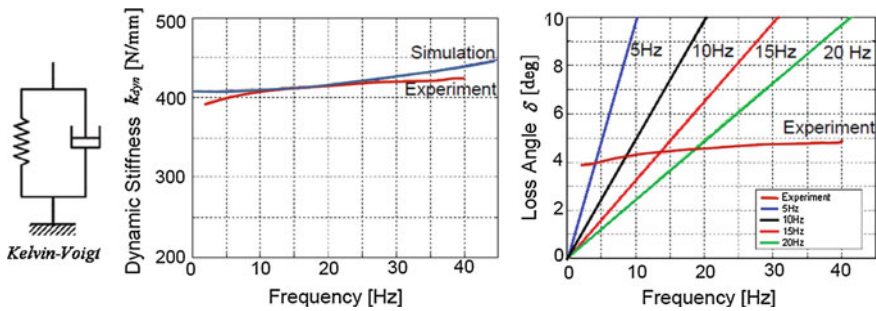


Fig. 2 Evaluation of spring-damper model (Kelvin-Voigt) with experimental data: dynamic stiffness is accurately mapped over frequency but damping characteristics (loss angle) are only correct around layout frequency. Simulation results are shown for different layout frequency; results are identical for any excitation amplitude

for elastomer mounts and bushings is presented and a practical process for linearization of such nonlinear models is discussed.

2 Characteristics of Elastomer Mounts and Bushings

In order to derive the requirements for model development elastomer behaviour is described in the following. Elastomer parts in general exhibit the following characteristic behaviour:

- Stiffness characteristics at quasi-static excitation are usually nonlinear. Therefore, the following characteristics more or less depend on the preload; behaviour varies at different operating points.
- Under dynamic excitation the measured dynamic stiffness (k_{dyn}) is much higher than the static stiffness (k_{stat}). The parameter dynamic hardening refers the dynamic stiffness to the static stiffness: $DH = k_{dyn}/k_{stat}$.

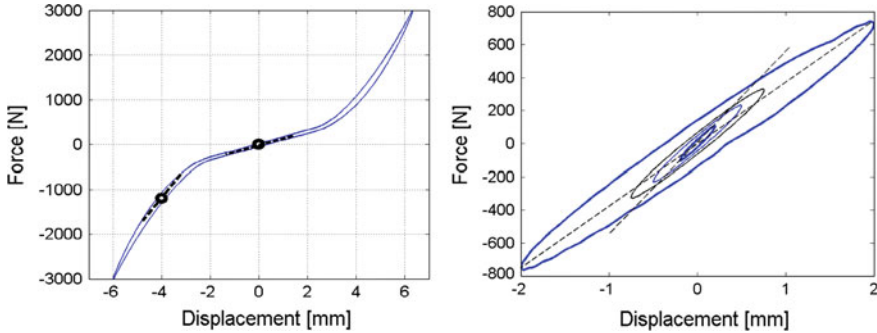


Fig. 3 Measured nonlinear static displacement-force characteristics at 10 mm/min and calculation of average static stiffness k_{stat} at various operating points (*left*). Behaviour at dynamic sinusoidal excitation at 10 Hz with hysteresis characteristics (*right*): Note that the average stiffness at small excitation amplitudes is higher than at high amplitudes. This behaviour is independent from the static characteristic curve which shows almost constant stiffness around this operating point

- The material exhibits some damping which can be seen in the hysteresis loops (force over displacement) for static and dynamic excitation. The loss angle is calculated from the integral of force over displacement (loss energy per cycle) divided by a reference area. It can also be interpreted as the phase shift between stress and strain and is widely used to characterise the damping behaviour of mounts and bushings (Fig. 3).
- Dynamic stiffness significantly decreases over excitation amplitude; known as the Payne effect. Damping slightly increases over amplitude but a maximum is often reached; depending on the tested amplitude range as shown in Fig. 4.
- Damping and stiffness increases noticeably over frequency.
- After end of excitation relaxation behaviour is observed; materials internal stress gradually decreases over time.
- Preconditioning is necessary before starting measurement because of the Mullin's Effect: Highly filled elastomer compounds reduce their stiffness during the first loading cycles.
- The material's characteristics also depend on temperature and aging.

All the above effects depend on the amount of filler in the elastomer matrix of the rubber compound. The term elastomer refers to any rubber parts including synthetic rubber compounds. In this project no material samples have been tested but complete metal-rubber bushings and mounts; so, the part's geometry also highly affects the behaviour. The next figure shows the typical amplitude and frequency dependent characteristics of elastomer bushings, using dynamic stiffness and loss angle for characterisation.

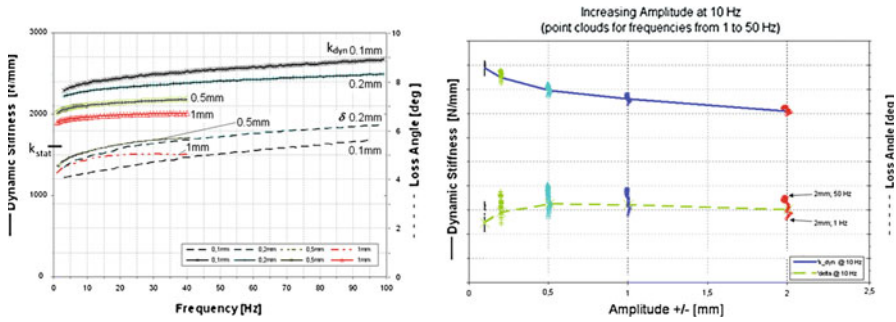


Fig. 4 Frequency response (left) and amplitude response (right) for two different elastomer bushings; amplitude response includes point cloud for increasing frequency: Impact of amplitude dependence (Payne effect) and frequency dependence

3 New Nonlinear Model for Elastomer Bushings

3.1 Objectives for Model Development

This paper focuses on modelling elastomer bushings for vehicle dynamics and ride comfort applications; emphasising the latter. Here, frequency range from 5 to 30 Hz is of main interest but the presented approach can also be used for ride handling; misuse simulation; acoustics and other application fields due to its very modular concept. Main focus is to simulate dynamic behaviour correctly within MBS environment under the assumption the bushing behaviour is roughly known; it is not a constitutive or FEA based model for prediction of characteristics depending on material and geometry design parameters. Key goals for model development were numerical stability under MBS environment; user-friendliness; model flexibility for a wide range of application and computing time; in the priority as listed. More specifically, the model could be used for real-time applications. Because these requirements are contrary to a high level of detail, in some applications a linear model layout neglecting amplitude dependence is preferred; e.g. for analyses in the frequency domain. In the following simulation results are validated for the complete new nonlinear model. Next, a concept for practical linearization of such a model will be explained. Equations and model structure of the linear frequency dependent model are given and the implementation into MBS environment is briefly described.

3.2 Model Description

The new nonlinear model is of a modular concept; Fig. 5 schematically shows the model structure (9). The overall model behaviour is a combination of:

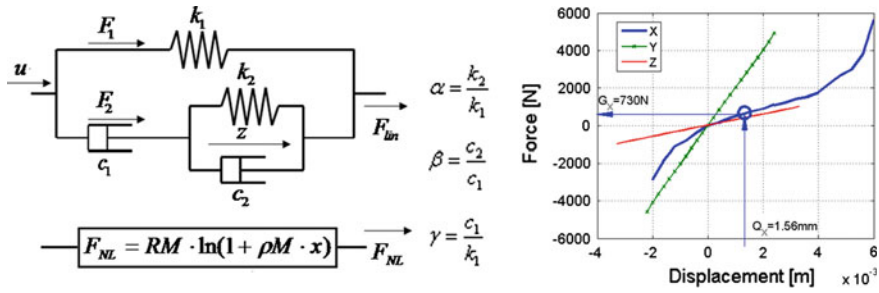


Fig. 5 Scheme for model structure of nonlinear model: In the following the nonlinear force F_{NL} is assumed to be zero; k_1 represents the main spring which may or may not be directly referred to measured static stiffness k_{stat} ; if nonlinear static characteristics are relevant they can be implemented within a table that calculates k_1 for the specific operation point from a given displacement offset Q_x or a given force preload G_x as shown in the right picture

- Nonlinear static stiffness characteristics from a table which represents the main spring k_1 in the following picture.
- Frequency dependent behaviour resulting from two dampers and one spring in parallel to the main spring.
- Amplitude dependent behaviour represented by nonlinear friction force characteristics at dynamic sinusoidal excitation.

The nonlinear part of this model leads to a logarithmic increase of nonlinear force F_{NL} over amplitude that gives the known dynamic hardening and damping attributes. The logarithmic force increase has originally been adapted from Lambertz [2]. It is described in [3] and has been continuously further developed within the last years [4–6]. In general, similar approaches can also be used such as smoothed Coulomb friction elements, the approach used from Berg [7] and Sjöberg [8] or Sedlaczek [9]. In this paper, linearization of such nonlinear model is discussed without explaining the nonlinear part in detail.

The described nonlinear model proved numerical stability and high accuracy for a great variety of different sorts of mounts and bushings. Model performance at transient excitations was improved due to an extension of the amplitude dependent part of the model that takes into account relaxation behaviour. The basic model has also been extended for hydraulic engine mounts and it was further improved particularly for hydraulic suspension bushings. Numerical implementation into MBS environment will be further discussed in the future.

3.3 Model Evaluation

Nonlinear models do give a very good fit over a wide range of amplitudes and the frequency dependence can also be seen under sinusoidal excitations like shown in Fig. 6.

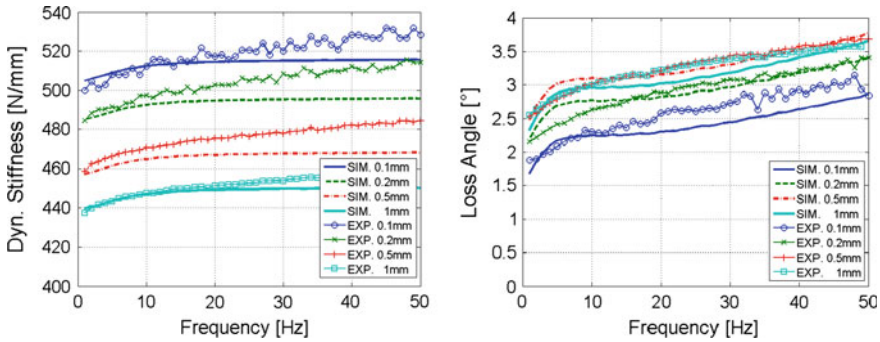


Fig. 6 Evaluation of full nonlinear Pfeffer model for elastomer mounts and bushings: nonlinear models are capable of predicting amplitude dependence as well as frequency dependence correctly over a wide range of frequencies and amplitudes. Model input: static stiffness k_{stat} ; dynamic stiffness $k_{dyn} \pm 0.1 \text{ mm}@10 \text{ Hz}$; $k_{dyn} 1 \text{ mm}@10 \text{ Hz}$; loss angle for $\pm 0.1 \text{ mm}@10 \text{ Hz}$

Even though similar nonlinear models are increasingly used within MBS environment and computing time is not significantly higher than other approaches, there are certain typical numerical issues and the parameter identification for such models could be very challenging. E.g. such modelling approaches may in some cases lead to unexpected results under superimposed sinusoidal excitation or at transient excitation in the time domain. These issues may be due to used modelling principle but can also occur as a result of different numerical details in various software tools. Hence, particular care needs to be taken for accurate implementation into the specific MBS software environment; model behaviour must be validated under different constant or variable integration time step sizes and different types of solvers; the virtual test rig setup in the development software should be identical to the one used in the target MBS environment.

Due to unexpected behaviour in the target software environment and a more complex parameter identification process, nonlinear modelling approaches are not widely used within MBS environments. On the other hand, if limited measurement data for the bushing exists or frequency domain analyses are of main interest, a linearization of nonlinear modelling approaches needs to be provided. Therefore, linear models which do only take frequency dependence into account are still preferred for a great variety of applications whereas nonlinear models currently are only used for particular analyses in the time domain.

4 New Linearization Concept

For frequency domain analyses any nonlinear model approach needs to be linearized around an operating point. A comprehensive nonlinear model must therefore be able to be simply linearized in a way to give satisfactory simulation results with a minimum effort in computing time and model parameter identification and

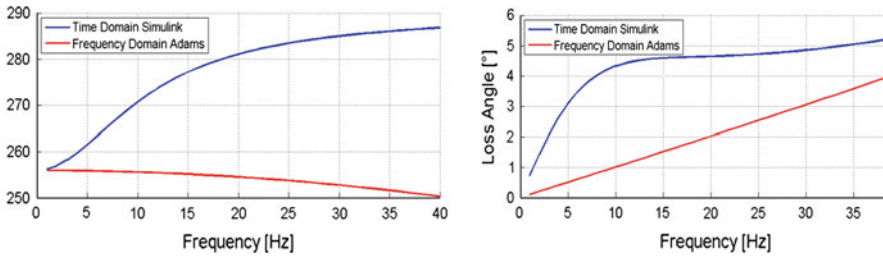


Fig. 7 Automatic linearization procedure in MSC.Adams/Car (2008-r1) does not calculate the frequency response accurately over the whole frequency range. Using the new model, frequency domain analysis gives exactly the same result as the time domain simulation carried out in Simulink (*blue curve*)

without any numerical restrictions. During this linearization, the full nonlinear model is changed into a more simple version which only consist of a combination of springs and dashpot elements that can only map frequency dependence but achieve similar results to the nonlinear model if the excitation amplitude is estimated correctly.

The investigation showed that some MBS software tools provide similar linear models which are more accurate than a simple spring damper approach. However, the automatic linearization carried out for frequency domain analysis often does not work accurately if these models are used. For example MSC.Adams/Car Ride offers a model which is a simplified version of the described linear model; referred to as the Frequency Bushing. This model is capable of giving very similar results in the time domain but as a severe drawback the model behaviour is very different when used for frequency domain analyses as shown in Fig. 7:

During automatic model linearization the principle model behaviour changes:

- the model becomes a simple spring-damper model as shown in Fig. 2.
- the approximation around the operating point is not correct but all nonlinear parts are simply set to zero

Therefore, a new method for linearization has been developed to offer a model which can be used for both, time domain simulation and frequency domain analyses with the same accuracy.

4.1 Frequency Dependent Part of Elastomer Model

The following refers to the linear, frequency dependent part of the model where F_{NL} is zero after linearization of the full nonlinear model. The overall force is then given by

$$F = F_{lin} = F_1 + F_2$$

At very slow excitation the overall stiffness of the model is dominated by the main spring k_1 because the dashpot element c_1 causes negligible force ($F_2 = c_1 \cdot du/dt$). The resulting force of the overall model therefore only depends on the main spring and excitation displacement u .

$$F_{lin} = F_1 = k_1 \cdot u$$

For further simplification the main spring k_1 is assumed to be linear around the regarded operation point; nonlinear static stiffness characteristics are neglected. Alternatively, an average stiffness is given for the particular operating point out of table data.

In the program routine the model parameters are related to each other in the following way:

$$\alpha = k_2/k_1 \quad \beta = c_2/c_1 \quad \gamma = c_1/k_1$$

Using these new model parameters alpha beta and gamma the resulting force of the model can be calculated using the following equation:

$$F = k_1 \left(u + \frac{c_1}{k_1} \cdot (\dot{u} - \dot{z}) \right) = k_1 (u + \gamma(\dot{u} - \dot{z}))$$

Where z is the displacement at the second spring k_2 and \dot{z} is the derivative of z . \dot{z} is estimated by:

$$\dot{z} = \frac{1}{1 + \beta} \cdot \left(\dot{u} - \left(\frac{\alpha}{\gamma} \right) \cdot z \right)$$

The force F_1 at the main spring is $F_1 = k_1 \cdot u$.

And the force F_2 at the dashpot is

$$F_2 = k_2 z + c_2 \dot{z} = c_1 (\dot{u} - \dot{z})$$

This simplified model version can now be used for frequency domain analyses if the force development is calculated correctly. Frequency dependence is simulated accurately and results will be the same for any excitation amplitude as long as the static stiffness does not change. If static stiffness is nonlinear the model will lead to a sort of amplitude dependence; however, this amplitude dependence does not take into account the dynamic hardening due to the Payne effect.

4.2 Transfer Function

Using the following equations, the described models frequency response could be calculated easily; by embedding the equations into code as sub-routine or via co-simulation the represented model can be implemented into any MBS software tool. This model is already of a linear type, so that simulation results in the time domain and from frequency analyses are almost identical.

For frequency domain analyses displacement and force is considered to be sinusoidal with the excitation frequency Ω ; the equations can be described in complex form as follows:

$$\begin{aligned} u &= \hat{U}e^{i\Omega t} \\ \dot{u} &= i\Omega\hat{U}e^{i\Omega t} \\ z &= \hat{Z}e^{i\Omega t} \\ \dot{z} &= i\Omega\hat{Z}e^{i\Omega t} \\ F &= \hat{F}e^{i\Omega t} \end{aligned}$$

Leading to:

$$i\Omega\hat{Z}e^{i\Omega t} = \frac{1}{1+\beta} \left(i\Omega\hat{U}e^{i\Omega t} - \left(\frac{\alpha}{\gamma}\right) \cdot \hat{Z}e^{i\Omega t} \right)$$

Rearranging:

$$\hat{Z} = \hat{U} \left((1+\beta) + \frac{\alpha}{i\Omega\gamma} \right)^{-1}$$

Substituting into

$$\hat{F} = k_{stat}\hat{U} \left(1 + i\Omega\gamma \left[1 - \left(1 + \frac{\alpha}{i\Omega\gamma} \right)^{-1} \right] \right)$$

Hence the loss angle δ is:

$$\delta = \arg\left(\frac{\hat{F}(\Omega)}{\hat{U}(\Omega)}\right) = \arg\left(k_{stat} \left(1 + i\Omega\gamma \left(1 - \left((1+\beta) + \frac{\alpha}{i\Omega\gamma} \right)^{-1} \right) \right)\right)$$

During parameter identification one parameter set is identified for the full nonlinear model and another one for a linearized form of the model that gives identical results in the time domain and frequency domain but does not change with different excitation amplitudes as can be seen in Fig. 8.

In order to compensate the missing stiffness and damping from the nonlinear friction force a specific parameter set for the linear model version is parameterized separately; using this parameter set, frequency domain analysis [2] and time domain simulation [1] give exactly the same results. The easiest way is to increase the main stiffness k_l by the amount of stiffness due to the nonlinear friction force that is missing after linearization process. As a drawback the real static stiffness k_{stat} does not correspond to the models stiffness k_1 . This could lead to inaccurate calculation of the operating point and hence an error or numerical stability issues at the start-up of overall vehicle simulation. For compensation the operating point has to be shifted e.g. by an additional displacement offset onto the bushings position if the static preload of the particular bushing may not change.

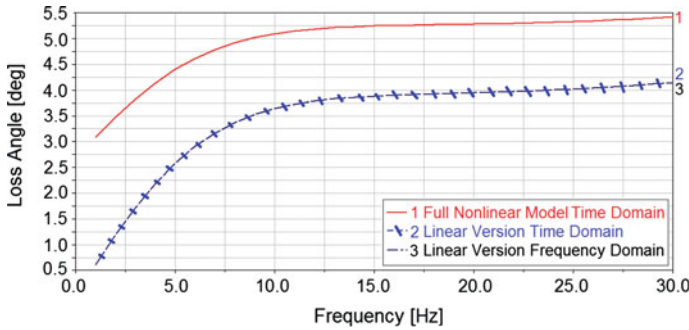


Fig. 8 Linearization procedure in MBS software using new bushing models: the loss angle for the full non-linear model version (1) is higher than for the linearized version for the regarded excitation amplitude (2)

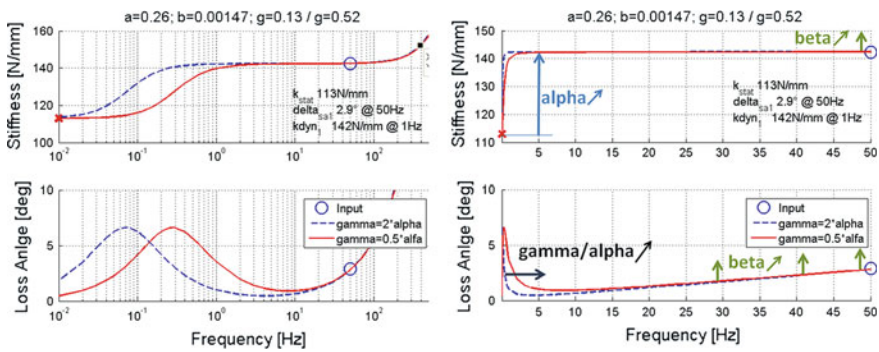


Fig. 9 Impact of changing model parameters alpha ($\alpha - a$), beta ($\beta - b$) and gamma ($\gamma - g$) on frequency response of the simplified model used for linearization: For $\gamma = 2.\alpha$ the peak loss angle of the model is reached at approx. 0.07 Hz. With a smaller relation gamma/alpha the impact of spring k_2 and damper d_1 shows at higher frequencies. Note, that alpha and gamma mainly affect the behavior for frequencies below 10 Hz in this example. The model parameter $beta = d_2/d_1$ defines the increase of damping at higher frequencies

4.3 Parameter Identification Process

In the following the method for parameter identification of the linearized model is discussed. Here, accuracy over the frequency range is slightly worse but as a benefit, the real static stiffness k_{stat} can still be used for the main spring k_1 . Besides, this description clarifies the impact of the model internal parameters α , β and γ for analytical parameter identification.

In Fig. 9 the effect of changing the main model parameters α , β and γ is shown:

- α defines the increase of stiffness over frequency
- increasing β results in increasing damping at high frequencies

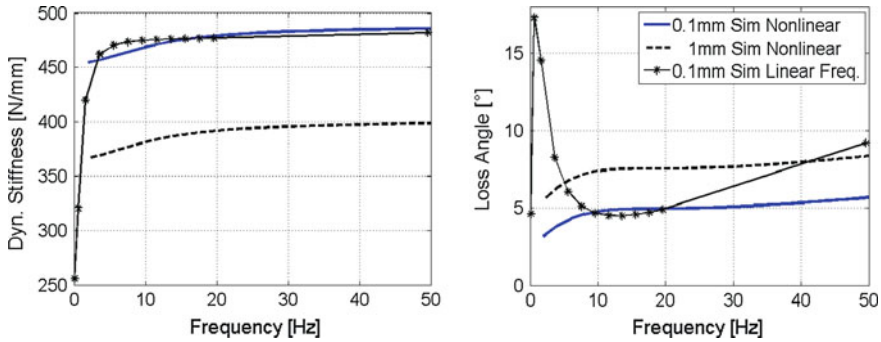


Fig. 10 Analytical parameter identification with the goal to use real measured static stiffness for main spring k_1 and to achieve sufficient dynamic hardening with only linear part of the new bushing model

- the relation α/γ defines the resonant frequency; changing the relation shifts the peak of damping to another frequency range.

The parameter α sets the maximum increase of stiffness over frequency due to the linear part of the model. The static stiffness and dynamic stiffness are known from experiment. Without any nonlinear contribution, all of the increase of stiffness must come from the frequency dependent part of the model. Hence, the parameter k_2 can be found by:

$$k_2 = k_{dyn} - k_1 = k_{dyn} - k_{stat} = (k_{stat} \cdot DH) - k_{stat} = k_{stat}(DH - 1).$$

The dashpot d_2 additionally gives increasing loss angle over frequency; in case d_2 was zero the loss angle at 50 Hz would also be zero. After α and γ have been chosen, the damping coefficient d_2 and thus the model parameter β is increased until the loss angle at the specified frequency is within a certain tolerance of the input loss angle. The right picture in Fig. 9 shows the used example with loss angle $\delta = 2.9^\circ$ at the layout frequency of 50 Hz.

Figure 10 shows parameter identification in a way that all dynamic hardening is high enough to reach measures dynamic stiffness for 0.1 mm within approx. 3 Hz. In this case the loss angle below 3 Hz and above 10 Hz is much too high but around the layout frequency of 15 Hz the model behavior is much better than a simple spring damper model (compare Fig. 2) Main benefit of this method is that the real static stiffness can be used for k_1 and still very high dynamic hardening ratios are possible.

In contrast, the standard procedure (compare to Fig. 8) uses given relations between α , β and γ to give a good fit over frequency. Because the dynamic hardening cannot exceed a certain value, the stiffness k_1 has to be significantly higher than the real static stiffness k_{stat} . Beneficially, the model parameters α , β and γ are usually taken from experience and do not have to be varied for each particular bushing; instead only the main stiffness k_1 and eventually α are changed and the rest of the model parameters remain within the same ratio.

5 Conclusion

A new nonlinear model for elastomer mounts and bushings has been developed and successfully validated within an MBS environment. For frequency domain analyses nonlinear models need to be accurately linearized around an operating point. A new concept for practical linearization of such models has been discussed in this paper. Without giving details of numerical computation of the full nonlinear model, a simplified linearized version has been described that gives accurate results in the frequency domain but does not take into account the amplitude dependence due to the Payne Effect. Using these equations, a linear version of the new model can be implemented into any MBS environment which is more accurate than a simple spring-damper model in the time domain and can also be used for frequency domain analyses.

References

1. Payne AR (1962) The dynamic properties of carbon black-loaded natural rubber vulcanizates. *J Appl Polym Sci* 6(19):57–63
2. Lambertz, Stefan (1993) Nichtlineares Materialgesetz für technische Gummiwerkstoffe mit deformationsabhängigen Eigenschaften und seine experimentelle Überprüfung an Gummifederelementen (Berichte aus der Werkstofftechnik). PhD Thesis, Aachen:Shaker
3. Pfeffer, Peter E. Hofer, Karl (2002) Simple non-linear model for elastomer and hydro mountings. to optimise overall vehicle simulation. *ATZ worldwide* 2002–05
4. Pfeffer, Peter E (2010) Modelling and simulation of the elastomer and hydro mounts models generation 2 and the implementation in MSC Adams. 3rd VI-grade Users' Conference, Bad Nauheim
5. Scheiblegger Christian, Pfeffer Peter E, Karrer Hannes, Geiger Nicolas (2011) Modelling of elastomer and hydro mounts for ride comfort and handling simulation. 13th International VDI Congress Tires-Chassis-Road
6. Scheiblegger Christian, Pfeffer Peter E (2012) New models for elastomer and hydro mounts for ride comfort and handling simulation. 6th Car Training Institute Conference, Federung und Daempfung im Kfz, Stuttgart
7. Berg Mats (1998) A non-linear rubber spring model for rail vehicle dynamics analysis. *Vehicle Syst Dyn* 30(3–4):197–212
8. Sjöberg M, Kari L (2002) Non-linear behavior of a rubber isolator system using fractional derivatives. *Vehicle Syst Dyn* 37(3):217–236
9. Sedlaczek K, Dronka S, Rauh J (2011) Advanced modular modelling of rubber bushings for vehicle simulations. *Vehicle Syst Dyn* 49(5):741–759

Research on Variable Steer Ratio of Active Front Steering System with Fluctuating Velocity

Jun Wang, Zhenhai Gao and Fangming Lou

Abstract Active Front Steering System (AFS) combines the advantages of Steer-by-Wire system and traditional mechanical steering system, and it has been developed rapidly recently. This paper focuses on the design of Variable Steer Ratio (VSR) for AFS, which is the key of AFS development. The objective of this study is to investigate a better approach of steer ratio design for AFS. Firstly, the typical piecewise linear style steer ratio presented in most early studies is introduced and its imperfection is analyzed. Then the guideline for VSR design is derived and a smooth curve style steer ratio is designed based on sigmoid function. Finally, the two different types of steer ratio (piecewise linear and smooth curve style steer ratio) are tested with CarSim and Simulink and analyzed comparatively. The simulation show that not only the steer ratio fluctuation effected by the smooth curve style is smaller than the piecewise linear steer ratio when vehicle velocity oscillates around the demarcation speed, but also the front road wheel angle superimposed by the smooth curve style is more smooth when vehicle speed changes in a wide range.

Keywords Active front steering system · Variable steer ratio · Variable vehicle velocity · Vehicle chassis electronic control system

F2012-G06-023

J. Wang (✉) · Z. Gao · F. Lou

State Key Laboratory of Automotive Simulation and Control, Jilin University, Changchun, China

e-mail: wangjunrabbit@163.com

Z. Gao

e-mail: gaozh@jlu.edu.cn

1 Introduction

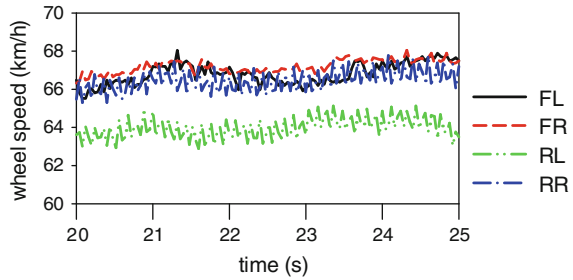
Active Front Steering System (AFS) has become an active area in the fields of vehicle active safety and integrate vehicle chassis control after it was introduced together with the new BMW 5 Series for the first time in 2004. AFS System combines the advantages of Steer-by-Wire system and traditional mechanical steering system [1, 2], and AFS system has been developed rapidly recently. Due to AFS system could implement an electronically controlled superposition of an angle to the hand steering wheel angle that is prescribed by the driver, it is possible to design the vehicle steering ratio as a function with vehicle speed. However, the permanent mechanical connection between steering wheel and road wheels remains [1, 2]. AFS could adjust the vehicle performance by means of intervening the road wheel angle in condition of the driver has top priority, which avoids the people's concerns about the Steer-by-Wire system. The functionality of AFS is classified into the stabilization functions (e.g. yaw rate control) and the assistance functions (e.g. variable steering ratio) [2]. A lot of studies about the active steering system carried out by engineers and scholars all over the world. But most of the studies focus on the stabilization functions, and the researches aimed at the assistance functions are rarely posted.

As a basic function of the active steering system, the driver will experience the performance of the assistance functions at first, and more attention is paid to assistance functions development for AFS in this paper. To design the steer ratio as a function with vehicle speed, which is called Variable Steer Ratio (VSR), is the key of AFS system development [2, 3]. AFS enables continuous and situation-dependent variation of the steering ratio and therefore adaptation of the transmission behaviour between the steering wheel and the vehicle's reaction to the relevant driving situation. Comfort, steering effort, handling and directional stability have been extensively optimized as a result of this. So the performance of Variable Steer Ratio function reflects the performance of a whole AFS System to a large extent.

Recently, a few researches are involved the development of VSR for AFS system. Gaogao put forward a piecewise linear function to describe the profile of steer ratio which is dependent on vehicle speed for VSR [4]. Shimizu and Yu Yanlei etc. present a method to design the steer ratio based on the vehicle yaw rate gain [5, 6]. Abe etc. carried out a study using a simple fixed base type of simulator which showed the upper and lower limit of the appropriate gain of the steering system [7]. It can be inferred from above studies that it is not difficult to find some common ground in designing variable steer ratio: a, the steer ratio of AFS increases with increasing speed in a wide range; b, the steer ratio of AFS trends to level out at low speed and high speed, in other words, the steer ratio of AFS almost change a little or even keep a constant value when vehicle speed changes at low speed and high speed.

All the above researches cover the two common grounds, but transient performance of variable steer ratio when the speed varies from low speed to high

Fig. 1 Speed of road wheels in 65 km/h circular driving test



speed is paid little attention, moreover, the VSR performance is not discussed in detail in a condition of velocity fluctuating, accelerating or decelerating. Due to all AFS functions are implemented by the electronic control system, it will be influenced by the particularity of the electronic control system. For instance, the actual vehicle velocity is not able to be measured by low cost sensors at present. So the vehicle velocity is estimated from the four road wheel speed sensors. Due to the physical wheel speed signal is inevitably interfered by noise and the wheel speeds always fluctuate in a range, it will result in a fluctuation of vehicle velocity [8, 9], as shown in Fig. 1. The VSR adopted the piecewise linear style steer ratio will cause steer ratio vibrate seriously especially at turning points when vehicle speed changes. The steer ratio vibration will make the AFS actuator motor run continuously and repeatedly, which will bring about a bad effect on VSR performance and even more energy consumption. Furthermore, because acceleration and deceleration are essential parts in ordinary driving, it is necessary to discuss the VSR performance with speed varying in a large range resulted from acceleration or deceleration.

In order to improve the transient performance defect of the piecewise linear style variable steer ratio, the design of variable steer ratio illustrated as a smooth curve is introduced in this paper. Moreover, the kinematics model of AFS actuator and a variable steer ratio controller are established in the study and simulation tests are implemented with CarSim & Simulink.

2 Modelling of Active Front Steer System

Compared with traditional mechanical steering system, active steering system is comprised of a double planetary gear and an electric actuator motor additionally, besides the primary mechanical steering system. Because all the links from the steering wheel to road wheel are mechanical, it is indubitable that AFS is reliable and safe. AFS could ensure that the vehicle is under driver’s control all the time, and make the driver have a clear road feel [2]. The planetary gear of AFS have two degrees of freedom (DOF), the output of the planetary gear connects with the steering gear’s pinion, and one input connects with the steering wheel, and the

other input connects with an electric actuator motor. The steering gear's pinion angle δ_V is dependent up on the steering wheel angle δ_S and motor angle δ_M , and there is a nonlinear relationship between the average front road wheel steering angle δ_f and the pinion angle δ_V . Hence, the front wheel angle δ_f relied on the pinion angle δ_V would be changed with variation of the motor angle δ_M when given a certain hand steering wheel angle δ_S , such is the function of variation of steering ratio. The above relationships are shown as follow Eq. (2):

$$\delta_V(t) = i_V \cdot \delta_S(t) + i_M \cdot \delta_M(t) \quad (1)$$

$$\delta_f(t) = F(\delta_V(t)) \quad (2)$$

$$\delta_f(t) = 1/i \cdot \delta_S(t) \quad (3)$$

Where δ_V denotes the steering gear's pinion angle, δ_S the hand steering wheel angle, δ_M the motor angle, δ_f the average front road wheel angle, i_S the factor of conversion from hand steering wheel angle to the steering gear's pinion angle, i_M the factor of conversion from motor angle to the steering gear's pinion angle, $F(\cdot)$ denotes the nonlinear relationship between the average front road wheel steering angle δ_f and the pinion angle δ_V , i is defined as the steer ratio of active steering system.

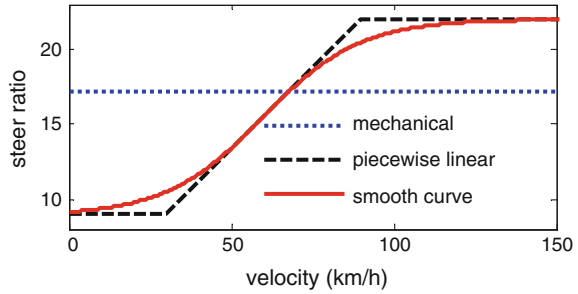
The core of the AFS system actuator is primarily comprised of a double planetary gear, an electric actuator motor, a worm gear, an electromagnetic locking unit in case of a safety relevant malfunction. The previous paper [10] gives a detailed description of modelling of AFS planetary gear, whereas this one focuses on the variable steer ratio functionality of the system.

3 Design of Variable Steer Ratio for Active Front Steer System

3.1 Design Variable Steer Ratio as a Function with Velocity

A driver needs to turn the steering wheel for a desired lateral acceleration and yaw rate if the driver wants to make a vehicle turn. When a vehicle turns the same corner, as known to all, a big steer ratio requires more steering wheel angular displacement than a small steer ratio, which even makes the driver cross his hands to turn a large angle. So it requires a driver to pay more physical effort, and it makes the driver feel vehicle steer response slowly and insensitively. However, a small steer ratio requires less steering wheel angular displacement, but it makes driver fell vehicle much too sensitive to control accurately, and the handling problem becomes more serious especially at high speed. The problem can be solved perfectly by variable steer ratio of active front steer system. The Variable

Fig. 2 Velocity dependent steering gear ratio



Steer Ratio is the first function of AFS which is experienced by driver, and the variable steer ratio is the basis of active front steer system.

To improve the performance of the piecewise linear style steer ratio, a smooth curve is introduced to describe the variable steer ratio in the study, which is named as smooth curve style steer ratio. With comparing performance of the two types steer ratio, the design requirements and guidelines for Variable Steer Ratio could be concluded from the research results.

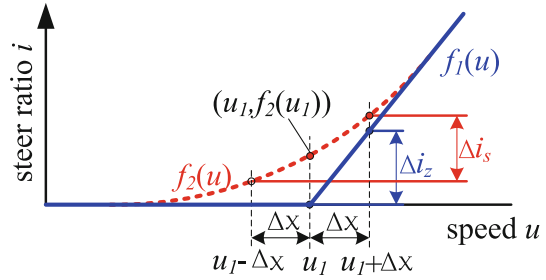
The piecewise linear style steer ratio is illustrated by black dotted line as shown in Fig. 2. The piecewise linear style steer ratio can be divided into three parts: high gain steer ratio at low speed, low gain steer ratio at high speed and linear gain steer ratio at medium speed. In order to guarantee vehicle mobility, the steer ratio is set to i_{min} if vehicle velocity is lower than a fixed value u_1 ; to improve the manipulation accuracy at high speed, the steer ratio is set to i_{max} if vehicle velocity is higher than a fixed value u_2 ; the steer ratio increases with velocity linearly. The piecewise linear style steer ratio is shown as follow equations.

$$i_l(u) = \begin{cases} i_{min} & u \leq u_1 \\ (i_{max} - i_{min}) / (u_2 - u_1) \cdot (u - u_1) + i_{min} & u_1 < u < u_2 \\ i_{max} & u \geq u_2 \end{cases} \quad (4)$$

Where $i_l(u)$ is defined as the piecewise linear style steer ratio of active steering system, u denotes vehicle velocity, u_1, u_2 are the boundaries of low speed and high speed respectively, i_{min}, i_{max} is the constant steer ratio at low speed and high speed.

The piecewise linear function is simple and easy to implement in AFS system control algorithm, so it has been adopted to represent the various steer ratio in most early studies. But the steer ratio will be influence greatly due to the discontinuousness of piecewise function, especially when the vehicle speed fluctuates wildly around the points of demarcation of the piecewise linear function (e.g. speed is near u_1, u_2). It has been proven to have a bright prospect to alleviate the problem by promoting the steer ratio form (e.g. the smooth curve type steer ratio presented in the study). And the requirements which are needed to meet by new style steer ratio will be derived in detail in this section. As shown in Fig. 3, the piecewise linear style steer ratio is shown as the dash line, its equation is $i = f_l(u)$, and the gradient of linear part is defined as k . the smooth curve style steer ratio is shown as

Fig. 3 Linear steer ratio and smooth steer ratio zoom in at u_1



the solid line, and its equation is $i = f_2(u)$. When vehicle velocity varies in the range of $[u_1 - \Delta x, u_1 + \Delta x]$, the change of steer ratio is depicted as follows:

$$\Delta i_l = f_1(u_1 + \Delta x) - f_1(u_1 - \Delta x) \tag{5}$$

$$\Delta i_s = f_2(u_1 + \Delta x) - f_2(u_1 - \Delta x) \tag{6}$$

Where $\Delta i_l(u)$, $\Delta i_s(u)$ are defined as the variation of the piecewise linear and the smooth curve style steer ratio, Δx denotes the vehicle velocity variation.

It can be inferred from the Eqs. (4) and (5):

$$\Delta i_l = k \cdot \Delta x \tag{7}$$

Where the gradient of the linear steer ratio $k = (i_{\max} - i_{\min}) / (u_2 - u_1)$.

The first order Taylor series expansion replaces Eq. (6) at u_1 :

$$\Delta i_s \approx 2f_2'(u_1) \cdot \Delta x \tag{8}$$

Where $f_2'(u_1)$ is the value of the first order derivative of the smooth curve $f_2(u)$ at u_1 .

It will make the variation of the smooth curve style steer ratio $f_2(u)$ at turning points milder than the piecewise linear style $f_1(u)$, if $\Delta i_l > \Delta i_s$. Thus, Eq. (9) can be deduced as follow.

$$f_2'(u_1) < k/2 \tag{9}$$

It can be inferred from above equation that the sufficient condition, which could ensure the fluctuation of the smooth style steer ratio resulted from speed noise smaller than the linear style, is to make the gradient $f_2'(u_1)$ of smooth curve $f_2(u)$ smaller than half the slope of linear steer ratio at u_1 .

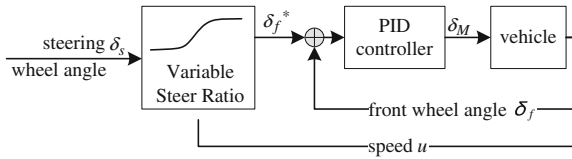
The smooth steer ratio can be designed by curve fitting. The sigmoid function has been chosen to design smooth steer ratio in the study. A smooth style steer ratio with independent vehicle velocity has been introduced by modifying sigmoid function, as shown in Eq. (10). Moreover the parameters in the equation have clear physical significance and easy to understand by engineers.

$$i_s(u) = (i_{\max} - i_{\min}) / (1 + e^{-\frac{u - (u_1 + u_2)/2}{15}}) + i_{\min} \tag{10}$$

Table 1 Parameters in equations of steer ratio

Parameter	u_1	u_2	i_{min}	i_{max}
Value	30 km/h	90 km/h	9	22

Fig. 4 Structure of variable steering ratio function controller



where $i_s(u)$ is defined as the smooth curve style steer ratio, other variables is same as Eq. (4).

It can be calculated with parameters in Table 1 like that $i_s'(u_1) = 0.091 < k/2 = 0.2167/2 = 0.1083$, the result shows that the smooth curve style steer ratio depicted by Eq. (10) has met the sufficient condition Eq. (9). When Δx is set to a given value of 0.8 (the fluctuation amplitude of vehicle velocity from the road test results is around 0.8 km/h), it can be inferred that $\Delta i_s = 0.1467 < \Delta i_l = 0.1733$, that is to say, the fluctuation of steer ratio induced by speed noise of the smooth curve style is smaller than the piecewise linear style, which will be validated by simulation tests in next paragraph.

4 Simulation Tests and Results Analysis

In order to implement the Variable Steer Ratio function of AFS and compare the above two styles steer ratio, the kinematics model of AFS actuator has been established with CarSim and Simulink and a PID controller for VSR has been designed in this paper. The structure of the controller is shown in Fig. 4 and control system block diagram is depicted in Fig. 5.

In order to compare the performance of above two styles of steer ratio, steady-state circular driving tests have been carried out in CarSim virtual test environment, and the radius of turn is 100 m according to ISO 1438 [11]. As shown in Fig. 6, a car accelerates with a fixed acceleration of 1 km/h/s from 0 to 100 km/h to imitate actual speed signal closely, some noise has been added to the speed signal from the CarSim vehicle model.

In the steady-state circular driving test, the steering wheel angle profiles are represented in Fig. 7. The VSR equipped vehicle requires a smaller steering wheel angle than the conventional vehicle in the same radius cycle test when speed is lower than 98 km/h, the advantage is more obvious especially at low speed. With increasing speed, the superposition angle generated by VSR of AFS will decrease gradually and even superpose an angle reversely which makes it easy to control vehicle direction accurately because the driver could steer hand wheel to turn a

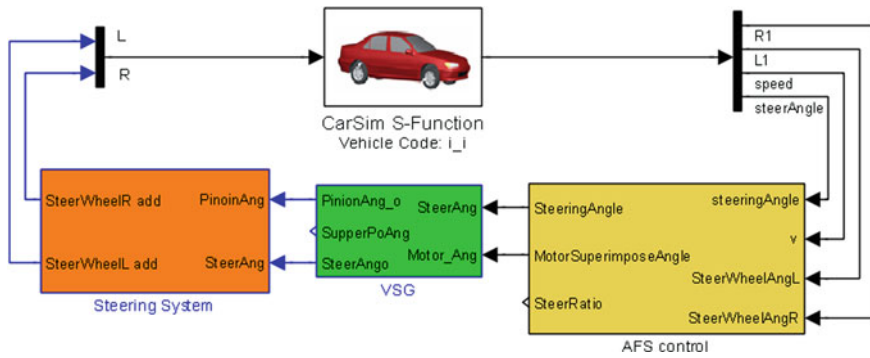
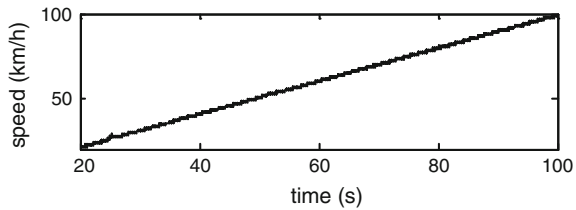


Fig. 5 VSR control system block

Fig. 6 Speed signal in the circular driving test



finer road wheel angle at high speed. It can be revealed from Fig. 2 that VSR will superpose a reverse angle to front road wheel which will makes the steering wheel angle increase when vehicle speed becomes higher than the speed (about 70 km/h) at the intersection of variable steer ratio and conventional steer ratio. However, the test results show that the steering wheel angle doesn't increase obviously when speed becomes higher than 70 km/h. The reason of above unexpected phenomenon is that the feedback of VSR controller is the pinion angle not the front road wheel angle and the compliance character of the vehicle chassis is not considered in the VSR controller which has an effect upon road wheel alignment. The vehicle lateral acceleration increase rapidly with increasing speed. Lateral tire force saturation and compliance steer will reduce the front wheel angle in the condition of large lateral acceleration, which will make the actual steer ratio greater than nominal steer ratio so that the actual steering wheel angle becomes greater than the calculated value with traditional steer system in the same radius turn test [12]. Therefore, the steering wheel angle of VSR equipped vehicle is closer to the traditional vehicle at high speed.

As shown in Figs. 2 and 7, there are few entire differences between piecewise linear style steer ratio and smooth curve style. Hence overall performance of the two styles steer ratio is similar to each other, and most part of the result plot (e.g. steering wheel angle) overlays each other except when speed is near 30 or 90 km/h.

It can be concluded from test results that when speed fluctuates on a large scale (for example, as shown in Fig. 6, a vehicle accelerates from 20 to 100 km/h) the superposition angle profile generated by the smooth style steer ratio is more

Fig. 7 Steering angle signal in the circular driving test

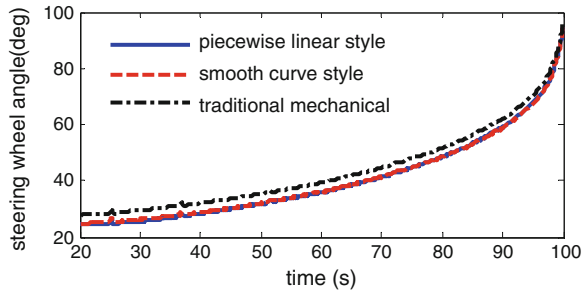


Fig. 8 Time history of superimposition angle of front road wheel in the circular driving test

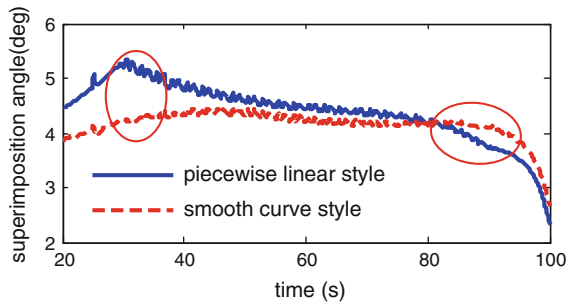
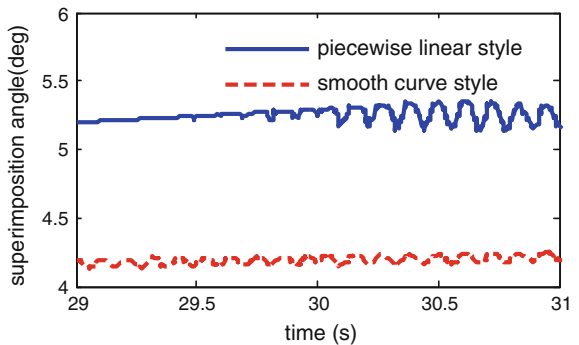


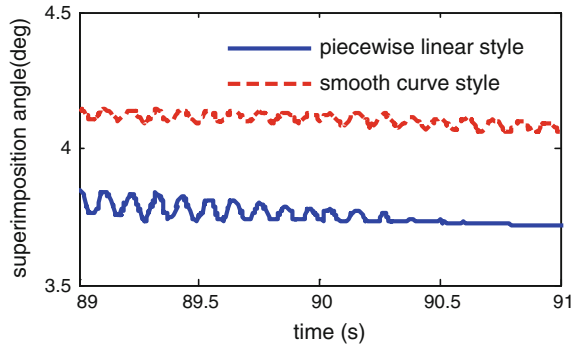
Fig. 9 Superimposed angle of front road wheel zoom in at speed of 30 km/h



smooth and continuous than the linear style and an abrupt change appears in the superposition angle curve of linear style VSR at a speed of 30 km/h, as shown in Fig. 8. To achieve the VSR function, AFS need to increase the superposition angle along with increasing vehicle velocity, in addition the affect of understeer has to be compensated. The superposition angle profile generated by the smooth style steer ratio is smooth because the steer ratio profile is smooth.

There are great differences between the two styles steer ratio at speed of 30 and 90 km/h, as shown in Figs. 9 and 10. The fluctuating velocity results in superposition angle variation, whose amplitude in smooth style VSR is smaller than linear style. Hence it provides evidence for the advantages of smooth curve style steer ratio

Fig. 10 Superimposed angle of front road wheel zoom in at speed of 90 km/h



discussed in the above paragraph. The superposition angle variation amplitude is close to zero in linear style VSR because the steer ratio is set to a fixed value when vehicle speed is lower than 30 or higher than 90 km/h.

5 Conclusions

In order to solve the defect of typical piecewise linear style steer ratio, a new style of variable steer ratio depicted as a smooth curve is introduced in this paper. And the parameters in the equation are easy to be understood and applied by engineers because they have clear physical significance. The sufficient condition is derived from mathematical method, which makes the steer ratio fluctuation of smooth curve style caused by vehicle velocity noise more smooth than the piecewise linear style variable steer ratio. Based on the derivation, a sigmoid function has been chosen to formula the smooth curve style steer ratio. Then the two different types of steer ratio (piecewise linear and smooth curve style steer ratio) are tested with CarSim and Simulink and analyzed comparatively. The simulation results show that not only the steer ratio fluctuation effected by the smooth curve style is smaller than the piecewise linear steer ratio when vehicle velocity oscillates around the demarcation speed, but also the front road wheel angle superimposed by the smooth curve style is more smooth when vehicle speed changed in a wide range. The research results proved in this paper may be a guide to contrive variable steer ratio function. In future, road tests will be carried out, and then an approach to find the optimal steer ratio at low speed as well as high speed and subjective evaluation method for variable steer ratio function in AFS system will be promoted.

Acknowledgments This paper is supported by National Natural Science Foundation of China (50975120), Fok Ying Tung Education Foundation (114025), the Key Project of Chinese Ministry of Education (108041) and Chang jiang Scholars, Program for New Century Excellent Talents in University (NCET-08-0247) and Innovative Research Team in University (No. IRT1017), People's Republic of China.

References

1. Koehn P. Active steering—the BMW approach towards modern steering technology. SAE Paper 2004-01-1105
2. Klier W, Reinelt W Active front steering (Part 1): mathematical modelling and parameter estimation. SAE Paper 2004-01-1102
3. Reinelt W et al Active front steering (Part 2): safety and functionality. SAE Paper 2004-01-1101
4. Gaogao S, Ze H, Hongdang Z et al (2010) Modeling of variable steering ratio with steady-state gain for active steering system. *J Jiangsu Univ (Nat Sci Ed)* 31(3):278–282
5. Shimizu Y, Kawai T Improvement in driver-vehicle system performance by varying steering gain with vehicle speed and steering angle-VGS (variable gear-ratio steering system). SAE Paper 1999-01-0395
6. YU L, Lin Y, SHI G (2007) A research of steer-by-wire system's steering ratio. *Trans Chin Soc Agric Mach* 38(8):190–192
7. Abe M, Shibahata Y Analysis on steering gain and vehicle handling performance with variable gear-ratio steering system (VGS). SAE Paper 2000-05-0250
8. Cai Y, Jian S (2009) A research on algorithms for calculating vehicle reference speed and slip ratio in ABS/TCS/AYC systems. *Automot Eng* 31(1):24–27
9. Pu L, Song J, Yu L (2009) Treatment method of anti-interference of abs wheel speed signal. *Automobile Technol* 31(1):24–27
10. Gao Z, Wang J, Wang D (2011) Dynamic modelling and steering performance analysis of active front steering system. *Procedia Eng* 15:1030–1035
11. ISO (2004) ISO 4138:2004 Passenger cars—Steady-state circular driving behaviour—Open-loop test methods
12. Millsap SA (1996) Handling enhancement due to an automotive variable ratio electric power steering system using model reference robust tracking control. SAE Paper 960931

Suspension Kinematic and Compliance Correlation: Test and Simulation

Da Xu, Bo Zhu, Shigen Hu, Zhonghui Zhang, Bingyong Wang,
Wei Chen and Yanghui Xu

Abstract Kinematic and Compliance (K&C) characteristics are the critical attribution to evaluate suspension performance. ADAMS-Car is a popular tool to simulate for suspension K&C characteristics simulation. Engineering experience has proved that even with all the component ratings as input, it is not guaranteed that the simulation could accord with physical testing, a lot of idealized simplification has their effects, e.g.: Difference on ride height, Friction, Hysteresis, Simplification of tyre mechanism, Assembly tolerance, Problem with small magnitude parameters. This paper will exemplify all this.

Keywords ADAMS · Correlation · Optimization · Kinematic · Compliance

F2012-G06-030

D. Xu (✉) · B. Zhu · S. Hu · Z. Zhang · B. Wang · W. Chen · Y. Xu
Beijing Automotive Technology Center, Beijing, China
e-mail: xuda2@163.com

B. Zhu
e-mail: zhubo02@beijing-atc.com.cn

S. Hu
e-mail: husg@beijing-atc.com.cn

Z. Zhang
e-mail: zhangzhonghui@beijing-atc.com.cn

B. Wang
e-mail: wangbingyong@beijing-atc.com.cn

W. Chen
e-mail: chenwei@beijing-atc.com.cn

Y. Xu
e-mail: xuyanghui@beijing-atc.com.cn

Before a valid simulation is conducted, the input parameters of the ADAMS model have been verified. Hardpoint information is obtained from design value, actually measurement on the physical vehicle shows that the hardpoints are within the error tolerance. All elastic component characteristics are from measured results. Based on these premises, a comparison between simulated result and physical testing result has been made. While most of these results shows consistency, there are certain aspect of the results demonstrate discrepancies.

Follow sections will try to explain the findings:

1 Difference on Ride Height

Oftentime, the loading conditions on the physical testing and simulated model are not totally identical, which leads to different ride height, thus the direct comparison will show differences. Figure 1 exemplifies this problem on wheel force-wheel travel plot, the results shows a horizontal shift on the abscissa. After adjusting the ride height of the simulated model, a rectified version is shown in Fig. 2, which shows accordance between the two. Another example is given on Figs. 3 and 4 on camber angle-wheel travel plot.

2 Friction

A visit back to Fig. 2 also reveal that friction does exist for vertical bounce test, which is shown by the difference on wheel force for bouncing and droop direction. However, current simulation does not take into account friction, the wheel forces are identical for two different directions.

3 Hysteresis

Due to the hysteresis nature within rubber bushes, after load is removed from rubber, the rubber component won't recover to its original shape before loading was applied. This phenomenon can be seen in Fig. 5, for the toe angle-wheel force compliance steer plot, toe angle in loading and unloading directions are different. On the other hand, simulation model does not taken into account hysteresis, the toe angle is identical between loading and unloading conditions.

Fig. 1 Wheel force–wheel travel (without adjustment) [1]

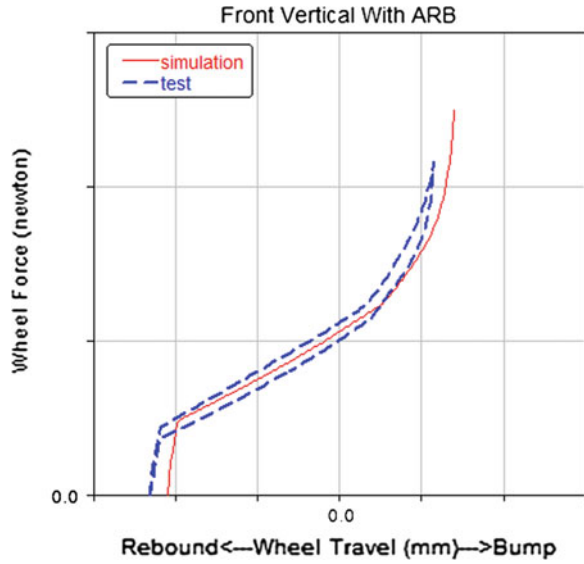


Fig. 2 Wheel force–wheel travel (with ride height adjustment)

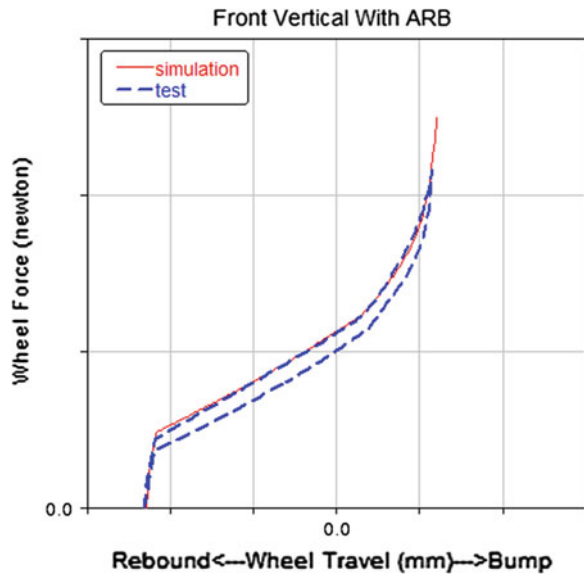


Fig. 3 Camber angle–wheel travel(without ride height adjustment)

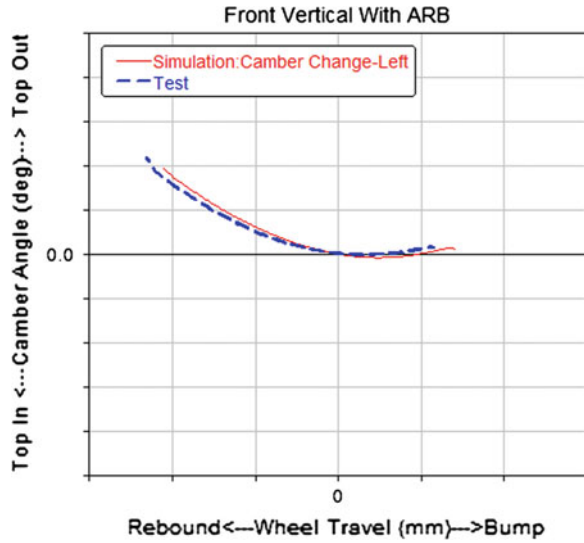
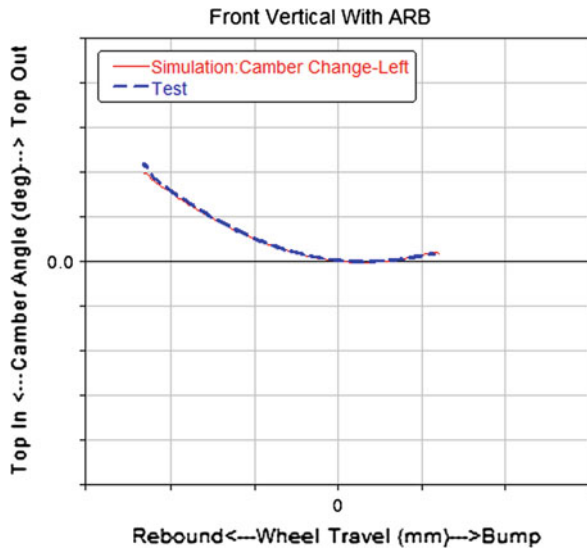


Fig. 4 Camber angle–wheel travel (with ride height adjustment)



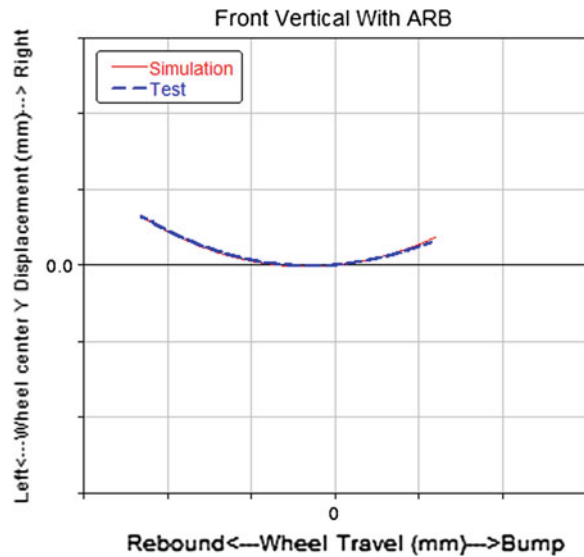
4 Simplification of Tyre Mechanism

Tyre model utilized now are specialized for certain application only. Figure 6 shown good accordance while Fig. 7 does not demonstrate same level of accordance, the reason is that tyre model is simplified for tyre force, which results in large deviation of the tyre contact point in high camber situation. This is again supported with the camber variation shown in Fig. 4.

Fig. 5 Toe angle–wheel force



Fig. 6 Wheel centre y displacement–wheel travel



5 Assembly Tolerance

Due to the existence of assembly tolerance, asymmetry of left and right may result in discrepancy on test result from left to right. In which situation, the simulated result will have to be compared with physical testing results from both left and right. An extreme example is shown in Figs. 8 and 9, the big discrepancy is due to the problem on the vehicle, which is not a useful data and must be eliminated on the correlation process.

Fig. 7 Track change–wheel travel

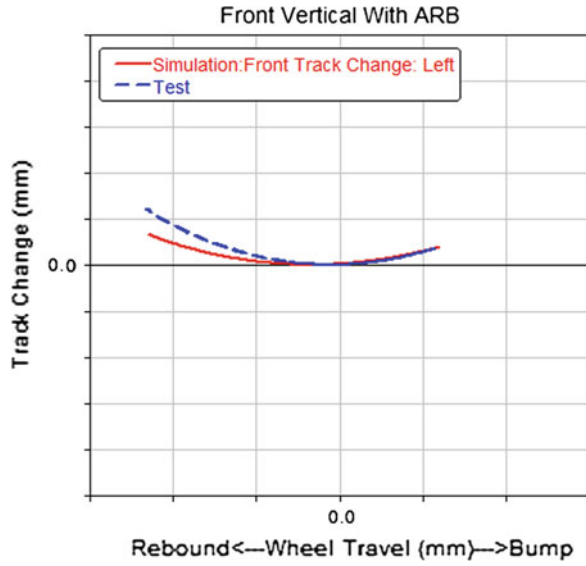


Fig. 8 Toe angle–wheel travel(*left*)

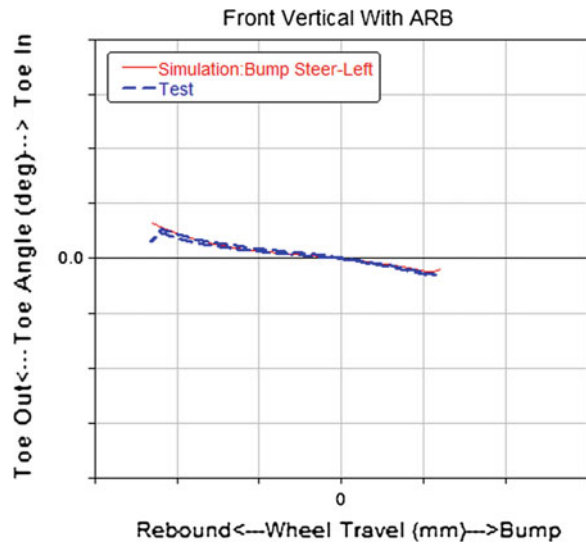


Fig. 9 Toe angle-wheel travel(right)

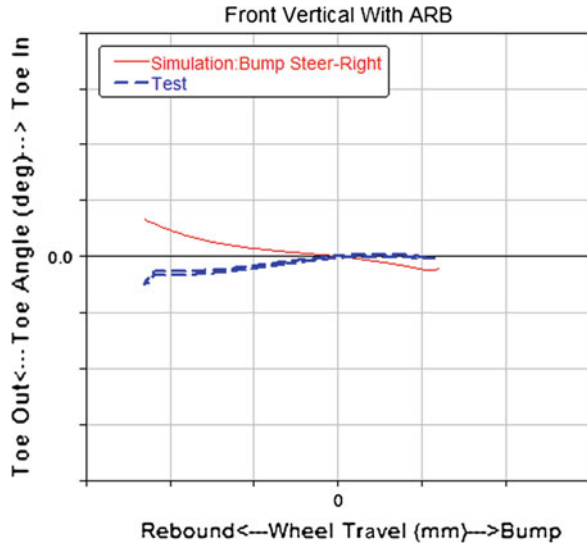


Fig. 10 Wheel center Y displacement-wheel travel (range of Y-coordinate: -2.5-2.5 mm)

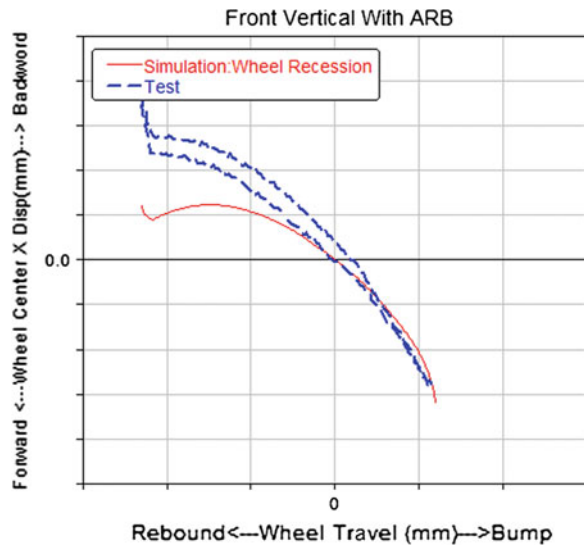
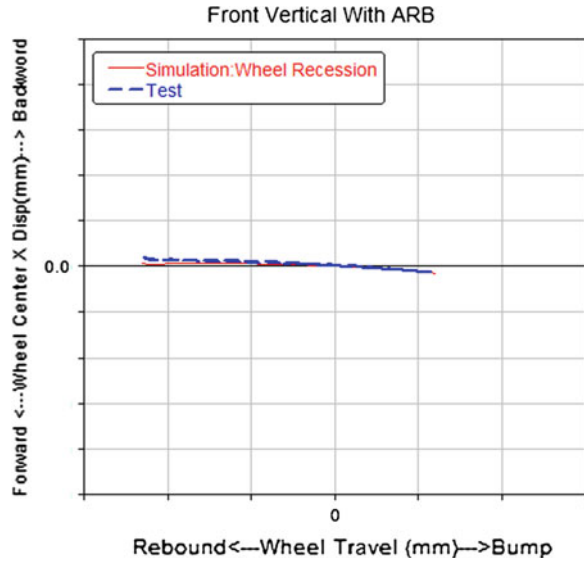


Fig. 11 Wheel center Y displacement–wheel travel (range of Y-coordinate: –50–50 mm)



6 Problem with Small Magnitude Parameters

For parameters that changes little with loading, the plotted result will show big difference especially in small scale. As shown in Fig. 10, it was deemed well correlated although the plot shape is different; the rationale is that we won't evaluate the parameter in such amplified level of magnitude. Alternatively, the scale in Fig. 11 is the proper scale for evaluating lateral migration of wheel centre in bounce test.

Reference

1. MSC. Software ADAMS Help

Decrease in Dynamic Loading of Transmission Elements of the Vehicle

Alexandr Taratorkin, Viktor Derzhanskii and Igor Taratorkin

Abstract The research is devoted to forecasting resonances of metal-ceramic disks (MCD) of transmission frictional elements for transport vehicles and determining the ways of increasing useful life. The analysis of the nature of destructions allowed for putting forward a hypothesis about MCD destruction due to the high-frequency resonance oscillations generated by the torque converter. Such an effect is new and has never been investigated before. The method of computation of natural high frequencies of MCD is developed for deleting resonant modes. Taking into account complexity of the disk design, natural frequency is analytically defined under many assumptions. In order to evaluate consistency of the assumptions in identifying natural frequencies and forms of MCD oscillations the method of nondestructive control based on identifying frequency characteristics during acoustic radiation of the test disk is developed by dominating values of spectral density of the process. Fine precision of theoretical and experimental investigations allows predicting possibility for occurrence of resonant modes of functioning of MCD frictional elements, essentially specifying the technique of design calculation, as well as solving an inverse problem of resonant mode deletion.

Keywords Dynamics · Resonance · Frictions · Durability

F2012-G06-031

A. Taratorkin (✉)

Bauman Moscow State Technical University, Moscow, Russia
e-mail: alexandr_tar@mail.ru

V. Derzhanskii · I. Taratorkin

Engineering Science Institute UrO RAN, Ekaterinburg, Russia
e-mail: dvb_47@mail.ru

I. Taratorkin

e-mail: ig_tar@mail.ru

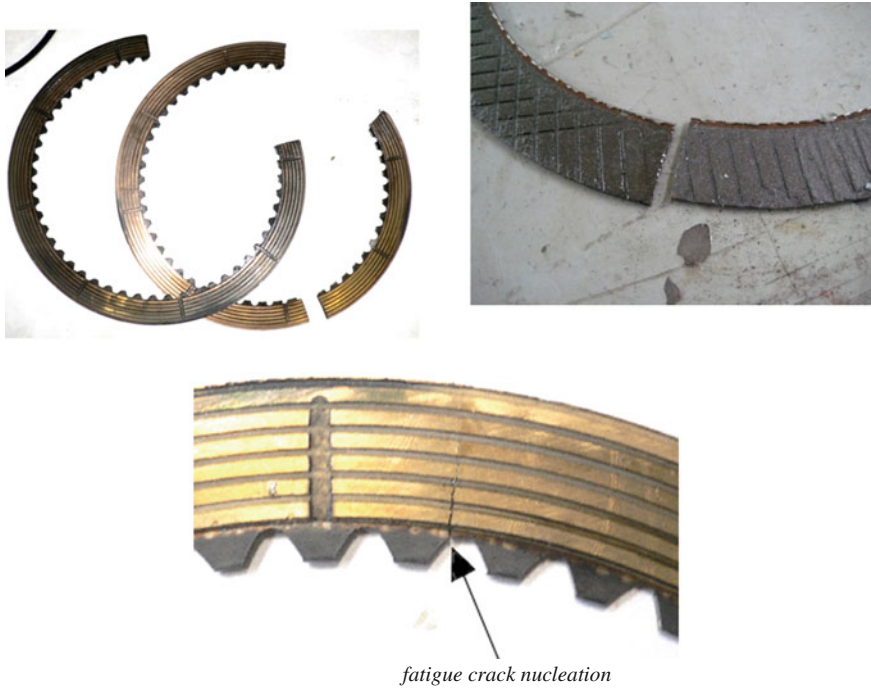


Fig. 1 Specific disruption of MCD (on the *left*: the prototype transmission; on the *right*: Allison transmission)

In the designs of multi-purpose tracked and wheel vehicles operated in the rugged environment, hydromechanical transmissions are widely used. Despite the progress in creating the prototype models of electromechanical, hybrid and variator transmissions, the hydromechanical ones retain their competitiveness. Therefore, at present more and more perfect designs of hydromechanical transmissions are developed for vehicles of the specified class, which are being developed or modernized. Testing experimental models of vehicles speaks for high dynamic loading, limiting durability of the details, in particular, of metal-ceramic disks of frictional control elements and components joined with them. The paper considers a new kind of breakdown—disk disruption, which is observed in transmissions under development and in designs of the world leader—Allison Company (Fig. 1).

The metallographic examination of the disrupted disks shows that formation of cracks has a fatigue character, which occurs during a limited time of trial operation. In this regard the hypothesis about parts failure due to occurrence of high-frequency oscillations in a resonant mode is put forward.

The research objective is to increase useful life of vehicle transmission elements by an exclusion of resonant modes in metal-ceramic disks of frictional elements of the control system.

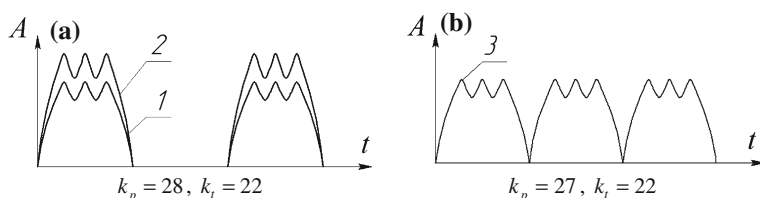


Fig. 2 Shape of pulse formed by the torque converter: 1–single pulse; 2–pair pulse; 3–impulse formed by the TC with $k_p = 27, k_t = 22$

The target goal is reached by creating a method of forecasting the conditions for exciting resonant modes in frictional elements of the control system and by solving the inverse problem.

The resonant mode is observed during torque converter (TC) operation in a hydrocoupling mode at insignificant, from 10 to 15 %, turbine sliding against the pump. The engine torque, a before-torque-converter zone, as well as gear systems do not contain such high order harmonics. In this regard the hypothesis about occurrence of a new, unexplored dynamic phenomenon—excitation of resonant oscillations by the torque converter—is put forward.

The hypothesis is proved by the character of spectral density: when the TC is blocked it comes as white noise, i.e. oscillations occur in a wide range of frequencies without resonances.

During further investigation it is revealed that one of natural frequencies of a collapsing metal-ceramic disk is equal to 703 Hz (see Fig. 6). Thus, while designing a HMT (hereinafter—Hydro Mechanical Transmission) it is obviously important to be able to estimate correctly torque converter disturbing properties and frequency characteristics of MCD of transmission frictional elements, for solving the problem of changing resonant modes out of limits of the working range.

For this purpose hydrodynamic processes in the inter-blade space of the torque converter are studied for an operating mode preceding transition to the hydrocoupling mode (when the highest vibration acceleration on the transmission case is observed in the above-stated range of frequencies).

On the basis of imitation of hydrodynamic streams in the inter-blade space, in relative motion of blade wheels of widely used and power-consuming torque converter GTK-XV with the number of blades of the blade wheels of the pump $k_p = 28$, turbine $k_t = 22$, it is defined that in transition of the pump and turbine in relative sliding 30–200 rpm a simultaneous interaction of two pairs of blades of the pump and turbine blade wheels occurs. In this regard hydrodynamic impulses with frequency of 703 Hz (Fig. 2a) that corresponds to frequency of the oscillations identified during test studies of the HMT (700–730 Hz) are formed. Besides, modeling of a series of hydrodynamic impulses in the form of a truncated cosinusoid with slip frequency of less than 136 rpm and the spectral analysis have revealed existence of harmonic components of the high order falling within the

range of a resonant mode. For the purpose of identifying the ways of tuning out disturbance from natural frequency of the disk, computation of impulses in the transition “pump-turbine” is executed with the reduced number of blades $k_p = 27$. In this case splitting of pair pulses occurs and, respectively, a 2-times increase in disturbance frequency with a simultaneous decrease in its amplitude (Fig. 2b). Thus, the given result can be used while defining the number of blades of wheels in design calculations. The exclusion of torque converter operating conditions, under which it turns to be an oscillator, is possible also under relevant control of the block system, of the synthesis of the turbine dynamic damper tuned to a resonant frequency. While installing MCD on the epicyclical gear of planetary gear set, antiphase damping realized through a two-line power supply—namely through carrier gear and a sun gear—is effective.

To confirm the hypothesis about MCD breakdown due to occurrence of high-frequency oscillations caused by close agreement between natural frequency and disturbance from TC it is necessary to have an authentic method of determining natural frequencies of MCD.

Natural frequencies of MCD are defined in the following manner. Structurally, MCD, applied in the HMT frictional elements in gross production, are made from a steel ring (steel 65 G) with the moment of inertia for a rectangular section ($J = b \cdot h^3/12$) with a gear rim internally toothed and with the frictional metal-ceramic plates (MC-5) baked to copper-plated surfaces of a steel ring at temperature of 750 °C through the adhesive layer. To define natural frequencies of MCD in an analytical way presents certain difficulties due to mechanical and physical material property difference. In this regard, natural frequency of a steel ring with reduced bulk mass m_o and modulus of stiffness E is analytically estimated. The influence of a gear rim and a metal-ceramic plate on the values of natural frequencies is determined experimentally.

Natural frequency of the steel ring is determined in accordance with the wave theory and is based on the researches of Timoshenko [1], Suryaninov [2], Pfeifer [3], Den-Gartog [4] etc.

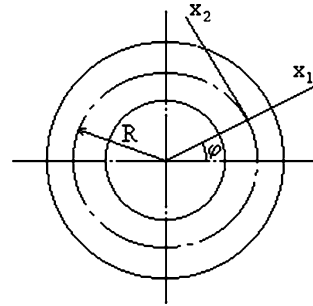
The design of the steel ring agrees with the main assumptions accepted in researches of circular rings. The ring is considered as a circular bar of a bounded curvature R^{-1} of a uniform cross section.

According to the wave theory oscillations of the circular ring, irrespective of the methods offered by various authors, are reduced to the system of partial differential equations (structural model in Fig. 3) which, considering bending oscillations in the ring plane, exclusion of a part of coordinates, are reduced to the sixth order differential equation describing tangential movement x_2 of annular cross section, defined by an angular coordinate φ :

$$\frac{\partial^6 x_2}{\partial \varphi^6} + 2 \frac{\partial^4 x_2}{\partial \varphi^4} + \frac{\partial^2 x_2}{\partial \varphi^2} + \frac{m_0 R^4}{EI} \cdot \frac{\partial^2}{\partial t^2} \left(\frac{\partial^2 x_2}{\partial \varphi^2} - x_2 \right) = 0 \quad (1)$$

The solution of the motion equation is determined in the form of radial x_1 and tangential x_2 movements (Fig. 3):

Fig. 3 Structural model for determination of ring oscillations. In this regard for U_2 it results in a ordinary differential equation



$$x_1 = U_1(\varphi)\text{Cos } \omega t; \quad x_2 = U_2(\varphi)\text{Sin } \omega t.$$

$$\frac{d^6 U_2}{d\varphi^6} + 2\frac{d^4 U_2}{d\varphi^4} + \frac{d^2 U_2}{d\varphi^2} - \frac{m_0 R^4 \omega^2}{EI} \left(\frac{d^2 U_2}{d\varphi^2} - U_2 \right) = 0 \tag{2}$$

$$U_1 = -\frac{dU_2}{d\varphi}$$

According to the general rules for solution of differential equations, it is necessary to find the common solution of the Eq. (2) including six constants, and to subdue it to the boundary conditions. Equality to zero of the system determinant expressing boundary conditions, leads to the frequency equation.

For the closed ring the boundary conditions are changed by periodicity conditions which hold true, if to assume

$$U_1 = K\text{Sin}K\varphi; \quad U_2 = \text{Cos}K\varphi \tag{3}$$

Placing (3) in (2), determine that the latter is satisfied identically if the frequency ω equals to

$$\omega = \omega_k = \frac{K(K^2 - 1)}{\sqrt{K^2 + 1}} \sqrt{\frac{EI}{m_0 R^4}} \tag{4}$$

where K is the whole number defining the number of waves being stacked along the ring length $2\pi R$ ($K = 1, 2..N$).

Depending on the parameter points K , the form of oscillations in the ring plane changes. The zero frequency agrees with $K = 1$, so as with $K = 1$ the formula (4) describes a ring movement as a rigid body. With $K = 2$ the disk takes the form of an ellipse, in this regard its natural frequency makes 703 Hz. With $K = 3$ the disk takes the form of a triangle and natural frequency makes 1,914 Hz.

This conclusion is verified by the exact solution of the system of the partial differential equations (numerical simulations), the forms and frequencies of oscillations are defined in the Unigraphics package based on the finite elements method (Fig. 4).

It follows from the given that with certain structural parameters of MCD the form of oscillations and natural frequency are defined by the parameter K .

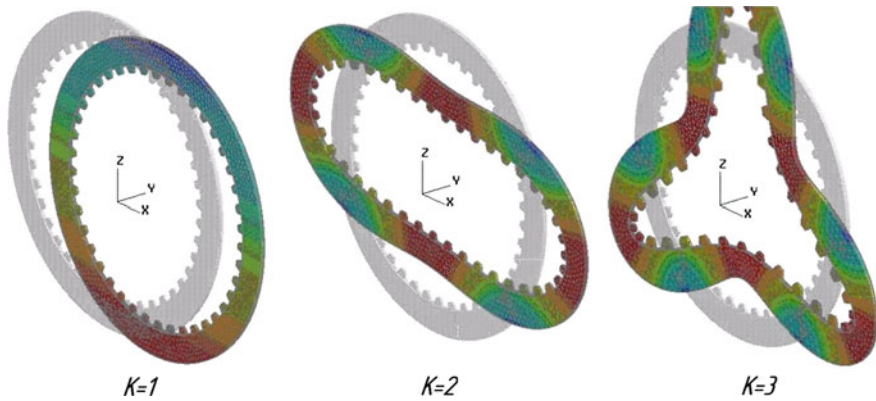


Fig. 4 Oscillation forms of the metal ceramic disk

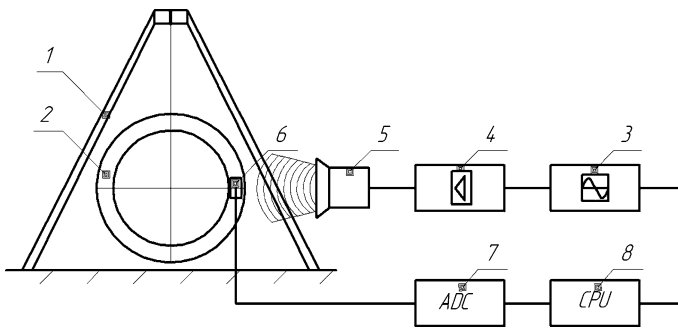


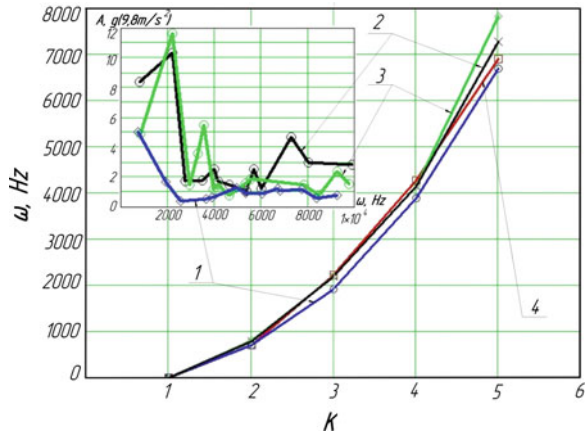
Fig. 5 Diagram of a test bed for determining the range of natural frequencies of metal-ceramic disks for torque converters

To estimate consistency of assumptions accepted at determining natural oscillation frequencies of MCD as well as the conclusion about exciting high-frequency range by the torque converter it is necessary to carry out experimental investigations. To solve the first task the way based on the method of nondestructive control and a corresponding device for its implementation is offered.

In Fig. 5 the diagram of a test bed for determining the range of natural frequencies of metal-ceramic disks for torque converters is depicted.

The test bed consists of a support 1, on which the ceramic-metal disk 2 under test is suspended, the low-frequency signal generator 3, which output is connected through the power amplifier 4 to the acoustic radiator 5 affecting the ceramic-metal disk 2 under study, on which the accelerometer 6 is fixed, the output of the accelerometer is connected via the analog-digital converter 7 to the personal electronic computer 8 which output is connected to the control unit of the low-frequency signals generator 3.

Fig. 6 Spectrum density of disk vibration acceleration: **1**–MCD; **2**–metal basis of MCD; **3**–ideal metal ring; **4**–estimated frequencies



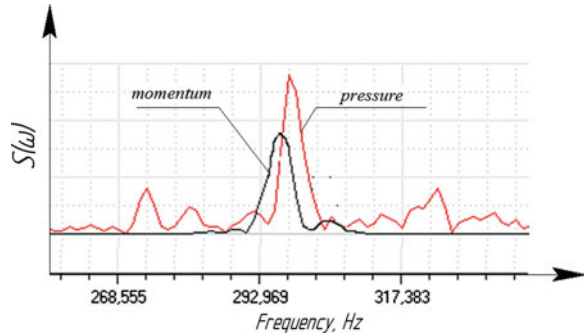
The test bed operates in the following way. For defining a range of natural frequencies on a fixed support 1 the MCD 2 under study with the accelerometer 6 fixed on it is established. When turning on the low-frequency signal oscillator 3, the sinusoidal signal through the power amplifier 4 moves to the acoustic radiator 5. Thus, an impact of an acoustic signal on the MCD 2 takes place. The analog signal from the accelerometer 6 via the analog–digital converter 7 is transmitted to an input of the personal computer 8 in a digital form. On a real time basis in terms of realization of the algorithm of direct Fourier transformation the spectral density of oscillations of MCD 2 is estimated, reaction parameters are determined, i.e. the amplitude, the phase and oscillation frequency of MCD. The spectral density of oscillation process is displayed. The values of natural frequencies of MCD are determined by local maximum of spectral density of oscillation process of MCD. The variation of frequency rate formed by the low-frequency signal oscillation 3 is carried out in software according to the set steps.

The suggested test bed structure allows experimentally for defining a range of natural frequencies of MCD with high precision, including batches of disks, defusing a subjective factor, increasing performance, reducing labor input of measurements by spectrum measurement automation, subsequent procession of the results, analysis and data storage.

During theoretical research MCD was considered as a homogeneous ring of a rectangular cross section. To check adequacy of the assumptions experimental determination of natural frequencies and investigation of an impact of availability of a metal-ceramic plate, an adhesive layer and a gear rim for the values of MCD natural frequencies was carried out. During the experimental investigation sound wave radiation of the metal disk without a gear rim (MD), of the metal disk with a gear rim (MZ) and of the MCD was carried out. The undertaken research has established close agreement of estimated and experimental values of MCD natural frequencies which is testified by Fig. 6.

Comparing the results of research of MD, MZ and MCD allow for drawing a conclusion about insignificant deviation of values of MCD natural frequencies

Fig. 7 Spectrum analysis of the process of changing the momentum at the input and pressure of hydraulic liquid



from the estimated. But within all the range of exciting frequencies oscillation amplitude of disks differ considerably, in this regard at frequency of 700–750 Hz of oscillation amplitudes of MCD and MZ are equal to 1.1 g, and MD is equal to 1.8 g. Availability of a gear rim and of ceramic–metal plates on the friction disk reduces the value of oscillation amplitude.

The result adequacy estimation of theoretical and experimental researches is made by comparison of a range of natural frequencies (Fig. 6) of the steel ring (Line Chart 1), rings with a gear rim (Line Chart 2) and MCD (Line Chart 3). The availability of the gear rim influences the value of natural frequencies insignificantly. Metal-ceramic frictional plates does not influence frequency spectrum though increase dissipative properties of the elastic system reducing oscillation amplitudes from 1.8 to 1.1 g at resonant frequency (703 Hz). Oscillation forms (the number of nodes) also correspond to the estimated.

The consistency of determining a range of high-frequency disturbance formed by the torque converter is executed while studying two torque converters of a various design and dimension sizes but with identical number of blades of the wheels (GTK XV-380 and GTR-140) at the test bed of the brake type used for determination of torque converter converting properties. The actuation of the torque converter impeller was carried out from a suspended change-speed motor. Turbine load was created by a Schenk Ltd electro-dynamic brake assembly. The pressure of the hydraulic liquid in the torque converter, its feed was created by the hydraulic system of the test bed. The supply and removal of hydraulic liquid was carried out between the reactor and the pump, herewith the channels were placed from each other at the angle of 90° . In the course of tests the following parameters were registered: torsion torque at the input and output, pressure of hydraulic liquid and its ripple frequency at the input in the torque converter, rotation frequency of pump and turbine impellers, as well as the level of vibration acceleration of torque converter casing. Parameter registration and processing was carried out by the L-CARD modular-type station of data accumulation using the Power Graph Professional 3.3.8 software package. The spectral analysis of the process of changing the momentum at the input and the pressure of hydraulic liquid showed (Fig. 7) that real dynamic processes of turbine disturbance formation are much more complicated than assumed estimates.

The disturbance frequency of the turbine momentum corresponds to the estimated, i.e. $\omega = 0,5k_p k_p \Delta n$. At the same time, the process of hydraulic liquid oscillation at the input in the torque converter formed by the feeding pump closely agrees with the oscillation frequency of the turbine momentum which also increases probability of resonance occurrence.

Agreement between the results of theoretical and experimental researches allows forecasting a possibility of occurrence of resonant modes of operation of MCD of the HMT frictional elements, it is essential to specify a technique of design calculation, as well as to solve a return problem about exclusion of resonant modes. Possibility of varying the values of MCD natural frequencies is determined on the basis of the analysis of the equation (4). Physical and mechanical properties of these materials for MCD are stable, and the change of geometrical parameters is limited by the conditions of frictional elements configuration in HMT case. An effective way of changing natural frequency is to change the number of waves stacked along the length of a disk, i.e. K parameter determining a form of oscillations. To change resonant frequency radial cuts are made on the disk.

In this regard the range of natural frequencies essentially changes: with two pairs of cuts the frequency (703 Hz) ceases to be dominating as the amplitude of spectral density decreases by 60 %. The maximum value of the amplitude moves towards lower values of frequencies. Similar process is observed with six pairs of cuts. The sizes of cuts are chosen due to the condition of strength retention of MCD with centrifugal effect in operation. Besides, the disk should not lose stiffness stability when wave propagation velocity along the disk becomes equal to rotation velocity. Some oscillation damping can be reached by creating the cone-shaped or corrugated form of the steel disks running together with MCD.

Due to the fact that the main reason for MCD breakdown in the conditions of transport vehicle operation is agreement between disk natural frequency and the frequency agitated by the torque converter, the required useful life is provided by the way of changing MCD natural frequency and of decreasing oscillation amplitude agitated by hydrodynamic processes in the inter-blade space of the TC and of pressure pulsation in its feeding system. Exclusion of the resonance can be also obtained by correction of the program for TC blocking control, by dynamic damping (antiphase) MCD oscillations or by synthesis of turbine oscillation damper. Removal of resonant modes out of the limits of an operating range is obtained by correcting the spectrum of MCD natural frequencies or by structural changes, i.e. by creating a special form of steel disks along with introduction of technological measures on decreasing load concentration at the foot of the tooth.

References

1. Timoshenko SP (1960) Strength of Material, vol 1. Phisimatgiz, Moscow, p 379
2. Suryaninov NG (2000) Theoretical Foundation of Machine Dynamics. Publishing House of Odessa GPU, Odessa, p 302

3. Pfeifer P (2006) Oscillations of Elastic Bodies. Translated from German, Edition of Lurie A.I.–2nd edn. Kom Kniga, Moscow, p 152
4. Den-Gartog GP (1960) Mechanic oscillations. State Publishing House of Physics and Mathematics Literature, Moscow, p 580

A Study on Pitching Characteristics of the Passenger Car in Braking Process

Xuanfeng Wang, Guang Shi, Lingge Jin, Guozeng Ying and Hongwei Yang

Abstract The passenger car will take on a strong pitching movement in the process of emergent braking, which makes a great impact on the ride comfort. The paper aims at resolving the practical problems of vehicle pitching. First, the variation characteristics of swing arm instant center of the front and rear suspensions are analyzed, and the suspensions adapted in the passenger car are under the combined effect of braking force and vertical force. Secondly, the calculation model of pitching characteristics and braking deceleration is established. Thirdly, test data of suspension K&C characteristic are analyzed so as to get the vertical and longitudinal displacement variation characteristics of the wheel center. Based on the calculation model of pitching characteristics and the tests of brake pitching characteristic, two conclusions are obtained. One is putting forward two evaluation indexes of vehicle pitching characteristics, the relationships of pitch angle versus braking deceleration and changing rate of longitudinal deceleration versus braking deceleration are used to comprehensively evaluate the pitching characteristics of

F2012-G06-033

X. Wang (✉) · G. Shi · L. Jin · G. Ying · H. Yang

State Key Laboratory of Comprehensive Technology on Automobile Vibration and Noise and Safety Control, FAW R&D Center, Changchun, People's Republic of China
e-mail: wangxuanfeng@rdc.faw.com.cn

G. Shi

e-mail: shiguang@rdc.faw.com.cn

L. Jin

e-mail: jinlingge@rdc.faw.com.cn

G. Ying

e-mail: yingguozeng@rdc.faw.com.cn

H. Yang

e-mail: yanghongwei@rdc.faw.com.cn

vehicle; the other is taking advantage of four process parameters to control the pitching characteristics of vehicle in braking process, and the four parameters are respectively. The anti-dive control of front and rear suspensions, the variation of vehicle wheelbase, the displacement of the centre of gravity in vertical direction. According to the aforementioned study results, the ideal brake pitching characteristics can be reached through rationally matching the longitudinal inclination balance characteristics of front and rear suspensions.

Keywords Brake pitching characteristics · Swing arm instant center · Kinematics & compliance · Changing rate of longitudinal deceleration · Anti-dive control

1 Introduction

Due to the inertia force and the braking force, mass transfer of the passenger car in the braking process leads to dynamic increase in the front axle load and decrease in the rear axle load, synchronously, the vehicle presents vertical and pitching vibrations. As a result, the car body inclines observably in the longitudinal plane, the phenomenon of brake dive appears and the ride comfort goes down considerably. The pitch degree is not only related to vibration characteristics, deceleration, braking force distribution ratios and moment of inertia, but also be affected by the forms of suspensions. In case the pitch angle of the car comes to be inordinate, the passenger will get a strong feeling of forward moving. At the instant the car stops, the passenger is compelled to receive a momentary bounce against the seat, and the uncomfortable pitch feel always results in consumers' complaints. The paper aims at resolving the aforementioned practical problems, making a theoretical analysis of the influencing factors for pitching characteristics during braking, and putting forward effective plans to ameliorate this kind of technical problem.

Earlier research reports on braking pitching characteristics can be seen in Sharp [1] and Reimpell et al. [2]. Sharp analyzed the impacts of suspension spring stiffness, damp coefficient and tire spring stiffness on the deformation of vehicle suspension, established the semi-vehicle pitch plane calculation model to identify the pitch angle of the vehicle, but characteristics analysis of suspension swing arm instant center was not described. Reimpell, Stoll, Betzler made a study on the swing arm instant center characteristics of double wishbone suspensions and longitudinal trailing arm suspension, furthermore, they pointed out that the swing arm instant center of the front suspension should be designed behind the wheel center, while the swing arm instant center of the rear suspension in front of the wheel center. In this way, the reaction of vertical force that acting on swing arm instant center of car body will reduce the pitch angle, which simultaneously improves the ability of withstanding brake dive. Moreover, Reimpell took the nonlinear suspension stiffness into account in the analysis of pitch angle, so as to keep the calculation model closer to actual working conditions, however, only steady-state characteristics of brake pitch angle and

variation of centre of gravity were calculated. Subjective evaluation tests of brake pitching show that when vehicles brake quickly to stop, which means that the vehicle speed is close to zero, the rebound and jerk characteristics of vehicle body seriously affect the comfort of the passengers, and the transient variability characteristics of the brake pitching must be analyzed so as to make a study on the before-mentioned aspects. Manfred Mitschke, Henning Wallentowitz [3] made a careful analysis of brake pitch in detail. They not only took account of the characteristics of swing arm instant center of suspension, suspension spring stiffness, damp coefficient, tire spring stiffness and the pitch inertia, but also calculated the transient variation characteristics and steady-state asymptotic values of the above-mentioned factors in the braking process, and gave the appropriate range of values which are the ratio of pitch angles and brake decelerations. We have conducted a large number of kinematics & compliance characteristic curves of the suspension longitudinal flexibility tests, and the results showed that the brake reaction support angle of suspension decreases as the braking force increases, especially for the rear suspension, which changes more dramatically. Consequently, the calculation model of vehicle pitching characteristics adapted the characteristic curves of suspension swing arm instant center measured by the K&C tests. In addition, the brake pedal feel is suggested to be researched and evaluated together with the pitching characteristics in the braking process, for that they both consider the action of brake pedal-motivating device as an input. During braking, the driver synchronously perceived five subjective evaluations, namely pedal force, pedal travel, pitch angle of vehicle body, longitudinal deceleration and changing rate of longitudinal deceleration.

Based on the careful study of pitch and stabilization characteristics in the braking process, a calculation model of some passenger car is built. It takes the longitudinal and vertical displacements and pitching actions into account, and considers the kinematics & compliance characteristic curves of the suspension as an input. After an integrated consideration of road tests for pitching characteristics and brake pedal feel, evaluation methods are proposed to do research in vehicle pitching. First, pitch angle versus deceleration and changing rate of longitudinal deceleration versus deceleration are came up with to evaluate the pitching characteristics. Second, anti-dive controls of front and rear suspensions, variation of vehicle wheelbase and vertical displacement of centre of gravity are adopted to control the pitching characteristics of vehicle in the braking process.

2 Characteristics Analysis of Suspension Swing Arm Instant Center During Braking

This car to be studied in the paper adapts double wishbone independent suspensions in the front suspension, and a five-link independent suspension is used in the rear suspension, as shown in Figs. 1 and 2. Analysis of swing arm instant center characteristics for the two types of suspension is respectively carried out in the following sections.

Fig. 1 Mechanics characteristics analysis of swing arm instant center of double wishbone independent suspensions

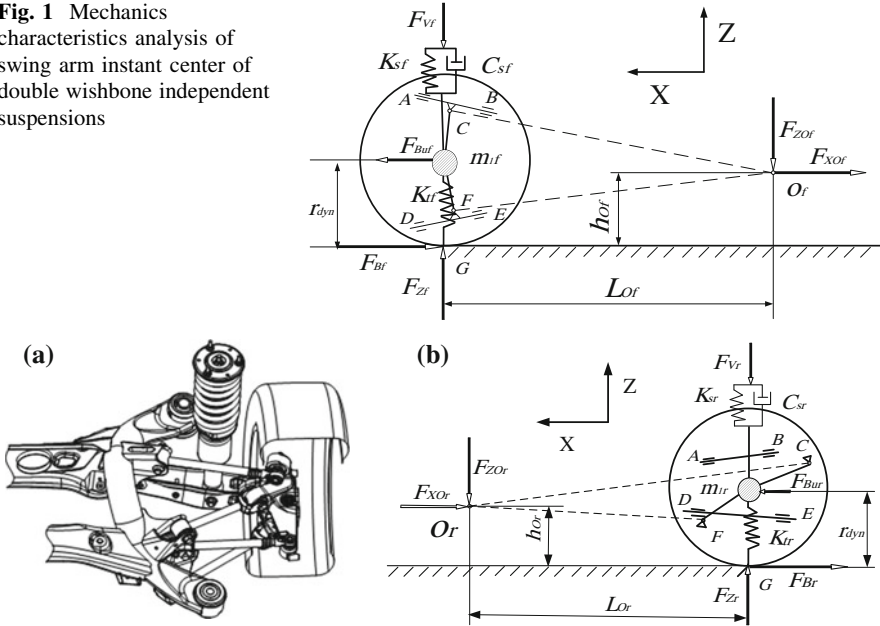


Fig. 2 Mechanics characteristics analysis of swing arm instant center of the five-link independent suspension

2.1 Swing Arm Instant Center of Double Wishbone Independent Suspensions

According to the side view of the double wishbone independent suspensions, point C is the spherical joint of the upper control arm and the steering knuckle, which moves up and down along the oscillation axis AB of the upper control arm. As a result, the longitudinal instantaneous rotation center of point C should be located at a straight line which passes through point C and parallels line AB . Similarly, for the point F which is the spherical joint of lower control arm, the longitudinal instantaneous rotation center should be located at a straight line which passes through point F and parallels line DE . O_f is the intersection of these two straight lines which is also defined the swing arm instant center of the double wishbone suspensions. Point G , the tire contact point, instantaneously rotates around point O_f , consequently, the position of swing arm instant center O_f alters along with the changes of braking force and vertical force that suspension and tires withstand [4].

Analysis of Fig. 1 reveals that both of the braking force F_{XOf} and the vertical force F_{ZOf} act on point O_f . F_{XOf} is the force that car body withstands and F_{ZOf} is the force resisting brake dive. Point G suffers the ground supporting force F_{Zf} , the ground braking force F_{Bf} , the spring and damping force F_{vf} . From inspection of Fig. 1, the mechanical equation of the double wishbone suspensions can be got and described as Eq. (1).

$$\begin{cases} F_{B_{uf}} - F_{X_{Of}} - F_{B_f} = 0 \\ F_{B_{uf}}r_{dyn} - F_{X_{Of}}h_{Of} - F_{Z_{Of}}L_{Of} = 0 \\ F_{B_{uf}} = -m_{1f}\ddot{X} \\ F_{Z_f} - m_{uf}g - F_{Z_{Of}} - F_{V_f} = 0 \end{cases} \quad (1)$$

2.2 Swing Arm Instant Center of the Five-Link Independent Suspension

The rear suspension of the passenger car adopts the five-link independent suspension, as shown in Fig. 2a and b, so as to ensure the comfort and handling stability of the vehicle. Referring to the mechanics analysis of swing arm instant center of the double wishbone independent suspensions, the five-link independent suspension is presented as Eq. (2).

$$\begin{cases} F_{B_{ur}} - F_{X_{Or}} - F_{B_r} = 0 \\ F_{B_{ur}}r_{dyn} - F_{X_{Or}}h_{Or} + F_{Z_{Or}}L_{Or} = 0 \\ F_{B_{ur}} = -m_{1r}\ddot{X} \\ F_{Z_r} - m_{1r}g - F_{Z_{Or}} - F_{V_r} = 0 \end{cases} \quad (2)$$

3 Analysis of Vehicle Pitching Characteristics During Braking

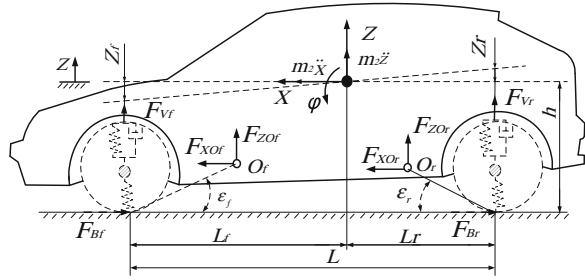
In the establishment of calculation model of vehicle pitching characteristics, the following assumptions are advanced: the vehicle is symmetrical; the vertical section of the road that left and right wheels of the car running on are the same; the elastic vibration of the frame and the vibration of the engine transmission are left out of account; the vibration of the wheel is ignored; air resistance and tire damp are overlooked and the tire stiffness was considered into the suspension spring stiffness; the car body was assumed to be rigid [5].

The calculation model of vehicle pitching characteristics during braking has three degrees of freedom: the displacement X of the vehicle in the driving direction, the displacement Z of the centre of gravity in the vertical direction and the pitch angle φ around the centre of gravity [6, 7]. The dynamics analysis can be seen in Fig. 3.

Dynamic equations of the sprung mass:

$$\begin{cases} -m_2\ddot{Z} + F_{Z_{Of}} + F_{Z_{Or}} + (F_{V_f} - F_{V_f0}) + (F_{V_r} - F_{V_r0}) = 0 \\ m_2\ddot{X} + F_{X_{Of}} + F_{X_{Or}} = 0 \\ -J_y\ddot{\varphi} + (F_{V_r} - F_{V_r0})L_r - (F_{V_f} - F_{V_f0})L_f - F_{X_{Of}}(h - h_{Of}) \\ - F_{Z_{Of}}(L_f - L_{Of}) + F_{Z_{Or}}(L_r - L_{Or}) - F_{X_{Or}}(h - h_{Or}) = 0 \\ Z_f = Z - L_f\varphi; \quad Z_r = Z + L_r\varphi \end{cases} \quad (3)$$

Fig. 3 The calculation model of vehicle pitching characteristics during braking



Longitudinal dynamics equation of the vehicle:

$$\begin{cases} (m_2 + m_{1f} + m_{1r})\ddot{X} = F_{Bf} + F_{Br} \\ F_{Bf} = \beta(m_2 + m_{1f} + m_{1r})\ddot{X} \\ F_{Zf} = F_{Zf0} + \frac{h(m_2 + m_{1f} + m_{1r})\ddot{X}}{L} \\ F_{Zr} = F_{Zr0} - \frac{h(m_2 + m_{1f} + m_{1r})\ddot{X}}{L} \end{cases} \quad (4)$$

Spring and damping forces of the front and the rear suspensions:

$$\begin{cases} F_{Vf} = F_{Vf0} - \frac{K_{Sf}K_{df}}{K_{Sf}+K_{df}}Z_f - C_{Sf}\dot{Z}_f \\ F_{Vr} = F_{Vr0} - \frac{K_{Sr}K_{dr}}{K_{Sr}+K_{dr}}Z_r - C_{Sr}\dot{Z}_r \end{cases} \quad (5)$$

According to Eqs. (1)–(6) is obtained as follows:

$$\begin{cases} m_2\ddot{Z} + (C_{Sf} + C_{Sr})\dot{Z} + (k_f + k_r)Z - (C_{Sf}L_f - C_{Sr}L_r)\dot{\varphi} - (k_fL_f - k_rL_r)\varphi \\ = \ddot{X}\left[\frac{m_{1f}(h_{Of} - r_{dyn})}{L_{Of}} + \frac{m_{1r}(r_{dyn} - h_{Or})}{L_{Or}}\right] \\ + (m_{1f} + m_{1r} + m_2)\left[\beta\frac{h_{Of}}{L_{Of}} - (1 - \beta)\frac{h_{Or}}{L_{Or}}\right] \\ J_y\ddot{\varphi} + (C_{Sf}L_f^2 + C_{Sr}L_r^2)\dot{\varphi} + (k_fL_f^2 + k_rL_r^2)\varphi - (C_{Sf}L_f - C_{Sr}L_r)\dot{Z} \\ - (k_fL_f - k_rL_r)Z = \ddot{X}\{(m_{1f} + m_{1r})(h - r_{dyn}) \\ - \frac{m_{1f}(h_{Of} - r_{dyn})L_f}{L_{Of}} - \frac{m_{1r}(h_{Or} - r_{dyn})L_r}{L_{Or}} \\ + (m_{1f} + m_{1r} + m_2)\left[h - \beta\frac{h_{Of}L_f}{L_{Of}} - (1 - \beta)\frac{h_{Or}L_r}{L_{Or}}\right]\} \end{cases} \quad (6)$$

make $\begin{cases} p = Z \\ q = \dot{Z} \\ r = \varphi \\ s = \dot{\varphi} \end{cases}$,

By selecting p, q, r, s as the system state variables and Eq. (6) can be changed into a vector–matrix representation:

$$\begin{bmatrix} \dot{p} \\ \dot{q} \\ \dot{r} \\ \dot{s} \end{bmatrix} = \begin{bmatrix} 0 & 1 & 0 & 0 \\ -\frac{k_f+k_r}{m_2} & -\frac{C_{Sf}+C_{Sr}}{m_2} & \frac{k_f L_f - k_r L_r}{m_2} & \frac{C_{Sf} L_f - C_{Sr} L_r}{m_2} \\ 0 & 0 & 0 & 1 \\ \frac{k_f L_f - k_r L_r}{J_y} & \frac{C_{Sf} L_f - C_{Sr} L_r}{J_y} & -\frac{k_f L_f^2 + k_r L_r^2}{J_y} & -\frac{C_{Sf} L_f^2 + C_{Sr} L_r^2}{J_y} \end{bmatrix} \begin{bmatrix} p \\ q \\ r \\ s \end{bmatrix} + \begin{bmatrix} 0 \\ C_1 \\ 0 \\ C_2 \\ J_y \end{bmatrix} \quad (7)$$

Where:

$$K_f = \frac{K_{Sf} K_{tf}}{K_{Sf} + K_{tf}} ; \quad K_r = \frac{K_{Sr} K_{tr}}{K_{Sr} + K_{tr}}$$

$$C_1 = \ddot{X} \left[\frac{m_{1f}(h_{Of} - r_{dyn})}{L_{Of}} + \frac{m_{1r}(r_{dyn} - h_{Or})}{L_{Or}} + (m_{1f} + m_{1r} + m_2) \left(\beta \frac{h_{Of}}{L_{Of}} - (1 - \beta) \frac{h_{Or}}{L_{Or}} \right) \right]$$

$$C_2 = \ddot{X} \left\{ (m_{1f} + m_{1r})(h - r_{dyn}) - \frac{m_{1f}(h_{Of} - r_{dyn})L_f}{L_{Of}} - \frac{m_{1r}(h_{Or} - r_{dyn})L_r}{L_{Or}} + (m_{1f} + m_{1r} + m_2) \left[h - \beta \frac{h_{Of} L_f}{L_{Of}} - (1 - \beta) \frac{h_{Or} L_r}{L_{Or}} \right] \right\}$$

After solving the differential Eq. (7), the displacement Z of the centre of gravity in the vertical direction and the pitch angle φ around the centre of gravity will be obtained.

4 Results and Discussion

In the process of braking, the positions of swing arm instant center of the front and rear suspensions change with the increase of the braking force. At the same time, mass transfer occurs, the front axle load dynamically grows and the rear axle load dynamically lessens. Since the elastic curves of the front and rear suspensions are non-linear, the suspension stiffness shows a real-time variation along with the dynamic axle load during braking. This paper makes use of the K & C test rig of British ABD Corporation to measure the parameters of front and rear suspension stiffness, tire stiffness, swing arm instant center of suspension etc.

4.1 Measurement of Suspension K&C Characteristics Parameters

Figure 4 depicts the parameters of front and rear spring stiffness, tire stiffness and suspension stiffness measured by K&C test rig. Inspection of Fig. 4 reveals that the suspension stiffness is basically linear in a small load region. However, the suspension stiffness increases rapidly when the load comes to certain limits.

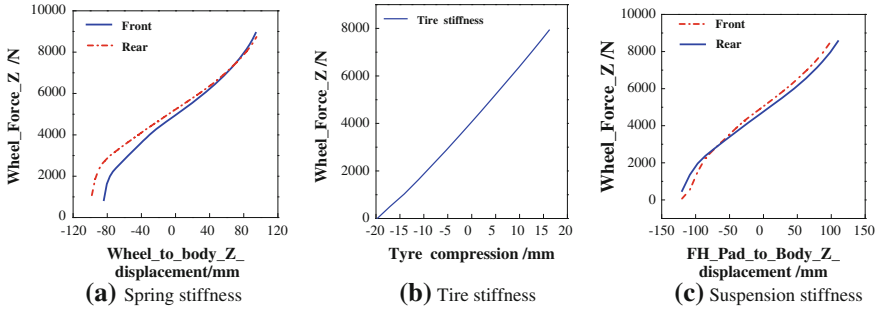
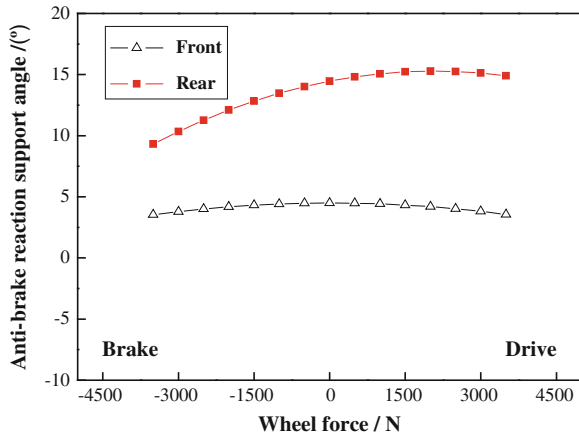


Fig. 4 Parameters of suspension stiffness measured by K&C test rig

Fig. 5 Anti-brake reaction support angles of front and rear suspensions



The initial value of the swing arm instant center of the front and rear suspensions in Figs. 1 and 2 can be identified through the method of graphing. Eqs. (8) and (9) indicate how to calculate the brake reaction support angle ϵ_f , ϵ_r of front and rear suspensions shown in Fig. 5. Figure 5 also gives the metrical results of anti-brake reaction support angles that got from K&C test rig, of which the front and rear suspension are under different longitudinal forces.

$$\text{Front suspension : } \tan \epsilon_f = h_{of} / L_{of} \tag{8}$$

$$\text{Rear suspension : } \tan \epsilon_r = h_{or} / L_{or} \tag{9}$$

4.2 Evaluation Indexes of the Brake Pitching Characteristics

For the reason that driver and passenger mainly apperceives the changes of vehicle characteristic in the braking process, such as brake pitch angle, braking

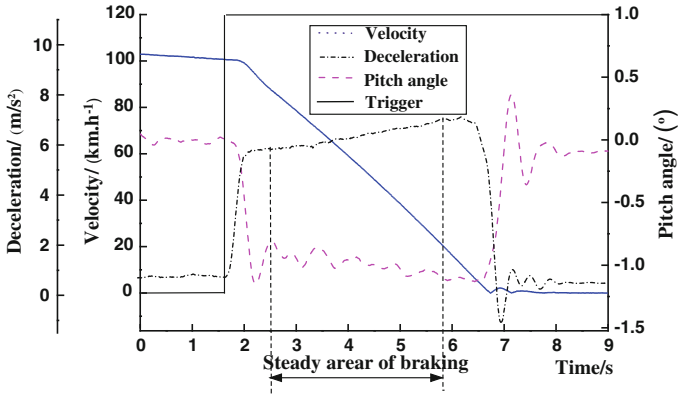
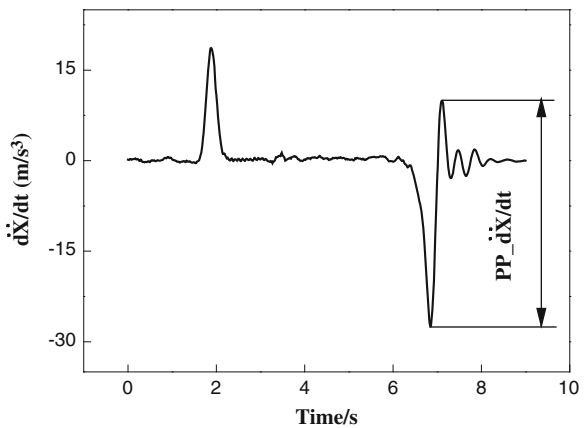


Fig. 6 The steady pitching characteristics of vehicle in successive braking

Fig. 7 The peak value of longitudinal braking deceleration rate $PP_{d\ddot{x}/dt}$



deceleration and longitudinal braking deceleration rate, therefore, two evaluation indexes of braking pitching characteristics in whole vehicle class are proposed [8]:

1. Pitch angle φ at different braking decelerations \ddot{X} , as shown in Fig. 6. It mainly reflects the steady pitching characteristics of vehicle in successive braking;
2. The peak value of longitudinal braking deceleration rate $d\ddot{X}/dt$ at different braking decelerations, as shown in Fig. 7. It mainly reflects the transient braking pitching characteristics of the rebound at the end of the braking process.

During braking, the variations of suspension characteristics and displacement characteristics of the centre of gravity in vertical direction are lesser, and the human can't feel it insensitively, but the changes have a relatively great impact on vehicle pitching. Therefore, four process-control parameters are proposed to analyze the changing trend of brake pitching characteristics:

1. The anti-dive control of front suspension, K_{ef}
2. The anti-dive control of rear suspension, K_{er}
3. The variation of vehicle wheelbase, ΔL
4. The displacement of the centre of gravity in vertical direction Z .

The anti-dive controls of front and rear suspensions reflect the impact of forces that swing arm instant center withstands on the braking pitch angle of the vehicle. K_{ef} stands for the ability to counteract the decline of head and K_{er} stands for the ability to counteract the elevation of after body [2].

The formulas are as follows:

The anti-dive control of front suspension, K_{ef} :

$$K_{ef} = \frac{F_{Vf} - F_{Vf0}}{F_{Zf} - F_{Zf0}} \quad (10)$$

The anti-dive control of rear suspension, K_{er} :

$$K_{er} = \frac{F_{Vr} - F_{Vr0}}{F_{Zr} - F_{Zr0}} \quad (11)$$

The variation of vehicle wheelbase ΔL focuses on reflecting the longitudinal withdrawing capability of suspensions and the vertical bounce withdrawing capability of wheels when brakes are applied. The displacement of centre of gravity in vertical direction Z reflects the variation of vehicle elastic potential energy. If the two numerical values were big, it indicates that more elastic potential energy is absorbed by the vehicle suspension during braking; and the rotational kinetic energy of vehicle pitching actions was inevitably small, as a result passengers get a better feel of brake pitching.

4.3 Test Methods of Brake Pitching Characteristics

In the test of vehicle brake pitching, the facility of VBOX3i manufactured in British Racelogic Company is used to measure vehicle speed, meanwhile, the brake decelerations in X and Z directions are manufactured by their triaxial inertial sensor of RLVBIMU01. Four non-contact laser height sensor manufactured in German CORRSYS DATRON are utilized to measure the vehicle pitch angles indirectly during braking. Brake pedal robot product by ABD Company of UK is used to measure brake pedal force and brake pedal travel, and all the test data are uniformly gathered by applying the VBOX3i host computer at a data acquisition sampling frequency of 100 Hz. The installation of equipments for brake pitching test is shown in Fig. 8.

The initial braking speed is set to be 100 km/h in the vehicle brake pitching test. The vehicle is first accelerated to a speed of 105 ± 1 km/h, and then the accelerator pedal is released without changing the gear, keeping the vehicle sliding. At

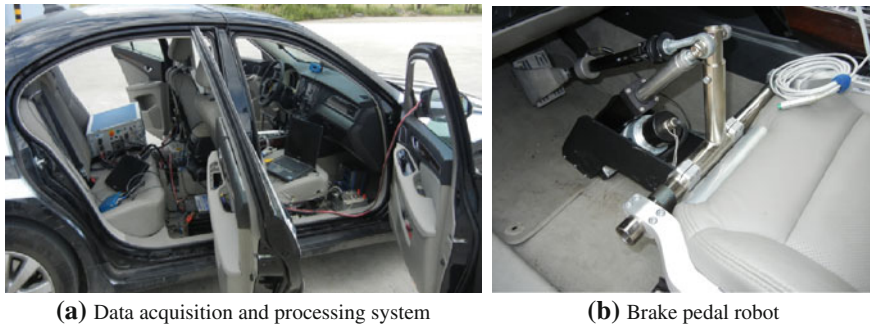


Fig. 8 The installation of brake pitching test

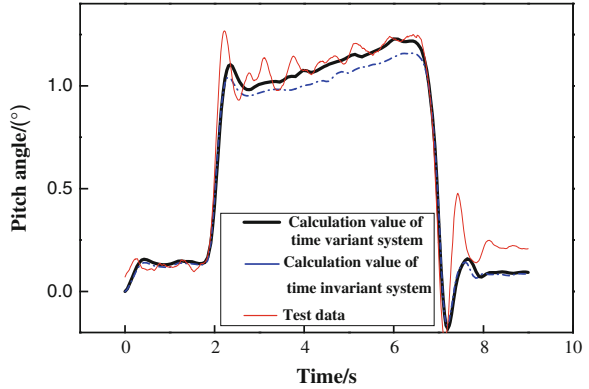
the same time, start the data acquisition system to record test data of each channel, and trigger the control button of the brake robot when the vehicle speed decreases to the provisions initial velocity, make the pedal-motivating device to step on the brake pedal at a constant speed (finish the pedal trampling process within 0.2 s) until the vehicle reaches the braking deceleration of 0.2 ± 0.05 g. Then adjust the stroke rate of the pedal-motivating device of the brake robot, so as to make the braking deceleration reach 0.3–0.9 g in turn each time at the same initial braking speed. During the test, the values of brake time, speed, brake pedal force and brake pedal travel, braking deceleration, pitch angle of the vehicle, acceleration of vehicle in the Z direction should be recorded simultaneously.

4.4 Analysis of Brake Pitching Characteristics

4.4.1 Analysis of Calculation Results and Experimental Results

Inspection of Figs. 4, 5 and 6 reveals that the parameters of suspension rate, brake reaction support angle and braking deceleration show a real-time variation along with the braking force during braking. These before-mentioned time-varying variables are substituted into Eq. (7) and it comes to be a time-varying system. Under such a condition, the pitch angle φ around the centre of gravity and the vertical displacement Z of centre of gravity will be calculated in this time-varying state. Suspension rate and brake reaction support angle are treated as fixed values in literature [3], in other words, the Eq. (7) is regarded as a constant system in this state and simulative calculations of pitching characteristics are carried out. Besides, the pitch angle of the vehicle is measured according to test methods of brake pitching characteristics mentioned above, and the calculation results and test results are shown in Figs. 9 and 10. Owing to the consideration of time-varying variables of suspension stiffness and brake reaction support angle, the calculation model of vehicle pitch angle is more in line with the actual braking condition. Figure 9 also shows that the calculated results are closer to the measured values.

Fig. 9 The pitch angle characteristics of vehicle in braking process



Duo to the under damp characteristics of shock absorber, the curves of pitch angle and vertical displacement present peaks at the beginning of the braking action. As the damp coefficients of front and rear shock absorbers are relatively large, analysis of Figs. 9 and 10 reveals that the oscillation period of the above two curves are relatively short and then they quickly converge into steady-state region. In addition, the position of centre of gravity goes down during braking which indicates that the suspensions accumulate elastic potential energy and the rotatable kinetic energy of pitching weakens, yet the amplitude of the displacement of the centre of gravity is so small that the driver could hardly feel any change.

4.4.2 Calculation Results Analysis of Front and Rear Suspensions at Different Stiffness Ratio

Originally, the rate ratio of front suspension to rear suspension is 1:1. After subjective evaluation test, the drivers point out that the brake pitching characteristics is not well and the pitch angle is relatively large. The stiffness ratio of front suspension to rear suspension is adjusted to 1:1.14 afterwards which increases the stiffness of the rear suspension, and the subjective evaluation test reflects that the brake pitching characteristics turn to be better. The calculation model of vehicle pitching characteristics is used to calculate the two different ratios of suspension stiffness, and the results are shown in Fig. 11. The adjustment of suspension stiffness ratio increases the vertical displacement of centre of gravity and the elastic potential energy of the suspension system during braking, and reduces the rotatable kinetic energy and the pitch angle. The calculation results shown in Fig. 11 are consistent with the subjective feelings of the evaluation staff.

4.4.3 Analysis of Suspension Anti-Dive Control Versus Brake Rate

The anti-dive controls of front and rear suspension are calculated according to Eqs. (10) and (11), as shown in Fig. 12. The brake anti-dive control of front and

Fig. 10 Characteristics of vertical displacement of the centre of gravity during braking

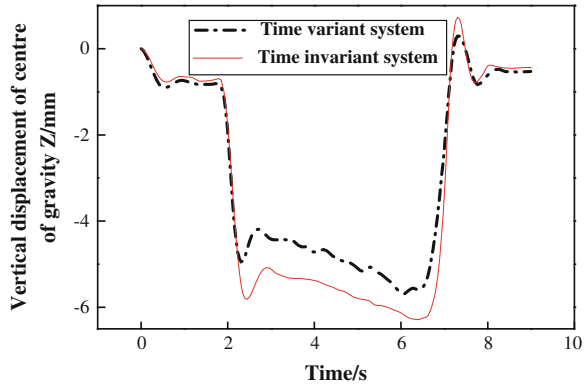
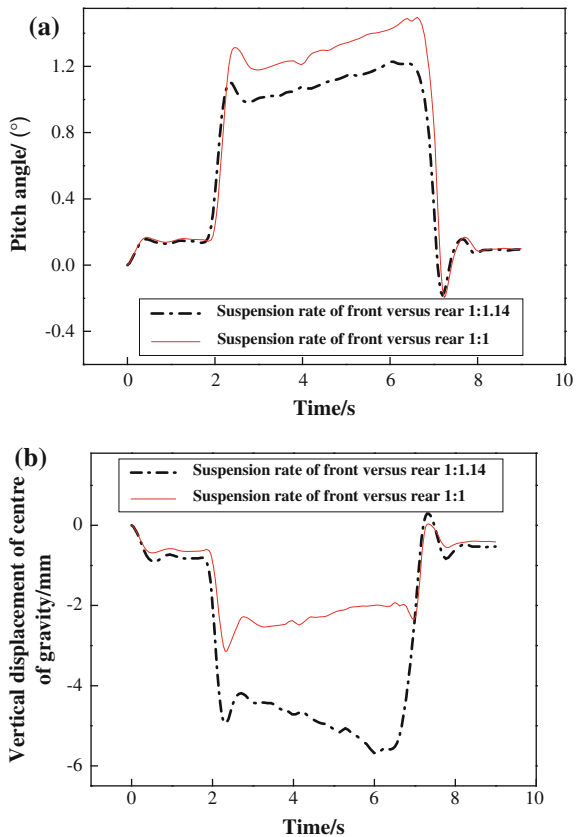
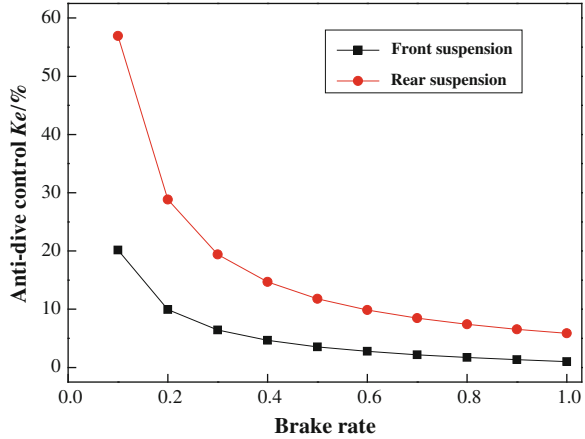


Fig. 11 Calculation results contrast of front and rear suspensions at different stiffness ratio. **a** The characteristics of pitch angle. **b** The characteristics of displacement of the centre of gravity in vertical direction



rear suspensions gradually decreases with the increase in brake rate z , but the amplitude of the rear suspension reduces relatively larger. This phenomenon indicates that the ability to counteract the decline of head and the ability to counteract the elevation of after body weakens. The brake pitch angle of vehicle

Fig. 12 Analysis of anti-dive control versus brake rate



grows fast with the increases of brake rate, but the effect is not very obvious, as the curves of brake anti-dive controls of front and rear suspensions become gentle when the brake rate exceeds 0.3.

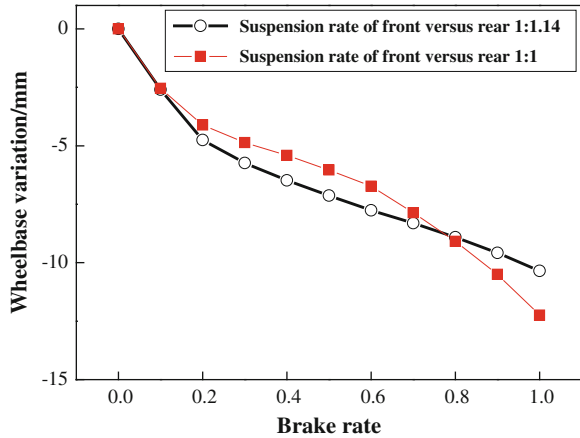
4.4.4 Analysis of Vehicle Wheelbase Variation Versus Braking Rate

The front and rear suspensions bear both the longitudinal braking force and the dynamic vertical forces during braking, and the wheelbase of vehicle significantly shortens under the combined effects of longitudinal braking force and vertical force. The following content is the analysis of this problem.

The variation of vehicle wheelbase ΔL focuses on reflecting the longitudinal withdrawing capability of suspensions in the process of braking and the vertical bounce withdrawing capability of wheels caused by vertical load changes. Under the action of longitudinal braking force, both of the front and rear wheel centers have a backward longitudinal displacement due to the vertical withdrawing capability of front and rear suspensions. The braking force of front axle is 85 % larger than that of the rear axle, therefore, the backward longitudinal displacement of the front axle wheel center is relatively larger, and the wheelbase of vehicle shortens due to the difference in front and rear longitudinal braking forces.

The mass transfer during braking leads to the vertical bounce withdrawing capability of front and rear suspensions. In terms of this car to be studied in the paper, the wheel center of the front suspension moves backward under compression, and that of the rear suspension moves forward as the rear suspension stretches. The relative movement of front and rear wheel centers shortens the wheelbase of the car. K and C experiments are carried out respectively on the original suspension design plan (the stiffness ratio of front suspension to rear suspension is 1:1) and the improved design plan (the stiffness ratio of front suspension to rear suspension is 1:1.14). Based on comprehensive consideration of the longitudinal withdrawing

Fig. 13 Analysis of wheelbase variation versus brake rate



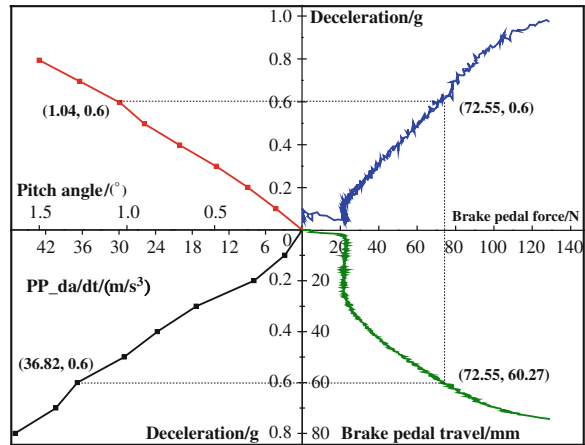
capability and the vertical bounce withdrawing capability of front and rear suspensions, the variations of wheelbase in the two design plans under different brake rate are calculated, as shown in Fig. 13. When the brake rate z is less than 0.8 g, the variation of wheelbase of the original test vehicle is smaller than that of the improved one. In this way, the rotatable kinetic energy of pitching absorbed by the suspension are reduced and the pitch angle of vehicle is inevitably enlarged, as shown in Fig. 11a. Meanwhile, the passengers' subjective evaluations of brake pitching feel get worse.

4.5 Comprehensive Evaluation of Brake Pitching Characteristics and Brake Pedal Feel Characteristics by Four-Quadrant Diagram

The above analysis focuses on the brake pitching feel of the passengers during braking, and three subjective variables of pitch angle, longitudinal deceleration and changing rate of longitudinal deceleration are the main objects to be evaluated. In the process of depressing brake pedal, the brake pedal force and pedal travel are also be perceived except the three subjective feels above. For the sports car which put emphasis on driving characteristics, the subjective evaluation of the driver is mainly concerned. In this case, a four-quadrant graphic shown in Fig. 14 is used to evaluate the brake pitching characteristics and the brake pedal feel characteristics. The right half-plane, expresses the brake pedal feel characteristics, the left half-plane expresses the brake pitching characteristics, and the upper half-plane expresses the two most important indexes of brake feel characteristics: brake pedal force and pitch angle of vehicle at different decelerations.

If the target vehicle aspires after comfort, braking feel should focus on the indexes shown in the second and third quadrants of Fig. 14, that is the response

Fig. 14 The four-quadrant graphic of brake feel



characteristics of the passengers to the brake pitching characteristics; if the market positioning of the car aspires after sport sector, as described in this paper, braking feel should adopt the following indexes shown in the four-quadrant graphic, as the driver not only apperceive the brake pitching characteristics but also the brake pedal characteristics.

5 Conclusion

The vehicle will take on a sharp pitching movement in the hurry-up stop, and this may badly impact on ride comfort. The paper takes into consideration of the real-time changes of suspension stiffness, brake reaction support angle and deceleration in the actual process of braking, and constructs a 3-DOF calculation model. Based on the foregoing preparation, a study is carried out to analyze the dynamic changes of pitch angle and the vertical displacement of the centre of gravity. Research results indicate that this time-varying calculation model is more in line with the values measured in the test. According to the vehicle characteristics that passenger could feel in the braking process, two evaluation indexes are put up with to evaluate the pitching characteristics. They are the peak values of pitch angle rate and braking deceleration rate. Besides, the achievements of the paper point out that the pitch movement could be mild once the suspension systems absorb more elastic potential energy during braking. In other words, the rotatable kinetic energy of pitching would be less when changes in the wheelbase and the vertical displacement get bigger. For sports car which concentrates on driving characteristic, the drivers not only endure the pitch angle change and the changing rate of longitudinal deceleration, but also feel the brake pedal force and brake pedal travel. Therefore, a four-quadrant graphic is used to evaluate the characteristics of brake pitching and brake pedal feel.

Appendix

Notation

C_{sf}	Damp coefficient of front shock absorber
C_{sr}	Damp coefficient of rear shock absorber
K_{sf}	Spring stiffness of front suspension (N/m)
K_{sr}	Spring stiffness of rear suspension (N/m)
K_{jf}	Stiffness of front tire (N/m)
K_{jr}	Stiffness of rear tire (N/m)
F_{Buf}	Braking force acting on centre of under spring mass of front axle (N)
F_{Bur}	Braking force acting on centre of under spring mass of rear axle (N)
F_{Xof}	Braking force that car body suffers acting on swing arm instant center of front suspension (N)
F_{Xor}	Braking force that car body suffers acting on swing arm instant center of rear suspension (N)
F_{Zof}	The force resisting brake dive that car body suffers acting on swing arm instant center of front suspension (N)
F_{Zor}	The force resisting brake dive that car body suffers acting on swing arm instant center of rear suspension (N)
F_{Bf}	Braking force that acting on front tyre contact point (N)
F_{Br}	Braking force that acting on rear tyre contact point (N)
F_{Zf}	The ground supporting force that acting on front tyre contact point (N)
F_{Zf0}	The static ground supporting force that acting on front tyre contact point (N)
F_{Zr}	The ground supporting force that acting on rear tyre contact point (N)
F_{Zr0}	The static ground supporting force that acting on rear tyre contact point (N)
F_{Vf}	The spring and damping force of front suspension (N)
F_{Vf0}	The static spring and damping force of front suspension (N)
F_{Vr}	The spring and damping force of rear suspension (N)
F_{Vr0}	The static spring and damping force of rear suspension (N)
r_{dyn}	Rolling radius (m)
h	Height of centre of gravity (m)
h_{of}	Height of swing arm instant center of front suspension (m)
h_{or}	Height of swing arm instant center of rear suspension (m)
L	Wheelbase between front axle and rear axle (m)
L_f	Distance between front axle and centre of gravity (m)
L_r	Distance between rear axle and centre of gravity (m)
L_{of}	Distance between centre of gravity of front axle and swing arm instant center of front suspension (m)
L_{or}	Distance between centre of gravity of rear axle and swing arm instant center of rear suspension (m)
m_1	Under spring mass (kg)
m_{1f}	Under spring mass of front axle (kg)

m_{1r}	Under spring mass of rear axle (kg)
m_2	Sprung mass (kg)
J_y	Rotational inertia (kg.m ²)
Z	The original displacement of the centre of gravity of the car (m)
Z_f	Vertical displacement of the centre of gravity of front sprung mass (m)
Z_r	Vertical displacement of the centre of gravity of Rear sprung mass (m)
φ	The pitch angle around the centre of gravity Slope angle (rad)
β	Braking force distribution ratio

References

1. Sharp RS (2002) Wheelbase filtering and automobile suspension tuning for minimizing motions in pitch. *Automob Eng* 216:933–946
2. Reimpell J, Stoll H, Betzler JW (2001) *The automotive chassis engineering principles*, 2nd edn. SAE International, Warrendale
3. Manfred M, Henning W (2009) *Dynamik der Kraftfahrzeuge*, 4th edn. In: Chen Y, Yu Q (eds) Tsinghua University Press, Beijing
4. Chen Y (1985) Unsteady state description of vehicle during braking. *Automob Eng*
5. Wang J, Lu S (1995) *Vibration of vehicle during braking*. Xian Road College Paper
6. Cao D, Rakheja S, Su CY (2008) Dynamic analyses of heavy vehicle with pitch-interconnected suspensions. *Heavy Vehicle Syst* 15:272–308
7. Dongpu C, Subhash R, Su CY (2008) Heavy vehicle pitch dynamics and suspension tuning part I: unconnected suspension. *Vehicle Syst Dyn*
8. Chou H, d'Andrea-Novell B (2005) Global vehicle control using differential braking torques and active suspension forces. *Vehicle Syst Dyn*

Part VII
Other

Development of Cost Saing and Sloshing Noise Reductive Baffles of Fuel Tant Using Triz and Taguchi Engineering Method

Kim YunSeok, Jeong ChiWeon, Lee MinSup and Yoo JaeGon

Abstract Since the movement of fuel by the force of inertia in tank always generates crashes to the wall of tank inside or surface wave motion of fuel, noise and vibration problems are easily observed under the condition of vehicle acceleration, deceleration or the stand still. In order to solve this problem, optimization of tank form, addition of damping pad to the structure, and baffle plate to the tank interior have been tried currently. This paper suggests a new concept development of cost effective device and optimization of the design. We have applied Triz and Taguchi method among Design For Six Sigma to approach this problem to achieve noise and cost reduction at the same time. In addition to that, the steps for solving this problem and the design guide of new concept including new sound quality index will be suggested.

Keywords Sloshing noise · Baffle · Fuel tank · Loudness · Triz · Taguchi

1 Introduction

The sudden motion change of vehicle, such as the aggressive vehicle start from stand still or the hard braking, generate the strong fuel sloshing noise, especially in quiet condition as in enclosed parking lot. Since this disturbing noise from the fuel

F2012-G07-005

K. YunSeok (✉) · J. ChiWeon · L. MinSup · Y. JaeGon
Hyundai-Motor Group, Seoul, Republic of Korea
e-mail: oz-tech@hyundai.com

tank is easily audible to the customer in vehicle cabin, serious customer complain can be happen frequently. In general, the fuel sloshing noise is categorized into three types by the sound generating mechanism, fluid waving, or bursting sound, bubbling sound and fluid impact sound. These noises are mainly caused by the behaviour of entrapped air inside the tank and the structural characteristics of the tank and also, the body structure of the vehicle is another influencing factor [1]. Currently well known solutions are as follows, the installation of a number of baffles for preventing excessive movement of the fuel, design change of the tank itself by giving an inclination to the front side for decreasing the impact pressure, and inserting vibration absorbing pad between the tank and the vehicle body for blocking the vibration transfer. Normally, analytical methods are adapted to predict and verify the noise improvement of the target level [2]. But in spite of lowering the level of noise, large portion of solutions tend to increase the cost. One of the main reasons is that the evaluation of the sloshing noise depends on the subjective evaluation at the last stage of the development which has a limit for the design change and applies the countermeasure to add baffles in order to reduce the noise. For that reason, it is requested that establishing the reasonable development process including rig test steps and clear definition of sound quality index corresponding to the real vehicle subjective evaluation results. Therefore, it is acutely required to establish the cost reducing measure and the product development process including noise index development and rig evaluation with the identical results of real vehicle subjective evaluation from the manufacturing stage of fuel tank.

1.1 Device of Sloshing Noise Reduction

Figure 1 is the analytical simulation results that show the flowing impact at the rear side of the tank by sloshing wave, and the concentration of pressure and formation of air pocket (occurs the noise) on the upper side of tank's curved surface. And the baffles are installed to reduce the concentration of pressure. Figure 2 shows the baffle installed to the fuel tank interior. The graph on the right side of Fig. 1 is showing the acceleration of fuel and the vehicle speed profile during 0.4 G mild braking conditions.

2 Concept Development

2.1 Definition of Requirements

- (1) Customer requests: "Fuel sloshing noise should not be audible to the customer in vehicle cabin"
- (2) Business requests: "Cost saving up to 20 %"

Fig. 1 Analytical simulation model (upper right) and graph (left)

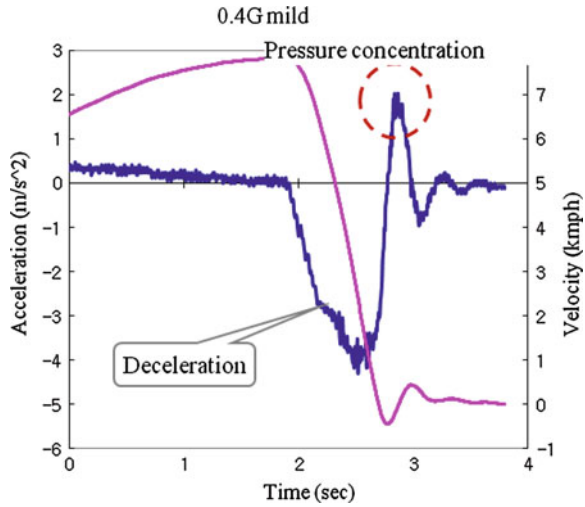
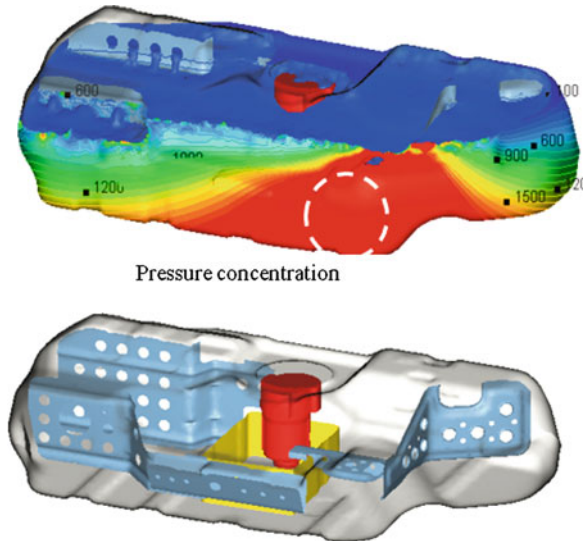


Fig. 2 Configuration of baffles installed



(3) Constraints

- Subjective evaluation rating of sloshing noise: 7 (0 ~ 10 scale)
- Prohibiting the change of layout, external and internal shape and relevant parts

(4) Target

- Cost saving up to 20 %,—Subjective rating: 7,—Establishing the design guide for baffle device and development process,—Setting up the rig test process and sound quality index for the sloshing noise.

Fig. 3 [A] matrix of tank design frame

		DP0: Fuel tank	DP1: tank	DP2: pump	DP3: baffles
FR0: Storing, Moving	X				
FR1: storing		X	O	O	
FR2: moving		O	X	O	
FR3: blocking		X	X	X	

2.2 Design Frame Analysis

The relation between the requirements function and the design parameter is as shown in Eq. (1) and design matrix [A] is defined as Fig. 3. Based on the matrix in Fig. 3, the design frame of the tank is in “decoupled state” while it still is an acceptable design. But it requires the optimization of information and re-construction of design parameters due to cost saving requirements [3].

$$\{FRs\} = [A]x\{DPs\} \tag{1}$$

2.3 Modelling of System Interaction Analysis

Figure 4 shows the system modelling of fuel tank based on the function flow analysis. The states of functional interactions between the system components are expressed with the lines. For example, if one function affects useful to one another it is showed with black solid line and if it is harmful, red dotted line is appeared. Interesting point of this modelling in Fig. 4, contradiction between fuel and tank is observed because they can simultaneously have both useful and harmful effect each other. In this modelling, function analysis, Su-Field of Triz [4] concept is applied for improving the problem solving efficiency. Based on this modelling, it is easily understood that the crashing noise and vibration between the fuels, tank surface, gas (air) occurs due to inertia force. Figure 4 is a system model while the vehicle is in motion, it displays the status without the noise reduction device (baffle).

2.4 Identification of Core Problem

(1) Fuel sloshing noise mechanism

The fuel fluid crashes to the front side and rear side of the tank wall by the inertia force due to acceleration/deceleration of vehicle. After those impacts, the fuel crashes to the top side of the wall by the mass force. Also, the surface wave motion generated by the turbulence flowing at the fuel surface becomes the main source of

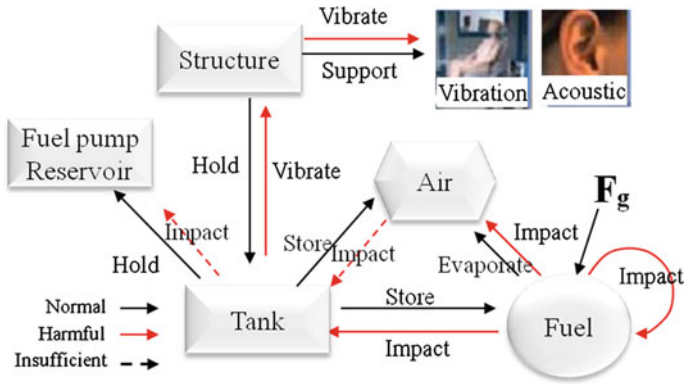


Fig. 4 System modelling

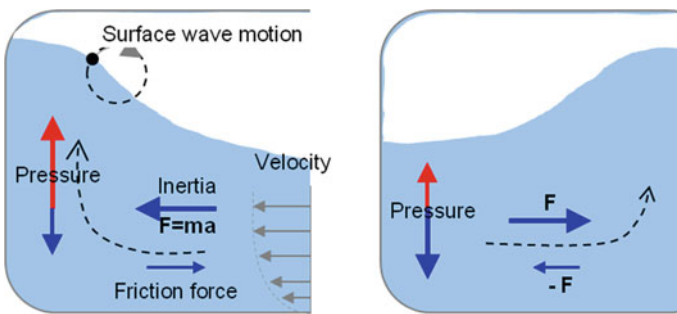


Fig. 5 Fluid movement and surface wave motion

fluid crash noise. Figure 5 shows the crashing and the mechanism of surface wave motion of fluid fuel.

(2) Operation event analysis

Operation event analysis is used for establishing the solution by analyzing the core problem with respect to the time by analyzing the system operational status, energy, manufacturing cost, generated problems and their effect to the other functions. Table 1 shows the analysis matrix of this type.

(3) The definition of physical contradiction

The general physical contradiction [4] of the fuel fluid of vehicle in motion can be expressed as “To operate the vehicle, fuel should exist in fuel tank but may be the fuel should not exist, because of the vibration and noise while the vehicle is under the accelerating, decelerating and stand still condition”. Based on the concept shown in Figs. 4, 5, Table 1, additional contradictions of the other properties are expressed below.

Table 1 System operation event analysis

Time	Before ΔT_1	Operation of tank					After ΔT_3
		ΔT_{21}	ΔT_{22}	ΔT_{23}	ΔT_{24}	ΔT_{2n}	
Model(state)	-	Driving	Accelerating	Decelerating	Stopping	-	-
Environment	-	Noisy	Quiet	←	←	-	-
Resource		Road	Parking area				
Space		Tank, fluid	Tank, fluid				
Energy field	Gravity	-	Inertia force	←	←	-	Gravity
			Velocity, area pressure, specific gravity quantity, air				
Design	Baffle coating	←	Baffle, hole, position, coating material, Q-value	←	←	←	←
Added cost	₩17,000	←	←	←	←	←	←
Symptom (customer)	-	-	Vibration noise	←	←	←	-
Problem (customer)	-	-	Uncomfortable fear	←	←	←	-

- The fuel may either have or not have the inertia force.
- The fuel may either have or not have the volume (mass).
- The mass of fuel may be either fast or slow.

One of the ways to resolve the physical contradictions is to separate the contradiction demands. And the principle of separation has 4 sub-methods, that are ‘Separation in Space/Time/Relation/System level’ [4], and it proposes ‘40 Inventive Principle’ [4]. The physical contradictory demands of fuel tank should be separated by using the ‘Separation in Time’ method as it is required to occur at different times. That is, ‘Inertia force of fuel should be exit’ is required while driving time, ‘Inertia force of fuel should be not exist’ is required while accelerating or decelerating or stopping the time. Using several principles among the ‘40 Inventive Principles’ could be suggested in order to analyze the physical contradiction by using the ‘Separation in Time.’ The solution is drawn by utilizing the proposed inventive principles and science effect. Principles are as follows. Principle 1: Segmentation, 3: Local quality, 4: Asymmetry, 7: Nested doll, 9: Preliminary anti-action, 10: Preliminary action, 11: In-advance “cushioning”, 15: Dynamics, 31: Porous materials.

2.5 Definition of Solution

To find out the solution for this problem, the definition of X-element is required. In this sloshing noise case, it is as follows. X-element is the solution for the physical contradiction. X-elements should be defined within the boundary of the facts that it should operate by itself, utilize the minimum resources, and should not have additional adverse action. Also, it should be determined or verified, if the physical contradictory that is mentioned can be solved.

- X-1: tank removes the inertia force by itself,
- X-2: controls the volume (mass) of fuel
- X-3: restrains the inertia force of fuel,
- X-4: controls the velocity (pressure) of the fuel
- X-5: softens the fuel,X-6: absorbs the noise and vibration.

2.6 Building of Concept

Each members of the cross functional team composed for the establishment of the concept have created the idea by utilizing the proposed inventive and scientific principles, established the concept through the group brainstorming as shown in Table 2, and selected 4 concepts as a final.

Table 2 Story board of concept

X-No	Concept deployment		Remarks
X-1	Change the fluid motion of straight (inertia force) to rotating flow rotary motion	1. Round the tank shape condition 2. Change the installation angle of the tank	Constraint
3.	Install the plate that rotates the fluid flow		
X-2	Holds the volume and mass of the fuel	4. Install the small tank that holds the fuel 5. Install the open foam-rubber made of porous	Melting
X-3	Weaken the inertia force by using the fluid speed, pressure, surface area enhancement, and frictional force	6. Install the baffle with multiple holes by piling up	Current
X-4		7. Install the 2-layer baffle applied with different sized holes by utilizing Bernoulli effect 8. Install the Bernoulli effect utilized cyclone baffle 9. Install the baffle cylinder 10. Install the coil type plastic (PA6) cylinder	Design
X-5	Soften the surface motion by giving cushion in order to weaken the noise.	11. Make foams to always stick together by utilizing the magnet in closed foam-rubber .	
X-6	Weaken the wave by dividing the tank wall.	12. Install the plate on the tank wall	
Add	Weaken the wave and rotary motion by mixing the concept of No 1-3 and 6.	13. Install the wave reduction plate to the fluid flowing direction controlling plate	

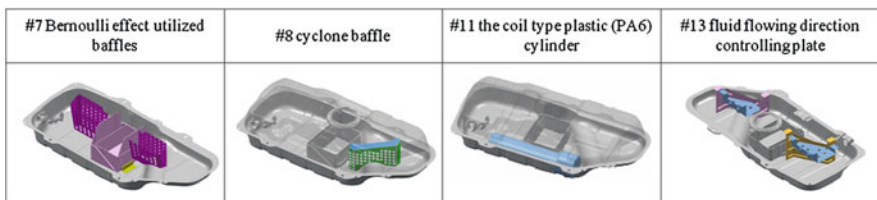


Fig. 6 4 concept solutions

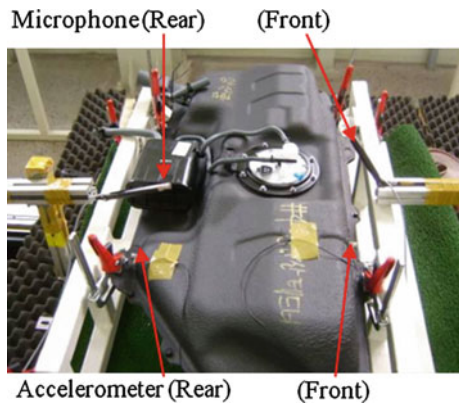
2.7 Selection of Concept

As the solution for sloshing noise, the 4 concepts, (1) Bernoulli effect utilized baffles, (2) rotational plate and space partition, (3) Bernoulli effect utilized cyclone baffle (4) the coil type plastic (PA6) cylinder, are selected among the 10 concepts that are designed by using the existing designs as datum through Pugh method [5].

Table 3 Rig test condition

Condition	Value	
Quantity of fuel	1/2, 3/4, 7/8, full	
Stage travel length	6 m	
Acceleration	0.2 G/0.4 G/0.6 G	
Max. speed	2 m/s	
Accelerometer	Type	ICP
	Sensitivity	100 mV/g
	Positions	100 mm away from tank (front and rear)
Microphone	Freq. range	3.15 Hz ~ 40 kHz
	Max. level	171 dB
	Positions	100 mm away from tank (front and rear)

Fig. 7 Sensor installed to the fuel tank



2.8 The Verification of Solution Concepts

These 4 concept solutions are produced as trial samples as they are shown in Fig. 6. Radiated noise on the rig was measured and compared with the current tank. By combining the measured data with the subjective evaluation results, Bernoulli effect utilized baffles was selected at last, because this solution has the same level of noise with the existing design.

3 Experimental

3.1 Rig Tests

(1) Test method

The test is performed under the rapid acceleration, deceleration mode from the rig test as a standard, while having a correlation with the acceleration, deceleration vehicle test which realizes the sloshing noise from the vehicle.

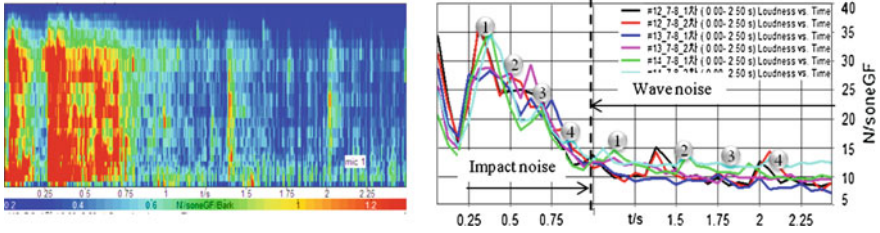


Fig. 8 Slashing noise measurements (left) and sound quality index graph (right)

No	Control Factor	1-Level	2-Level	3-Level
A	Height of Reservoir	5%	10%	20%
B	Position of baffle	Front	Center	Rear
C	Hole area of baffle	100%	80%	60%
D	Width of baffle	70mm	90mm	110mm

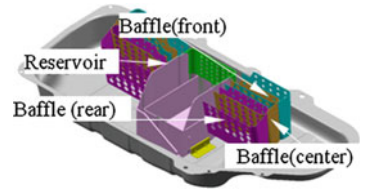


Fig. 9 Control factors and baffles

Table 3 shows the position of installation including the rig test condition and the sensor. Figure 7 shows the equipments and the location of sensor installed to the fuel tank during the rig test.

(2) Judgement criterion

Loudness (unit: sone) [6] among the psychoacoustic indexes is used for representing the acoustical characteristics of slashing noise, because this sound quality index corresponds the most with the subjective evaluation. Figure 8 shows the 3-D color map graph of loudness and the 2-D levels of loudness with respect to the time. The fluid flowing sound is defined as the sound pressure level of impact from the 1st, 2nd, 3rd, 4th peaks at 0 ~ 1 s and as the sound energy of flow from the 1st, 2nd, 3rd, 4th peaks at 1 ~ 2.25s. The criterion for defining the impact sound and the flowing sound was set based on the engineering experiences and analysis of rig/vehicle test expert, NVH engineer, and fuel tank designer.

(3) Design of experiment

We have optimized the information of design parameters by using the experimental design of

Taguchi robust engineering. The type of response has selected the Loudness(=y) by ‘Smaller-the Better type’ [7] Eq. (2) shows the formula for Signal-to-Noise ratio.

$$S/N = \eta_{dB} = 10 \log \frac{1}{MSD} = 10 \log \frac{1}{\frac{1}{n} \sum_{i=1}^n y_i^2} \tag{2}$$

Table 4 Conduct experiment and S/N ratio, mean

N O #	A	B	C	D	1/2, 3/4, 7/8, Full												S/N	Mean				
					0.2 G, 0.4 G, 0.6 G						Front, Rear											
					Test-1																	
					Test-2																	
					P1	P2	P3	P4	P1	P2	P3	P4	P1	P2	P3	P4	P1	P2	P3	P4		
1	1	1	1	1	13.2	13.2	11.7	10.7	14.9	14.0	12.5	11.0	13.7	13.2	12.5	12.3	15.0	12.8	10.8	10.0	-23.0	13.9
2	1	2	2	2	19.9	14.0	12.9	12.2	13.0	12.5	11.5	11.2	20.7	13.5	13.0	13.0	12.7	10.7	10.7	10.0	-23.5	14.5
3	1	3	3	3	19.0	11.5	10.8	9.0	15.0	13.9	13.5	13.2	18.8	9.0	8.0	8.0	14.9	13.5	13.0	12.5	-22.8	13.3
4	2	1	2	3	15.9	14.0	13.2	11.0	18.5	14.2	11.0	11.0	13.0	13.0	12.5	10.3	17.0	16.5	13.0	11.8	-23.4	14.4
5	2	2	3	1	16.8	12.7	12.0	12.0	12.8	11.9	11.9	11.9	16.0	15.0	13.0	12.0	15.0	14.8	12.0	11.0	-23.3	14.4
6	2	3	1	2	13.5	12.0	11.7	11.0	20.8	13.0	12.5	11.8	12.2	12.0	10.2	10.0	24.9	14.5	13.0	12.0	-23.7	14.6
7	3	1	3	2	16.3	11.5	10.2	10.0	10.5	10.2	10.0	9.9	17.0	15.8	12.0	10.2	11.0	10.5	10.2	10.1	-22.6	12.9
8	3	2	1	3	11.0	11.0	10.0	10.0	10.8	11.0	10.2	10.0	12.0	10.2	10.2	10.0	14.0	11.5	11.0	11.0	-21.3	11.5
9	3	3	2	1	13.0	11.0	8.2	8.0	13.5	11.3	10.8	10.0	13.8	11.3	11.0	10.3	15.0	11.8	10.5	10.0	-22.0	12.34

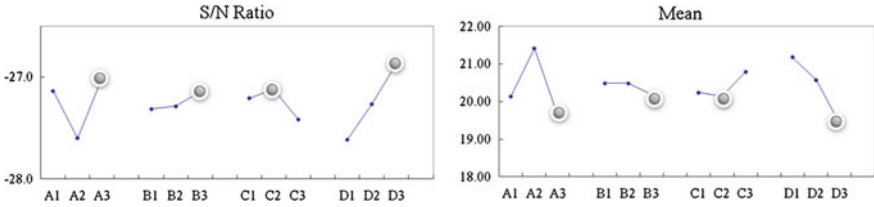


Fig. 10 Response graph

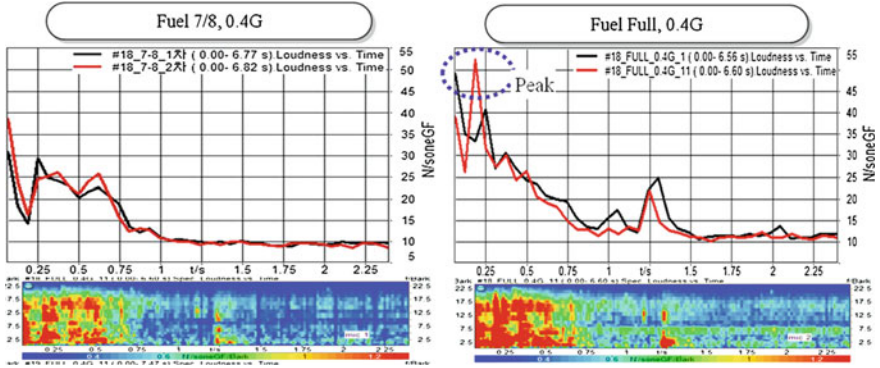


Fig. 11 Loudness graph of No. 7 in rig test

(4) Establishing control factors and levels

Through pressure and velocity of Bernoulli effect, 2 of the baffle hole sizes were selected and the set value of the control factors, levels including the location of baffle, distance are set as an engineering guide, enabling the other models to utilize Fig. 9.

(5) Develop noise strategy

Noise factors are the variables that affect system function, and are either uncontrollable or too expensive to control. For example, these are the system interface, environment conditions, usage and operating environment, aging, wear, and etc. The fuel amount (1/2, 3/4, 7/8, full), acceleration (0.2/0.4/0.6G), position of the sensor (Front/Back), number of testing times (twice), Impact sound/moving sound (peak 1 ~ 8) are selected for the noise factors of this test condition.

(6) Conducting experiment and calculating S/N ratio, Mean

Control factors of baffles were formulated for each combination of the orthogonal array of L9 (3⁴), Table 3 below displayed below shows collected loudness data after conducting the experiment. Also, S/N ratio and mean are calculated for each run of L9 orthogonal array. S/N ratio is a metric in decibels (dB) to variability. The

Table 5 Results of No7 in vehicle evaluation

Class	Fuel quantity				Overall
	1/2	3/4	7/8	Full	
Current design	7	7 ⁻	7 ⁻	7 ⁻	7 ⁻ ~ 7
No. 7	7	7	7	6 ⁺	6 ⁺ ~ 7

Table 6 Confirmation of optimum design

	Confirmation	
	S/N ratio	Mean
Current design	-26.9 dB	19.99
Optimum design	-26.1 dB	18.59
Gain	0.8 dB	1.4
%	3 % [↑]	7 % [↑]

larger the S/N, the smaller the variability of loudness. The smaller the mean, this mean is the smaller the noise Table 4.

(7) Response graphs for S/N ratio and Mean

Through the two response graph (Fig. 10), the effect of each control factor has on S/N and Mean can be observed. Performance optimization: maximize S/N to reduce functional variability, minimize Mean for reducing the sloshing noise. Selection of factors and level: A3, B3, C2, D3.

3.2 Verification of Loudness Index

To verify the validity of loudness index, sample No 7 is mounted on the vehicle rather than the other psychoacoustic indexes and simple sound pressure level. This sample shows good aspect in all ranges, except in “0.4 G” and “Full” condition due to large impact sound at this point. Figure 11 and Table 5 present the identical results between the rig test measured objective data and the vehicle test subjective evaluation showing the correlation of the evaluation result. These test results show the validity of the loudness index for sloshing noise. On the other hand, peak sound pressure level simultaneously measured with the microphone is used as the data base for sloshing noise guide line.

3.3 Verification of Performance

(1) Conduct confirmation run

Final optimum design has improved 3 % of noise variability and 7 % of mean noise loudness level compare to the current tank at the rig test. (See Table 6) Also the subjective evaluation of the tank with modified design shows the improvement

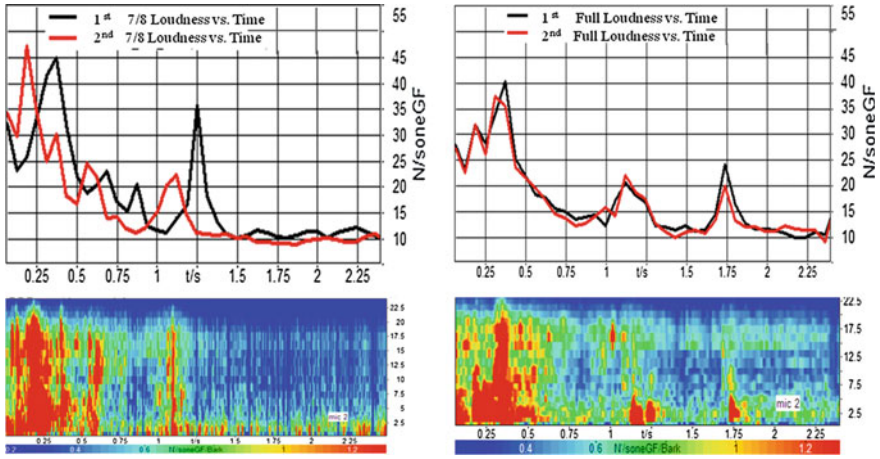


Fig. 12 Loudness graph of current design (left)

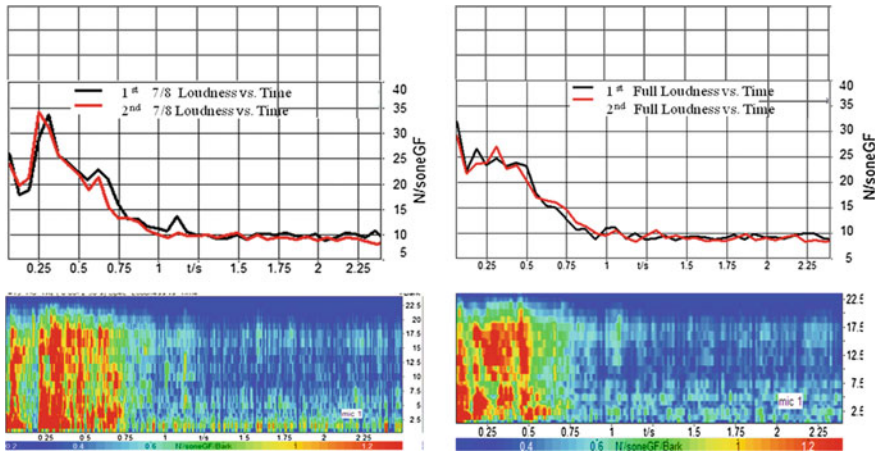


Fig. 13 Loudness graph of optimum design (right)

Fig. 14 Current design

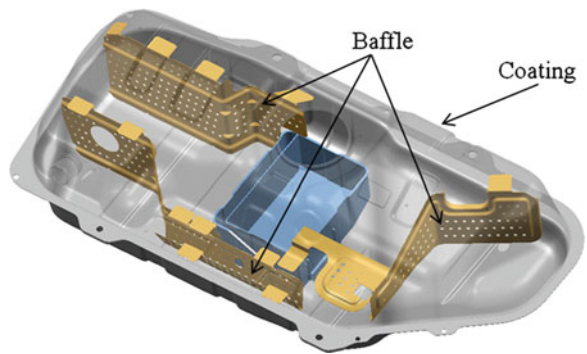
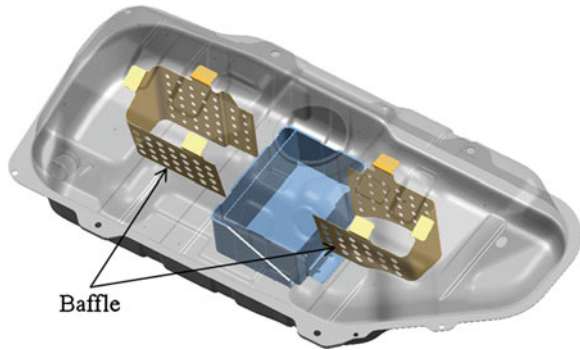


Fig. 15 Optimum design

as shown in Fig. 12, 13 present another test result of loudness at 0.4 G and '7/8, Full' condition in graph.

(2) Vehicles driving tests

Put 1/2, 3/4, 7/8, full amount of fuel to vehicle and evaluate under the specific mode (braking, turning, etc.). Subjective evaluations are conducted while the NVH experts are seated in the front and rear seat. And the judgment criterion could be passed when the evaluation rating score is above the certain score. This newly devised simple and smart baffle design reduces not only the disturbing fuel tank sloshing noise but also the overall cost of tank up to 30 % (deleted baffles and tank surface coating for noise) (Figs. 14, 15).

4 Conclusions

In this study, use of conceptual design process by utilizing Triz and Taguchi method has been suggested for the low noise baffle developing process. In addition to that, the sound quality index suitable for fuel tank sloshing noise rig test evaluation is applied based upon the reasonable test results. Using this innovative process, noise and cost reducing baffle was developed successfully and have reached the following conclusions.

- (1) Commonly applicable 10 concepts of reducing fuel sloshing noise were induced. One of the concepts is the new baffle device using Bernoulli theory and friction force. By the rig and vehicle test, the validity of this innovative design was proven by saving 30 % of the cost level, reducing 7 % and improving S/N ratio 3 % of the sloshing noise, compare to the current design for noise reduction.
- (2) Through the Taguchi optimization test, the interval length of 2 baffles, relative size of the holes, and the position of installation are found to be the main factors to reduce the concentration of pressure by the fuel inertia force.

- (3) In the rig test, loudness analysis among the psychoacoustic indexes was adapted. According to the time based analysis, the sloshing noise was divided into the impacting noise and the waving noise, and the 8 peak values are used for calculating S/N ratio and mean value.
- (4) The tank with optimized baffle shows the identical noise pattern both in vehicle subjective test and rig test measured data. Based upon this, validity of rig test was proven and sloshing noise guide line was set.
- (5) The validity of the sound quality index as loudness was proven at the rig test of fuel tank sloshing noise.

Based on this research, evident cost saving and acceptable noise reduction can be achieved more effectively and systemically, if the tank is developed in earlier stage of the development with the suggested process. Moreover, the conceptual design process using TRIZ and Taguchi method played an important role in proving its engineering validity by establishing the product developing process.

References

1. Kamei M, Hanai J, Fukasawa W, Makino T (2007) Establishment of a method for predicting and confirming fuel tank sloshing noise. SAE Technical Paper 2007-01-1538
2. Jong-Suh Park, Seung-Chan Choi, Seok-Gil Hong (2011) The prediction of fuel sloshing noise based on fluid-structure interaction analysis. SAE Technical Paper 2011-01-1695
3. Nam Pyo Suh (2001) Axiomatic design. Oxford university Press, New York
4. Philatov V, Zlotin B, Zusman A, Altshuller G (1999) Tools of classical TRIZ. Ideation Intl Inc, Detroit
5. Pugh S (1991) Total design. Addison-Wesley Publishing, New York
6. Fastl H, Zwicker E (2007) Psycho-acoustics: facts and models, 3rd edn. Springer, New York
7. Fowlkes WY, Creveling CM (1995) Engineering methods for robust product design. Addison-Wesley, Massachusetts